

TECHNISCHE MECHANIK

Editor:
Magdeburger Verein für Technische Mechanik e.V.
und Otto-von-Guericke-Universität Magdeburg



TECHNISCHE MECHANIK

Wissenschaftliche Zeitschrift für Grundlagen und Anwendungen der Technischen Mechanik
Scientific Journal for Fundamentals and Applications of Engineering Mechanics

The journal **Technische Mechanik** publishes refereed original articles on Engineering Mechanics in its broadest sense. It is intended to provide a forum for a rapid transfer of research results to industry and science. In that sense contributions are encouraged which demonstrate the practical application of new results and scientific findings.

In der **Technischen Mechanik** werden begutachtete Beiträge aus allen Gebieten der Mechanik publiziert. Ein Hauptanliegen besteht in der raschen Verfügbarmachung von Forschungsergebnissen für Industrie und Wissenschaft. In diesem Sinne werden vor allem auch solche Beiträge bevorzugt, die neben neuen Ergebnissen und Erkenntnissen auch deren praktische Anwendung beinhalten.

Editorial Board / Herausgeberkollegium:

Holm Altenbach (Magdeburg)
Albrecht Bertram (Magdeburg)
Daniel Balzani (Dresden)
Stefan Diebels (Saarbrücken)
Paweł Dłużewski (Warsaw)
Christoph Egbers (Cottbus)
Victor Eremeyev (Rzeszów)
Samuel Forest (Paris)
Michael I. Friswell (Bristol)
Ulrich Gabbert (Magdeburg)
Daniel Juhre (Magdeburg), editor-in-chief
Richard Markert (Darmstadt)
Reinaldo Rodriguez (Havanna)
Miroslav Šilhavý (Prague)
Paul Steinmann (Erlangen-Nuremberg)
Jens Strackeljan (Magdeburg)
Bob Svendsen (Aachen)
Dominique Thévenin (Magdeburg)
Kerstin Weinberg (Siegen)

Copyright

Submission of a manuscript implies that the work described has not been published before (except in the form of an abstract or as part of a published lecture, review, or thesis); that it is not under consideration for publication elsewhere; that its publication has been approved by all co-authors, if any, as well as by the responsible authorities at the institute where the work has been carried out; that, if and when the manuscript is accepted for publication, the authors agree to automatic transfer of the copyright to the publisher (society).

All articles published in this journal are protected by copyright, which covers the exclusive rights to reproduce and distribute the article (e.g. as offprints), as well as all translation rights. No material published in this journal may be reproduced photographically or stored on microfilm, in electronic data bases, video disks, etc., without prior written permission of the publisher.

Urheberrecht

Voraussetzung für die Einreichung eines Manuskriptes an die Redaktion der Zeitschrift ist, dass die Arbeit noch nicht publiziert oder an anderer Stelle zur Publikation eingereicht wurde. Ferner wird vorausgesetzt, dass die Publikation von allen beteiligten Autoren einer Arbeitsgruppe genehmigt ist und dass die Arbeit, wenn sie zur Publikation angenommen wurde, nicht an anderer Stelle in gleicher Form publiziert wird. Die Zeitschrift sowie alle in ihr enthaltenen einzelnen Beiträge und Abbildungen sind urheberrechtlich geschützt. Jede Verwertung, die nicht ausdrücklich vom Urheberrechtsgesetz zugelassen ist, bedarf der vorherigen schriftlichen Zustimmung der Redaktion. Das gilt insbesondere für Vervielfältigungen, Bearbeitungen, Übersetzungen, Mikroverfilmungen und die Einspeicherung und Verarbeitung in elektronischen Systemen.

Fotokopien für den persönlichen und sonstigen eigenen Gebrauch dürfen nur von einzelnen Beiträgen oder Teilen daraus als Einzelkopien hergestellt werden.

Redaktion/Editorial Office

W. Lenz (Chefredakteur)

Bezugsmöglichkeiten

A volume of the journal regularly consists of 2-4 issues per year. The subscription rate is € 60 / annum for the printed volume. Individual numbers are available at a price of € 20. Prices quoted include postage and VAT. Subscription enquiries and orders should be send to the Editorial Office address listed. All articles can be freely downloaded from the website.

Die Technische Mechanik erscheint in der Regel zwei- bis viermal im Jahr. Der Jahresbezugspreis im Abonnement beträgt € 60,00 für die gedruckte Ausgabe. Der Preis eines Einzelheftes beträgt € 20,00. Die angegebenen Preise beinhalten die Mehrwertsteuer und die Versandkosten. Die Bestellungen sind an die Redaktion zu richten. Alle Artikel können kostenfrei von unserer Webseite herunter geladen werden.

Anschrift der Redaktion/Editorial Office

Redaktion Technische Mechanik
Institut für Mechanik
Otto-von-Guericke-Universität
Postfach 4120
D-39016 Magdeburg
Telefon: +49 391 67-52 459
Telefax: +49 391 67-12 439-12 863
e-mail: Technische.Mechanik@ovgu.de
<http://www.ovgu.de/techmech/>

Herausgeber/Publisher

Magdeburger Verein für Technische Mechanik e.V.
und Otto-von-Guericke-Universität Magdeburg
Geschäftsführender Herausgeber: D. Juhre
Stellvertr. geschäftsführender Herausgeber: E. Woschke

Druck/Printer

Buch- und Offsetdruckerei Schlutius Magdeburg

Inhalt / Contents

Vorwort / Preface	107
B. Pfau, R. Markert: A two-lobe Journal Bearing with adjustable Gap Geometry for Vibration Reduction of flexible Rotors	109
S. Rother, M. Beitelschmidt: Strength Assessment of a Precession Driven Dynamo	120
A. Burov, E. Shalimova: Bifurcations of Relative Equilibria Sets of a Massive Point on Rough Rotating Surfaces	129
A. Marn, F. Schönleitner, M. Mayr, F. Heitmeir: Comparison of Numerical Forced Response Predictions with Experimental Results Obtained in a Subsonic Test Turbine Facility	139
L. Quurck, M. Richter, M. Schneider, D. Franz, S. Rinderknecht: Design and practical Realization of an innovative Flywheel Concept for industrial Applications	151
C. Zahalka, K. Ellermann: Determining a Function for the Damping Coefficient of a laminated Stack	161
N. Norrick, S. Neeb: Calculation of Torsional Vibrations and Prediction of Print Quality in Sheetfed Offset Printing Presses	171
S. Nitzschke, E. Woschke, C. Daniel: Dynamic Behaviour of EHD-contacts using a regularised, mass conserving Cavitation Algorithm	181
F. Schönleitner, T. Selic, M. Zenz, F. Heitmeir, A. Marn: On the Influence of a Five-Hole-Probe on the Vibration Characteristics of a Low Pressure Turbine Rotor while Performing Aerodynamic Measurements	196
T. Pumhössel, B. Hopfner, H. Ecker: Enhanced Utilization of structural Damping of rotating Machines using impulsively shaped torsional Moments	208
S. Haas, K. Ellermann: Development and Analysis of radial Force Waves in electrical rotating Machines	218
R. Hoffmann, C. Kayo, R. Liebich: Experimental Analysis of the nonlinear Vibrations of a rigid Rotor in Gas Foil Bearings	226
U. Werner: Influence of electromagnetic Field Damping on the Vibration Stability of soft mounted Induction Motors with Sleeve Bearings, based on a Multibody Model	239
G. Mikota: Modal Analysis of Rotors under Special Support Conditions	250
A. Hartung, H.-P. Hackenberg, U. Retze: More Flexible Damping Systems for Blades and Vanes	258
T. Szolc: On Dynamics and Stability of the Automotive Engine Turbocharger Rotor Supported by the Electrodynamic Passive Magnetic Bearings	268

T. Leister, C. Baum, W. Seemann:	On the Importance of Frictional Energy Dissipation in the Prevention of Undesirable Self-Excited Vibrations in Gas Foil Bearing Rotor Systems	280
S. von Osmanski, J. S. Larsen, I. F. Santos:	On the Incorporation of Friction Into a Simultaneously Coupled Time Domain Model of a Rigid Rotor Supported by Air Foil Bearings	291
Z. Racic, M. Racic:	Practical Approach for Solving Vibrations of Large Turbine and Generator Rotors - Reconciling the Discord between Theory and Practice	303
S. Willeke, L. Panning-von Scheidt, J. Wallaschek:	Reduced Order Modeling of Mistuned Bladed Disks under Rotation	314
M. Clappier, L. Gaul:	Rotordynamic Computation of a Permanent-Magnetic excited Synchronous Machine due to Electromagnetic Force Excitation	326
G. Żywica, P. Bagiński, J. Kiciński:	Selected operational Problems of high-speed Rotors supported by Gas Foil Bearings	339
T. P. Holopainen, A. Arkkio:	Simple Electromagnetic Motor Model for Torsional Analysis of Variable Speed Drives with an Induction Motor	347
C. Wagner, W. Tsunoda, O. Matsushita, T. Berninger, T. Thümmel , D. Rixen:	Prediction of Instability in Rotor-Seal Systems using Forward Whirl Magnetic Bearing Excitation	358
S. Neeb, N. Norrick:	Stability Analysis of parameter-excited linear Vibration Systems with Time Delay, using the Example of a Sheetfed Offset Printing Press	367
J. Zapoměl, P. Ferfecki:	Study of the Influence of a Delayed Yielding Phenomenon in Magnetorheological Damping Devices on the Vibration Attenuation of a Jeffcott Rotor	377
F. Boy, H. Hetzler:	The Effect of Field Damping on Rotordynamics of Non-salient Pole Generators	384
E. Shalimova, L. Klimina, K.-H. Lin:	On Behavior of a Double Rotor HAWT with a Differential Planet Gear ..	394
G. Nowald, R. Schmoll, B. Schweizer:	Transient Run-Up Simulations of Rotors in Journal Bearings Considering Mass-Conserving Cavitation Approaches	400
S. Bukovnik, G. Offner, A. Diemath, L. Smolik:	Turbocharger Dynamic Analysis: Advanced Design Simulation in Time Domain Using CFD Predicted Thermal Boundary Conditions	409
N. Mokhtari, M. Grzeszkowski, C. Guhmann:	Vibration Signal Analysis for the Lifetime-Prediction and Failure Detection of Future Turbofan Components	422
A. Boyaci, W. Seemann:	Vibro-acoustical Behavior of a Turbocharger Housing Excited by Oil-film Induced Rotor Oscillations	432
L. Spannan, C. Daniel, E. Woschke:	Run-up Simulation of Automatic Balanced Rotors Considering Velocity-dependent Drag Coefficients	442
A. Krinner, W. Tsunoda, C. Wagner, T. Berninger, T. Thummel, D. Rixen:	Simulation and Experimental Validation of a Misaligned Rotor in Journal Bearings using Different Levels of Detail	450

Preface

This volume contains selected papers presented at the 12th International Conference on vibrations in rotating machines, SIRM, which took place February 15-17, 2017 at the campus of the Graz University of Technology.

By all meaningful measures, SIRM was a great success, attracting about 120 participants (ranging from senior colleagues to graduate students) from 14 countries. Latest trends in theoretical research, development, design and machine maintenance have been discussed between machine manufacturers, machine operators and scientific representatives in the field of rotor dynamics.

SIRM 2017 included thematic sessions on the following topics: Rotordynamics, Stability, Friction, Monitoring, Electrical Machines, Torsional Vibrations, Blade Vibrations, Balancing, Parametric Excitation, and Bearings. The papers struck an admirable balance between theory, analysis, computation and experiment, thus contributing a richly diverse set of perspectives and methods to the audience of the conference.

All participants were invited to submit full-length papers to a special issue of *Technische Mechanik*. The contributed papers were peer-reviewed and appear in this volume.

Horst Ecker, Katrin Ellermann, Franz Heitmeir, Elmar Woschke
October 2017

A two-lobe Journal Bearing with adjustable Gap Geometry for Vibration Reduction of flexible Rotors

B. Pfau, R. Markert

Flexible rotors in journal bearings can exhibit large vibration amplitudes during the passage of bending critical speeds. To reduce these vibrations, a two-lobe journal bearing with adjustable gap geometry is presented. By an adjustment of the gap height, stiffness and damping properties of the bearing and as a consequence the damping ratio of the rotor system can be varied during the operation. When the system passes a critical speed in a run-up process, a large gap is adjusted for higher damping. After the resonance pass through, the gap height is reduced to increase the load carrying capacity and to enlarge the stability margin. Investigating the Jeffcott rotor in adjustable journal bearings demonstrates the basic effects. For a validation, a test rig is set up and a related mathematical model is created. Various experiments are made and compared with numerical results.

1 Introduction

Journal bearings exist in different geometric designs. At this, the classical cylindrical bearing has the simplest geometry with respect to calculation and manufacturing. A disadvantage is a high susceptibility to self-excited vibrations. Hence, multi-lobe bearings having better stability properties are used for applications with low Sommerfeld numbers¹, e.g. due to high rotational speeds. Depending on the designing with respect to resonance behavior, onset speed of instability and load carrying capacity, large vibrations amplitudes may occur passing bend-critical speeds. To reduce these vibrations, a journal bearing with adjustable gap geometry is presented.

In recent years, different types of active and controllable journal bearings were developed and are increasingly found in the literature. The current state of research on controllable oil film bearings can be found in an overview article from Santos (2011). Many of the existing concepts incorporate movable (Ulbrich and Althaus (1989); Althaus (1991); Wu and de Queiroz (2010)) or flexible bearing pads (Krodkiewski et al. (1997)). Other concepts apply external forces on the bearing shell or on the journal, for example magnetically (El-Shafei and Dimitri (2010); Fürst and Ulbrich (1988)) or piezo-mechanically (Przybylowicz (2004); Túma et al. (2013)), without changing the bearing's gap geometry. Furthermore there are also bearings that utilize an active oil injection as suggested from Santos and Scalabrin (2003) and Santos (2011). An unconventional bearing is shown by Martin and Parkins (2002), here the outer part is rotating and the inlying stator is able to vary the gap geometry by use of adjustable pins. In most of the cases, a PID controller is used.

The concept of a journal bearing with variable gap geometry for vibration reduction during the resonance pass trough was firstly presented in a previous project. The results are to find in papers of Chasalevris and Dohnal (2012, 2014, 2015). In this paper a new design is introduced, which differs significantly from the first version, since the adjustment mechanism is installed in the upper part of the bearing. This has the advantage, that the mechanism is not loaded by the self-weight of the rotor. Figure 1 shows the working principle of the adjustable bearing, which is basically a lemon bore bearing in horizontal construction design. The lower segment is fixed, the upper one can be moved along the vertical direction. The movement, which is in the shown investigations constant for certain values, leads to a change of the fluid film thickness h as well as to a change of the geometric shape. The related mathematical quantity is called preload factor δ , a measure for the geometric deviation of the lemon bore shape ($0 < \delta < 1$) in comparison to the cylindrical shape ($\delta = 0$). The basic idea of an adjustable lemon bore bearing was for the first time presented by Pfau et al. (2015) and somewhat later by Becker and Seemann (2015), whereby both publications deal with a time-periodic preload factor to increase the stability limit. This topic is also investigated by Breunung et al. (2017). A constructional realization of the bearing is shown in detail by Pfau and Markert (2016).

¹ $So = F_{stat} \psi^2 / (BD \eta_{oil} \Omega)$

Due to an adjustment of the gap geometry, stiffness and damping properties of the bearing are varied during the operation in dependence of the rotational speed. When the system passes a bend-critical speed in a run up process, a low preload factor (larger gap) is adjusted for higher damping. Since this setup is susceptible to stability problems and the load carrying capacity is comparatively low, the preload factor is increased after passing the resonance.

2 Description and Modeling of the Journal Bearing

At first, figure 1 is explained in detail. The journal rotates with an angular velocity Ω , the deflection is described by the eccentricity e and the angle ϑ (respectively w_L in z -direction and v_L in y -direction). The radius of the journal is given by R_Z . The segments of the sliding surfaces are all having the same radius of R_S . Thus, the gap function of the i -th ($i=1, 2$) segment is expressed by

$$h_i = (R_S - R_Z) - e \cos(\vartheta - \gamma) + h_{p,i} \cos(\vartheta - \psi_i). \quad (1)$$

At this, the latter term describes an offset between the centre of the i -th segment and the origin of ordinates (see also Pfau et al. (2015)). In the following, the term $(R_S - R_Z) = h_n$ is denoted as *nominal clearance*. It is appropriate to use it as reference quantity, due to the fact that it is constant and independent of the segment's movement. Since the lower segment is fixed ($h_{p,1} = 0$), the preload factor can be calculated to

$$\delta = h_{p,2}/(2h_n). \quad (2)$$

The calculation of the bearing forces is performed separated for the individual segments by numerical integration of the Reynolds differential equation of lubricating film theory, see e. g. Lang and Steinhilper (1978),

$$\frac{1}{R_S^2} \frac{\partial}{\partial \vartheta} \left(h^3 \frac{\partial p}{\partial \vartheta} \right) + \frac{\partial}{\partial x} \left(h^3 \frac{\partial p}{\partial x} \right) = 6 \eta_{oil} \left(\Omega \frac{\partial h}{\partial \vartheta} + 2 \frac{\partial h}{\partial t} \right), \quad (3)$$

which describes the pressure distribution $p(\vartheta, x)$ in dependence of the segment radius R_S , the gap function h , the angular velocity Ω and the oil viscosity η_{oil} . Integrating the pressure distribution yields the forces acting on the journal, F_z and F_y . The solution procedure is based on a finite volume method (see Pfau (2012) or Köhl (2015) for details). The bearing model is verified by experimentally determined data from Glienike (1966) and numerically determined data from Someya (1989).

The fluid-film forces depend on vertical and horizontal position (w_L and v_L) and the corresponding velocities of the journal, which is in general expressed by a nonlinear relationship, $F_{z,y} = F_{z,y}(w, v, \dot{w}, \dot{v}) = F_{z,y}(e, \vartheta, \dot{e}, \dot{\vartheta})$. If the journal performs small vibrations around an equilibrium position ($w_{L,0}|v_{L,0}$), the fluid film force can be linearized which yields

$$\begin{bmatrix} \Delta F_z \\ \Delta F_y \end{bmatrix} = \begin{bmatrix} b_{zz} & b_{zy} \\ b_{yz} & b_{yy} \end{bmatrix} \begin{bmatrix} \Delta \dot{w}_L \\ \Delta \dot{v}_L \end{bmatrix} + \begin{bmatrix} k_{zz} & k_{zy} \\ k_{yz} & k_{yy} \end{bmatrix} \begin{bmatrix} \Delta w_L \\ \Delta v_L \end{bmatrix}. \quad (4)$$

Equation (4) contains the stiffness coefficients k_{ij} as well as the damping coefficients b_{ij} . Both depend on the Sommerfeld number as well as on the preload factor. For simplicity, the letter Δ is neglected hereinafter.

3 Vibration Behavior of a Jeffcott Rotor supported by adjustable Journal Bearings

First of all, the vibration behavior of a Jeffcott rotor supported by adjustable journal bearings is investigated. This model represents a simplification of real-world rotors, but it is sufficient to show the elementary phenomena. The rotor consists of a flexible massless shaft (stiffness k) with a centered disc (mass m_S) and two journals (each mass m_Z) mounted at its ends. The mass of the disc is not balanced, which is described by an eccentricity ε . The phasing of ε is – without any loss of generality – set to zero. The journals are, in contrast to the disc, assumed to be perfectly balanced. The coordinates are given by w_W and v_W for the geometric center of the disc and w_L and v_L for the journals in the z - and y -direction. The equation of motion for a constant rotational velocity and linearized bearing forces is given by

$$\begin{bmatrix} m_S & m_S \\ m_S & 2m_Z \\ & 2m_Z \end{bmatrix} \begin{bmatrix} \ddot{w}_W \\ \ddot{v}_W \\ \ddot{w}_L \\ \ddot{v}_L \end{bmatrix} + \begin{bmatrix} & & & \\ & 2b_{zz} & 2b_{zy} \\ & 2b_{yz} & 2b_{yy} \end{bmatrix} \begin{bmatrix} \dot{w}_W \\ \dot{v}_W \\ \dot{w}_L \\ \dot{v}_L \end{bmatrix} + \begin{bmatrix} k & -k & -k \\ k & k+2k_{zz} & 2k_{zy} \\ -k & -k & 2k_{yz} \\ & & k+2k_{yy} \end{bmatrix} \begin{bmatrix} w_W \\ v_W \\ w_L \\ v_L \end{bmatrix} = m_S |\varepsilon| \Omega^2 \begin{bmatrix} \cos(\Omega t) \\ \sin(\Omega t) \end{bmatrix}. \quad (5)$$

A sketch of the system can be found in a contribution of [Dohnal et al. \(2015\)](#) or in any book on rotor dynamics. By means of the reference frequency ω_0 and the bend-critical speed in rigid bearings ω_k ,

$$\omega_0^2 = \frac{(m_S + 2m_Z)g}{h_n m_S} = \frac{2F_{stat}}{h_n m_S} \quad \text{and} \quad \omega_k^2 = \frac{k}{m_S},$$

equation (5) is converted into a dimensionless form. It turns out, that the behavior of the system is described by some few parameters. These are: the stiffness ratio κ , the Sommerfeld number So_0 , the mass ratio μ and the ratio of the bearings width and diameter B/D . The definitions are given by

$$\kappa = \frac{2F_{stat}}{h_n} \frac{1}{k} = \frac{\omega_0^2}{\omega_k^2}, \quad So_0 = So \frac{\Omega}{\omega_0} = \frac{F_{stat} \psi^2}{BD \eta_{oil} \omega_0} \quad \text{and} \quad \mu = \frac{2m_Z}{m_S}.$$

The parameter κ can be interpreted as a ratio between the bearing's and the shaft's stiffness. For $\kappa \rightarrow 0$ the system behaves like a rigid rotor in journal bearings. The Sommerfeld number So_0 is a dimensionless load parameter. It is calculated with the reference frequency ω_0 and thus constant for a specific rotor design. For the most cases, the Sommerfeld number is defined using the minimal clearance (see also [DIN \(1996\)](#)), $\psi_{min} = h_{min}/R_S$. Due to the fact that h_{min} is varying in dependence of the preload factor δ , the nominal gap is chosen to calculate the Sommerfeld number, $\psi = h_n/R_S$. The parameter μ describes the ratio between the two journal masses and the mass of the disc. The B/D ratio of the bearing is set to 0.5 in the shown investigations.

To begin with the systems behavior at constant rotational speeds Ω , figure 2 shows the vibration amplitude of the disc $G_S/|\varepsilon|$ (semi-major axis) and the onset speed of instability for different preload factors δ . It can be seen that in the vicinity of the bend-critical speed at $\eta_0 \approx 1.3$ the maximal amplitudes are getting larger, the higher the preload factor is. This arises due to different stiffness and damping properties, what results in a lower damping ratio.

Hence, for the passage trough the resonance a low preload factor is set. For higher rotational speeds, the preload factor is increased to have a larger stability reserve as well as a higher load carrying capacity. Even if figure 2 is only valid for constant rotational speeds, the tendency is also given for non-stationary processes like run-ups. An experimental investigation at constant speeds is quite difficult, due to the fact that the amplitudes of the journals are getting to large, what violates the assumption of an equilibrium position (see equation (4)) at a certain value.

The individual subjects of maximal resonance amplitude, onset speed of instability and load carrying capacity are discussed in the following subchapters.

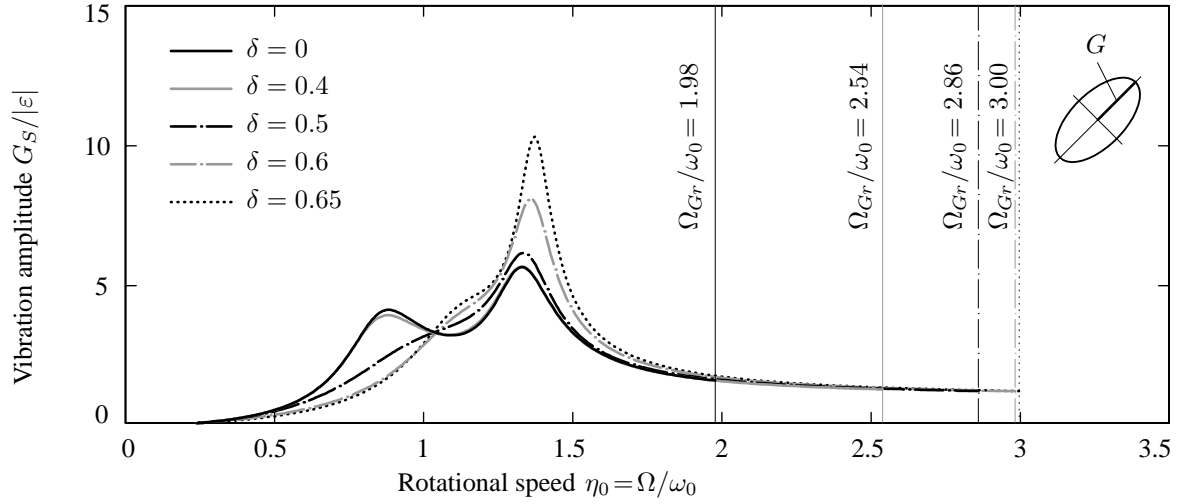


Figure 2. Vibration amplitude of the disc $G_S/|\varepsilon|$ and onset speed of instability for different preload factors δ (parameters: $So_0=1$, $\kappa=0.5$, $\mu=0$, $B/D=0.5$)

3.1 Reduction of the Amplitudes during Resonance pass trough

Figure 3 shows the maximum amplitudes of $G_S/|\varepsilon|$ in dependence of the specific Sommerfeld number So_0 for a constant value of $\kappa=1$. It can be seen, that especially for low Sommerfeld numbers the maximum amplitudes differ significantly. Concerning to the amplitude reduction, this is the application area of the adjustable journal bearing. For high Sommerfeld numbers the effect vanishes. This is because the journal center is located at low position on the locus (Gümbel curve) and the pressure build-up occurs mainly in the lower segment.

To evaluate the potential for vibration suppression, the maximum amplitudes are compared to a lemon bore bearing with a typical preload factor of $\delta=0.65$ (see also DIN (1996) or Glinicke (1966)). As a measure, the quantity

$$R = 1 - \frac{G_{max,\delta_i}}{G_{max,\delta=0.65}} \quad \text{with} \quad \delta_i = 0, 0.4, 0.5 \text{ and } 0.6 \quad (6)$$

is defined. Figure 4 shows R for different values of κ . As already mentioned, a vibration suppression can only be achieved for small specific Sommerfeld numbers. Beyond this, the parameter κ plays an important role. For small values of κ , the gradient of R with respect to So_0 is relatively weak in comparison to bigger values of κ , which results in a larger application area. If κ is getting larger, in other words the shaft stiffness decreases in comparison

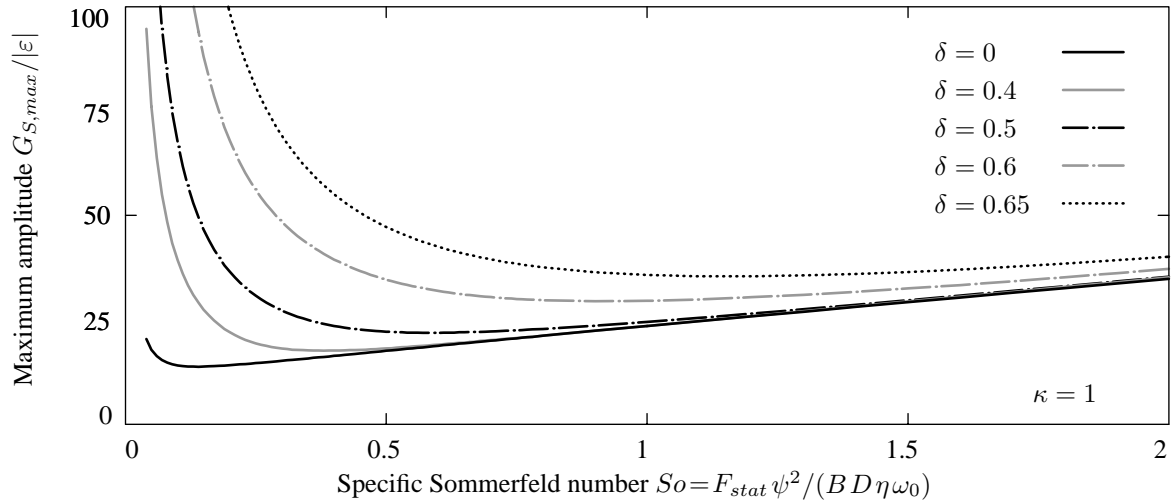


Figure 3. Maximum amplitudes $G_{S,max}/|\varepsilon|$ in dependence of the specific Sommerfeld number So_0 for different preload factors δ (parameters: $So_0=1$, $\kappa=1$, $\mu=0$, $B/D=0.5$)

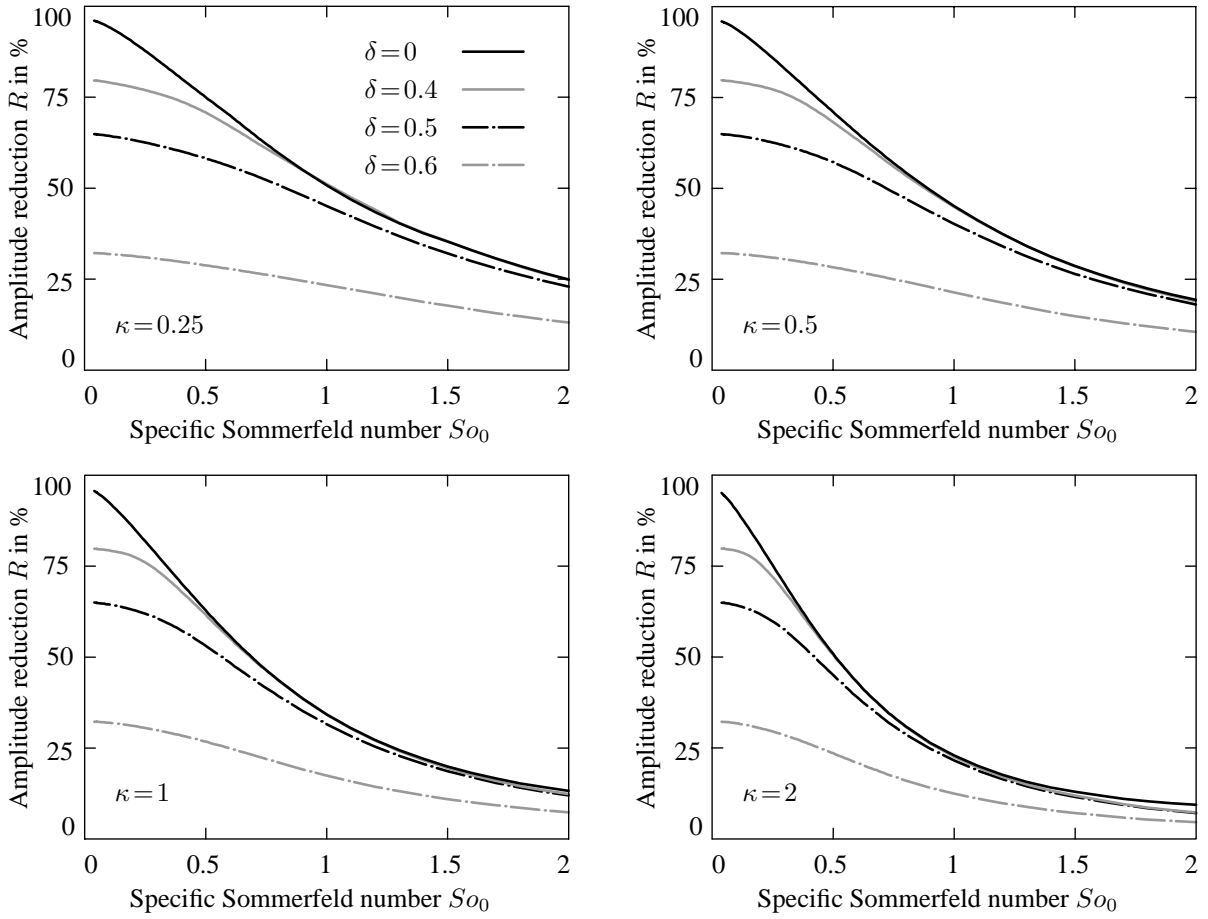


Figure 4. Comparison of the potential for vibration suppression R for different values of κ
(parameters: $\mu = 0$, $B/D = 0.5$)

to the bearing stiffness, the damping properties of the bearings can not entirely reach the disc, what narrows the effect. For $\kappa \rightarrow \infty$ the system behaves like a Jeffcott rotor in rigid bearings (concerning the resonance behavior), an influencing by the bearings is not possible.

3.2 Change of the Onset Speed of Instability

For a safe operation of a rotor system, the operational rotating speed should have a certain margin to the onset speed of instability. Above this speed, self-excited vibrations will occur, which lead to a damage or in the worst case to a destruction of a machine. Multi-lobe bearings are known for its good stability behavior in comparison to cylindrical bearings (comparison at $So_{min} = F_{stat} \psi_{min} / (B D \eta_{oil} \Omega) = \text{const.}$), see also the book of [Gasch et al. \(2001\)](#).

Figure 5 shows the onset speeds of instability for the same system parameters already used in figure 4. Generally, the onset speed of instability decreases with a decreasing shaft stiffness k . Furthermore it can be said, that the higher the specific Sommerfeld number is, the higher is the onset speed of instability (except for very small values of So_0). Comparing the graphs based on different preload factors, it turns out that for a decreasing shaft stiffness k (increasing κ) the individual onset speeds of instability are getting closer to each other. This is especially the case for low specific Sommerfeld numbers. For example for $\kappa = 2$, here the difference nearly vanishes, the onset speed of instability depends mainly on ω_k .

As a conclusion, the application area for an adjustable journal bearing concerning the onset speed of instability is given for tendentially high specific Sommerfeld numbers and small values of κ .

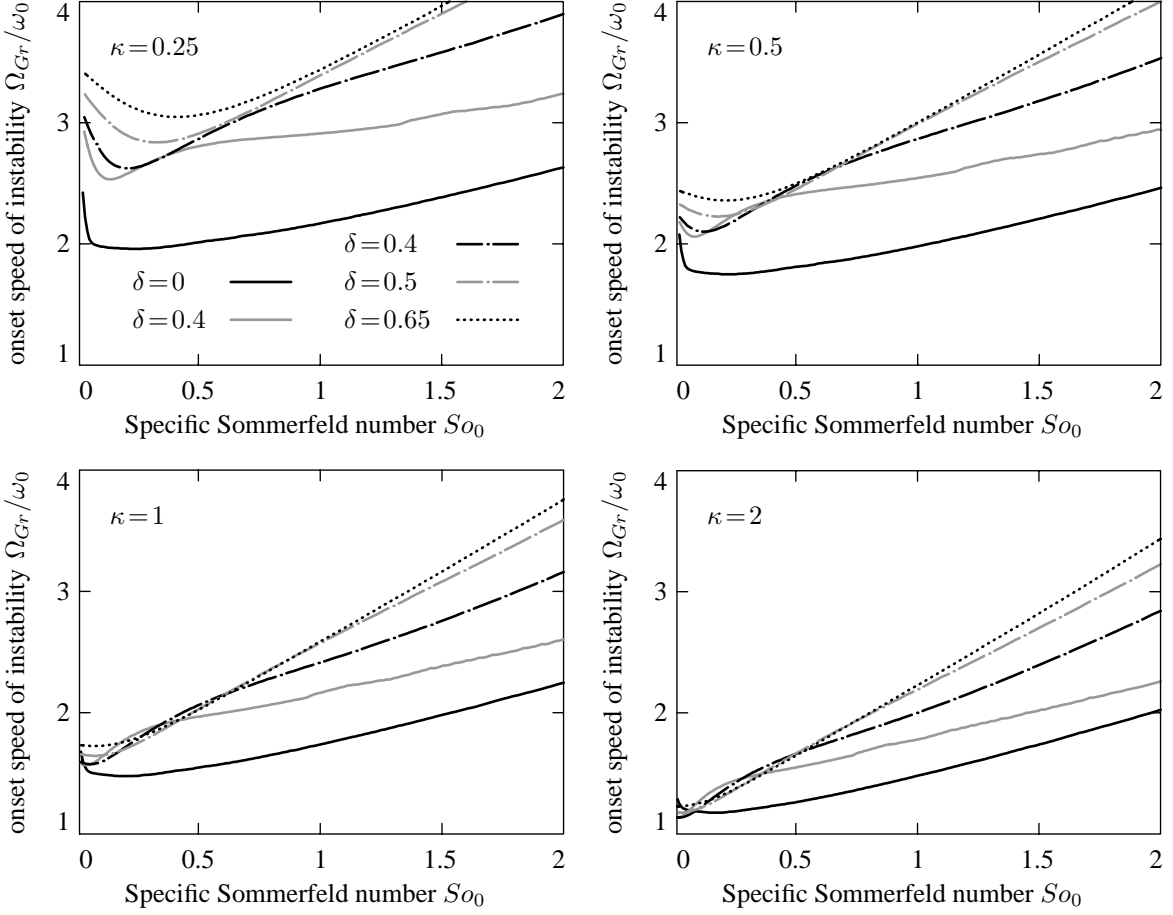


Figure 5. Comparison of the onset speeds of instability Ω_{Gr}/ω_0 for different values of κ
(parameters: $\mu=0$, $B/D=0.5$)

3.3 Load carrying Capacity

A further subject is the load carrying capacity of the bearing. For this, the residual gap related to the minimal gap,

$$\frac{h_{res}}{h_{min}} = \frac{h_{res}}{h_n} \frac{1}{1-\delta}, \quad (7)$$

can be used as a measure, see also the book from [Lang and Steinhilper \(1978\)](#).

The higher the residual gap h_{res}/h_{min} , the higher is the load carrying capacity. A comparison of different bearing types (comparison at $So_{min} = F_{stat} \psi_{min} / (BD \eta_{oil} \Omega) = \text{const.}$) yields, that the cylindrical bearing has the highest load carrying capacity (see also [Lang and Steinhilper \(1978\)](#)). In the presented bearing design, the geometric shape and the minimal gap is changed due to the adjustment, at what the latter one has a higher influence.

Figure 6 shows the load carrying capacity for different preload factors. Mind that the curves are plotted against the Sommerfeld number So , due to the fact, that the load carrying capacity is a pure bearing property. For $\delta=0$, or in other words for the largest gap, the load carrying capacity is relatively low. Increasing the preload factor, respectively decrease the minimal gap, leads to a significant higher pressure build-up in the bearing and thus to a higher load carrying capacity. This effect is for lower Sommerfeld numbers more distinct. Note, that the load carrying capacity has to be reduced during the resonance pass trough.

It is to mention, that the non-referenced residual gap h_{min} is decreasing with an increasing preload factor δ for $So < 1$, for $So > 1$ it is nearly independent from δ .

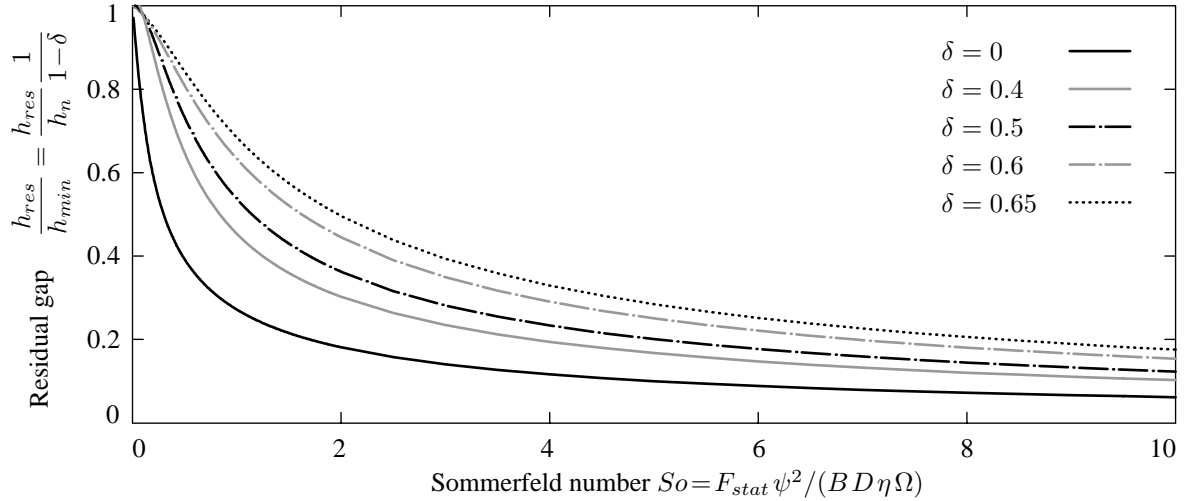


Figure 6. Residual lubrication gap in dependence of the Sommerfeld number for different preload factors

3.4 Conclusion

The investigation of a simple flexible rotor in adjustable journal bearings showed the fundamental effects concerning amplitude reduction, onset speeds of instability and load carrying capacity. If an application is useful in a real machine, these (and surely more) subjects have to be investigated for a specific machine design. As a simple rule it can be said, that the stiffness of the bearing and the shaft should be of the same order, respectively $\kappa = \mathcal{O}(1)$.

4 Experimental Setup and Validation

To validate the effect of amplitude reduction during the resonance pass trough, a test rig is set up, see figure 7. An AC-servomotor is used as drive, it is connected with a double cardan joint to the shaft. The shaft is supported by two ball bearings at the driving end, which function as simple suspension, and the adjustable journal bearing at the opposite side. The position of the upper bearing segment is adjusted by a high voltage piezo stack actuator with a maximum stroke of $200 \mu\text{m}$. By means of an active magnetic bearing, additional stiffness and damping properties can be generated. In this manner, a change of the shaft stiffness and the influence of other damping sources can be investigated. Furthermore, the test rig contains two discs including retainer bearings.

Disc 1 is located between the magnetic bearing and the journal bearing, disc 2 is overhanging at the end of the test rig. Their deflections are measured using eddy current sensors. Due to its overhanging position, disc 2 shows the largest deflections, therefore it is mainly used for the analysis of the measurements.

The systems behavior is described by a MDOF model, see figure 8, using a modular system based on a finite element formulation. The shaft is modeled as Euler–Bernoulli beam, each individual element has a constant bending stiffness EI_j and a column mass density ρA_j . The journals of the magnetic bearing and the journal bearing are approximated as point masses, for the discs the moments of inertia are additionally considered. The forces from magnetic and journal bearing are indicated as F_{AMB} and F_L .

To update the model, a hammer testing of the running rotor (at $\delta = 0$) was performed. In a first step, masses and E -moduli were optimized to fit the first two bend-critical frequencies. After this, the damping was optimized using Rayleigh damping (stiffness term only), $\mathbf{B} = \beta \mathbf{K}$. The first bend-critical speed is about 1020 min^{-1} .

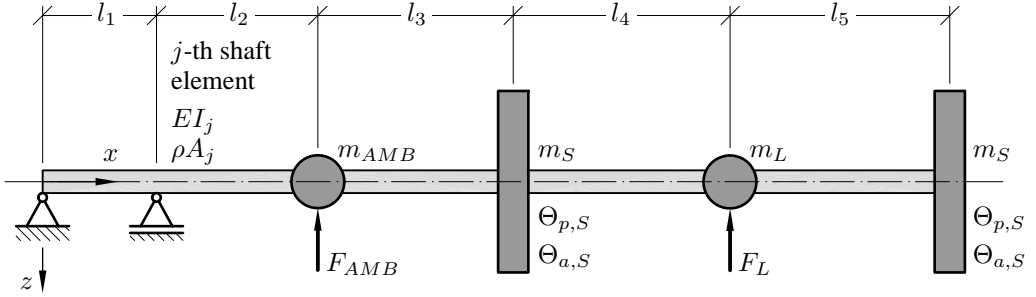


Figure 8. Mechanical model of the test rig

4.1 Run-up Processes

Figure 9 shows the measured and simulated results of two exemplary run-up processes. Here, the deflection of disc 2

$$|r_{S,2}| = \sqrt{w_{S,2}^2 + v_{S,2}^2}, \quad (8)$$

whose steady component is eliminated, is plotted against the time. The bearing forces were calculated with a non-linear force model (equation 3). Both, experiment and simulation exhibit that the maximum amplitude is increasing with the preload factor δ , as predicted in subchapter 3.1. The amplitude reduction for this example is about 24.2 %. The agreement between experiment and simulation is satisfying.

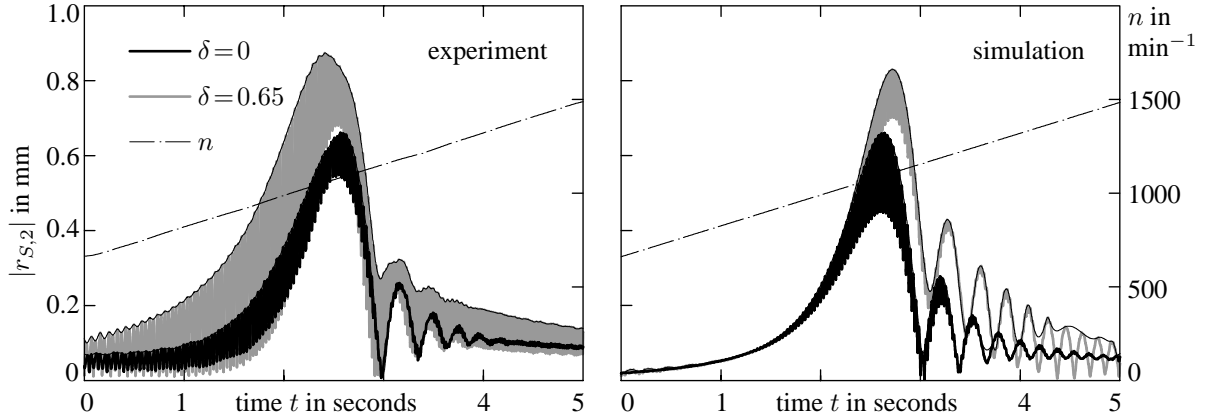


Figure 9. Exemplary run-up processes with different preload factors δ ; experiment (left) and simulation (right)

Run-up processes were carried out for different preload factors δ . Figure 10 shows the resulting maximum amplitudes in a bar graph. For low preload factors $\delta = 0 \dots 0.4$, the maximum amplitude is de facto the same. This is also predicted by the model (see also figure 2). A further increase of δ leads to higher maximum amplitudes. The reduction between $\delta = 0.7$ and $\delta = 0$ amounts to 25.2 % and between $\delta = 0.7$ and $\delta = 0.3$ it is about 23.5 %. Hence, the adjustment must not be accomplished over the full range of δ . For an application, the travel range of an actuator can be chosen smaller. Furthermore, the decrease of the load carrying capacity is not that large during the adjustment. The agreement between experimental and simulated results is satisfactory. The maximum deviation (at $\delta = 0.7$) is about 5 %. A good result, considering that the model has been optimized for the value of $\delta = 0$. An optimization of the bearing model itself was not performed.

After the passage of the bending critical speed, the preload factor δ is set to larger value. A change of the stiffness and damping properties during the operation leads to natural vibrations. These vibrations decay quickly, due to the fact, that the damping ratios even after the resonance are relatively high. In general, the lower the change rate of the preload factor δ , the lower the arising natural vibrations.

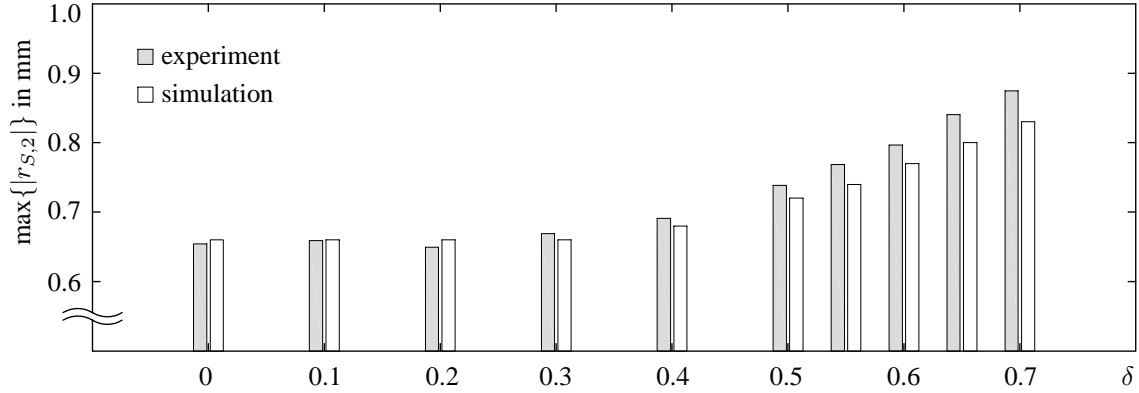


Figure 10. Comparison between measured and simulated resonance amplitudes for different preload factors δ

4.1.1 Additional stiffness and damping due to an active magnet bearing

To investigate the influence of a modified stiffness relation between shaft and bearing and to examine the influence of other damping sources in the system, experiments using the magnetic bearing were performed. The force of a magnetic bearing, here exemplary for the z -direction, operating with a PD controller is calculated and linearized to

$$F_{AMB} = (k_i P - k_s) w_1 + k_i D \dot{w}_1 = k_{AMB} w_1 + b_{AMB} \dot{w}_1. \quad (9)$$

At this, the parameters k_i and k_s are physical constants, P and D describe proportional and derivative gains. An operation with a pure P or D controller is not possible due to technical reasons, so both quantities have at all times values greater than zero.

For an adjustment of the stiffness relation, the proportional gain P is varied. The bend-critical frequency increases about 2.5 Hz, this corresponds to a decrease of κ . According to the theory, see figure 4, the amplitude reduction increases. Table 1 lists the result. A difference is detectable, but it is relatively weak. The standard deviation, calculated on a base of four measurements for each experiment, is one order smaller. However, the difference in amplitude reduction between minimal and maximal P -gain mounts to 3.8 percentage points.

Table 1. Maximum amplitudes $\max\{|r_{S,2}|\}$ in dependence of different proportional gains P ($D = 0.01$ As/mm)

proportional gain	$\delta = 0$	$\delta = 0.65$	Reduction
$P = 10$ A/mm	0.790 mm	1.045 mm	24.3%
$P = 15$ A/mm	0.762 mm	1.041 mm	26.8%
$P = 20$ A/mm	0.743 mm	1.034 mm	28.1%

In a real-world rotor, there are several sources of damping, for example due to a surrounding fluid, material damping or other bearings. To capture this influence, experiments with different derivative gains D have been carried out. The results are listed in table 2. At these experiments, the difference between minimal and maximal D gain is about 7 percentage points. Hence, additional damping can decrease the effect of amplitude reduction. For an eventual designing of a rotor system with an adjustable journal bearing, potential damping sources should be considered.

Table 2. Maximum amplitudes $\max\{|r_{S,2}|\}$ in dependence of different derivative gains D ($P = 10$ A/mm)

derivative gain	$\delta = 0$	$\delta = 0.65$	Reduction
$D = 0.01$ As/mm	0.795 mm	1.078 mm	26.3%
$D = 0.03$ As/mm	0.622 mm	0.788 mm	21.1%
$D = 0.05$ As/mm	0.551 mm	0.682 mm	19.3%

4.2 Measured and calculated Onset Speeds of Instability

Besides the run-up simulations, also the onset speeds of instability were measured. For this purpose the rotational speed is raised in small steps. If the rotor starts to carry out vibrations with the bend-critical frequency, what is good to observe in a real-time FFT, the onset speed of instability is found and the rotational speed has to be lowered immediately to avoid damage. This procedure is repeated for several values of the preload factor δ .

Figure 11 shows the experimental and numerical results. The present behavior – a decrease of the onset speed of instability for high preload factors – is not observed in this extent investigating the Jeffcott rotor. The reasons for this are effects, which are not shown by the investigated Jeffcott rotor, this is for example a shift of the onset speed of instability caused by gyroscopic effects due to the overhung disc. An important point is, that experiment and simulation show a similar global behavior. However, the differences between measured and simulated results are with values up to 15% satisfying only to a limited extent. Even comparing theoretical results based on different bearing data results in a relatively high scattering.

The determination of onset speeds of instability is especially for non-circular bearings difficult, due to the fact that a small change in the Sommerfeld number (e. g. by a change of the oil temperature) can lead to a significant change of the results (see also [Gasch et al. \(2001\)](#)).

5 Conclusions

In this paper, an adjustable journal bearing for the vibration reduction of flexible rotors is presented. An investigation of the Jeffcott rotor supported by such bearings shows the basic effects. It turns out, that a designing has to be made among others with respect to the reduction of the maximum amplitude during the resonance pass trough, the onset speed of instability and the load carrying capacity. For a validation, a test rig is set up. The experimental results show, that the effect of amplitude reduction arises. Numerical results using a simple mechanical model agree with the experiments. Furthermore, the influence of additional stiffness and damping properties is investigated, which influence the maximum amplitude more or less. Finally, measured and calculated onset speeds of instability were compared.

References

Althaus, J.: *Eine aktive hydraulische Lagerung für Rotorsysteme*. Fortschritt-Berichte VDI Reihe 11 Nr. 154, VDI-Verlag, Technische Universität München (1991).

Becker, K.; Seemann, W.: A journal bearing with actively modified geometry for extending the parameter-based stability range of rotor dynamic systems. In: *Euromech Colloquium 573 - Coupling and Nonlinear interactions in Rotating Machinery* (2015).

Breunung, T.; Dohnal, F.; Pfau, B.: An approach to account for multiple interfering parametric resonances and anti-resonances applied to examples from rotor dynamics. In: *Proceedings of the 12th International Conference on Vibrations in Rotating Machines (SIRM)*, Graz, Austria (February 2017).

Chasalevris, A.; Dohnal, F.: A journal bearing with variable geometry for the reduction of the maximum amplitude during passage through resonance. *Journal of Vibration and Acoustics*, 134, (2012), 061005–1–061005–8.

Chasalevris, A.; Dohnal, F.: Vibration quenching in a large scale rotor-bearing system using journal bearings with variable geometry. *Journal of Sound and Vibration*, 333, (2014), 2087–2099.

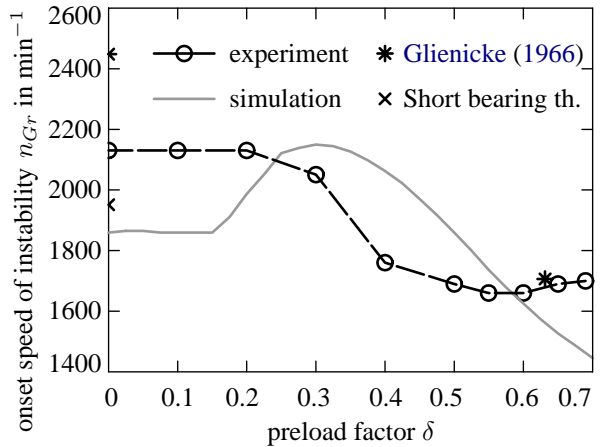


Figure 11. Measured and calculated (based on bearing data from different sources) onset speeds of instability

Chasalevris, A.; Dohnal, F.: A journal bearing with variable geometry for the suppression of vibrations in rotating shafts: Simulation, design, construction and experiment. *Mechanical Systems and Signal Processing*, 52-53, (2015), 506–528.

DIN: DIN-Norm 31657-1 Hydrodynamische Radial-Gleitlager im stationären Betrieb, Teil 1: Berechnung von Mehrflächen- und Kippsegmentlagern (1996).

Dohnal, F.; Pfau, B.; Chasalevris, A.: Analytical predictions of a flexible rotor in journal bearings with adjustable geometry to suppress bearing induced instabilities. In: *Proceedings of the 13th International Conference on Dynamical Systems - Theory and Applications*, Łódź, Poland (December 2015).

El-Shafei, A.; Dimitri, A. S.: Controlling journal bearing instability using active magnetic bearings. *Journal of Engineering for Gas Turbines and Power*, 132(1), (2010), 012502–012502–9.

Fürst, S.; Ulbrich, H.: An active support system for rotors with oil-film bearings. In: *Proceedings of the 4th International Conference on Vibrations in Rotating Machinery of the Institution of Mechanical Engineers*, pages 61–68, Edinburgh, UK (1988).

Gasch, R.; Nordmann, R.; Pfützner, H.: *Rotordynamik*. Springer-Verlag (2001).

Glienicker, J.: *Feder- und Dämpfungskonstanten von Gleitlagern für Turbomaschinen und deren Einfluß auf das Schwingungsverhalten eines einfachen Rotors*. Ph.D. thesis, Technische Hochschule Karlsruhe (1966).

Köhl, W.: *Stabilisierung von leichten Rotoren in Schwimmbuchsenlagern durch statisch unbestimmte Lagerung*. Ph.D. thesis, Technische Universität Darmstadt (2015).

Krodkiewski, J. M.; Cen, Y.; Sun, L.: Improvement of stability of rotor system by introducing a hydraulic damper into an active journal bearing. *International Journal of Rotating Machinery*, 3, 1, (1997), 45–52.

Lang, O.; Steinhilper, W.: *Gleitlager – Berechnung und Konstruktion von Gleitlagern mit konstanter und zeitlich veränderlicher Belastung (Konstruktionsbücher Band 31)*. Springer-Verlag (1978).

Martin, J. K.; Parkins, D. W.: Theoretical studies of a continuously adjustable hydrodynamic fluid film bearing. *Journal of Tribology*, 124, (2002), 203–211.

Pfau, B.: *Numerische Untersuchung eines Rotors in Schwimmbuchsenlagern*. Masterthesis, Technische Universität Darmstadt (2012).

Pfau, B.; Markert, R.: Konstruktion und Erprobung eines Zweiflächengleitlagers mit verstellbarer Spaltgeometrie zur Reduzierung der Schwingungen von flexiblen Rotoren. In: *Second IFTOMM D-A-CH Conference 2016*, Innsbruck, Austria (February 2016).

Pfau, B.; Rieken, M.; Markert, R.: Numerische Untersuchungen eines verstellbaren Gleitlagers zur Unterdrückung von Instabilitäten mittels Parameter-Antiresonanzen. In: *First IFTOMM D-A-CH Conference*, Dortmund, Germany (March 2015).

Przybylowicz, P.: Active stabilisation of a rigid rotor by a piezoelectrically controlled mobile journal bearing system. *Australian Journal of Mechanical Engineering*, 1(2), (2004), 123–128.

Santos, I. F.: On the future of controllable fluid film bearings. *Mécanique & Industries*, 12, (2011), 275–281.

Santos, I. F.; Scalabrin, A.: Control system design for active lubrication with theoretical and experimental examples. *Journal of Engineering for Gas Turbines and Power*, 125, (2003), 75–80.

Someya, T.: *Journal-Bearing Databook*. Springer-Verlag (1989).

Túma, J.; Šimek, J.; Škuta, J.; Los, J.: Active vibrations control of journal bearings with the use of piezoactuators. *Mechanical Systems and Signal Processing*, 36, (2013), 618–629.

Ulbrich, H.; Althaus, J.: Actuator design for rotor control. In: *12th Biennial ASME Conference on Vibration and Noise*, pages 17–22, Montreal, Quebec, Canada (September 1989).

Wu, A.; de Queiroz, M.: A new active tilting-pad bearing: Nonlinear modeling and feedback control. *Tribology Transactions*, 53, 5, (2010), 755–763.

Strength Assessment of a Precession Driven Dynamo

S. Rother, M. Beitelschmidt

A pressure vessel, which shall be filled with eight tons of liquid sodium, has to be designed for a large-scale experimental setup to investigate flow-induced magnetic fields. In addition to the centrifugal forces and gyroscopic loads induced by the rotation about two non-parallel axes, the complex internal pressure distribution, the imbalance of the container, as well as the thermal loads resulting from the elevated temperatures, which are required for the experiments, must be taken into account. This leads to several millions of load cases. That is why a calculation procedure is developed using the finite element method, which strongly reduces the computational complexity by utilizing sector symmetry, load case decomposition and superposition. Here, the focus is to determine the most critical load cases, which will be used for the strength assessment, regarding both the static and the fatigue strength. Besides the structural strength, the welded joints and the bolted joints are analyzed. Therefore, nonlinear effects are considered, for example the contact status of the bolted joints. The submodelling technique is used to investigate structural details.

1 Introduction

Within the framework of the project DRESDYN (DREsden Sodium facility for DYNamo and thermohydraulic studies) at the Helmholtz-Zentrum Dresden-Rossendorf (HZDR) experimental investigations of flow-induced magnetic fields will be performed (Stefani et al., 2012). This is comparable to the processes in the outer earth's core, in which iron and nickel are present in liquid form. In conjunction with an existing magnetic field, the flows of the liquid metal induce an electric current, which in turn produces a magnetic field. If the flows show a sufficiently helical shape, the original field is amplified and a stable magnetic field develops, called the homogeneous dynamo effect. The aim of the experiment is to investigate whether rotation and precession of astronomical objects serve as source for the described self-excitation of magnetic fields. The rotation and precession corresponds to the rotation of the earth about its axis within 24 h and the rotation of the earth's axis around the normal of the ecliptic plane with a cycle of 25,700 years.

According to Stefani et al. (2008) the formation of the described flow phenomena requires a critical magnetic Reynolds number $R_m = \mu_0 \sigma v L$, where μ_0 describes the magnetic field constant, σ the electrical conductivity, v the flow velocity, and L a characteristic length. Since the dimensions that can be realized in the test facility are limited, high rotational speeds are necessary. Sodium is chosen as liquid metal, which on the one hand is characterized by a low density, a low melting temperature and a high electrical conductivity, but on the other hand ignites when exposed to air humidity and thus requires strict safety precautions. To avoid corrosion, all components being in contact with sodium will be made of austenitic steel 1.4571.

The test facility designed by SBS Bühnentechnik GmbH is shown in Figure 1. A cylindrical pressure vessel with an inner diameter and a length of two meters, which has conical ends and can be filled with about eight tons of liquid sodium, is located in its center. The vessel shall rotate with a maximum frequency of 10 Hz and is positioned on a platform, which itself can rotate with up to 1 Hz about the vertical axis. The angle between the two rotation axes can be varied between 45° and 90° by a swivel frame.

The required flows should develop inside the cylindrical volume in the center of the pressure vessel (Figure 2). Rectangular wings can be extended into the flow to guide the fluid and thus reduce the turbulence. 40 sensor flanges in total are distributed on the cylinder wall allowing access for the measurement equipment. Because of the two rotations, no equalization of the volume expansion to the outside is possible. Therefore, the thermal expansion due to the warming of the sodium must be internally compensated. For this purpose, two argon-filled compensators in the cones prevent a critical rise of pressure. The conical shape is necessary to empty the container completely at a swivel angle of 42°.

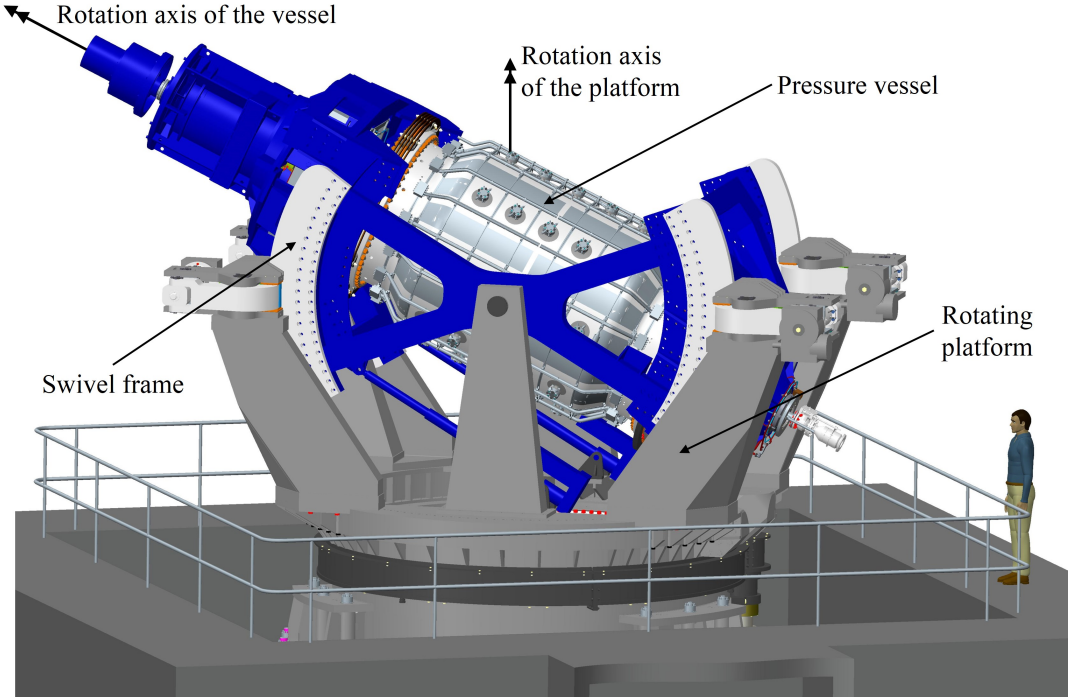


Figure 1: Setup of the test facility (provided by SBS Bühnentechnik GmbH).

As a result of the high rotational speeds and the hazard potential of the sodium, failure during operation must be reliably excluded. That is why the strength assessment of the vessel is performed in accordance with the FKM Guideline (FKM, 2012), using the finite element method (FEM) to determine the stresses. The FKM Guideline is also used to assess the welded joints, while the bolted joints are evaluated according to VDI 2230 Part 1 (2014). For the following experimental validation of the numerically calculated pressure distributions water is used instead of sodium.

2 Loads

Determining the stresses requires the consideration of all loads present at the structure, which are shown in Figure 3. The mechanical loads result from the rotation about two non-parallel axes, leading to a gyroscopic moment of almost $8 \cdot 10^6$ Nm. The rotation about the longitudinal axis of the container is described by the angular velocity ω_1 in the model, while the platform rotation is expressed by the angular velocity of the global reference system ω_2 . The ratio of the angular velocities describes the precession ratio

$$\eta = \frac{\omega_2}{\omega_1}. \quad (1)$$

In addition, the radial and the axial imbalance have to be taken into account. Since the latter directly results from the asymmetric structure, especially at the bearings, it is explicitly included in the finite element model and thus does not require a separate consideration. In contrast, the radial imbalance due to manufacturing-related inaccuracies cannot be completely compensated during balancing. The defined balancing quality limits its maximum value, but its direction is unknown. As a consequence, the most unfavorable load combination has to be used for the strength assessment. The weight force is also considered, although it is of minor importance because of its small magnitude.

Much higher loads result from the fluid-structure interaction, whereby the pressure distribution strongly depends on the precession ratio (Figure 4). In case of no precession ($\eta = 0$), the pressure distribution is equal to that of a solid-body rotation. Hence, the pressure p increases with the radius r corresponding to $p \sim r^2$ and reaches a maximum of 20.7 bar. With rising precession ratio, the gyroscopic moment acting on the fluid leads to a pressure difference in the circumferential direction. Since the pressure distribution is constant in the coordinate system of the platform and does not rotate with the container, a cyclic load is caused. At high precession ratios ($\eta \rightarrow 0.1$), the former laminar flow turns into a turbulent flow, which accompanies with a significant decrease of the pressure

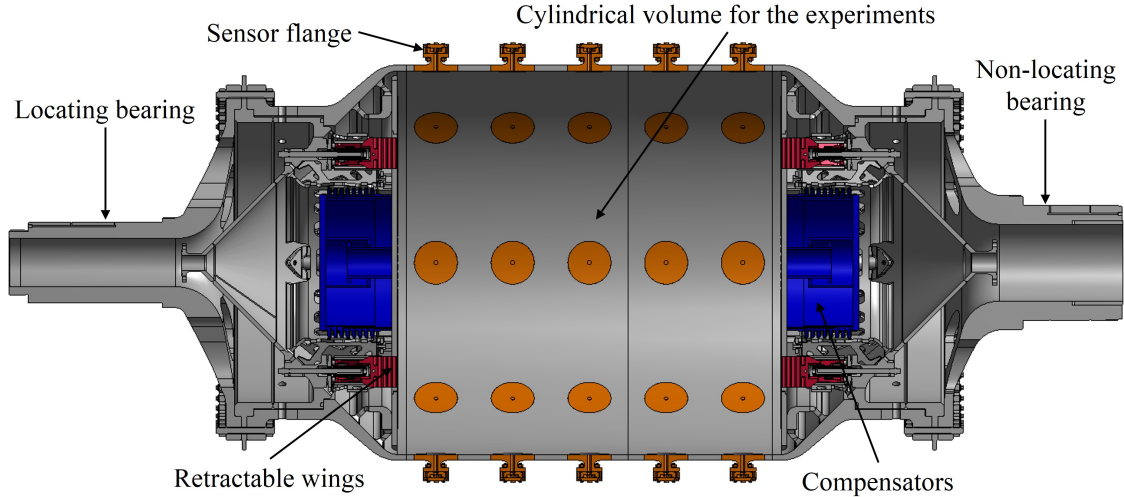


Figure 2: Sectional view of the pressure vessel.

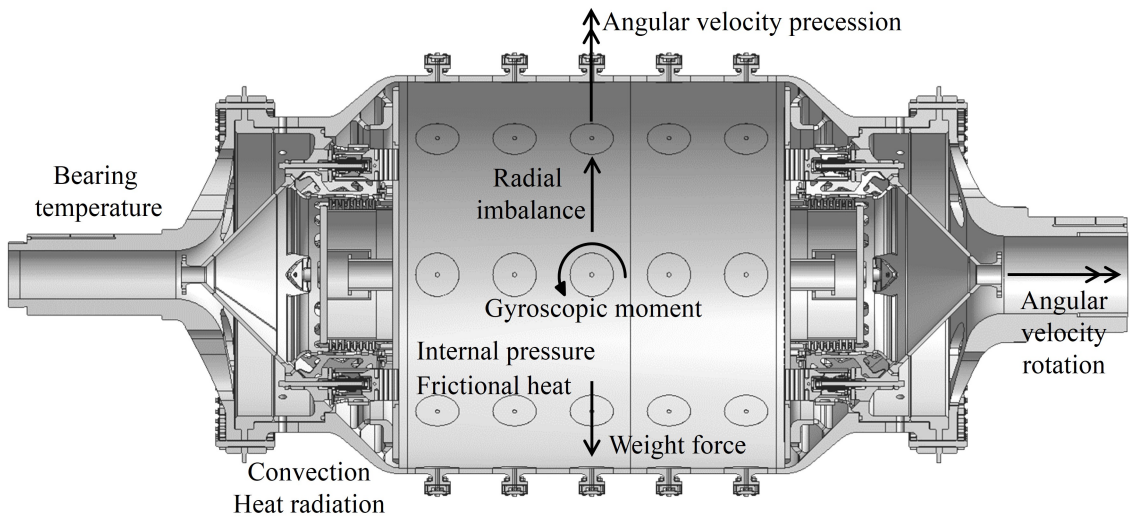


Figure 3: Overview of the loads present at the vessel for a swivel angle of 90°.

maximum. Because of the strong guidance of the fluid in the conical volumes of the vessel due to the numerous internal installations, the pressure distribution corresponds to a solid-body rotation for all precession ratios. This can lead to high pressure differences at the internal walls between the cylinder and the cones.

As the sodium experiments will be performed in a temperature range between 110 °C and 170 °C, thermal loads have to be taken into account to determine the thermal stresses. The ambient air is restricted to a maximum temperature of 60 °C in order to ensure the functionality of all electronic devices. The temperature difference between the surface and the environment causes a heat transfer by convection and heat radiation. Due to the high surface speed of the vessel ($\approx 65 \text{ m/s}$), forced convection is of particular importance even for the water experiment where the maximum temperature is limited to 85 °C. At high precession ratios, a large portion of the applied engine power of 800 kW is converted into heat by friction due to turbulence. So, the sodium warms up from 110 °C to 170 °C within about 25 minutes. In contrast, at low precession ratios corresponding to a laminar flow the sodium cools down from the selected initial temperature of 170 °C, since no appreciable heat conversion occurs. As a result of the low heat conductivity of the stainless steel, high temperature gradients are obtained in the vessel, which are determined in a transient analyses and are accompanied by high thermal stresses.

All described loads are superimposed for the strength assessment of the vessel. Due to the numerous influencing variables such as precession ratio, swivel angle, angle of rotation, direction of the radial imbalance and number of time steps for the computation of the thermal stresses, several millions of load cases occur. Thereby, the rotational

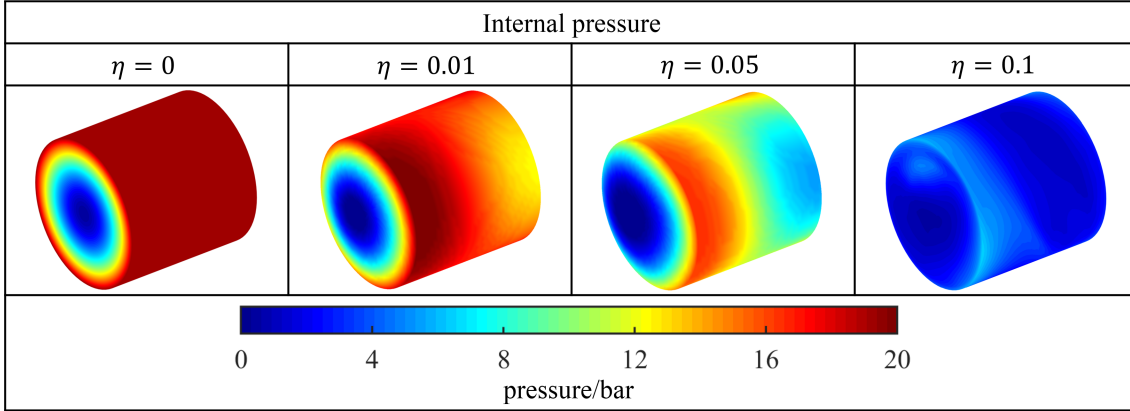


Figure 4: Pressure distribution on the cylinder wall as a function of the precession ratio (Giesecke et al., 2014; Stefani et al., 2014).

motion is discretized in steps of 5° . Since a numerical solution of all load cases is not possible, the number of load steps has to be reduced by several orders of magnitude. For this purpose, a calculation algorithm has been developed which will be discussed in more detail in the next section.

3 Computation Algorithm

Figure 5 illustrates the general calculation process starting with the geometry, which is provided by the construction department, ending with the visualization of the utilization ratios. Here, the focus is on the computation of the stresses and the determination of the most critical load cases. Hence, the number of load cases solved within the finite element software has to be reduced from several millions to a manageable level. This requires a more precise analysis of the loads, the geometry and the material properties. The aim is to decompose the complex loads and afterwards to superpose the resulting stresses. The decoupling of the thermal and the mechanical field problem resulting from neglecting the piezocaloric effect, is an essential precondition. Therefore, the temperature field is computed in the first step before determining the thermal stresses. The temperature dependence of the material properties is negligible in the examined temperature intervals. In accordance with the FKM Guideline linear-elastic material behavior has been assumed (FKM, 2012). Furthermore, the bolted joints are linearized for the load case identification and the components are connected by bonded contact in the clamping area as described for model class I of VDI 2230 Part 2 (2014). Since a large sliding distance at the interface has to be avoided in general, this linearization does not constitute a restriction with respect to the global structural behavior. The resulting linear model is valid for the applied load case superposition. However, a separate analysis of the bolted joints has to be performed afterwards.

3.1 Computation of Stresses

Three different angles between the two angular velocity vectors are considered for the strength assessment. On the one hand, the horizontal position of the container (swivel angle 90°) and on the other hand a swivel angle of 45° , taking into account both directions of platform rotation. It is necessary to distinguish between these two variants of rotation directions, as for one case the effective angular velocity of the container increases while it decreases for the other one. This has a strong influence on the expected pressure distribution. Preliminary numerical studies proved that a restriction to four precession ratios ensures a safe dimensioning. In addition to the cases of no precession ($\eta = 0$) and maximum precession ($\eta = 0.1$), these precession ratios are $\eta = 0.03$, where the highest pressure amplitude occurs, and $\eta = 0.08$. This latter is a combination of a high pressure amplitude and a large gyroscopic moment, because it is present shortly before turning from the laminar to the turbulent flow.

As it can be seen in Figure 6, the stress computation is divided into three parts and is performed for each swivel angle and all four precession ratios. First, the thermal stresses are calculated, which is connected to the transient solution of the temperature field and takes place at intervals of 100 s. Because of the model symmetry and the symmetrical thermal load, the use of a quarter model is sufficient at this point. This is followed by the determination of the stresses due to the radial imbalance and the other mechanical loads. In the latter case, the rotation angle of

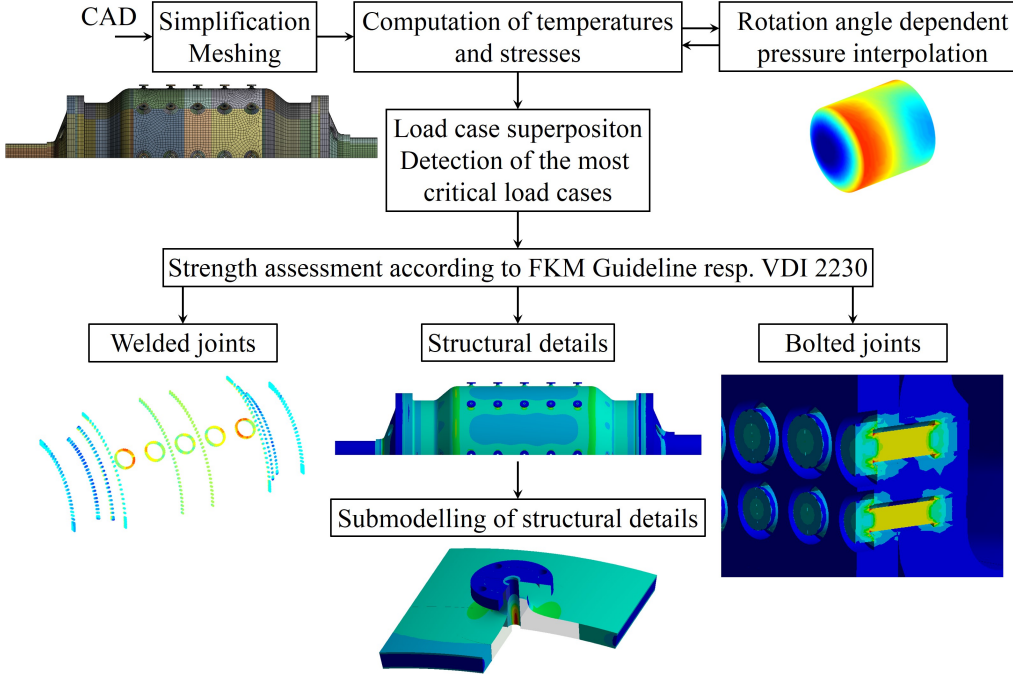


Figure 5: Flowchart of the calculation algorithms for the strength assessment.

the vessel, which is discretized in steps of 5° , represents the crucial parameter. Regarding the mechanical loads, it is necessary to evaluate a complete stress period. Except for the weight force, all loads appear either in the body-fixed or in the platform-fixed coordinate system. However, since the direction of the weight force coincides with the axis of rotation of the platform, it is identical in the inertial system and in the platform-fixed coordinate system. For this reason, the investigation of one rotation of the vessel about its longitudinal axis is sufficient. Here, in general the load is not symmetric, which requires a full model. The sector-symmetrical design of the pressure vessel allows the reconstruction of a full rotation from a quarter turn. When the load is rotated through 90° , the stress distribution is equivalent to the case where the container is rotated through 90° with an unchanged load direction. The load resulting from the imbalance can be composed of two perpendicular components. That is why one load step is sufficient to determine a complete revolution by using sector symmetry. Due to the complex pressure distribution this procedure cannot be applied for the other mechanical loads.

In order to minimize both the effort involved in the preprocessing and in the postprocessing, a quarter model is created and completed to the full model by 90° rotation. The nodes at the interfaces are merged in order to connect the segments. This procedure ensures that each node in the original quarter model has three corresponding nodes in the other segments. Thus, no stress interpolation is needed and the quarter model is sufficient for the strength assessment.

The reduction of the computational effort is demonstrated using the example of the sodium experiment with the precession ratio $\eta = 0.1$ and a certain swivel angle. Instead of computing all combinations of 72 rotation angles, 72 imbalance directions and 16 time steps, the finite element model system only has to be solved for 18 rotation angles, 1 imbalance direction and 16 time steps. Hence, the number of load cases reduces from 82,944 to 35.

The load of the radial imbalance can be adapted to the current angular velocity by scaling and thus to the swivel angle. Besides, this load does not depend on the precession ratio. Furthermore, for the precession ratio $\eta = 0$ a distinction between the platform rotation directions becomes superfluous. Instead of many millions of load cases, the calculation effort is reduced to a few hundred, as illustrated in Figure 7.

In addition, the used linearization has a further advantage. The stiffness matrix always remains constant, while the load vector changes between each load case. As a consequence, the factorization of the system matrix must be performed only once for the quarter model and the full model. Afterwards, the load vector is varied, which reduces the computational costs drastically, especially if sufficient internal memory is available to store the factorized matrix.

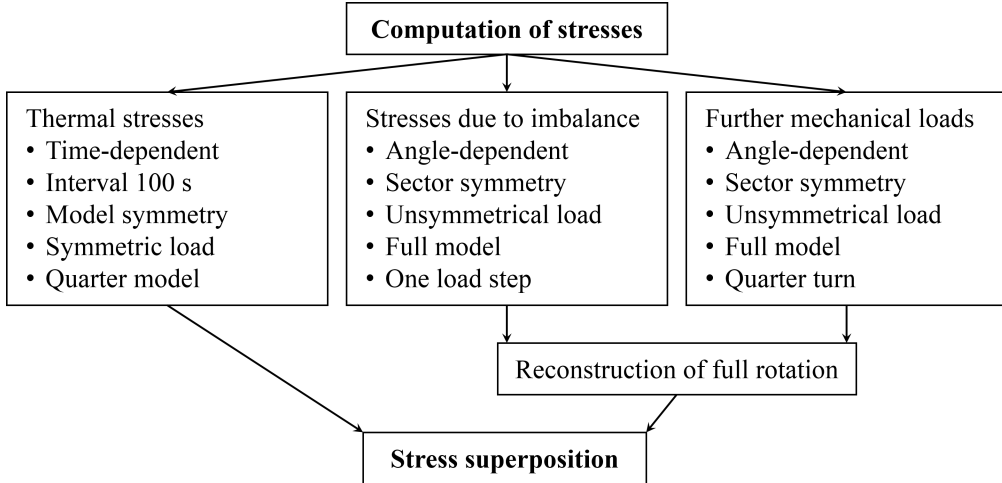


Figure 6: Segmentation of the stress computation to reduce the number of load cases combining the rotational speeds, the gyroscopic effects, the internal pressure and the weight force under further mechanical loads.

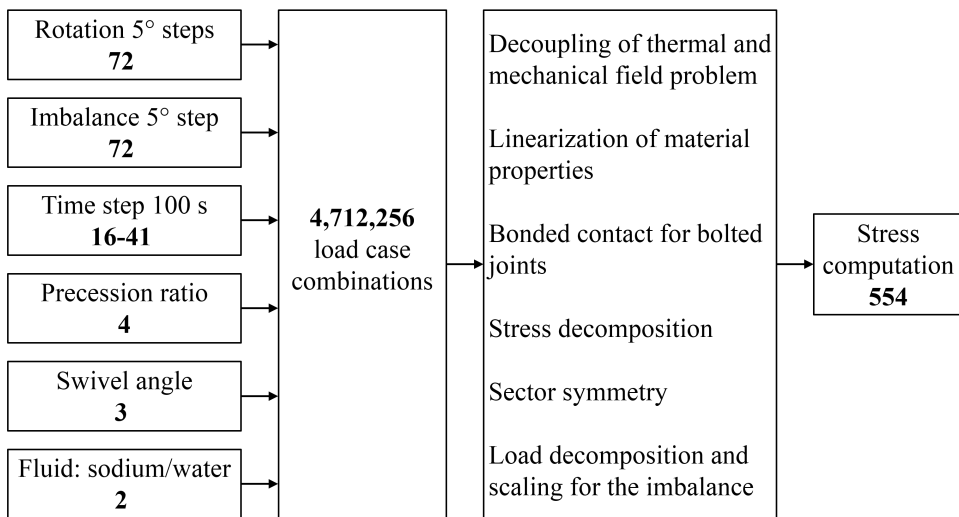


Figure 7: Load case combination and methods to reduce the computational effort. The number of variants is indicated below the variables.

3.2 Load Case Superposition and Strength Assessment

All possible load combinations are reconstructed from the calculated stresses in order to identify the most critical load case for the strength assessment. This is done separately for the static strength and the fatigue strength. According to the FKM Guideline (FKM, 2012) different concepts are applied to assess the non-welded sections and the welded joint. In addition, the bolted joints are examined via VDI 2230 Part 2 (2014).

The evaluation is conducted separately for each node and each bolt respectively with the strength values being always related to the maximum temperature. The fatigue assessment is carried out for an infinite number of load cycles, since the planned operating time of 2000 h with the maximum rotation frequency of 10 Hz corresponds to $7.2 \cdot 10^7$ cycles. This also allows the user-specific distribution of the different swivel angles and precession ratios, because no stress spectrum has to be predefined. The stresses due to the imbalance are constant as the direction does not change during operation. Furthermore, the thermal stresses can be regarded as quasi-static because one temperature cycle consisting of heating and cooling takes several hours, resulting in a frequency, which is many orders of magnitude lower than the rotational frequency. Therefore, the determination of the stress amplitudes is limited to the mechanical loads.

Due to a sufficiently fine mesh, the stresses can be interpreted as local stresses for the non-welded areas. The

computational effort is reduced by analyzing only the surface nodes of the quarter model because of the sector symmetry and the fact that a potential crack is expected to start at the surface. For the static strength assessment the maximum von Mises stress is evaluated for all load case superpositions and then the combination with the highest value is determined. Plastic deformations are only taken into account for structural details, where the assessment cannot be provided otherwise. However, the material has high strength reserves by strain hardening that are considered during the strength assessment.

The largest stress amplitude is determined separately for each stress component during a full rotation. In order to obtain an equivalent utilization ratio, the amplitudes are combined according to the von Mises hypothesis. The load case combination with the highest equivalent stress amplitude is considered for the strength assessment. In a second step the influence of the mean stress is taken into account, whereby the fatigue resistance decreases with increasing mean stress. That is why the load case combination with the maximum mean stress is detected including the constant stresses due to the imbalance and the quasi-static thermal stresses, which is used for the calculation of the utilization ratio. Since this is performed separately for every node, supporting effects in the case of high stress gradients are not considered because the determined stresses at adjacent nodes do not necessarily belong to the same load case.

During the strength assessment of welded joints it is necessary to distinguish between butt welds and fillet welds. The stresses at the butt welds can be directly interpreted as local nominal stresses. As the welds are positioned at a sufficient distance from geometrical notches, no high stress gradients occur allowing the use of the fatigue resistance values (FAT classes) for nominal stresses. For the fillet welds structural stresses are considered. However, surface extrapolation (hot-spot method) as recommended by the International Institute of Welding (Hobbacher, 2007) is not feasible for the given geometry. For this reason, the concept of Haibach (Haibach, 1968) is used, according to which the structural stress is determined at a distance of 2 mm from the weld toe. The obtained structural stresses are used only to identify the most critical load cases, which are assessed by effective notch stresses afterwards. Therefore, the weld toes are rounded with a radius of 1 mm (Fricke, 2008). This can only be applied in combination with submodelling techniques because of the very fine mesh and the large number of degrees of freedom. Hence, it is necessary to identify the critical load cases and places for crack initiation in the global model.

The static strength assessment is mainly analogous to the non-welded areas, since only the equivalent stress σ_v

$$\sigma_v = \sqrt{\sigma_{\perp}^2 + \tau_{\parallel}^2} \quad (2)$$

differs taking into account the stress perpendicular to the weld σ_{\perp} and the shear stress parallel to the weld τ_{\parallel} (FKM, 2012). In the first step of the fatigue strength assessment again the highest stress amplitude is determined, while in the second step the load case combination with the maximum mean stress is detected. According to FKM (2012) the equivalent stress amplitude σ_{av}

$$\sigma_{av} = \frac{1}{2} \cdot \left(|\sigma_{a\perp} + \sigma_{a\parallel}| + \sqrt{(\sigma_{a\perp} - \sigma_{a\parallel})^2 + 4 \cdot \tau_{a\parallel}^2} \right) \quad (3)$$

follows, where $\sigma_{a\perp}$ and $\sigma_{a\parallel}$ describe the amplitudes of the stress components perpendicular and parallel to the weld while $\tau_{a\parallel}$ stands for the amplitude of the shear stress.

For the bolted joints, the linearized model is used to identify the most critical load cases and the most heavily loaded bolts. Since the components, which should be bolted together, are connected within the non-overlapping clamping area, the contact loads can be used to infer the transmitted load at each bolt. Here, the tensile force as well as the shear force and the bending moment are of particular interest. If materials with different coefficients of thermal expansion are screwed, as in case of the flanges connecting the main assemblies of the vessel, the change of pretension due to heating must be considered. The load case identification is performed separately for the different load components as a weighting with respect to their effect in the nonlinear model is not yet possible. Afterwards, a finite element model of model class III according to VDI 2230 Part 2 (2014) is used for a detailed analyses and the strength assessment. Therefore, the bolts are modeled as equivalent cylindrical volumes. Both the pretension of the bolts and the contact status, including the friction between the clamped components, are taken into account, which inevitably leads to a nonlinear model. However, due to the restriction to a few load cases the computational effort remains manageable. For the static strength assessment the stresses at maximum preload are of interest. In contrast, for the fatigue strength assessment the minimum preload must be applied, considering the tightening factor and the amount of embedding, since the highest stress amplitudes result in this case. The simplified screw model leads to stress singularities under the bolt head and in the thread. That is why the nodal reaction forces are used for the computation of the nominal stresses, which are needed for the strength assessment.

4 Results

The complexity of the vessel does not allow to include all structural details within one finite element model, since the resulting degree of freedom would clearly exceed the computational feasibility. Therefore, a global model is used, first considering only the outer wall of the container and the parts connected to the bearings in detail. The conical ends and the interior walls have a coarse mesh, which does not allow the evaluation of local stresses. However, the model contains the inertial effects and the global deformations of these assemblies. Figure 8 displays the results of the static strength assessment for the outer wall of the vessel. Here, the utilization ratio which is defined as the quotient of the acting stresses and the allowed stress reaches a maximum of approximately 89 %.

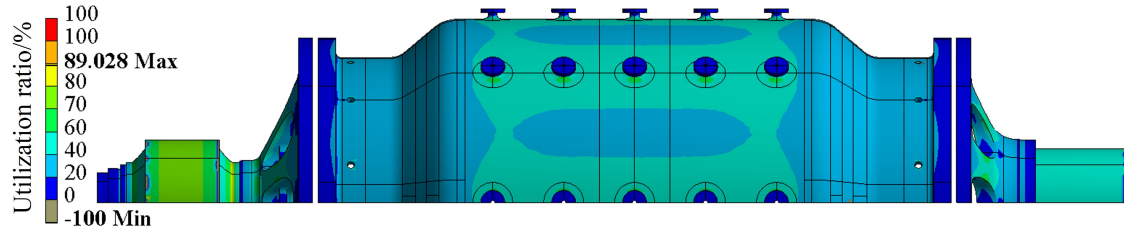


Figure 8: Utilization ratio for the static strength assessment of the vessel.

The result of the fatigue strength assessment of the welded joints is shown in Figure 9. Here, the maximum utilization ratio is 96 %, thus both assessments are fulfilled. The guideline-specific safety factors are already included in these values. The sensor flanges, the cones, the interior assemblies and the bolted joints are examined separately using submodels. Furthermore, the strength assessment of the fillet welds with effective notch stresses requires additional submodels.



Figure 9: Utilization ratio for the fatigue strength assessment of the welded joints.

5 Summary

A concept was developed for the computational strength assessment of a precession driven dynamo to explore planetary magnetic fields. The various thermal and mechanical loads acting on the pressure vessel lead to several millions of load cases. By decoupling the thermal and mechanical field, linearization, utilization of sector symmetry and dividing the stresses into the thermal stresses, the stresses due to imbalance and the stresses resulting from the other mechanical loads, the computational effort is drastically reduced by several orders of magnitude. Stress superposition allows to identify the most critical load cases and load case combinations respectively needed for the strength assessment. Therefore, it must be distinguished between the non-welded structure and the welded joints. In both cases the FKM Guideline is used, while the bolted joints are proved according to VDI 2230.

References

FKM Forschungskuratorium Maschinenbau: *FKM-Richtlinie Rechnerischer Festigkeitsnachweis für Maschinenbauteile aus Stahl, Eisenguss- und Aluminiumwerkstoffen*, vol. 6. VDMA-Verlag GmbH, Frankfurt (2012).

Fricke, W.: Guideline for the Fatigue Assessment by Notch Stress Analysis for Welded Structures. In: *Annual Assembly of International Institute of Welding*, IIW-Doc. XIII-2240r2-08/XV-1289r2-08 (2008).

Giesecke, A.; Albrecht, T.; Gerbeth, G.; Gundrum, T.; Stefani, F.: Numerical simulations for the DRESDYN precession dynamo. *Magnetohydrodynamics*, 51, (2014), 293–302.

Haibach, E.: Die Schwingfestigkeit von Schweißverbindungen aus der Sicht einer örtlichen Beanspruchungsmessung. Tech. rep., Fraunhofer-Inst. für Betriebsfestigkeit, Darmstadt (1968).

Hobbacher, A.: Recommendations for the Fatigue Design of Welded Joints and Components. Tech. rep., International Institute of Welding, Paris (2007).

Stefani, F.; Albrecht, T.; Gerbeth, G.; Giesecke, A.; Gundrum, T.; Herault, J.; Nore, C.; Steglich, C.: Towards a precession driven dynamo experiment. *Magnetohydrodynamics*, 51, (2014), 275–284.

Stefani, F.; Eckert, S.; Gerbeth, G.; Giesecke, A.; Gundrum, T.; Steglich, C.; Weier, T.; Wustmann, B.: DRESDYN - A new facility for MHD experiments with liquid sodium. *Magnetohydrodynamics*, 2012, (2012), 103–113.

Stefani, F.; Gailitis, A.; Gerbeth, G.: Magnetohydrodynamic experiments on cosmic magnetic fields. *ZAMM - Zeitschrift für Angewandte Mathematik und Mechanik*, 88(12), (2008), 930–954.

VDI-Fachbereich Produktentwicklung und Mechatronik: *VDI 2230 Part 1 Systematic calculation of highly stressed bolted joints - Joints with one cylindrical bolt*. VDI-Gesellschaft Produkt- und Prozessgestaltung (2014).

VDI-Fachbereich Produktentwicklung und Mechatronik: *VDI 2230 Part 2 Systematic calculation of highly stressed bolted joints - Multi bolted joints*. VDI-Gesellschaft Produkt- und Prozessgestaltung (2014).

Address: TU Dresden, Chair of Dynamics and Mechanism Design, Marschnerstr. 30, 01307 Dresden, Germany
email: stephan.rother@tu-dresden.de

Bifurcations of Relative Equilibria Sets of a Massive Point on Rough Rotating Surfaces

A. Burov, E. Shalimova

Dynamics of a massive point on a rotating wire or surface under dry friction force action is considered. Existence, stability and bifurcations of non-isolated relative equilibria sets of the point located

- on a sphere uniformly rotating about an inclined fixed axis;
- on a thin circular hoop rotating about an inclined fixed axis;
- on a paraboloidal bowl uniformly rotating about its axis

are studied. The results are represented in the form of bifurcation diagrams.

1 Introduction

Problems similar to those considered in the present paper arise when we study dynamics of mechanical systems with rotating parts performing various operations such as mixing, grinding, drying, etc. of diverse substances (Joshi et al. (1995)), as well as, self-compensating systems (van de Wouw et al. (2005)).

Modern advances in computer simulation (Fleissner et al., 2010; Alkhaldi et al., 2008) allow to investigate dynamics of systems with a large number of moving parts numerically. However it is usually difficult to perform the qualitative analysis of the obtained results. That is why it is reasonable to consider some simple problems such as the motion of a material particle on some mobile surface or curve under the action of a friction force. It turns out that appropriate mechanical systems exhibit rather complicated behaviour even be considered in this simple formulation.

One of the main points relates to existence of non-isolated equilibria, in particular, of relative equilibria. Though existence of non-isolated equilibria for systems with dry friction has been known for a long time (cf. Kauderer (1958); Magnus (1976)), systematic investigation of their stability properties and dependence on parameters attracted attention of specialists much later (Pozharitsky, 1962; Matrosov and Finogenko, 1998; Leine and van de Wouw, 2008; Ivanov, 2009; Burov, 2010; Biemond et al., 2012; Burov and Yakushev, 2014; Ivanov, 2015; Burov and Shalimova, 2015, 2016; Várkonyi and Or, 2016)).

2 Formulation of problem and equations of motion in redundant coordinates

Consider a massive point P of mass m moving on a rotating surface A . Let O be an origin of a moving frame $Ox_1x_2x_3$ (MF). In this frame $\overrightarrow{OP} = \mathbf{x} = (x_1, x_2, x_3)^T$, and the surface A is given as

$$\varphi = \varphi(\mathbf{x}) = 0. \quad (1)$$

Furthermore we assume that the point P is moving under the action of potential active forces with a potential

$$U'(\mathbf{x}) = mU(\mathbf{x}). \quad (2)$$

A Coulomb friction force \mathbf{F} with a coefficient of friction μ appears between the point P and the surface A . This surface is assumed being in rotation with an angular velocity $\boldsymbol{\omega} = (\omega_1, \omega_2, \omega_3)^T$.

The motion of the point can be described by

$$\ddot{\mathbf{x}} = \mathbf{F}_C + \mathbf{F}_c + \mathbf{F}_N + \mathbf{N} + \mathbf{F}. \quad (3)$$

Here, $\mathbf{F}_C = 2\dot{\mathbf{x}} \times \boldsymbol{\omega}$, $\mathbf{F}_c = (\boldsymbol{\omega} \times \mathbf{x}) \times \boldsymbol{\omega}$, $\mathbf{F}_N = -U_x \mathbf{i}$, $\mathbf{N} = \lambda \varphi_{\mathbf{x}} \mathbf{n}$ and \mathbf{F} are Coriolis force, centrifugal force, potential force, normal reaction force and friction force, respectively;

$$\mathbf{n} = \varphi_{\mathbf{x}} |\varphi_{\mathbf{x}}|^{-1}, \quad \left(\varphi_{\mathbf{x}} \stackrel{\text{def}}{=} \frac{\partial \varphi}{\partial \mathbf{x}} \right)$$

is a unit external normal to the surface. All these forces are divided by m . A magnitude of the normal reaction reads

$$N = (\mathbf{N}, \mathbf{n}) = \lambda (\varphi_{\mathbf{x}}, \varphi_{\mathbf{x}}) |\varphi_{\mathbf{x}}|^{-1} = \lambda |\varphi_{\mathbf{x}}|.$$

The multiplier λ can be determined via a standard way. It reads

$$\lambda = -(\varphi_{\mathbf{x}}, \varphi_{\mathbf{x}})^{-1} [(\varphi_{\mathbf{xx}} \dot{\mathbf{x}}, \dot{\mathbf{x}}) + (\varphi_{\mathbf{x}}, \mathbf{F}_C + \mathbf{F}_c + \mathbf{F}_N)], \quad \left(\varphi_{\mathbf{xx}} \stackrel{\text{def}}{=} \frac{\partial^2 \varphi}{\partial \mathbf{x}^2} \right). \quad (4)$$

The sign of λ determines the direction of the normal reaction.

Determining the friction force, one must distinguish two cases (see, for example, Levi-Civita and Amaldi (1930)). In the case of slipping of the point P on the rotating surface the friction force \mathbf{F} is perpendicular to the vector of the normal reaction \mathbf{N} , i.e. $(\varphi_{\mathbf{x}}, \mathbf{F}) \equiv 0$, and the direction of this force is opposite to direction of slipping.

In the case of the resting point P with respect to the rotating surface the friction force is directed to the side, opposite to direction of possible slipping. Its magnitude does not exceed the magnitude of the normal reaction, multiplied by the coefficient of friction. It means that

$$\mathbf{F}_c + \mathbf{F}_N + \mathbf{N} + \mathbf{F} = 0, \quad \text{and} \quad |\mathbf{F}| \leq \mu |\mathbf{N}| \quad (5)$$

yields

$$|\mathbf{F}_c + \mathbf{F}_N + \mathbf{N}| \leq \mu |\mathbf{N}|, \quad (6)$$

which determines a set of relative equilibria.

Further assume that coefficient of static friction is equal to coefficient of sliding friction.

2.1 Equations of relative equilibria in redundant coordinates

Inequality (6) gives the condition of existence of relative equilibria and depends, in particular, on the vector $\boldsymbol{\omega}$. It allocates regions on the surface A , ‘filled’ by relative equilibria (RFbRE). By virtue of inequality (6) boundaries Σ of these regions are determined as

$$f = 0, \quad (7)$$

$$\begin{aligned} f &= (\mathbf{F}_c + \mathbf{F}_N + \mathbf{N}, \mathbf{F}_c + \mathbf{F}_N + \mathbf{N}) - \mu^2 (\mathbf{N}, \mathbf{N}) = \\ &= (\varphi_{\mathbf{x}} \times ((\boldsymbol{\omega} \times \mathbf{x}) \times \boldsymbol{\omega} - U_x \mathbf{i}), \varphi_{\mathbf{x}} \times ((\boldsymbol{\omega} \times \mathbf{x}) \times \boldsymbol{\omega} - U_x \mathbf{i})) - \mu^2 (\varphi_{\mathbf{x}}, (\boldsymbol{\omega} \times \mathbf{x}) \times \boldsymbol{\omega} - U_x \mathbf{i})^2. \end{aligned}$$

The curve $\Gamma = \Sigma \cap A$ bounds a set of relative equilibria. Equilibria correspond to points $P : f \leq 0$ for all instants of time.

Remark. The similar approach can be used for describing the sliding of the point P along a curve, if this curve is given as an intersection of a couple of surfaces.

3 A point on a sphere

3.1 Description of the mechanical system

A heavy material point P moves on the ‘standard’ sphere S^2 under the action of dry friction force. The sphere is rotating with a constant angular velocity ω about a fixed axis, passing through the center of the sphere O . Let α be an angle of inclination of the axis. A dry friction force F with a friction coefficient μ acts between the point and the sphere (Figure 1).

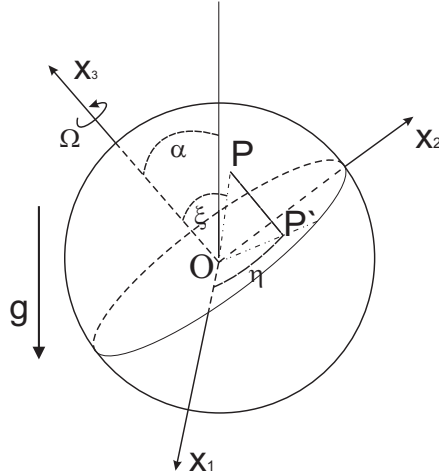


Figure 1. A point on a rotating sphere.

Let $Ox_1x_2x_3$ be a rectangular coordinate system fixed to the sphere with the axis Ox_3 coinciding with rotation axis. The position of the point in this system will be specified by two spherical angles ξ and η . Let ξ be an angle between the axis Ox_3 and \overrightarrow{OP} and η be an angle between the axis Ox_1 and $\overrightarrow{OP'}$, where P' is the projection of the point P onto the plane Ox_1x_2 .

Now introduce dimensionless time $t \mapsto t \sqrt{\ell/g}$ and dimensionless parameter $\Omega^2 = \omega^2 \ell/g$. The derivatives with respect to the new time will be denoted by a stroke. Then the system of motion in the relative coordinate system can be written as

$$\begin{aligned} \sin^2 \xi \eta'^2 + \xi'^2 &= (\sin \xi \sin \alpha \sin(\omega t + \eta) + \cos \xi \cos \alpha) - \tilde{N}_r - \Omega \sin^2 \xi (\Omega + 2\eta'), \\ \xi'' - \sin \xi \cos \xi \eta'^2 &= -(\cos \xi \sin \alpha \cos \eta \sin(\omega t + \eta) - \sin \xi \cos \alpha) - \tilde{F}_\xi + \Omega \sin \xi \cos \xi (\Omega + 2\eta'), \quad (8) \\ \sin \xi \eta'' + 2\xi' \eta' \cos \xi &= -\sin \alpha \cos(\omega t + \eta) - \tilde{F}_\eta - 2\Omega \cos \xi \xi', \end{aligned}$$

where $\tilde{F}_\xi = F_\xi/mg$, $\tilde{F}_\eta = F_\eta/mg$ are dimensionless projections of the friction force on the coordinate axes \vec{e}_ξ and \vec{e}_η , $\tilde{N}_r = N_r/mg$ is a dimensionless normal reaction.

3.2 Sets of equilibria

Introducing the angle $\gamma = \eta - \pi/2 + \omega t$, the equilibria can be found from these equations by supposing $\xi' = 0$, $\eta' = 0$, $\xi'' = 0$, $\eta'' = 0$. If the point is in a state of equilibrium then

$$F_\xi^2 + F_\eta^2 \leq \mu^2 N_r^2, \quad (9)$$

$$N_r = \sin \xi \sin \alpha \cos \gamma + \cos \xi \cos \alpha - \Omega^2 \sin^2 \xi,$$

$$F_\xi = \cos \xi \sin \alpha \cos \gamma + \sin \xi \cos \alpha + \Omega^2 \cos \xi \sin \xi, \quad F_\eta = \sin \alpha \sin \gamma.$$

Using these expressions and inequality (9) one obtains

$$\begin{aligned} & (-\cos \xi \sin \alpha \cos \gamma + \sin \xi \cos \alpha + \Omega^2 \cos \xi \sin \xi)^2 + \sin^2 \alpha \sin^2 \gamma \leq \\ & \leq \mu^2 (\sin \xi \sin \alpha \cos \gamma + \cos \xi \cos \alpha - \Omega^2 \sin^2 \xi)^2. \end{aligned} \quad (10)$$

Figure 2 represents the bifurcation diagrams for different values of the inclination angle α and $\mu = 0.7$. The equilibria sets can be obtained by a rotation of the angle 2π around an axis that coincides with the rotation axis. When $\alpha = 0$ the diagram represents a half of a ‘fat fork’, denoted with F , and a equilibrium set in a form of a ‘needle’, denoted with G , near the axis $\xi = 0$ that converges to zero when $\omega \rightarrow \infty$ (Figure 2a, see also Burov (2010)). With increasing of the angle α the area G and the middle ‘prong’ converge to zero and $\xi = \pi$ respectively (Figure 2b), then if $\alpha = \alpha_*$ there is only one point between the ‘prongs’ (Figure 2c), and when $\alpha > \alpha_*$ there is only the bigger jag left (Figure 2d) that straightens itself with the further increase of α (Figure 2e). When $\omega \rightarrow \infty$ the bifurcation diagram for every α is a strip with the boundaries $\xi = \pi/2 - \alpha_*$ and $\xi = \pi/2 + \alpha_*$.

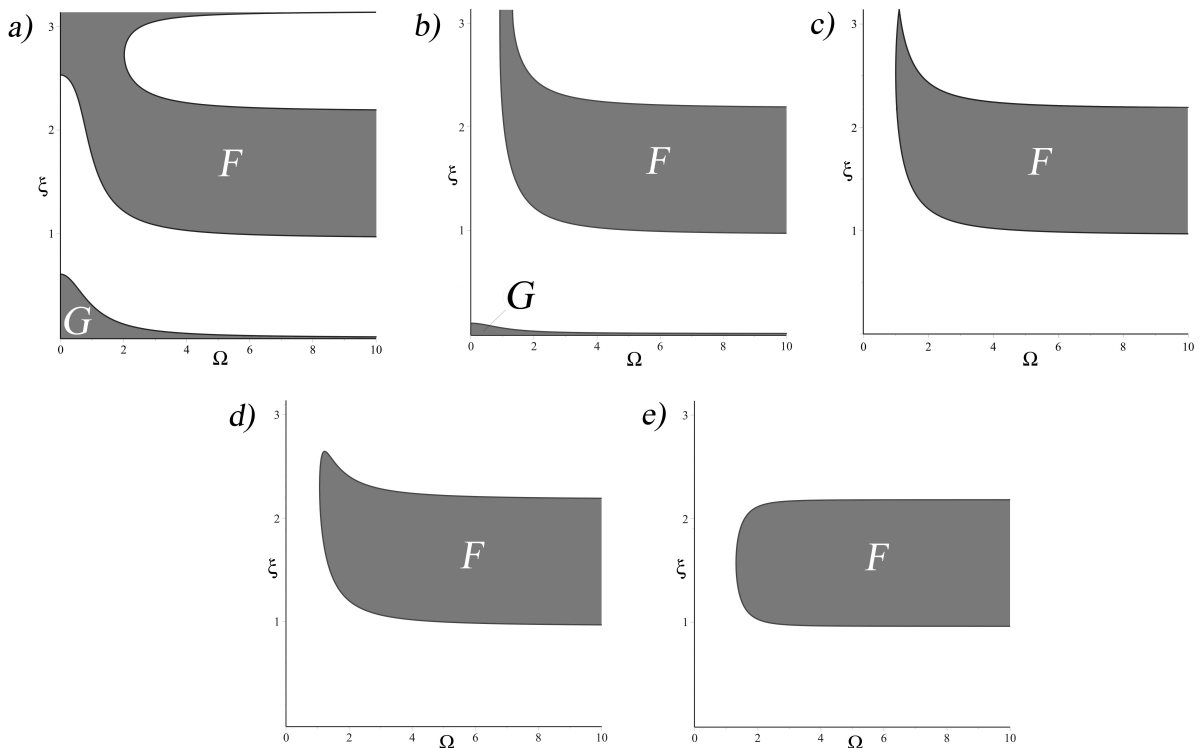


Figure 2. Bifurcation diagrams for $\alpha = 0$, $\alpha = \arctan(0.7) - 0.1$, $\alpha = \arctan(0.7)$, $\alpha = \arctan(0.7) + 0.1$, $\alpha = \pi/2$.

4 A bead on a circle

4.1 Description of the mechanical system

The motion of a heavy bead P of mass m on a circular hoop with radius ℓ with its center at the point O is considered. The hoop rotates with a constant angular velocity ω about an inclined axis lying in its plane and passing through its center. The angle of inclination of the axis α is constant. A dry friction force \mathbf{F} with a friction coefficient μ acts between the bead and the hoop (Figure 3).

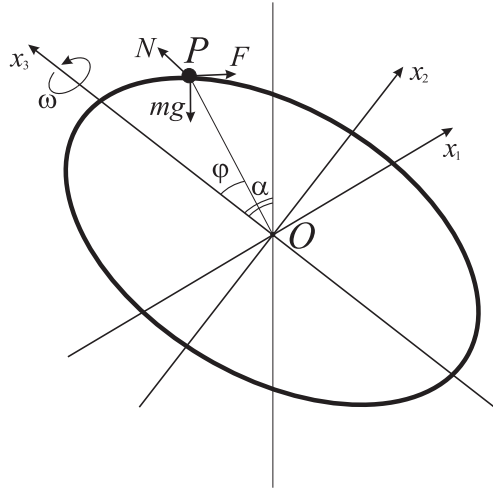


Figure 3. A bead on a circular hoop.

Suppose $Ox_1x_2x_3$ is a moving coordinate system (MCS) with origin at the center of the hoop, the x_3 axis of which is directed along its axis of rotation, the x_2 axis lies in the plane of the hoop and the x_1 axis is perpendicular to this plane.

In the MCS, the bead position is given by coordinates (x_1, x_2, x_3) . For the sake of convenience, represent the constraints restricting its motion as

$$f_1 = \frac{1}{2} (x_2^2 + x_3^2 - \ell^2) = 0, \quad f_2 = x_1 = 0. \quad (11)$$

Suppose $\mathbf{v}_r = (\dot{x}_1, \dot{x}_2, \dot{x}_3)$ is the bead velocity in the MCS, $v_r = (\mathbf{v}_r, \mathbf{v}_r)^{1/2}$, and the transfer velocity $\mathbf{v}_e = (-\omega x_2, \omega x_1, 0)$. The kinetic energy of the system, free from constraints, and the potential energy in the MSC are given by the relations

$$\begin{aligned} T &= \frac{m}{2} ((\dot{x}_1 - \omega x_2)^2 + (\dot{x}_2 + \omega x_1)^2 + \dot{x}_3^2), \\ U &= mg(x_1 \sin \omega t \sin \alpha + x_2 \cos \omega t \sin \alpha + x_3 \cos \alpha). \end{aligned} \quad (12)$$

Putting

$$\begin{aligned} x_1 &\mapsto x'_1 \ell, \quad x_2 \mapsto x'_2 \ell, \quad x_3 \mapsto x'_3 \ell, \quad t \mapsto t' \sqrt{\frac{\ell}{g}}, \quad \omega \mapsto \omega' \sqrt{\frac{g}{\ell}} \\ \lambda_1 &\mapsto \lambda'_1 m \frac{g}{\ell}, \quad \lambda_2 \mapsto \lambda'_2 mg, \quad L \mapsto L' mg \ell, \quad F_{x_2} \mapsto mg F'_{x_2}, \quad F_{x_3} \mapsto mg F'_{x_3}. \end{aligned} \quad (13)$$

where λ_1, λ_2 are Lagrange multipliers:

$$\lambda_1 = -(\dot{x}_1^2 + \dot{x}_2^2) - \omega^2 x_2^2 + x_2 \cos \omega t \sin \alpha + x_3 \cos \alpha, \quad \lambda_2 = -2\omega \dot{x}_2 + \sin \omega t \sin \alpha, \quad (14)$$

and dropping the strokes we obtain the equations of motion in the form:

$$\ddot{x}_2 = \omega^2 x_2 - \cos \omega t \sin \alpha + \lambda_1 x_2 + F_{x_2}, \quad \ddot{x}_3 = -\cos \alpha + \lambda_1 x_3 + F_{x_3}, \quad (15)$$

According to Amontons-Coulomb law

$$F^2 = F_{x_2}^2 + F_{x_3}^2 \leq \mu^2 (\lambda_1^2 + \lambda_2^2). \quad (16)$$

4.2 Sets of equilibria

If the point is in equilibrium, then the friction force compensates the sum of the tangential components of the gravitational force and the centrifugal force, so

$$F = \omega^2 x_2 x_3 - x_3 \cos \omega t \sin \alpha + x_2 \cos \alpha.$$

Then condition (16) can be rewritten as

$$(\omega^2 x_2 x_3 - x_3 \cos \omega t \sin \alpha + x_2 \cos \alpha)^2 \leq \mu^2 (x_2 \cos \omega t \sin \alpha + x_3 \cos \alpha - \omega^2 x_2^2)^2 + \mu^2 \sin^2 \omega t \sin^2 \alpha. \quad (17)$$

For equilibria this inequality must be fulfilled identically for all time instances.

The sets of relative equilibria depend on three parameters (μ, α, ω) . Let us now introduce an angular coordinate φ , measured clockwise from the Oz axis of the MCS (Figure 3). Then $x_2 = \sin \varphi$, $x_3 = \cos \varphi$, and the condition (17) reads

$$\begin{aligned} & (\omega^2 \sin \varphi \cos \varphi - \cos \varphi \cos \omega t \sin \alpha + \sin \varphi \cos \alpha)^2 \leq \\ & \leq \mu^2 (\sin \varphi \sin \alpha \cos \omega t + \cos \varphi \cos \alpha - \omega^2 \sin^2 \varphi)^2 + \mu^2 \sin^2 \omega t \sin^2 \alpha. \end{aligned} \quad (18)$$

Putting in (18) $\cos \omega t = 1$ and $\cos \omega t = -1$, respectively, one obtains the regions Σ_+ and Σ_- in the (φ, ω) plane. These regions are bounded by the curves Γ_+ and Γ_- respectively. The intersection $\Sigma_+ \cap \Sigma_-$ is a set of relative equilibria.

The part of the (φ, ω) plane enclosed between the lines $\varphi = 0$ and $\varphi = \pi$ is shown in Figure 4. The relation between the equilibrium positions and the angular velocity of rotation of the sphere ω is depicted in this figure for different values of the inclination angle of the rotation axis, assuming the friction coefficient $\mu = 0.7$. The Σ_+ regions are denoted by the lightest shading, the Σ_- regions are denoted by the darker shading, and their intersection is distinguished by the darkest shading. It has been shown by Burov (2010) that, when $\alpha = 0$, the set of relative equilibria is the half region F of the ‘bold-face fork’ that is symmetrical about the axis $\varphi = \pi$, and also the region of equilibria G in the form of a ‘needle’ stretched along the line $\varphi = 0$ that converges to zero when $\omega \rightarrow \infty$ (Figure 4a). When α is increased, the regions Σ_+ and Σ_- , which coincide when $\alpha = 0$, diverge (in Figure 4b the case of $\alpha = \arctg(0.7) - 0.04$ was chosen for purposes of convenience), and, when $\alpha = \arctg(0.7)$, the region G vanishes and only one point of the middle prong of the ‘fork’ remains (Figure 4c). When $\arctg(0.7) < \alpha < \pi/2 - \arctg(0.7)$ these prongs split completely and diverge (Figure 4d). When $\alpha > \pi/2 - \arctg(0.7)$ a new region I appears for small ω (Figure 4e) that becomes larger as α increases (Figure 4f) and it joins the region F when $\alpha = \pi/2$. In this case the bifurcation diagram is a strip.

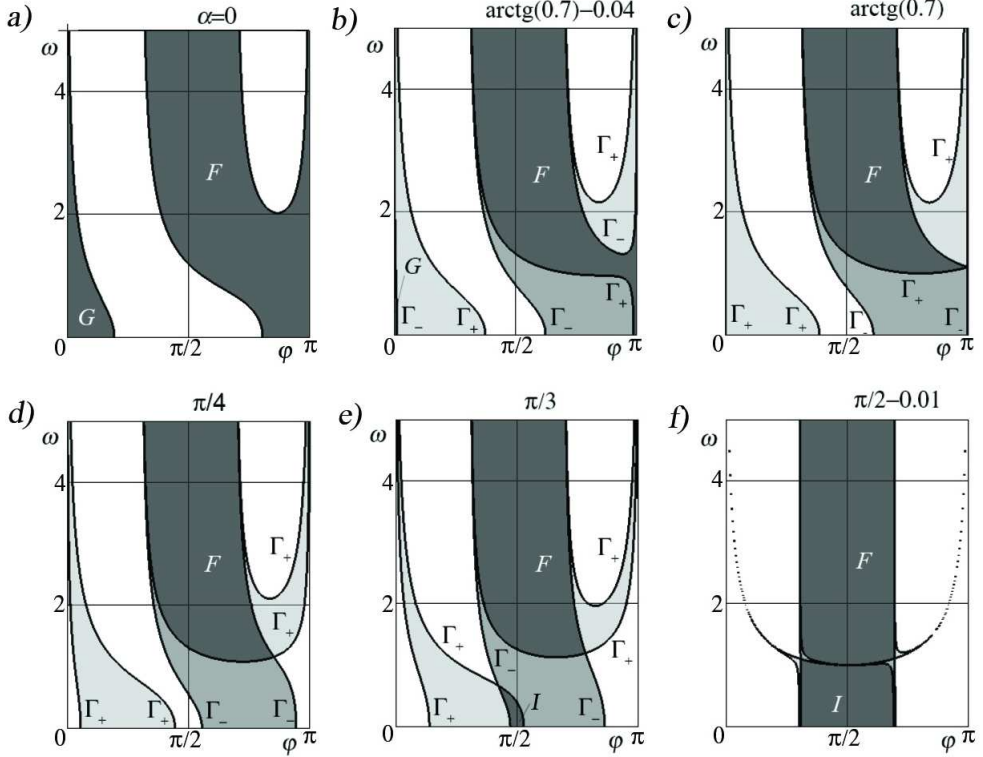


Figure 4. Bifurcation diagrams for different angles of inclination α , $\mu = 0.7$.

5 A point on a paraboloidal cup

5.1 Description of the mechanical system

A heavy material point P moves on the surface of a paraboloidal cup under the action of a dry friction force. The cup is rotating with a constant angular velocity ω about its symmetry axis (Figure 5). The coefficient of dry friction is μ .

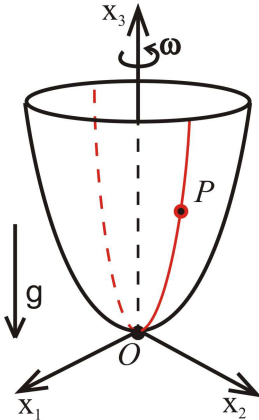


Figure 5. A point in a paraboloidal cup.

Let $Ox_1x_2x_3$ be a moving frame, uniformly rotating about an axis Ox_3 directed along the upward vertical. In this system the position of the point is given by the coordinates (x_1, x_2, x_3) , and the constraint restricting its motion is defined by the relation

$$f = x_3 - \frac{1}{2} \left(\frac{x_1^2}{a_1} + \frac{x_2^2}{a_2} \right) = 0. \quad (19)$$

5.2 Relative equilibria sets

Introduce dimensionless variables and parameters

$$\begin{aligned} x_1 &= \sqrt{a_1 a_2} x'_1, & x_2 &= \sqrt{a_1 a_2} x'_2, & x_3 &= \sqrt{a_1 a_2} x'_3, \\ p' &= \sqrt{a_1 a_2} p, & p &= \omega^2 / g, & b_1 &= \sqrt{a_1 / a_2}, & b_2 &= \sqrt{a_2 / a_1}, & (0 < b_1 \leq 1 \leq b_2). \end{aligned}$$

Dropping the strokes over the symbols and using (6) with $\mathbf{F}_N = mg$ for determination of relative equilibria, we obtain the boundary of the equilibria sets as follows:

$$(p^2 (x_1^2 + x_2^2) + 1) \left(\frac{x_1^2}{b_1^2} + \frac{x_2^2}{b_2^2} + 1 \right) - (1 + \mu^2) \left(p \left(\frac{x_1^2}{b_1} + \frac{x_2^2}{b_2} \right) + 1 \right)^2 = 0. \quad (20)$$

At first we consider the symmetrical case, i.e. $b_1 = b_2 = b$. If $x > 0$: $x^2 = x_1^2 + x_2^2$ is a new coordinate, then the boundary of the equilibria sets can be rewritten as

$$P(x, p, b, \mu) = x^2 \left(1 - \mu^2 \frac{x^2}{b^2} \right) p^2 - 2(1 + \mu^2) \frac{x^2}{b} p + \frac{x^2}{b^2} - \mu^2 = 0. \quad (21)$$

Consider this expression as an equation on $y = x^2$. It is possible to show that this equation has only one root if

$$p = p_{\pm} = \frac{\left(\sqrt{1 + \mu^2} \pm \mu \right)^2}{b} = \frac{1 \pm \sin \alpha_*}{b(1 \mp \sin \alpha_*)}.$$

The relative equilibria sets on the (p, x) -plane are depicted on Figure 6. If $p = 0$ the set of equilibria is a disk that contains the point $(x_1, x_2) = (0, 0)$. If $0 < p < p_-$ the set of equilibria is a plane except for an annulus, the center

of which is the point $(x_1, x_2) = (0, 0)$. The radius of the outer circle of the annulus increases indefinitely when $p \mapsto 0$. If $p_- < p < p_+$, then the whole cup becomes the set of equilibria. When $p > p_+$ the set of equilibria is again a whole cup except for an annulus. When $p \mapsto \infty$ the radius of the inner circle of the annulus converges to zero and the radius of an outer circle approaches $\sqrt{b/\mu}$.

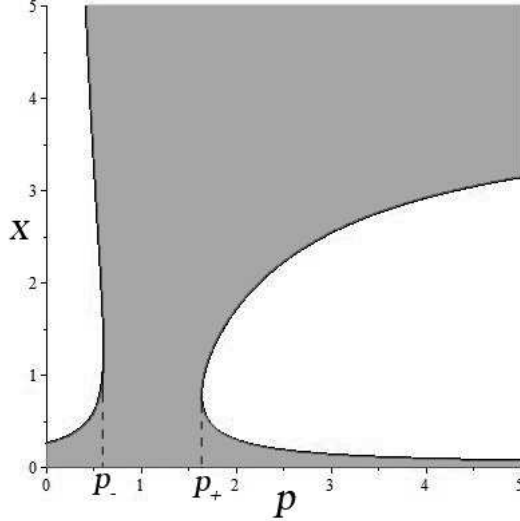


Figure 6. Relative equilibria sets in the symmetrical case.

Now, consider the asymmetrical case. Since Ox_1 and Ox_2 are symmetry axes of the boundary of equilibria sets, it is reasonable to study topological restructuring of the equilibria sets on these axes.

Let

$$p_{\pm k} = \frac{(\sqrt{1 + \mu^2} \pm \mu)^2}{b_k} = \frac{1 \pm \sin \alpha_*}{b_k(1 \mp \sin \alpha_*)}, \quad k = 1, 2$$

be parameters, similar to p_{\pm} used above.

Consider a section of sets of equilibria by a plane $x_2 = 0$. This section is a curve

$$P(x_1, p, b_1, \mu) = 0. \quad (22)$$

This curve bifurcates for $p = p_{\pm 1}$.

Similarly, the section of sets of equilibria by a plane $x_1 = 0$ is

$$P(x_2, p, b_2, \mu) = 0. \quad (23)$$

This curve bifurcates for $p = p_{\pm 2}$.

Topologically, there are four types of “regular” sets of equilibria and three types of “singular” sets in this problem. The regular, topologically coarse, sets are

- D : a disk;
- $D \cup 4T$: a disk and four tongues;
- $S_i \cup 2T_j$: a strip and two tongues;
- C : a cross.

These sets are structurally stable.

The singular sets are

- $S2S_i \cup 2T_j$: a strip with 2 straps;

- $C2S_i$: a cross with 2 straps;
- $C4S$: a cross with 4 straps,

respectively. Quarters of sets of these types are depicted in Figure 7.

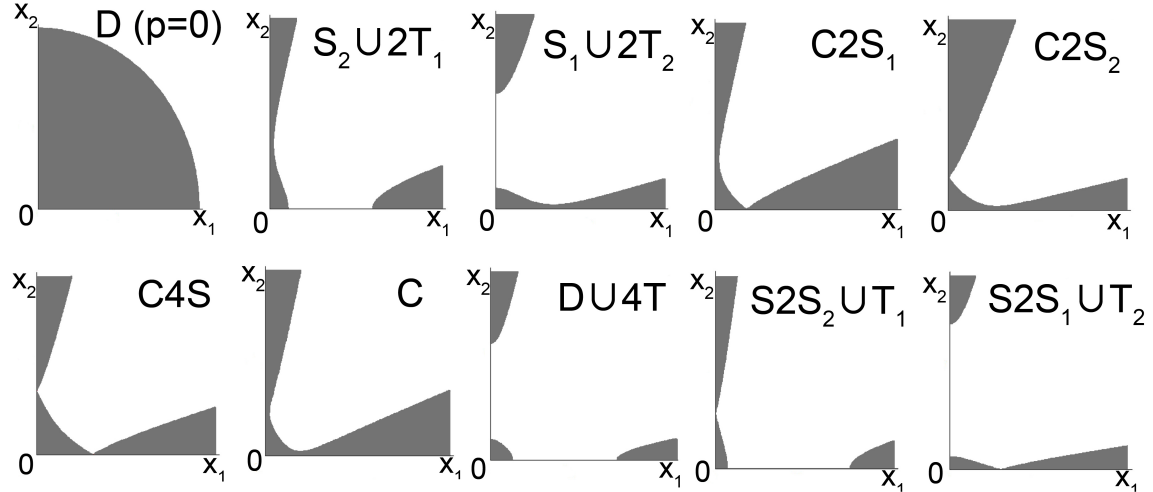


Figure 7. Possible types of equilibria sets.

It is supposed that $b_1 < b_2$, so $p_{+1} > p_{+2}$ and $p_{-1} > p_{-2}$. Thus there are three possible cases of mutual arrangement of p_{-1} and p_{+2} , and so there are three possible ways of the evolution of equilibria sets:

- 1) $p_{+1} > p_{-1} > p_{+2} > p_{-2}$,

$$D \rightarrow D \cup 4T \rightarrow S2S_2 \cup 2T_1 \rightarrow S_2 \cup 2T_1 \rightarrow S2S_2 \cup 2T_1 \rightarrow D \cup 4T \rightarrow S2S_1 \cup 2T_2 \rightarrow S_1 \cup 2T_2 \rightarrow S2S_1 \cup 2T_2 \rightarrow D \cup 4T$$

- 2) $p_{+1} > p_{-1} = p_{+2} > p_{-2}$

$$D \rightarrow D \cup 4T \rightarrow S2S_2 \cup 2T_1 \rightarrow S_2 \cup 2T_1 \rightarrow C4S \rightarrow S_1 \cup 2T_2 \rightarrow S2S_1 \cup 2T_2 \rightarrow D \cup 4T$$

- 3) $p_{+1} > p_{+2} > p_{-1} > p_{-2}$

$$D \rightarrow D \cup 4T \rightarrow S2S_2 \cup 2T_1 \rightarrow S_2 \cup 2T_1 \rightarrow C2S_1 \rightarrow C \rightarrow C2S_2 \rightarrow S_1 \cup 2T_2 \rightarrow S2S_1 \cup 2T_2 \rightarrow D \cup 4T$$

6 Conclusions

In this paper three problems of motion of a heavy point on rotating surfaces under the action of dry friction force were considered. For these problems the equations of motion were obtained and the condition of equilibrium and its dependence on parameters of the system was studied. The evolution of relative equilibria sets was represented graphically.

Investigation is partially supported by RFBR, grant no. 16-0-00625a.

References

Alkhaldi, H.; Ergenzer, C.; Fleissner, F.; Eberhard, P.: Comparison between two different mesh descriptions used for simulation of sieving processes. *Granul. Matter*, 10(3), (2008), 223 – 229.

Biemond, J.; van de Wouw, N.; Nijmeijer, H.: Bifurcations of equilibrium sets in mechanical systems with dry friction. *Physica D*, 241(22), (2012), 1882–1894.

Burov, A.: On bifurcations of relative equilibria of a heavy bead sliding with dry friction on a rotating circle. *Acta mech.*, 212(3-4), (2010), 349–354.

Burov, A.; Shalimova, E.: On the motion of a heavy material point on a rotating sphere (dry friction case). *Regul. Chaot. Dyn.*, 20(3), (2015), 225–233.

Burov, A.; Shalimova, E.: Bifurcations of relative equilibria of a heavy bead on a rotating parabolic bowl with dry friction. *Mechanics of Solids*, 51(4), (2016), 395–405.

Burov, A.; Yakushev, I.: Bifurcations of relative equilibria of a heavy bead on a rotating hoop with dry friction. *J. Appl. Maths Mech.*, 78(5), (2014), 645–655.

Fleissner, F.; Lehnart, A.; Eberhard, P.: Dynamic simulation of sloshing fluid and granular cargo in transport vehicles. *Vehicle Syst. Dyn.*, 48(1), (2010), 3–15.

Ivanov, A.: Bifurcations in systems with friction: Basic models and methods. *Regul. Chaotic Dyn.*, 14(6), (2009), 656–672.

Ivanov, A.: The equilibrium of systems with dry friction. *J. Appl. Maths Mech.*, 79(3), (2015), 217–228.

Joshi, P.; Nigam, K.; E., B. N.: The kenics static mixer: new data and proposed correlations. *Chem. Eng. J.*, 59(3), (1995), 265–271.

Kauderer, H.: *Nichtlineare Mechanik*. Springer-Verlag, Berlin (1958).

Leine, R.; van de Wouw, N.: *Lecture Notes in Applied and Computational Mechanics: Stability and convergence of mechanical systems with unilateral constraints*. Springer, Berlin (2008).

Levi-Civita, T.; Amaldi, U.: *Lezioni di Meccanica Razionale. Volume primo.* Zanichelli, Bologna. (1930).

Magnus, K.: *Schwingungen*. B.G.Teubner, Stuttgart (1976).

Matrosov, V.; Finogenko, I.: The stability of the set of equilibrium positions of autonomous mechanical systems with sliding friction. *J. Appl. Maths Mech.*, 62(6), (1998), 863–871.

Pozharitsky, G.: Stability of equilibria for the systems with dry friction. *J. Appl. Maths Mech.*, 26(1), (1962), 5–14.

van de Wouw, N.; van Den Heuvel, M.; Nijmeijer, H.; van Rooij, J.: Performance of an automatic ball balancer with dry friction. *Int. J. Bifurc. Chaos*, 15(1), (2005), 65–82.

Várkonyi, P.; Or, Y.: Lyapunov stability of a rigid body with two frictional contacts. *arXiv*, [abs/1603.09672](https://arxiv.org/abs/1603.09672).

Address: 1, Michurinckiy prospect, Moscow, 119192, Russia
 email: ekateryna-shalimova@yandex.ru, jtm@narod.ru

Comparison of Numerical Forced Response Predictions with Experimental Results Obtained in a Subsonic Test Turbine Facility

A. Marn, F. Schönleitner, M. Mayr, F. Heitmeir

In order to achieve the ACARE targets regarding reduction of emissions it is essential to reduce fuel consumption drastically. Reducing engine weight is supporting this target and one option to reduce weight is to reduce the overall engine length (shorter shafts, nacelle). However, to achieve a reduction of engine length the spacing between stator and rotor can be minimised, thus changing rotor blade excitation. Related to the axial spacing, a number of excitation mechanisms in respect to the rotor blading have to be considered already during the design process. Based on these facts several setups have been investigated at different engine relevant operating points and axial spacing between stator and rotor in the subsonic test turbine facility for aerodynamic, acoustic, and aeroelastic investigations (STTF-AAAI) at the Institute for Thermal Turbomachinery and Machine Dynamics at Graz University of Technology. In order to avoid upstream effects of supporting struts, these struts are far downstream of the stage which is under investigation.

In this paper the capability to predict forced response vibrations of selected rotor blades is evaluated with experimental results for two different axial gaps between rotor blade and stator vane row. The investigation is done for engine relevant operating conditions. For rotor blade vibration measurements a novel telemetry system in combination with strain gauges is applied. The stage was modelled using the software package ANSYS. Flow fields up and downstream of the turbine stage are analysed and visualised for two axial gaps and compared to the forced response of the blading. Detailed structural dynamic investigations show critical modes during operation which are identified by the telemetry measurements as well. Finally, the influence of the axial spacing regarding the rotor blade excitation and vibration can be elaborated and is prepared to get a better understanding of basic mechanism. The paper shows that reducing axial spacing is a promising option when reducing engine weight. However, prediction of forced response vibrations is still challenging due to the variety of unknown parameters of a real life engine such as coupling stiffness, damping, blade mass, etc.

1 Introduction

Anthropogenic climate change has become more and more evident during the last decades. It is well known that it is primarily caused by emissions of mainly carbon dioxide. Therefore, it is essential to reduce the emissions of pollutants at every region where they are formed. That means that engineers have to develop techniques and/or strategies to reduce fuel consumption that is directly linked to the formation of carbon dioxide. In case of air traffic aero engines can be named as the only polluters and here it is highly necessary to set measures when considering that the number of passengers is growing fast. There are mainly two options to decrease fuel consumption of aero engines. Firstly, increase of efficiency which is indeed challenging and secondly decrease of engine weight. The latter one can be "easily" achieved by e.g. reducing axial spacing between blade and vane rows or increasing stage loading by decreasing the number of vane and blade counts. However, as simple these measures seem to be many new problems have to be accounted for. E.g. smaller axial gaps lead to altered blade-vane interaction and therefore, a more reliable forced response prediction is crucial in order to ensure a safe design of aero engines. Aerodynamic excitation and response of the blading is dependent on the damping especially close to and in resonance. However, it is known that in general the available aerodynamic theories are less reliable for evaluating the (out-of-phase with displacement) damping forces than those forces in-phase with displacement (Acum, 1988). Nevertheless, the aero elastic response is essential to the analysis of fatigue of turbomachinery blades. The question of crack initiation, propagation and destructive failure cannot be addressed without giving attention to the type of excitation, damping and the parametric dependencies on the unsteady aerodynamic forces. In resonance (blade eigenfrequency=excitation frequency) damping is responsible for limiting vibration amplitudes, that means damping also limits the cyclic stresses in oscillating blades and thus has a direct (positive) impact on high cycle fatigue.

In turbomachines damping is the sum of structural damping, material damping, and aerodynamic damping, which is a phenomenon that occurs as a consequence of the blade vibration and its interaction with the flow. While structural damping is always positive and limits the vibration amplitude, and material damping is in general negligibly small, aerodynamic damping can become negative and instead of reducing the amplitudes it would induce a self-excited condition where the vibration amplitude increases rapidly and leads to failure of the complete engine. This is referred as flutter. (Mayorca, 2011) stated that a closer attention should be given to the aerodynamic damping (numerical and experimental) predictions. This implies a major challenge since it requires high quality test data that allows a one to one validation only accounting for the aerodynamic damping. However, there is only a minimal amount of published experimental data at engine conditions (Kielb et al., 2001)).

Within the last years a lot of literature became available dealing with numerical investigations of flutter or fluid-structure-interaction, respectively. In the following only a few of them are cited. For example (Carstens et al., 2001) who stated that non-linear fluid-structure-interaction may significantly influence the aerodynamic damping and hence shifts the stability boundaries. (Cinnella et al., 2004) presented an accurate and efficient numerical method for turbomachinery flutter and simulated the 11th Aeroelastic Standard Configuration, which is a well known test case. They same authors extended the afore mentioned numerical method to the computation of 3D problems. (Petrie-Repar et al., 2014) presented a flutter analysis of a long steam turbine blade. The logarithmic decrements of the aeroelastic modes were calculated. (Rzadkowski et al., 2006) presented numerical simulations of 3D viscous flutter and compared the results with the available experimental results. The calculations were carried out for bending oscillations of the 11th Aeroelastic Standard Configuration. Recently, fully coupled fluid-structure-interaction and flutter simulations were conducted as reported by (Tateishi, et al., 2014). (Srinivasan, 1997), (Marshall et al., 1996). (Hall et al., 2005) surveyed papers investigating aeroelastic problems. Aerodynamic damping has been studied more carefully by (Chiang et al., 1993) and (Abhari et al., 1997). (Li et al., 2003) conducted a parameter study numerically and showed that the rotor aerodynamic damping could be changed by up to 100% when varying the rotor-stator gap. (Yamaguchi et al., 2000) presented an analytical approach to predict flutter limits of a thin sheet in high speed flow. (Yamaguchi et al., 2000) also presented experimental results and made a comparison between the prediction and the experimental results. Compared to the amount of numerical work there have been only few experiments regarding to axial turbomachinery conducted. (Stepanov et al., 2014) investigated three different counter rotating fan models, aerodynamically and acoustically. However, the authors had the opportunity to measure blade vibrations by means of tip-timing measurements and strain gauges. (Gubran et al., 2014) investigated three different blade faults of a generic rotor and showed the influence of the faults on the spectrum. (Hentschel et al., 2014) presented an experimental setup for specimen specific structural damping determination in a vacuum chamber. Further, different clamping mechanisms, temperature, and static stress are applied and the results are compared to each other. Also (Kubin et al., 2013) measured structural damping for different blade couplings and compared the results to a new type of blading. (Vega et al., 2014) have shown the stabilizing effect of rotor blades in pairs experimentally and numerically. The authors stated that there is a shielding effect of the neighbouring rotor blade. (Heinz et al., 2010) measured mechanical and aerodynamic damping parameters for different mass flow densities (including vacuum). In a next step (Heinz et al., 2011) showed the influence of mistuning on the circumferential blade amplitude distribution at different operating points. (Glodic et al., 2011) investigated experimentally and numerically the effect of aerodynamic damping in an oscillating low-pressure turbine cascade taking mistuning into account. (Vogt et al., 2007) used the same cascade to show that the main influence of a vibrating blade is limited to the adjacent blades. (Petrov, 2010) and (Petrov, 2011) investigated the effect of mistuning on aerodynamic damping and explained the effect that for very low engine orders the amplification factor may become even lower than one. In the survey of (Ewins, 1991) many papers on the effect of mistuning on flutter are listed, also with the uniform conclusion that mistuning always raises the flutter threshold. A current overview of mistuning literature can be found in the review paper of (Castanier, et al., 2006), including intentional mistuning. (Kielb et al., 2001) presented some results of an experimental method and data analysis study of multiple engine relevant damping sources. The contributions of aerodynamic and structural damping for several vibration modes were determined. (Nowinsky et al., 2000) presented a series of experiments in an annular cascade to investigate torsional flutter in low-pressure turbines. They showed that relatively small changes to the location of the torsion axis had a dramatic effect on the stability behaviour. (Kovats, 1980) determined time histories of aerodynamic forces interferometrically and showed experimentally that at large negative flow incidence blades are becoming unstable in the twist mode. Experimental research in the field of forced response for a fan under engine representative conditions was performed in detail by (Manwaring et al., 1991) and (Manwaring et al., 1990). The experiments quantified the effect of the inlet flow conditions and the blade pressure distribution on the vibratory response of the blades. (Chen et al., 2012) investigated the combined effects of both axial gap and blade count ratio numerically. They have found that the excitation of a downstream rotor is reduced when increasing the blade count ratio. The excitation is also reduced exponentially with increased axial gap. However, the response of the blades is not analysed in their paper.

There are a lot of papers dealing with damping, mistuning vibration suppression but there is not much about measured response of low pressure turbine rotor blades at engine realistic conditions. This paper focuses on that response of the rotor blades and compares experimental and numerical results of different axial gaps between rotor and stator. The aim of this paper is to show the differences one have to deal with between experiments and simulations due to necessary simplifications of the numerical model.

2 Experimental Facility and Instrumentation

Test Facility

The Institute for Thermal Turbomachinery and Machine Dynamics at Graz University of Technology operates a 3MW compressor station in order to supply a couple of test facilities continuously with pressurized air. For the subsonic turbine test facility the maximum pressure ratio is limited to 2. The maximum mass flow rate is 15 kg/s at a temperature at stage inlet of 100°C. This inlet temperature can be adjusted by coolers within a wide range. The pressurized air enters the facility through a spiral inlet casing where the flow turns into axial direction. Within this spiral inlet casing the front bearing of the overhung-type turbine shaft is mounted. The shaft is coupled to a water brake.

In order to provide well defined and uniform inflow conditions a de-swirler and a perforated plate is located upstream of the stage inlet. Further, upstream of the stage, inlet guide vanes (IGV) can be found that should simulate additional wakes of other upstream low pressure turbine stages. The air leaves the rig through an acoustic measurement section, supporting struts, exhaust casing, and the exhaust stack to ambient. The rig is designed to be able to perform aerodynamic, acoustic and aeroelastic investigations (AAAI). A detailed description of the STTF-AAAI is given in (Moser, et al., 2007). To be able to change the distance between blade/vane rows interchangeable rings (rings upstream of IGV and rotor in Figure 1) are available and have been changed to adjust the axial gap between stator and rotor. However, the rotor was always on the same axial position, only IGVs and stator vanes have been moved upstream. Also, the relative position of the five-hole-probe measurement planes A and C have been the same.

Turbine Stage

The aerodynamic design of the low pressure turbine (LPT) stage and the IGVs was performed by MTU Aero Engines. Considerable effort was put into the adjustment of relevant model parameters to reproduce the full scale LPT configuration. The turbine diameter is approximately half of that of a commercial aero engine LPT and therefore the rig is operated at higher rotational speeds. The blade count ratio (BCR) is chosen to fulfil an acoustic design intent. A meridional section of the rig is shown in Figure 1. The rig is characterised by a high aspect ratio unshrouded rotor. Relevant geometry parameters can be seen in the upper half of Table 1.

For this investigation three different operating points have been chosen. Operating Point OP1 represents an acoustically relevant operating point ("approach"). For this investigation two additional operating points OP2 and OP3 were chosen. With OP2 the behaviour of the turbine stage at the same pressure ratio as for OP1 but lower rotational speeds was investigated. Further, blade vibrations have been measured at the same lower rotational speed as for OP2 but at a lower stage total pressure of 1.14 (=OP3).

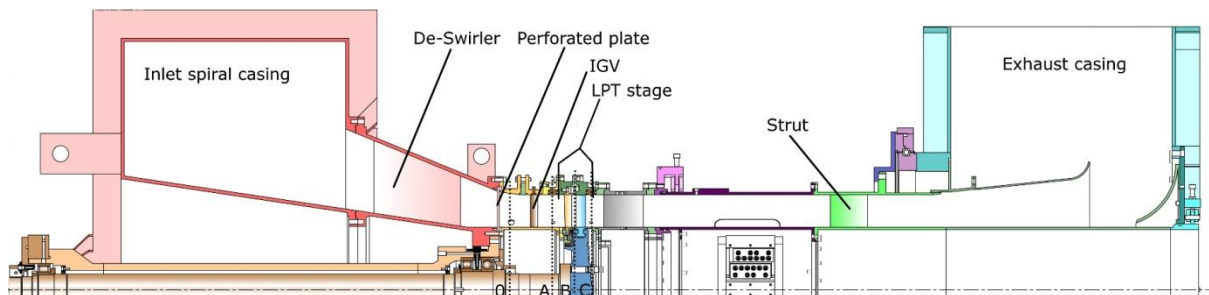


Figure 1. Meridional section of the STTF-AAAI

Operating Conditions

Based on the intended use of the LPT rig for aeroelastic, acoustic and aerodynamic investigations, the main operating points are selected according to the typical noise certification points. They have been defined using an aero design point of the last stage LPT, derived from current LPT design practice using scaling along reduced speed, reduced mass flow (both referred to 288.15 K and 1013.25 mbar) and pressure ratio. For this investigation

the operating point approach (=OP1) was chosen. Based on that point the rotational speed was reduced to investigate "near-resonance" behaviour at the same stage total pressure and temperature (=OP2). A third operating point (OP3) was investigated with decreased total pressure at the same temperature and rotational speed. The lower half of Table 1 shows the operating conditions. Although, the reduced values for the rotational speed are given, in the experiment it was crucial to keep also the mechanical rotational speed constant for each operating point. Also, all vibration measurements have been performed at the same day in order to have the same ambient pressure. That is important to ensure that different stage pressure ratios are only related to the inlet pressure.

Table 1. Geometry details and operating conditions

Geometry details	
Number of blades/vanes	
IGV	83
Stator	96
Rotor	72
Tip gap to blade height ratio	1.0%
Hub to tip radius ratio	$\approx 2/3$
Operating conditions	
Reduced mass flow OP3	6.86kg/s
Reduced rotational speed OP2 and OP3	3000rpm
Reduced mass flow OP1	6.94kg/s
Reduced rotational speed OP1	3653rpm
Stage pressure ratio OP3	1.14
Stage pressure ratio OP1 and OP2	1.16
Stage total inlet temperature OP1 and OP2	100°C

Instrumentation

Five-hole-probes (from Institute of Jet Propulsion and Turbomachinery, RWTH Aachen University) with a probe head of 2.5 mm diameter were applied in measurement plane C (see Figure 1). The probes are calibrated for Mach numbers between 0.1 and 0.8, yaw angles between -20 deg and +20 deg, pitch angles between -16 deg and +20 deg. Negative values of the yaw angle indicate a counter-rotating flow and negative values of the pitch angle indicate the flow direction towards the hub.

The correlation between the calibration characteristics and the value to be measured is given by a multi-parameter approximation.

The axial positions of measurement planes can be seen in Figure 1. Plane C is located downstream of the rotor trailing edge (TE) in a distance of 60% of the axial rotor blade chord length.

The grid covers two stator pitches and about 95% passage height. Traversing was done along radial lines. In each measurement point the probe was turned into the flow to reach the highest accuracy and to ensure to be always within the calibration range of the probe (with these probes it would not have been necessary, if one ensures to be always within the calibration range). Unfortunately, it was not possible to reliable measure in plane B between stator and rotor because of the very small (engine realistic) axial gap.

The rotor blading which had to be instrumented was already characterized and results presented by (Schönleitner, et al., 2015). A number of numerical and experimental studies showed the optimum strain gauge positions for blade vibration measurements.

Basically, the telemetry system used in the experiments provides 12 ports for strain gauge measurements. Therefore, 12 strain gauges were applied on different blades of the rotor and on three different blade surface positions near maximum strain positions for eigenmodes. Additional to that 12 ports for strain gauge measurements the telemetry system provides 8 ports for temperature measurements and is extendable with pressure sensors. The maximum sampling rate is 400 ksamples/second with a simultaneous data acquisition of 12bit. The strain gauge data is transmitted by rotor stator principle via antenna outside of the test rig where it is recorded. Further information can be found in (Schönleitner, et al., 2015). The system is able to operate at rotational speeds up to 11000rpm and temperature ranges up to 150°C. Data is acquired for the investigations presented in this paper with a sampling rate of 204.8 ksamples/second.

For this investigation only one strain gauge SG3 was evaluated. SG3 is marked in Figure 2 with a circle.

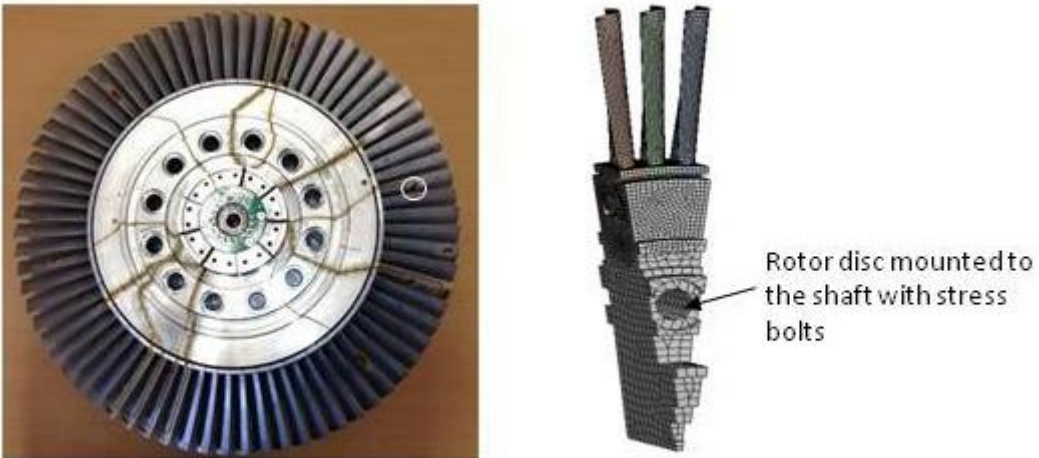


Figure 2. Rotor strain gauge application and FE model

Measurement Uncertainties

Instrumentation has to meet not only high demands on accuracy and repeatability but requires higher numbers of channels, too. Therefore, the measurement system is made up by eleven multi channel pressure transducers PSI 9016 with a total amount of 176 channels and an accuracy of 0.05% full scale and four National Instruments Field Point FP-TC-120 eight-channel thermocouple input modules and one FP-RTD-122 resistance thermometer input module. Table 2 shows the measurement uncertainties (within a 95% confidence interval) of the five-hole-probe measurements. From these measurements the Mach number Ma , flow angle α as well as static p and total pressure p_t is obtained. The uncertainty of these values are positive and negative deviations and contain the error due to the approximation, random error and the systematic error of the PSI Modules. The difference between the positive and the negative direction is a result of the multiparameter approximation, because the calibration surface is not symmetrical. The measurement uncertainties of the static pressure and the total pressure at rig and stage inlet are ± 1 mbar.

The variation of speed is below 0.2% of the current operating speed and the measurement uncertainty of the temperature measurement is about ± 0.5 K.

The variation of the operating parameters (pressure ratio, corrected speed, speed, total pressure and temperature at rig inlet) between different measurement days has been below 0.5%.

Table 2. Measurement uncertainties of the five-hole-probe

Ma	+0.006	-0.003	[/]
α	+0.5	-0.08	[deg]
p_t	+3.3	-3.0	[mbar]
p	+5.3	-5.2	[mbar]

3 Numerical Setup

Numerical simulations have been performed using ANSYS 16.2. CFx was used for fluid dynamic simulations and ANSYS mechanical for the structural simulation. In order to capture the effect of the deformed blades on the fluid flow this deformation has to be feed back into the CFD solver and therefore a two-way coupled fluid-structure-interaction simulation was performed.

For the transient CFD simulation (time step: 0.000025 [s]) 4 stator vanes and 3 rotor blades have been modelled for periodicity reasons, although the calculated frequencies are about 1% higher compared to a five blade model that also contains a solid part between two holes. The IGV's have not been modelled to reduce mesh size. As boundary conditions a constant backpressure at outlet was set according to measurement results. Measured total pressure, total temperature, pitch angle, and yaw angle distribution at inlet are given (see Figure 4) as well as turbulence intensity at inlet of 10% was set.

The CFD mesh consists of approx. 6.3 million hexahedral elements. As turbulence model $k - \omega$ SST with automatic wall functions ($y^+ \sim 60$) was applied.

The FE mesh for the transient structural (time step 0.0002451 [s]) computation consists of approx. 75000 elements. The blade (made of aluminium) is modelled with hexahedral elements and the disc with tetrahedral elements. The contact type between rotor disc and blades is set as frictional ($\mu = 0.19$) and bonded (see Figure 3) and between the blades as frictional ($\mu = 1.05$). A study showed that the combination frictional and bonded with that specific standard values of μ reproduces best agreement between calculation and experiment. Further, it

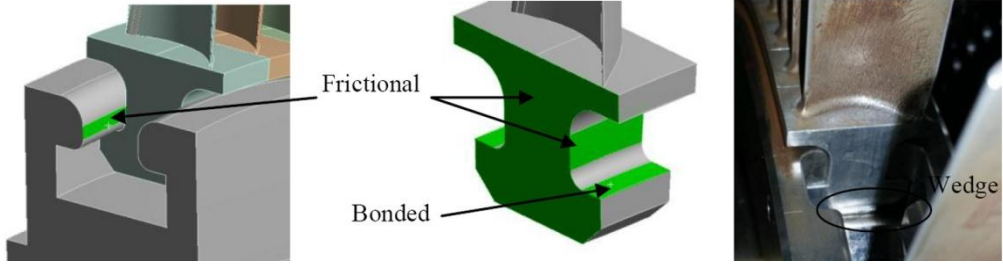


Figure 3. Contact types

has to be mentioned that in that case the blade is fixed with a wedge beneath the root pressing the surfaces together in radial direction. Surfaces with slight contact are modelled as frictional contact.

4 Excitation and Eigenfrequencies

According to (Tyler, et al., 1962) following pressure patterns can occur (assuming zero swirl):

$$m = n \cdot B + k \cdot V; \quad k = -\infty, \dots, -1, 0, 1, \dots + \infty \quad (1)$$

For multiple blade/vane rows this equation can be extended to:

$$m = n \cdot B + k_1 \cdot V_1 + k_2 \cdot V_2 \quad (2)$$

Again $k_{1,2} = -\infty, \dots, -1, 0, 1, \dots + \infty$. V_1 is the number of stator vanes and V_2 the number of IGVs. Table 3 lists the main airfoil interaction modes m and the respective frequency for the easiest case of a non-spinning pressure pattern. The left side shows the interaction modes for $n=0$ and the right side for $n=1$. The sign indicates the sense of rotation of the pressure pattern. Every peak in the measured spectra in the results section belongs to one of these calculated values. That means that the strain gauges have been able to detect also very small excitations resulting in small response amplitudes at the respective frequency. Due to the large number of vanes (IGV and stator) and blades a lot of interaction modes are possible as can be seen in the following tables. Here it should be mentioned that the higher the mode number the less energy the mode carries.

Table 3. Airfoil interaction modes

OP1				OP2 and OP3			
m	k_1	k_2	Frequency [Hz]	m	k_1	k_2	Frequency [Hz]
140	-2	4	9660	140	-2	4	7933
57	-2	3	3933	57	-2	3	3230
-26	-2	2	-1794	-26	-2	2	-1473
-109	-2	1	-7521	-109	-2	1	-6177
-96	-1	0	-6624	-96	-1	0	-5440
-13	-1	1	-897	-13	-1	1	-737
70	-1	2	4830	70	-1	2	3967
153	-1	3	10557	153	-1	3	8670
-166	0	-2	-11454	-166	0	-2	-9407
-83	0	-1	-5727	-83	0	-1	-4703
0	0	0	0	0	0	0	0
83	0	1	5727	83	0	1	4703
166	0	2	11454	166	0	2	9407
-153	1	-3	-10557	-153	1	-3	-8670
-70	1	-2	-4830	-70	1	-2	-3967
13	1	-1	897	13	1	-1	737
96	1	0	6624	96	1	0	5440
109	2	-2	7521	109	2	-2	6177
26	2	-2	1794	26	2	-2	1473
-57	2	-3	-3933	-57	2	-3	-3230
-140	2	-4	-9660	-140	2	-4	-7933

5 Results and Discussion

Figure 4 shows the measured stage inlet conditions (plane A). On the upper left hand side the total pressure distribution is depicted. The IGV wakes can be clearly identified. The total temperature distribution can be seen on the right hand side. It is quite uniform and constant with minor variations. The yaw angle distribution can be

seen at bottom on the left side and at the bottom right the pitch angle is depicted. From these four parameters the inlet boundary conditions for Ansys CFx have been deduced.

Figure 6 shows measurement results obtained by one strain gauge indicated in Figure 2. The spectrum of the larger gap is intentionally shifted by 100 Hz for the sake of clarity. Details of that results are given in (Marn et al., 2016). The percentage in Figure 6 middle gives the increase in amplitudes regarding to OP3. Table 4 shows the predicted eigenfrequencies by means of a numerical modal analysis performed prior to the beginning of the test campaign. It can be seen that all peaks in the frequency spectra (Figure 6) except at 2718 Hz and 6624 Hz belong to blade-disc vibrations close to resonance. The highest amplitude in the spectra at 5540 Hz for OP3 and OP2 is due to rotor-stator interaction (engine order 96).

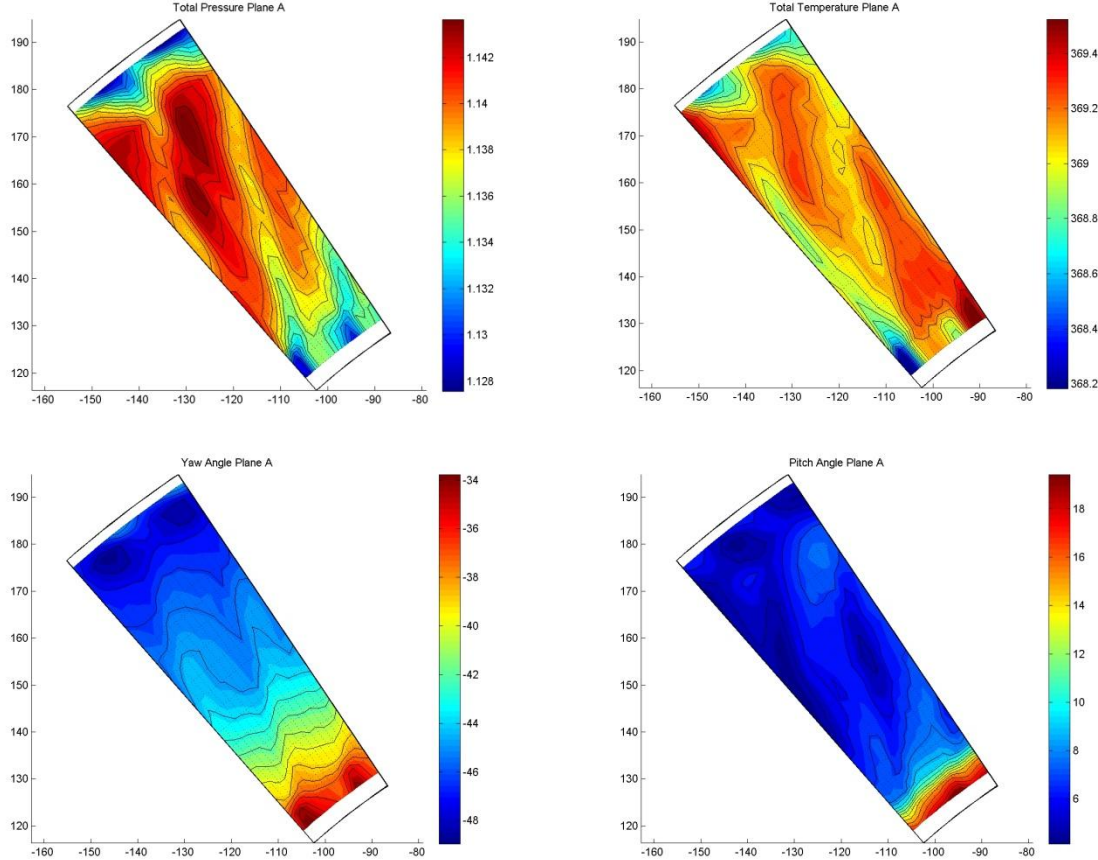


Figure 4. Measured stage inlet condition

Figure 5 shows an example of a time snap shot of the total pressure distribution in plane C downstream of the rotor. On the left side the numerical result is depicted and on the right side the experimental result is shown. Except the absolute level the simulations is able to capture the flow physics very well. It is most essential to capture the flow physics in order to get realistic structural dynamic results.

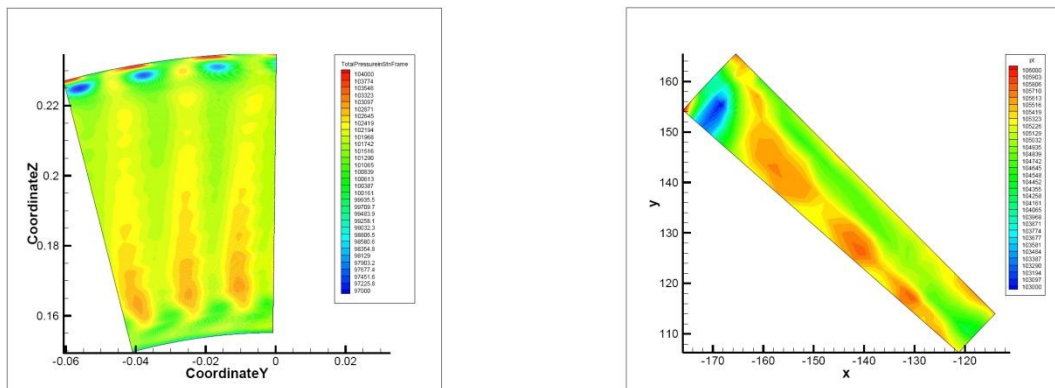


Figure 5. Total pressure plane C; left: numerical result and right: experiment

Table 4. Predicted eigenfrequencies

Mode No.	Operating Point		
	0rpm	OP1	OP2&3
1 st	923 [Hz]	955 [Hz]	939 [Hz]
2 nd	1648 [Hz]	1649 [Hz]	1648 [Hz]
3 rd	3270 [Hz]	3303 [Hz]	3274 [Hz]
4 th	5404 [Hz]	5472 [Hz]	5424 [Hz]
5 th	8180 [Hz]	8288 [Hz]	8223 [Hz]

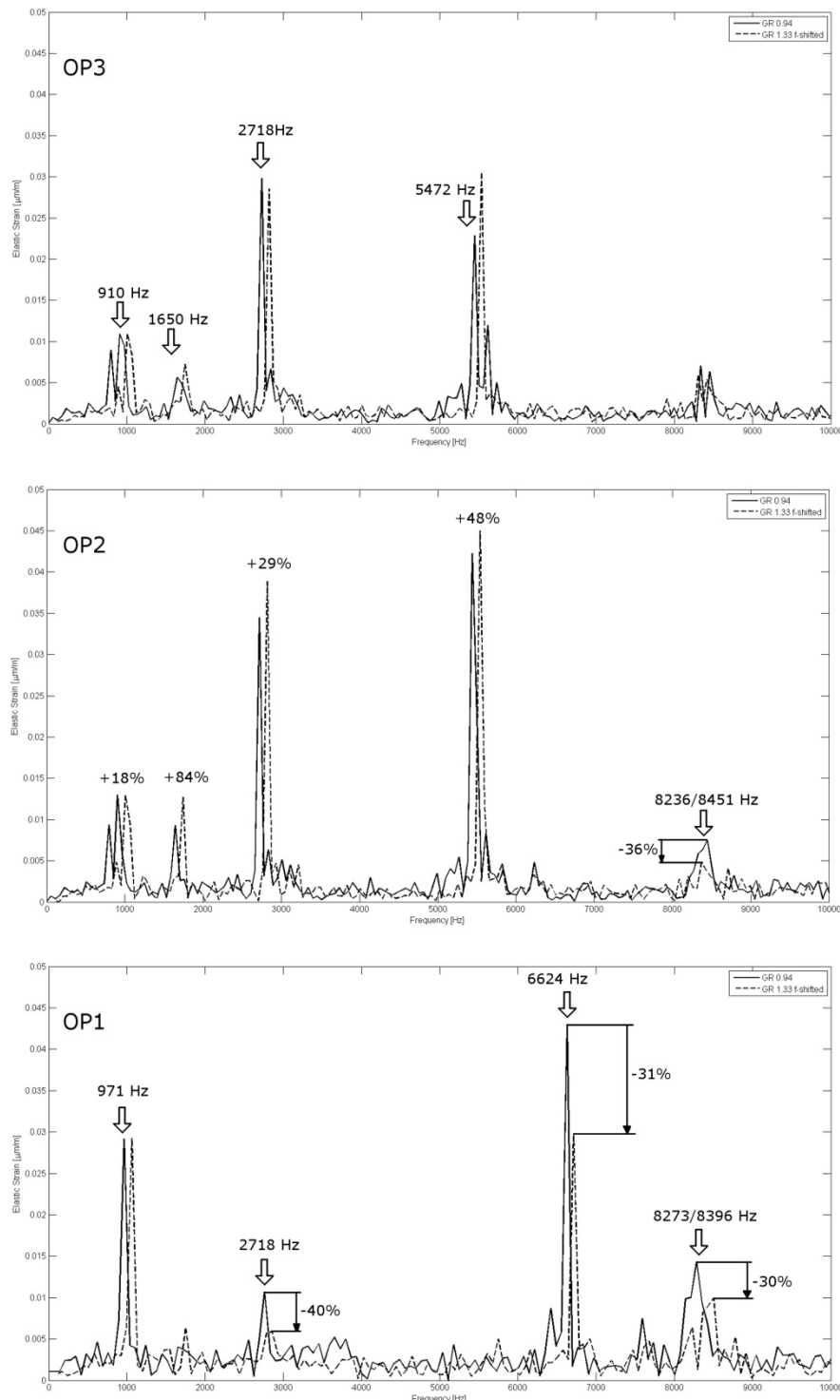


Figure 6. Spectra (experiment) for OP3 (top), OP2 (middle), and OP1 (bottom)

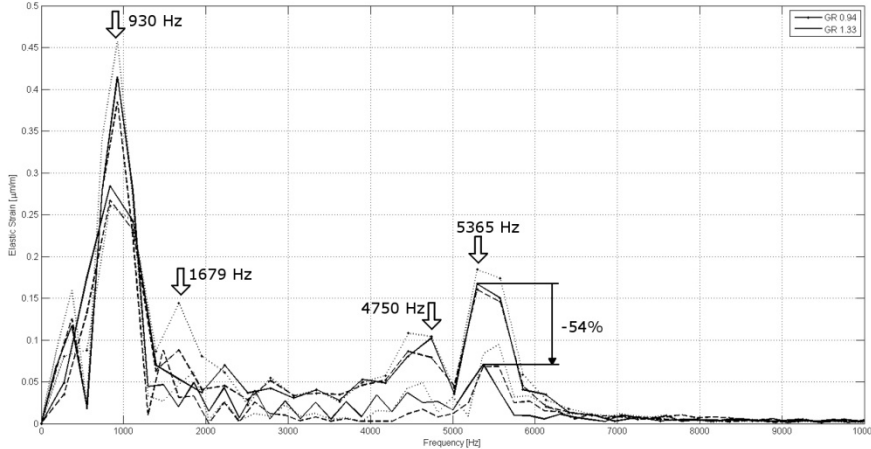


Figure 7. Spectra (simulation) for OP3

Figure 7 shows the spectrum for OP3 of the blade vibration evaluated at the same position of the strain gauge in the experiment. Depicted are the spectra for all three blades. Also both axial gaps have been evaluated. Firstly, it can be seen that the simulation overpredicts the vibration amplitudes tremendously, especially at ~ 930 Hz. Although, structural damping parameters have been set according to the experiment the amplitude is much too high. That shows clearly, that the aerodynamic damping (neglecting material damping) is not predicted in the right order of magnitude and/or that the excitation force is much stronger than in the experiment. The latter one could be due to less mixing of the IGV or stator wakes and other upstream flow features. Also the amplitude for the small gap is predicted to be lower than for the larger gap, but it seems only that due to the frequency step the amplitude is not captured. All blades show a peak at 1679 Hz, which corresponds to the 2nd mode. In the simulation a large amplitude at 5365 Hz is visible that is close to a excitation frequency due to a higher harmonic of the rotor-IGV interaction ($m=-94$). Although, the IGVs have not been modelled but are considered in the inlet boundary conditions this peak can be reproduced. However, in the measurements this peak does not appear. Again, this fact shows that although the flow field at the rotor exit shows a good agreement with the measurements the wakes of the IGVs may be stronger in the simulation and strongly excite the rotor blades. Further, it seems that the rotor-stator interaction ($m=-96$) resulting in a frequency of 5440 Hz is not resolved but is part of the broad band peak at 5365 Hz. This peak could be therefore a combined effect of rotor-stator as well as rotor-IGV interaction. The peak at 2718 Hz visible in the experiment belongs to the rotor shaft and therefore it is obvious that the simulation cannot predict this peak due to the necessary simplification of the simulation model. The simulation also predicts a peak at 4750 Hz which is close to 4703 Hz that is again due to rotor-IGV interaction. The experiment subsequently does not show this peak for the same reason as for the peak at 5365 Hz. Further, the simulation does not predict any frequencies higher than approx. 6500 Hz. The experiment also shows clearly a peak at 8263 Hz that is close to the 5th mode. Whether the experiment nor the simulation shows the blade passing frequency of 4080 Hz at OP2 and OP3.

6 Conclusion

Blade vibration measurements and aerodynamic measurements have been conducted in the subsonic test turbine facility for aerodynamic, acoustic and aeroelastic investigations. Additionally, a coupled fluid structure interaction simulations was performed for one operating point and two different gaps. The aim of this investigation was to compare the numerical with experimental results. It is shown that the simulation was able to capture the flow physics downstream of the rotor quite well but totally failed to predict the vibration amplitudes. This is mainly due to the fact that some flow features such as the IGV wakes are more or less mixed out in the experiment while they are still dominating the flow field in the simulation. The reason is simply that some very important inlet boundary conditions are usually not known. Although, in this case turbulence intensity (usually it is also unknown) was set to the level of the experiment the turbulence length scale is unknown. Further, when simplifying the model for the simulation it should be always kept in mind that many excitation frequencies cannot be captured due to the simplifications. E.g. torsional vibrations of the shaft can be measured as blade bending vibrations. From that investigation it can be concluded that the overall agreement between experiment and simulation is poor when considering the numerical effort.

7 Acknowledgements

This work has been carried out in the framework of the national funded TAKE-OFF programme within the research project AdMoNt (contract no. 839008) regarding aeroelastic investigations of low pressure turbine blading at Graz University of Technology at the Institute for Thermal Turbomachinery and Machine Dynamics. The authors therefore want to thank the Austrian Research Promotion Agency (FFG) and the Austrian Ministry for Transport, Innovation and Technology (bmvit) for funding this project. The authors would like to thank Prof. Dr.techn. H.P. Pirker for his great support and the discussions during all experimental investigations and for operating the compressor station.

References

Abhari, R. and Giles, M.: A Navier-Stokes Analysis of Airfoils in Oscillating Transonic Cascades for the Prediction of Aerodynamic Damping. *ASME Journal of Turbomachinery*, vol. 119, January 1997.

Acum, W.: The Comparison of Theory and Experiment of Oscillating Wings. *AGARD Manual on Aeroelasticity in Axial Flow Turbomachines*, vol. 2, 1988, Chapter 10.

Carstens, V. and Belz, J.: Numerical Investigation of Nonlinear Fluid-Structure Interaction in Vibrating Compressor Blades. *ASME Journal of Turbomachinery*, vol. 123, pp. 402-408, April 2001.

Castanier, M. and Pierre, C.: Modeling and Analysis of Mistuned Bladed Disk Vibration: Status and Emerging Directions. *Journal of Propulsion and Power*, vol. 22, no. 2, pp. 384-396, 2006.

Chen, T.; Patel, K.; Millington, P.: Combined Effects of Both Axial Gap and Blade Count Ratio on the Unsteady Forces of a Steam Turbine Stage. *Proceedings of the ASME TurboExpo*, 2012, ASME Paper GT2012-68874.

Chiang, H. and Kielb, R.: An Analysis System for Blade Forced Response. *ASME Journal of Engineering for Gas Turbines and Power*, vol. 115, October 1993.

Cinnella, P.; De Palma, P.; Pascazio, G., Napolitano, M.: A Numerical Method for Turbomachinery Aeroelasticity. *ASME Journal of Turbomachinery*, vol. 126, pp. 310-315, April 2004.

Ewins, D.: The Effect of Blade Mistuning on Vibration Response – A Survey. IFToMM Conference on Theory of Machines and Mechanisms, 1991.

Glodic, N.; Vogt, D.; Fransson, T.: Experimental and Numerical Investigation of Mistuned Aerodynamic Influence Coefficients in an Oscillating LPT Cascade. *Proceedings of the ASME TurboExpo*, 2011, ASME Paper GT2011-46283.

Gubran, A. and Sinha, J.: Comparison between Long and Short Blade Vibration Using Shaft Instantaneous Angular Speed in Rotating Machine. *Proceedings of ASME TurboExpo*, 2014, ASME Paper GT2014-25904.

Hall, K.; Kielb, R.; Ekici, K.; Thomas, J.: Recent Advancements in Turbomachinery Aeroelastic Analysis. *Proc. 43rd AIAA Aerospace Sciences Meeting and Exhibit*, 2005, AIAA 2005-0014.

Heinz, C.; Schatz, M.; Casey, M.; Stürer, H.: Experimental and Analytical Investigation of a Low Pressure Model Turbine During Forced Response Excitation. *Proceedings of the ASME TurboExpo*, 2010, ASME Paper GT2010-22146.

Heinz, C.; Schatz, M.; Stürer, H.; Casey, M.: Impact of Mistuning on the Vibration Behaviour of the Last Stage in a Model Three Stage Low Pressure Steam Turbine. *Proceedings of ASME TurboExpo*, 2011, ASME Paper GT2011-45784.

Hentschel, O.P.; Panning-von Scheidt, L.; Wallaschek, J.; Denk, M.; Masserey, P.-A.: Influential Parameters on Structural Damping Values of Turbine Blades. *Proceedings of ASME TurboExpo*, 2014, ASME Paper GT2014-25656.

Kielb, J. and Abhari, R.: Experimental Study of Aerodynamic and Structural Damping in a Full-Scale Rotating Turbine. *Proceedings of the ASME TurboExpo*, 2001, 2001-GT-0262.

Kovats, Z.: Interferometrically Measured Aerodynamic Forces on a Vibrating Turbine Blade Group, *Journal of Engineering for Power*, vol. 102, July 1980.

Z. Kubin, Z.; Polreich, V.; Cerny, V.; Babkova, P.; Prchlik, L.: Damping Identification and its Comparison For Various Types of Blade Couplings. *Proceedings of ASME TurboExpo*, 2013, ASME Paper GT2013-95438.

Li, H.D. and He, L.: Blade Aerodynamic Damping Variation with Rotor-Stator Gap-A Computational Study Using Singe-Passage Approach. *Proceedings of ASME TurboExpo*, 2003, ASME Paper GT2003-38199.

Manwaring, S.R. and Fleeter, S.: Forcing Function Effects on Rotor Aerodynamic Response. *Journal of Turbomachinery*, vol. 113, no. 2, 1991.

Manwaring, S.R. and Fleeter, S.: Inlet Distortion Generated Periodic Aerodynamic Rotor Response. *Journal of Turbomachinery*, vol. 112, no. 2, pp. 298-307, 1990.

Marn, A.; Schönleitner, F.; Mayr, M.; Selic, T.; Heitmeir, F.: On the Effect of Axial Spacing Between Rotor and Stator onto the Blade Vibrations of a Low Pressure Turbine Stage at Engine Relevant Operating Conditions. *Proceedings of the ASME TurboExpo*, pp. 1-13, 2016, ASME Paper GT2016-56069.

Marshall, J. and Imregun, M.: A Review of Aeroelasticity Methods with Emphasis on Turbomachinery Applications. *Journal of Fluids and Structures*, vol. 10, pp. 237-267, 1996.

Mayorca, M.A.: Numerical Methods for Turbomachinery Aeromechanical Predictions. Stockholm, Sweden, 2011, Doctoral Thesis.

Moser, M.; Kahl, G.; Kulhanek, G.; Heitmeir, F.: *Construction of a Subsonic Test Turbine Facility for Experimental Investigations of Sound Generation and Propagation for Low Pressure Turbines*. Beijing, China, ISABE-2007-1366, 2007.

Nowinsky, M. and Panovsky, J.: Flutter Mechanisms in Low Pressure Turbine Blades. *Journal of Turbomachinery*, vol. 122, January 2000.

Petrie-Repar, P.; Makhnov, V.; Shabrov, N.; Smirnov, E.; Galaev, S.; Eliseev, K.: Advanced Flutter Analysis of a Long Shrouded Steam Turbine Blade. *Proceedings of ASME TurboExpo*, 2014, ASME Paper GT2014-26874.

Petrov, E.P.: A Method for Forced Response Analysis of Mistuned Bladed Discs with Aerodynamic Effects Included. *Journal of Engineering for Gas Turbines and Power*, vol. 132, pp. 062502-1/-10, June 2010.

Petrov, E.P.: Reduction of Forced Response Levels for Bladed Discs by Mistuning: Overview of the Phenomenon. *Journal of Engineering for Gas Turbines and Power*, vol. 133, pp. 072501-1/-10, July 2011.

Rzadkowski, R.; Gnesin, V.; Kolodyazhnaya, L.: 3D Viscous Flutter in Turbomachinery Cascade by Godynov-Kolgan Method. *ASME TurboExpo*, 2006, ASME Paper GT2006-90157.

F. Schönleitner, F.; Selic, T.; Traussnig, L.; Heitmeir, F.; Marn, A.: Experimental Blade Vibration Measurements on Rotating Turbomachinery. 20th Blade Mechanics Seminar, 2015.

Schönleitner, F.; Traussnig, L.; Heitmeir, F.; Marn, A.: Modal Characteristics, Strain Gage Setup and 1-way FSI of a Low Pressure Turbine Rotor as Preparation for Upcoming Experimental Aeroelastic Investigations. *Proceedings of the ASME TurboExpo*, 2015, ASME Paper GT2015-42717.

Srinivasan, A.V.: Flutter and Resonant Vibration Characteristics of Engine Blades, *Journal of Engineering for Gas Turbine and Power*, vol.119, pp. 741-775, October 1997.

Stepanov, A.; Fateev, V.; Milesin, V.: Study of Rotor Vibration Behavior of Counter Rotating Fan Models. *Proceedings of ASME TurboExpo*, 2014, ASME Paper GT2014 26310.

Tateishi, A.; Watanabe, T.; Himeno, T.; Inoue, C.: Multimode Flutter Analysis of Transonic Fan Using FSI Simulation. *Proceedings of ASME TurboExpo*, 2014, ASME Paper GT2014-26702.

Tyler J.M. and Sofrin, T.G.: Axial Flow Compressor Noise Studies. *SAE Transactions*, vol. 70, pp. 309-332, 1962.

Vega, A.; Corral, R.; Zanker, A.; Ott, P.: Experimental and Numerical Assessment of the Aeroelastic Stability of Blade Pair Packages. *Proceedings of ASME TurboExpo*, 2014, ASME Paper GT2014-25607.

Vogt, D.M. and Fransson, T.: Experimental Investigation of Mode Shape Sensitivity of an Oscillating Low Pressure Turbine Cascade at Design and Off-Design Conditions. *Journal of Engineering for Gas Turbines and Power*, vol.129, pp. 530-541, April 2007.

Yamaguchi, N.; Sekiguchi, T.; Yokota, K.; Tsujimoto, Y.: Flutter Limits and Behavior of a Flexible Thin Sheet in High Speed Flow—II: Experimental Results and Predicted Behaviors for Low Mass Ratios. *Journal of Fluids Engineering*, vol. 122, pp. 74-83, 2000.

Yamaguchi, N.; Yokota, K.; Tsujimoto, Y.: Flutter Limits and Behaviors of a Flexible Thin Sheet in High-Speed Flow—I: Analytical Method for Prediction of the Sheet Behavior. *Journal of Fluids Engineering*, vol. 122, pp. 65-73, 2000.

Address: Dr. Andreas Marn, Mathias Mayr, Univ.-Prof. Dr.-Ing. Franz Heitmeir; Graz University of Technology, Institute for Thermal Turbomachinery and Machine Dynamics, Inffeldgasse 25A, A-8010 Graz, Austria. Dr. Florian Schönleitner, Semperit AG Holding, Modecenterstraße 22, A-1031 Vienna, Austria
email: andreas.marn@tugraz.at, mathias.mayr@student.tugraz.at, franz.heitmeir@tugraz.at, florian.schoenleitner@semperitgroup.com

Design and practical Realization of an innovative Flywheel Concept for industrial Applications

L. Quurck, M. Richter, M. Schneider, D. Franz, S. Rinderknecht

The joint industry project 'ETA-Fabrik' at TU Darmstadt demonstrates different approaches to improve the energy efficiency of manufacturing processes. Within this project an innovative flywheel concept was designed and realized in order to provide energy storage and load smoothing services. The flywheel design is an outer-rotor setup. The rotor is a hubless hollow cylinder made of fiber reinforced plastic (FRP). All functional components are fully integrated into the rotor. For the radial suspension homopolar active magnetic bearings (AMBs) made of soft magnetic composite are used. A permanent magnetic bearing provides axial levitation. In order to increase the systems robustness a newly developed backup bearing system in a planetary arrangement with multiple independent bearing elements is integrated. The motor generator unit is a permanent magnet synchronous machine which is connected to the factory gird via a frequency inverter. The system is operated in high vacuum in order to reduce gaseous friction. Design challenges are the segmented sensor planes for the AMBs, the diametric enlargement of the rotor due to centrifugal forces, the anisotropic FRP as well as the thermal stability of the rotor in vacuum environment which leads to the demand of very low rotor losses. The paper describes the system and component design process and solutions which were incorporated in order to meet the design restrictions and challenges.

1. Background

The demand for energy storage systems in industrial applications has risen over the last years. They can fulfill different tasks such as peak shaving or load smoothing to improve the energy efficiency and stability of the supply system as well as to save power dependent cost. The joint industry project 'ETA-Fabrik' at TU Darmstadt demonstrates different approaches to improve the energy efficiency of manufacturing processes. Within this project an innovative kinetic energy storage system (KESS) was designed and realized in order to provide the mentioned services. Figure 1 shows the layout of the system as a CAD model and the KESS set up in the 'ETA-Fabrik'. The design is based on the first realized outer rotor type flywheel which was introduced by Schaede (2013) as a proof of concept. This first outer rotor flywheel was brought into operation in 2012 in the laboratory of the 'Institut für Mechatronische Systeme im Maschinenbau' (IMS) in Darmstadt.

Magnetically suspended flywheels provide reliable high power density with maintenance- and wear-free operation and without calendric and cyclic degradation. High energy conversion efficiency compensates the occurring standby losses particularly when dynamic load profiles with frequent high power demands have to be smoothed or cut. Figure 2 shows a simulation of a representative industrial load profile with and without the used flywheel as well as the corresponding power and state of charge of the flywheel. The used flywheel is the 1.4 kWh, 60 kW flywheel ETA290 which will be described in this paper. Another application could be the reduction of diesel consumption in island grids with high shares of renewable energy production (Schaede et al. 2015).

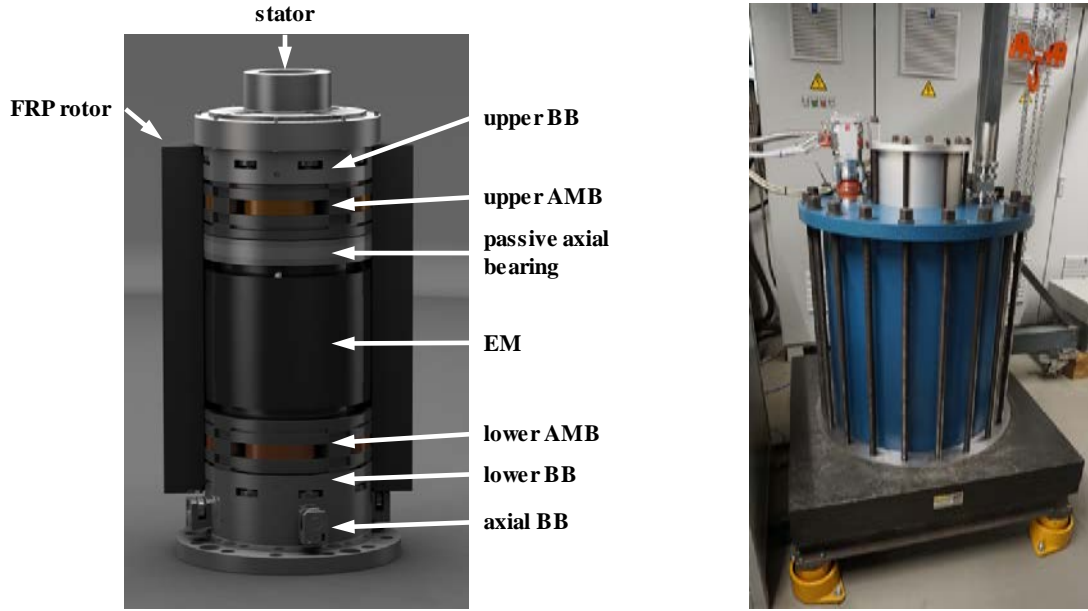


Figure 1. Left: CAD Cut-away model of the rotor mounted on the stator. Right: Photograph of the KESS in the factories utility compartment.

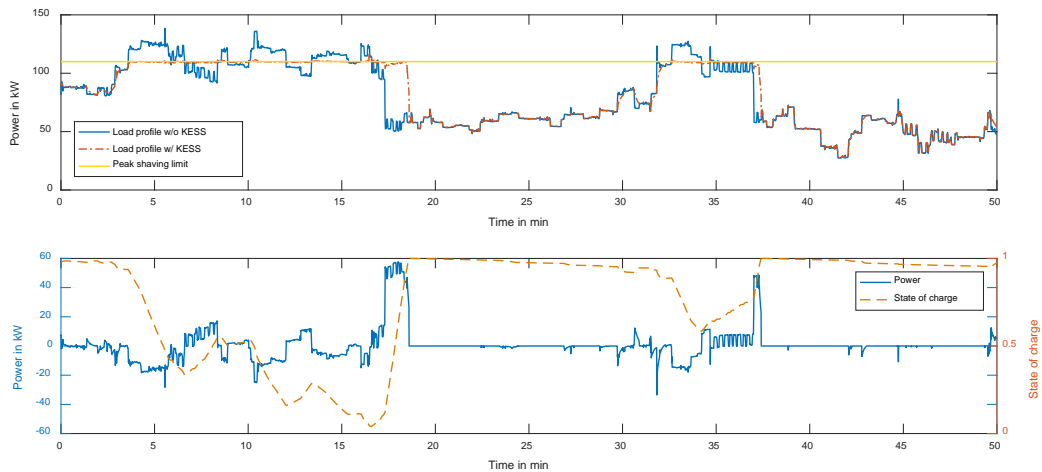


Figure 2. Simulation results of the peak shaving operation in the factory (top: factory load profiles, bottom: storage power and state of charge)

2. Design Goals and Design Process

In order to be able to design a suitable energy storage system for a specific application the individual requirements have to be analyzed. For load smoothing and peak shaving applications in an industrial environment the storage system needs medium to high electric power and moderate energy. As can be seen in Figure 2, more than 1 cycle per hour can be expected. Therefore, modern flywheel systems with low conversion losses, low self-discharge losses and a high cycle life can be an interesting alternative to other technologies. General design goals are minimal maintenance and wear even during continuous service, leading to the requirement of thermal stability. In order to be able to adapt to different industrial processes the system should be independently scalable in terms of output power and stored energy. The design of the flywheel should also allow for an efficient serial manufacturing. Due to the industrial environment liquid cooling and a connection to the 400 V AC grid can be assumed.

The outer-rotor design has potentially high energy densities because every active rotor component rotates with the maximum radius leading to a highly integrated system. Due to the large inner rotor radius high electric output power is possible. A general design conflict lies in the simultaneous optimization of energy density and energetic

losses. High energy densities can be reached at high rotational speeds and large radii. For the electric machine and the magnetic bearings, high speeds lead to high remagnetization frequencies resulting in high hysteresis and eddy current losses. The optimization of energy density and energetic losses can also be motivated from an economic point of view. The energy density can be interpreted as an indicator for the material dependent initial costs of the storage system. The losses that are generated during operation have to be compensated by electricity from the grid and can thus be interpreted as operating costs. An optimal system is characterized by the minimal sum of both dimensions over its lifetime.

In order to minimize the drag losses due to gaseous friction the system is operated at high vacuum levels ($<10^{-4}$ mbar). This operation condition in combination with the magnetic levitation of the rotor, however, leads to a poor thermal connection between the rotor and stator. Heat exchange can only be obtained by radiation. During the design of the magnetic bearings and the electric machine, losses on the rotor thus have to be minimized in order to prevent overheating and enable high energy efficiency.

From a methodologic point of view, a serial or independent design of the relevant system components (rotor, active magnetic bearings (AMB), electric drive (ED) and stator) is not promising due to the system's high degree of integration. Therefore, a simultaneous initial design process is carried out by Schneider (2014) using detailed component models in combination with optimization algorithms.

3. System Design

The following subsections describe the challenges within the design process of the main components. This includes rotor design, electric machine design, magnetic bearing design and back-up bearing (BB) design. The chapter concludes with an overview of the final parameters and the integration concept into the factory.

3.1. Rotor Design

The flywheel design is an outer-rotor setup. The rotor is a thick walled, hubless hollow cylinder made out of fiber reinforced plastic (FRP). The FRP rotor is produced in an industrial filament winding process with mainly circumferential fiber orientation to encounter the tangential stress. The state of stress can be assumed as plane due to the axially almost constant density distribution. This circumstance generally meets the orthotropic material strengths and reduces shear stresses in the composite. The maximum rotational speed, and therefore the kinetic energy content of the rotor, is restricted by the transverse strength in radial direction which is dominated by the resin matrix, while the utilization of longitudinal fiber strengths is comparably low. Another restriction is the diametric enlargement of the rotor by the centrifugal forces. At high speed, the diametric enlargement can be up to 1% of the inner diameter, what is the ultimate strain of common conventional FRPs. The ETA290 flywheel utilized about 0,5% of strain. The resulting significant enlargement of the air gap has to be taken into account at the design of the magnetic bearings, the electric machine and the backup bearings.

The allowable strain of most functional components is considerably lower than 0.5%, especially for the soft- and hard-magnetic components of the active and passive bearing. To avoid high stresses and failure in these components they are segmented circumferentially. This terminates the tangential hoop stresses under rotation. Further effects of this segmentation are discussed later in this paper. Despite the speed restriction due to maximum strain the ETA290 rotor reaches a specific energy density of 8.8 Wh/kg, while further design improvements will allow 14 to 20 Wh/kg by decreasing the weight of the functional components and simultaneously increase the maximum speed without changing the main diameters or mechanical strain.

The lack of a hub and an inner shaft simplifies rotordynamics and control. Due to the hollow and thick walled design the elastic eigenfrequencies are comparably high. Figure 3 shows the Campbell diagram of a 3D FE modal analysis of the rotor. The first three elastic eigenfrequencies are axially symmetric modeshapes with comparably low gyroscopic influence. The first bending eigenfrequency is above 1011 Hz. This simplifies the control of the AMB and gives the opportunity to enlarge the rotors length and adapt the energy content to the specific applications preferences without a significant influencing on the control design. For example, increasing the rotor length and thereby the kinetic energy content to 140%, lowers the first elastic eigenfrequency (1st bending mode) to 502 Hz which is still two times the maximum rotational frequency. The rigid body eigenfrequencies are defined by the magnetic bearing properties. The passive magnetic bearing, which is stabilizing the axial degree of freedom, creates an 11 Hz eigenmode which does only change slightly due to thermal influences and due to diametric enlargement. Its negative stiffness in radial direction is compensated by the AMB. The four parallel and conical mode shapes are crossed below 50 Hz while design of the bearing and controller contains the rotor position within a 100 μ m radius.

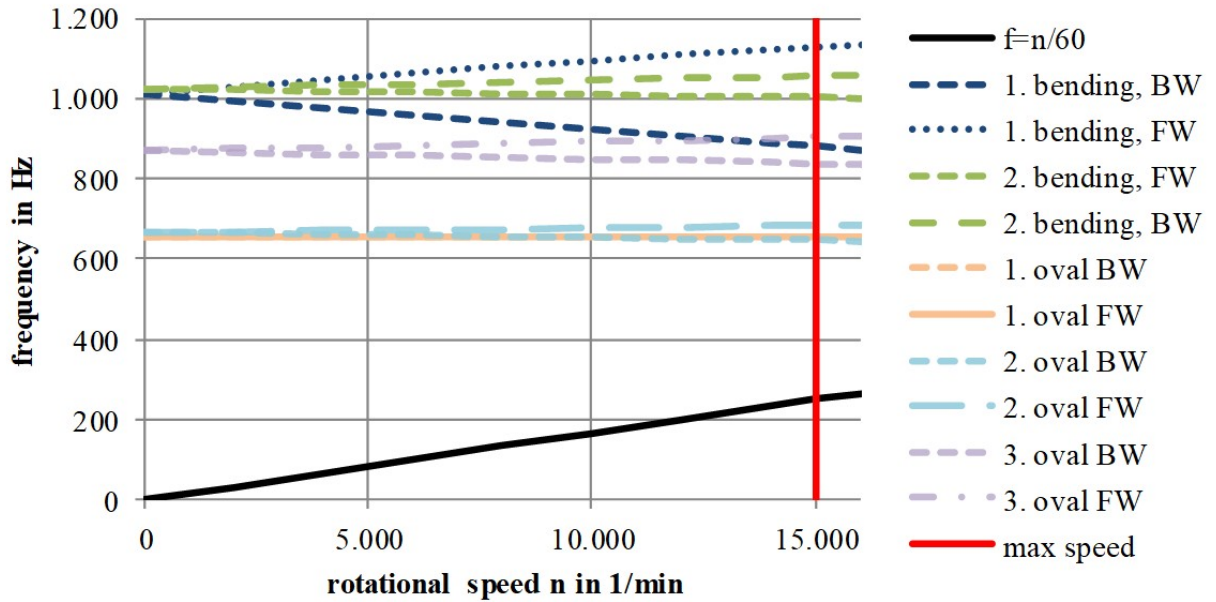


Figure 3. Campbell diagram of the 3D-FE-modalanalysys of the ETA290 flywheel rotor in free-free configuration

3.2. Electric Machine Design

In general, different electric machine types are suitable for flywheel systems. Due to the specific requirements from the field of application a permanent magnet synchronous machine (PMSM) is selected. As mentioned before, the rotor losses have to be minimized which excludes asynchronous machines due to their power dependent high copper losses. Synchronous reluctance machines are suited for high frequency applications due to the very low drag losses during idling. But due to the high power demand of the factory with many charging and discharging cycles, higher conversion efficiency is desired. Even though the PMSM creates drag losses when no power is requested from the flywheel it is the best option considering all factors of this industrial application.

As mentioned before, the all functional components have to be integrated into the rotor by segmentation considering the resulting stresses due to centrifugal forces. This circumstance leads to the requirement of a very thin PMSM rotor in radial direction in order to reduce the centrifugal forces applied to the FRP rotor. The goal can be achieved by increasing the number of pole pairs of the machine because the magnetic flux in the rotor in circumferential direction per pole is reduced. At the same time the active axial length of the machine decreases leading to shorter copper windings and thus lower copper losses. The EM rotor design uses permanent magnets which are embedded in electrical sheets. An ironless Halbach array would also be possible but it is much more expensive due to a higher magnetic volume and complex magnetization directions.

A high number of pole pairs, however, leads to high remagnetization frequencies and thus to high core losses. Typically, a high number of pole pairs can be found in so-called torque motors that run at low to medium frequencies. A high speed motor typically has a lower number of pole pairs and can thus be operated at higher frequencies. In this case this results in a design of the EM with four pole pairs and a rotor speed of 250 Hz. Therefore, the output frequency of the inverter has to be 1000 Hz which demands switching frequencies of at least 8 kHz. Furthermore, the control of the inverter operates without a rotor position signal because no commercial encoder system is available for outer-rotor designs with time variant air gap in high vacuum environment. The sensor-less drive mode results in reduced dynamics of the power control compared to encoder drive mode.

In order to design the EM in detail, a transient magnetic finite element analysis is carried out. The influence of the switching of the inverter is neglected, therefore electric currents in sine wave form are assumed. Figure 4 shows the exemplary results for a low speed operating point of 7500 rpm and a positive (charging) electric power of 60 kW. From this analysis the machine losses can be estimated using material-specific loss coefficients for the electrical sheets and the copper windings for different operating point (specified by electrical power and rotational speed).

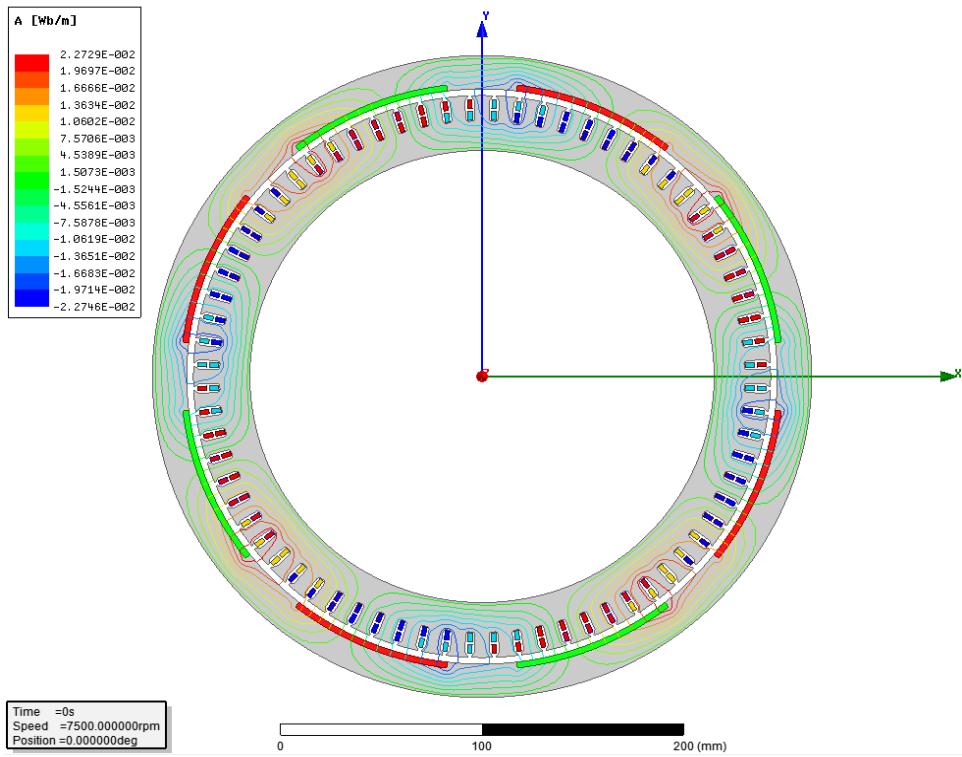


Figure 4. Results (2D magnetic flux) of the finite element simulation of the EM at 7500 rpm and +60 kW

By calculating the steady state losses, given as root mean square values, for 6 rotational speeds and 9 electrical powers, a loss map of the system can be defined. Figure 5 shows the loss map for the electric machine including rotor and stator losses. Due to the poor thermal coupling of rotor and stator, the rotor losses of all components have to be reduced. Rotor losses of the EM lie below 50 W. For the analysis sinusoidal currents and voltages are assumed. In a practical application pulse width modulated inverters are used that create current and voltage harmonics which again lead to core losses in the rotor. These losses can be reduced by installing inductors but have to be taken into account for practical applications.

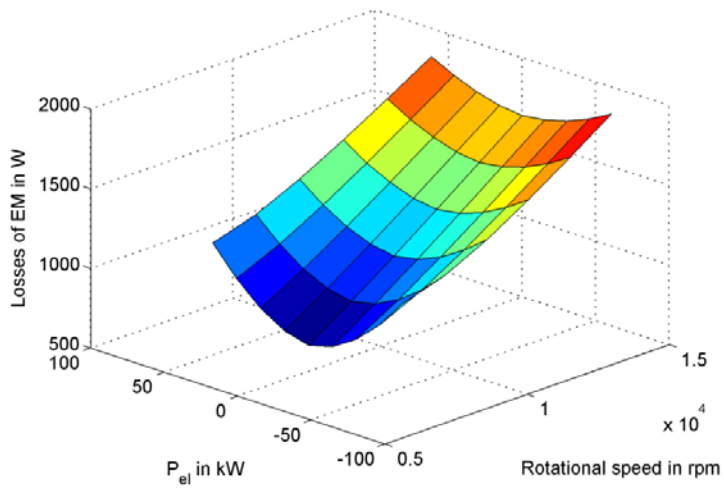


Figure 5: Loss map of the EM (rotor and stator losses) derived by a FE simulation

Analytical and numerical loss models of the AMBs and the gaseous friction losses of the rotor show that the flywheel's loss structure is mainly dominated by the losses of the EM. Losses of magnetic bearings and air friction losses lie in the range of 140-180 W and below 10 W respectively. A loss optimization should thus focus on an efficient EM design.

3.3. Magnetic Bearing Design

The goals during the design of the active magnet bearing system are stable levitation over the entire operation range with as low losses as possible especially with respect to rotor losses which lead to rotor heating. As a special design feature, the speed dependent diametric enlargement of the air gap has to be faced. In order to keep hysteresis and eddy current losses low, a homopolar AMB configuration is used. In Figure 6 the two axis radial AMB design, air gaps (magnified) magnetic flux path and the position sensors in differential arrangement are visualized.

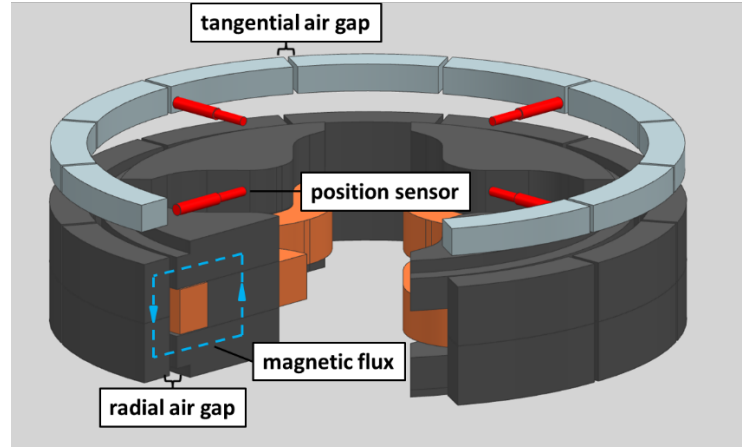


Figure 6: Homopolar AMB configuration with differential sensor configuration and corresponding air gaps

Despite a homopolar configuration a near constant, non changing pre-magnetization flux on the rotor is obtained keeping both losses low. Unfortunately, the homopolar configuration makes it hard to use thin electric sheet as the flux conducting material to further reduce eddy current losses. Thus soft magnetic composite is used as an alternative which allows isotropic 3-dimensional flux. As a result of the diametric enlargement of the rotor, the segmented sensor and actor planes of the rotor create tangential air gaps which increase with the rotor speed. When looking at the tangential air gaps one has to distinguish between those on the bearing side and those on the position sensor side. The first can be neglected due to the homopolar configuration as the tangential air gap does not lie in the path of the flux and thus does not further influence the behavior of the bearing. The latter is more crucial to the system. The tangential air gap has significant influence on the measured position as the air gap is being misinterpreted as a change in the rotor position whenever it passes the position sensor head. In Figure 7 exemplary position signals are shown. Looking at the single sensor signals (S_P and S_N) high peaks can be seen.

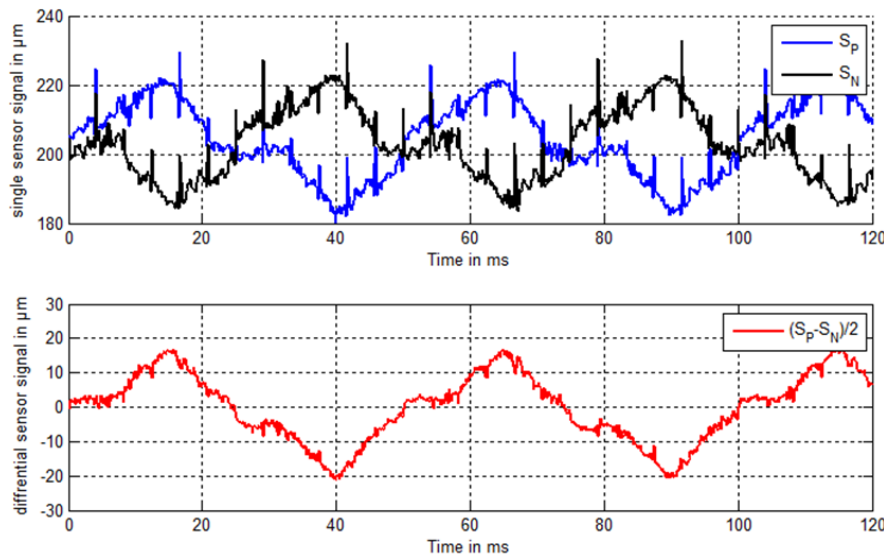


Figure 7: Single sensor signals (top) and differential sensor signal (bottom)

To overcome this undesired behavior, the mathematical difference ($S_P - S_N$) between two counter positioned sensors is used. Ensuring a symmetrical construction of the rotor segments, tangential gaps occur at the same time at both sensors and are thus not present in the difference of their signals (shown in Figure 7 at the bottom). This further holds for elastic axial symmetric eigenmodes of the rotor. Possible sensor errors like temperature drift and the speed dependent enlargement of the radial air gap between the sensor head and rotor are not present to this position signal anymore.

Unfortunately, the influences of the radial air gap enlargement on the actuator part of the magnet bearing cannot be circumvented in a same manner. With an increasing radial air gap the magnetic force drops by the power of two with the air gap, resulting in a highly nonlinear magnetic force over the rotational speed range. One way to overcome this undesired behavior from a control point of view is to increase the initial air gap. As the absolute change of the air gap remains the same, the relative change of the air gap as well as the linked nonlinear magnetic force characteristics decrease. The enlarged initial air gap on the other hand has the drawback of an increased magnetic bearing size due to the higher number of coil turns which is needed to overcome the additional air gap reluctance.

The rotor itself can be seen rigid from a control point of view since its first bending mode is more than 3.5 times higher than the highest rotational frequency, as shown in section 3.1. Due to its high moment of inertia the rigid body eigenfrequencies of the levitated suspended split up. Thus the highest rigid body eigenfrequency to be stabilized by the AMB are below 50 Hz and gives an upper limit of the desired frequency range of the AMB system. Despite these specific rotordynamic characteristics and the previously mentioned influences of the diametric enlargement of the rotor, a decentralized PID position control with a subordinated PI current control is sufficient to stabilize the system.

3.4. Backup Bearing Design

As most magnetically suspended rotors, the ETA290 flywheel uses rolling element bearings as backup bearings (BB). During regular operation the BB rests on the stator without mechanical contact to the rotor. When overload, malfunction or power loss of the AMB arise, the BB should prevent touching and damaging of other parts. Mechanical failures of the BB system can be classified as critical to the systems integrity because destructive whirl movements and very high bearing loads can occur as well as rapid momentum transfer from rotor to the stator when friction excessively rises. For high energy flywheels the preferences towards reliability and service times are notably challenging because of the kinetic energy density and the long spin down times even if high electric power braking is applied. For emergency braking during grid black out an additional passive brake resistor is added, spin down times are still above 2 minutes from full speed.

The size of inner diameter of the ETA290 flywheel together with the high rotational speed complicates the use of conventional bearing components. The bearing speed expressed in the DN number is higher than 4e6 mm/min, which classifies the bearing situation as high speed application. This is aggravated by the vacuum environment resulting in an unfavorable lubrication and a lack of cooling. Therefore, an alternative BB design was chosen. First introduced by Chen et al. (1997) and similarly published by Jansen et al. (2014) the basic idea of this new approach is to use multiple small bearing units circumferentially distributed around the stator in each BB plain. This planetary arrangement of independent bearings leads to better high speed capability, lower BB inertia and lower friction. Further information is given by Quurck et al. (2014). In Figure 8 an illustration of the ETA290 BB design is given as well as a photograph of the components during built up.

For the ETA290 flywheel, bearing units with full complement hybrid spindle bearings, mounted on a steel roller element are chosen. The roller element contacts the rotor's BB plain, while the outer bearing races are placed into the stator. In each of the two BB plains, eight bearing units form a polygon shaped free orbit in which the rotor can move contact-free.

Beside the higher speed capability of these bearing units, another advantage is given by the polygon shaped orbit. Due to the noncircular orbit, the rotor does not perform forward or backward whirls with high frequencies, what is often the case with circular BBs which are comparably stiff. Bearing loads of the polygon shaped BB are comparably low and plastic deformation can be prevented as long, as friction inside the bearing elements is low. The global behavior of a vertical and gyroscopic rotor in this kind of planetary bearing is described by Quurck et al. (2016). It can be described as a jumping character with a low speed, friction driven backward whirl component. Exemplary simulation data of a rotor drop event with a 150 kg flywheel from 12000 rpm in a planetary BB with six bearing elements is given in Figure 9.

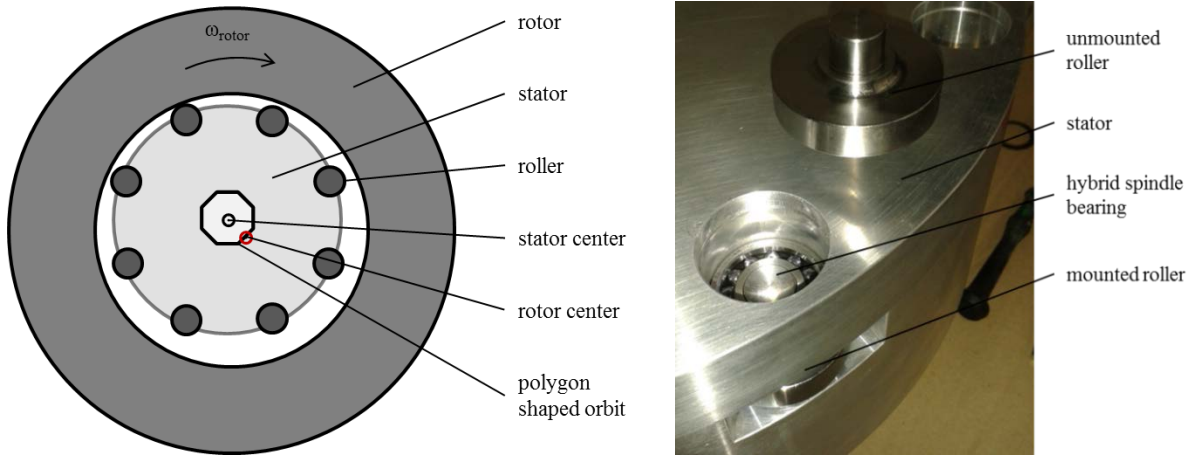


Figure 8: Planetary BB design in schematic drawing (left), photograph of the BB system during build up (right)

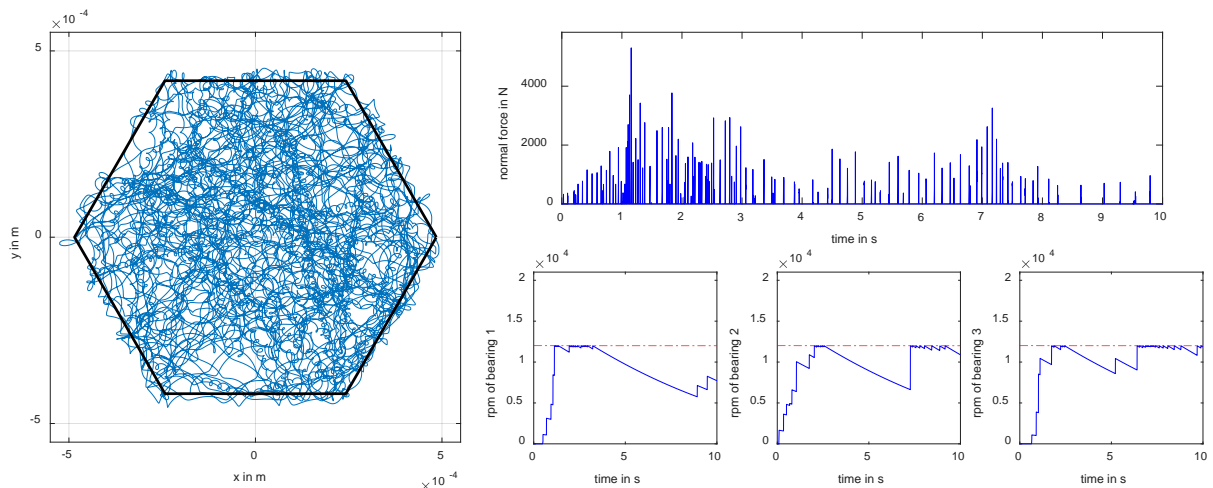


Figure 9: Rotor drop simulation in a planetary BB with six bearing units. Simulation time is 10 seconds, displayed is data of the lower BB plain. Left: Rotor position data. Right top: Normal force applied to the rotor. Right bottom: Rotational speed of bearing unit 1, 2 and 3 in solid, rotor speed as chain dotted line.

4. Final Design and Integration into the Factory

Using synthetic load profiles from measured single machines of the 'ETA-Fabrik' the dimensioning of electric power and capacity was finished before the factory was built. To enable significant peak shaving and load smoothing capability the storage demand was defined by 1.4 kWh and 60 kW. The factories electric protection is rated by 170 kW. Minimum 60 kW are available from 7500 rpm. While the electric power is easy to achieve, the kinetic energy is more challenging. Derived by the first prototype the inner diameter was enlarged to 290 mm and the outer diameter rose to 430 mm to meet the demands. The upper speed limit was set to 15000 rpm for secure long time operation with low risk of rotor fatigue. The resulting surface speed is 227 m/s at the inner diameter, and 337 m/s at the outer diameter of the FRP rotor. The total rotor weight is 153 kg, while the non-FRP components take two thirds of the weight. This ratio is responsible for the comparably low energy density of 8.9 Wh/kg and shows a high potential for improvement.

The nominal air gap of the BB system is 0.25 mm, the air gap of the AMB was set to 1 mm at zero rpm. Both air gaps enlarge radially up to 0.6 mm because of the centrifugal forces. The static load capacity of one BB unit with two spindle bearings is 4200 N. The lubricant of the bearing is MoS₂, as it is resistant to evaporation and its dry friction is calculable by the theory of Birkhofer and Kümmerle (2012). The physical dry friction model provides information for a thermal and a wear model of the BB which enables lifetime prognosis of these components. The system's first run up was performed in middle of 2015 in the laboratory of the IMS. In early 2016 the whole KESS was moved into the utility compartment in the basement of the 'ETA-Fabrik' where it is connected to the

factories point of common coupling in order to influence the residual load of the factory. The factories load is measured in the electrical main cabinet and transmitted via PROFIBUS to the programmable logic control (PLC) where the control strategy is implemented. A control loop running at 1 kHz can be used to control the electric power of the KESS.

5. Conclusion and Outlook

In the paper a novel type of flywheel was introduced for industrial applications. The high degree of integration of active magnetic bearings, permanent magnet synchronous machine and composite rotor together with the outer-rotor topology lead to many challenges during practical realization. Development, construction, and assembly of the prototype are completed so far. Open tasks are the implementation of the KESS controller on a PLC and its integration into the factory's energy management communication bus. This is going to be completed within the mentioned research project.

Based on research questions that rose from this research project, follow-up projects were started. One project focuses on an intensive modelling and testing on component level. Here a special test rig for the experimental validation of back-up bearings and novel failure tolerant magnetic bearing concepts is set up. A second test rig focuses on the long life fatigue strength of the composite rotor. Due to the uncommon stress state in the outer-rotor configuration induced by centrifugal forces, special test configurations have to be developed on material level. On component level flywheel shaped probes have to be cycled until they disintegrate to evaluate fatigue and failure modes of high thick walled, high speed FRP rotors.

By implementing design improvements concerning the radial thickness of the AMB and EM the centrifugal loads can be reduced and the rotational speed heightened. A prototype with a maximum speed of 17500 rpm and 2.4 kWh is currently implemented at the IMS. The specific energy of this system is 13.9 Wh/kg. Heightening the maximum allowable stress in the FRP to around 50% of the static ultimate strength would further raise these values to 4.8 kWh and 27.8 Wh/kg respectively, but the fatigue tests have to be done first and results have to proof these less conservative design restrictions.

A further research project called 'SWIVT' focuses on a different field of application. Smart micro grids with decentralized generation can be stabilized using energy storage systems. For such a task an electric hybrid energy storage system consisting of a lithium-ion battery and a flywheel is developed. The flywheel design is based on the described prototype and tries to improve it further on a system level.

In general, the main future challenges lie in the further integration of the component design on a system level. Also the power electronics (frequency inverter and magnetic bearing amplifiers) have to be adapted to the flywheel concept. The detailed knowledge about the reliability in terms of rotor fatigue and back-up bearing failure play a major role in order to increase the technology readiness of the design.

Acknowledgments

The referred projects 'ETA-Fabrik' and 'SWIVT' are funded by the Federal Ministry for Economic Affairs and Energy and are administrated by Projektträger Jülich. The Project 'ETA-Fabrik' is additionally supported by the federal state of Hessen.

Gefördert durch:



Bundesministerium
für Wirtschaft
und Technologie

Betreut vom:



Unterstützt durch:



aufgrund eines Beschlusses
des Deutschen Bundestages

References

Birkhofer H., Kümmerle T. *Feststoffgeschmierte Wälzlager* Springer-Verlag Berlin Heidelberg (2012)

Chen, M. H., Walton, J., Heshmat, Hooshang, International Gas Turbine & Aeroengine Congress & Exhibition Orlando, Florida, ASME, New York, USA (1997)

Jansen, R. H., Storozuk R. J., *High speed, compliant, planetary flywheel touchdown bearing*. World Intellectual Property Organizazion, 14.08.2016, WO 2014/123507 A1 (2014)

Quurck, L., Schaeede, H., Richter, M., Rinderknecht S.: *High Speed Backup Bearings for Outer-Rotor-Type Flywheels - Proposed Testrig Design*. Proceedings of ISMB14. Linz, Austria (2014)

Quurck, L., Schuessler B., Franz D., Rinderknecht S.: *Planetary backup bearings for high speed applications and service life estimation Methodology*. Proceedings of ISMB15. Kitakyushu, Japan (2016)

Schaeede, H.: *Dezentrale elektrische Energiespeicherung mittels kinetischer Energiespeicher in Außenläufer-Bauform*. Dissertation, Technische Universität Darmstadt, Shaker Verlag Aachen (2013)

Schaeede, H., Schneider, M. Vandermeer J., Mueller-Stoffels, M., Rinderknecht S. (2015) Development of kinetic energy storage systems for islanded grids Conference: 9th International Renewable Energy Storage Conference (IRES), Düsseldorf, Germany (2015)

Schneider, M. *Multicriteria Design Process for Outer-Rotor Kinetic Energy Storage Systems*. (2014)

“ETA-Fabrik” Project homepage: <http://www.eta-fabrik.de>

Addresses:

M.Sc. Lukas Quurck¹
quurck@ims.tu-darmstadt.de

M.Sc. Michael Richter¹
richter@ims.tu-darmstadt.de

M.Sc. Maximilian Schneider¹
schneider@ims.tu-darmstadt.de

M.Sc. Daniel Franz¹
franz@ims.tu-darmstadt.de

Prof. Dr.-Ing. Stephan Rinderknecht¹
rinderknecht@ims.tu-darmstadt.de

¹ Institut für Mechatronische Systeme im Maschinenbau (IMS), TU Darmstadt, Otto-Berndt-Str. 2, 64287, Darmstadt, Germany

Determining a Function for the Damping Coefficient of a laminated Stack

C. Zahalka, K. Ellermann

The design of electrical machines is determined by electrical as well as mechanical requirements. Possible losses due to eddy currents in the stator or the rotor are commonly reduced by using stacks of laminated sheet metal. On the other hand, the design of the stator and the rotor has a significant influence on the mechanical properties: Vibrations depend on the stiffness and the damping of the laminated stack. There are different methods to determine the stiffness coefficient of a stack, but it is much more difficult to obtain suitable values for the damping as there are more influencing factors.

This paper describes an experimental procedure, which determines the influence of different parameters on the damping of a stack. The stack used during the experiments consists of 200 quadratic steel sheets with a side length of 80 mm and a thickness of 0.5 mm. In accordance with the measurement data, a functional dependance based on three variables is derived. The first one is the surface pressure between the steel sheets, the second one is the frequency of the applied lateral force, and the third one is the displacement between the steel sheets.

It is the aim of this investigation to determine the influence of variations of these parameter values on the damping. The forces are applied onto the stack with hydraulic cylinders. The mechanical deformation of the stacked metal sheets is measured by a laser-speckle-based measurement system. This system detects the displacement of single steel sheets. The displacement is measured on two steel sheets, but they are not side by side. The difference between the two measurement points is equal to the displacement of the stack.

Through the synchronization of the time signal of the lateral force and the displacement of the stack, a hysteresis loop can be calculated. This hysteresis depends on the lateral force and the displacement of the stack. The area of the hysteresis corresponds to the dissipation energy between the two measurement points on the stack, 140 sheets apart from each other. This area is calculated by numerical integration based on the trapezoidal rule. Through the conservation of energy for this system, it is possible to calculate an effective damping coefficient for the stack. Considering different influencing parameters, a function for the damping coefficient can be identified by the least square method. This function can be used for the parameters in a numerical simulation of an electrical machine.

Nomenclature

A	[m]	Amplitude of the displacement of the dynamic cylinder
d	[$\frac{\text{Ns}}{\text{m}}$]	Structural damping
f_E	[Hz]	Excitation frequency
F_D	[N]	Dynamic force
\hat{F}_D	[N]	Amplitude of the dynamic force
F_{Stat}	[N]	Static force
m	[kg]	Mass
p	[$\frac{\text{N}}{\text{m}^2}$]	Surface pressure
t	[s]	Time
x	[m]	Displacement
\hat{x}	[m]	Amplitude of the displacement
W_{Diss}	[Nm]	Dissipation energy
η	[—]	Loss factor
ψ	[rad]	Phase shift
ω_0	[$\frac{\text{rad}}{\text{s}}$]	Angular eigen frequency
ω_E	[$\frac{\text{rad}}{\text{s}}$]	Angular excitation frequency

1 Introduction

Information about the material properties of the laminated stack is necessary to simulate the dynamics of a rotor or a stator of an electrical machine. Due to the structure of the stack, the material properties vary in the different directions: in radial direction, the metal of the sheets dominates the tensile stiffness. Different layers of the stack act in parallel and the material with the highest value of Young's modulus contributes most significantly to the effective stiffness of the stack. In axial direction, the contact- and lamination-zone between the sheets becomes much more important as layers act in series. In this direction, the material with the smallest value of Young's modulus influences the tensile stiffness much more. These zones are also considered to be highly important for non-conservative effects: The transversal deformation of the stack due to a shearing motion between the metal sheets contributes significantly to the overall damping of the structure. This is mainly due to the softer material in the lamination zone.

The stiffness of a component can be determined experimentally or numerically – given the geometry and tabulated material properties. Damping values are much harder to determine and are rarely available in literature. In this paper, an experimental set-up is described in order to determine a function for the damping coefficient of a stack caused by a shearing motion in transversal direction. There are many different parameters which have an influence on the structural damping of a component. In this work, three variables are considered: The surface pressure between the steel sheets, the frequency of the lateral force and the amplitude of the displacement of the stack. All others, like the height of the stack or the size of the steel sheets, are being kept constant.

In practice, the displacement and the frequency vary with the operating states. The pressure on the other hand is mostly caused by the design and by compressing the stack in the production process: In electrical machines, the laminated sheets are – more or less loosely – stacked, then compressed and finally held in place by a welded structure of tension elements and end plates. This design and production process make the pressure difficult to be determined – leading possibly to significant variations in mechanical parameters of the machine.

There are different methods to determine the stiffness and the structural damping of a laminated stack. Luchscheider et al. (2012) describes a set-up to measure the stiffness of a lamination stack. Two plungers compress nine circular samples, cut out from a typical lamination sheet material. With two extensometers, clamped on the plungers, and a load cell, a force-displacement diagram is created. With this diagram the stiffness in stacked direction of the laminated stack can be derived.

Mogenier et al. (2010) predicted the modal parameters of an induction motor with an undamped finite-element model. The minimization of the error between the predicted and the measured modal parameters with the Levenberg-Marquardt algorithm. This leads to the equivalents constitutive properties of the laminated stack.

Clappier and Gaul (2015) and Clappier et al. (2015) determine the structural damping and the stiffness in axial and in shear direction of a laminated stack. The measurement set-up for this evaluation consists of two laminated stacks and three plates. The stack is axial pretensioned with a screw connection between the plates. The excitation is effected with a shaker to one of the plates. To calculate the stiffness and the structural damping, the acceleration of the plates and the force on the excited plate are measured. The structural damping is calculated through the determination of the dissipated energy. The same principle is used by Bograd et al. (2008). The difference between these works is that Bograd determines the structural damping in shear direction from a thin layer element and not from a laminated stack.

2 Experimental set-up

The complete test stand is placed on a foundation, which is isolated from the surrounding with an air suspension. This is necessary to be independent from the environmental influences of the building. The measurement system is not placed on this foundation, but the offset between the measurement system and the test bench can be removed through an differential measurement of the displacement. The test bench consists of two hydraulic cylinders and the clamping device for the stack (see Fig. 1). The vertical cylinder (4) applies the surface pressure on the laminated stack. To avoid an inclined position of the pressure plate, there are four linear guides in axial directions around the laminated stack. These guides are not shown in Fig. 1. The second cylinder (1) on the right side applies the oscillating lateral force on the stack.

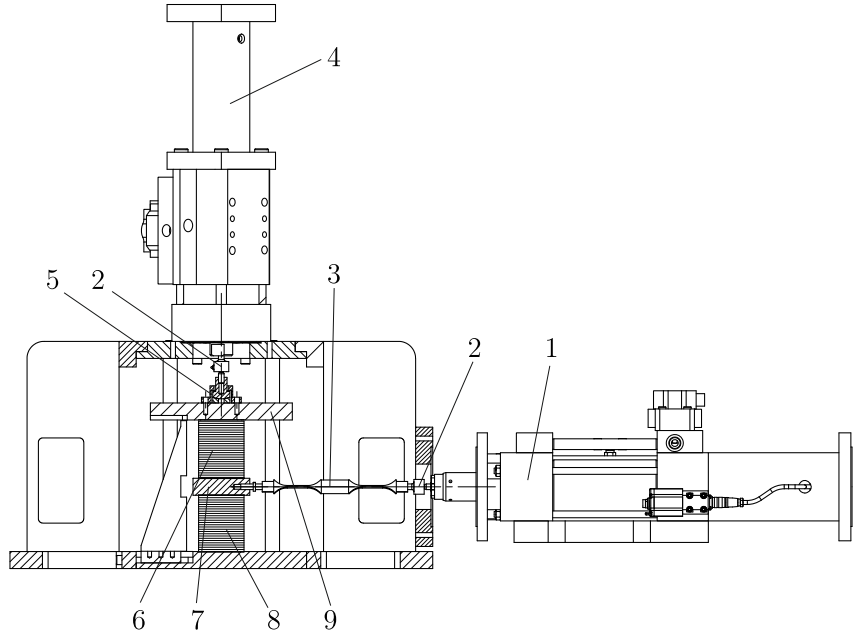


Figure 1: Experimental set-up 1. Dynamic hydraulic cylinder 2. Load cell 3. Flexure 4. Static hydraulic cylinder 5. Ball joint 6. Upper lamination stack 7. Intermediate plate 8. Lower lamination stack 9. Pressure plate

There are two stacks, one is above the intermediate plate and the other one is below. Each of the stacks consists of 200 steel sheets with a side length of 80 mm and a thickness of 0.5 mm. Between the static hydraulic cylinder and the pressure plate are a load cell and a ball joint. The load cell measures the force for the surface pressure in the laminated stack and the ball joint corrects the inaccuracies of the concentricity between the pressure plate and the cylinder. A load cell and a flexure are situated between the dynamic cylinder and the intermediate plate. The load cell records the damping force and the flexure is used for the correction of the vertical position of the intermediate plate. This is necessary, because the vertical position of the intermediate plate depends on the surface pressure in the laminated stack. The static hydraulic cylinder is force controlled based on the load cell and the second one is stroke controlled based on the magnetostrictive measurement method of the cylinder. Both systems are controlled with one dual-channel controlling system.

The basic construction of the measurement system for the displacement of the steel sheets was described in Halder et al. (2014) based on the laser-speckle principle. For the application in the test bench, the measurement system has been adapted. The measurement construction is positioned so that the axes of the two high speed cameras are orthogonal to the front site of the laminated stack, shown on the left picture of Fig. 2. This cameras record the Regions of Interest (RoI) and the software calculates the displacement of each ROI. The displacement of the laminated stack is the difference between the two ROI in horizontal direction. The maximum sampling rate of the system is 150 Hz by recording two measure points at each ROI. In combination with the maximum excitation frequency of 12.5 Hz, there are at least twelve measurement points during one vibration period. In order to get different measurement points in the hysteresis loop, the sampling frequency is not an integral multiple of the excitation frequency.

The position of the two ROI is shown on the right side of Fig. 2 and marked with a red rectangle. The distance between the ROI is limited by the image of the camera in relation to the thickness of the sheets. For the setup under consideration the ROI are separated by 140 sheets of steel. The speckle pattern is produced through a laser light beam which is redirected with a mirror to a beam expander. This expanded beam is divided into two beams with an splitter cube and must be projected exactly on the two ROI. The detailed description of this measurement system is in Halder et al. (2014).

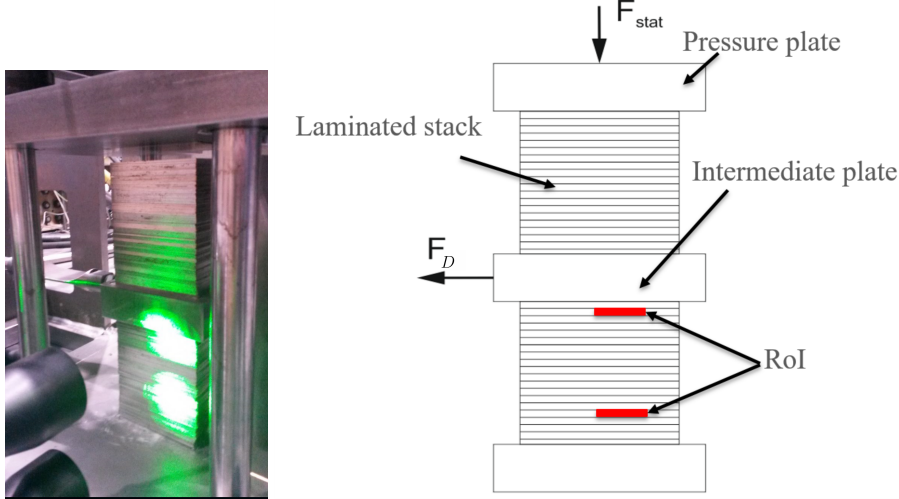


Figure 2: Principle of the measurement system

3 Calculation of the damping coefficient

Through the structural damping in the laminated stack, the force-displacement graph is a hysteresis loop. The area inside this hysteresis corresponds to the dissipated energy W_{Diss} . The energy can be calculated from the damping force F_D acting over a displacement x

$$W_{Diss} = \int F_D \, dx. \quad (1)$$

In the considered case, W_{Diss} determined from the horizontal displacement of F_D as indicated in the right hand side of Fig. 2.

Another definition for the dissipation energy is the approach of Kelvin-Voigt, which is described in Dresig and Fidlin (2014). This approach uses the damping coefficient d and replaces the integration over x by an integration over time t

$$W_{Diss} = \int_0^T d \dot{x}^2 \, dt = d \omega_E^2 \int_0^T \dot{x}^2 \sin^2(\omega_E t) \, dt. \quad (2)$$

Here, the excitation is assumed to be a sinusoidal function with frequency ω_E and amplitude \dot{x} . Furthermore, the response is assumed to have reached steady state with constant amplitude and angular frequency. As a result of these assumptions, the damping coefficient d determined from Eq. (2) leads to

$$d = \frac{W_{Diss}}{\omega_E \pi \dot{x}^2}. \quad (3)$$

In addition to the structural damping, the loss factor η can be calculated. This factor is defined by the dissipation energy divided by the maximum energy of the system. In Fig. 3, the maximum energy is shown in the dark gray triangle and the dissipation energy is the gray area of the hysteresis loop.

On the other hand, the maximum energy can be calculated from the amplitude of the dynamic force and the displacement. Thereby, the loss factor becomes

$$\eta = \frac{W_{Diss}}{1/2 F_D \dot{x}}. \quad (4)$$

The damping coefficient can also be evaluated from the equation of motion of a forced oscillator:

$$\ddot{x} + \frac{d}{m} \dot{x} + \omega_E^2 x = \frac{F_D}{m} e^{i\omega_E t}. \quad (5)$$

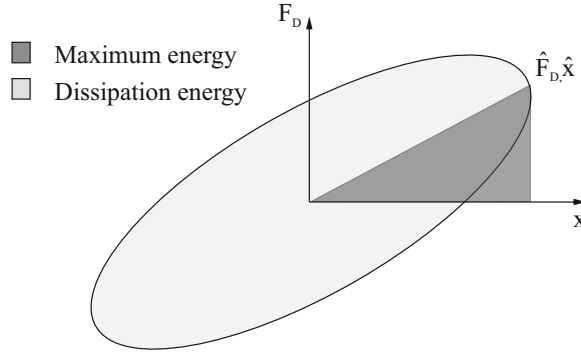


Figure 3: Maximum and dissipation energy

This essentially reduces the vibrating stack to a one-degree of freedom oscillator. The mass m is the effective mass of the stack. The fact, that parts of the experimental setup also move is accounted for in the force F_D . For the evaluation, only the steady state solution is relevant. A solution is given by the complex function

$$x = \hat{x} e^{i(\omega_E t - \psi)}, \quad (6)$$

where ψ is the phase shift between excitation and response. Substituting Eq. (6) and its derivatives into the equation of motion Eq. (5) leads to

$$\omega_0^2 - \omega_E^2 + i \frac{d}{m} \omega_E = \frac{F_D}{\hat{x} m} e^{i\psi}. \quad (7)$$

In Fig. 4, the left side of Eq. (7) is plotted in the complex plane.

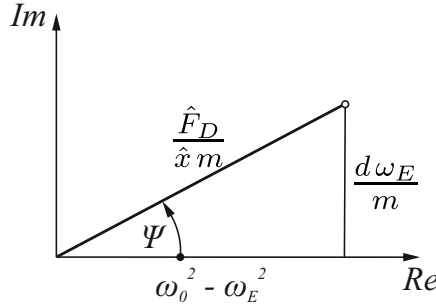


Figure 4: Complex plane

From trigonometric functions applied to the rectangular triangle in the complex plane, the structural damping becomes

$$d = \frac{F_D \sin \psi}{\hat{x} \omega_E}. \quad (8)$$

With this equation, it is possible to calculate the damping coefficient from the phase shift ψ between the vibration excitation and the vibration response. This function is used for the evaluation of the calculation of the area from the hysteresis loop.

4 Experimental evaluation

The aim of this experiment is to derive a function for the damping coefficient depending on the excitation frequency, the displacement and the surface pressure between the steel sheets. A total of 120 measurement series were considered: five different pressure values, four different amplitudes and six different frequencies. The pressure was varied from $0.8 - 2.4 \text{ N/mm}^2$ in steps of 0.4 N/mm^2 , the amplitude from $0.1 - 0.55 \text{ mm}$ in steps of 0.15 mm . Frequencies included were $1, 2.5, 5, 7.5, 10, 12.5 \text{ Hz}$. Each of these 120 series was repeated ten times.

In order to exclude systematic measurement errors, the chronological order of the measurement was randomized. All of these measurements were considered in this study, but for the illustration of the method, we subsequently focus on the measurement series with a pressure of 1.2 N/mm^2 as given in Table 1.

Table 1: Measurement series with $p = 1.2 \text{ N/mm}^2$

Series	f_E [Hz]	A [mm]	Series	f_E [Hz]	A [mm]
25	1	0.1	37	7.5	0.1
26	1	0.25	38	7.5	0.25
27	1	0.4	39	7.5	0.4
28	1	0.55	40	7.5	0.55
29	2.5	0.1	41	10	0.1
30	2.5	0.25	42	10	0.25
31	2.5	0.4	43	10	0.4
32	2.5	0.55	44	10	0.55
33	5	0.1	45	12.5	0.1
34	5	0.25	46	12.5	0.25
35	5	0.4	47	12.5	0.4
36	5	0.55	48	12.5	0.55

Fig. 5 shows the dynamic force and the displacement of the laminated stack versus time. The first three seconds of the signal include the approach of the hydraulic cylinder and the transient response. After this time, the steady state solution is reached. For the determination of the damping coefficient, the steady state solution is significant, see Section 3. Furthermore, only the measurement points after five seconds will be considered. After the transient response, the amplitude of the displacement and the dynamic force is nearly constant. The reason for small fluctuations lies in the stroke control of the hydraulic cylinder.

The comparison of the plotted measurement data and the parameter of the measurement series (see Table 1) shows a difference in the amplitude of the displacement. This difference is caused by the elastic deflection of the flexure (see Fig. 1). The hydraulic cylinder is stroke controlled, which is measured inside the piston. So, on one side there is the displacement of the piston and, on the other side, the displacement of the laminated stack. Consequently, the difference between these two displacements is the elastic deformation of the flexure.

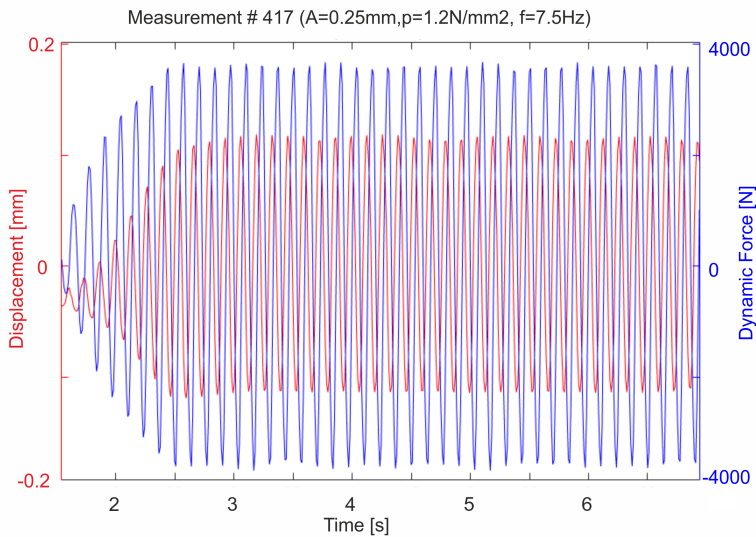


Figure 5: Measurement signal from the measurement number 417 (series 38)

The signal of the dynamic force and the displacement includes a phase-shift. This results from the structural damping in the laminated stack. To get a graph (see Fig. 6) with the dynamic force over the displacement, the two signals must be equal. In order to remove fluctuations from the measurements, several points are grouped into one by averaging. With this operation, there is a minor error from the calculation of the area. The area is calculated with a numerical integration, based on the trapezoidal rule. A linear connection between the points is

satisfactory exact, because the error from the measurement is higher than the error through the linearization. Such linear connections are shown in the right graph of Fig. 6.

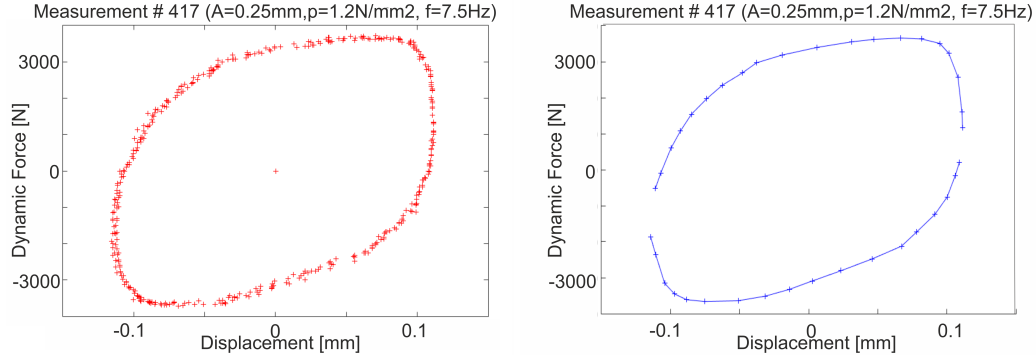


Figure 6: Hysteresis loop left: measurement data; right: linearized data

Fig. 7 shows the boxplots of the measurement series with a surface pressure of 1.2N/mm^2 . All measurements which are in one marked rectangle have the same excitation frequency and from left to right an increasing amplitude (see Table 1). The damping coefficient decreases with an ascending amplitude and by an ascending frequency. Both of these connections have a similar behavior and can be approximated through an exponential function with a negativ exponent. Another detail is shown in Fig. 7: Lower amplitudes and frequencies lead to a larger difference between the first and the third quartile. The reason for this lies in the absolut measurement and calculation error which is in all cases roughly the same, but through the smaller measurement values the relative error is much bigger.

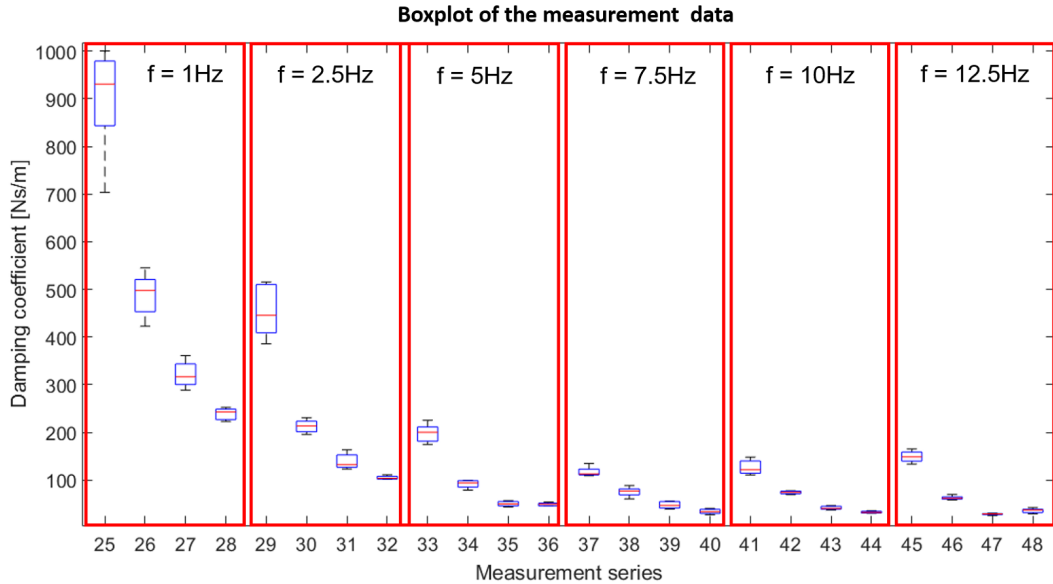


Figure 7: Boxplot of the measurement series with a surface pressure of 1.2 N/mm^2

Corresponding to the five different pressure values, five different functions for the damping coefficient are determined. These functions depend on the frequency and the displacement of the laminated stack and are assumed to take the form

$$d(f, A) = \frac{C_1}{f} + \frac{C_2}{A} + \frac{C_3}{fA}. \quad (9)$$

Parameters C_1 , C_2 and C_3 are calculated from a least squares approximation separately for each pressure value: For each variation of the parameters (C_1, C_2, C_3) the sum of all squared differences between each measurement point and the function value is calculated. The best approximation of the function is found when the sum reaches

a minimum. In order to control the quality of the solution, the coefficient of determination (R^2) is calculated. It is defined in Birkes and Dodge (1993) as

$$R^2 = \frac{\sum(\hat{y}_i - \bar{y})^2}{\sum(y_i - \bar{y})^2}. \quad (10)$$

The range of R^2 is from 0 to 1, whereby 1 corresponds to the best approximation of the data values.

As an example, the function for a constant surface pressure of 1.2 N/mm^2 is found to be

$$d(f, A) = \frac{386.64}{f} + \frac{3 \cdot 10^{-3}}{A} + \frac{5.15 \cdot 10^{-3}}{f A} \quad \left[\frac{\text{Ns}}{\text{m}} \right]. \quad (11)$$

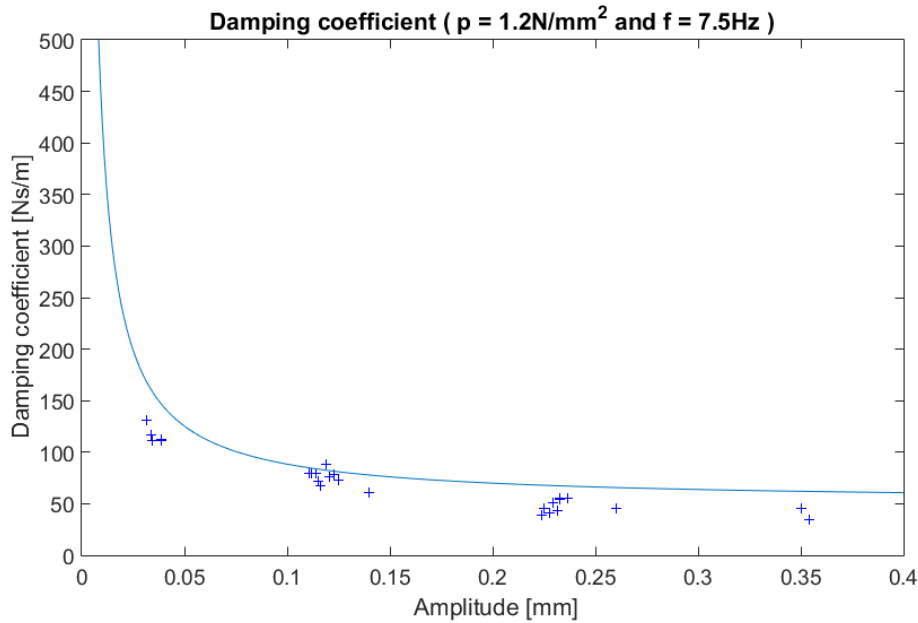


Figure 8: Damping coefficient for a surface pressure of 1.2 N/mm^2 and an excitation frequency of 7.5 Hz

Fig. 8 illustrates Eq. (11) using a frequency of 7.5 Hz and the results of the corresponding measurements. Inserting the value of the frequency into eq. (11) gives

$$d(A) = \frac{3.69 \cdot 10^{-3}}{A} + 51.552 \quad \left[\frac{\text{Ns}}{\text{m}} \right]. \quad (12)$$

Again, as an example, the function for the damping coefficient at a surface pressure of 1.2 N/mm^2 in Fig. 9 is shown. The measurement points are marked with red crosses in this figure. The two-sided 95 % confidence interval is built from all 120 measurement series. The calculation of the confidence interval is described in Mittag (2015). The complete function is inside most of the confidence intervals.

Comparing the results from the different pressure values, only the parameter C_1 is found to differ significantly. The correlation between the parameter values and the associated pressures is nearly linear. With a linear regression, the complete function for the damping coefficient can be derived and this function is

$$d(f, A, p) = \frac{0.3072 \cdot 10^{-3} p + 18}{f} + \frac{3 \cdot 10^{-3}}{A} + \frac{5.15 \cdot 10^{-3}}{f A} \quad \left[\frac{\text{Ns}}{\text{m}} \right]. \quad (13)$$

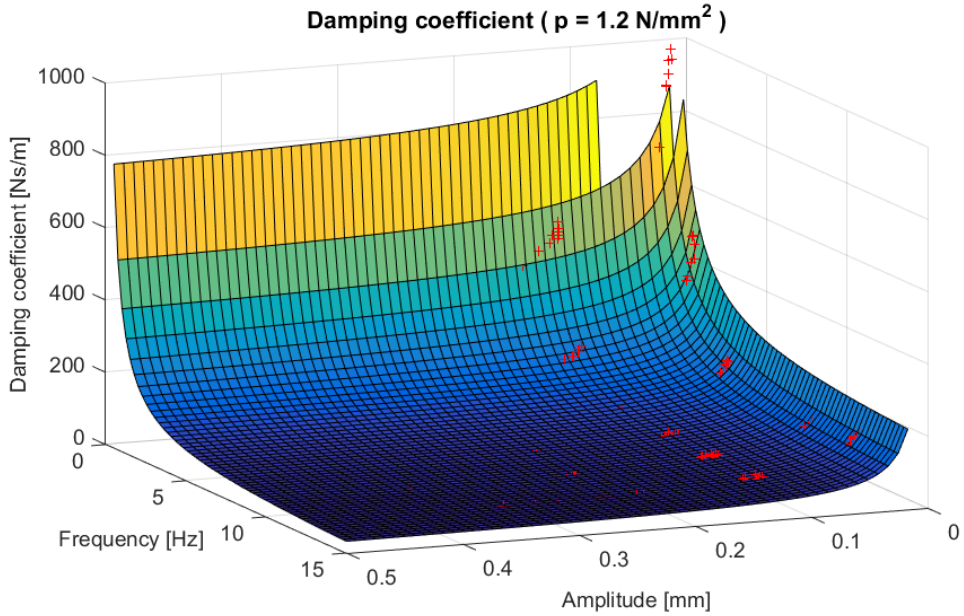


Figure 9: Damping coefficient for a surface pressure of 1.2N/mm^2

5 Conclusion

This paper describes a method to identify a parametric model for a damping coefficient of a stack of sheet metal. This function depends on the surface pressure, the excitation frequency and the displacement of the stack. A test stand was developed and 120 measurement series were recorded. From this measurement data, the damping coefficient was determined by means of the dissipated energy. In order to control the obtained coefficients, a second approach was used. All the calculated damping coefficients were fitted into a global function. The best approximating function was derived by the least square method. At last, the function was compared with the confidence interval of the measurement data.

The function reveals a significant dependance of the damping on the different parameters for the considered test case. The results may be used for multibody simulation analyses of a stack, which is loaded by an oscillated force with a constant excitation frequency.

References

Birkes, D.; Dodge, Y.: *Other Methods*, pages 205–213. John Wiley & Sons, Inc. (1993).

Bograd, S.; Schmidt, A.; Gaul, L.: Joint damping prediction by thin layer elements. In: *Proceedings of the IMAC XXVI: Conference & Exposition on Structural Dynamics, Orlando, FL, USA* (2008).

Clappier, C.; Gaul, L.; Westkmper, E.: Experimental determination of material properties in stacking direction of laminated stacks belonging to electrical machine rotors using a dilatation test. In: *Proceedings of the 22nd International Congress on Sound and Vibration, Florence, Italy* (2015).

Clappier, M.; Gaul, L.: *Experimental Investigation of Structural Damping of Laminated Stacks of Electrical Machine Rotors*, pages 613–624. Springer International Publishing, Cham (2015).

Dresig, H.; Fidlin, A.: *Schwingungen mechanischer Antriebssysteme: Modellbildung, Berechnung, Analyse, Synthese*. Springer Berlin Heidelberg (2014).

Halder, C.; Thurner, T.; Mair, M.: Development of a laser-speckle-based measurement principle for the evaluation of mechanical deformation of stacked metal sheets. In: *Proc. SPIE*, vol. 9132, pages 91321F–91321F–8 (2014).

Luchscheider, V.; Willner, K.; Maidorn, M.: Development of a model to describe the stiffness of an electric motor lamination stack. In: *2012 2nd International Electric Drives Production Conference (EDPC)*, pages 1–5 (Oct 2012).

Mittag, H.: *Statistik: Eine Einführung mit interaktiven Elementen*. Springer-Lehrbuch, Springer Berlin Heidelberg (2015).

Mogenier, G.; Dufour, R.; Ferraris-Besso, G.; Durantay, L.; Barras, N.: Identification of lamination stack properties: Application to high-speed induction motors. *IEEE Transactions on Industrial Electronics*, 57, 1, (2010), 281–287.

Address: Graz University of Technology, Institute for Mechanics, Kopernikusgasse 24/IV, Graz, A-8010 Austria
email: ellermann@tugraz.at

Calculation of Torsional Vibrations and Prediction of Print Quality in Sheetfed Offset Printing Presses

N. Norrick, S. Neeb

In sheetfed offset printing presses the synchronous drive of the paper-carrying cylinders is achieved by a continuous geared drive train. Due to the mechanical compliance of the drive train, the system is capable of torsional oscillations, which are excited by a multiplicity of phenomena. The oscillations of the gear train have a direct effect on print quality. The color register must not fluctuate from sheet to sheet, since fluctuations on the order of a few μm lead to unacceptable printing results. The excitation frequencies or orders in the printing press lead to register errors with corresponding orders on the printed sheets. Using a mechanical model of the printing press, the effects of the excitations on the system can be simulated and, thus, predictions of register variation can be made using a sheet-tracking algorithm. In a practical example, it is shown how due to a harmonic disturbance acting on the main drive motor, register variations occur with a corresponding rhythm. By compensating the excitation (feed-forward control), the torsional vibrations of the machine can be suppressed and the print quality can thus be ensured. This is shown both in the simulation and on the basis of measured data. It is thus possible to predict the effect of mechanical or control-related changes in the design of the printing machine, which ultimately saves time and money during machine development and manufacturing.

1 Introduction

Sheetfed offset printing presses offer high print quality due to the exact hand-over of sheets from one inking unit to the next (Kipphan, 2000). The exact hand-over of sheets at high speeds of up to 18000 sheets/hour (corresponding to five sheets/s or 7.6 m/s sheet velocity for the machine type discussed in this paper) is attained by using cam-driven grippers. A continuous geared drive train connects the paper-carrying cylinders. This drive train is powered by a single electric main drive motor. In this way, sheets can be transported through machines with lengths of 30 m or more with errors on the order of 10 μm . The cutaway view in Figure 1 shows the cylinder layout as well as important components of a modern large format printing press (sheet format up to 1210 mm \times 1620 mm) with six inking units and one varnishing unit (Heidelberg Speedmaster XL162-6+L). The sheets are taken from a paper pile in the feeder (on the right) and accelerated to machine speed, then transported through the machine via grippers, printed with multiple colors on the way, and dried and piled in the delivery (on the left).

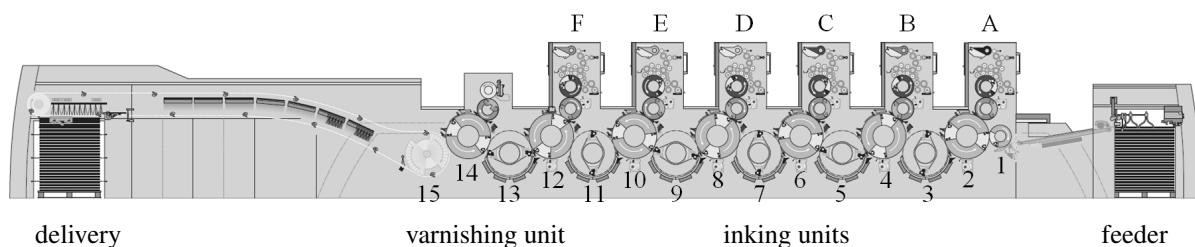


Figure 1. Cutaway view of a Heidelberg Speedmaster XL162-6+L sheetfed offset printing press with six inking units (marked A to F), one varnishing unit and 15 degrees of freedom (marked 1 to 15). The degrees of freedom of the main drive motor and the intermediate gear are not shown. Paper feed direction is from right to left.

Due to the mechanical compliance of the gear coupling, the printing machine is a system capable of torsional oscillation, which is excited by a multiplicity of phenomena. In addition to the reaction torques of the aforementioned gripper mechanisms, examples of predominant excitations are the drive belt (Langer, 2013; Messer, 2013), the

vibrating roller for ink transport (Hummel et al., 1998; Heiler and Hieronymus, 2009), and the rotary encoder of the main drive. In the following, these three excitation mechanisms are briefly described:

a) Drive belt: Due to the manufacturing process of the drive belt, the transmission ratio fluctuates during one belt circumference as described by Langer (2013). This results in an oscillation of the driving torque. The excitation is periodic with respect to the belt loop, allowing it to be divided into harmonic parts using Fourier analysis. These harmonics correspond to non-integer machine orders when calculated in machine coordinates due to the non-integer transmission ratio.

b) Vibrating roller for ink transport: The vibrating roller is an integral part of each inking unit and responsible for the transport of ink from the ink supply fountain into the inking unit. The roller oscillates back and forth between the ductor roller, where it receives ink, and the first ink roller, where it expends ink into the inking unit. It is not driven so that it must be re-accelerated to machine speed at every stroke. This provides a shock-like excitation for the machine, which responds with harmonic vibrations at non-integer machine orders.

c) Rotary encoder of the main drive motor: The errors of the rotary encoder mounted to the shaft of the main drive motor are passed on to the machine via the motor control. The excitation mechanism will be explained in detail in section 4.

The excited torsional vibrations have a direct effect on the printing quality, since the individual colors are transferred successively to the sheet during multicolor printing, but the positions of the colors must match exactly. The correlation of the independently printed colors is called color registration or register. Only minimal variations of the color register from sheet to sheet are tolerable, whereby fluctuation amplitudes of a few μm lead to unacceptable printing results. The excitation frequencies or orders in the printing press can be found as register variations with corresponding orders on the printed sheets. It is a prime example of (inevitable) undersampling: High frequency vibrations of the machine, e.g. the effect of the vibrating roller with an excitation order $f_o = 2.3$ are sampled with one sheet per machine revolution (sampling frequency $f_s = 1$). After a Fast-Fourier-Transform (FFT) into the order domain aliasing leaves us with an amplitude error at the order 0.x because of the formula

$$f_{\text{alias,principal}} = \min |f_o - Nf_s| \quad N \in \mathbb{N}, \quad (1)$$

which yields an order of 0.3 in the current example. Figure 2 shows the connection between the machine vibration, the sampling with one sheet per machine revolution and the transformation of the signal into the order domain. Although an error is made due to undersampling, important information can be obtained from the analysis of the register data.

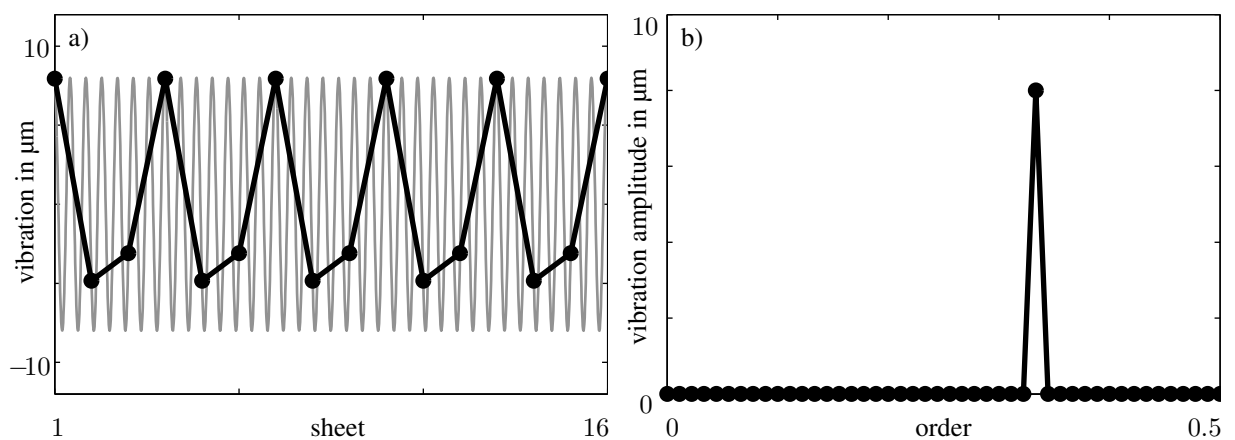


Figure 2. a) High-frequency vibrations of the machine (thin gray curve, machine order 2.3) are sampled with one sheet per machine revolution (black dots). b) Sheet signal transformed into the order domain.

In this context it is important to note that vibrations at integer orders do not result in register variation since they are always sampled at the same phase angle. This is the case, for example, for the reaction torques of the gripper systems. Vibrations with non-integer orders, on the other hand, such as the aforementioned mechanisms, produce disturbances in the printed image.

In the case of web printing machines, a large number of publications dealing with the modeling of the printing machine and the prediction of registration values can be found. A comprehensive process model for web printing was derived for the first time in the 1970s in the groundbreaking works of Brandenburg (1971, 1976). Publications from various research groups followed. This trend has continued up to the present day, as shown by more current research papers (Wolfermann, 1995; Zitt, 2001; Galle, 2007; Schnabel, 2009; Brandenburg, 2011). The overall aim is always dynamic and precise control of print quality in order to increase productivity while at the same time minimizing energy and raw material use. In the case of sheetfed printing presses, this broad basis of publications is missing, although the objectives are fundamentally the same. This paper is one building block in the filling of this gap.

Using a mechanical model of the printing press, the effects of the excitations on the system can be simulated and, with a suitable post-processing algorithm, predictions of register variation can be calculated. The mechanical model and the post-processing algorithm for the prediction of register variation are explained in detail in the following two sections.

2 Mechanical Modeling

Torsional vibration models of the complete printing press have been used for many years to aid in the understanding and design of sheetfed offset printing press dynamics (Buck et al., 2005; Wiese, 1998; Norrick, 2015). Naturally, the necessary modeling depth and complexity are different depending on the questions that need to be answered.

For this work, a discrete torsional degree of freedom (DoF) q_n is assigned for each paper-carrying cylinder. In addition, degrees of freedom are assigned to the drive motor and the intermediate gear. The moments of inertia can be calculated from CAD models of the assembled components. The moments of inertia of the other cylinders and rollers in each printing unit are added to the corresponding printing cylinder. The coupling of the DoF is attained by discrete spring-damper elements which also include the nonlinearity due to gear tooth clearance (backlash). Because of this, the spring-damper elements are dependent on the relative angular position of adjacent cylinders Δq . A schematic of the discrete modeling incorporating backlash is shown in Figure 3. Stiffness and damping values can be evaluated by model updating using measured machine natural frequencies and modal damping.

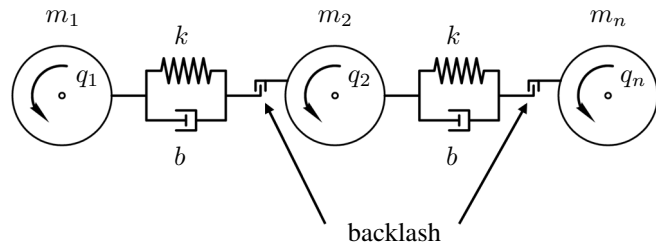


Figure 3. Schematic of the discrete modeling incorporating backlash.

The system equations in matrix form are

$$\mathbf{M}\ddot{\mathbf{q}} + \mathbf{B}(\Delta\mathbf{q})\dot{\mathbf{q}} + \mathbf{K}(\Delta\mathbf{q})\mathbf{q} = \mathbf{T}, \quad (2)$$

with \mathbf{M} being the mass matrix, \mathbf{B} being the damping matrix and \mathbf{K} being the stiffness matrix. The vector of excitation torques \mathbf{T} is described by

$$\mathbf{T} = \mathbf{T}_A(\mathbf{q}, \dot{\mathbf{q}}) + \mathbf{T}_G(\mathbf{q}, \dot{\mathbf{q}}) - \mathbf{T}_R(\dot{\mathbf{q}}). \quad (3)$$

\mathbf{T}_A is the torque from the main motor control, which is only applied to the DoF of the motor. Input values for the motor feedback control are machine angle and machine angular velocity. The control strategy is a cascade control with a proportional (P-) position control and a PI-velocity control. The filtering of the input signals and the signal delay times are accounted for, since these influence the system behavior.

\mathbf{T}_G are the reaction torques of the gripper cams which are dependent on machine angle and angular velocity. The torque values are gained from kinetostatic analysis or detailed multibody simulations, e.g. MSC/ADAMS.

\mathbf{T}_R is the speed-dependent friction torque which is known from many measurements and distributed on the DoF

according to the machine configuration. For example, a printing unit and a varnishing unit have different friction torque values.

The calculation is carried out in the time domain utilizing Matlab/Simulink. To manage the large number of possible machine configurations it is of the utmost importance to ensure a well-structured and automated design of the models.

For the case that the machine behavior is linear, i.e. no backlash occurs during operation, the complex transfer function between the torque of the main drive motor and the relative cylinder rotation

$$\underline{H}(\Omega) = \frac{q_{12} - q_2}{T_A} \quad (4)$$

can be measured as well as calculated from the model. Figure 4 shows the amplitude and phase curves of measured transfer functions for seven printing presses of the same configuration and the comparison with the simulated transfer function for the same configuration. The coherence function γ^2 (as defined by Markert (2013)) gives us information about the reproducibility of the system's behavior. Where the transfer function amplitudes are significant, the coherence is near 1, making it obvious that the system behavior from one machine to the next is reproducible. In addition it is evident that the natural frequencies and modal damping of the mechanical model fit the measured values very well.

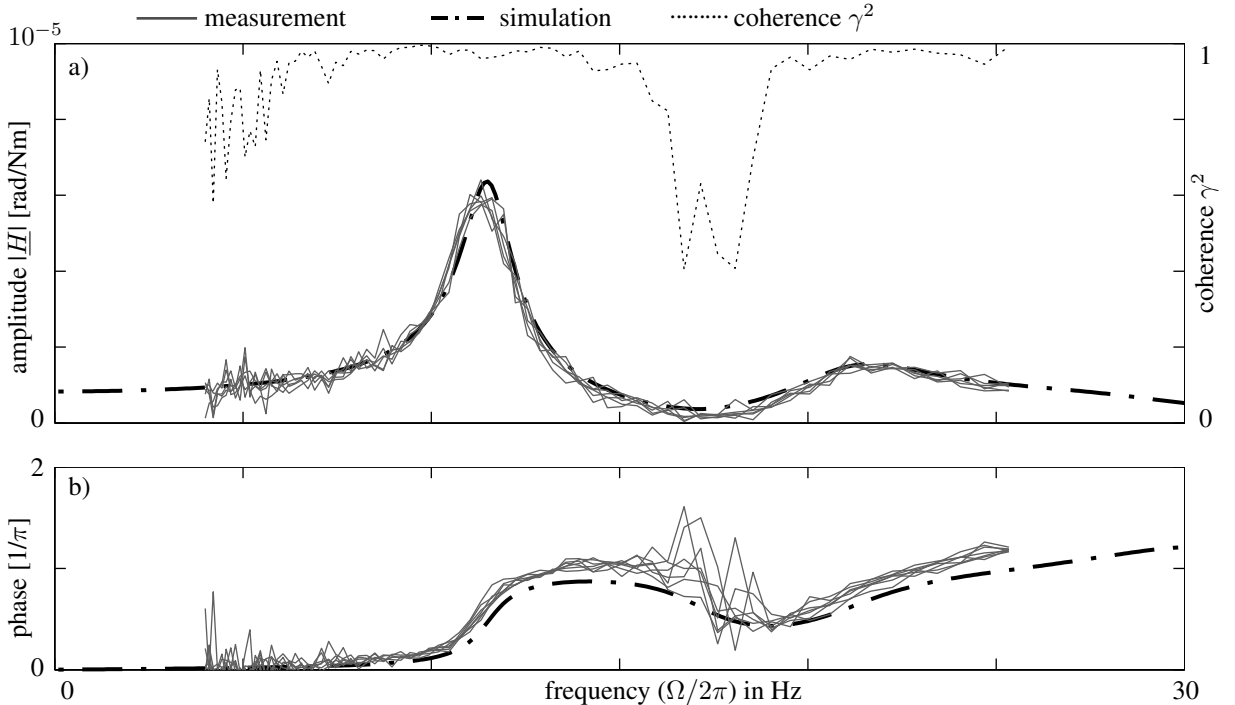


Figure 4. Comparison of measured transfer functions for seven printing presses of the same configuration and simulated transfer function (amplitude (a) and phase (b)) as well as the coherence function γ^2 (reproduced from Norrick, 2015).

3 Post-Processing: Sheet-tracking Algorithm

To predict print quality, starting point is the calculated machine vibration for the operating point of interest. To calculate print quality during stationary operation it is sufficient to simulate the steady state vibrations at a constant printing speed. The algorithm presented here is not limited to steady state operation though, but also suited for transient operation such as emergency stop scenarios.

Preliminary results are rotation angle data for all paper-carrying cylinders at simulation time points ($q_n(t)$). The handover angles, i. e. the nominal cylinder angles at which the sheet transfer takes place, are part of the machine design and known for a certain machine. To track a sheet through the machine, the following steps must be taken: First, for n paper-carrying cylinders the points in time are calculated at which the cylinder angles are equal to the

handover angles. If necessary, interpolation between simulation time points yields more exact results. Next, from this matrix of handover times, the points in time are extracted that correspond to a certain sheet moving through the machine. Then, for each of the $n - 1$ handovers, the difference between the rotation angle of the "giving" cylinder $n - 1$ and the "receiving" cylinder n is calculated. The receiving cylinder is used as a reference. The giving cylinder hands the sheet over too early or too late, depending on the state of vibration of the machine. The angle-based handover errors multiplied by the cylinder radius r are converted into circumferential handover errors u . Finally, the cumulative handover error can be calculated which is equal to the color register from one printing unit to the next. The color register values can be specified relative to the first printing unit or as a register difference between neighboring units.

As an example, the machine model can be subjected to an excitation with the machine order $2\bar{3}$. The simulation is carried out during steady state at printing speeds from 10000 to 14000 sheets/hour for time spans corresponding to 100 sheets. The time domain data are transferred to the sheet-tracking algorithm. Figure 5 shows the simulated machine vibrations at 12000 sheets/hour (relative vibration at the cylinder circumference between the first printing cylinder q_2 und the sixth printing cylinder q_{12}) as a time signal as well as the calculated register variation between printing unit one (DoF 2) and printing unit six (DoF 12) as a sheet signal as well as the values transformed into the order domain.

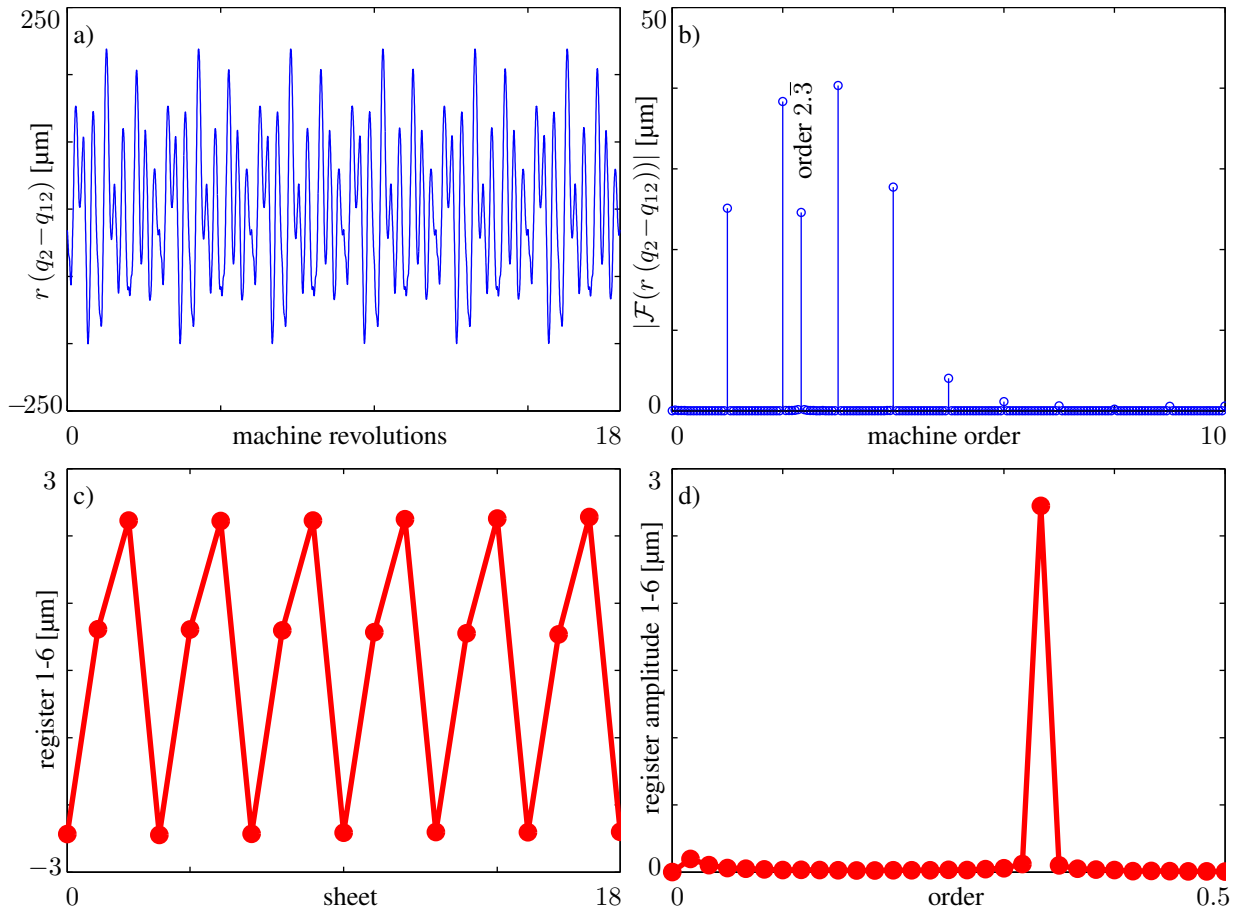


Figure 5. a) Calculated machine vibrations $r(q_2 - q_{12})$ in μm at a printing speed of 12000 sheets/hour, b) amplitude spectrum of the machine vibrations $|\mathcal{F}(r(q_2 - q_{12}))|$ in the order domain in μm at a printing speed of 12000 sheets/hour, c) Calculated color register variation in μm at a printing speed of 12000 sheets/hour, d) Order spectrum of the color register variation in μm at a printing speed of 12000 sheets/hour.

From the plots it is evident that the machine vibrations do not translate directly into register variations. The relative circumferential vibration of the printing cylinders is around $\pm 250 \mu\text{m}$, but this results in only about $\pm 3 \mu\text{m}$ of register variation. This has two reasons. First, only the non-integer machine order $2\bar{3}$ is visible in the register variation, since integer machine orders have no effect on the register as detailed in section 1. Second, the sheets are not handed over at the vibration peaks (in general), but rather at various points of one oscillation. Depending on the mode shape or shapes being excited and the offset angle from one printing unit to the next, a superposition

takes place which can be positive or negative.

Figure 6 shows a summary of the results for the order $2\bar{3}$ and $0\bar{3}$, respectively, over printing speed. It is apparent that the vibration amplitudes of the machine and the register variation exhibit a maximum value around 12300 sheets/hour. This is due to resonance of the first elastic mode of the machine at 8 Hz, excited by the machine order $2\bar{3}$ (12300 sheets/hour $\hat{=} 3.42$ Hz; 3.42 Hz $\times 2\bar{3} = 8$ Hz). Because the damping matrix is not diagonalizable, the mode shape is complex. The motions of the DoF are not in phase with each other, meaning the mode reaches its maximum value at different times for every location. The mode shape is visualized in Figure 7. The S-shape is characteristic of oscillator chains, as Dresig and Holzweißig (2009) have shown. The three-dimensional plot emphasizes the mode shape's twist in the complex plane.

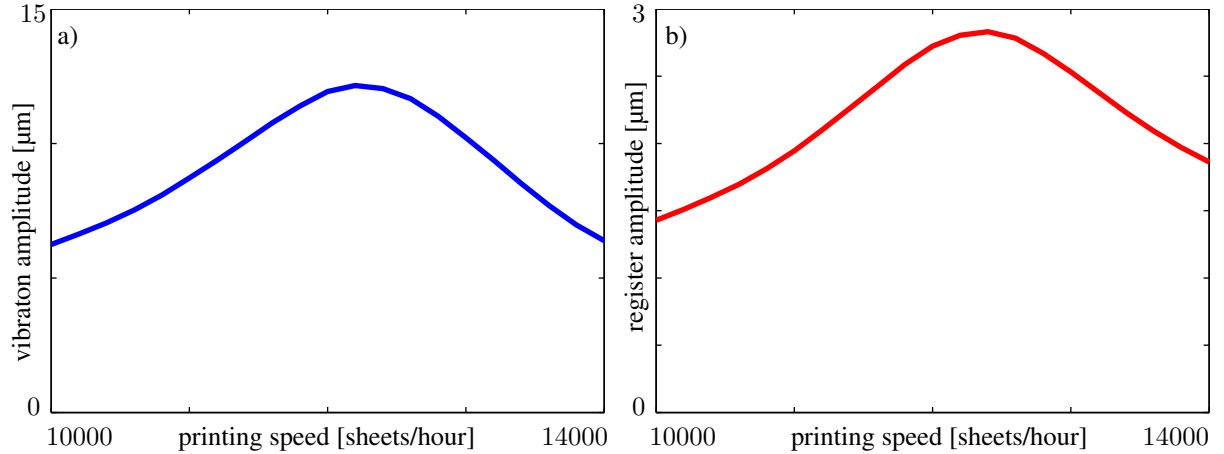


Figure 6. Calculated amplitude of the machine vibrations r ($q_2 - q_{12}$) at order $2\bar{3}$ in μm for printing speeds from 10000 to 14000 sheets/hour, b) Calculated amplitude of the register variation at order $0\bar{3}$ in μm for printing speeds from 10000 to 14000 sheets/hour.

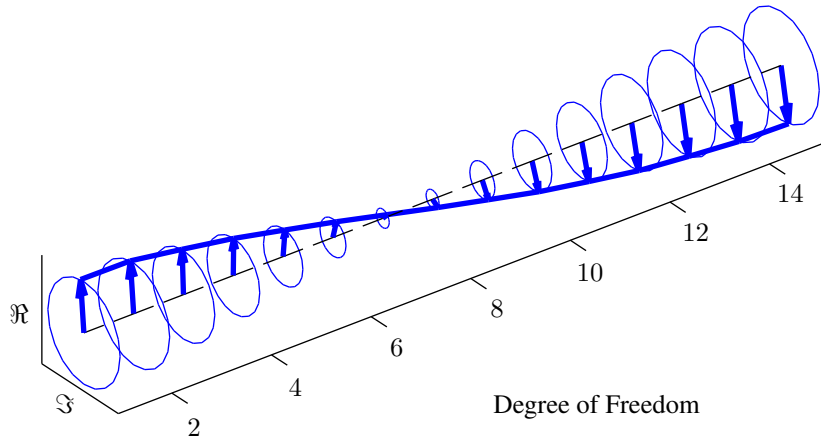


Figure 7. First elastic mode shape of the printing press at 8 Hz. The degrees of freedom of the main drive motor and the intermediate gear are not shown.

4 Example: Disturbance at the Main Drive Motor

A rotary encoder mounted to the shaft of the main drive motor of the printing press is used to generate the speed input signal for the motor control. Internal errors of the rotary encoder as well as external errors due to eccentric mounting of the encoder are responsible for modulating the encoder signal at constant speed with a harmonic error function. A pointer diagram (Figure 8a) shows the vector addition of internal and external encoder errors to a total error vector.

The frequency of this error function is visible in a motor torque variation, which in turn excites high-frequency

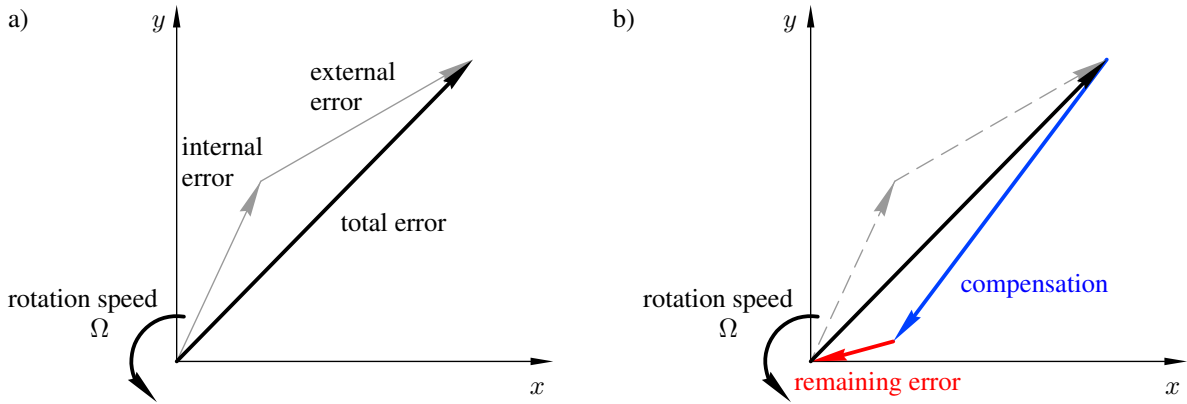


Figure 8. a) Summation of internal and external encoder errors to a total error vector. b) Remaining error after addition of the compensation signal.

vibrations of the printing press. Finally, these vibrations cause register variations with a corresponding rhythm on the printed sheets, leading to unacceptable print quality.

Measurements carried out on a Heidelberg Speedmaster XL162-6+L at a printing speed of 14200 sheets/hour show a variation in the motor torque T_A at machine order 10.06 – a non-integer value. On the printed sheets a register variation at the order 0.06 is visible, corresponding to the value calculated from equation (1). The register variation is mainly visible between printing units one and two. The measurement of the color register is done via optical acquisition of special measurement fields on the printed sheets. When observing the measurement instructions and good print quality in the single colors is given, the measurement uncertainty of this process reaches $< 2 \mu\text{m}$ as detailed by the Polygraphische innovative Technik Leipzig GmbH (2016).

If the amplitude and phase values of the systematic error of the rotary encoder can be determined, the excitation can be compensated. In this way, the control does not "see" the eccentricity of the rotary encoder, so that the machine vibrations are not excited in the first place. Ideally, a signal with the exact amplitude and a phase angle shifted by π is added to the encoder signal. This would result in perfect compensation. Figure 8b shows a pointer diagram of the effect of the addition of a non-ideal compensation value, which corresponds to an error in the determined values of amplitude and phase angle.

The effectiveness of the compensation method can be demonstrated through simulation. In the model the encoder signal is superimposed by a sinusoidal disturbance with known amplitude and phase. Figure 9 shows the simulated amplitude spectra of the drive torque and the register variation without and with compensation of the encoder error. Naturally, when applying an ideal compensation in the model, there is no remaining error. Therefore, for the simulation results shown here, it was assumed that the value for the phase angle of the encoder error was incorrectly entered with $\Delta\varphi = 10^\circ$, so that only an incomplete compensation of the error takes place. Since

$$|1 - e^{i\Delta\varphi}| \approx 0.83 \quad (5)$$

we expect a reduction of the motor torque vibration as well as the register variation of 83%, which is verified by the simulation.

With the help of the machine model, it is clear why the register error develops mainly between the first and second printing units: The order 10.06 excites a frequency of 40 Hz at 14200 sheets/hour. At this frequency, a mode shape of the machine is excited in which mainly the main drive motor and the first cylinders (degrees of freedom one to four) of the machine are involved. The eigenvector has hardly any deflections in the rear part of the machine, as shown in Figure 10.

The simulated behavior without and with compensation was tested on a real machine. The driving torque was recorded parallel to the printing of test sheets. After a first run without compensation, the compensation algorithm was activated in the main drive control and a second run with compensation was performed. In the measurements, a reduction of the driving torque fluctuation of 94% and a reduction of the register variation of 93% were achieved, as shown in Figure 11. In the amplitude spectrum of the drive torque it is evident that only the 10.06 is affected

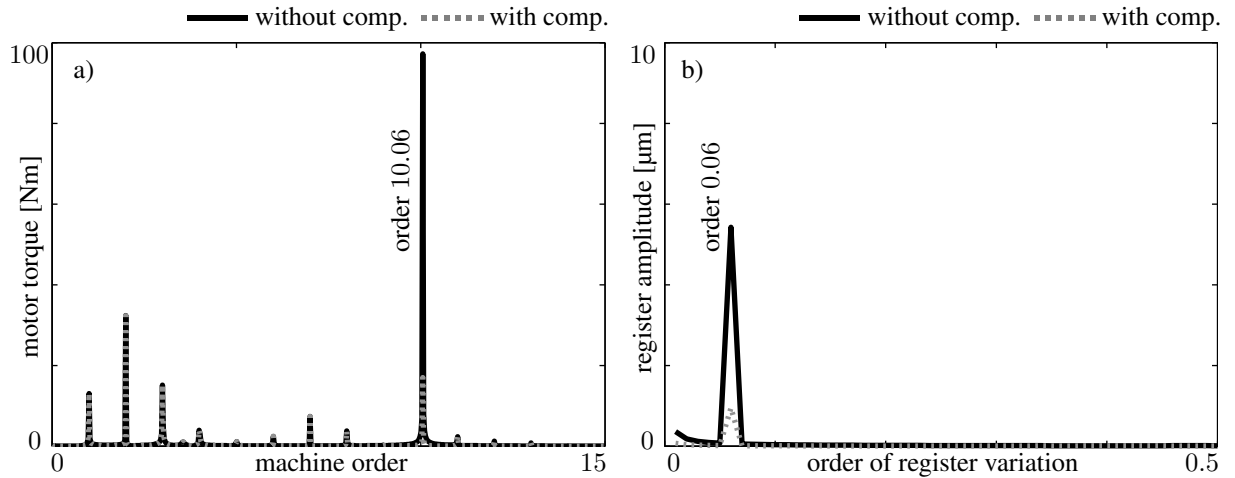


Figure 9. a) Calculated amplitude spectrum of the motor torque in machine coordinates [Nm] without and with compensation of the rotary encoder error. b) Calculated amplitude spectrum of the register variation from 100 consecutive sheets [μm] without and with compensation of the rotary encoder error.

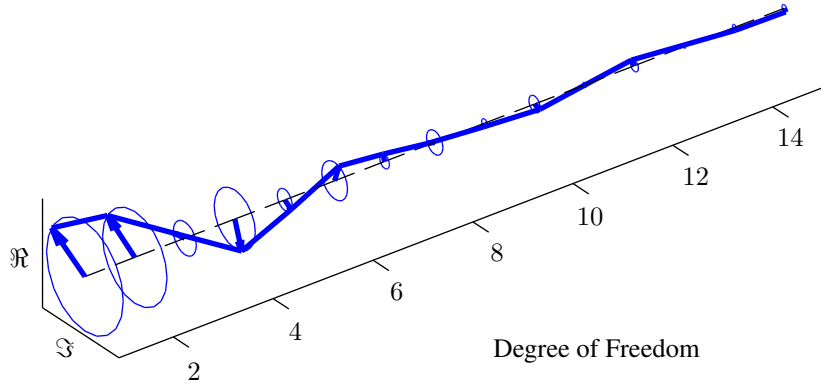


Figure 10. Elastic mode shape of the printing press at 40 Hz. The degrees of freedom of the main drive motor and the intermediate gear are not shown.

by the compensation algorithm, as was the case in the simulation. The amplitudes of the other orders remain the same. This is also the case for the measured register variation where only the order 0.06 is influenced by the compensation.

Table 1 shows a summary of the results for direct comparison. The erroneous torque on the order of magnitude of 100 Nm generates a register variation of several μm in the measurement as well as in the simulation. Both simulation and measurement show the proportional relationship between torque and register variation.

		amplitude motor torque order 10.06	amplitude register variation order 0.06
simulation	without compensation	97.2 Nm	5.4 μm
	with compensation	17.0 Nm	0.9 μm
	reduction	83%	83%
measurement	without compensation	92.2 Nm	7.1 μm
	with compensation	5.6 Nm	0.4 μm
	reduction	94%	93%

Table 1. Summary of the simulation and measurement results.

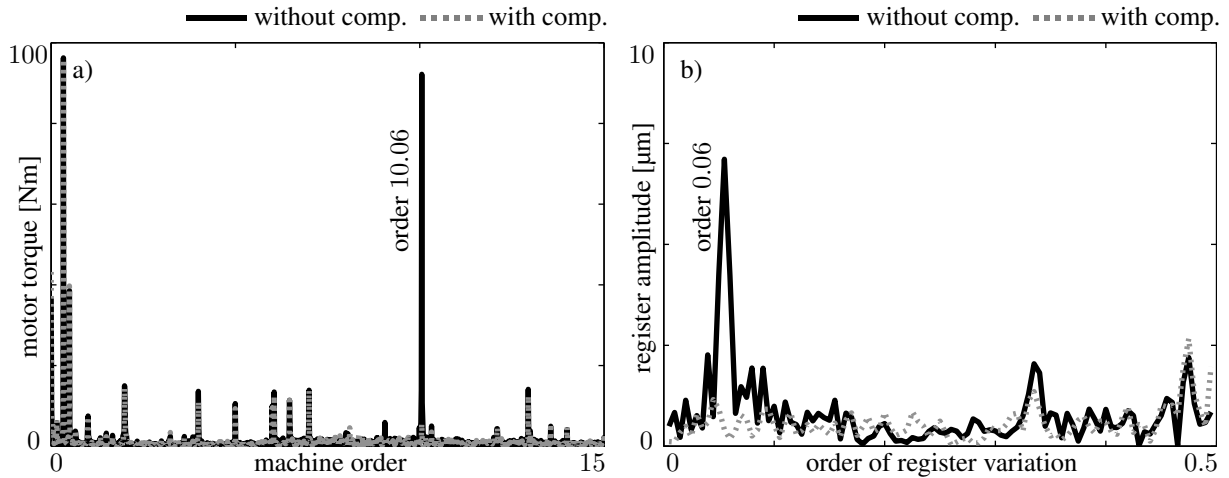


Figure 11. a) Measured amplitude spectrum of the motor torque in machine coordinates [Nm] without and with compensation of the rotary encoder error. b) Measured amplitude spectrum of the register variation from 100 consecutive sheets [μm] without and with compensation of the rotary encoder error.

5 Summary and Conclusions

Using the presented mechanical model in conjunction with the post-processing sheet-tracking algorithm, it is possible to predict the effect of mechanical or control-related changes on the sheetfed offset printing press directly with regard to print quality. The method is suitable for steady-state printing at constant printing speed but also for transient processes such as emergency stop. The comparison of simulation and measurement in a case study shows a good agreement. In the range of a few μm , the effects of vibration excitations on the printed image can be predicted. These predictions can ultimately save time and money in machine development and production.

References

Brandenburg, G.: *Über das dynamische Verhalten durchlaufender elastischer Stoffbahnen bei Kraftübertragung durch Coulomb'sche Reibung in einem System angetriebener, umschlungener Walzen*. Dissertation TU München, München (1971).

Brandenburg, G.: *Verallgemeinertes Prozessmodell für Fertigungsanlagen mit durchlaufenden Bahnen und Anwendung auf Antrieb und Registerregelung bei Rotationsdruckmaschinen*, vol. 1(46). VDI-Verlag, Düsseldorf (1976).

Brandenburg, G.: New mathematical models and control strategies for rotary printing presses and related web handling systems. *IFAC Proceedings Volumes*, 44, (2011), 8620–8632.

Buck, B.; Knopf, E.; Schreiber, S.; Seidler, M.: Nichtlineare Schwingungsphänomene in Bogenoffsetdruckmaschinen. *VDI-Berichte*, Nr. 1917, (2005), 345–361.

Dresig, H.; Holzweißig, F.: *Maschinendynamik*. Springer-Verlag, Berlin Heidelberg (2009).

Galle, A.: *Regelungstechnische Untersuchung der Bedruckstoffförderung in Rollendruckmaschinen*. TU Chemnitz, Chemnitz (2007).

Heiler, P.; Hieronymus, J.: Farbwerk einer Druckmaschine. *Patent DE 102009008778 A1*, (2009).

Hummel, P.; Ortner, R.; Hinz, M.: Farbwerk für eine Rotationsdruckmaschine. *Patent DE 19715614 A1*, (1998).

Kipphan, H.: *Handbuch der Printmedien: Technologien und Produktionsverfahren*. Springer-Verlag, Berlin Heidelberg (2000).

Langer, P.: Bestimmung der Übertragungsgüte von Riementrieben. *VDI-Berichte*, Nr. 2197, (2013), 129–140.

Markert, R.: *Strukturdynamik*. Shaker, Aachen (2013).

Messer, M.: Parametererregte Drehschwingungen im Antriebsstrang von Bogenoffsetdruckmaschinen. *VDI-Berichte*, Nr. 2197, (2013), 1–12.

Norrick, N.: Statistical consideration of uncertainties in bolted joints of the drive train of sheet-fed offset printing presses. *Applied Mechanics and Materials*, 807, (2015), 3–12.

Polygraphische innovative Technik Leipzig GmbH: Produktdatenblatt Passer-Messsystem Luchs III and Pitsid. (2016).

Schnabel, H.: *Entwicklung von Methoden zur Registerregelung in Abhängigkeit der Bahnzugkraft bei Rollen-Tiefdruckmaschinen*. Sierke-Verlag, Göttingen (2009).

Wiese, H.: Antriebsdynamische Untersuchungen an Bogenoffsetmaschinen. *VDI-Berichte*, Nr. 1416, (1998), 105–118.

Wolfermann, W.: Tension control of webs - a review of the problems and solutions in the present and future. In: *Proceedings of Third International Conference on Web Handling*, pages 198–228, Stillwater, Oklahoma (1995).

Zitt, H.: *Entwicklung einer Modell-Bibliothek zur Simulation von Bahnspannung und Tänzerbewegung beim Transport von Materialbahnen*. Dissertation Universität des Saarlandes, Saarbrücken (2001).

Address: Nicklas Norrick, Heidelberger Druckmaschinen AG, Alte Eppelheimer Str. 26, 69115 Heidelberg, Germany
email: nicklas.norrick@heidelberg.com

Dynamic Behaviour of EHD-contacts using a regularised, mass conserving Cavitation Algorithm

S. Nitzschke, E. Woschke, C. Daniel

The paper deals with the holistic simulation of systems supported in journal bearings, which is demonstrated using the example of a conrod's big end bearing. For that purpose, primarily the interactions of multibody-, structure- and hydrodynamics have to be described. Based on the time integration of the global equations of motions, the non-linear bearing forces in the fluid film and the elastic deformation of the bearings surfaces have to be modelled adequately concerning their mutual influence. The implementation of the elastic structure is carried out by means of a hierachised, IRS-based modal reduction in order to represent its eigenbehaviour as realistic as possible and to fulfil the requirement of low computational costs by reducing the number of degree of freedoms. Additionally, the journal bearing is considered by an online solution of the Reynolds equation, whereat the cavitation is handled by a transient acting, mass-conserving algorithm. This is based on the classical Elrod algorithm, but was extended by a regularisation, which enables a faster and more stable solution. Due to the general approach, both mechanical and tribological output quantities are accessible. This provides the possibility to draw a comparison with simpler approaches and to emphasize the benefit of the described procedure.

1 Introduction

The transient simulation of systems supported in journal bearings and exposed to high dynamic loads requires the description of the interaction between different field problems to determine the vibrations of the structure.

Firstly, the global behaviour due to the external loads has to be modelled including the elastic deformations. Taking large non-linear rigid body motions with superimposed small elastic deformations into account, an elastic MBS² approach based on the SID-formulation³ is state of the art. To assure an adequate description of the transient behaviour, the hydrodynamic properties have to be considered.

In transient rotor-dynamics often a look-up table approach, which involves a stepwise linearisation of the bearing forces w.r.t. the displacements, is used in order to keep the numerical effort at a low level. Here it is not possible to represent the transient elastic deformations, which result from high dynamic forces. In contrast, a direct solution of the Reynolds equation is necessary yielding the actual hydrodynamic pressure in the fluid film. Whereas compressive loads are unproblematic for fluids, tensile loads lead to cavitation effects in the form of fluid vaporisation and emission of dissolved air. To consider these phenomena in the numerical scheme of EHL⁴ analyses, several approaches exist. A pragmatical way is to postulate all negative pressure values to become zero, which is known as Half-Sommerfeld or Gumbel condition. The resulting drawback is the violation of the mass conservation, which was used to derive the Reynolds equation. Furthermore, differences concerning the minimal film thickness, the maximum pressure and especially the damping property can be expected.

Sophisticated approaches, which fulfil the mass conservation are given by Elrod's algorithm (Elrod and Adams (1974); Elrod (1981); Kumar and Booker (1991); Shi and Paranjpe (2002); Ausas et al. (2009)), the bi-phase model (Feng and Hahn (1986); Zeidan and Vance (1989); Tao et al. (2000); Gienicke et al. (2000)) as well as the ALE-approach⁵ (Hu and Liu (1993); Martinet and Chabrand (2000); Boman and Ponthot (2004); Schweizer (2008)).

¹Improved Reduction System

²Multibody System

³Standard Input Data

⁴Elasto-Hydrodynamic Lubrication

⁵Augmented-Lagrangian-Eulerian approach

The first one is widely-used also in EHL applications (Boedo et al. (1995); Shi and Paranjpe (2002); Rho and Kim (2003); Hajjam and Bonneau (2007)), whereat often the rotating structure is oversimplified to a mass point. Nevertheless – due to the necessarily fine discretisation of the cavitation boundary and the elastic structure on the bearing surface – high computational efforts arise. Aiming for stationary results, good solutions are achievable, whereas under dynamic conditions (depending on position, velocity, deformation and the numerical discretisation) cyclic repetitions of non-convergent iteration states during the solution of the Reynolds equation occur preventing a convergent pressure distribution in the fluid film.

As a consequence the time integration would fail, unless the solution strategy is able to assure a valid pressure distribution under all kinematic conditions. For that purpose a regularised variant of Elrod's algorithm was developed, which solves the problem by the introduction of a fuzzy cavitation state (Nitschke et al. (2016)).

Using the example of a crank-drive and the support of the conrod's big end bearing, the differences between the Gumbel and the modified Elrod algorithm are discussed in the context of the numerical results and the necessary cpu-time. Beside the hydrodynamic properties, the increased level of detail concerning the film-fraction is also relevant for the interaction with further field problems, e.g. thermodynamics of the bearing and its surrounding.

2 Theoretical Principles

The main part of the presented approach is the implementation of the non-linear stiffness and damping properties of the bearing into the overall transient simulation. Starting with the numerical solution of the Reynolds equation using a regularised Elrod algorithm, the bearing reaction forces and torques are derived. Afterwards, the elastic behaviour of the bearing elements is taken into account via FEM⁶. Additionally, the global movement of the deformable components is modelled by an E-MBS⁷ approach, which involves a model-reduction due to simulation time issues.

2.1 Hydrodynamics

2.1.1 Regularised Cavitation Approach

The pressure distribution in the fluid film of journal bearings due to the movement of shell and pin is described by the Reynolds PDE⁸, which can be derived from Navier-Stokes equations and conservation of mass regarding the geometrical relations in the fluid gap. Elrod and Adams transformed this equation leading to the density relation $\theta = \varrho / \varrho_c$ as universal unknown, which depends on the compression modulus β

$$\underbrace{\frac{\partial}{\partial x} \left(\frac{h^3}{12\eta} g(\theta) \beta \frac{\partial \theta}{\partial x} \right) + \frac{\partial}{\partial y} \left(\frac{h^3}{12\eta} g(\theta) \beta \frac{\partial \theta}{\partial y} \right)}_{\text{Poiseuille-flow}} = \underbrace{\frac{U_s + U_j}{2} \frac{\partial(\theta h)}{\partial x}}_{\text{Couette-flow}} + \underbrace{\frac{\partial(\theta h)}{\partial t}}_{\text{squeeze-flow}}. \quad (1)$$

As a result, the conservation of mass is ensured even in cavitating regions – i.e. in regions with divergent film height. This involves the implementation of a switch-function $g(\theta)$, which suppresses the Poiseuille-flow in these regions. The disadvantage of the resulting formulation is the calculation of the pressure from the film-fraction. Due to the magnitude of the compression modulus ($\beta \approx 10^9 \text{ Pa}$), restrictive error tolerances for the film-fraction are needed to assure sufficient accuracy of pressure and thereby bearing forces as well as torques.

Utilising the fact that in the cavitation region a mixture of fluid and air occurs, Kumar and Booker introduced the application of the following approaches for density ϱ and viscosity η of the mixture depending on the film-fraction ϑ

$$\varrho = \vartheta \varrho_{\text{liq}} + (1 - \vartheta) \varrho_{\text{gas}} \approx \vartheta \varrho_{\text{liq}} \quad \text{and} \quad \eta = \vartheta \eta_{\text{liq}} + (1 - \vartheta) \eta_{\text{gas}} \approx \vartheta \eta_{\text{liq}} \quad (2)$$

⁶Finite Element Method

⁷Elastic Multibody System

⁸Partial Differential Equation

leading to a modified form of Eq. (1)

$$\frac{\partial}{\partial x} \left(\frac{\varrho_{\text{liq}} h^3}{12\eta_{\text{liq}}} \frac{\partial p}{\partial x} \right) + \frac{\partial}{\partial y} \left(\frac{\varrho_{\text{liq}} h^3}{12\eta_{\text{liq}}} \frac{\partial p}{\partial y} \right) = \frac{U_S + U_J}{2} \frac{\partial(\vartheta \varrho_{\text{liq}} h)}{\partial x} + \frac{\partial(\vartheta \varrho_{\text{liq}} h)}{\partial t} . \quad (3)$$

This form is now depending on the pressure p as well as the film-fraction ϑ , which show a complementary relation. To obtain a solution, firstly the following relations are introduced in order to get a dimensionless formulation

$$H = \frac{h}{\Delta r^*}, \quad X = \frac{x}{r^*}, \quad Y = \frac{y}{r^*}, \quad \bar{\eta} = \frac{\eta_{\text{liq}}}{\eta^*}, \quad u_m = \frac{U_S + U_J}{2}, \quad P = \frac{p(\Delta r^*)^2}{\eta^* |u_m| r^*}, \quad T = \frac{t |u_m|}{r^*} . \quad (4)$$

Furthermore, the definition of a common variable Π is useful

$$\Pi(x, y) \stackrel{!}{=} \begin{cases} \vartheta(x, y) - 1 & (x, y) \in \Omega_{\vartheta} \\ P(x, y) & (x, y) \in \Omega_p \end{cases} , \quad (5)$$

which has to be interpreted depending on its actual value: In the pressure region Ω_p it correlates with the dimensionless pressure P , whereas in the cavitation region Ω_{ϑ} it contains the film-fraction. Defining a switch-function in analogy to Eq. (1)

$$g(\Pi) \stackrel{!}{=} \begin{cases} 0 & \forall \Pi < 0 \\ 1 & \forall \Pi \geq 0 \end{cases} , \quad (6)$$

the equivalents to Eq. (5) and Eq. (6) read by reversal conclusions

$$\vartheta(x, y) = (1 - g)(\Pi(x, y) + 1) + g \quad \text{and} \quad (7)$$

$$P(x, y) = g \Pi(x, y) , \quad (8)$$

which can be inserted in Eq. (3)

$$\begin{aligned} & \left[\frac{\partial}{\partial X} \left(\frac{H^3}{12\bar{\eta}} \frac{\partial(g\Pi)}{\partial X} \right) + \frac{\partial}{\partial Y} \left(\frac{H^3}{12\bar{\eta}} \frac{\partial(g\Pi)}{\partial Y} \right) - \text{sgn}(u_m) \frac{\partial H}{\partial X} - \frac{\partial H}{\partial T} \right] \\ & + \left[\text{sgn}(u_m) \frac{\partial((g-1)\Pi H)}{\partial X} + \frac{\partial((g-1)\Pi H)}{\partial T} \right] = 0 . \end{aligned} \quad (9)$$

In order to solve Eq. (9) numerically, the bearing surface is discretised using a FVM⁹ approach. Therefore, in the pressure region central differences replace the differential quotient, whereas in the cavitation region due to the transport character of Couette-flow backward differences are applied. Finally, this leads to the non-linear system of equations

$$\mathbb{A}(g) \mathbb{p} = \mathbb{r}(g) , \quad (10)$$

with a sparse, unsymmetric matrix \mathbb{A} and a vector \mathbb{p} , which contains the unknown values of Π . The partition of the regions Ω_p and Ω_{ϑ} is initially unknown. Hence, Eq. (10) has to be solved by a fix-point iteration of the form

$$\mathbb{p}^{(i+1)} = \mathbb{A}(g^{(i)})^{-1} \mathbb{r}(g^{(i)}) . \quad (11)$$

A convergent state of iteration is found, if the values of the switch-function remain constant. Under transient loads the described algorithm tends to poor convergence, whereat cyclic repetitions in the solution of Eq. (11) occur. This behaviour complicates the application within rotor- or structredynamic models. Obviously, in these cases the cavitation boundary is represented insufficiently, as its discretisation is coupled to the numerical grid. Therefore, a finer mesh is able to improve the situation, but the computational costs increase and the general problem remains: A given finite volume is either associated to the pressure *or* to the cavitation region. A redefinition of the Heaviside-like switch-function Eq. (6), e.g. by

$$g(\Pi) = \frac{1}{\pi} \arctan \left(\frac{\Pi}{1 - \Pi^*} \right) + \frac{1}{2} , \quad (12)$$

⁹Finite Volume Method

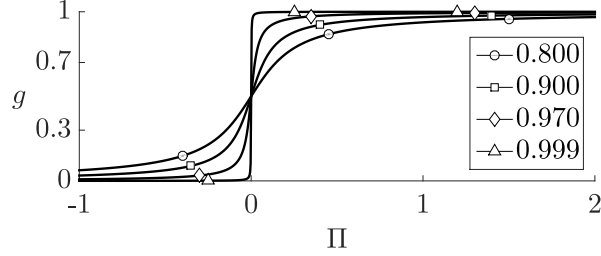


Figure 1: Influence of regularisation parameter Π^* on the smoothed switch-function Eq. (12).

allows a finite volume to be part of both regions. The stepwise respectively discrete non-linearity of Eq. (10) is thereby regularised. Additionally, by the smooth transition a Newton-Raphson algorithm is applicable to solve the non-linear system of equations. For that purpose, Eq. (10) is to be seen as a function of p

$$f(p) \mapsto r(p) - A(p) = 0 \quad , \quad (13)$$

whereof using a Taylor series interrupted after the first term yields

$$p^{(i+1)} = p^{(i)} - J(p^{(i)})^{-1} f(p^{(i)}) \quad (14)$$

with the Jacobian

$$J(p^{(i)}) = \frac{\partial f}{\partial p} \Big|_{p^{(i)}} = \frac{\partial r}{\partial p} \Big|_{p^{(i)}} - \left(A(p^{(i)}) + \frac{\partial A}{\partial p} \Big|_{p^{(i)}} p^{(i)} \right) \quad . \quad (15)$$

The partial derivatives of r and A can be expressed analytically and in addition only the derivative of Eq. (12) is required

$$\frac{\partial g}{\partial \Pi} = \left(\pi (1 - \Pi^*) \left[1 + \left(\frac{\Pi}{1 - \Pi^*} \right)^2 \right] \right)^{-1} \quad . \quad (16)$$

2.1.2 Validation of Hydrodynamics

The described approach was benchmarked in [Nitschke et al. \(2016\)](#) against simulation results published in the literature [Vijayaraghavan and Keith \(1989\)](#) under static conditions. Furthermore, a convergence study was performed concerning the meshsize and the influence of the regularisation parameter Π^* . It was found, that from approximately 1000 unknowns and in the region of $\Pi^* = 0.9 \dots 0.95$ the influences on the pressure distribution and the bearing force as well as its direction can be neglected.

Concerning dynamic loads, another example stated in [Ausas et al. \(2009\)](#) was used. Therein, a transient calculation of a single journal bearing under a load as it occurs in a main bearing of a crank-drive is examined. The equations of motion are restricted to a planar motion of the pin, which was modelled as a point mass. The shell features

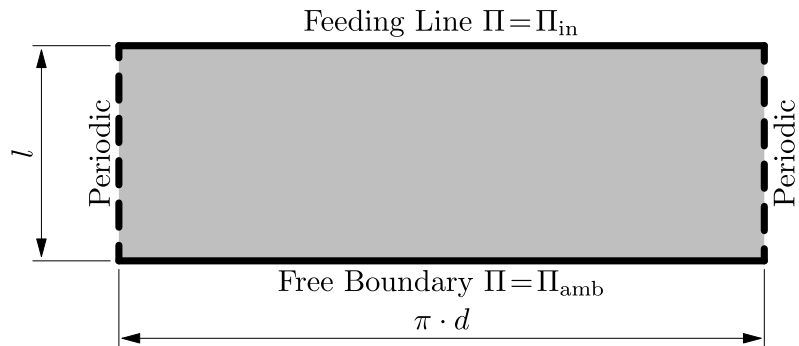


Figure 2: Scheme of half bearing surface with boundary conditions as stated in [Ausas et al. \(2009\)](#).

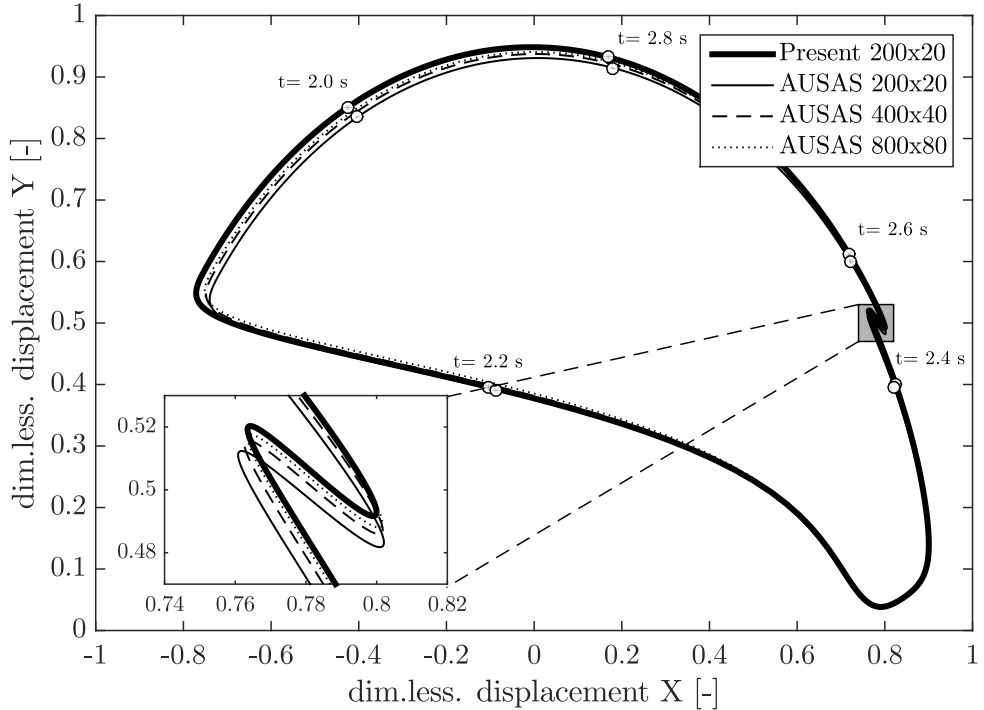


Figure 3: Orbit of the pin under transient conditions during one working cycle: comparison of the regularised algorithm against the classic algorithm of reference [Ausas et al. \(2009\)](#) with variation of the reference meshsize.

an axially centred circumferential groove ensuring the oil supply. Hence, only one bearing half is modelled, cf. Fig. 2.

As the reference solution and the corresponding source code is publicly available, the present approach can be opposed to the reference. The calculated orbits of the pin are displayed in Fig. 3 for one working cycle. In general, using an equal meshsize of 200x20, a good correlation between both approaches can be stated, whereas the reference tends to show the smaller orbit. It is interesting that, a refinement of the *reference mesh* leads to convergence against the 200x20 solution of the approach presented here. In reverse it can be concluded, that the latter shows a better solution quality even on a coarse mesh. This is caused by the property of Eq. (9) respectively Eq. (14) to allow grid point to be part of pressure as well as the cavitation region: The boundary between both is not longer restricted to run on the grid lines, but in contrast is able to cross a finite volume, cf. Fig. 4.

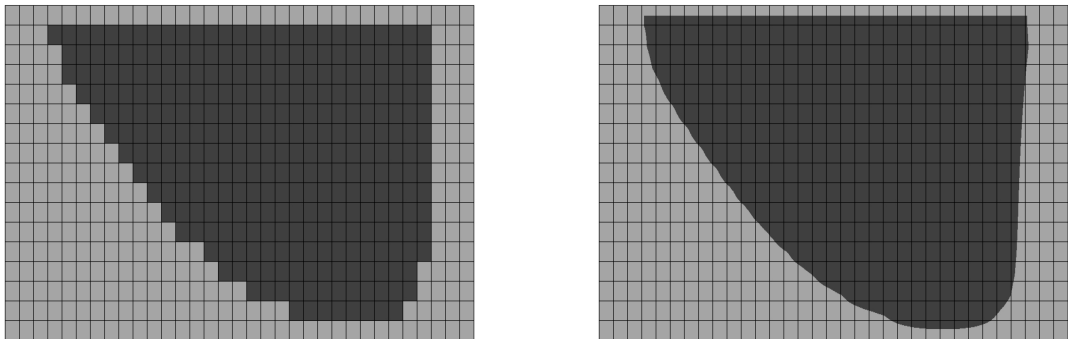


Figure 4: Representation of the boundary between pressure and cavitation region with the classic algorithm of reference (left) and the regularised algorithm (right) ([Nitzschke et al. \(2016\)](#)). The pressure region is indicated by light and the cavitation region by dark gray.

Table 1: Comparison of cpu-time under otherwise identical conditions concerning the results shown in Fig. 3.

regularised algorithm		classic algorithm	
meshsize	cpu-time [s]	meshsize	cpu-time [s]
200 × 20	254	200 × 20	480
		400 × 40	5790
		800 × 80	≈ 70000

Supplementary, due to the application of the Newton-Raphson algorithm the cpu-time is reduced by a factor of two under otherwise identical conditions. If the achieved accuracy is taken into account, the finest reference mesh has to be used for the comparison leading to a remarkable benefit of the regularised algorithm, cf. Tab. 1.

2.2 Elastic Deformations and Modal Reduction

Within the hydrodynamic contact in a crank shaft, the deformations in a conrod bearing show the same magnitude as the clearance. Hence, the elastic deformation of the bearing contour due to the mechanical loads and the appropriate surface velocity have to be taken into account. A proper method to provide the elastic behaviour during simulation is the FEM.

2.3 Structural Dynamics

2.3.1 FEM-approach of non-moving Structures

Starting from the Hamiltonian principle, according to discretisation and formulation of suitable shape functions of the variational function, a linear system of equations can be derived

$$\mathbb{M} \ddot{\mathbf{u}} + \mathbb{D} \dot{\mathbf{u}} + \mathbb{K} \mathbf{u} = \mathbf{f} \quad , \quad (17)$$

in which \mathbb{M} represents the mass-, \mathbb{D} the damping- and \mathbb{K} the stiffness matrix. The vector \mathbf{f} represents the external forces and \mathbf{u} the displacements of nodal degrees of freedom. To minimise the numerical effort in the context of time integration algorithms, a reduction of the degree of freedoms is mandatory. This can be achieved by a reduction based on the master-slave concept or by a modal reduction.

2.3.2 Master-Slave Reduction

Firstly, the degrees of freedom of the overall structure are subdivided in master- and slave-degrees of freedom and sorted according to the following scheme

$$\begin{bmatrix} \mathbb{M}_{MM} & \mathbb{M}_{MS} \\ \mathbb{M}_{SM} & \mathbb{M}_{SS} \end{bmatrix} \begin{bmatrix} \ddot{\mathbf{u}}_M \\ \ddot{\mathbf{u}}_S \end{bmatrix} + \begin{bmatrix} \mathbb{D}_{MM} & \mathbb{D}_{MS} \\ \mathbb{D}_{SM} & \mathbb{D}_{SS} \end{bmatrix} \begin{bmatrix} \dot{\mathbf{u}}_M \\ \dot{\mathbf{u}}_S \end{bmatrix} + \begin{bmatrix} \mathbb{K}_{MM} & \mathbb{K}_{MS} \\ \mathbb{K}_{SM} & \mathbb{K}_{SS} \end{bmatrix} \begin{bmatrix} \mathbf{u}_M \\ \mathbf{u}_S \end{bmatrix} = \begin{bmatrix} \mathbf{f}_M \\ \mathbf{f}_S \end{bmatrix} \quad , \quad (18)$$

whereat the master-group is still present after the reduction and the slave-group will be expressed as a function of the master degrees of freedom using a suitable transformation matrix \mathbb{Q}_{red}

$$\begin{bmatrix} \mathbf{u}_M \\ \mathbf{u}_S \end{bmatrix} = \mathbb{Q}_{red} \mathbf{u}_M \quad . \quad (19)$$

Different variants with specific advantages and disadvantages exist: The simplest form of reduction dates back to Guyan (1965) and neglects all dynamic effects of the slave structure, which is widely known as static condensation

$$\begin{bmatrix} \mathbf{u}_M \\ \mathbf{u}_S \end{bmatrix} = \begin{bmatrix} \mathbb{I} \\ -\mathbb{K}_{SS}^{-1} \mathbb{K}_{MS}^T \end{bmatrix} \mathbf{u}_M = \mathbb{Q}_G \mathbf{u}_M \quad . \quad (20)$$

The application of the transformation matrix to all system matrices and the subsequent symmetrisation

$$\mathbb{S}_G = \mathbb{Q}_G^T \mathbb{S} \mathbb{Q}_G \quad \text{with} \quad \mathbb{S} = \mathbb{M}, \mathbb{D}, \mathbb{K} \quad (21)$$

leads to the differential equation of the reduced system

$$\mathbb{M}_G \ddot{\mathbf{u}}_M + \mathbb{D}_G \dot{\mathbf{u}}_M + \mathbb{K}_G \mathbf{u}_M = \mathbf{f}_G \quad . \quad (22)$$

However, as the excitation frequency rises, increasing deviations occur compared to the dynamic behaviour of the unreduced structure. An improvement can be made by consideration of the dynamic behaviour of the slave degrees of freedom. A popular method of improvement without the usage of additional modal degrees of freedom (as done in the Craig-Bampton- ([Craig \(2000\)](#)) or the SEREP-reduction ([O'Callahan \(1989b\)](#))) is the IRS-method by [O'Callahan \(1989a\)](#). Therein, the Guyan approach is extended with pseudostatic inertial forces, which leads after some conversions to the following transformation matrix

$$\begin{bmatrix} \mathbf{u}_M \\ \mathbf{u}_S \end{bmatrix} = \mathbb{Q}_{IRS} \mathbf{u}_M = (\mathbb{Q}_G + \mathbb{P} \mathbb{M} \mathbb{Q}_G \mathbb{M}_G^{-1} \mathbb{K}_G) \mathbf{u}_M \quad \text{with} \quad \mathbb{P} = \begin{bmatrix} 0 & 0 \\ 0 & \mathbb{K}_{SS}^{-1} \end{bmatrix} \quad . \quad (23)$$

The procedure can be extended iteratively ([O'Callahan \(1989b\)](#)), whereby the eigenfrequencies of the reduced system are converging to that of the unreduced system

$$\mathbb{Q}_{IRS,i+1} = \mathbb{Q}_G + \mathbb{P} \mathbb{M} \mathbb{Q}_{IRS,i} \mathbb{M}_{IRS,i}^{-1} \mathbb{K}_{IRS,i} \quad . \quad (24)$$

However, the drawback of this iteration is an increasing condition of the system matrices. Hence, it has to be terminated after reaching a sufficient accuracy or exceeding a critical condition number.

2.3.3 Modal Reduction

Alternatively, the reduction can be based on the eigenvectors. The homogeneous solution of the boundary value problem consists of the n_k eigenfrequencies ω_k and the corresponding eigenvectors $\hat{\mathbf{u}}_k$

$$[\mathbb{K}_{red} - (\omega_k)^2 \mathbb{M}_{red}] \hat{\mathbf{u}}_k = 0 \quad . \quad (25)$$

This results in a transition from the physical coordinates \mathbf{u} to the modal coordinates $\mathbf{q} = [q_1 \dots q_k]$

$$\mathbb{M}_{red} \ddot{\mathbf{u}} + \mathbb{D}_{red} \dot{\mathbf{u}} + \mathbb{K}_{red} \mathbf{u} = \mathbf{f}_{red} \Rightarrow \quad (26)$$

$$\mathbb{M}_{mod} \ddot{\mathbf{q}} + \mathbb{D}_{mod} \dot{\mathbf{q}} + \mathbb{K}_{mod} \mathbf{q} = \mathbf{f}_{mod} \quad (27)$$

using the transformation

$$\mathbf{u} = \mathbb{Q}_{mod} \mathbf{q} = \hat{\mathbf{U}} \mathbf{q} \quad \text{with} \quad \hat{\mathbf{U}} = [\hat{\mathbf{u}}_1 \dots \hat{\mathbf{u}}_k] \quad . \quad (28)$$

This transformation is initially exact and it can be shown that each deformation state can be represented as the superposition of different eigenvectors.

The reduction is achieved by eliminating those eigenvectors $\hat{\mathbf{u}}_j$ of the modal matrix $\hat{\mathbf{U}}$ which – due to the frequency spectrum of the external loads – result in modal amplitudes q_j with insignificant magnitude ([Dietz \(1999\)](#)). These are predominantly high-frequency components of the deformation, which in addition usually show a strong damping.

2.4 Elastic Multi Body Dynamics

For the application example of the crank drive, the individual components are subject to large rigid body movements, on which small elastic deformations are superimposed. With this background, the use of a FEM description, which would inevitably have to be geometrically non-linear, is numerically very complex. For this reason, elastic multi-body algorithms are preferred which have been specifically developed with this focus using the floating-frame-of-reference approach.

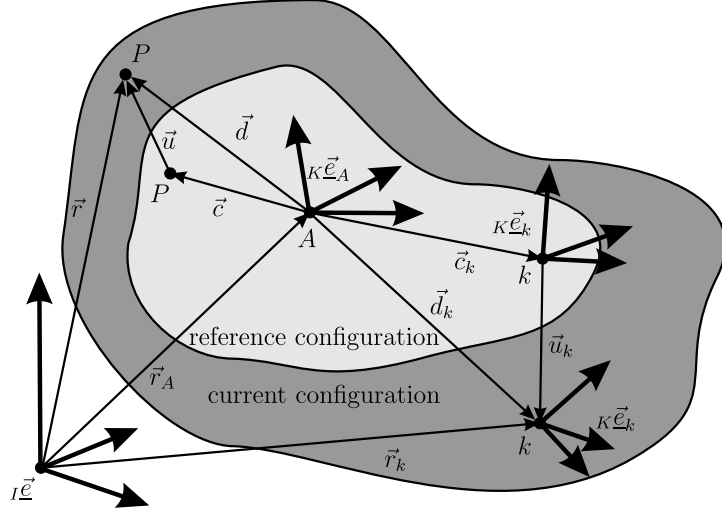


Figure 5: Representation of the position vector \mathbf{r} in initial- and deformed configuration and its segmentation in rigid body part \mathbf{c} as well as the elastic deformation \mathbf{u} according to Woschke (2013).

As a starting point for their description, the integral over the difference of the variations of the internal and the kinetic energy can be used, which must be in equilibrium with the virtual work of the external loads, consisting of volume- and single-forces

$$0 \equiv \int_{t_1}^{t_2} (\delta E_{\text{kin}} - \delta E_{\text{in}} + \delta W) dt \quad (29) \\ = \int_{t_1}^{t_2} \left(\int_V \delta \dot{\mathbf{r}}^T \dot{\mathbf{r}} \rho dV - \int_V \delta \varepsilon^T \sigma dV + \int_{V^s} \delta \mathbf{r}^T \mathbf{s}^v dV + \sum_i (\delta \mathbf{r}_i^T \mathbf{f}_i) \right) dt .$$

Using the fundamental lemma and the fact that the variation vanishes at the times t_1 and t_2 yields

$$0 \equiv \underbrace{\int_V \delta \mathbf{r}^T \ddot{\mathbf{r}} \rho dV}_{\text{inertia effects}} + \underbrace{\int_V \delta \varepsilon(\mathbf{u})^T \sigma(\mathbf{u}) dV}_{\text{inner forces}} - \underbrace{\left[\int_{V^s} \delta \mathbf{r}^T \mathbf{s}^v dV + \sum_i (\delta \mathbf{r}_i^T \mathbf{f}_i) \right]}_{\text{external loads}} . \quad (30)$$

The equation of motion now contains volume integrals with non-linear dependence on location and time. If, at the same time, the elastic deformation \mathbf{u} is replaced by the modal coordinates \mathbf{q} by utilising the described reduction methods, the following relationships according to Fig. 5 are obtained

$$\begin{aligned} \mathbf{r} &= \mathbf{Q}_{IK} K(\mathbf{r}_A + \mathbf{c} + \mathbf{u}) = \mathbf{Q}_{IK} K(\mathbf{r}_A + \mathbf{c} + \hat{\mathbf{U}}\mathbf{q}) , \\ \ddot{\mathbf{r}} &= \mathbf{Q}_{IK} K \left(\ddot{\mathbf{r}}_A + \left(\mathbf{c} + \hat{\mathbf{U}}\mathbf{q} \right)^T \times \dot{\mathbf{w}} + \hat{\mathbf{U}}\ddot{\mathbf{q}} + 2\mathbf{w} \times \hat{\mathbf{U}}\dot{\mathbf{q}} + \mathbf{w} \times (\mathbf{w} \times (\mathbf{c} + \hat{\mathbf{U}}\mathbf{q})) \right) , \\ \delta \mathbf{r} &= \mathbf{Q}_{IK} K \left(\delta \mathbf{r}_A + \delta \mathbf{w} \times \mathbf{r}_A + \left(\mathbf{c} + \hat{\mathbf{U}}\mathbf{q} \right) \times \delta \mathbf{w} + \hat{\mathbf{U}}\delta \mathbf{q} \right) . \end{aligned} \quad (31)$$

Thereby, all terms are expressed as a function of the angular velocity \mathbf{w} as well as the modal coordinates \mathbf{q} and their derivatives $\dot{\mathbf{q}}$, which leads to a formulation of Eq. (30) in the form of

$$\mathbf{M}_{\text{MBS}}(\mathbf{q}) \mathbf{a} + \mathbf{h}_\omega(\mathbf{w}, \mathbf{q}, \dot{\mathbf{q}}) + \mathbf{h}_{\text{el}}(\mathbf{q}, \dot{\mathbf{q}}) = \mathbf{h}_o(\mathbf{q}) \quad \text{mit} \quad \mathbf{a} = \begin{bmatrix} \ddot{\mathbf{r}}_A \\ \dot{\mathbf{w}} \\ \ddot{\mathbf{q}} \end{bmatrix} . \quad (32)$$

The modal reduction is an integral part of the implementation of elastic bodies into MBS applications. Due to the orthogonality properties, they allow a decoupling of the equation of motions into n linearly independent differential equations. At the same time, a master-slave reduction can be pre-set to the modal reduction, in order to limit the

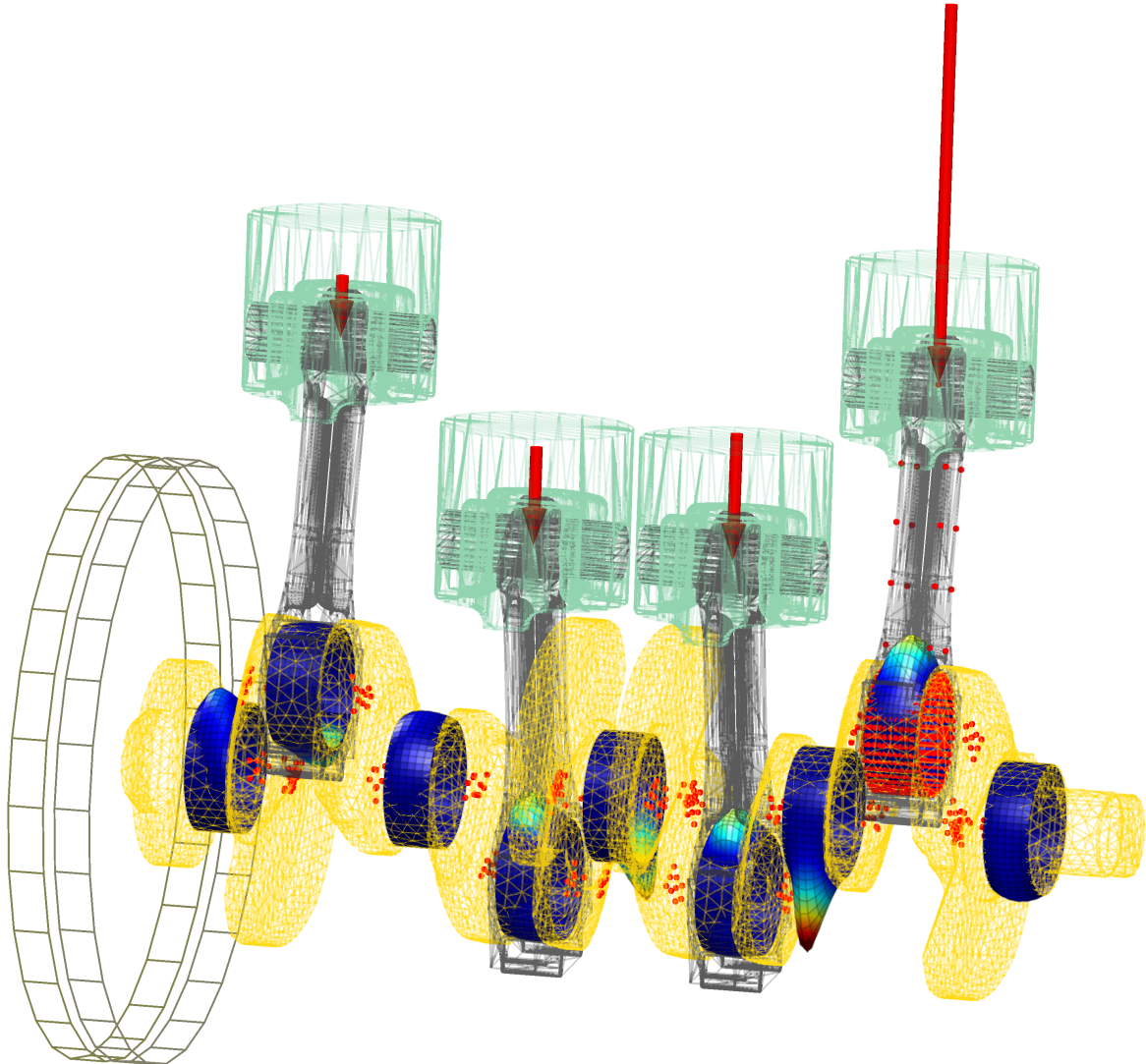


Figure 6: Model of the crankdrive with elastic crankshaft and elastic conrod on cylinder 1 (C_1) shortly after TDC¹⁰ of C_1 . The dots indicate the markers resulting from the master degree of freedoms. In addition, the lubrication film pressures are visualised on the main bearings and on the conrod's big end bearings. The arrows on the pistons represent the forces due to the gas pressure in the cylinders.

eigenvectors to the information essential for the deformation description. This results in the following substitution

$$\mathbf{u} = \mathbf{Q}_{IRS} \mathbf{u}_M = \mathbf{Q}_{IRS} \hat{\mathbf{U}} \mathbf{q} \quad , \quad (33)$$

which can be applied in Eq. (31) instead of the straight modal reduction.

3 Model

The combination of the described approaches with regard to hydrodynamics and elastic multi-body simulation is demonstrated by means of a conrod big end bearing of a crankdrive, cf. Fig. 6.

Conrod For this purpose, the conrod is first discretised by finite elements and then reduced to 1503 degrees of freedom using the described IRS-based master-slave approach. The master nodes are arranged on the one hand uniformly over the shank of the conrod and, on the other hand, are concentrated in the bearing shell in order to be

¹⁰Top Dead Centre

able to accurately represent the deformation in the fluid gap. The distribution of the nodes is coupled to the mesh required for the hydrodynamics, in order to avoid interpolation of the deformations and the associated velocities. Subsequently, a modal reduction is used, in order to achieve decoupling of the equations of motion. The eigenforms to be considered depend primarily on the excitation frequency spectrum. But in addition, special eigenforms have to be taken into account to inclose the local deformations in the bearing shell. These deformations are described by eigenforms whose natural frequency is clearly above each frequency contained in the load spectrum. In this case, the influence of the deformation on the pressure build-up in the journal bearing and thus in the loads is decisive, whereat a renouncement of the corresponding eigenforms results in exaggerated hydrodynamic pressures. The decisive point of the modal reduction is thus given by the selection of the eigenforms used to describe the deformation.

Neglecting the effect of all inertia forces and influences from damping compared to those from stiffness, the equation of motion of a modal reduced elastic body Eq. (26) can be formulated by

$$\mathbb{M}_{\text{mod}} \ddot{\mathbf{q}} + \mathbb{D}_{\text{mod}} \dot{\mathbf{q}} \ll \mathbb{K}_{\text{mod}} \mathbf{q} \quad \rightsquigarrow \quad \mathbb{K}_{\text{mod}} \mathbf{q} = \mathbb{f}_{\text{mod}} \quad . \quad (34)$$

This assumption applies formally only to slowly moving elastic bodies, taking into account a low attenuation as well as a low rate of change concerning the external loads. However, the results obtained are also applicable to dynamically loaded systems in the context of journal bearing simulation because the local deformations primarily result from the acting external loads and the deformation rate remains moderate.

Assuming that the forces acting on the structure are known, the modal deformations q_i can be determined. If they are weighted with regard to their share in the overall deformation state using the modal participation factor

$$\text{MPF}_i = \frac{|q_i|}{\sum_i |q_i|} \cdot 100\% \quad , \quad (35)$$

an explicit selection of significant eigenforms can be achieved. Also a set of load collectives – e.g. obtained from dynamic simulations – can be considered by superposition of significant eigenforms of each load step.

For the knowledge of the external loads of the deformed model, formally a complete simulation with a high number of modal state variables is necessary. However, it could be shown that the general trend of hydrodynamic loads using a simulation with a rigid bearing shell is similar to an elastic one. Hence, the hydrodynamic loads of a rigid calculation – which are obtainable with a lower numerical effort – can be used as input data for the selection of the participating eigenvectors.

The minimal percentage contribution to the deformation, which must be taken into account, is not comprehensively algorithmic, but is always associated with the actual load case. Further details concerning the choice of eigenforms are shown in [Woschke \(2013\)](#), [Woschke et al. \(2007\)](#) and [Wallrapp \(1999\)](#). For the conrod considered here, 74 suitable eigenforms from the first 200 eigenforms were selected and taken into account for the calculation.

Depending on the algorithm used for the master-slave reduction, deviations of the eigenfrequencies between reduced and unreduced structure result. These are summarised in Tab. 2 using the example of the lowest and highest natural frequency selected for the deformation. The reduction methods consistently predicate a stiffer behavior than is represented by the unreduced structure, whereat the differences increase as the order of the eigenfrequencies increases. The deviations are greatest in the Guyan reduction due to the disregarded dynamic properties of the slave structure. The IRS reduction converges with increasing number of iterations monotonously against the values of the unreduced model. The highest eigenfrequency to be considered defines the numerical stiffness of the resulting differential equation system and thus represents an important indicator for time integration with respect to the maximum step size.

Table 2: Influence on the conrod's eigenfrequencies due to the master-slave-reduction method

method	1 st EF [Hz]	...	188 th EF [kHz]	rel. deviation to unreduced [%]
unreduced	2058	...	120.9	-
Guyan	2063	...	262.1	117
IRS (5 iterations)	2063	...	134.7	11
IRS (10 iterations)	2063	...	123.0	2

Crank shaft The local deformations at the bearing area in radial direction are negligibly small on the crankshaft due to the solidly designed pins on the main and conrod bearings. However, in the course of the ignition sequence of the individual cylinders, a time delay concerning the introduction of the gas forces occurs leading to a global deformation. Subsequently, the crankshaft is also reduced by the described methods. The selection of the master nodes was made with a restriction on the degrees of freedom required for the force application into the bearing points. For this purpose, the bearing pin surfaces were assumed to be non-deformable and rigidly connected to a master node, which is central with respect to the pin – nine nodes remain after reduction. According to the highest frequency contained in the excitation, the consideration of the 13 first eigenforms is sufficient here.

4 Results

In this section, the results concerning the big end bearing of the conrod are discussed depending on different modelling approaches of MBS and hydrodynamics, cf. Tab. 3.

Table 3: Modelling approaches

variant	label	description MBS	description hydrodynamics
a)	CR _{el} + HD _{reg/reg}	conrod as well as crankshaft elastic	conrod bearing and main bearings with regularised cavitation algorithm
b)	CR _{el} + HD _{reg/spring}	conrod as well as crankshaft elastic	conrod bearing with regularised cavitation algorithm, main bearings with isotropic spring-damper elements
c)	CR _{el} + HD _{gue/spring}	conrod as well as crankshaft elastic	conrod bearing with Gümbel cavitation algorithm, main bearings with isotropic spring-damper elements
d)	CR _{rig} + HD _{reg/spring}	conrod rigid, crankshaft elastic	conrod bearing with regularised cavitation algorithm, main bearings with isotropic spring-damper elements
e)	CR _{rig} + HD _{gue/spring}	conrod rigid, crankshaft elastic	conrod bearing with Gümbel cavitation algorithm, main bearings with isotropic spring-damper elements

Due to the transient load, the elastic deformation and the associated surface velocity are varying during the working cycle and influence the hydrodynamic film thickness and its derivative w.r.t. time, further details can be found in Daniel (2013). As a consequence of the online approach for solving the Reynolds equation, the pressure distribution and the resulting bearing reactions can be analysed. Additionally, due to the mass-conserving cavitation algorithm, the transient development of the film-fraction ϑ is accessible. The mentioned quantities are displayed exemplarily at the TDC in Fig. 7: The radial deformation of the bearing surface is dominated by a global ovalisation due to inertia forces, which is superimposed by local deformations in the region of maximum hydrodynamic pressure. The gap function consist of the radial deformation plus the gap due to the rigid body kinematics. As a consequence, the maximum pressure arises in the region with minimal gap. The pressure build-up is also influenced by the transient film-fraction – only in regions with sufficient fluid filling pressure values above the cavitation pressure can occur. Furthermore, in the visualisation of the film-fraction the oil-supply is noticeable.

The evaluation of these quantities for every time step of a complete working cycle is not practicable at this point, therefore integral quantities like the orbit of the crankpin w.r.t. the conrod's big end as well as the maximum pressure and the minimal film thickness are discussed in correlation to the modelling approaches, cf. Tab. 3.

The orbit is displayed normalised relative to the bearing clearance. Firstly, in Fig. 8 the different parts of the orbit are assigned to the four strokes of cylinder 1. In particular, during compression and power stroke sharp peaks occur in the orbit, which result from the changing gas force due to the pressure in the combustion chamber. Basically, Fig. 9 shows the evident difference between the elastic and the rigid modelling of the conrod. Due to the elastic deformation values of the normalised total displacement $v_{\text{total}} = \sqrt{v_x^2 + v_y^2} > 1$ occur.

Both, the elastic as well as the rigid results show a significant deviation in the utilisation of the clearance concerning the modelling of the cavitation algorithm. The regularised Elrod algorithm tends to larger displacements caused by the delayed pressure build-up as a result of the film-fraction's transient development. In contrast, the Gümbel approach leads, apparently due to the violation of mass conservation, to larger reserves before solid contact occurs.

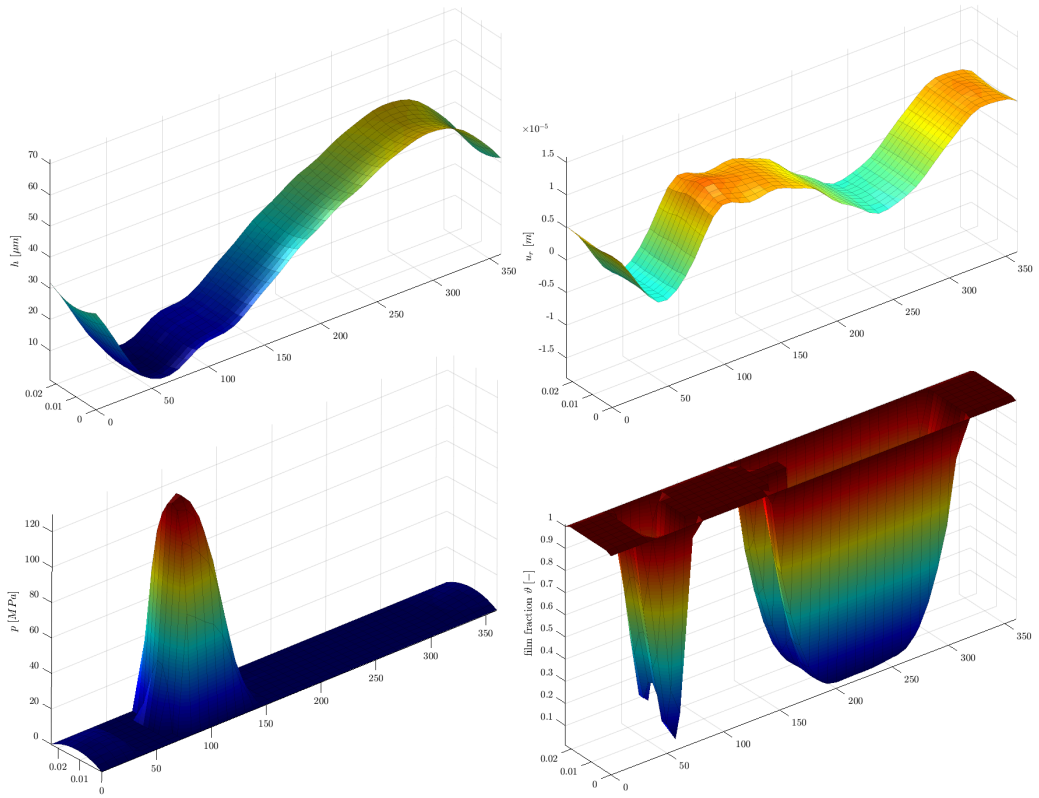


Figure 7: Input and result field-quantities of Reynolds equation at TDC: gap function (top left), radial deformation of bearing surface (top right), pressure (bottom left), film-fraction (bottom right).

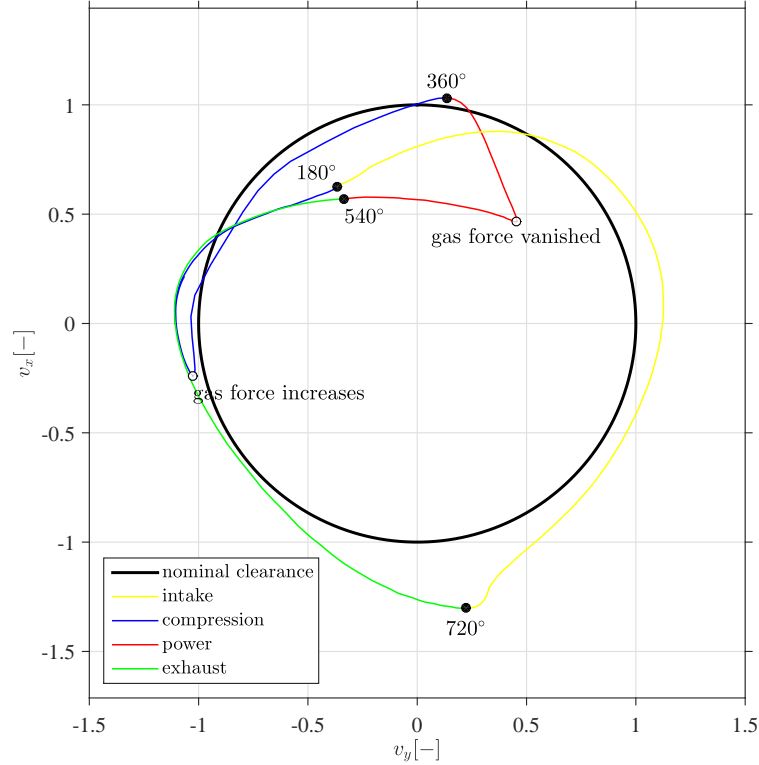


Figure 8: Orbit of crank pin w.r.t. the conrod's big end: correlation to the four strokes of the working cycle.

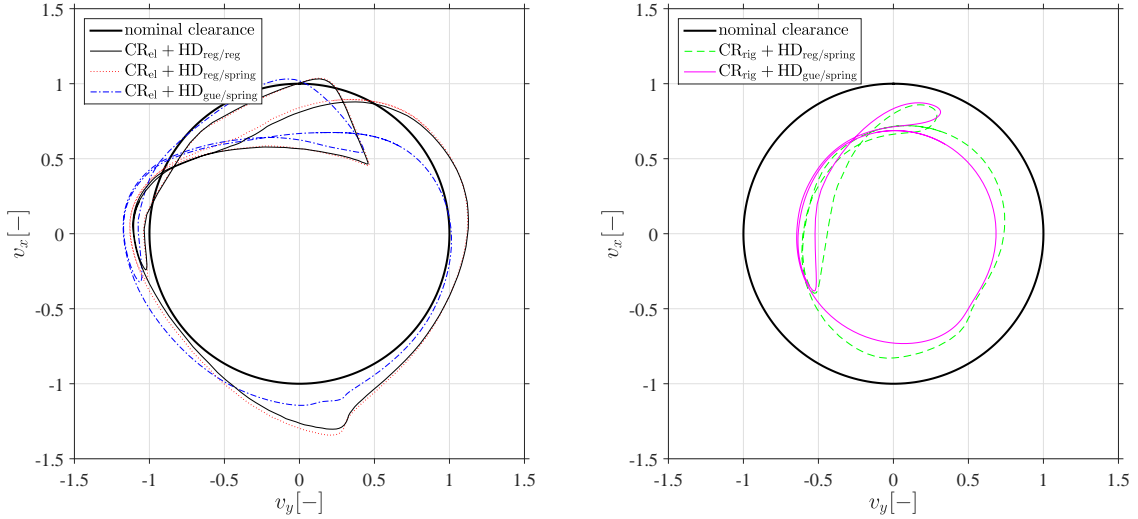


Figure 9: Orbit of crank pin w.r.t. the conrod's big end using different modelling approaches: elastic conrod (left), rigid conrod (right). Additionally, the nominal clearance is displayed as a bold line, which visualises the undeformed contour.

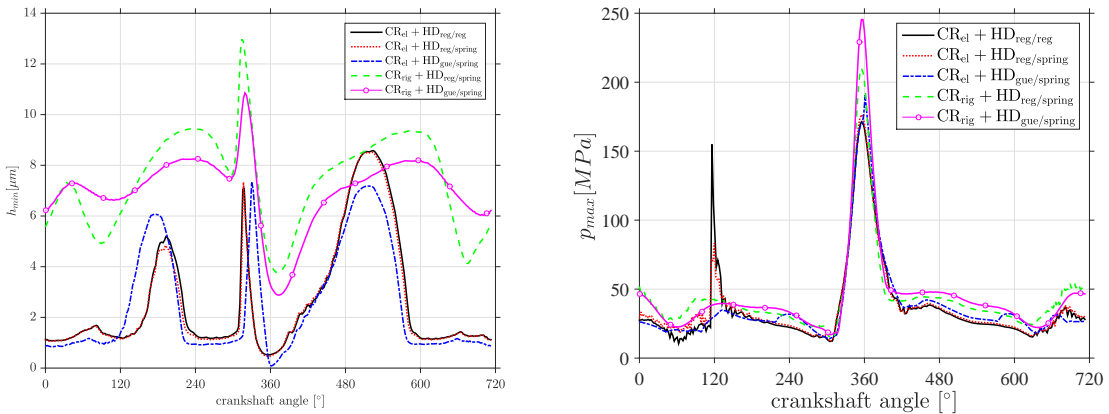


Figure 10: Tribological quantities during a working cycle: minimal film thickness (left) and maximum pressure (right).

With regard to the influence of the main bearings and the remaining conrod bearings on the crankpin orbit, only slightly differences occur, which hardly legitimate the extended effort.

Concluding, the minimal film thickness and the maximum hydrodynamic pressure are investigated as tribological indicators of the bearing's operating grade, cf. Fig. 10 left. Contrarily to the crankpin orbit, which is meaningful only at the bearing mid, here the film thickness is evaluated in the whole bearing, whereby potential wear on the bearing's edges due to tilting of the bearing surfaces can be identified. But coinciding with the results obtained on the crankpin orbit, the influence of tilting is negligible in the present case.

The maximum pressure in the fluid film shows in wide ranges of the working cycle only minor differences between the modelling approaches, cf. Fig. 10 right. Merely on TDC a decrease can be observed with increasing modelling grade. This behaviour is caused by the increasing compliance due to elasticity of the conrod, which results in an enlargement of the load zone. This trend is amplified by the cavitation as the partly filled fluid gap leads to a softer bearing reaction resulting in lower pressure values.

Referring to the tribological quantities, the modelling of the remaining bearings is also of minor importance.

5 Summary and Outlook

The paper at hand shows exemplarily the implementation of dynamic loaded components or systems supported in journal bearings into a holistic MBS-based simulation. Therein, the level of detail concerning the hydrodynamics is extended by introducing a regularised Elrod-algorithm, which is compared to existing simplified approaches. Firstly, a significant deviation from these assumptions can be shown, which e.g. results in smaller minimal film thickness preventing an overestimation of carrying reserves. Furthermore, a significant advantage in cpu-time of the new approach appeared compared to the classic Elrod-algorithm. It can also be concluded, that the modelling depth of adjacent bearings has only a small impact on the bearing on the investigated conrod.

The presented approach can be transferred in a similar manner to other tribological contacts (axial or floating ring bearings) and cavitation models (bi-phase-model). Regarding the floating ring bearing appropriate results are published in [Nitzschke \(2016\)](#). In addition to the improved model quality, a basis for the integration of the thermal field problem is given through the mass-preserving cavitation algorithm, because the transient gap filling is required as an input of the energy equation, as mentioned in [Woschke \(2013\)](#).

Acknowledgment

The results were generated in the framework of the project WO 2085/2 "Numerische Analyse des transienten Verhaltens dynamisch belasteter Rotorsysteme in Gleit- und Schwimmbuchsenlagern unter Berücksichtigung kavitations Effekte", which is supported by the DFG. This support is gratefully acknowledged.

References

Ausas, R. F.; Jai, M.; Buscaglia, G. C.: A mass-conserving algorithm for dynamical lubrication problems with cavitation. *Journal of Tribology*, 131, 3, (2009), 031702–031702.

Boedo, S.; Booker, J.; Wilkie, M.: A mass conserving modal analysis for elastohydrodynamic lubrication. *Tribology Series*, 30, (1995), 513–523.

Boman, R.; Ponthot, J.-P.: Finite element simulation of lubricated contact in rolling using the arbitrary lagrangian–eulerian formulation. *Comput. Methods Appl. Mech. Engrg.*, 193, (2004), 4323–4353.

Craig, R. R.: Coupling of substructures for dynamic analysis: An overview. *AIAA Journal*, 41.

Daniel, C.: *Simulation von gleit- und wälzgelagerten Systemen auf Basis eines Mehrkörpersystems für rotordynamische Anwendungen*. Ph.D. thesis, Magdeburg, Universität, (2013).

Dietz, S.: *Vibration and Fatigue of Vehicle Systems Using Component Modes*. Ph.D. thesis, Technische Universität Berlin (1999).

Elrod, H. G.: A cavitation algorithm. *Journal of Tribology*, 103, 3, (1981), 350–354.

Elrod, H. G.; Adams, M. L.: A computer program for cavitation and starvation problems. In: D. Dowson; M. Godet; C. Taylor, eds., *Cavitation and related phenomena in lubrication (Proc. 1st Leeds-Lyon Symposium on Tribology, Leeds, England)*, pages 37–41, Mechanical Engineering Publications (1974).

Feng, N. S.; Hahn, E. J.: Density and viscosity models for two-phase homogeneous hydrodynamic damper fluids. *A S L E Transactions*, 29, 3, (1986), 361–369.

Glienicke, J.; Fuchs, A.; Peng, D.; Lutz, M.; Freytag, C.: Robuste Lagerungen. Abschlussbericht Vorhaben 662 Heft 694, FVV (2000).

Guyan, R. J.: Reduction of stiffness and mass matrices. *AIAA Journal*, 3, 2, (1965), 380.

Hajjam, M.; Bonneau, D.: A transient finite element cavitation algorithm with application to radial lip seals. *Tribology International*, 40, (2007), 1258–1269.

Hu, Y.-K.; Liu, W. K.: An ale hydrodynamic lubrication finite element method with application to strip rolling. *International Journal for Numerical Methods in Engineering*, 36, (1993), 855–880.

Kumar, A.; Booker, J. F.: A finite element cavitation algorithm. *Journal of Tribology*, 113, 2, (1991), 279–284.

Martinet, F.; Chabrand, P.: Application of ale finite elements method to a lubricated friction model in sheet metal forming. *International Journal of Solids and Structures*, 37, (2000), 4005–4031.

Nitzschke, S.: *Instationäres Verhalten schwimmbuchsengelagerter Rotoren unter Berücksichtigung masseerhaltender Kavitation*. Ph.D. thesis, Otto-von-Guericke Universität Magdeburg (2016).

Nitzschke, S.; Woschke, E.; Schmicker, D.; Strackeljan, J.: Regularised cavitation algorithm for use in transient rotordynamic analysis. *International Journal of Mechanical Sciences*, 113, (2016), 175–183.

O'Callahan, J.: A procedure for an improved reduced system (irs). *Proceedings of the 7th International Modal analysis conference, Society of Experimental Mechanics*, 7, (1989a), 17 – 21.

O'Callahan, J.: System equivalent reduction and expansion process. *Proceedings of the 7th International Modal analysis conference, Society of Experimental Mechanics*, 7, (1989b), 29 – 37.

Rho, B.-H. R.; Kim, K.-W.: Acoustical properties of hydrodynamic journal bearings. *Tribology International*, 36, (2003), 61–66.

Schweizer, B.: Ale formulation of reynolds fluid film equation. *ZAMM*, 88, 9, (2008), 716–728.

Shi, F.; Paranjpe, R.: An implicit finite element cavitation algorithm. *Computer modeling in engineering and sciences*, 3, 4, (2002), 507–516.

Tao, L.; Diaz, S.; San Andres, L.; Rajagopal, K.: Analysis of squeeze film dampers operating with bubbly lubricants. *Journal of tribology*, 122, 1, (2000), 205–210.

Vijayaraghavan, D.; Keith, T. G.: Development and evaluation of a cavitation algorithm. *Tribology Transactions*, 32, 2, (1989), 225–233.

Wallrapp, S. M., O.; Wiedemann: Multibody system simulation of deployment of a flexible solar array. In: *4th International Conference on Dynamics and Control of Structures in Space* (1999).

Woschke, E.: *Simulation gleitgelagerter Systeme in Mehrkörperprogrammen unter Berücksichtigung mechanischer und thermischer Deformationen*. Dissertation, Otto-von-Guericke-Universität Magdeburg (2013).

Woschke, E.; Daniel, C.; Strackeljan, J.: Reduktion elastischer Strukturen für MKS Anwendungen. In: *Tagungsband 8. Magdeburger Maschinenbau-Tage* (2007).

Zeidan, F. Y.; Vance, J. M.: Cavitation leading to a two phase fluid in a squeeze film damper. *Tribology Transactions*, 32, 1, (1989), 100–104.

Address: S. Nitzschke, E. Woschke , C. Daniel,
 IFME, Otto-von-Guericke-Universität Magdeburg, Universitätsplatz 2, 39106 Magdeburg, Deutschland
email: {steffen.nitzschke,elmar.woschke, christian.daniel}@ovgu.de

On the Influence of a Five-Hole-Probe on the Vibration Characteristics of a Low Pressure Turbine Rotor while Performing Aerodynamic Measurements

F. Schönleitner, T. Selic, M. Zenz, F. Heitmeir, A. Marn

For many reasons it is essential to know and assess the flow field and its characteristics up- and downstream of a turbine stage. For these purpose measurements are conducted in test rigs such as the STTF-AAAI (subsonic test turbine facility for aerodynamic, acoustic, and aeroelastic investigations) at the Institute for Thermal Turbomachinery and Machine Dynamics at Graz University of Technology. A low pressure turbine is operated in engine relevant operating conditions. The turbine is experienced high mechanical loads and is excited to vibrate (forced response). In the rotor design process forced response predictions and structural assessments are performed. However, it is not common to include instrumentation (e.g. total pressure and temperature rakes, five-hole-probes, fast response aerodynamic pressure probes) in these forced response predictions. But, these measurement devices are essential and therefore this paper investigates the influence of such an instrumentation onto the vibrational behaviour of a low pressure turbine rotor of the STTF-AAAI. Several vibration measurements at distinct circumferential and radial positions of the five-hole-probe in the flow channel are conducted. These measurement results are compared to measurements performed without a five-hole-probe in the flow channel. A clear influence of the five-hole-probe on the vibration level is shown.

1 Introduction

Aerodynamic investigations of turbine stages are the main part of every turbomachinery research. After the design and numerical predictions of the flow through turbine stages and its mechanical and dynamical behaviour it is indispensable to perform measurements in test rigs especially if the design is at the limits of the known and established design space. Since many years the Institute for Thermal Turbomachinery and Machine Dynamics at Graz University of Technology has been operating a test rig to investigate sound propagation and blade vibrations. For sure, instrumentation is a necessary and essential part of the test rig. The influence of the instrumentation and measurement devices should be as less as possible, but it is still there. This is true for the flow itself but also for the excitation of blade vibrations. Within a national funded project AdMoNt a sensor telemetry system is used in the subsonic test turbine facility for aerodynamic, acoustic and aeroelastic investigations (STTF-AAAI) in order to measure blade vibrations by means of strain gauges on the blade surfaces in the rotating frame of reference. These investigations have been conducted under engine representative conditions. (Schönleitner, 2016) investigated blade vibrations due to the potential effect of different turbine exit casings (TEC) and due to the downstream effect of the upstream low pressure turbine stator vane row. He has shown a clear evidence of both effects. Also, due to blade-vane interaction the vibrational characteristics of the rotor is affected. This is true for the rotor blades and rotor disc.

Because of the small axial distance between rotor and TEC and hence a small distance between the five-hole-probe (shaft diameter 7mm) and the rotor blades the influence of this probe onto the blade vibrations is determined. Blade vibrations have been measured for different circumferential and radial positions of the probe.

2 Literature Survey

Public experimental data of vibrations of low pressure turbine blades under engine relevant operating conditions are limited. A lot of numerical data can be found in literature, also analytical data and literature about the development of methodology is available. Also, a lot of theoretical work dealing with flutter, forced response and mistuning can be found. Experimental data is mostly obtained in cascades due to the simpler test set up and easier measurements. These tests however neglect essential 3D phenomena and effects that occur. Thus they cannot be simulated in linear cascades.

(Bell, et al., 2000) show the influence of the tip leakage onto the blade vibration of a oscillating blade in a linear cascade. (Huang, et al., 2006) investigated the effect of the tip leakage vortex onto the flutter behaviour of turbine blades. The authors conducted their experiments also in a linear cascade. Shock induced vibrations has been investigated by (Urban, et al., 2000) in a linear cascade utilising flexible supported blades. (Nowinski, et al., 2000) did experiments with low pressure turbine blades and showed some aspects of flutter occurrence in an annular cascade. (Vogt, et al., 2007) reported the influence of negative incidence on the mode shape of oscillating blades. Also these authors conducted their experiments in an annular cascade. The influence of mistuning on aerodynamic damping of an oscillating low pressure turbine blade was shown by (Glodic, et al., 2011). In the same cascade (Vogt, et al., 2007) showed that the influence of a vibrating blade is limited to the adjacent blades. (Kielb, et al., 2001) give detailed insight into the effect of damping of a turbine. The authors showed that aerodynamic damping is inversely proportional to the square of the rotational speed.

There have been no publications found in open literature dealing with low pressure turbine blade vibration measurements in the rotating frame of reference under engine representative operating conditions. Also, there is no literature available that shows the influence of the upstream stator vane row (downstream effect) on the blade vibration excitation and the influence of the downstream turbine exit casing (upstream effect). Therefore, within the project AdMoNt (Schönleitner, 2016) created a novel database with data obtained in the rotating frame of reference under engine representative conditions in order to support the development of future innovative low pressure turbine stages. Main focus was on the upstream effect of different turbine exit casings on the forced response of low pressure turbine blading combined with the downstream effect of the stator vanes.

Also investigations in order to identify and clarify the influence of a five-hole-probe on the blade vibrations during a measurement campaign has been conducted and are reported in this paper.

3 Experimental Facility and Instrumentation

3.1 Subsonic Test Turbine Facility for Aerodynamic, Acoustic and Aeroelastic Investigations (STTF-AAAI)

Figure 1 shows the meridional section of the subsonic test turbine facility. Figure 1 a) illustrates the leaned TEC configuration while in b) the measurement plane is depicted. Air, delivered by a 3 MW compressor station, enters the open loop test facility through a spiral casing. There, the tangential inlet flow is turned into axial direction. The remaining swirl is further reduced by a de-swirler that is also located in the inlet casing. In order to ensure a uniform and homogeneous inflow of the turbine stage a perforated plate is located downstream of the de-swirler. Upstream of the turbine stage an additional inlet guide vane (IGV) can be found. With that IGV different inlet flow angles for the turbine stage can be realised in order to be able to test different stages and/or different operating conditions. The IGVs are followed by the low pressure turbine stator and rotor. Downstream of the rotor the turbine exit casing (TEC) with the turbine exit guide vanes (TEGV) is located.

Additional design details of the test rig are summarised in (Moser, et al., 2007). Due to the design of the test rig it is possible to easily adopt all parts. Inlet guide vanes, stator, rotor, and turbine exit casing can be changed fast and different designs can be integrated in the test rig.

Within this paper the influence of a five-hole-probe during a measurement campaign in plane C between rotor and turbine exit casing will be determined and its effect on the rotor blade vibrations are reported.

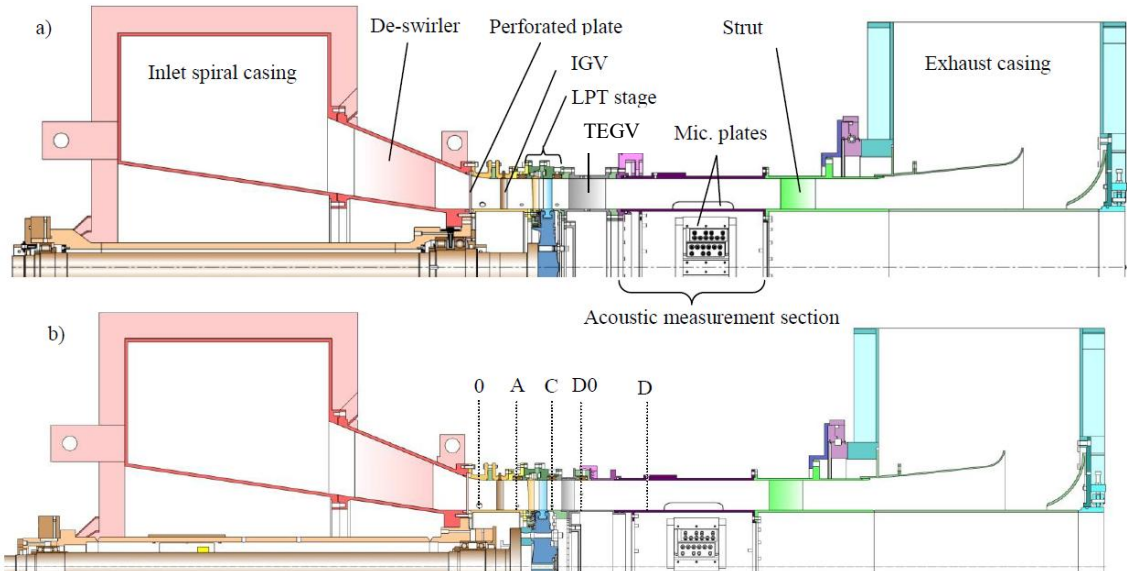


Figure 1. Meridional section of the STTF-AAAI; a) leaned TEC, b) measurement locations

3.2 Turbine Exit Casing

For this investigation the leaned TEC is used. It is an acoustically modified state-of-the-art TEC. The optimisation of the TEC was done by MTU Aero Engines and is reported in (Broszat, et al., 2010). In a parameter study the number of TEGV as well as the angle of the stagger line in circumferential direction (=lean angle) was optimised in order to obtain lowest sound power levels. A strong dependency of the sound power level on the rotor wakes have been observed. Figure 2 left shows a picture of the entire TEC and on the right side a close up view of the TEGV leading edge can be seen as well as a lean angle of 20 deg.



Figure 2. Lean TEC

Table 1 lists the most important technical details. Reynolds number is calculated using inlet flow velocity and chord length of the turbine exit guide vanes.

Table 1. Technical details of the leaned TEC and the turbine stage

No. of TEGV/stator/IGV	-	15/96/83
No. of rotor blades	-	72
Axial Chord Length TEGV	mm	100
Aspect ratio TEGV	-	0.8
Diffusion No. TEGV @ADP	-	0.5
Reynolds No. TEGV@ADP	-	375000

3.3 Five-Hole-Probe

Steady flow field measurements are usually performed by means of five-hole-probes in the measurement locations given in Figure 1 b). Measurements have been performed over one TEGV pitch. The five-hole-probe used for this investigation was manufactured and calibrated at the Institute of Jet Propulsion and Turbomachinery, RWTH Aachen University and is a state-of-the-art probe commonly in use for turbomachinery experiments. In general, five-hole-probes are pneumatic probes to measure the time averaged (steady) flow quantities, total pressure, static pressure, Mach number, and flow angles. Geometrical dimensions of this probe can be seen in Figure 3.

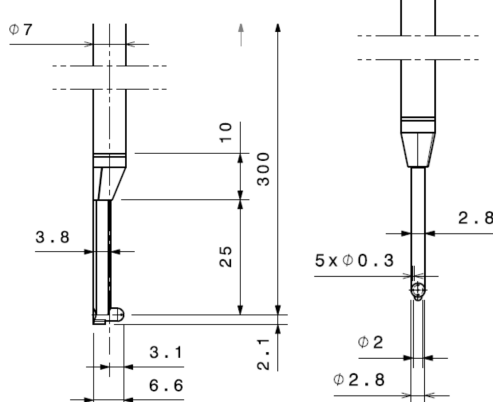


Figure 3. Geometrical details of the five-hole-probe

3.4 Sensor Telemetry System

Blade vibration measurements have been performed by means of strain gauges on different blades at different positions on the blade surfaces and a sensor telemetry system. Details of the strain gauge applications can be found in (Schönleitner, et al., 2015). The sensor telemetry system has a modular design, therefore not only strain gauge signals can be read but also temperature and unsteady pressure signals. For this work at hand 12 channels for strain gauge measurements have been used and 8 for temperature measurements. Technical data can be found below.

- Sensor telemetry system with radial antenna (air gap 2 mm)
- Optimised for turbine rig applications
- Simultaneous data acquisition with 12 bit resolution
- Max. sampling frequency 400 kSamples/s
- Strain gauge resistant 300Ω
- Quarter-bridge circuit
- Vibration analysis up to 100kHz
- Max. rotational speed 11.000 rpm
- Temperature range -10°C to $+125^{\circ}\text{C}$

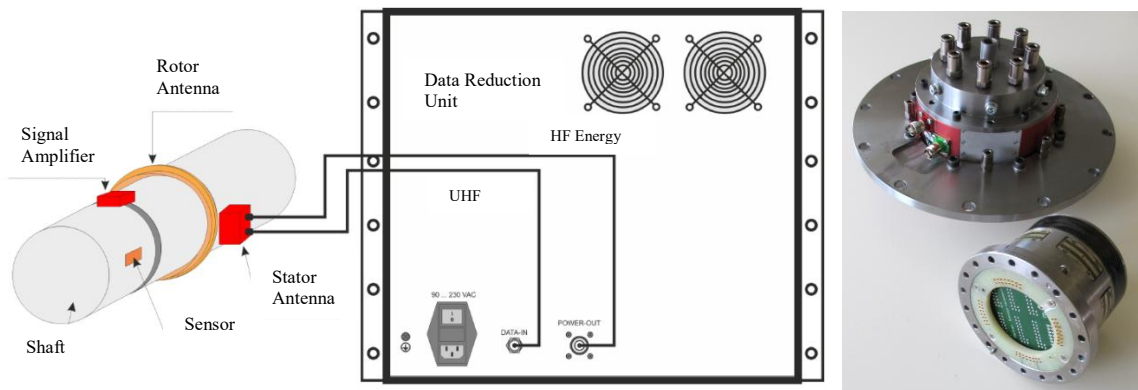


Figure 4. Sensor telemetry system

3.5 Operating Point

The operating point parameters for operating point ADP (aerodynamic design point) are given in Table 2. Due to the fact that the STTF-AAAI is an open loop test facility it is important to adjust the reduced operating parameters in order to have the same comparable operating conditions.

For this investigation the operating point ADP which is the aero design point was chosen.

Table 2 Operating point parameters

			ADP
Total Temperature Inlet	$T_{t,IN}$	°C	100
Stage Pressure Ratio	$p_{t,IN}/p_{t,OUT}$	-	1.131
Mass Flow Rate	\dot{m}	kg/s	7.07
Reduced Mass Flow	m_{red}	kg/s	6.86
Speed	n	min ⁻¹	3400
Reduced Speed	n_{red}	min ⁻¹	2997
Rotor Reynolds No.	-	-	165000

3.6 Measurement Uncertainties

Within this work vibration frequency up to 10 kHz are analysed. With a chosen sampling frequency of 204.8 kSample/s the Shannon-Nyquist criteria is maintained. Simultaneously with the strain gauge signals, temperatures of the applied thermo couples and rig operating parameters are recorded. A trigger signal is provided by the Bentley Nevada shaft monitoring system of the test rig and is also simultaneously recorded. Additionally, the signal of a reference microphone is recorded in order to be able (at a later stage) to perform additional data reduction and evaluation for e.g. trigger on non-synchronous vibrations. The reference microphone (1/4" G.R.A.S. 40BD as in (Selic, 2016)) is located in the TEC close to the trailing edge of the TEGV. For the investigation channels 0 to 11 are used for strain gauge data, channel 14 for trigger data and channel 15 for reference microphone data, respectively.

Strain gauges have a resistance of 350Ω (+/-0.30%). The k-factor is 2.05 (+/-1.0%) and a temperature coefficient of the k-factor of 101 [$10^{-6}/K$] (+/-10).

The signal amplifier of type MSV_M_1#2_PCM12 of the telemetry system has a zero drift and amplification drift of 0.02 %/°C. The amplification was set to 0.4 mV/V according to the expected vibration amplitude. The bandwidth of the signal is 0 to 100 kHz (-3dB).

The signal amplifier of type MSV_M_8_PCM12 for the temperature data acquisition has a zero drift and amplification drift of 0.02 %/°C (linearity <0.1%) and a bandwidth of 0 to 5 Hz.

The reference microphone can be used for measurements of sound pressure levels up to 174 dB and frequencies of up to 70 kHz. In a range between 10 Hz and 25 kHz the frequency response is linear (+/- 1 dB). The preamplifier (type 26AC) has a dynamic frequency range between 2 Hz and 200 kHz (+/- 0.2 dB). For the acoustic measurement chain a measurement uncertainty of 1 dB can be assumed.

4 Rotor Characteristics

The low pressure turbine rotor used for this investigation is optimised for highest stage loading. The reference configuration was acoustically investigated within the EU project VITAL. Knowledge of the system properties is essential for the assessment of the operational behaviour. Different numerical and experimental methods are available for system identification. The modal parameter of the rotor have been reported in (Schönleitner, 2016), and (Schönleitner, et al., 2015). Figure 5 shows the rotor with all applied strain gauges 1-12 and thermo couples T_1 and T_2 (left) and one blade with strain gauge no. 3 (right).

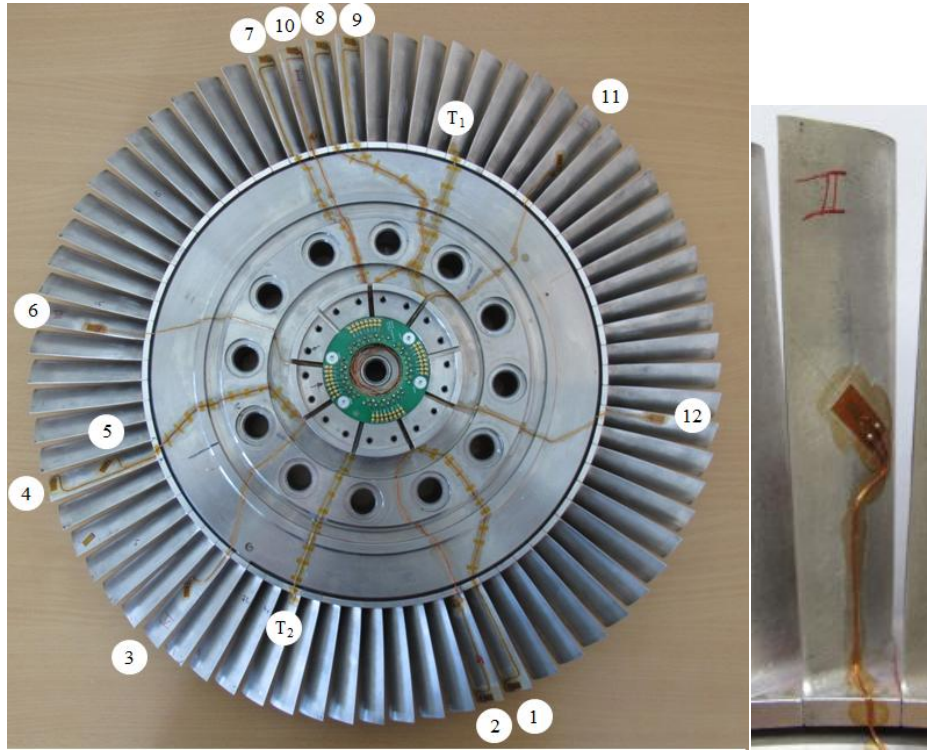


Figure 5. Instrumented rotor (left) and blade with strain gauge #3 (right)

Data of strain gauge no. 3 was used for this paper and is representative for all measurement positions (Schönleitner, 2016).

Campbell diagrams are shown in Figure 6 for the blades (left) and for the rotor disc (right). For the sake of clarity it was decided to draw separate diagrams for the rotor disc and blades. Also, the dashed line indicates the operating rotational speed for this investigation at 3400 rpm. Engine order (EO) lines according to blade-vane-row interactions are also indicated in the diagrams. These lines are dependent of the number of blades and vanes. The origin of the excitation is additionally marked, either with D or U. D represents all effects from upstream vane rows such as stator and inlet guide vane wakes and denotes downstream effects. U represents effects from downstream components such as the turbine exit guide vanes and denotes upstream effects. Modes can also have an upstream and a downstream effect and will be then marked with D/U.

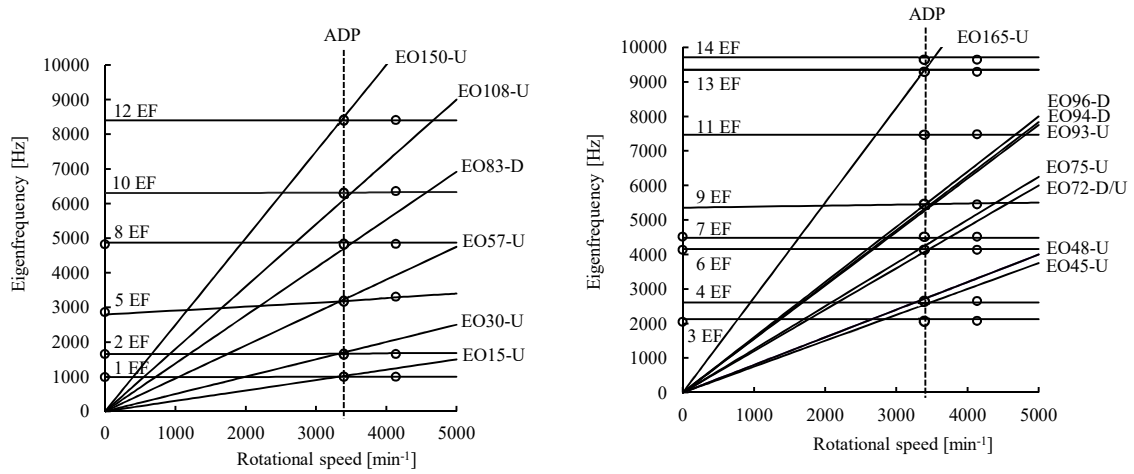


Figure 6. Campbell diagrams; blade (left) and rotor disc (right)

There are 15 turbine exit guide vanes and therefore an EO15 excitation of the first eigenfrequency can be seen. The second harmonic of EO15 excites the second blade eigenfrequency (left diagram). Further, EO45 and EO75 excite rotor disc eigenfrequencies (right diagram). Also EO83 (IGV excitation) and EO96 (stator excitation) are depicted in the diagrams. The operating point was chosen that an excitation of mode 9 due to the stator wakes can be measured. This is one of the most important excitation mechanism in a turbomachine. Also (Tyler, et al.,

1962) reported the importance of vane-blade interaction modes originally for acoustics but these modes are also relevant for forced response.

5 Five-Hole-Probe Measurement Positions

The influence of a five-hole-probe downstream of a low pressure turbine rotor (plane C in Figure 1 b)) onto the rotor and disc vibration was measured. Plane C is important to evaluate the flow field downstream of the rotor and is crucial for aerodynamic investigations of the turbine stage and the turbine exit casing. Usually a turbine exit guide vane pitch is measured in that plane.

For this investigation three typical circumferential and three typical radial positions of the probe are chosen for vibration measurements, see Figure 7. The worst position is expected to be in the middle of the pitch between two turbine exit guide vanes and radial at the most inner position (see Figure 7, bottom right).

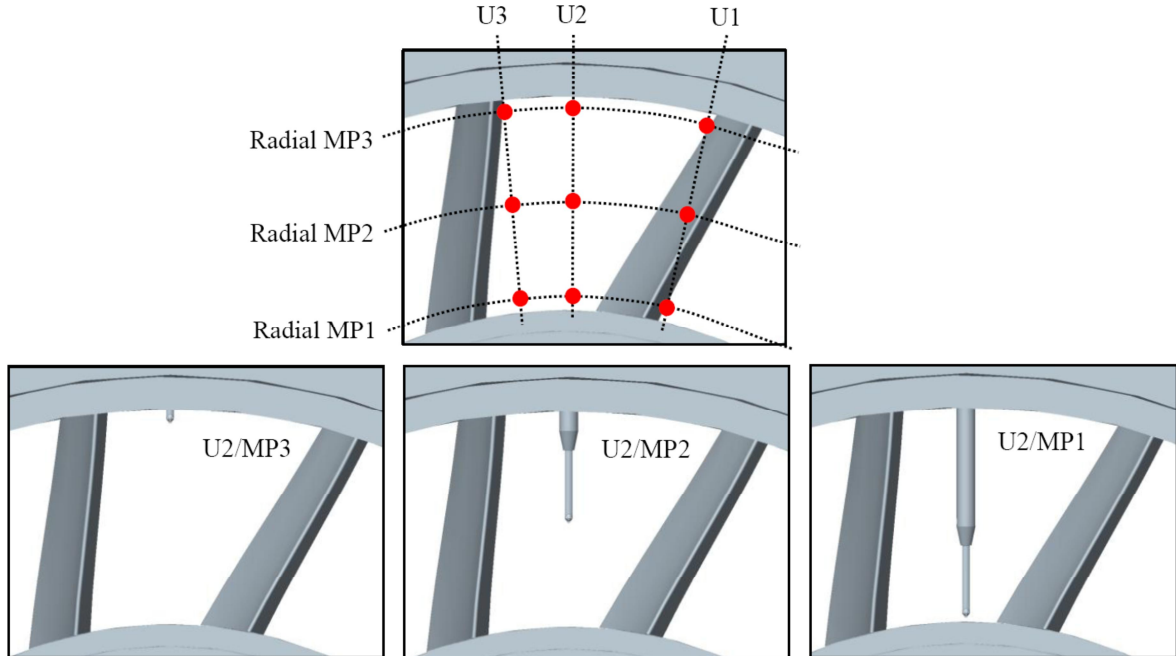


Figure 7. Probe positions for blade vibration measurements

The probe positions where vibration measurements have been performed are shown in Figure 7 at the top and are marked with dots.

6 Blade Vibration Measurements

For the evaluation of the blade vibrations all amplitudes of the respective mode of the different configurations are used. By means of numerical simulations the peaks in the spectra can be clearly identified and assigned to a specific blade or disc mode. These modes can be evaluated separately or together and compared to other configurations. By means of an amplitude weighting a quantitative comparison is possible. For a better representation of the results a net diagram is used.

Figure 8 shows the results of the experimental investigation of the lean TEC compared with the reference configuration (state-of-the-art TEC) presented in (Schönleitner, 2016). The weighted amplitudes for each mode is depicted in the net diagram (Figure 8 left). Amplitudes for the lean TEC as solid line and in amplitudes of the reference configuration as dotted line is shown. A lower vibration level can be seen for the leaned TEC configuration. In Figure 8 on the right side it is distinguished between disc modes and blade modes. Depicted is the sum of all excited modes. It can be seen that 66% of the modes belong to disc modes and 34% to blade modes. The dominant disc modes are a result of the excitation of EO96, EO94, and EO93, where mode 9 show a crossing in the Campbell diagram. For the following discussion mode 1 (blade vibration) and mode 9 (disc vibration) will be analysed in more detail.

Figure 9 shows the spectra without five-hole-probe on the left side and for the worst probe position (circumferential position U2, radial position MP1) on the right side. The influence can be clearly seen when comparing both spectra. Mode 1 (ca. 1000 Hz) and mode 9 (ca. 5400 Hz) show clearly higher amplitudes.

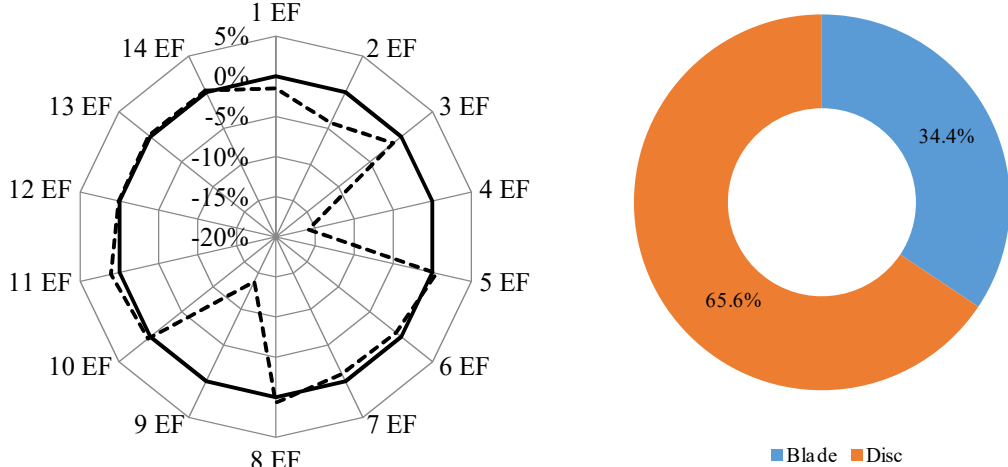


Figure 8. Amplitude levels; net diagram (left) and amplitude distribution of the lean TEC (right)

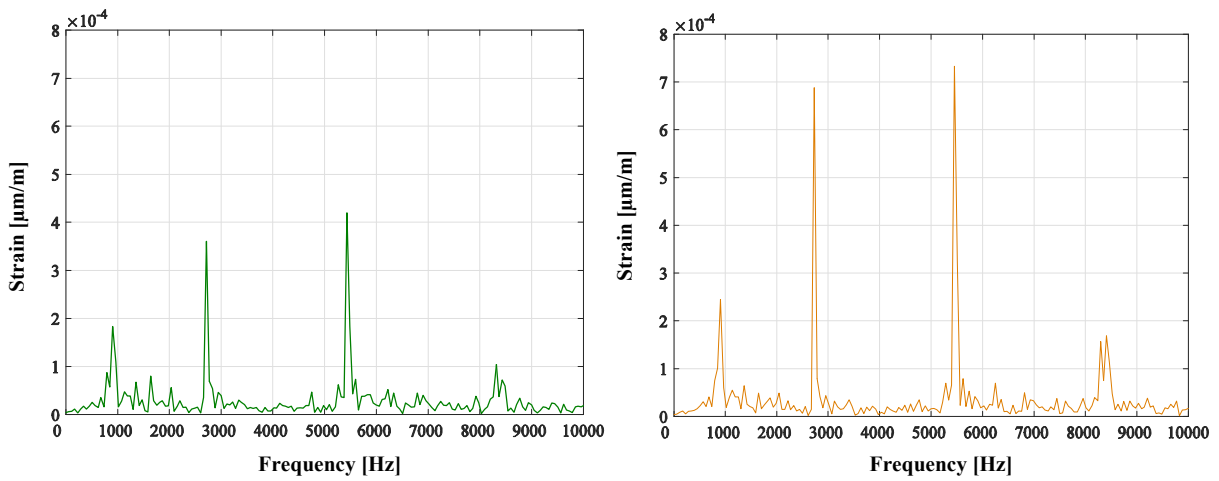


Figure 9. Spectra of strain gauge #3, ADP, without probe (left) and probe position U2/MP1 (right)

7 Results and Discussion

7.1 Amplitude Weighting

For a better comparison of the spectra the amplitudes are weighted based on the amplitudes of the blade vibrations without a probe. The procedure is as follows. All max. amplitudes of the single modes a_i are summed up and give an equivalent amplitude $A_{\text{equivalent}}$ independent from the frequency. Related to the equivalent amplitude of a state-of-the-art TEC (standard TEC) a weighting factor is calculated. For other TEC configurations a weighted amplitude $A_{\phi i}$ can be determined. With that amplitude a quantitative comparison is possible.

$$A_{\text{equivalent,standard TEC}} = \sum a_{i,\text{standard TEC}} \quad (1)$$

$$\phi_{i,\text{standard TEC}} = \frac{a_{i,\text{standard TEC}}}{A_{\text{equivalent,standard TEC}}} \quad (2)$$

$$A_{\phi i,\text{TEGV}} = \left[\frac{a_{i,\text{TEGV}}}{a_{i,\text{standard TEC}}} - 1 \right] \phi_{i,\text{standard TEC}} \quad (3)$$

The procedure was already introduced and applied to compare different TEC configurations in (Schönleitner, 2016) and in (Schönleitner, et al., 2016). This weighting does not take into account if amplitudes of higher frequency are more harmful than amplitudes of lower frequency. For a further lifetime prediction modern methods of durability analysis under consideration of the number of load cycles have to be used.

7.2 Influence of Circumferential Position

The influence of the five-hole-probe onto the blade vibrations changes with the circumferential position of the probe relative to the TEGV downstream of the rotor. Figure 10 shows the weighted amplitudes for blade mode 1 (left) and disc mode 9 (right). The dashed line indicates the blade vibrations without a probe. This vibration level is set as reference value. It can be clearly seen that the vibration level is dependent on the circumferential position as well as on the radial position. In Figure 10 the radial positions are also drawn. The amplitudes are increasing dependent on the radial position. That means that the more the probe is inserted into the channel the higher is the vibration amplitude of the rotor. This is a clear evidence of the negative influence of the probe onto the vibrations of the rotor blades and the rotor disc.

The dependency of the amplitudes on the circumferential positions shows different characteristics for blades and disc. Blade mode 1 is more affected if the probe is in line with the trailing edge of the TEGV (circumferential position U1).

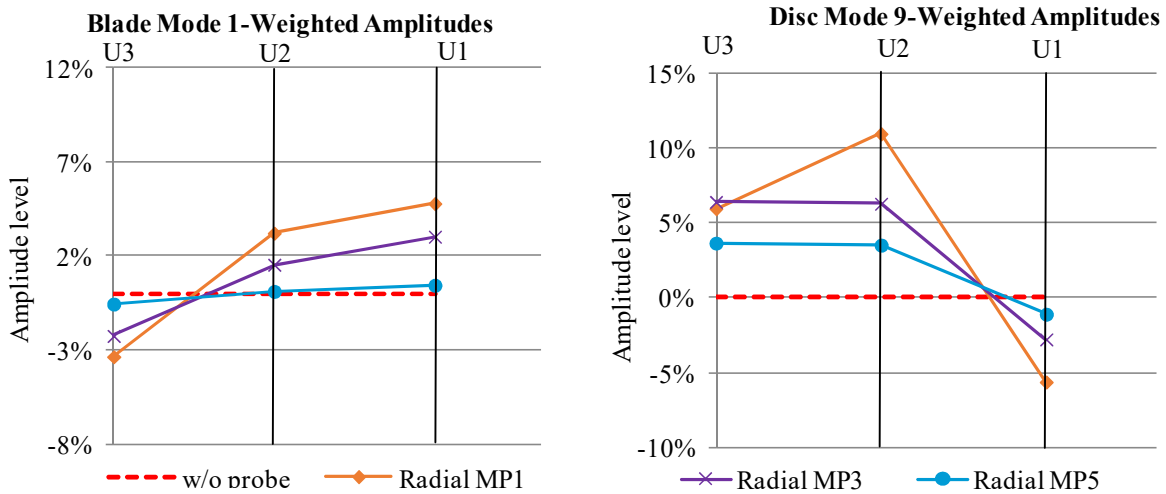


Figure 10. Influence of the circumferential position of the five-hole-probe

The amplitudes decrease if the probe is moved towards the middle of the flow channel between suction and pressure side of TEGVs. These higher amplitudes for circumferential position U1 may be caused by an amplification of the potential effect of the turbine exit guide vanes or it is the sum of the effect of the probe. Looking at the disc mode it is seen that the strongest influence and highest amplitudes occur at circumferential position U2 in the middle of the flow channel. The stronger excitation could be caused by additional blockage effects of the probe and hence a changed flow field through the machine. Contrary to that, the additional blockage effect is less pronounced in circumferential position U1, because the TEGV still produces some blockage.

7.3 Influence of Radial Position

For circumferential position U2 the increase of blade vibrations (left) and the increase of disc vibrations (right) (compared to the vibrations without a probe) for three radial probe positions are plotted in Figure 11. The rotor vibration amplitudes increase the more the probe is inserted into the flow channel. The change is almost linear for the blade vibrations as well as for the disc vibrations. The influence of the probe leads to an increase of blade vibration amplitudes up to 45%. Further, it can be seen, that also in MP3 where only the small probe head of 2.5 mm is in the flow channel, the vibration amplitudes are increased.

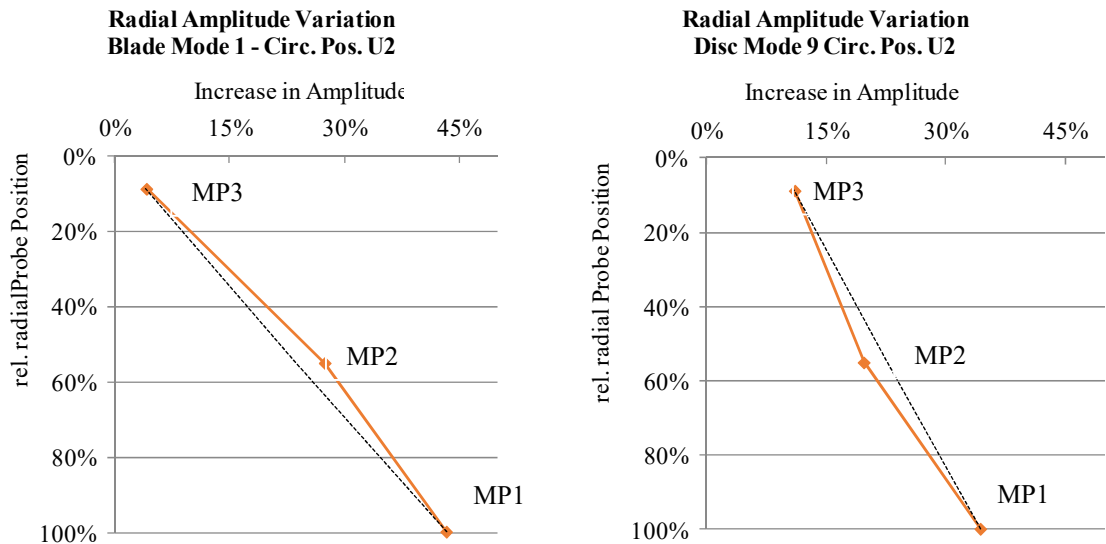


Figure 11. Radial distribution of amplitude variation; blade mode (left), disc mode (right)

7.4 Overall Vibration Levels

To get a better overall view on the vibration amplitudes the data is depicted in net diagrams. Figure 12 shows the amplitudes of all blade modes (left) and disc modes (right) in a frequency range up to 10 kHz.

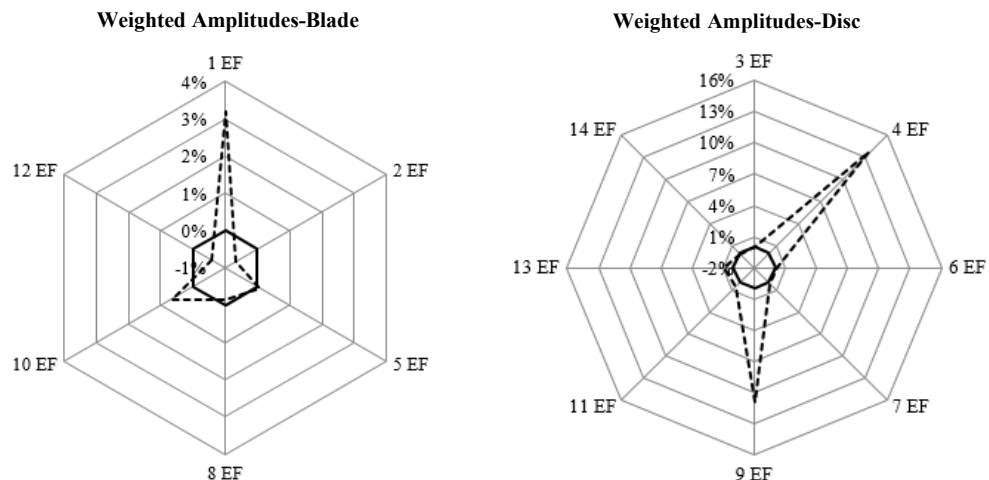


Figure 12. Weighted amplitudes for circumferential position U2 and radial position MP1; blade modes (left) and disc modes (right)

The solid line indicates the case without a probe as a reference with 0% amplitude. Compared to the solid line the amplitudes can be higher, lower or equal. It was shown in previous chapters that the probe position U2/MP1 was the worst one regarding vibration excitation. Therefore Figure 12 shows the amplitudes for that specific probe position. From that figure it can be seen that the influence of the probe is up to 15%. For almost every blade and disc mode an increase of the vibration amplitudes can be seen.

Figure 13 shows the non-weighted amplitudes for all blade and disc modes. Again a large influence of the five-hole-probe is seen clearly. Further, it can be seen that an amplitude increases of up to 80% is measured.

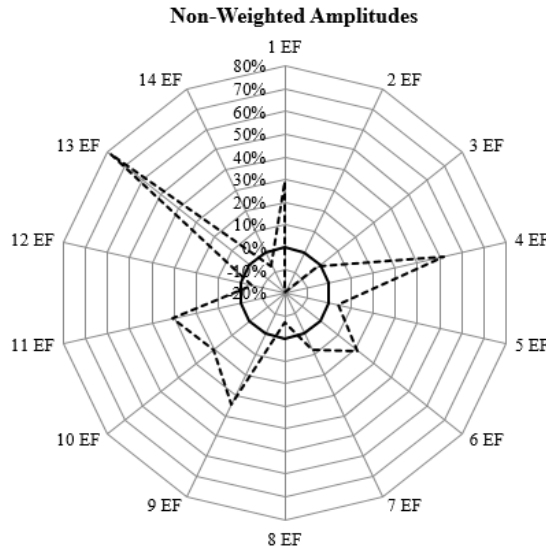


Figure 13. Non-weighted amplitudes of blades and disc at circumferential position U2 and radial position MP1

8 Conclusion

In this paper the influence of a five-hole-probe onto the blade vibrations of a low pressure turbine rotor under engine relevant operating conditions was shown. Further, the dependency on radial and circumferential probe position was reported. For blade and disc modes large vibration amplitude amplifications dependent on the probe position was measured. As expected, the worst probe position was identified if the probe is fully in the flow channel and therefore the largest potential effect and influence of the flow field is assumed, thus increasing the vibration amplitudes of the rotor. In circumferential direction the largest influence has been found if the probe is directly upstream of the TEGV leading edge. Here, the upstream potential effect of the probe and the TEGV are assumed to sum up. Considering the disc modes, the largest influence was found if the probe is in the middle of the flow channel. Here the blockage effect of the vane passage is assumed to play a major role. Amplitude amplification of single modes up to 80% have been measured and shows the importance of considering probes and instrumentation and their position in the design process of rotors intended to be used in test rigs for flow measurements.

9 Acknowledgements

This work has been carried out in the framework of the national funded TAKE-OFF programme within the research project AdMoNt (contract no. 839008) regarding aeroelastic investigations of low pressure turbine blading at Graz University of Technology at the Institute for Thermal Turbomachinery and Machine Dynamics. The authors therefore want to thank the Austrian Research Promotion Agency (FFG) and the Austrian Ministry for Transport, Innovation and Technology (bmvit) for funding this project. The authors would like to thank Prof. Dr.techn. H.P. Pirker for his great support and the discussions during all experimental investigations and for operating the compressor station.

References

Bell, D.L. and He, L.: Three-Dimensional Unsteady Flow for an Oscillating Turbine Blade and the Influence of Tip Leakage. *ASME Journal of Turbomachinery*. January 2000, Vol. 122, S. 93-101.

Broszat, D., Kennephol, F., Tapken, U., Moser, M. and Heitmeir, F.: Validation of an Acoustically 3d-designed Turbine Exit Guide Vane. *16th AIAA/CEAS Aeroacoustics Conference*. 2010. AIAA-2010-3806.

Glodic, N., Vogt, D. and Fransson, T.: Experimental and Numerical Investigation of Mistuned Aerodynamic Influence Coefficients in an Oscillating LPT Cascade. *Proceedings of the ASME TurboExpo*. 2011. ASME Paper GT2011-46283.

Huang, X.Q., He, L. and Bell, D.L.: An Experimental Investigation Into Turbine Flutter Characteristics at Different Tip-Clearances. *Proceedings of the ASME TurboExpo*. June 2006. ASME Paper GT2006-90541.

Kielb, J. and Abhari, R.: Experimental Study of Aerodynamic and Strutural Damping in a Full-Scale Rotating Turbine. *Proceedings of the ASME TurboExpo*. 2001. 2001-GT-0262.

Moser, M., Kahl, G., Kulhanek, G. and Heitmeir, F.: *Construction of a Subsonic Test Turbine Facility for Experimental Investigations of Sound Generation and Propagation for Low Pressure Turbines*. Beijing, China : s.n., 2007. ISABE Conference. ISABE-2007-1366.

Nowinski, M. and Panovsky, J.: Flutter Mechanism in Low Pressure Turbine Blades. *Journal of Engineering for Gas Turbine and Power*. January 2000, Vol.122, S. 82-88.

Schönleitner, F.: Schwingungsanregung unterschiedlicher Turbinenaustrittsgehäuse zukünftiger Flugtriebwerkskonzepte. *Dissertation, Technische Universität Graz*. 2016.

Schönleitner, F., Traussnig, L., Marn, A. and Heitmeir, F.: Detection of blade mistuning in a low pressure turbine rotor resulting from manufacturing tolerances and differences in blade mounting. *11th International Conference Vibrations in Rotating Machines*. 2015

Schönleitner, F., Selic, T., Schitter, C., Heitmeir, F. and Marn, A.: Experimental Investigation of the Upstream Effect of Different Low Pressure Turbine Exit Guide Vane Designs on Rotor Blade Vibration. *Proceedings of the ASME TurboExpo*. 2016. ASME Paper GT2016-56067.

Schönleitner, F., Traussnig, L., Heitmeir, F. and Marn, A.: Modal Characteristics, Strain Gage Setup and 1-way FSI of a Low Pressure Turbine Rotor as Preparation for Upcoming Experimental Aeroelastic Investigations. *Proceedings of the ASME TurboExpo*. 2015. ASME Paper GT2015-42717

Selic, T.: Experimental Investigation of the Aerodynamics and Acoustics of Exit Guide Vanes for Future Aircraft Engines. *Dissertation, Technische Universität Graz*. 2016.

Tyler, J.M. and Sofrin, T.G.: Axial Flow Compressor Noise Studies. *SAE Transactions*. 1962, Bd. 70, S. 309-332.

Urban, B., Stetter, H. and Vortmeyer, N.: Experimental Investigation of Shock-Induced Blade Oscillation at an Elastically Suspended Turbine Cascade in Transonic Flow. *Proceedings of the ASME TurboExpo*. 2000. ASME Paper 2000-GT-378.

Vogt, Damian M., Fransson, T. and Torsten H.: Experimental Investigation of Mode Shape Sensitivity of an Oscillating Low Pressure Turbine Cascade at Design and Off-Design Conditions. *Journal of Engineering for Gas Turbines and Power*. April 2007, Vol.129, S. 530-541.

Addresses: Dr. Andreas Marn, Dipl.-Ing. Manuel Zenz, Univ.-Prof. Dr.-Ing. Franz Heitmeir; Graz University of Technology, Institute for Thermal Turbomachinery and Machine Dynamics, Inffeldgasse 25A, A-8010 Graz, Austria. Dr. Florian Schönleitner, Semperit AG Holding, Modecenterstraße 22, A-1031 Vienna, Austria. Dr. Thorsten Selic, Elin Motoren GmbH, Elin-Motoren-Straße 1, A-8160 Preding/Weiz, Austria.
email: andreas.marn@tugraz.at, manuel.zenz@tugraz.at, franz.heitmeir@tugraz.at,
florian.schoenleitner@semperitgroup.com, thorsten.selic@elinmotoren.at

Enhanced Utilization of structural Damping of rotating Machines using impulsively shaped torsional Moments

T. Pumhössel, B. Hopfner, H. Ecker

The reduction of torsional vibrations of rotating machines is an important issue, as they may lead to a decrease of the performance, or in the worst case, to a damage of the machinery. In particular, self-excited vibrations have to be suppressed in any case due to their hazardous nature.

In this contribution, a method is proposed, which allows utilizing the structural damping inherent to every rotating machine much more effectively by introducing impulsively shaped torsional moments, resulting in repeated modal transfers of vibration energy. Depending on the chosen impulsive strength, the energy transfers are accompanied by feeding external energy to, or extracting energy from the mechanical system. It is shown theoretically by approximating the impulses by Dirac-delta functions that an impulsive strength exists, where no energy crosses the system boundary, i.e. energy extracted from one mode is fed entirely to another mode of vibration. In the case of a conservative system, a repeated application of such impulses induces a periodic exchange of energy between lower and higher modes. Taking into account the structural damping reveals the advantages of transferring energy across modes. As higher modes possess higher damping ratios than lower ones, the structural damping of the rotating machine can be utilized much more effectively, which leads to a significant reduction of torsional vibrations. The underlying equations of motion of the impulsively excited system can be written as recursive difference equations with constant coefficients. Hence, the stability properties of the system can be investigated according to the Floquet theory. It is shown that the proposed concept is capable of suppressing self-excited vibrations. Stability charts are presented which allow to identify stable areas of operation. Finally, some numerical results of a test-rig are shown, underlining the effectivity of the proposed method.

1 Introduction

Torsional vibrations of rotating machines have been investigated for a long time. This is founded in the fact that they may decrease the performance of such machines, or in the worst case, result in a damage or breakdown. Especially, self-excited vibrations, due to several mechanisms, have led to catastrophic failures of rotating machines. Therefore, a lot of measures have been developed to suppress or at least to reduce such vibrations.

Reduction of vibrations of mechanical systems means to reduce the energy content. A natural approach is to introduce additional devices which allow a rapid dissipation of vibration energy. Within this context, an interesting concept are nonlinear energy sinks (NES), see Vakakis et al. (2009). They consist of a lightweight vibrating system which is coupled in an essential nonlinear manner to the primary structure. It is shown that, under certain conditions, an unidirectional energy flow from the primary structure to the NES occurs, where energy is dissipated effectively. Another method is the modal redistribution of energy. As higher modes usually possess enhanced damping properties compared to lower ones, it is beneficial to shift vibration energy to higher modes, where it can be dissipated more effectively. This is demonstrated in Al-Shudeifat et al. (2015), where vibro-impact NES are used to achieve a modal redistribution of energy of mechanical structures to utilize the damping properties of the structure more efficiently. Hence, transient vibrations decay much faster compared to the case where no NES is used. Methods for tracking energy flows in dynamical systems can be found in Quinn et al. (2012), for example. A continuous and repeated transfer of energy from low to high modes and vice versa can also be achieved by a periodic variation of system stiffness parameters at certain frequencies, see Tondl (1998). To induce the modal energy transfer, external energy has to be fed to the system and energy has to be extracted from the system in a periodic manner. In the following years, a variety of investigations focused on this effect, see Ecker (2005); Tondl (2000); Dohnal (2008); Ecker and Pumhössel (2012), for example.

Dynamical systems subjected to periodic impulsive parametric excitation were investigated in Hsu (1972), wherein the question of stability of such systems has been addressed extensively. In Pumhössel et al. (2013) and Pumhössel (2016a), the effect of stiffness variation of impulsive type on the energy content of mechanical systems was inves-

tigated. It was shown that stiffness impulses, whose strength depends in a nonlinear manner on the state-vector, allow to transfer discrete amounts of energy from pre-defined low-modes, to a target set of higher modes. The existence of energy-neutral transfers, i.e. energy transfers where neither external energy is fed to the mechanical system, nor energy is extracted from the system while energy is transferred across modes, was discovered and reported. In Pumhössel (2016b), the general case of modal energy transfers using impulsive forcing of mechanical systems was investigated.

The present contribution addresses targeted modal energy transfers in rotor systems, induced by applying impulsive torsional moments. It is shown that energy can be transferred periodically from low to high modes and vice versa. In a further development of the work presented in Pumhössel (2016b), the stability of a rotor system subjected to self-excitation is addressed in a comprehensive manner. The proposed approach allows to write the equations of motion of the impulsively excited system as a set of difference equations with constant coefficients. Hence, the stability properties can be investigated easily. Stability charts demonstrate which combinations of system parameters allow to stabilize the self-excited rotor system. Finally, some numerical results of a test-rig under construction are shown.

2 Modal Energy Transfers - analytical Investigations

The n -dimensional equations of motion of a rotor system consisting of flexible shafts with isotropic properties, and rigid disks with zero unbalance eccentricity may be written as

$$\mathbf{I}\ddot{\mathbf{q}} + \mathbf{C}\dot{\mathbf{q}} + \mathbf{K}\mathbf{q} = \sum_{k=1}^N \varepsilon_k \delta(t - t_k) \mathbf{f}, \quad (1)$$

where $\mathbf{q} = [q_1, q_2, \dots, q_n]^T$ represents the vector of rotational degrees of freedom, and $\mathbf{I} = \text{diag}(I_1, I_2, \dots, I_n)$ and \mathbf{K} denote the constant and symmetric mass-, and stiffness-matrices. The damping matrix \mathbf{C} is assumed to be decomposable in a damping and a self-excitation part, according to $\mathbf{C} = \mathbf{C}_{damp} + \mathbf{C}_{self}$, where \mathbf{C}_{damp} is assumed to be stiffness-proportional, i.e. $\mathbf{C}_{damp} = \beta \mathbf{K}$ holds. The rotor system is subjected to a sequence of N torsional moments of impulsive type, see right hand side of Eq. (1), where $\delta(t - t_k)$ represents the Dirac-delta function, and $\mathbf{f} = [f_1, f_2, \dots, f_n]^T$, $f_i = 1 \vee 0$, $i = 1, \dots, n$ denotes the constant vector, which allows to select specific disks. The scalar ε_k , which will be state-dependent, as described later, represents the strength of the impulses. To investigate the effect of the impulsive excitation to the rotor system, especially discrete modal energy transfer effects, the equations of motion are transformed to modal coordinates \mathbf{u} according to $\mathbf{q} = \Phi \mathbf{u}$, where Φ represents the modal matrix of the undamped rotor system. This yields to the equations of motion in the modal form

$$\bar{\mathbf{I}}\ddot{\mathbf{u}} + (\beta \bar{\mathbf{K}} + \bar{\mathbf{C}}_{self})\dot{\mathbf{u}} + \bar{\mathbf{K}}\mathbf{u} = \sum_{k=1}^N \varepsilon_k \delta(t - t_k) \bar{\mathbf{f}}. \quad (2)$$

In the case of no self-excitation, i.e. $\bar{\mathbf{C}}_{self} = \mathbf{0}$, the left hand side of Eq. (2) is decoupled. Hence, modal energy transfers can occur only at the instants of time t_k , where an impulse is applied. In the following, it is assumed that the instants of time t_1, t_2, \dots where impulses are applied, are equidistant in time, i.e. $t_{k+1} - t_k = T_P$, $k = 1, \dots, N - 1$, $T_P = \text{const.}$ holds. This assumption allows to relate the state-vector of the system at an instant of time t , to the state-vector at $t + T_P$ using a constant matrix-mapping. Therefore, the equations of motion (1) are written in first order form according to

$$\dot{\mathbf{x}} = \underbrace{\begin{bmatrix} \mathbf{0} & \mathbf{E} \\ -\mathbf{I}^{-1}\mathbf{K} & -\mathbf{I}^{-1}\mathbf{C} \end{bmatrix}}_{\mathbf{A}} \mathbf{x} + \begin{bmatrix} \mathbf{0} \\ \sum_{k=1}^N \varepsilon_k \delta(t - t_k) \mathbf{I}^{-1} \mathbf{f} \end{bmatrix}, \quad (3)$$

where the state-vector is given by $\mathbf{x} = [q_1, q_2, \dot{q}_1, \dot{q}_2]^T$, and \mathbf{E} denotes the unity-matrix. The solution of the autonomous set of differential equations $\dot{\mathbf{x}} = \mathbf{A}\mathbf{x}$ is of the well-known form

$$\mathbf{x}(t) = \mathbf{e}^{\mathbf{A}(t-t_0)} \mathbf{x}_0, \quad (4)$$

with an initial state-vector \mathbf{x}_0 . Hence, the state-vectors at the beginning and at the end of an autonomous timespan T_P are related to each other by

$$\mathbf{x}(t_{k+1})_- = \mathbf{e}^{\mathbf{A}T_P} \mathbf{x}(t_k)_+ = \mathbf{D} \mathbf{x}(t_k)_+, \quad (5)$$

where the \pm signs indicates instants of time just after and just before an impulse. At this point, the question about the effect of a force impulse to the state-vector arises. This was investigated extensively in the past, see Angeles

(2012), for example. Therefore, only a brief description is given in the following. The momentum balance for a single impulse is given by

$$\mathbf{I}[\dot{\mathbf{q}}(t_k)_+ - \dot{\mathbf{q}}(t_k)_-] = \varepsilon_k \mathbf{f}, \quad (6)$$

which can be written in the form

$$\dot{\mathbf{q}}(t_k)_+ = \dot{\mathbf{q}}(t_k)_- + \varepsilon_k \mathbf{I}^{-1} \mathbf{f}, \quad (7)$$

and hence, provides a relation of the velocities $\dot{\mathbf{q}}$ just before and just after an impulse. From Eq. (7) one can easily see that the velocities exhibit a jump at the instant of time the impulse is applied. By contrast, the displacements remain continuous, see Angeles (2012), for example, i.e.

$$\mathbf{q}(t_k)_+ = \mathbf{q}(t_k)_-. \quad (8)$$

Summarizing Eqs. (7) and (8) yields to

$$\begin{bmatrix} \mathbf{q}(t_k)_+ \\ \dot{\mathbf{q}}(t_k)_+ \end{bmatrix} = \begin{bmatrix} \mathbf{E} & \mathbf{0} \\ \mathbf{0} & \mathbf{E} \end{bmatrix} \begin{bmatrix} \mathbf{q}(t_k)_- \\ \dot{\mathbf{q}}(t_k)_- \end{bmatrix} + \begin{bmatrix} \mathbf{0} \\ \varepsilon_k \mathbf{I}^{-1} \mathbf{f} \end{bmatrix}. \quad (9)$$

The equation above holds for any arbitrary impulsive strength ε_k . In the following, the special case, where an impulse neither extracts energy from the mechanical system, nor adds external energy to the system, which means that the variation of the kinetic energy ΔT_k is equal to zero, i.e. $\Delta T_k = T_{k+} - T_{k-} = 0$, is investigated. With Eq. (7) the total kinetic energy of the mechanical system after an impulse is given by

$$T_{k+} = \underbrace{\frac{1}{2} [\varepsilon_k^2 \mathbf{f}^T \mathbf{I}^{-1} \mathbf{f} + 2\varepsilon_k \mathbf{f}^T \dot{\mathbf{q}}(t_k)_-]}_{\Delta T_k} + \underbrace{\frac{1}{2} \dot{\mathbf{q}}^T(t_k)_- \mathbf{I} \dot{\mathbf{q}}(t_k)_-}_{T_{k-}}, \quad (10)$$

which leads to the variation ΔT_k in the form

$$\Delta T_k = \frac{1}{2} \varepsilon_k [\varepsilon_k \mathbf{f}^T \mathbf{I}^{-1} \mathbf{f} + 2\mathbf{f}^T \dot{\mathbf{q}}(t_k)_-]. \quad (11)$$

The zeros of the equation $\Delta T_k = 0$ are

$$\varepsilon_{k,1} = 0 \quad \text{and} \quad \varepsilon_{k,2} = -2 \frac{\mathbf{f}^T}{\mathbf{f}^T \mathbf{I}^{-1} \mathbf{f}} \dot{\mathbf{q}}(t_k)_-. \quad (12)$$

If an impulse with $\varepsilon_k = \varepsilon_{k,2}$ is applied, the overall energy content of the mechanical system remains unchanged. However, this does not prevent energy transfers from one mode to another. It has to be pointed out that $\varepsilon_{k,2}$ remains bounded, as the denominator of $\varepsilon_{k,2}$ in Eq. (12) is positive definite. For the following investigations, the impulsive strength ε_k is rewritten in the form $\varepsilon_k = \vartheta \varepsilon_{k,2}$, with the scalar ϑ . Therewith, ΔT_k is given by

$$\Delta T_k(\vartheta) = 2\vartheta(\vartheta - 1) \frac{(\mathbf{f}^T \dot{\mathbf{q}})^2}{\mathbf{f}^T \mathbf{I}^{-1} \mathbf{f}} = \begin{cases} < 0 & \text{if } 0 < \vartheta < 1 \\ = 0 & \text{if } \vartheta = 0 \vee \vartheta = 1 \\ > 0 & \text{if } \vartheta < 0 \vee \vartheta > 1 \end{cases}. \quad (13)$$

The sign of ΔT_k depends only on the selected value for ϑ , as the fraction in Eq. (13) is always positive. If $0 < \vartheta < 1$, ΔT_k is negative, which means that kinetic energy is extracted from the mechanical system by the impulse. Energy is fed into the mechanical system, i.e. ΔT_k is positive, if $\vartheta < 0$ or $\vartheta > 1$ holds. No energy crosses the system boundary, if $\vartheta = 1$, denoted as the energy-neutral case introduced in Pumhössel (2016a). Inserting $\varepsilon_k = \vartheta \varepsilon_{k,2}$ into the expression for the velocity just after an impulse, Eq. (7) leads to

$$\dot{\mathbf{q}}(t_k)_+ = \dot{\mathbf{q}}(t_k)_- - 2\vartheta \underbrace{\frac{\mathbf{I}^{-1} \mathbf{f} \mathbf{f}^T}{\mathbf{f}^T \mathbf{I}^{-1} \mathbf{f}}} \dot{\mathbf{q}}(t_k)_- = \dot{\mathbf{q}}(t_k)_- - 2\vartheta \mathbf{G} \dot{\mathbf{q}}(t_k)_- = [\mathbf{E} - 2\vartheta \mathbf{G}] \dot{\mathbf{q}}(t_k)_-. \quad (14)$$

The relation between the state-vector just before and just after an impulse can now be written in the form

$$\begin{bmatrix} \mathbf{q}(t_k)_+ \\ \dot{\mathbf{q}}(t_k)_+ \end{bmatrix} = \underbrace{\begin{bmatrix} \mathbf{E} & \mathbf{0} \\ \mathbf{0} & \mathbf{E} - 2\vartheta \mathbf{G} \end{bmatrix}}_{\mathbf{J}} \begin{bmatrix} \mathbf{q}(t_k)_- \\ \dot{\mathbf{q}}(t_k)_- \end{bmatrix}, \quad (15)$$

where the matrix \mathbf{J} is denoted as *jump transfer matrix*, according to the notation introduced by C.S. Hsu, see Hsu (1972). With Eqs. (5) and (15) the state-vector after one period T_P is given by

$$\begin{bmatrix} \mathbf{q}(t_{k+1})_+ \\ \dot{\mathbf{q}}(t_{k+1})_+ \end{bmatrix} = \mathbf{J} \begin{bmatrix} \mathbf{q}(t_{k+1})_- \\ \dot{\mathbf{q}}(t_{k+1})_- \end{bmatrix} = \mathbf{J} \mathbf{D} \begin{bmatrix} \mathbf{q}(t_k)_+ \\ \dot{\mathbf{q}}(t_k)_+ \end{bmatrix}, \quad (16)$$

which is a set of linear difference equations with constant coefficients. For the following investigations, the abbreviation $\mathbf{Q} = \mathbf{JD}$ is used. Equation (16) allows to easily calculate the state-vector at instants of time $\dots t_{k-1}, t_k, t_{k+1} \dots$, and hence, the matrix \mathbf{Q} describes the growth of the state-vector. For this reason, the eigenvalues of \mathbf{Q} decide about the stability of the trivial solution of Eq. (3) for $N \rightarrow \infty$. The trivial solution is asymptotically stable if for all eigenvalues $\Lambda_i, i = 1 \dots n$, of \mathbf{Q} holds

$$|\Lambda_i| = |\text{eig}(\mathbf{Q})| < 1. \quad (17)$$

3 Example - 2 DOF System

A schematic of the investigated mechanical system is depicted in Fig. (1). It consists of two disks with inertias I_1 and I_2 as well as rotary degrees of freedom q_1 and q_2 . The disks are connected to each other and to the inertial

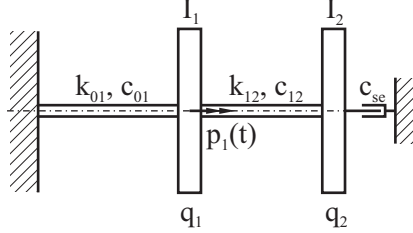


Figure 1: Schematic of the investigated mechanical system.

frame by shafts with stiffness k_{01} and k_{12} and damping coefficients c_{01} and c_{12} . A self-excitation mechanism is modelled by an element connected to disk two, which is capable of possessing a negative damping coefficient. Disk one is subjected to a sequence of impulsively shaped torsional moments $p_1(t)$. The following system-parameters are used for the numerical simulations $I_1 = I_2 = 1 \text{ kgm}^2$, $k_{01} = k_{12} = 1 \text{ Nm}$, $\beta = 0.01 \text{ s}$, $c_{se} = -0.02 \text{ Nsm}$. The periods of first and second mode vibration are $T_1 = 10.1664 \text{ s}$ and $T_2 = 3.3882 \text{ s}$. Two different initial conditions (ICs) are used for the numerical investigations, the scaled first eigenvector (IC 1) and an initial velocity of disk two (IC 2), representing a shock load, see Eq. (18).

$$\mathbf{x}_0 = \begin{cases} [0.6180, 1, 0, 0]^T & \text{IC 1} \\ [0, 0, 0, 1]^T & \text{IC 2} \end{cases} \quad (18)$$

Figure (2) depicts first numerical results of the undamped system without self-excitation to show the basic mechanism of modal energy transfer in the energy-neutral case, i.e. $\vartheta = 1$. As initial condition, a first mode deflection according to IC1 is used. Impulses are applied to disk one. By contrast to the physical coordinates q_1 and q_2 (see left column), the modal coordinates u_1 and u_2 (right column) clearly indicate the occurring modal energy transfer. A (local) minimum of u_1 is accompanied by a (local) maximum of u_2 and vice versa. Correspondingly, the energy content E_1 of the first mode minimizes, when the energy content E_2 of the second mode peaks. It has to be pointed out that the overall energy content E_{tot} of the mechanical system remains unchanged, i.e. neither energy is extracted from the system, nor external energy is fed to the system by the impulsive excitation, as the energy-neutral case $\vartheta = 1$ is investigated and natural damping is neglected.

Exemplary time-series for extracting energy from, or feeding external energy into the mechanical system are depicted in Fig. (3). Also in these cases, natural damping as well as self-excitation are switched off. In the left column, $\vartheta = 0.8$ and hence, the torsional moments of impulsive type extract energy from the mechanical system. The modal energy transfer is accompanied by a decreasing of the overall energy content E_{tot} . The right column shows results for $\vartheta = 1.02$, which means that external energy is fed into the system by the impulsively shaped torsional moments. As a consequence, the overall energy E_{tot} of the system increases beyond all limits, hence, the mechanical system becomes unstable.

The advantages of transferring energy across modes in a recurring manner becomes clear if natural damping is introduced. Figure (4) shows some corresponding results for $\vartheta = 1$, where as initial condition IC2 is used. Results, where no impulsive excitation is present, are depicted grey-colored. One clearly observes that the modal energy transfer induced by the impulsive excitation leads to a faster decrease of torsional vibrations q_1 and q_2 . The envelope of the modal coordinate u_1 is much smaller and that of u_2 is larger compared to the case, where no impulsive excitation is present. This means that impulsive excitation in the proposed manner decreases/increases the level of first/second mode vibrations. Hence, the damping properties, inherent to the mechanical structure due

to the natural damping are utilized in a more efficient way. This is underlined by the time-series of the total energy content E_{tot} , which decreases much faster with impulsive excitation than without.

Figure (5) depicts the maximum absolute value of the eigenvalues of the matrix \mathbf{Q} , $\max|\Lambda|$, which decides about the stability of the trivial solution of the impulsively excited system. For the sake of comparison, the maximum absolute eigenvalue of the matrix \mathbf{D} , $\max|\rho|$, describing the system without impulsive excitation is shown as well. The dotted lines represent the case, where no self-excitation is present. With increasing pulse-pause T_P , $\max|\rho|$ decreases linearly and is always below the stability threshold. By contrast, $\max|\Lambda|$ of the system with impulsive excitation shows some minima and maxima and is below $\max|\rho|$, i.e. has a larger distance from the stability limit. Two of the maxima of $\max|\Lambda|$ coincide with $\max|\rho|$ at a pulse-pause of $T_P = 0.5T_1$ and $T_P = T_1$. If self-excitation is introduced, i.e. $c_{se} = -0.02$, the system without impulsive excitation becomes unstable, see solid, grey-colored line in Fig. (5). For almost all values of T_P , also $\max|\Lambda|$ is above the stability limit. However, there exist some small intervals around $T_P = 5.5/8.785/10.98/14.29$ where the impulsively excited system is asymptotically stable. Hence, the modal energy transfer induced by the impulsive excitation is capable of stabilizing the otherwise unstable system.

In the following, the effect of a variation of system parameters on the stability is investigated. It has to be pointed out that for all values of system parameters, the mechanical system without impulsive excitation is unstable. Figure (6) depicts $\max|\Lambda|$ for different values of the pulse-pause T_P and the inertia I_1 of disk one. The stability threshold $\max|\Lambda| = 1$ is indicated by a black, solid line. A variety of areas is observed, where $\max|\Lambda| < 1$, and hence, the trivial solution is asymptotically stable for the corresponding values of T_P and I_1 . Besides, characteristic resonances occur if the pulse-pause T_P is close to $T_P = nT_1/2$, $n \in \mathbb{N}$, see Fig. (7) (left). Therein, grey/white colored areas denote unstable/asymptotically stable trivial solutions. Moreover, the values for $nT_1/2$ (red dashed line) and nT_1 (red solid line), $n \in \mathbb{N}$, indicating resonance areas, are depicted as well. One notes that the stable areas are located close to $nT_1/2$ and nT_1 . Moreover, a kind of self-similarity with increasing T_P is observed. The effect of a variation of the inertia I_2 of disk two is shown in Fig. (7) (right). Large areas of stability are observed with increasing I_2 . As previously shown, they are mainly located near $nT_1/2$ and nT_1 . The results for a variation of the stiffness k_{01} are shown in Fig. (8) (left). Only small tongues of stability are observed. By contrast, the stiffness k_{12} , see Fig. (8) (right), has a large effect on the stability. For almost all values of $k_{12} > \approx 2.3$, the trivial solution is asymptotically stable, except for small areas near $nT_1/2$ and nT_1 . The previous results were based on using impulsive excitation of Dirac-delta type, which allows to give a clear insight into the physical mechanism behind modal energy transfer effects.

In the following, some numerical results of a test rig are presented using half-sine shaped impulses. A sketch of the designed test-rig consisting of two connected disks is shown in Fig. (9). Impulsively shaped torsional moments are applied to the disks using permanent excited synchronous electrical engines (PSM 1 and PSM 2), where the

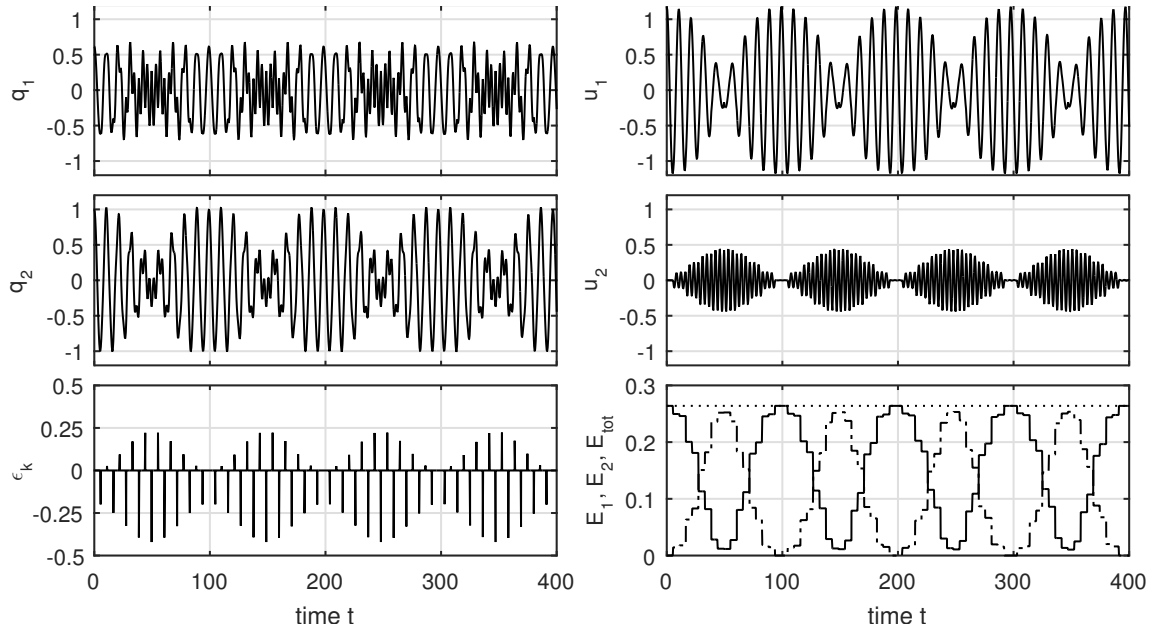


Figure 2: Time-series of physical coordinates q_1 and q_2 , impulsive strength ε_k (left column), modal coordinates u_1 and u_2 , modal energy contents E_1 (solid), E_2 (dashed-dotted) and overall energy content E_{tot} (dotted), (right column). Undamped system without self-excitation. Impulses applied to disk one. Initial condition: IC1. Energy-neutral case $\vartheta = 1$.

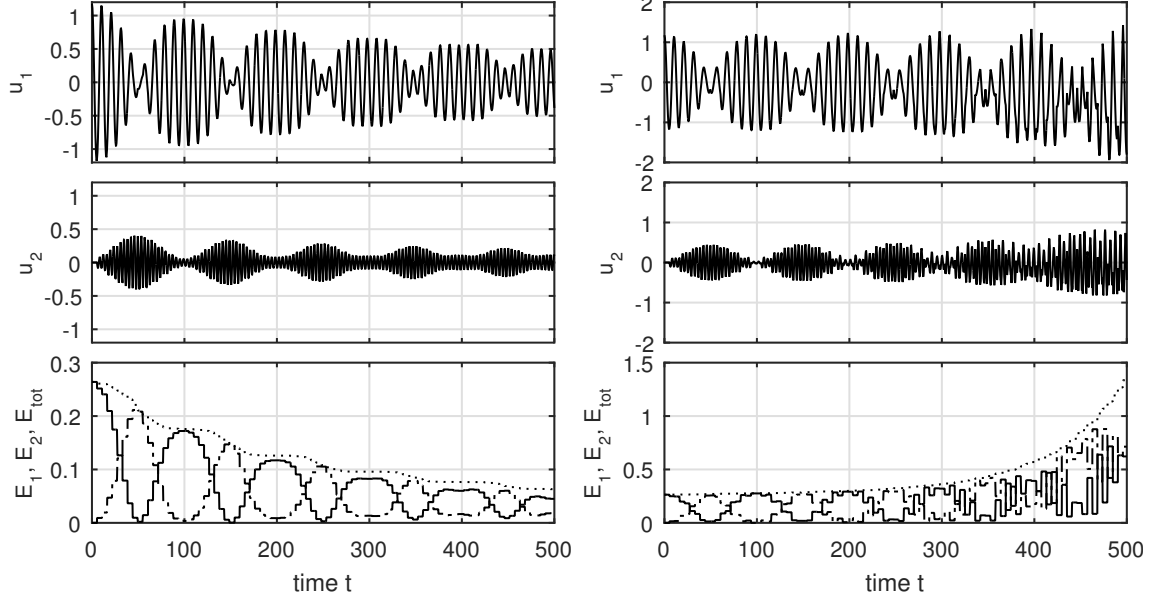


Figure 3: Modal coordinates u_1 and u_2 , modal energy contents E_1 (solid), E_2 (dashed-dotted) and overall energy content E_{tot} (dotted), for extracting energy from the system, $\vartheta = 0.8$, (left column) and feeding energy to the system, $\vartheta = 1.02$, (right column). Undamped system without self-excitation. Impulses applied to disk one. Initial condition: IC1.

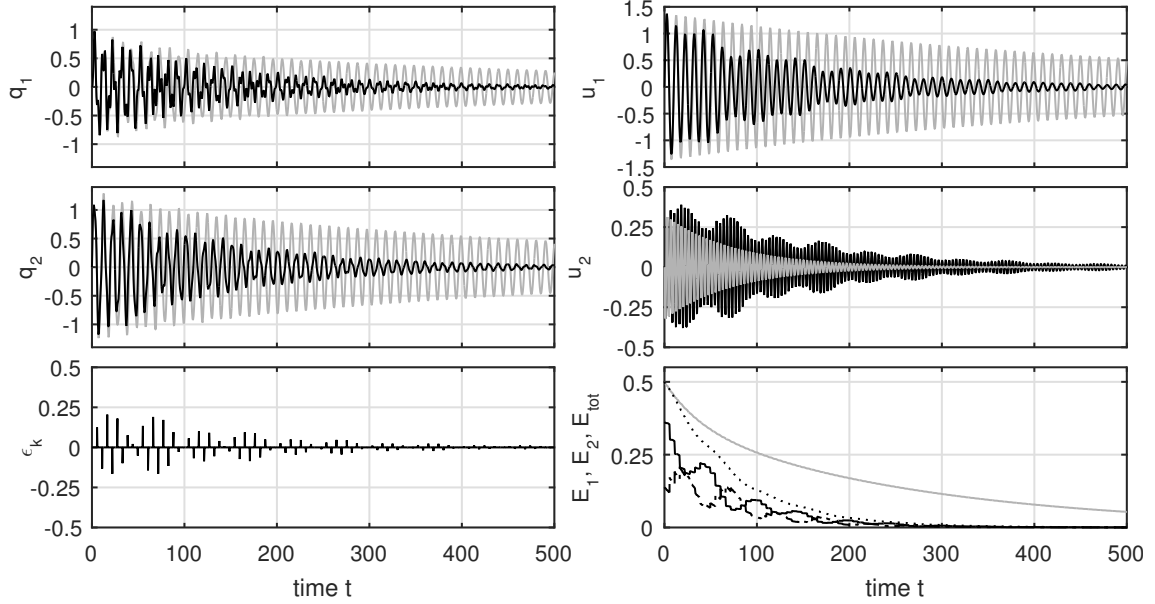


Figure 4: Time-series of physical coordinates q_1 and q_2 , impulsive strength ε_k (left column), modal coordinates u_1 and u_2 , modal energy contents E_1 (solid), E_2 (dashed-dotted) and overall energy content E_{tot} (dotted), (right column). Damped system without self-excitation. Impulses applied to disk one. Comparison with results where no impulsive excitation is present (grey colored). Energy-neutral case $\vartheta = 1$. Initial condition: IC2.

shaft of the first engine connects the part of the rotor to the left and to the right. In the general case, where impulses are applied to both disks, PSM1 and PSM2 require the actual values of the velocities \dot{q}_1 and \dot{q}_2 to apply impulses with the correct strength. The impulses are chosen to be of half-sine shape with a duration of 36 ms, which is equal to about 10% of the period of the second mode. Contrary to the previous investigations, the damping matrix is assumed to be of the form $\mathbf{C}_{damp} = \alpha \mathbf{I} + \beta \mathbf{K}$. The mass-proportional part allows to take the absolute damping, introduced by the electrical engines, into account. The following parameters are used for the numerical investigations: $I_1 = I_2 = 0.0065 \text{ kgm}^2$, $k_{01} = k_{12} = 0.75 \text{ Nm}$, $\alpha = 0.02$, $\beta = 0.0002$.

Figure (10) depicts the physical coordinates q_1 and q_2 , the torsional moment M (applied to disk 1), the modal

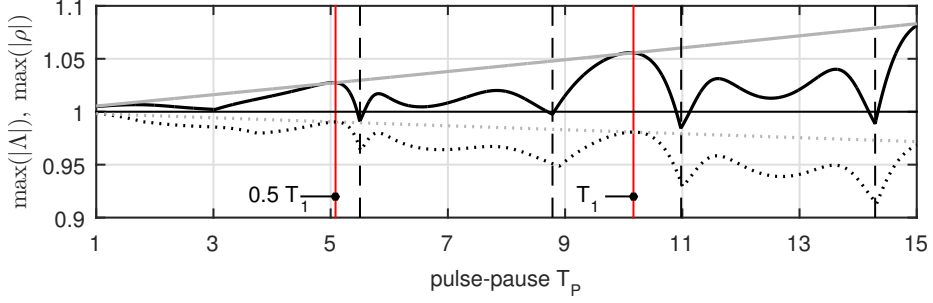


Figure 5: Maximum absolute value $\max|\Lambda|$ of the eigenvalues of the matrix \mathbf{Q} without (dotted, black) and with (solid, black) self-excitation for different values of the timespan T_P between impulses. Grey-colored lines depict the maximum absolute eigenvalue $\max|\rho|$ of the matrix \mathbf{D} . Energy-neutral case $\vartheta = 1$.

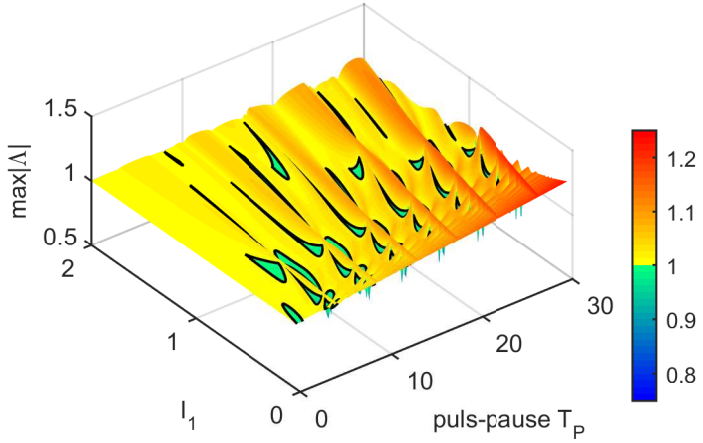


Figure 6: Maximum absolute value $\max|\Lambda|$ of the eigenvalues of the matrix \mathbf{Q} of the damped system with impulsive excitation for different values of the pulse-pause T_P and the moment of inertia I_1 . Energy-neutral case $\vartheta = 1$.

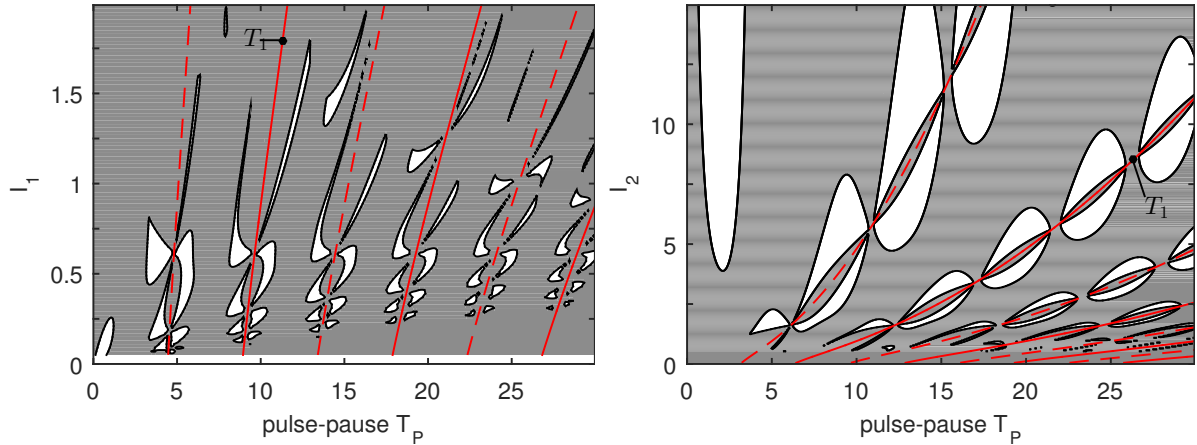


Figure 7: Stability chart for variation of system parameters I_1 (left) and I_2 (right) and T_P . Grey/white colored areas denote unstable/asymptotically stable trivial solutions. Energy-neutral case $\vartheta = 1$.

energy contents E_1 (solid) and E_2 (dashed-dotted) and the overall energy content E_{tot} (dotted). The selected pulse-pause $T_P = 2.30$ s corresponds to a local minimum of the maximum absolute value of the eigenvalues of the matrix \mathbf{Q} . One clearly observes the modal energy exchange between first and second mode. The overall energy content of the mechanical system E_{tot} decreases faster than the energy content of the corresponding system without impulsive excitation (see grey-colored line). The maximum required torque is about $M_{max} \approx 0.1$ Nm. Some results of the self-excited case are shown in Fig. (11). Therein, a self-excitation mechanism is introduced by a negative damping coefficient $c_{se} = -0.0005$ Nsm between disk two and the inertial frame, where c_{se} is tuned

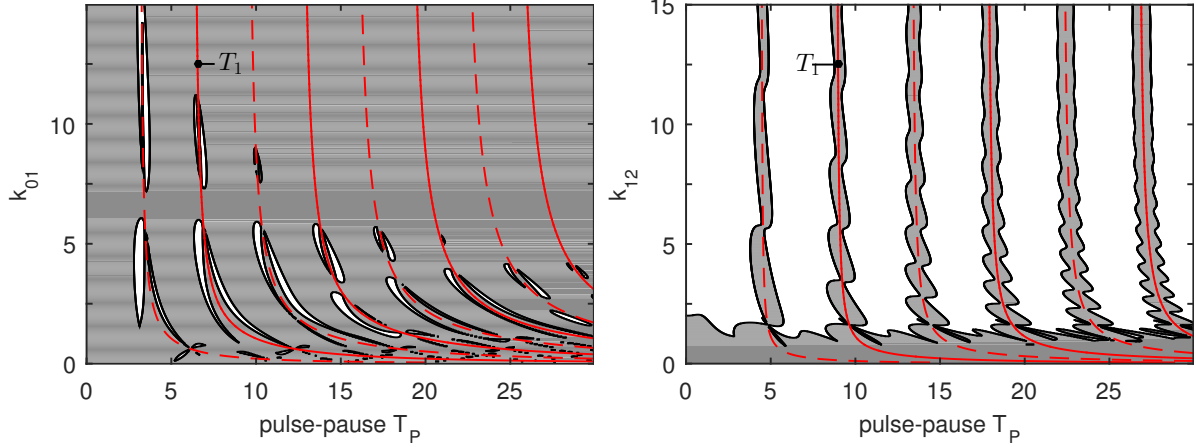


Figure 8: Stability chart for variation of system parameters k_{01} (left) and k_{12} (right), and T_P . Grey/white colored areas denote unstable/asymptotically stable trivial solutions. Energy-neutral case $\vartheta = 1$.

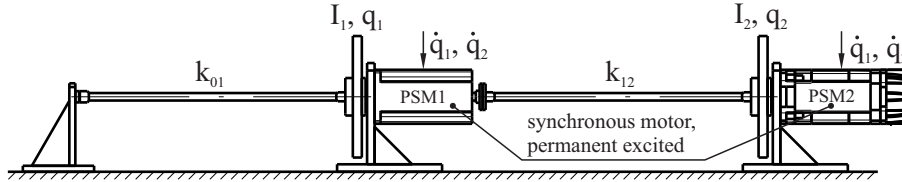


Figure 9: Test rig for investigating modal energy transfer effects in rotor systems.

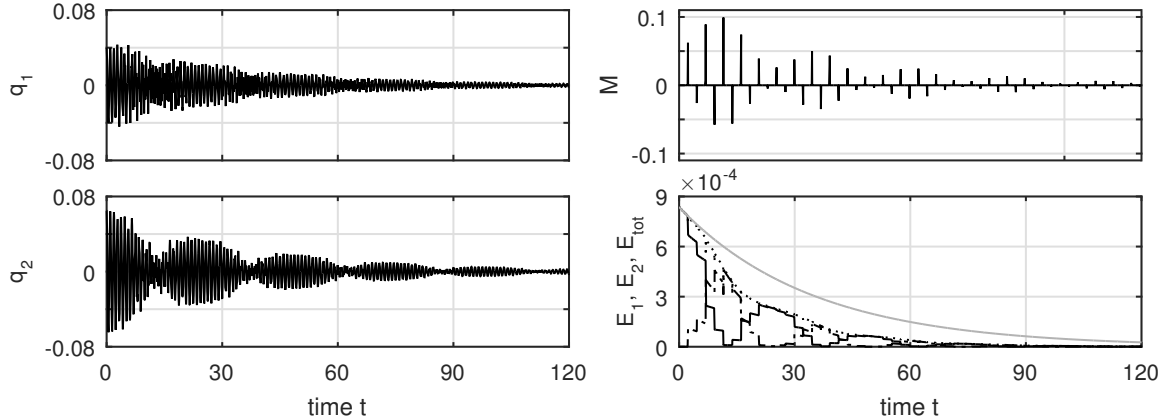


Figure 10: Physical coordinates q_1 and q_2 (left column), torsional moment M , modal energy contents E_1 (solid), E_2 (dashed-dotted) and overall energy content E_{tot} (dotted), (right column). Damped system without self-excitation. E_{tot} of corresponding system without impulsive excitation (grey-colored). Initial condition: IC 1. Sine-shaped impulses applied to disk one. Pulse-pause $T_P = 2.30$ s. Energy-neutral case $\vartheta = 1$.

in a way that the absence of impulsive excitation results in an unstable system. Introducing impulsive excitation to disk one according to the proposed approach causes a repeated modal energy exchange between modes one and two and, hence, allows to stabilize the mechanical system.

4 Conclusion

It was shown in this contribution that impulsively shaped torsional moments are capable of introducing modal energy transfers between low and high modes of vibration in a recurring manner. This allows to utilize the damping properties of the mechanical structure more efficiently and results in a faster decrease of transient vibrations. Moreover, it was shown that the proposed concept is capable of suppressing self-excited vibrations of rotor systems.

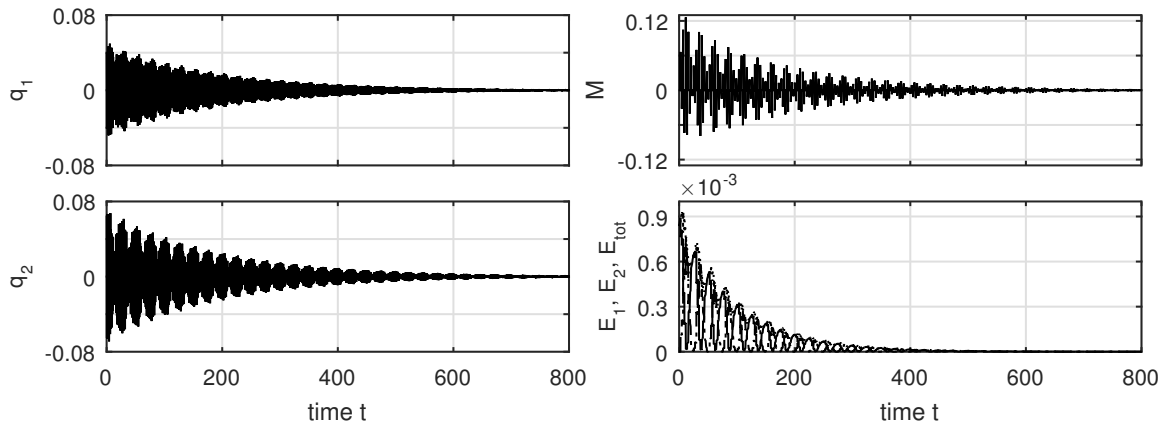


Figure 11: Physical coordinates q_1 and q_2 (left column), torsional moment M , modal energy contents E_1 (solid), E_2 (dashed-dotted) and overall energy content E_{tot} (dotted), (right column). E_{tot} of corresponding system without impulsive excitation (grey-colored). Damped system with self-excitation. Initial condition: IC 1. Sine-shaped impulses applied to disk one. Pulse-pause $T_P = 2.30$ s. Energy-neutral case $\vartheta = 1$.

Acknowledgement

This work has been supported by the Austrian COMET-K2 programme of the Linz Center of Mechatronics (LCM), and has been funded by the Austrian federal government and the federal state of Upper Austria.

References

Al-Shudeifat, M. A.; Vakakis, A. F.; Bergman, L. A.: Shock mitigation by means of low to high-frequency non-linear targeted energy transfers in a large-scale structure. *ASME J. Comput. Nonlinear Dynam.*, 11(2), (2015), 021006–021006–11.

Angeles, J.: *Dynamic Response of Linear Mechanical Systems*. Springer, US (2012).

Dohnal, F.: Damping by parametric stiffness excitation: Resonance and anti-resonance. *J. Vib. Control*, 14(5), (2008), 669 – 688.

Ecker, H.: Suppression of self-excited vibrations in mechanical systems by parametric stiffness excitation. In: *Fortschrittsberichte Simulation*, vol. 11, ARGESIM/ASIM-Verlag, Wien (2005).

Ecker, H.; Pumhössel, T.: Vibration suppression and energy transfer by parametric excitation in drive systems. *Proc. Inst. Mech. Eng., Part C*, 226(8), (2012), 2000 – 2014.

Hsu, C. S.: Impulsive parametric excitation: Theory. *ASME J. Appl. Mech.*, 39(2), (1972), 551 – 558.

Pumhössel, T.: Energy-neutral transfer of vibration energy across modes by using active nonlinear stiffness variation of impulsive type. *ASME J. Comput. Nonlinear Dynam.*, 12(1), (2016a), 011001–011001–11.

Pumhössel, T.: Suppressing self-excited vibrations of mechanical systems by impulsive force excitation. *Journal of Physics: Conference Series*, 744(1), (2016b), 012011–11.

Pumhössel, T.; Hehenberger, P.; Zeman, K.: On the effect of impulsive parametric excitation to the modal energy content of hamiltonian systems. In: *Proc. of the 11th Int. Conf. on Vibration Problems (ICOVP)* (2013), Lisbon, Portugal.

Quinn, D. D.; Hubbard, S.; Wierschem, N.; Al-Shudeifat, M. A.; Ott, R. J.; Luo, J.; Spencer, B. F.; McFarland, D. M.; Vakakis, A. F.; Bergman, L. A.: Equivalent modal damping, stiffening and energy exchanges in multi-degree-of-freedom systems with strongly nonlinear attachments. *Proc. Inst. Mech. Eng., Part K*, 226(2), (2012), 122 – 146.

Tondl, A.: To the problem of quenching self-excited vibrations. *Acta Technica CSAV*, 43, (1998), 109 – 116.

Tondl, A.: Self-excited vibration quenching in a rotor system by means of parametric excitation. *Acta Technica CSAV*, 45, (2000), 199 – 211.

Vakakis, A. F.; Gendelman, O. V.; Bergman, L. A.; McFarland, D. M.; Kerschen, G.; Lee, Y. S.: *Nonlinear Targeted Energy Transfer in Mechanical and Structural Systems*. Springer, Netherlands (2009).

Address:

Dipl.-Ing. Dr. Thomas Pumhössel, Institute of Mechatronic Design and Production, Johannes Kepler University Linz, Altenbergerstrasse 69, 4040-Linz, Austria

email: thomas.pumhoessel@jku.at

Dipl.-Ing. Bernhard Hopfner, Institute of Mechanics and Mechatronics, Vienna University of Technology, Getreidemarkt 9, 1060-Wien, Austria

Ao. Univ.Prof. Dipl.-Ing. Dr. Horst Ecker, Institute of Mechanics and Mechatronics, Vienna University of Technology, Getreidemarkt 9, 1060-Wien, Austria

email: horst.ecker@tuwien.ac.at

Development and analysis of radial force waves in electrical rotating machines

S. Haas, K. Ellermann

Vibrations in electrical machines lead to undesired operating conditions and noise. The reasons lie in the design of the machine and the lack of precision in manufacturing. In order to avoid excessive vibrations, complex numerical analyses are carried out. This work deals with the development and analysis of electromechanical excitations in asynchronous machines with a short circuit rotor. The time-dependent electromagnetic forces acting on the stator bore are simulated with the method of finite elements. Subsequently, the force waves with respect to the frequencies and amplitudes are analyzed.

1 Introduction

Asynchronous machines are used as drive units in many industrial applications and therefore have great practical importance. The increasing electromobility also leads to an increase in production of electrical motors and to changes in the specifications regarding vibration and sound emission. Numerical tools based on a physical model are often used in order to predict the dynamic behavior of a machine during the development. For the calculation of velocities of surface structures in the context of a vibration analysis, detailed information about eigenfrequencies and eigenforms of the structure is necessary. This information is derived from structural stiffness, damping and mass distribution. For the asynchronous machine, the main focus is set on the stator structure. However, there are vibration modes, which are very different, especially in terms of their form, see e.g. Haas et al. (2016). The different excitation forces and moments have different effects on these modes. The excitation of the structure is important for numerical calculations, as eigenmodes become especially important when excited externally.

This article discusses the magnetic force excitation in asynchronous motors with squirrel cage rotor. It focuses on the radial forces acting in the interface between air gap and the laminated stator core stack. An overview about excitation in induction machines as well as their analytical and numerical calculations are given by Seinsch (1992) and Seinsch (1993). A technique for calculating forces in electromagnetic fields is the finite element method. An essential contribution to the formulation of this method for electromagnetic application can be found in the articles Biro and Preis (1989), Biro et al. (1991) and Biro et al. (1992). This method was implemented in commercial software. One application to electric drives is described in the books Aschendorf (2014a) and Aschendorf (2014b).

Details about the analysis of resulting force waves can be found in the articles by Van der Giet et al. (2008) and Weilharter et al. (2012).

2 Forces in asynchronous squirrel-cage induction motors

One of the most important effect of forces in electrical machines is generating a torque. This desired force component is due to a current-carrying conductor in a magnetic airspace field. It is calculated via the Lorentz force

$$\vec{f} = i \cdot \int_l d\vec{s} \times \vec{B} \quad (1)$$

where, in electrical machines, the current i flows in the axial direction and thus the force solely has a tangential component, which results from the magnetic flux density \vec{B} along the length l of the rotor. A tangential vibration component has no influence on sound radiation of the surface of a stator core. Since the air gap torque is constant along the circumference of the stator bore and along the axial length, there is also no excitation through torsional

vibration. In machines with skewed stator or rotor slots, axial forces can occur. However, they have only a small technical significance, since the rotor itself adjusts to his axial mean and the axial load on the bearing is very small.

Forces at the interface are much more important for vibrations in electrical machines. These occur in the transitions of materials with very different permeability values. In the case of electrical machines, this transition area is located in the air gap between stator and rotor. The field lines emerge almost perpendicularly from the iron surface (permeability $\approx \mu_0$). Therefore, these interfacial stresses are mainly directed radially. They are determined from the relations

$$\sigma_n = \frac{B_n^2 - B_t^2}{2\mu_0} \quad , \quad (2)$$

$$\sigma_t = \frac{B_n \cdot B_t}{\mu_0} \quad . \quad (3)$$

The indices n and t represent the normal and tangential component of the surface. In order to calculate these forces for an asynchronous machine, a finite element model is created. As mainly radial force waves are considered, a two-dimensional model of the electrical machine is sufficient.

3 Simulation model

Figure 1 shows schematically the structure of an asynchronous machine in a sectional view. In the stator plate, slots are punched out for the coils. The stator consists of two layers of short-pitched coils, where the end turns are connected to a triangular circuit. The squirrel-cage rotor consists of oval bars distributed symmetrically along the circumference. The ends are connected with a short-circuit ring. The air gap is located at the interface between stator and rotor. At the boundary surfaces between the iron and the air gap, Maxwell forces occur. For a numerical

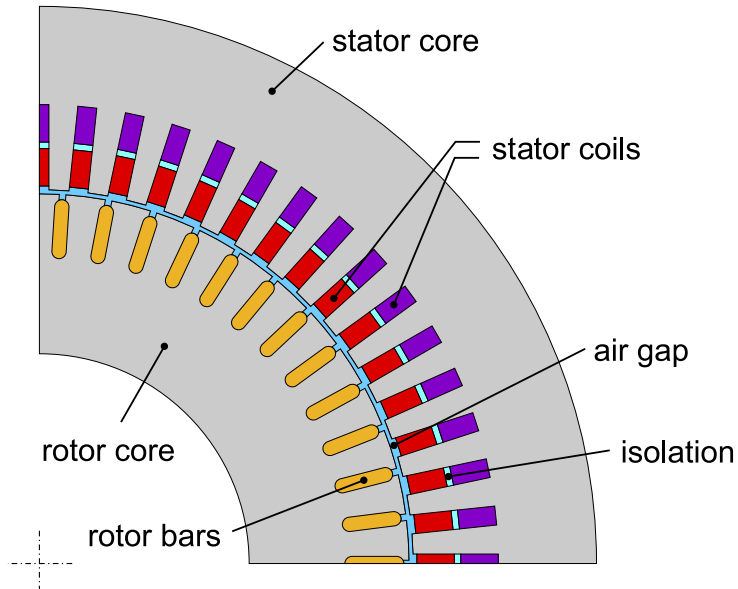


Figure 1: Sectional view of an asynchronous machine.

example, we assumed a parameter set for a machine, which is summarized in Table 1.

The geometry is meshed with a slice finite element for magnetic field calculations (see Figure 2). The element is defined by 8 nodes and has up to 3 degrees of freedom per node. It is based on a vector potential formulation with a magnetic vector potential A_z for each node. It can also be used for electrostatic field calculations with a scalar potential V or coupled to the magnetic field. The third degree of freedom EMF provides the coupling with electronic components, in order to be able and realize oscillating circuits or to interconnect the elements. These components were used for interconnecting the rotor.

The stator current is imposed onto the coils of the upper and lower rod by the specification of current densities. In the case of coils with several strands, a constant distribution of the current over the cross-section is assumed.

Table 1: Machine parameters of an asynchronous machine.

Symbol	Value	Unit	Description
m	3		number of strands
p	2		number of pole pairs
q	5		number of slots per pole and phase
f_n	50	Hz	mains frequency
J	1e6	A/m^2	current density
Q_s	60		number of stator slots
Q_r	50		number of rotor slots
d_{as}	0.85	m	outside diameter of stator
Δ	0.003	m	air gap

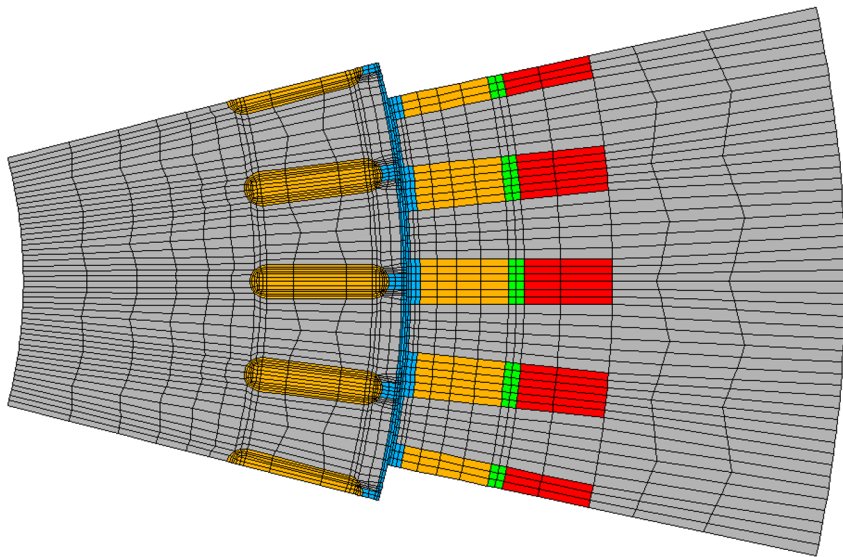


Figure 2: Mesh of the asynchronous machine – Partial segment of rotor and stator.

A suppression of the current can be expected in the massive conductor of the rotor. For verification of the model, static and harmonic analysis are carried out. In both analyses, the influence of the rotating rotor is neglected. In the static analysis, no current is induced in the short-circuit conductors. According to the induction law

$$u_i = \frac{d\Phi}{dt} = \frac{d(\vec{B} \cdot \vec{A})}{dt} = \vec{B} \frac{d\vec{A}}{dt} + \vec{A} \frac{d\vec{B}}{dt} \quad (4)$$

an induced voltage u_i is generated in a coil when a magnetic flux Φ changes in time. In this case, the cause of the flux changes has no influence: It can be either due to a moving coil in a stationary field that is equivalent to a shape change, or due to a time-changing magnetic field $d\vec{B}$. Both are not present in a static analysis. In the case of a harmonic analysis, the magnetic field changes with time due to the supply frequency. Here, the massive conductor in the rotor is assumed not to change its position. This means, that the analysis refers to a steady state, where the rotor is not rotating. The frequency of the current, which flows in the rotor conductors, is the same as the supply frequency f_n . The rotor conductors are short-circuited in rings. Due to the Lorentz force according to Eq. (1), the so-called short-circuit torque acts on the rotor.

4 Transient analysis

In order to detect the influence of the rotating rotor field in an operating point of the machine, a transient analysis is performed. The difficulty is, that the finite elements for magnetic field calculations have no degrees of freedom for displacement and so they do not allow a time dependent rotation of the elements. This problem is solved by turning the elements of the rotating system into position in each time step and taking the conditions of the last time step into account. Therefore, the system matrices are rebuilt for the finite element formulation at every stage. As a result of the rotation of the elements, the mesh between the stator and the rotor does not coincide. At the interface

in the air gap, coupling equations are formulated at the nodes located there. These equations ensure the correct transfer of the node results from the stator side to the rotor side. They must also be calculated for each step in the iteration.

In order to avoid excitations of all system eigenfrequencies, the external loads of the current densities to the stator coils are starting from zero and increase exponentially to their maximum amplitude. The time sequences of the load is shown in Figure 3. The current densities reach their maximum values after a mains period.

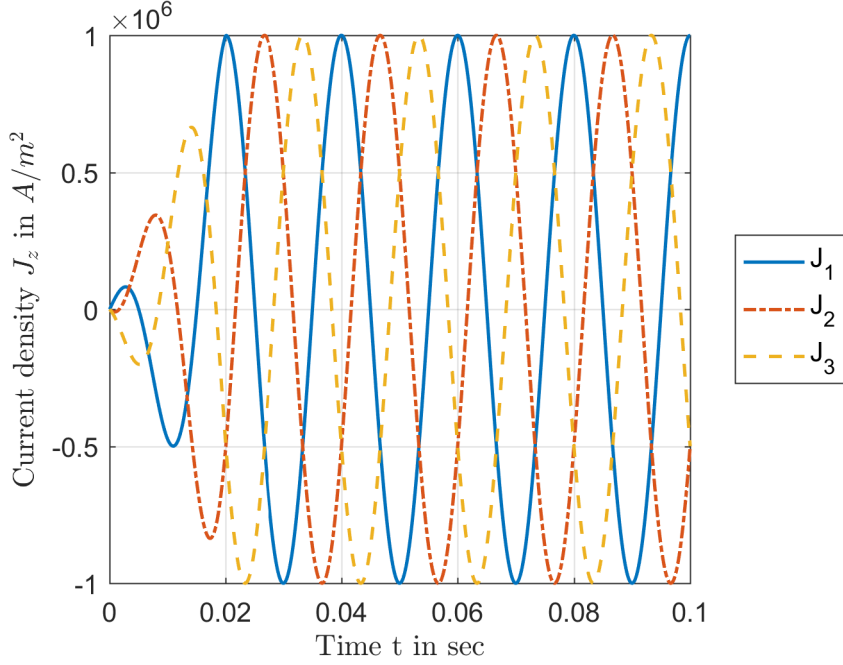


Figure 3: Chronological sequence of the current density.

4.1 Force calculation

The calculation of the force in the finite element method can be carried out in two ways: the first possibility is the calculation by means of a stress tensor

$$\mathbf{T} = \begin{bmatrix} H_x B_x - \frac{1}{2} |\mathbf{H} \mathbf{B}| & H_x B_y & H_x B_z \\ H_y B_x & H_y B_y - \frac{1}{2} |\mathbf{H} \mathbf{B}| & H_y B_z \\ H_z B_x & H_z B_y & H_z B_z - \frac{1}{2} |\mathbf{H} \mathbf{B}| \end{bmatrix} \quad (5)$$

which is also called Maxwell's stress tensor. The force calculation can be applied to any area which is enclosed by a surface Γ and is determined from the equation

$$\vec{f} = \int_{\Omega} \nabla \cdot \mathbf{T} \cdot d\Omega = \oint_{\Gamma} \mathbf{T} \cdot d\Gamma. \quad (6)$$

Another method of calculating the force is developed from the principle of virtual work. The external work of a small element, which is moved in an electromagnetic field, has to equal the internal work. This formulation is based on the law of conservation of energy,

$$\vec{f} \cdot d\vec{s} + dW = 0 \Rightarrow \vec{f} = -\text{grad}(\vec{W}). \quad (7)$$

Both methods are integrated in the FEM software "ANSYS \circledcirc ". The calculation of the force is activated by setting a flag. The relevant areas for electrical machines are the closed curves along the stator iron and the rotor. In the case of the rotor, the focus of interest is mainly in the calculation of the effective torque, while on the stator side the radial force wave is important for the oscillation excitation.

4.2 Results of transient analysis

In the investigation, the rotor speed is set and kept constant. Due to the supply frequency f_n and the number of pole pairs p of the machine, the synchronous speed of the rotor is obtained from

$$n_1 = \frac{f_n \cdot 60}{p} = \frac{50 \cdot 60}{2} = 1500 \text{ rpm.} \quad (8)$$

The slip

$$s = \frac{n_1 - n}{n_1} \quad (9)$$

is used as the deviation from synchronous speed.

The calculations for the transient behavior were carried out without slippage. As a first plausibility test and for a qualitative result of the numerical simulation, the time profile of the rotor currents in Figure 4 is considered. When synchronized, the rotor rotates at the same frequency as the magnetic rotating field. According to the induction law in Equation 4, only a voltage in a conductor is induced, when the conductor moves in a stationary field or the magnetic field changes in time. Both conditions are not met by synchronous speed. Therefore, no voltage is induced in the conductors and for this reason no current can flow into them. The decay of the current is also evident in the simulation results. The fluctuations are attributed to the counter-induction on the conductors. In order to validate this statement, studies on the model itself still have to be carried out. When the rotor is not turning, the same frequency of the winding currents is imposed onto the rotor rods by the stator field. This frequency is also clearly visible in the harmonic analysis.

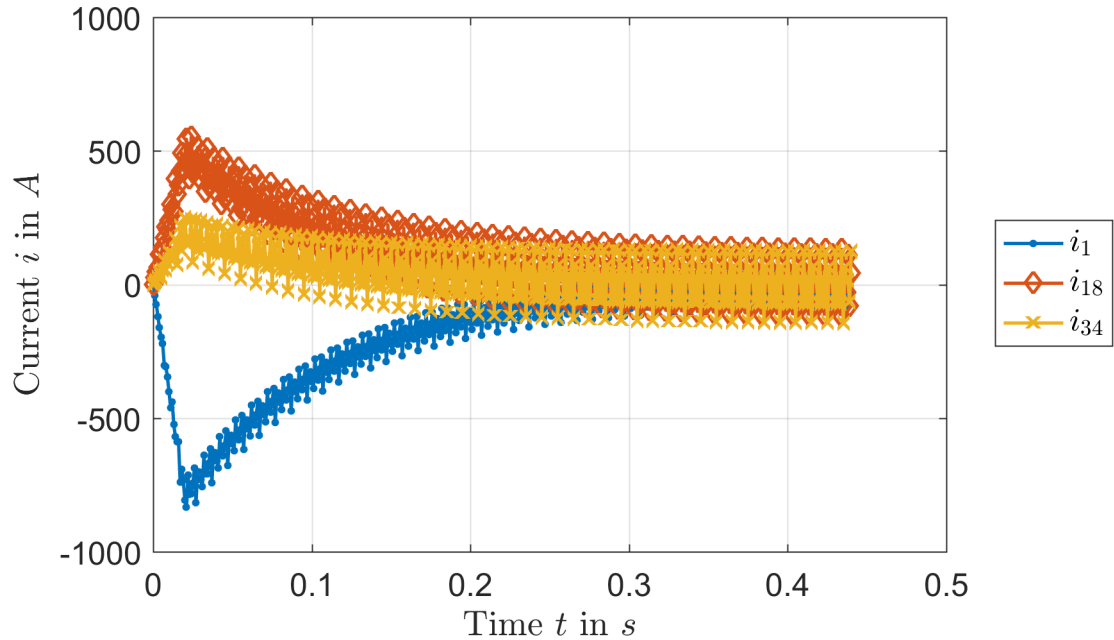


Figure 4: Chronological sequence of the rotor currents.

The consideration of the flux lines in the left part of Figure 5 ensures the functionality of the coupling equations for the interface at the air gap. The lines spread over the entire cross-section of the stator plate and the rotor plate. In addition, the number of poles is clearly shown by the closed curves. The right part of the figure shows the magnitude of the magnetic flux density. It provides information on the validity of the assumption of a linear model. The relationship between the magnetic field strength H and the flux density B is given by the material constant of the permeability μ

$$\vec{B} = \mu \cdot \vec{H}. \quad (10)$$

For dynamo sheets, the iron is saturated from a certain value of the flux density and the initial linear slope in the BH characteristic falls off. This area cannot be expected to be linear. The increased peak values in the sharp corners of the windings are due to constriction effects conditions.

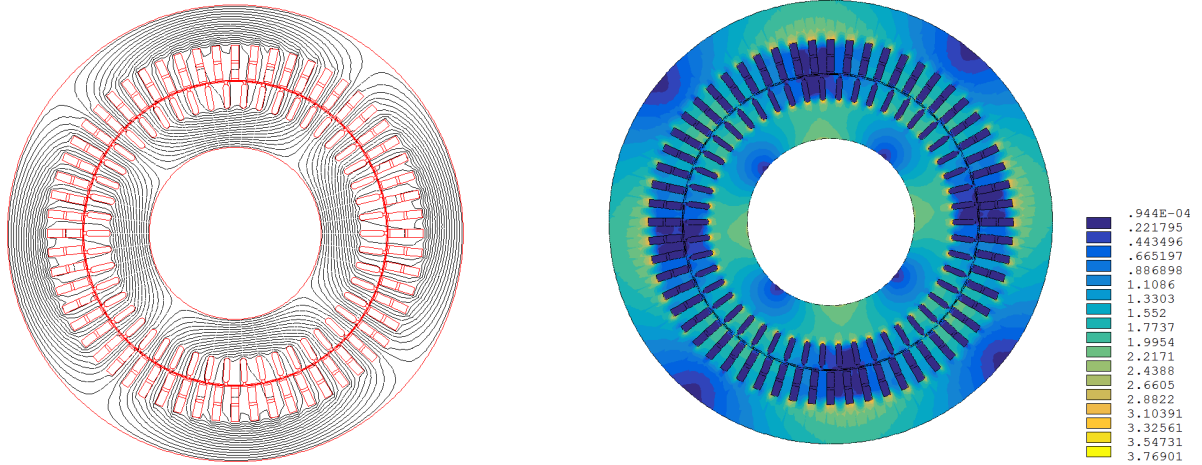


Figure 5: Results of a transient field calculation at stationary speed. Left: flux lines, right: magnetic flux density.

5 Analysis of force waves

The calculated forces are spatially distributed on the stator inner contour. Figure 6 shows the radial forces as vector plots and as quantities developed over the circumference. The force is directed radially inwards. The effect of the forces on the stator therefore corresponds to that of a tensile component. The discontinuity of the course of forces is due to the slots of the stator plate, since forces can only occur at the sudden transitions of strongly changing material properties. This condition is strongly present in electrical machines, especially at the boundary layers between air and iron. The force profile also rotates with the rotating field of the machine.

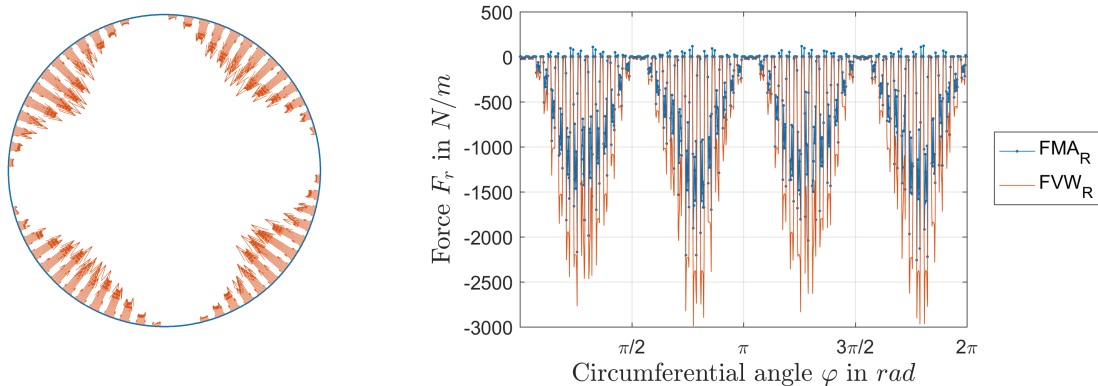


Figure 6: Radial force wave on the stator lamination stack.

A common method for analyzing the force waves is based on the conversion of the signal from time domain to a representation in the frequency domain, performed by a Fast Fourier Transformation. In this way, the temporally harmonic components of the signal are visualized in the form of amplitudes and frequencies (see Figure 7, left picture). This method is applied once more along the circumferential direction to the obtained Fourier spectrum. The result is a spatially harmonic ordinal number. It indicates the order of the occurring force wave for a certain frequency. The force wave is determined from equation

$$F_\nu = \bar{F}_\nu \cos(\nu \cdot \varphi - \omega_\nu t - \psi_n) \quad (11)$$

and is composed of the magnitude of the force \bar{F}_ν , the ordinal number ν , the spatial angle φ , the phase angle ψ_ν and the local angular frequency ω_ν .

From the graphs in Figure 7, it is to be recognized that the dominant forces occur at a frequency of $f = 100\text{Hz}$. This corresponds to the double of the mains frequency f_n . The spectrum also clearly shows an equal proportion. This acts constantly as a pulling force. The harmonic components oscillate around this force component. The force wave at this frequency has a dominant spatial order number of $\nu = -4$. This reflects the number of poles of the machine. The negative sign of the order means that the force wave rotates in the opposite direction to the magnetic rotating field. The other dominant orders occur at a distance of $\Delta\nu = 60$. This number coincides with the number of slots of the stator Q_s . The fundamental wave occurs with approximately twice the amplitude $\bar{F}_{-4} \approx 2 \cdot \bar{F}_{-64,56}$ opposite to the other two force waves.

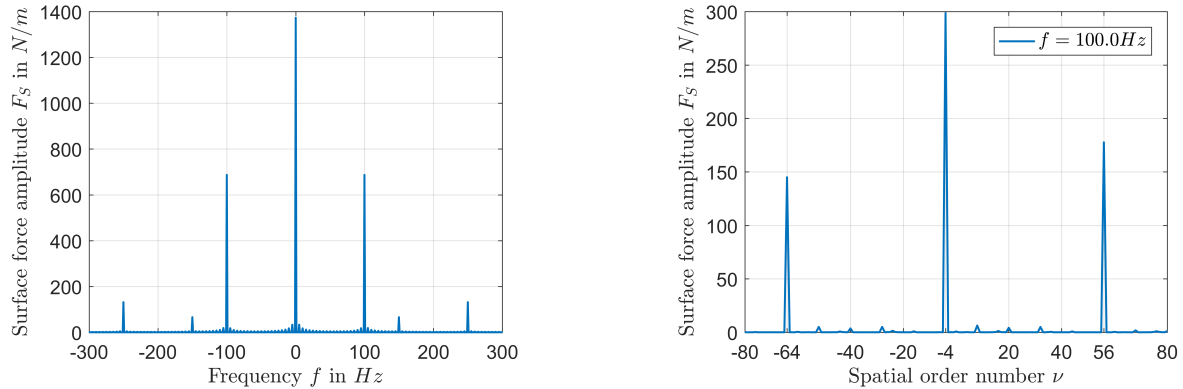


Figure 7: Frequency range and order number of the force wave. Left: the spectrum, right: the spatial order number.

6 Summary

By using the finite element method on an asynchronous machine, its electromagnetic rotating field was calculated at synchronous speed. Subsequently, the results were validated and a force calculation was carried out in the area of interest. These forces were analyzed with regard to their temporal as well as spatial development.

References

Aschendorf, B.: *FEM bei elektrischen Antrieben 1: Grundlagen, Vorgehensweise, Transformatoren und Gleichstrommaschinen*. Springer Vieweg, Wiesbaden (2014a).

Aschendorf, B.: *FEM bei elektrischen Antrieben 2: Anwendungen: Gleichstrommaschinen, Asynchronmaschinen, Synchronmaschinen, Linearmotoren*. Springer Vieweg, Wiesbaden (2014b).

Biro, O.; Preis, K.: On the use of the magnetic vector potential in the finite element analysis of three-dimensional eddy currents. *IEEE Transactions on Magnetics*, 25, (1989), 3145 – 3159.

Biro, O.; Preis, K.; Magele, C.: Numerical analysis of 3d magnetostatic fields. *IEEE Transactions on Magnetics*, 27, (1991), 3798 – 3803.

Biro, O.; Preis, K.; Magele, C.: Different finite element formulations of 3-d magnetostatic fields. *IEEE Transactions on Magnetics*, 28, (1992), 1056 – 1059.

Haas, S.; Mair, M.; Ellermann, K.; Lang, H.; Weilharter, B.: Material parameter estimation of a laminated stator core stack and vibrational behaviour. In: *VIRM 11 - Vibrations in rotating machinery*, pages 199 – 207, University of Manchester (September 2016).

Seinsch, O.: *Oberfelderscheinungen in Drehfeldmaschinen*. B.G. Teubner, Stuttgart (1992).

Seinsch, O.: *Grundlagen elektrischer Maschinen und Antriebe*. B.G. Teubner, Stuttgart (1993).

Van der Giet, M.; Rothe, R.; Hameyer, K.: Asymptotic fourier decomposition of tooth forces in terms of convolved air gap field harmonics for noise diagnosis of electrical machines. *Compel*, 28, (2008), 804 – 818.

Weilharter, B.; Biro, O.; Rainer, S.: Numerical investigation of the 3d vibrational behaviour of skewed induction machines due to rotating force waves. *Compel.*, 31, (2012), 1503 – 1512.

Address: Graz University of Technology, Institute for Mechanics, Kopernikusgasse 24/IV, Graz, A-8010 Austria
email: stefan.haas@tugraz.at

Experimental Analysis of the nonlinear Vibrations of a rigid Rotor in Gas Foil Bearings

Robert Hoffmann, Cédric Kayo, Robert Liebich

Air bearings and gas foil bearings (GFBs) in particular are characterized by a low-loss operation at high rotational speeds and temperatures, because of their adequate and relatively low lubrication viscosity. Further advantages are the simple design of the bearing and the omission of an oil system. A disadvantage is the low fluid viscosity, which limits the load capacity and damping capacity of the bearing. Even though the bearing wall, which is elastic and sensitive to friction, compensates the mentioned disadvantages by self-regulating the lubrication film and providing external damping. GFBs always show a tendency for nonlinear subharmonic vibrations. In this paper, the nonlinear vibration behavior of a rigid rotor in gas foil bearings is investigated. The rotor is accelerated to approx. 60 000 rpm by means of an impulse turbine. Waterfall charts for a variation of static and dynamic unbalance are recorded using transient coast-downs. The experiments show a variety of nonlinear effects. Their causes are analyzed experimentally. In addition to self-excitation by the fluid film, the rotor is sensitive to high unbalances and the resulting forced vibrations. The nonlinear, progressive system behavior results in excitation orders of $1/2\Omega$, $1/3\Omega$, and $1/4\Omega$ that modulate additional frequencies.

1 Introduction

Gas foil bearings (GFBs) are based on a fluid dynamic lubrication principle and possess a variety of benefits. Due to the use of ambient air, a conventional oil system is not necessary. At the same time, losses in the lubrication film are relatively low and high temperature applications are possible, which can be explained by the relatively low viscosity and the thermal behavior of gases. Nonetheless, a low viscosity results in low load capacity and poor damping properties. Apart from the external damping caused by friction in the foils, the elastic structure forms a self-regulating lubrication film, cf. Heshmat (1994). The latter particularly increases the load capacity when compared to rigid gas bearings, cf. DellaCorte and Valco (2000). However, systems with GFB-supported systems often manifest nonlinear subharmonic vibrations, cf. Heshmat (1994, 2000); Kim et al. (2010); Kim (2007); Sim et al. (2012); Larsen (2015). If the damping of the system is sufficiently large there are stable limit cycles, Kim (2007); Heshmat (1994). Moreover, the unbalance of the system significantly influences the nonlinear vibration behavior, Heshmat et al. (1982); San Andrés et al. (2007); Kim (2007); San Andrés and Kim (2008); Balducci (2013); Larsen (2015). Despite the large number of experimental rotordynamic investigations, no detailed classification of the vibration is available. In 2007, San Andrés and Kim (2008) labeled the nonlinear behavior as *Forced Nonlinearity*, which is influenced by the unbalance, whereby self-excitation has been completely excluded. Instead, Hoffmann et al. (2014) proved numerically the possibility of self-excitation in a nonlinear stability analysis. Consequently, in well balanced systems the subharmonic vibration starts at the rotational speed *noSSV* (*Onset Speed of Subharmonic Vibration*) and vibrates synchronously with the eigenfrequency of the system. The onset of subharmonic vibration is characterized by a Hopf-bifurcation resulting from a fluid film induced self-excitation. A possible classification of the nonlinear vibrations of a rotor in a GFB is displayed in Figure 1. The system behavior can take one of two paths: forced vibration and self-excited vibration.

1.1 Path 1: Forced Vibration

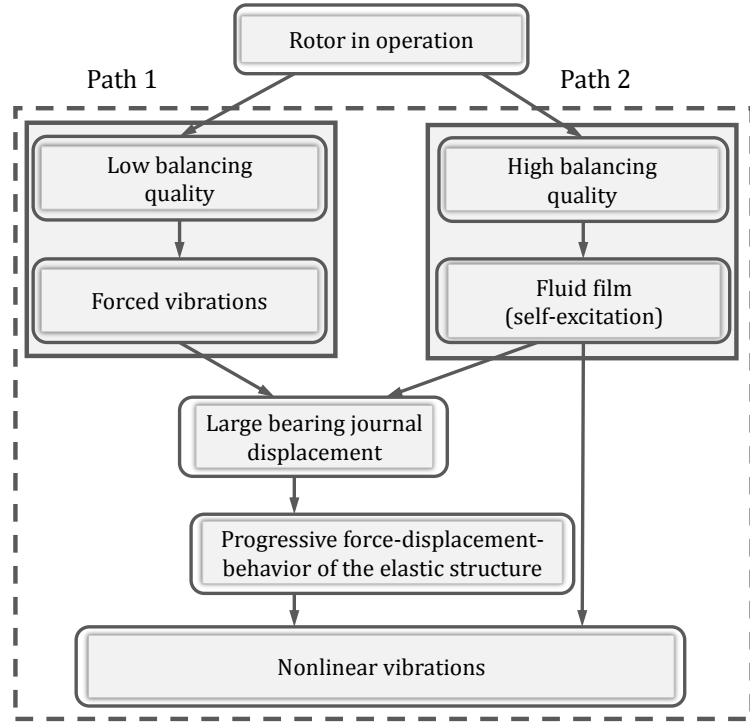


Figure 1: Classification of the vibration characteristic of a GFB mounted system

The generation of nonlinear vibration in path 1 is due to forced vibrations caused by poor balancing quality. Due to the progressive force-displacement-behavior of a gas foil bearing, the system behaves similarly to a Duffing-oscillator, cf. Yamamoto and Ishida (2001); Kovacic and Brennan (2011); Dresig et al. (2011); Magnus et al. (2013). The Duffing equation (Equation 1) is a differential equation for a damped elastic structure subjected to a large deformation, where m is the mass of the system, Ω the rotor speed, δ the damping coefficient and $r(x)$ the nonlinear elastic restoring forces.

$$\ddot{x} + 2\delta\dot{x} + r(x) = F \cos(\Omega t) \quad (1)$$

The nonlinear forces are induced by the elastic structure of the GFB and the gas film. The large displacement of the shaft in the bearing makes nonlinear elastic effects significant (Figure 2). Figure 3 shows the response amplitude of the Duffing equation by applying the harmonic balance method and assuming a solution of the form (Equation 2).

$$x_1(t) = C \sin(\Omega t + \varphi) \quad (2)$$

One particularity of the duffing oscillator is the jump phenomenon in the resonance peak of the frequency response function, which occurs when the system is excited by a harmonic force (Figure 3). When the frequency of excitation increases, there appears suddenly a jump down from point (A) to (B). If the frequency decreases, the amplitude jumps up from point (C) to (D). This phenomenon can be observed during the experiment (chapter 3). Jump phenomena, subharmonic resonances of the $1/2\Omega$, $1/3\Omega$ and $1/4\Omega$ etc. order and frequency modulations are characteristics of such an oscillator, cf Yamamoto and Ishida (2001); Kovacic and Brennan (2011).

1.2 Path 2: Self-excited Vibration

Nevertheless, a very well balanced rotor can also exhibit nonlinear vibrations during operation. The cause is fluid-induced, self-excited vibrations by the air lubrication (Whirl-vibration). At the OSSV-point, subharmonic fractions rise and vibrate synchronously with a system eigenfrequency. Due to the large displacements of the shaft, the progressive behavior of the bearing comes into effect, so that ultimately a mixture of path 1 and 2 occurs. The purpose of this work is the experimental rotordynamic analysis of a rotor supported by GFBs focusing on its nonlinear vibration and the classification of the same according to the scheme from Figure 1.

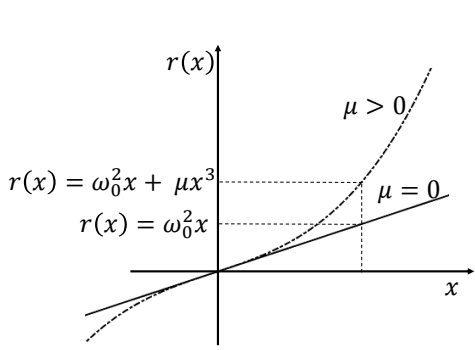


Figure 2: Nonlinear stiffness

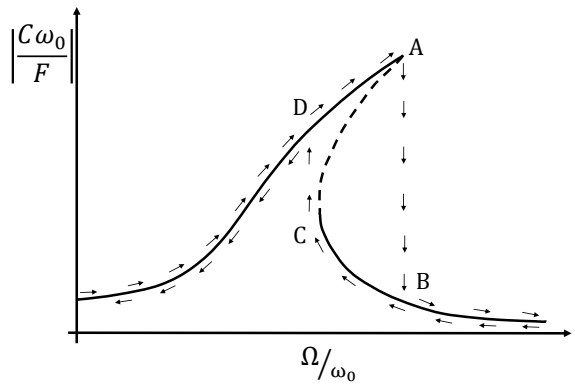


Figure 3: Frequency response of the resonant Duffing equation

2 Experimental Setup

Figure 4 (a)-(d) presents the experimental setup for the rotordynamic analysis in a section view (a) and in two further views (c) and (d). The cylindrical casing consists of precision turned components, so that a coaxial bearing seat is provided for the front (F) and rear (R), see Figure 4 (a). Two identically constructed radial GFBs of the 1st generation are investigated whose technical data are listed in Table 1. The mounting position of the bearing allows the rigid clamping of the foils (WP) to be at the 12 o'clock position and the bearing shaft to rotate from the free foil ending to the rigid clamp. The chassis is tightly connected to a vibration-isolated machine bed by means of a bracket. A numerical FE based modal analysis of the chassis structure shows no eigenfrequencies below 110 000 rpm, therefore no influence from the chassis at the operation range ($n_{\max} \approx 60 000$ rpm) is to be expected. The rigid rotor is driven by an impulse turbine (3) supplied with pressurized air, see Figure 4 (a) and (b), whose technical data can be found in Table 2. The rotor including the turbine is built symmetrically around the center of gravity (SP). Thus, similar radial loads are generated and axial thrust from the turbine is minimized in operation. If, however, axial forces occur during operation, these are absorbed via two axial start-up linings (4), see Figure 4 (a), (c) and (d). For this purpose, pressure pieces with a spring-loaded ceramic ball are used to keep the friction as well as the damping of vibrations low. At the same time, this allows for a small heat input into the shaft. The turbine is supplied via the pressure line (5), see Figure 4 (c) and (d). The control of the test rig, i.e. the turbine, is achieved with a proportional pressure control valve, which is steplessly electronically controlled by means of a PC. Furthermore, M2 x 6 x 60° thread holes are provided at the front sides of the bearing shaft for the attachment of unbalance weights.

3 Experimental Analysis

3.1 Measurement Instrumentation

Referring to Figure 4 (a) and (b), for the rotordynamic analysis the vibration behavior at the front (F) and rear (R) bearing positions is measured in vertical and horizontal directions by means of two fiber-optic displacement sensors. The rotational speed is detected simultaneously by an infrared sensor (7). A black and white marking is therefore placed next to the turbine, see Figure 4 (b). Furthermore, the temperature at the bearing seat is measured by means of thermocouples of the type T, see Figure 4 (a).

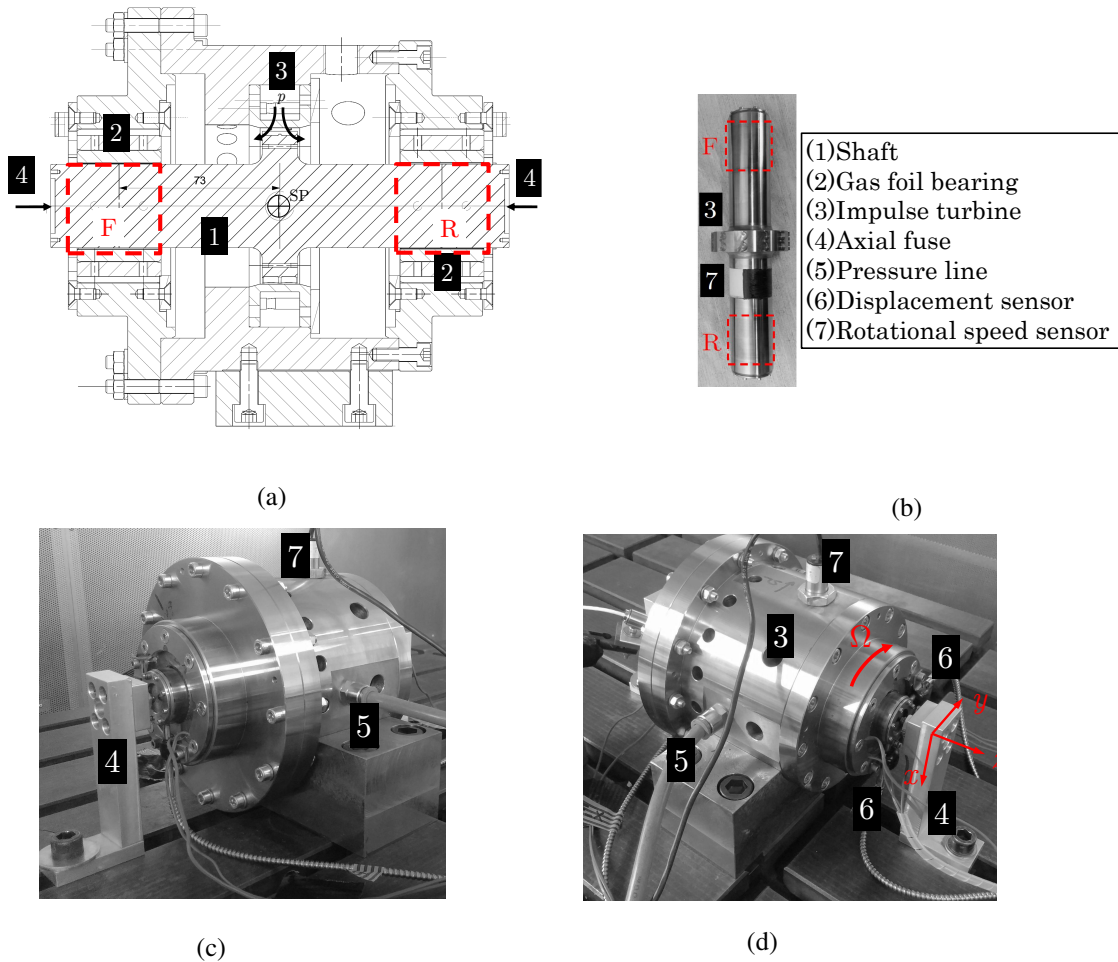


Figure 4: Experimental setup: cross-sectional (a) view, (b) shaft, (c) view 1 and (d) view 2.

Table 1: Geometrical data of a GFB of the 1st generation (Manufacturer MSI.Inc).

Parameter	Value
Bearing radius R	19.050 mm
Bearing length l	38.100 mm
Bump-height h_b	0.50 mm
Bump-thickness t_b	0.1 mm
Bump-range s_b	4.572 mm
Number of bumps N_b	26
Half the length of a bump l_b	1.778 mm
Foil cover thickness t_f	0.1 mm
Elastic modulus E	$2.07 \times 10^{11} \text{ N/m}^2$
Poisson's ratio ν	0.3
Foil material	Inconel X-750

The sensors and the measurement instruments are listed in Table 3.

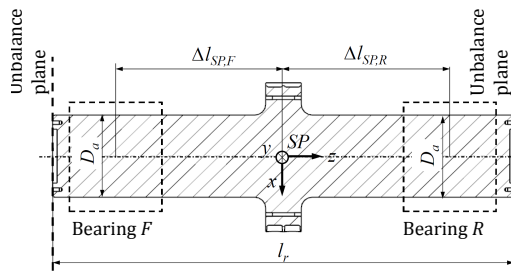
3.2 Test Procedure and Signal Processing

Two different experiments are carried out: first, the influence of the self-excitation is analyzed, see Figure 1, path 2. Hereto, the rotor is in the initial unbalanced state, i.e. no additional masses are attached to the balancing planes. According to DIN ISO 21940, a balance quality grade of G 0,4 is available. Second, the influence of the forced vibrations is investigated by different unbalance mass settings by means of static and couple unbalances. The

unbalance masses are listed in Table 4. This study is based on path 1 from Figure 1. Both studies are to demonstrate the classification shown in Figure 1. The tests are based on transient runs. For this purpose, the rotor is accelerated to its maximum rotational speed ($n_{max} \approx 60\,000$ rpm). This state is held until stationary operation is established. Thereafter the pressurization of the turbine is switched off, the rotor decelerates and the measurement takes place. Excitations due to the flow through the turbine are thereby minimized. This procedure is performed more than 10 times to verify the reproducibility of the results. The reproducibility of experimental results is very good, so that an averaging of the results is not performed. The results of the transient rotordynamic analyses are shown in waterfall charts. Hereby, the magnitude of the pointer $|r| = \sqrt{u^2 + v^2}$ of the displacement in x - and y -direction is plotted over the frequency component f and rotational speed n .

¹ Application field: tool spindle machines and propulsion of precision machines.

Table 2: Design data of the solid shaft



Parameter	Solid shaft
Material	42CrMo4 (1.7225)
Mass m_r	2.148 kg
Inertia J_z	568.425 mm ² kg
Inertia J_x, J_y	6775.878 mm ² kg
Rotor length l_r	212 mm
Bearing distance $\Delta l_{SP,F/R}$	72.5 mm
Shaft diameter (nominal) D_a	38 mm
Nominal gap bearing F $c_{0,F}$	55 $\mu\text{m} \pm 6 \mu\text{m}$
Nominal gap bearing R $c_{0,R}$	50 $\mu\text{m} \pm 6 \mu\text{m}$

Table 3: Measurement instrumentation of the rotordynamic experiment.

Sensor	Manufacturer	Type	Sensitivity/specification	Quantity
Rotational speed	Monarch	IRS- Infrared Sensor	1-999 999 min ⁻¹	1
Displacement	Philtec INC	RC 62	2.8 mV/ μm	4
Temperature	Omega	5TC-TT-KI-24-2M	Type T, max. 300 °C	10
PC-measurement electronics	NI	9215	AD-converter 16 Bit, ± 10 V	3
PC-measurement electronics	NI	9213	16 channel thermocouple module 16 Bit	1
PC-measurement electronics	NI	cDAQ 9127	Measurement Chassis	1
PC-measurement electronics	NI	9162	Measurement Chassis	1

Table 4: Unbalance values of the rotor.

Rotor	Type of unbalance	Unbalance U_F	Unbalance U_R
Solid shaft static		0 gmm	0 gmm
		6 gmm	6 gmm
		12 gmm	12 gmm
Solid shaft couple		0 gmm	0 gmm
		9 gmm	9 gmm
		12 gmm	12 gmm

For this purpose, the time signals of the displacement sensors are sampled with 40 kHz and converted into the frequency domain by means of a Fast Fourier Transform (FFT). A digital Butterworth low-pass filter (cutoff frequency: 20 kHz) and a Hanning window are also used for frequency analysis. Possible amplitude damping, caused by signal processing, in particular resulting from the choice of the window, have been neglected, since the absolute values of the vibration amplitude are less of interest than their frequency characteristics. Due to the low temporal variance of the temperature, the sampling frequency of the thermocouples has been set to 100 Hz. The temperature of the bearing relative to the environment T_a is not expected to vary much during the study, since the bearing load is relatively low.

3.3 Experimental Results

3.3.1 Assessment of the Self-excitation

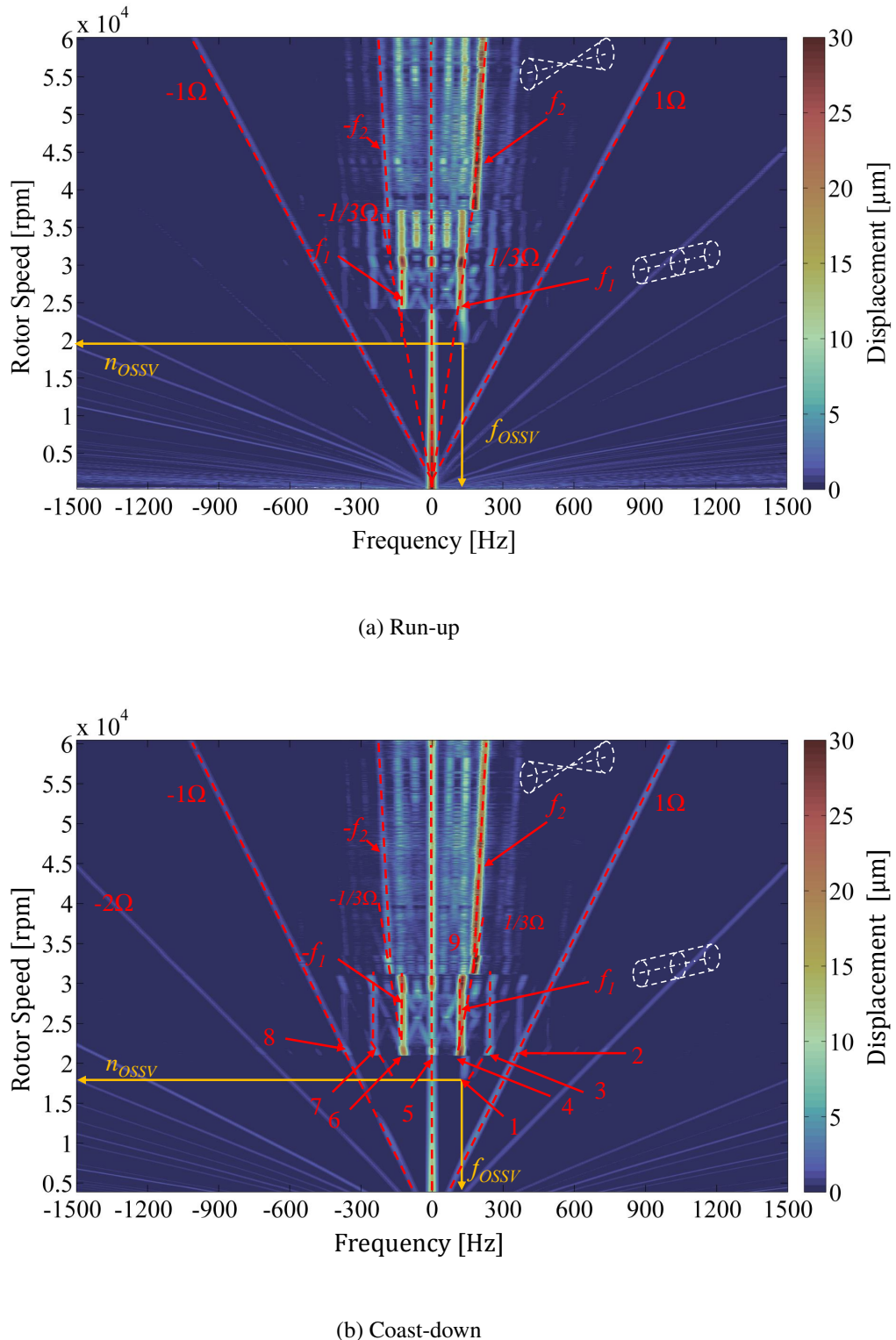


Figure 5: Waterfall charts of the solid shaft, measurement position: front bearing, (a) Run-up and (b) Coast-down

In Figure 5 the waterfall charts display the shaft displacement in forward and backward directions at the front

bearing (F) during (a) run-up and (b) coast-down. No additional unbalance is attached to the rotor. As a result, the nonlinear vibration behavior can be evaluated by means of a possible self-excitation by the gas film, see Figure 1 path 2. Figure 5 basically underlines that subharmonic vibrations start at the onset speed n_{OSSV} with the frequency f_{OSSV} . The results of the OSSV-point are summarized for the different measurements in Table 5. They reflect very well the behavior of the Duffing oscillator. During coast-down the OSSV is lower than during run-up. That reflects the Jump frequencies (C)-(D) respectively (A)-(B) in Figure 3. With the delayed onset of the subharmonic vibrations at higher rotational speeds of the run-up, a system with a positive feedback can be identified.

Table 5: OSSV at run-up and coast-down.

	Measurement cycle	f_{OSSV}	n_{OSSV}	Displacement amplitude r
Solid shaft	Coast-down	136.72 Hz	17 754 rpm	2.698 μm
	Run-up	136.7 Hz	19 992 rpm	4.804 μm

3.3.2 Assessment of the nonlinear Vibrations

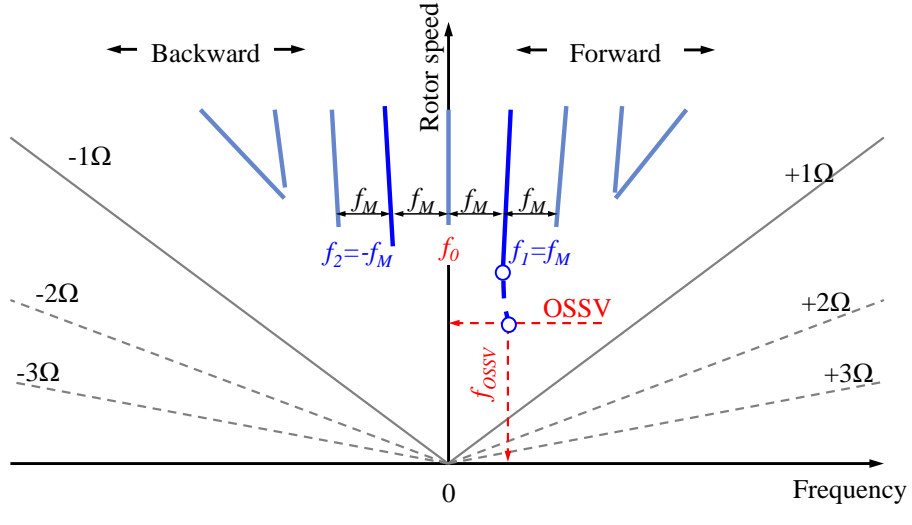
The waterfall chart in Figure 5 displays a variety of nonlinear vibrations as soon as the onset speed n_{OSSV} has been surpassed. In accordance with Figure 1, this is explained by the increased bearing shaft displacement due to the self-excitation. Thus, subharmonic vibrations are excited because of the existence of a positive feedback resulting from the progressive force-displacement-behavior. In Figure 5 (a), the frequency orders in forward and backward direction for $\pm 1/3\Omega$ (indicated by dashed lines) induce the subharmonic resonance of the $1/3\Omega$ order at the points (4) and (9). Behind the OSSV-point, the system oscillates in a self-excited manner synchronously with the first eigenfrequency f_1 . This slightly detunes the system so that a slight jump close to point (4) towards lower frequencies occurs. The system is strongly dominated by the first eigenfrequency f_1 (1st mode, cylindrical shape). At higher speeds, a further subharmonic resonance of the $1/3\Omega$ -order occurs at point (9), which leads to a jump of the eigenfrequency f_2 (2nd mode, cone shape). Furthermore, after the self-excitation and the nonlinear system behavior, a variety of combination frequencies, also known as frequency modulation, appears. For this purpose, Figure 6 (a) serves as an exemplary waterfall chart. In the case considered, self-excitation starts at the OSSV-point with the rotational speed n_{OSSV} and the frequency f_{OSSV} . Furthermore, the cylindrical mode f_1 is strongly excited up from the point (4) by these nonlinear vibrations. If the frequency f_1 up from point (4) is split between forward and backward motions and the half difference between backward and forward component is considered as the module frequency of action $f_M = f_1$ (Equation 5). The value of half of the sum of the forward and backward component is considered as the carrier frequency f_c (Equation 5), the so-called side bands vibrate next to the main vibration components f_1 due to the nonlinear feedback of the system. If a random frequency f is assumed, it may have higher and lower frequency side bands (index USB: upper side bands, index LSB: lower side bands). Kinetic energy will then be transferred from the basic vibration to the side bands. These side bands can, in combination with other frequencies, generate new frequencies according to the same scheme, see Figure 6 (a) and (b). The cascade-like modulation according to Figure 6 (b) can be calculated using Equation 3 and 4 for the side bands cf. Nguyen-Schäfer (2012).

$$f_{LSB} = \begin{cases} f_1 - 2f_M = f_c - f_M = f_2 \\ f_1 - 4f_M = f_c - 3f_M = 2f_2 - f_1 \\ f_1 - 6f_M = f_c - 5f_M = 3f_2 - 2f_1 \\ \dots \end{cases} \quad (3)$$

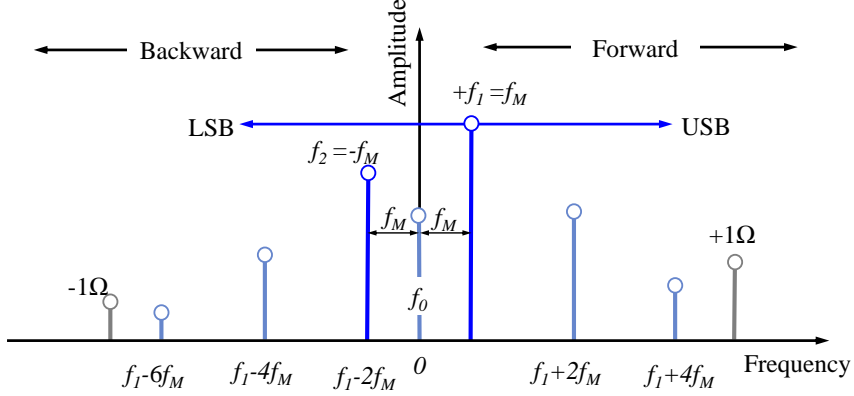
$$f_{USB} = \begin{cases} f_1 + 0f_M = f_c + f_M = f_1 \\ f_1 + 2f_M = f_c + 3f_M = 2f_1 - f_2 \\ f_1 + 4f_M = f_c + 5f_M = 3f_1 - 2f_2 \\ f_1 + 6f_M = f_c + 7f_M = 4f_1 - 3f_2 \\ \dots \end{cases} \quad (4)$$

$$f_M = \frac{1}{2}(f_1 - f_2) \quad f_c = \frac{1}{2}(f_1 + f_2) \quad (5)$$

Referring to the waterfall diagram of Figure 5 (b), combined frequency points (2-8) result. These points are summarized in Table 6. By applying Eq. (3) and (4) with the modulation frequency $f_M = 117.19 \text{ Hz}$ of the point



(a) Waterfall chart



(b) Spectrum

Figure 6: Diagram of a frequency modulation: (a) in waterfall chart and (b) frequency spectrum with cascade-like frequency modulation.

(6) of Figure 5 (b), identical frequencies are calculated. This comparison further underlines the nonlinear system behavior, which is initiated by the onset of self-excitation at the OSSV point.

Table 6: Side band modulation of the waterfall chart of Figure 5 (b), solid shaft, coast-down with $f_M = 117.19$ Hz.

Position	8	7	6	5	4	3	2
f_i	-351.56 Hz	-234.34 Hz	-117.19 Hz	0 Hz	117.18 Hz	234.375 Hz	351.56 Hz

3.3.3 Impact of Unbalance on the nonlinear Vibration Behavior

Path 1 is analyzed according to Figure 1 in order to prove the above hypothesis experimentally. The reason of nonlinear vibrations lies within forced vibrations due to a generally poorer balancing quality, so that nonlinear vibrations are generated even below the OSSV point. The unbalance values used are based on the data in Table 4. The results are plotted in the waterfall diagrams in Figures 7 and 8 for the cases of a static and couple unbalance. In principle, it can be stated: the higher the unbalance is, the more distinct a nonlinear rotor behavior due to the progressive force-displacement behavior of the bearing becomes. With exception of the 6 gmm measurement with static unbalance, see Figure 8 (a), subharmonic vibrations of the $1/2\Omega$ -order occur as a result of the forced

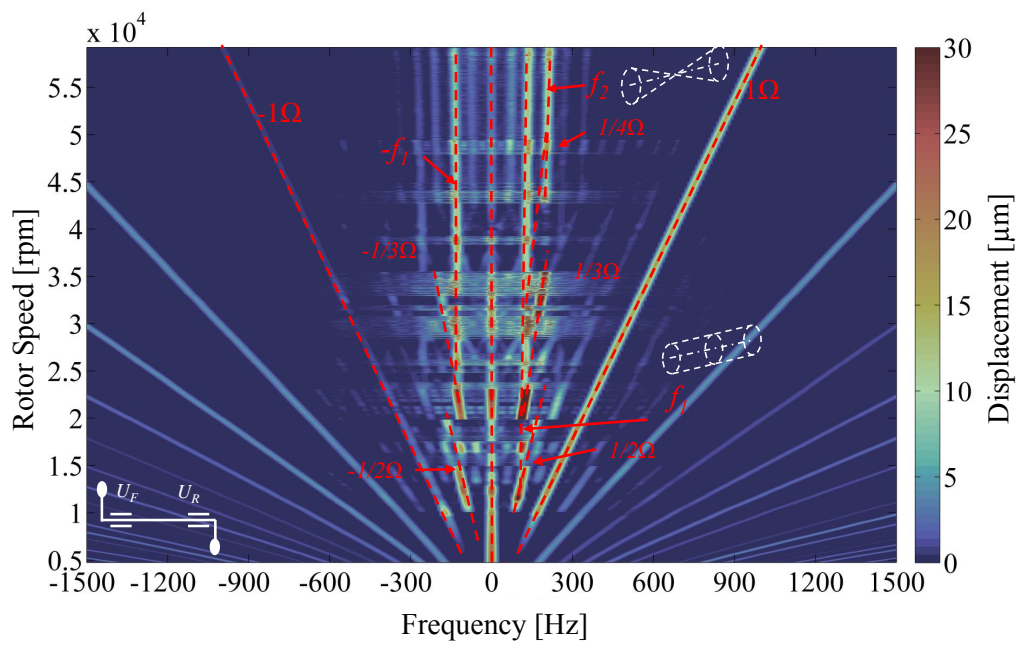
unbalance excitation already below the abovementioned OSSV point. The original unbalance state of the rotor has undergone little change by introducing this test mass, which is why the OSSV at 6 gmm is still present as a result of self-excitation. Subsequently, $\pm 1/3\Omega$ and $\pm 1/4\Omega$ orders are excited, which again implies the presence of a nonlinear system behavior due to the positive feedback and thus supports the hypothesis of the first path. Furthermore, the waterfall diagrams show that the second mode (cone shape) is strongly excited by the nonlinear oscillations $\pm 1/3\Omega$ or $\pm 1/4\Omega$ by means of the subharmonic resonances. The second mode oscillates with the frequency f_2 .

In addition to the side bands, continuous spectral components are clearly visible in the case of the couple unbalance with $U_i = 12$ gmm ($i=F,R$). These can be chaotic, stochastic or non-steady-state vibrations, cf. Magnus et al. (2013). Above all, the latter effect is to be assumed, since the coast-down runs were very short in the experiments. This resulted in a heavily unsteady state regime. A detailed investigation of this effect was not carried out within the framework of the work, since these are not of great importance for the purpose of the work. Moreover, it can be observed, that the mass of the couple unbalance causes a stronger nonlinear behavior with higher vibration amplitudes compared to the static unbalance, see Figures 7 and 8. As a result of the couple unbalance and its kinematic effect on the rotor, the displacements close to the front (F) and rear (R) bearings are larger in comparison to those obtained in the static unbalance case. This is due to the conical mode, which is dominated by a forced vibration particularly in the operational range and it is sensitive to the present unbalance mass, according to the analysis in the Campbell diagram, see Figure 9. Unfortunately, the results for the higher couple unbalance case do not show the high conical mode vibrations. It was not possible to run the rotor in the relevant speed range due to the extremely high vibration level, see Figure 7 (b). A possible reason for this is the strong excitation of the rotor due to the unbalance and the subharmonic resonance, which excite the cone mode, thereby transferring the rotational kinetic energy of the drive into the translational vibrations. The drive power of the turbine is not sufficient in this case to accelerate the rotor to higher speeds.

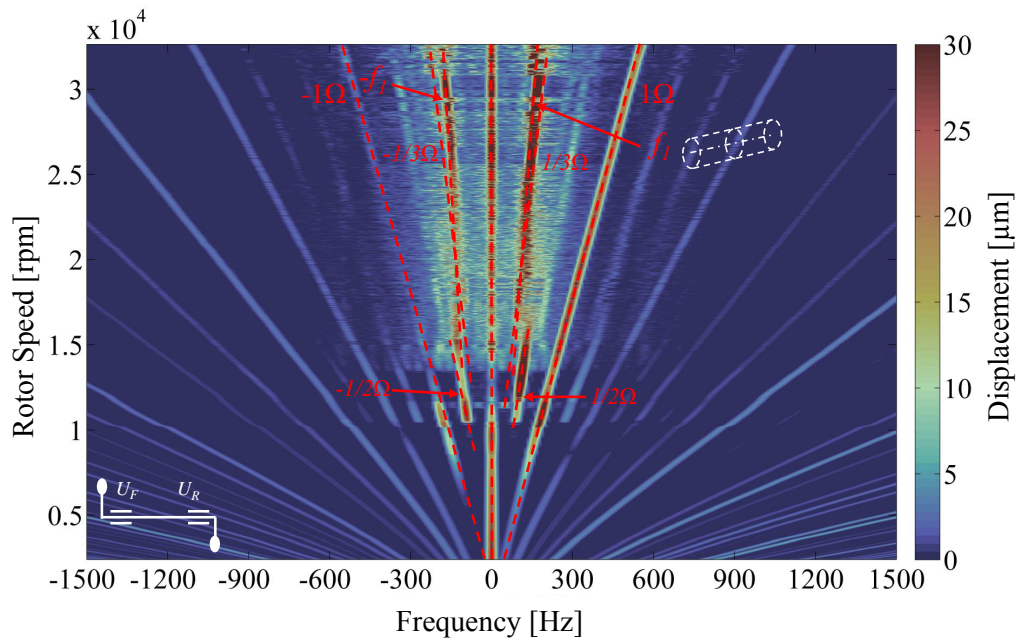
Based on the experimental results shown here, the path 1 of the classification of vibrations caused by driven vibration by a nonlinear progressive system is proven, whereby nonlinear vibrations occur before the self-excitation by the gas film, see Figure 1.

4 Summary

In order to confirm the claimed vibration classification of this work a rigid rotor supported by two gas foil bearings is tested experimentally. The following results can be summarized: According to path 2, self-excited vibrations by the fluid film occur as a subharmonic *Whirl*-vibration at the OSSV-point. After the onset of subharmonic vibration, which developed synchronously with the 1st mode (cylindrical shape), a variety of subharmonic resonances of the $\pm 1/3\Omega$ and $\pm 1/4\Omega$ orders occurs due to the progressive force-displacement behavior. In addition to the unstable cylindrical mode (1st mode), these also excite the conical mode (2nd mode). According to path 1, the unbalance has a great influence on the nonlinear vibrations. A variety of subharmonic resonances and vibrations of the $\pm 1/2\Omega$, $\pm 1/3\Omega$ and $\pm 1/4\Omega$ orders were identified as a result of the nonlinear progressive force-displacement behavior of the bearing. Even before self-excitation, $\pm 1/2\Omega$ orders occur due to nonlinear behavior. In addition, a variety of frequencies are modulated by the nonlinear behavior.

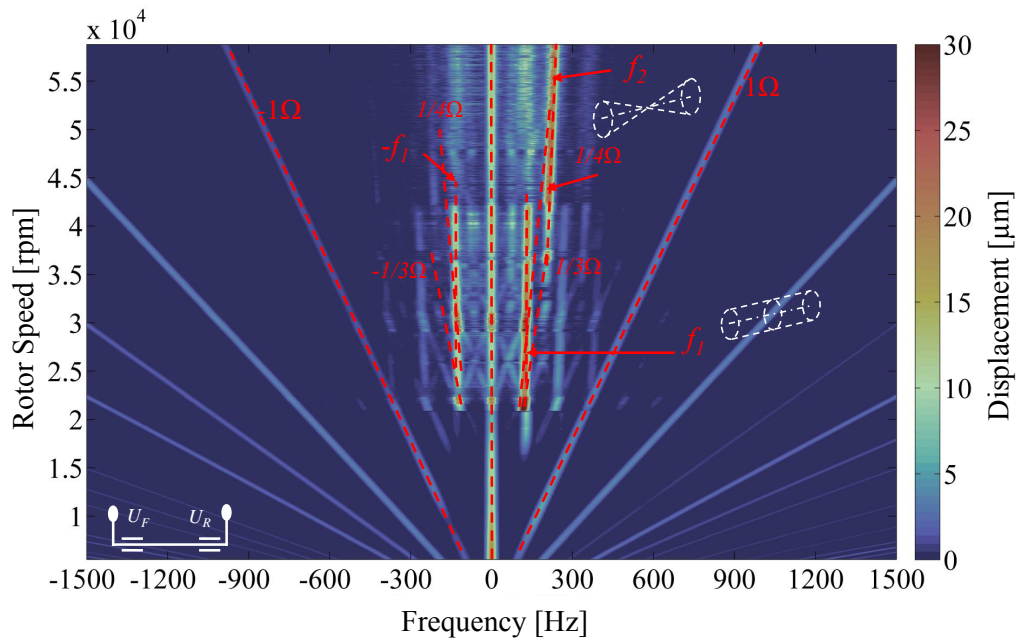


(a) $U_i = 9$ gmm ($i = F, R$)

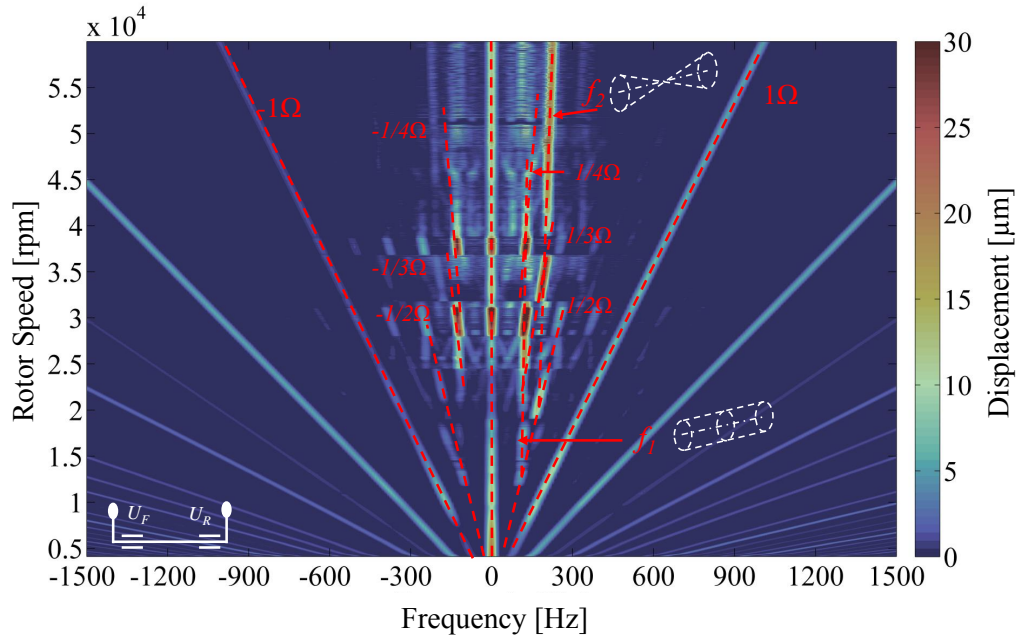


(b) $U_i = 12$ gmm ($i = F, R$)

Figure 7: Couple unbalance on the solid shaft: waterfall charts (a) and (b) (measurement location: front bearing, coast-down).



(a) $U_i = 6$ gmm ($i = F, R$)



(b) $U_i = 12$ gmm ($i = F, R$)

Figure 8: Static unbalance on the solid shaft: waterfall charts (a) and (b) (measurement location: front bearing, coast-down).

5 Appendix

Eigenbehavior of the test rig in operation.

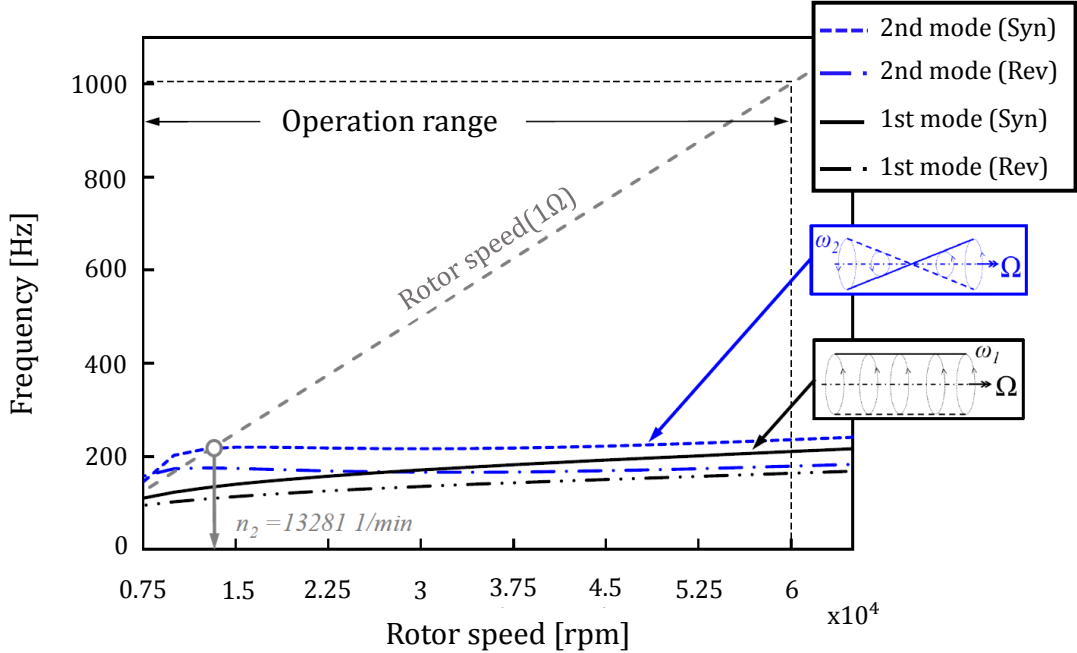


Figure 9: Campbell diagram of the solid shaft.

The following results are based on a rotordynamic model, which takes into account gyroscopic effects of the rotor as well as speed-dependent linearized stiffness and damping for the GFBs. The method for determining the linearized bearing parameters is given in Hoffmann et al. (2016); Hoffmann (2016). The forward and backward components of the two first modes in the operation range ($n_{\max} = 60\,000 \text{ rpm}$) are displayed. Due to the very high-frequency bending modes, their critical speeds are not reached. In operation, according to this linear view, critical speeds n_2 occur when there is a point of intersection between the spin speed line and the eigenfrequency of the 2nd mode (cone mode). This means that the rotationally synchronous excitation 1Ω is equal to the forward mode eigenfrequency f_2 of the rotor. Backward whirls are neglected. The low-frequency cylindrical mode has no resonance for a synchronous excitation with 1Ω in operation above $n = 7500 \text{ rpm}$.

References

Balducci, F.: *Analyse expérimentale des paliers et des butées aérodynamiques à feuilles*. Ph.D. thesis, Poitiers (2013).

DellaCorte, C.; Valco, M. J.: Load capacity estimation of foil air journal bearings for oil-free turbomachinery applications. *Tribology Transactions*, 43, 4, (2000), 795–801.

Dresig, H.; Rockhausen, L.; Holzweißig, F.: *Maschinendynamik*. Springer Berlin Heidelberg (2011).

Heshmat, H.: Advancements in the performance of aerodynamic foil journal bearings: high speed and load capability. *Journal of Tribology*, 116, 2, (1994), 287–294.

Heshmat, H.: Operation of foil bearings beyond the bending critical mode. *Journal of Tribology*, 122, 2, (2000), 478–479.

Heshmat, H.; Shapiro, W.; Gray, S.: Development of foil journal bearings for high load capacity and high speed whirl stability. *Journal of Lubrication Technology*, 104, 2, (1982), 149–156.

Hoffmann, R.: *Eine Methode für die Vorhersage nichtlinearer selbsterregter Schwingungen von Rotoren in Gasfolienlagern – Eine numerische und experimentelle Untersuchung*. Ph.D. thesis, Technische Universität Berlin (2016).

Hoffmann, R.; Munz, O.; Pronobis, T.; Barth, E.; Liebich, R.: A valid method of gas foil bearing parameter estimation: A model anchored on experimental data. *Proceedings of the Institution of Mechanical Engineers, Part C: Journal of Mechanical Engineering Science*, page 0954406216667966.

Hoffmann, R.; Pronobis, T.; Liebich, R.: Non-linear stability analysis of a modified gas foil bearing structure. Proceeding: IFToMM 2010 - 9th International Conference on Rotor Dynamics, Milano, Italy (2014).

Kim, K.-S.; Cho, B.-C.; Kim, M.-H.: Rotordynamic characteristics of 65 kw micro turbine with compliant air foil bearings. Proceeding: IFToMM 2010 - 8th International Conference on Rotor Dynamics, Seoul, Korea (2010).

Kim, T. H.: *Analysis of side end pressurized bump type gas foil bearings: A model anchored to test data*. Ph.D. thesis, Texas A&M University, College Station (2007).

Kovacic, I.; Brennan, M. J.: *The Duffing Equation: Nonlinear Oscillators and their Behaviour*. Wiley (2011).

Larsen, J. S.: *Nonlinear analysis of rotors Supported by air foil journal bearings–theory and experiments*. Ph.D. thesis, Technical University of Denmark (2015).

Magnus, K.; Popp, K.; Sextro, W.: *Schwingungen: Physikalische Grundlagen und mathematische Behandlung von Schwingungen*. Springer Fachmedien Wiesbaden (2013).

Nguyen-Schäfer, H.: *Rotordynamics of automotive turbochargers: Linear and nonlinear rotordynamics–Bearing design–rotor balancing*. Springer (2012).

San Andrés, L.; Kim, T. H.: Forced nonlinear response of gas foil bearing supported rotors. *Tribology International*, 41, 8, (2008), 704 – 715.

San Andrés, L.; Rubio, D.; Kim, T. H.: Rotordynamic performance of a rotor supported on bump type foil gas bearings: Experiments and predictions. *Journal of Engineering for Gas Turbines and Power*, 129, 3, (2007), 850–857.

Sim, K.; Lee, Y.-B.; Kim, T. H.; Lee, J.: Rotordynamic performance of shimmed gas foil bearings for oil-free turbochargers. *Journal of Tribology*, 134, 3, (2012), 031102–1–031102–11.

Yamamoto, T.; Ishida, Y.: *Linear and Nonlinear Rotordynamics: A Modern Treatment with Applications*. A Wiley-Interscience publication, Wiley (2001).

Address: Chair Engineering Design and Product Reliability, TU Berlin, Germany
email: gervais.c.djokokayo@campus.tu-berlin.de

Influence of electromagnetic Field Damping on the Vibration Stability of soft mounted Induction Motors with Sleeve Bearings, based on a Multibody Model

U. Werner

The paper shows an analytical vibration model for stability analysis of soft mounted induction motors with sleeve bearings, especially focusing on the influence of electromagnetic field damping on the limit of vibration stability. The model is a multibody model, considering the electromagnetic influence – including the electromagnetic field damping effect –, stiffness and internal material damping of the rotor structure, stiffness and damping of the bearing housings and end shields, stiffness and damping of the foundation elements and stiffness and damping of the oil film of the sleeve bearings. The aim of the paper is to unite all these influences in a model and to derive a procedure for calculating the limit of vibration stability, with considering the electromagnetic field damping effect. Additionally, a numerical example is presented, where the influence of electromagnetic field damping on the limit of vibration stability is shown, as well as the influence of the foundation elements and of the internal damping of the rotor. The procedure and conclusions can also be adopted into finite-element analysis.

1 Introduction

For analyzing rotating machinery, it is important to know the limit of vibration instability, which is e.g. influenced by the oil film of the sleeve bearings and internal material damping of the rotor (rotating damping), described by Rao (1996), Gasch (2002) and Genta (2005). In electrical machines, also electromagnetic fields occur, which couple the rotor to the stator and influences the vibration behavior, described by Schuisky (1972), Früchtenicht et al. (1982), Seinsch (1992), Smith et al. (1996), Arkkio et al. (2000), Holopainen (2004) and Werner (2006). Especially in induction motors an electromagnetic field damping effect occurs, which itself influences the electromagnetic forces and therefore the vibration behavior, shown by Früchtenicht et al. (1982), Seinsch (1992), Arkkio et al. (2000), Holopainen (2004), Werner (2006) and Werner (2016). Sometimes large induction motors (1MW-10MW) with sleeve bearings and high speeds (3000 rpm-6000 rpm) are mounted on soft foundation elements (rubber elements) to decouple the motor from the foundation (Fig.1). However, a soft mounting influences the vibration behavior of the machine clearly, which is demonstrated by Kirk et al. (1974), Gasch et al. (1984) and Werner (2008).

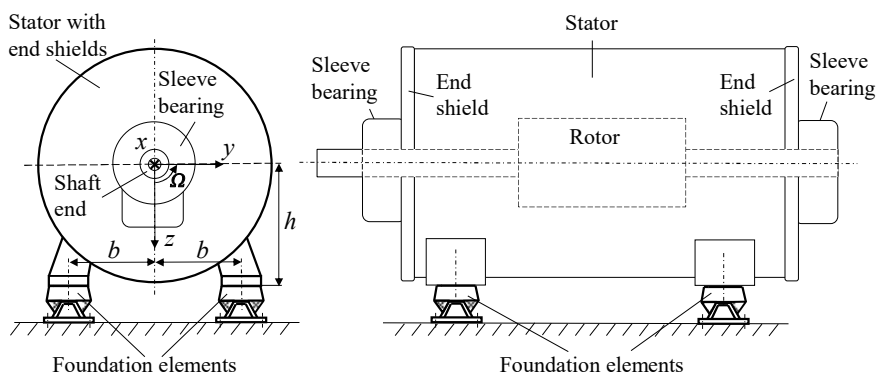


Figure 1. Soft mounted induction motor with sleeve bearings

Up to now, electromagnetic field damping of induction motors is often not considered for vibration analysis in the industry. Therefore the aim of the paper is now to present an analytical vibration model of a soft mounted induction motor with sleeve bearings and to derive a practicable method to consider the influence of electromagnetic field damping on the limit of vibration stability.

2 Electromagnetic Field Damping

An eccentricity \hat{e} between the shaft centre point W of the rotor and the centre of the stator bore leads to additionally electromagnetic eccentricity fields, which cause a radial magnetic force \hat{F}_{mr} in direction of the smallest air gap (Fig. 2a). If the rotor angular frequency Ω is different to the angular frequencies of the eccentricity fields, these fields induce voltage into the rotor cage, which reduces the magnitude of origin eccentricity fields. Therefore, the radial magnetic force \hat{F}_{mr} will be reduced and an additional magnetic force \hat{F}_{mt} in tangential direction is caused (Fig. 2a).

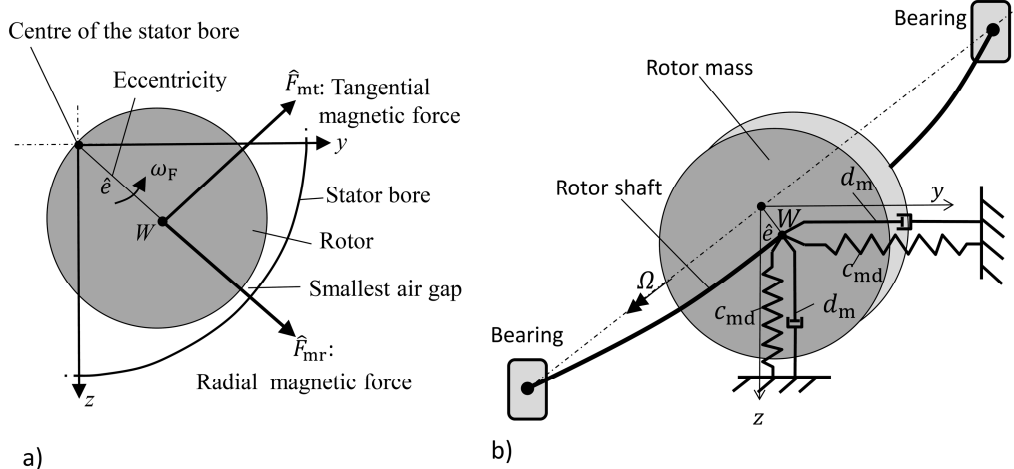


Figure 2. a) Electromagnetic forces; b) Magnetic spring and magnetic damper

The following equations are fundamentally based on the investigations of Früchtenicht et al. (1982) and Seinsch (1992). The radial magnetic force can be described by an electromagnetic spring element c_{md} (Fig. 2b):

$$p > 1: \quad c_{md} = \frac{c_m}{2} \cdot (\alpha_{p+1} + \alpha_{p-1}); \quad p = 1: \quad c_{md} = c_m \cdot \alpha_{p+1} \quad (1)$$

Where p is the number of pole pairs of the motor, c_m electromagnetic spring element without electromagnetic field damping, and α_{p+1} and α_{p-1} are the real parts of the complex field damping value. Without electromagnetic field damping, the real parts of the field damping coefficients get $\alpha_{p+1} = \alpha_{p-1} = 1$. For 2-pole motors ($p=1$) the component α_{p-1} gets zero, neglecting the homopolar flux.

$$p > 1: \quad c_m = \frac{\pi \cdot R \cdot l}{2 \cdot \mu_0 \cdot \delta''} \cdot \hat{B}_p^2; \quad p = 1: \quad c_m = \frac{1}{2} \cdot \frac{\pi \cdot R \cdot l}{2 \cdot \mu_0 \cdot \delta''} \cdot \hat{B}_p^2 \quad (2)$$

Where R is the radius of the stator bore, l is the length of the core, μ_0 is the permeability of air, δ'' is the equivalent magnetic air gap width – depending on mechanical air gap, saturation effects and CARTER-factors, described by Seinsch (1992) –, \hat{B}_p is the amplitude of fundamental air gap field. The tangential magnetic force can be described by the electromagnetic damper element d_m (with $\omega_F \neq 0$) (Fig. 2b):

$$p > 1: \quad d_m = -\frac{1}{\omega_F} \cdot \frac{c_m}{2} \cdot (\delta_{p+1} - \delta_{p-1}); \quad p = 1: \quad d_m = -\frac{1}{\omega_F} \cdot c_m \cdot \delta_{p+1} \quad (3)$$

Where ω_F is the whirling angular frequency of the rotor and δ_{p+1} and δ_{p-1} are imaginary parts of the complex field damping value. Without electromagnetic field damping, the field damping coefficients get $\delta_{p+1} = \delta_{p-1} = 0$. For 2-pole motors ($p=1$) the component δ_{p-1} gets also zero, neglecting the homopolar flux. If electromagnetic field damping has to be considered, the electromagnetic field damping coefficients $\alpha_{p+1}, \alpha_{p-1}, \delta_{p+1}, \delta_{p-1}$ have to be derived. With the ordinal number $v = p \pm 1$ for an eccentricity field wave, the electromagnetic field damping coefficients can be calculated:

$$\alpha_v = 1 - K_v \cdot s_v^2; \quad \delta_v = -K_v \cdot \beta_v \cdot s_v \quad (4)$$

$$\text{with: } \beta_v = \frac{R_{2,v}}{\omega_1 (L_{2h,v} + L_{2\sigma,v})} \quad \text{and } K_v = \frac{1}{\beta_v^2 + s_v^2} \cdot \frac{\xi_{Schr,v}^2 \zeta_{K,v}^2}{1 + \frac{L_{2\sigma,v}}{L_{2h,v}}}$$

Where $R_{2,v}$ is the resistance of a rotor bar and ring segment, ω_1 is the electrical stator angular frequency, $L_{2h,v}$ is the main field inductance of a rotor mesh, $L_{2\sigma,v}$ is the leakage inductance of a bar and ring segment, $\xi_{Schr,v}$ is the screwing factor and $\zeta_{K,v}$ is the coupling factor, which are all described in detail by Seinsch (1992).

The harmonic slip s_v can be described by:

$$s_v = \frac{\frac{\omega_v - \Omega}{\omega_1}}{\frac{\omega_1}{\omega_v}} \quad \text{with: } \Omega = \frac{\omega_1}{p} (1 - s) \quad (5)$$

Where s is the fundamental slip of the induction motor, ω_1 is the electrical stator angular frequency and ω_v/ν are the angular frequencies of the eccentricity fields, depending on the kind of eccentricity:

- Static eccentricity: $\omega_v = \omega_1$
- Dynamic eccentricity as a circular forward whirl: $\omega_v = \omega_1 \pm \omega_F$
- Dynamic eccentricity as a circular backward whirl: $\omega_v = \omega_1 \mp \omega_F$

To consider the electromagnetic field damping effect by a magnetic spring element c_{md} and by a magnetic damper element d_m , the compromise has to be made, that the calculation of c_{md} and d_m is here only based on circular forward whirls. With this simplification, the electromagnetic influence is supposed to be higher than it maybe in reality. If the absolute value of the harmonic slip $|s_v|$ is high – as it is for a circular backward whirl in conjunction with a small fundamental slip s – which is usual for steady state operation – the damped magnetic spring c_{md} gets very small as well as the magnetic damper d_m . In this case, the eccentricity fields induce strongly in the rotor cage and so the eccentricity fields get clearly reduced due to the harmonic rotor currents. Therefore, calculating c_{md} and d_m based on circular forward whirls presents the worst case regarding the height of the electromagnetic influence, when considering electromagnetic field damping, shown by Werner (2016).

3 Vibration Model

The model is an enhancement to the model, described by Werner (2008), where no electromagnetic field damping has been considered, no internal damping of the rotor, and no damping of bearing housings and end-shields. The vibration model is a simplified plane vibration model (plane y, z). It consists of two main masses, the rotor mass m_w , concentrated in the shaft centre point W , and the stator mass m_s , which has the inertia Θ_{sx} and is concentrated in the centre of gravity S (Fig. 3).

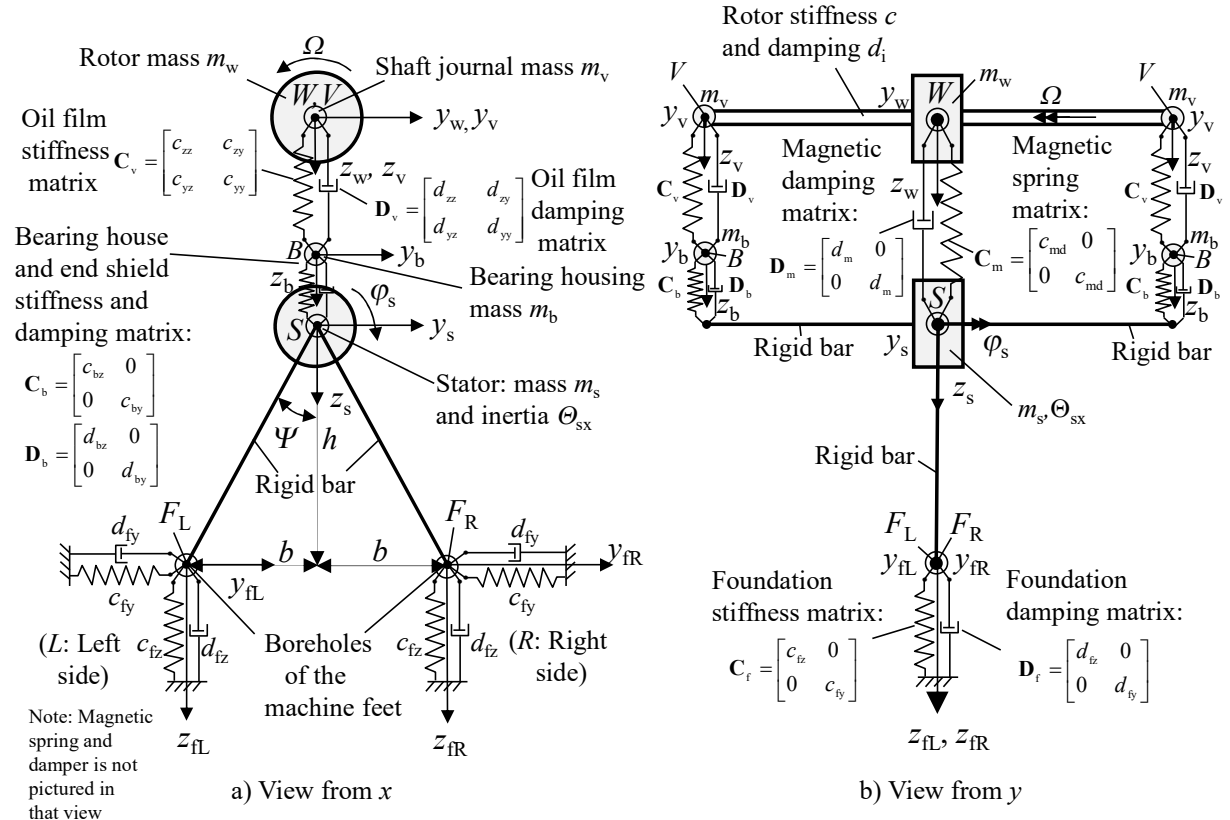


Figure 3. Vibration model

Additional masses are the mass of the shaft journal m_v and the mass of the bearing housing m_b , which are accounted separately, mostly to avoid zeros at the main diagonal of the mass matrix. Due to their low mass, their influence is only marginal. The rotor rotates with the rotary angular frequency Ω . The inertia moments of the

rotor are not considered and therefore also no gyroscopic effects. The shaft journal centre point V describes the movement of the shaft journal in the sleeve bearing. The point B is positioned in the axial middle of the sleeve bearing shell and describes the movement of the bearing housing. The rotor mass is linked to the stator mass by the stiffness c and internal damping d_i of the rotor, the oil film stiffness matrix \mathbf{C}_v and oil film damping matrix \mathbf{D}_v of the sleeve bearings, which are supposed to be equal for the drive side and the non-drive side, and the bearing house and end shield stiffness and damping matrix \mathbf{C}_b and \mathbf{D}_b , which are also assumed to be equal for the drive side and the non-drive side. The stator structure is assumed to be rigid, compared to the soft foundation. The foundation stiffness matrix \mathbf{C}_f and the foundation damping matrix \mathbf{D}_f connect the stator feet, F_L (left side) and F_R (right side), to the ground. The foundation stiffness and damping on the right side is the same as on the left side and the foundation stiffness values c_{fy} and c_{fz} and the foundation damping values d_{fy} and d_{fz} are the values for each motor side. The electromagnetism is considered by the electromagnetic spring and damper matrix \mathbf{C}_m and \mathbf{D}_m , where also electromagnetic field damping is included. All used coordinate systems are fixed.

For deriving the damping coefficients, it is important to consider here, that natural vibrations with the angular natural frequency ω_{stab} of the critical mode at the limit of stability with the rotary angular frequency Ω_{stab} has to be analyzed. Therefore the whirling frequency ω_F becomes ω_{stab} :

$$\omega_F = \omega_{stab} \quad (6)$$

The oil film stiffness and damping coefficients c_{ij} and d_{ij} ($i, j = z, y$) of the sleeve bearing are calculated by solving the Reynolds differential equation, shown by Tondl (1965), Gienicke (1966) and Lund et al. (1987).

$$c_{ij} = c_{ij}(\Omega) \text{ and } d_{ij} = d_{ij}(\Omega) \quad (7)$$

Referring to Gasch (2002), the internal material damping of the rotor d_i is described here by the mechanical loss factor $\tan \delta_i$ of the rotor, depending on the whirling angular frequency ω_F .

$$d_i(\omega_F) = \frac{c \cdot \tan \delta_i}{\omega_F} \quad (8)$$

With the stiffness of the bearing housing and end shield ($c_{bz}; c_{by}$), the damping of the bearing housing and end shield ($d_{bz}; d_{by}$) is here also described by the mechanical loss factor $\tan \delta_b$:

$$d_{bz}(\omega_F) = \frac{c_{bz} \cdot \tan \delta_b}{\omega_F}; \quad d_{by}(\omega_F) = \frac{c_{by} \cdot \tan \delta_b}{\omega_F} \quad (9)$$

The damping of the foundation elements is also described by the mechanical loss factor $\tan \delta_f$:

$$d_{fz}(\omega_F) = \frac{c_{fz} \cdot \tan \delta_f}{\omega_F}; \quad d_{fy}(\omega_F) = \frac{c_{fy} \cdot \tan \delta_f}{\omega_F} \quad (10)$$

The electromagnetic stiffness coefficient c_{md} and damping coefficient d_m are depending on the harmonic slip s_v , and therefore also depending on the whirling angular frequency ω_F (see chapter 2).

$$c_{md} = c_{md}(\omega_F) \text{ and } d_m = d_m(\omega_F) \quad (11)$$

4 Mathematical Description

To calculate the limit of stability, it is necessary to derive the homogenous differential equation. Therefore, d'Alemberts method is applied to the vibration system in order to derive the equations of motion, leading to the parts: a) rotor mass system, b) journal system, c) bearing house system and d) stator mass system – (Fig. 4).

Because of the small displacements of the stator mass (z_s, y_s, φ_s), compared to the dimensions of the machine (h, b, Ψ), following linearization is possible: The machine feet displacements on the left side (z_{fL}, y_{fL}) and the machine feet displacements on the right side (z_{fR}, y_{fR}) can be described by the displacements of the stator (z_s, y_s, φ_s) by:

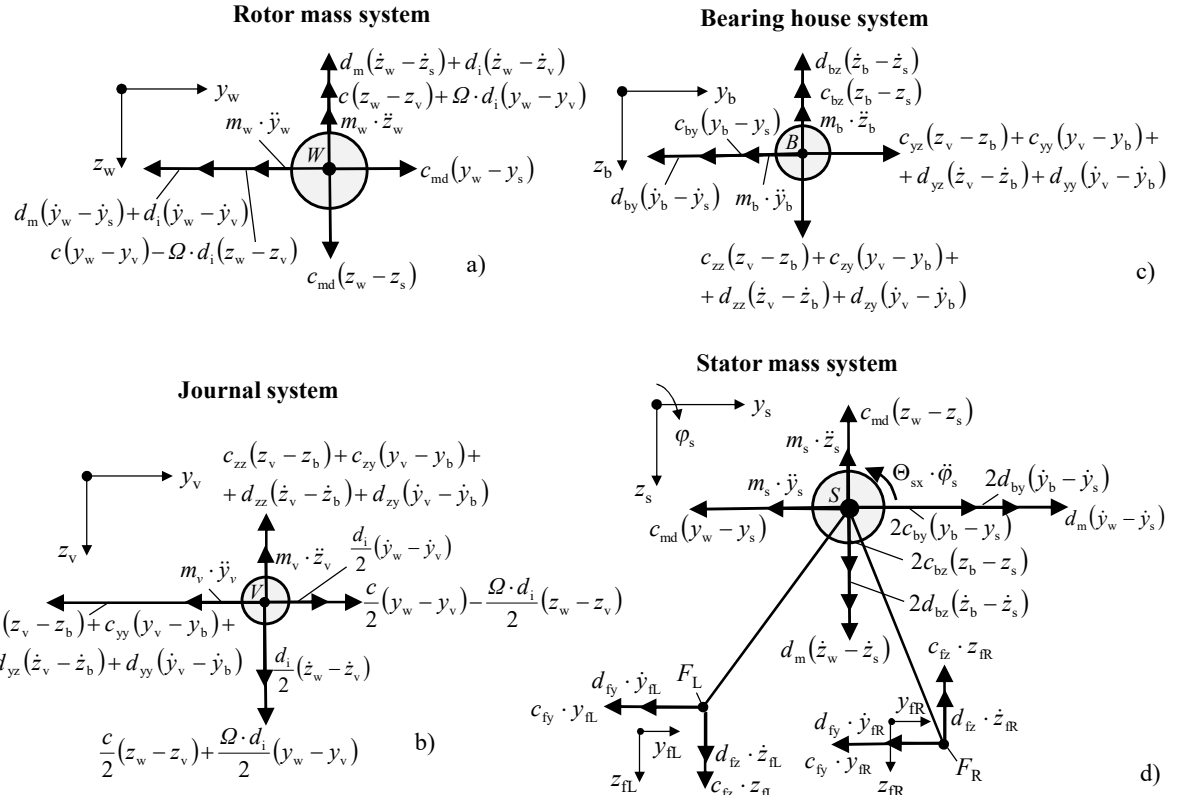
$$z_{fL} = z_s - \varphi_s \cdot b; \quad z_{fR} = z_s + \varphi_s \cdot b; \quad y_{fL} = y_{fR} = y_s - \varphi_s \cdot h \quad (12)$$

With the equilibrium of at each single system, the homogenous differential equation can be derived:

$$\mathbf{M} \cdot \ddot{\mathbf{q}} + \mathbf{D} \cdot \dot{\mathbf{q}} + \mathbf{C} \cdot \mathbf{q} = \mathbf{0} \quad (13)$$

Coordinate vector \mathbf{q} :

$$\mathbf{q} = [z_s; z_w; y_s; y_w; \varphi_s; z_v; z_b; y_v; y_b]^T \quad (14)$$



Note: The negative vertical displacement in F_L , relating to the coordinate z_{fL} , is considered by the direction of the vertical forces in F_L , so z_{fL} has to be described in the differential equation by: $z_{fL} = -z_s + \varphi_s \cdot b$

Figure 4. Vibration model, cut free into sub-systems

Mass matrix \mathbf{M} :

$$\mathbf{M} = \begin{bmatrix} m_s & 0 & 0 & 0 & 0 & 0 & 0 & 0 & 0 & 0 \\ 0 & m_w & 0 & 0 & 0 & 0 & 0 & 0 & 0 & 0 \\ 0 & 0 & m_s & 0 & 0 & 0 & 0 & 0 & 0 & 0 \\ 0 & 0 & 0 & m_w & 0 & 0 & 0 & 0 & 0 & 0 \\ 0 & 0 & 0 & 0 & \Theta_{sx} & 0 & 0 & 0 & 0 & 0 \\ 0 & 0 & 0 & 0 & 0 & 2m_v & 0 & 0 & 0 & 0 \\ 0 & 0 & 0 & 0 & 0 & 0 & 2m_b & 0 & 0 & 0 \\ 0 & 0 & 0 & 0 & 0 & 0 & 0 & 2m_v & 0 & 0 \\ 0 & 0 & 0 & 0 & 0 & 0 & 0 & 0 & 2m_b & 0 \end{bmatrix} \quad (15)$$

Damping matrix \mathbf{D} :

$$\mathbf{D} = \begin{bmatrix} 2(d_{fz} + d_{bz}) + d_m & -d_m & 0 & 0 & 0 & 0 & 0 & -2d_{bz} & 0 & 0 \\ -d_m & d_m + d_i & 0 & 0 & 0 & -d_i & 0 & 0 & 0 & 0 \\ 0 & 0 & 2(d_{fy} + d_{by}) + d_m & -d_m & -2d_{fy} \cdot h & 0 & 0 & 0 & 0 & -2d_{by} \\ 0 & 0 & -d_m & d_m + d_i & 0 & 0 & 0 & -d_i & 0 & 0 \\ 0 & 0 & -2d_{fy} \cdot h & 0 & 2(d_{fy}h^2 + d_{fz}b^2) & 0 & 0 & 0 & 0 & 0 \\ 0 & -d_i & 0 & 0 & 0 & 2d_{zz} + d_i & -2d_{zz} & 2d_{zy} & -2d_{zy} & 0 \\ -2d_{bz} & 0 & 0 & 0 & 0 & -2d_{zz} & 2(d_{zz} + d_{bz}) & -2d_{zy} & 2d_{zy} & 0 \\ 0 & 0 & 0 & -d_i & 0 & 2d_{yz} & -2d_{yz} & 2d_{yy} + d_i & -2d_{yy} & 0 \\ 0 & 0 & -2d_{by} & 0 & 0 & -2d_{yz} & 2d_{yz} & -2d_{yy} & 2(d_{yy} + d_{by}) & 0 \end{bmatrix} \quad (16)$$

Stiffness matrix \mathbf{C} :

(17)

$$\mathbf{C} = \begin{bmatrix} 2(c_{fz} + c_{bz}) - c_{md} & c_{md} & 0 & 0 & 0 & 0 & -2c_{bz} & 0 & 0 \\ c_{md} & c - c_{md} & 0 & \Omega d_i & 0 & -c & 0 & -\Omega d_i & 0 \\ 0 & 0 & 2(c_{fy} + c_{by}) - c_{md} & c_{md} & -2c_{fy}h & 0 & 0 & 0 & -2c_{by} \\ 0 & -\Omega d_i & c_{md} & c - c_{md} & 0 & \Omega d_i & 0 & -c & 0 \\ 0 & 0 & -2c_{fy}h & 0 & 2(c_{fy}h^2 + c_{fz}b^2) & 0 & 0 & 0 & 0 \\ 0 & -c & 0 & -\Omega d_i & 0 & 2c_{zz} + c & -2c_{zz} & 2c_{zy} + \Omega d_i & -2c_{zy} \\ -2c_{bz} & 0 & 0 & 0 & 0 & -2c_{zz} & 2(c_{zz} + c_{bz}) & -2c_{zy} & 2c_{zy} \\ 0 & \Omega d_i & 0 & -c & 0 & 2c_{yz} - \Omega d_i & -2c_{yz} & 2c_{yy} + c & -2c_{yy} \\ 0 & 0 & -2c_{by} & 0 & 0 & -2c_{yz} & 2c_{yz} & -2c_{yy} & 2(c_{yy} + c_{by}) \end{bmatrix}$$

Due to the non-symmetric stiffness matrix – caused by the oil film and internal material damping of the rotor – and due to a negative electromagnetic damping coefficient d_m , the vibration system will get instable, when the limit of stability is exceeded ($\Omega > \Omega_{stab}$). The limit of vibration stability Ω_{stab} can be derived, by increasing the rotary angular frequency Ω , and analyzing the eigenvalues.

When a real part of one eigenvalue gets zero, the limit of vibration stability is reached. If the rotary angular frequency Ω is increased furthermore, the real part gets positive and the vibration system gets instable. To find the limit of stability, the homogenous differential equation has to be analyzed. To calculate the eigenvalues, the state-space formulation is used here (with $\mathbf{q}_h = \mathbf{q}$; Index h for homogenous):

$$\underbrace{\begin{bmatrix} \dot{\mathbf{q}}_h \\ \ddot{\mathbf{q}}_h \end{bmatrix}}_{\mathbf{x}} = \underbrace{\begin{bmatrix} \mathbf{0} & \mathbf{I} \\ -\mathbf{M}^{-1} \cdot \mathbf{C} & -\mathbf{M}^{-1} \cdot \mathbf{D} \end{bmatrix}}_{\mathbf{A}} \cdot \underbrace{\begin{bmatrix} \mathbf{q}_h \\ \dot{\mathbf{q}}_h \end{bmatrix}}_{\mathbf{x}} \quad (18)$$

With the formulation $\mathbf{x} = \hat{\mathbf{x}} \cdot e^{\lambda \cdot t}$, the eigenvalues can be derived from:

$$\det[\mathbf{A} - \lambda \cdot \mathbf{I}] = 0 \quad (19)$$

At the limit of stability, the eigenvalue λ of the critical mode gets:

$$\lambda = \lambda_{stab} = \pm j \cdot \omega_{stab} \quad (20)$$

Knowing the eigenvalue λ_{stab} , the critical mode shape at the limit of stability can be derived. The real part of the critical eigenvalue λ_{stab} is zero and the whirling angular frequency ω_F is then identical to ω_{stab} , while the rotor is rotating with Ω_{stab} . It has to be considered, that the coefficients $d_i, d_{bz}, d_{by}, d_{fz}, d_{fy}, d_m, c_{md}$ are depending on the whirling angular frequency ω_F , which has to be determined.

Referring to Werner (2016) – where a rigid mounted induction motor was investigated –, an iterative solution has to be deduced, according to Fig. 5, for a soft mounted induction motor. First, the coefficients $d_i, d_{bz}, d_{by}, d_{fz}, d_{fy}, d_m$ and c_{md} , which depend on the whirling angular frequency ω_F , are set to zero, so that only the non-symmetric stiffness matrix of the oil film will cause instability. The eigenvalues are calculated according to (19), depending on the rotary angular frequency Ω .

To derive the limit of stability, the rotary angular frequency Ω is increased, till the real part of an eigenvalue gets zero. At this limit, the rotary angular frequency is $\Omega_{stab,1}$ – index “1” for the first calculation – and the natural angular frequency of the critical mode $\omega_{stab,1}$ can be derived from the eigenvalue. Afterwards the coefficients $d_i, d_{bz}, d_{by}, d_{fz}, d_{fy}, d_m$ and c_{md} are calculated with $\omega_F = \omega_{stab,1}$, and the limit of stability and the natural angular frequency are calculated again, leading to $\Omega_{stab,2}$ and $\omega_{stab,2}$. Then the new calculated natural angular frequency $\omega_{stab,2}$ will be compared to the origin natural angular frequency $\omega_{stab,1}$. If the ratio is less than Δ – an arbitrarily chosen value –, the calculation is finished and $\Omega_{stab} = \Omega_{stab,2}$ and $\omega_{stab} = \omega_{stab,2}$. If the ratio is larger as the chosen value Δ , a new calculation is deduced and the coefficients $d_i, d_{bz}, d_{by}, d_{fz}, d_{fy}, d_m$ and c_{md} are now calculated with $\omega_F = \omega_{stab,2}$. With these new coefficients, the new limit of stability $\Omega_{stab,n+1}$ and the natural angular frequency $\omega_{stab,n+1}$ are derived. Then again the new value $\omega_{stab,n+1}$ is compared to the previous value $\omega_{stab,2}$. If the deviation is still too large, the loop in Fig. 5 will run through, till the deviation is less than Δ . With this iterative process the limit of stability Ω_{stab} can be derived, as well as the corresponding natural angular frequency ω_{stab} of the critical mode. This procedure is useful, if the biggest influence on the limit of stability is caused by the non-symmetric stiffness matrix of the oil film, which is usually the case for common induction motors with sleeve bearings.

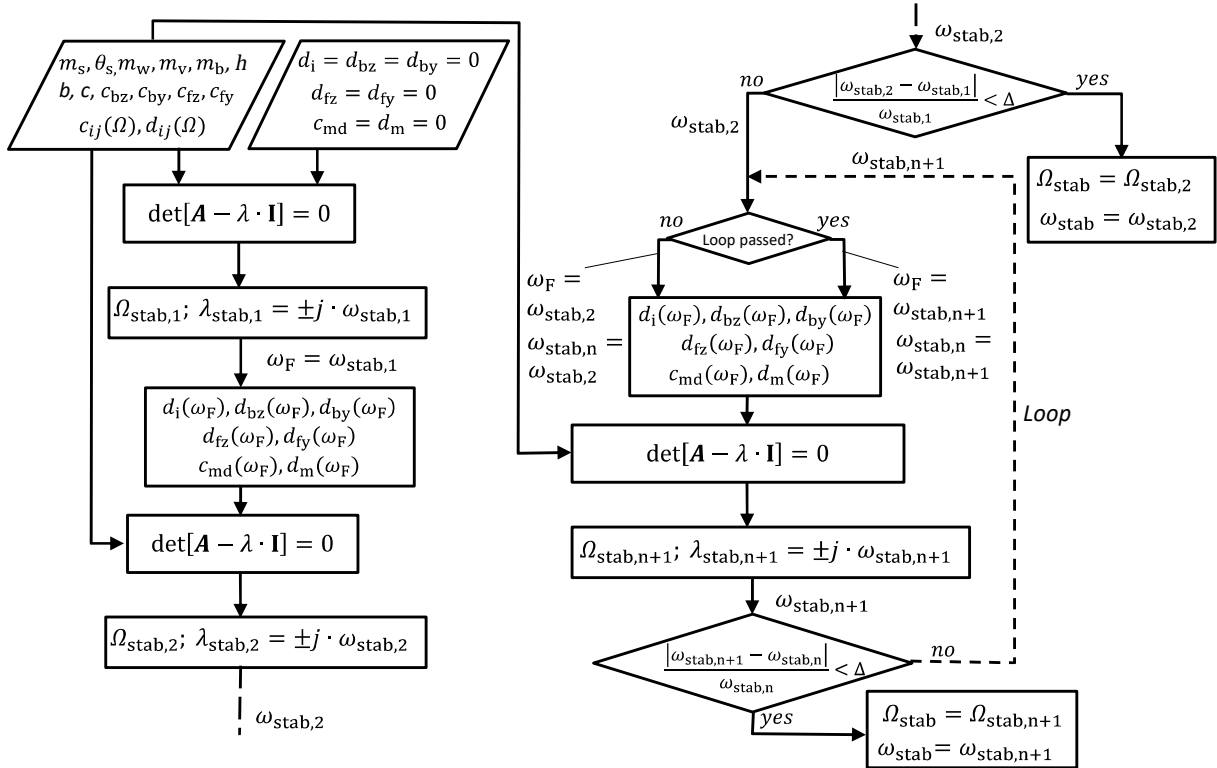


Figure 5. Flow diagram to derive the limit of stability for a soft mounted induction motor

5 Numerical Example

The limit of vibration stability for a 2-pole induction motor (Table 1), mounted on soft rubber elements, and driven by a converter with constant magnetization, is analyzed. The load machine is a pump and therefore the load torque is a quadratic function of the rotor speed n . At rated speed, the load torque is identical to the rated torque of the motor.

Table 1. 2-pole induction motor, mounted on soft rubber elements

Data of the motor:	
- Rated power	$P_N = 2400 \text{ kW}$
- Rated voltage	$U_N = 4160 \text{ V } (\Delta)$
- Rated frequency	$f_N = 60.15 \text{ 1/s}$
- Rated speed	$n_N = 3600 \text{ rpm}$
- Rated torque	$M_N = 6366 \text{ Nm}$
- Rated slip	$s = 0.0025$
- Number of pole pairs	$p = 1$
- Undamped magnetic spring constant	$c_m = 7.0 \cdot 10^6 \text{ kg/s}^2$
- Masse of the stator	$m_s = 7040 \text{ kg}$
- Mass inertia of the stator at the x-axis	$\theta_{sx} = 1550 \text{ kgm}^2$
- Mass of the rotor	$m_w = 1900 \text{ kg}$
- Mass of the rotor shaft journal	$m_v = 10 \text{ kg}$
- Mass of the bearing housing	$m_b = 80 \text{ kg}$
- Stiffness of the rotor	$c = 1.8 \cdot 10^8 \text{ kg/s}^2$
- Height of the centre of gravity S	$h = 560 \text{ mm}$
- Distance between motor feet	$2b = 1060 \text{ mm}$
- Horizontal stiffness of bearing housing and end shield	$c_{by} = 4.8 \cdot 10^8 \text{ kg/s}^2$
- Vertical stiffness of bearing housing and end shield	$c_{bz} = 5.7 \cdot 10^8 \text{ kg/s}^2$
- Mechanical loss factor of the bearing housing and end shield	$\tan \delta_b = 0.04$
- Mechanical loss factor of the rotor	$\tan \delta_i = 0.03$
Data of the sleeve bearings:	
- Bearing shell	Cylindrical
- Lubricant viscosity grade	ISO VG 32
- Nominal bore diameter / Bearing width	$d_b = 100 \text{ mm} / b_b = 81.4 \text{ mm}$

- Ambient temperature / Supply oil temperature	$T_{\text{amb}} = 20^\circ\text{C} / T_{\text{in}} = 40^\circ\text{C}$
- Mean relative bearing clearance (DIN 31698)	$\Psi_m = 1.6\%$
Data of the foundation elements (for each motor side):	
- Vertical stiffness for each motor side	$c_{fz} = 2.0 \cdot 10^7 \text{ kg/s}^2$
- Horizontal stiffness for each motor side	$c_{fy} = 1.0 \cdot 10^7 \text{ kg/s}^2$
- Mechanical loss factor of the foundation elements	$\tan \delta_f = 0.1$

The oil film stiffness and damping coefficients of the sleeve bearings have been calculated with the program SBCALC from RENK AG.

First, the coefficients d_i , d_{bz} , d_{by} , d_{fz} , d_{fy} , d_m and c_{md} are set to zero – according to the flow diagram in Figure 5 – and the real part and the imaginary part of the critical eigenvalue is analyzed. The critical vibration mode is the mode, which will get instable (Fig. 6).

Figure 6 shows, that at a rotor speed of 4595 rpm the real part of the critical eigenvalue becomes zero. Increasing the rotor speed, will lead to a positive real part and therefore to instability. So the limit of stability is reached at a rotor speed of $n_{\text{stab},1} = 4595 \text{ rpm}$ ($\Omega_{\text{stab},1} = 481.2 \text{ rad/s}$).

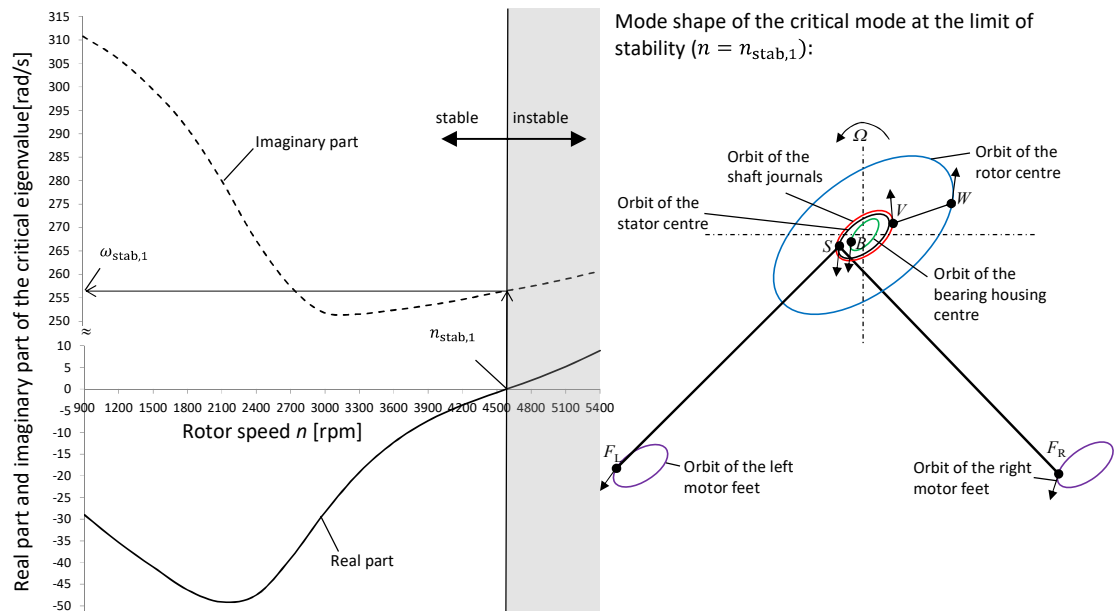


Figure 6. Real and imaginary part of the critical eigenvalue, depending on the rotor speed, with the boundary condition: $d_i = d_{bz} = d_{by} = d_{fz} = d_{fy} = d_m = c_{md} = 0$; Critical mode shape at the limit of stability

At this rotor speed the imaginary part, which represents the whirling angular frequency ω_F of the critical natural mode, becomes $\omega_F = \omega_{\text{stab},1} = 255.3 \text{ rad/s}$. According to the flow diagram this angular natural frequency $\omega_{\text{stab},1}$ can now be used to calculate the coefficients d_i , d_{bz} , d_{by} , d_{fz} , d_{fy} , d_m and c_{md} (Table 2).

Table 2. Coefficients d_i , d_{bz} , d_{by} , d_{fz} , d_{fy} , d_m and c_{md} at a rotor speed of $n_{\text{stab},1} = 4595 \text{ rpm}$ and at a whirling angular frequency of $\omega_F = \omega_{\text{stab},1} = 255.3 \text{ rad/s}$

Damping constant of the rotor	$d_i = 2.12 \cdot 10^4 \text{ kg/s}$
Damping constant of bearing housing and end shield (horizontal direction)	$d_{by} = 7.52 \cdot 10^4 \text{ kg/s}$
Damping constant of bearing housing and end shield (vertical direction)	$d_{bz} = 8.93 \cdot 10^4 \text{ kg/s}$
Damping constant of foundation elements for each motor side (horizontal direction)	$d_{fy} = 3.92 \cdot 10^3 \text{ kg/s}$
Damping constant of foundation elements for each motor side (vertical direction)	$d_{fz} = 7.83 \cdot 10^3 \text{ kg/s}$
Electromagnetic damping constant	$d_m = -61.7 \text{ kg/s}$
Electromagnetic spring constant	$c_{md} = 4.82 \cdot 10^5 \text{ kg/s}^2$

The large difference between rotor angular frequency $\Omega_{\text{stab},1} = 481.2 \text{ rad/s}$ and the whirling angular frequency $\omega_F = \omega_{\text{stab},1} = 255.3 \text{ rad/s}$, leads in combination with a very small fundamental slip $s = 0.0032$ to a large harmonic slip $s_v = -0.47$, and therefore to a strong electromagnetic field damping, and the electromagnetic coefficients d_m and c_{md} get very small. Fig. 7 shows, that the electromagnetic coefficients would be much higher, if the whirling angular frequency ω_F would be close to the rotor angular frequency Ω .

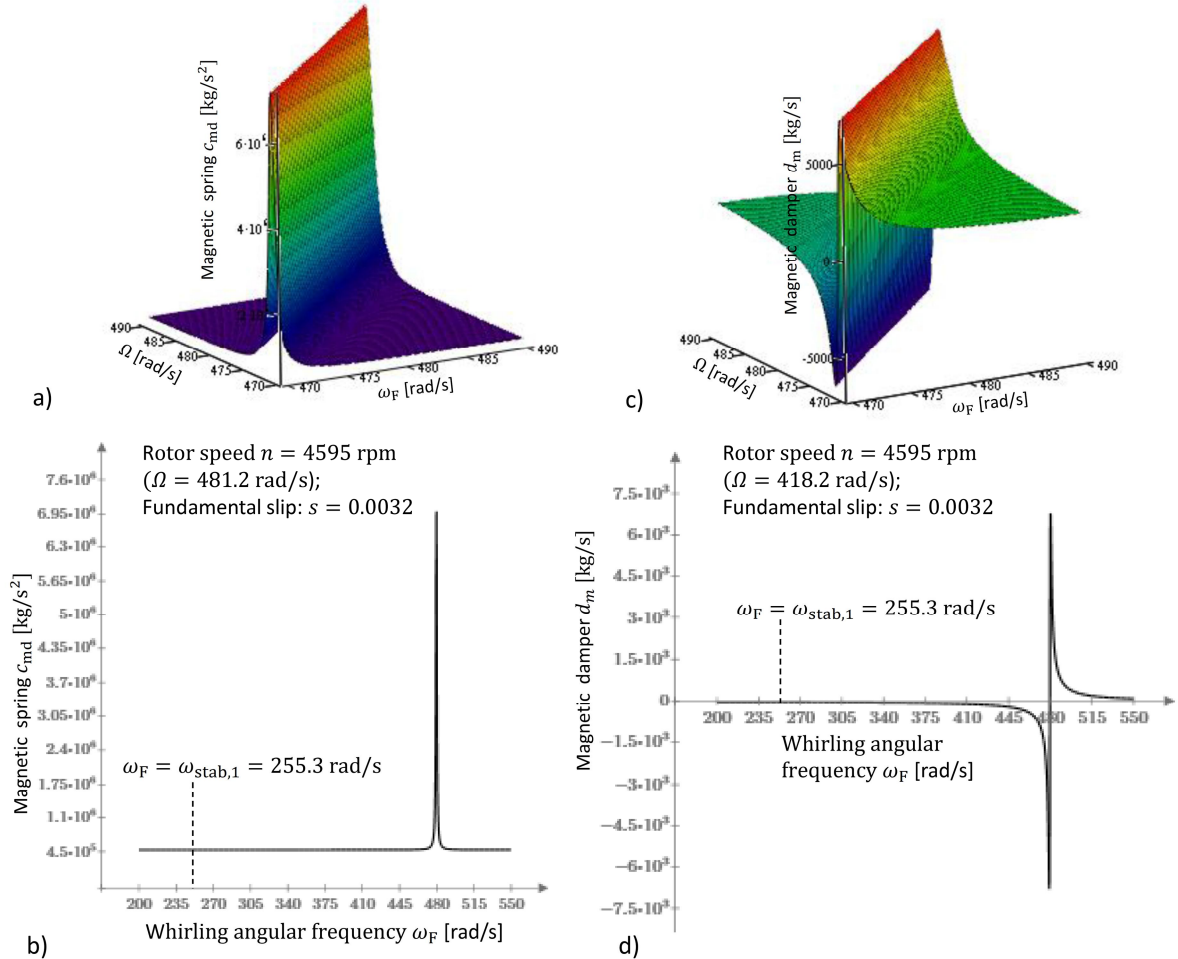


Figure 7. Magnetic spring constant a) and b) and magnetic damper constant c) and d) for different whirling angular frequencies and different rotor angular frequencies

With the basic coefficients from Table 2, the limit of stability is calculated again according to the flow diagram. To clarify this additional calculation, the index “2” is used instead of index “1”. So the limit of vibration stability is reached now at a rotor speed of $n_{stab,2} = 4554$ rpm and the whirling frequency is $\omega_F = \omega_{stab,2} = 255.6$ rad/s. According to the flow diagram a third calculation is not necessary, because $\omega_{stab,2}$ differs only marginal from $\omega_{stab,1}$ (+0.12%). Therefore, the values for the limit of stability are $n_{stab} = n_{stab,2} = 4554$ rpm; $\omega_{stab} = \omega_{stab,2} = 255.6$ rad/s. Now different cases are investigated. Table 3 shows, that the electromagnetic damper d_m and the electromagnetic spring constant c_{md} influence the limit of vibration stability only marginal (case b and c), because the large harmonic slip at the limit of stability causes a strong electromagnetic field damping and therefore leading to low values for d_m and c_{md} . Without considering electromagnetic field damping (case d), the magnetic spring value gets maximal ($c_{md} = c_m$) and the magnetic damper coefficient gets zero ($d_m = 0$). For this case, the limit of stability will be clearly reduced from 4554 rpm to 4377 rpm, which means -3.9%. When neglecting the internal damping of the rotor (case e), the limit of stability will be increased (+2.0%).

Table 3. Limit of stability for different cases

Case	Description	ω_{stab} [rad/s]	n_{stab} [rpm]	Δ of n_{stab} to a [%]
a)	Data Table 2 (Basic conditions)	255.6	4554	0
b)	Data Table 2 with $d_m = 0$	256.5	4556	+0.04
c)	Data Table 2 with $c_{md} = 0$	256.5	4566	+0.26
d)	Data Table 2 with $d_m = 0$; $c_{md} = c_m$ (no electromagnetic field damping)	248.1	4377	-3.9
e)	Data Table 2 with $d_i = 0$ (no internal damping of the rotor)	255.7	4645	+2.0
f)	Data Table 2 with $d_{by} = d_{bz} = 0$ (no damping of the bearing housing and end shield)	256.5	4509	-1.0
g)	Data Table 2 with $d_{fy} = d_{fz} = 0$ (no damping of the foundation elements)	256.1	4537	-0.37
h)	Data Table 2 with $c_{fy} = c_{fz} \rightarrow \infty$ (motor rigid mounted)	226.4	3922	-13.9

However, neglecting the damping of the bearing housings and end-shields (case f) will lower the limit of stability (-1%), as well as neglecting the damping of the foundation elements (-0.37%). The low influence of the damping of the foundation elements is caused by their low stiffness, which leads in conjunction with the loss factor to low damping values, which can be seen in Table 2. Figure 8 shows, that if the foundation element stiffness would be e.g. 4 times higher and the mechanical loss factor of the foundation elements would be the same ($\tan \delta_f = 0.1$), the limit of stability would increase from 4554 rpm to 4880 rpm (+7.2%). However, for a low loss factor ($\tan \delta_f = 0.01$) the limit of stability would only increase to 4730 rpm (+3.9%).

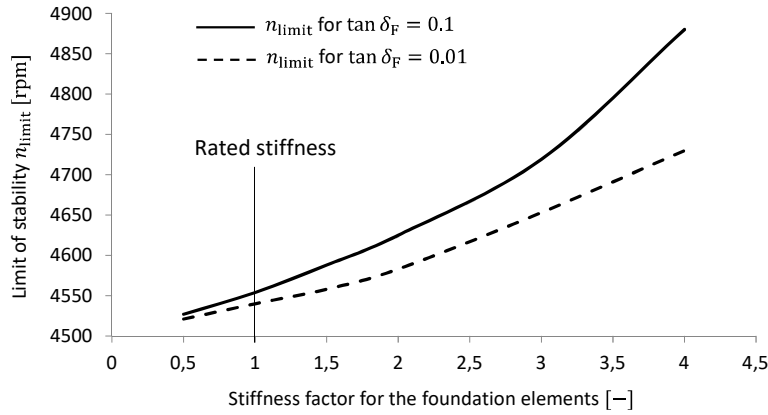


Figure 8. Influence of the foundation element stiffness on the limit of stability n_{limit}

Figure 9 shows the influence on the limit of stability and on the whirling angular frequency ω_{stab} , for stiffness variation of the foundation elements in a range of $c_{\text{fy}} = 1 \cdot 10^6 \dots 4 \cdot 10^7 \text{ kg/s}^2$; $c_{\text{fz}} = 1 \cdot 10^6 \dots 8 \cdot 10^7 \text{ kg/s}^2$.

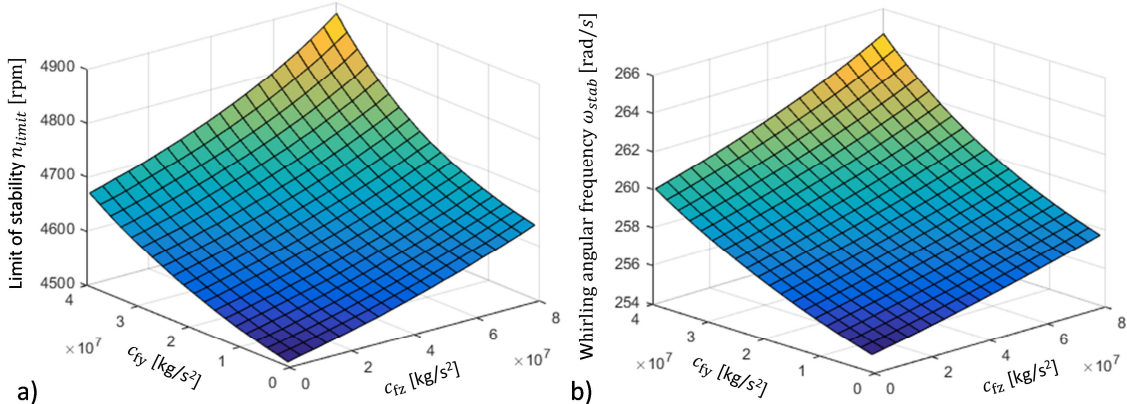


Figure 9. Influence of the arbitrary stiffness of the foundation elements on a) the limit of stability n_{limit} and on b) the whirling angular frequency ω_{stab} ; with a loss factor of $\tan \delta_f = 0.1$ for the foundation elements

If the motor would be rigid mounted (case h), which means $c_{\text{fy}} = c_{\text{fz}} \rightarrow \infty$, the limit of stability would be reached already at 3922 rpm, and the whirling frequency at the limit of stability ω_{stab} would be 226.4 rad/s instead of 255.6 rad/s, shown by Werner (2016). Therefore, putting here the motor on the soft foundation elements increases the limit of stability clearly (+16.1%), compared to the rigid mounted induction motor.

6 Conclusion

In the paper a multibody vibration model and a procedure are presented for stability analysis of soft mounted induction motors, with sleeve bearings. The focus of the paper is on the influence of electromagnetic field damping, regarding the limit of stability. After the mathematical coherences have been derived, a numerical example was presented, where the limit of stability was analyzed. It could be shown, that neglecting electromagnetic field damping leads to a lower limit of stability. Additionally the influence of the foundation elements and of the internal damping of the rotor on the limit of stability could be demonstrated. Although, the vibration model is a simplified multibody model, the procedure and conclusions can be adopted into finite-element analysis.

References

Arkkio, A.; Antila, M.; Pokki, K.; Simon, A.; Lantto, E.: Electromagnetic force on a whirling cage rotor. *Electr. Power Appl.*, Vol. 147, No. 5, (2000), 353-360.

Früchtenicht, J.; Jordan, H.; Seinsch, H.O.: Exzentrizitätsfelder als Ursache von Laufinstabilitäten bei Asynchronmaschinen. *Archiv für Elektrotechnik*, Vol. 65, Issue 4, Part 1, pp. 271-281, Part 2, (1982), 283-292.

Gasch, R.; Maurer J.; Sarfeld, W.: The influence of the elastic half space on stability and unbalance of a simple rotor-bearing foundation system, *Conference Vibration in Rotating Machinery*, C300/84, IMechE, Edinburg, (1984), 1-12.

Gasch, R.; Nordmann, R.; Pfützner H.: *Rotordynamik*. Springer-Verlag, Berlin-Heidelberg, (2002).

Genta, G.: *Dynamics of Rotating Systems*. Springer Science & Business Media, (2005).

Glienicker, J.: *Feder- und Dämpfungskonstanten von Gleitlagern für Turbomaschinen und deren Einfluss auf das Schwingungsverhalten eines einfachen Rotors*. Dissertation TH Karlsruhe, (1966).

Holopainen, T.P.: *Electromechanical interaction in rotor dynamics of cage induction motors*. VTT Technical Research Centre of Finland, Ph. D. Thesis, Helsinki University of Technology, Finland, (2004).

Kirk, R.G.; DeChowdhury, P.; Gunter, E.J.: The effect of support flexibility on the stability of rotors mounted in plain cylindrical bearings, *IUTAM Symposium Dynamics of Rotors*, (1974), 244-298.

Lund, J.; Thomsen, K.: *A calculation method and data for the dynamics of oil lubricated journal bearings in fluid film bearings and rotor bearings system design and optimization*, ASME, New York, (1978), 1-28.

Rao, J. S.: *Rotor Dynamics*. New Age International, (1996).

Schusky, W.: Magnetic pull in electrical machines due to the eccentricity of the rotor. *Electrical Research Association Trans.* 295, (1972), 391-399.

Seinsch, H.-O.: *Oberfelderscheinungen in Drehfeldmaschinen*. Teubner-Verlag, Stuttgart, (1992).

Smith, A.C.; Dorrell, D.G.: Calculation and measurement of unbalanced magnetic pull in cage induction motors with eccentric rotors. I. Analytical model. *Electric Power Applications*. Vol. 143, Issue 3, (1996), 193–201.

Tondl, A.: *Some Problems of Rotordynamics*. Chapman and Hall, London, (1965).

Werner, U.: *Rotordynamische Analyse von Asynchronmaschinen mit magnetischen Unsymmetrien*. Dissertation, Technical University of Darmstadt, (2006).

Werner, U.: Vibration stability of soft mounted asynchronous machines with flexible shafts and sleeve bearings considering electromagnetic effects. *ISMA 23rd International Conference on Noise & Vibration Engineering*, Leuven, Belgium, 15-17 September, (2008), 1167-1182.

Werner, U.: Stability analysis of induction rotors supported in sleeve bearings considering electromagnetic field damping and internal material damping of the rotor. *Vibration in rotating machinery*, Manchester, UK, Sept. 13-15, (2016), 155-166.

Address: Georg Simon Ohm University of Applied Sciences Nuremberg, Keßlerplatz 12, 90489 Nuremberg, Germany
email: ulrich.werner@th-nuernberg.de

Modal Analysis of Rotors under Special Support Conditions

G. Mikota

Gyroscopic rotors in rolling element or tilting pad bearings assume a particular model structure if the bearing load directions coincide. For simple bearing models in suitable coordinates, the stiffness and damping matrix are free from cross-coupling terms. Under these conditions, a relationship between right and left eigenvectors is derived. The rows of the frequency response matrix are related to its columns, and the elements of the frequency response matrix are expressed in terms of eigenvalues and right eigenvectors. The results are illustrated by a numerical example. The theory can be used to facilitate advanced applications of modal testing for a special class of rotors.

1 Introduction

Modal testing of rotors has been complicated by the fact that the right and left eigenvectors do not coincide. If a rotor is excited in one degree of freedom and the vibration responses are measured in all degrees of freedom, the right eigenvectors can be obtained, which correspond to the vibration mode shapes (Nordmann, 1984). Advanced applications such as model correlation or modification prediction require a complete modal model; the left eigenvectors can be obtained by exciting the rotor in all degrees of freedom, but this is often too much effort and sometimes even impossible. It would be helpful if a relationship between right and left eigenvectors could be established in advance. Zhang et al. (1988) as well as Lee (1991) found such relationships for several cases of isotropic rotors. However, bearings are often anisotropic and thus do not meet the assumptions made by these authors. For undamped gyroscopic rotors, Meirovitch (1974) and Meirovitch and Ryland (1979) proved that the left eigenvectors are the complex conjugates of the right eigenvectors. Bucher and Ewins (2001) used a perturbation analysis for lightly damped systems that was developed by Wang and Kirkhope (1994a,b); for a special type of anisotropic bearings, they simplified the relationship between frequency response functions and modal parameters and concluded that a complete modal model can be obtained from an excitation at one point along the shaft in both the x- and y-directions. Nevertheless, a considerable amount of damping may be present in practice. For damped gyroscopic rotors, Gutierrez-Wing (2003) published a general method whereby left eigenvectors can be derived from right eigenvectors; however, this method involves some matrix algebra and the solution of two eigenvalue problems.

As an alternative, one can take advantage of the model structure that is assumed by special types of bearings. Simple models of rolling element and tilting pad bearings indicate that in a coordinate system aligned with the load, the stiffness and damping matrix are free from cross-coupling terms. If bearing load directions coincide, this also applies for the contributions of bearings to the rotor's overall stiffness and damping matrix. A multi-degrees-of-freedom model of the rotor itself is, for instance, described in Genta (2005), where Timoshenko beam elements are used. With respect to the coordinate axes, the symmetric mass, damping, and stiffness matrices appear in separate blocks. The skew-symmetric gyroscopic matrix only contains symmetric off-diagonal submatrices. This leads to a special case of the vibro-acoustical model structure, for which a simple relationship between right and left eigenvectors is known. The rotor model may further include a skew-symmetric circulatory matrix from internal damping, which only contains symmetric off-diagonal submatrices.

In this paper, the cross-coupling properties of rolling element and tilting pad bearings are extracted from literature. The vibro-acoustical model is expressed in velocity and pressure state variables in order to demonstrate the analogy to a special case of the rotordynamic model. This model is extended by a circulatory matrix to account for internal damping. Under these conditions, a simple relationship between right and left eigenvectors is derived. The rows of the frequency response matrix are related to its columns, and the elements of the frequency response matrix are expressed in terms of eigenvalues and right eigenvectors. The results are illustrated by a numerical example. The theory can be used to facilitate advanced applications of modal testing for a special class of rotors.

2 Cross-coupling Properties of Supports

In rotordynamic models, bearings are often considered by 2×2 stiffness and damping matrices which need not be symmetric. These matrices can be split into symmetric and skew-symmetric parts, and principal axes can be found where the symmetric parts are free from cross-coupling terms. The skew-symmetric parts do not change with the angular position of the coordinate system, are cross-coupling in nature, and thus contribute to the overall circulatory and gyroscopic matrices. For journal bearings in general, the principal axes of stiffness and damping may differ among the individual supports of a rotor; any choice of coordinate system may lead to cross-coupling terms in the overall stiffness or damping matrix. The overall stiffness matrix could be decoupled for equally loaded identical journal bearings, but this is a somewhat unrealistic configuration.

Models of rolling element bearings include further restrictions. Krämer (1993) used 2×2 stiffness and damping matrices which are diagonal in a coordinate system aligned with the load. For a rotor whose bearing load directions coincide, this model does not contribute any cross-coupling terms to the overall stiffness or damping matrix. Dietl (1997) assembled 5×5 stiffness and damping matrices of rolling element bearings based on the stiffness and damping coefficients of the individual elasto-hydrodynamic lubrication contacts. One of his models describes the dry Hertzian contact with respect to stiffness and damping and uses an empirical law for elasto-hydrodynamic oil-film damping. For radial, axial, and tilting loads in a plane through the rotor axis, this model is symmetric to that plane. If x denotes the radial load direction, it follows that the resulting stiffness and damping matrices do not include any coupling terms between the local displacement vectors

$$\mathbf{x}_l = \begin{bmatrix} x \\ \varphi_y \end{bmatrix} \quad \text{and} \quad \mathbf{y}_l = \begin{bmatrix} y \\ \varphi_x \end{bmatrix}. \quad (1)$$

This conclusion still holds for a rotor whose bearing loads are confined to the x - z -plane. Such conditions may be realistic, especially if the load is constituted by the rotor's own weight.

Similar models are obtained for tilting pad bearings. According to Someya (1989), the cross-coupling stiffness and damping terms of four pad and five pad bearings disappear in a coordinate system aligned with the load. Dimond et al. (2011) stated that in tilting pad bearings, the cross-coupled stiffness terms are generally three orders of magnitude less than the direct stiffness terms. Experimental results for five pad and four pad bearings were published by Childs et al. (2011); cross-coupled stiffness and damping coefficients were always much smaller than direct ones.

These considerations are summarized as follows. For 2×2 matrix models of rolling element or tilting pad bearings, cross-coupling can be avoided if the coordinate system is aligned with the load. If radial and tilting loads are confined to a plane through the rotor axis, this also holds for a 4×4 matrix model of rolling element bearings.

3 From Vibro-acoustics to Rotordynamics

According to Wyckaert et al. (1996), the vibro-acoustical model can be described by

$$\begin{bmatrix} \mathbf{M}_s & \mathbf{0} \\ \mathbf{K}_c^T & \mathbf{M}_f/\rho \end{bmatrix} \begin{bmatrix} \ddot{\mathbf{s}} \\ \ddot{\mathbf{p}} \end{bmatrix} + \begin{bmatrix} \mathbf{C}_s & \mathbf{0} \\ \mathbf{0} & \mathbf{C}_f/\rho \end{bmatrix} \begin{bmatrix} \dot{\mathbf{s}} \\ \dot{\mathbf{p}} \end{bmatrix} + \begin{bmatrix} \mathbf{K}_s & -\mathbf{K}_c \\ \mathbf{0} & \mathbf{K}_f/\rho \end{bmatrix} \begin{bmatrix} \mathbf{s} \\ \mathbf{p} \end{bmatrix} = \begin{bmatrix} \mathbf{f}_s \\ \dot{\mathbf{q}} \end{bmatrix} \quad (2)$$

with the structural displacement vector \mathbf{s} , the sound pressure vector \mathbf{p} , the vector of external force loading \mathbf{f}_s , the vector of acoustical source loading $\dot{\mathbf{q}}$, the structural mass matrix \mathbf{M}_s , the structural damping matrix \mathbf{C}_s , the structural stiffness matrix \mathbf{K}_s , the fluid mass matrix \mathbf{M}_f , the fluid damping matrix \mathbf{C}_f , the fluid stiffness matrix \mathbf{K}_f , the coupling submatrix \mathbf{K}_c , and the fluid density ρ . Wyckaert et al. (1996) derived a simple relationship between right and left eigenvectors of such systems. If structural velocities \mathbf{v} are chosen as state variables instead of structural displacements \mathbf{s} , the vibro-acoustical model (2) becomes

$$\begin{bmatrix} \mathbf{M}_s & \mathbf{0} \\ \mathbf{0} & \mathbf{M}_f/\rho \end{bmatrix} \begin{bmatrix} \ddot{\mathbf{v}} \\ \ddot{\mathbf{p}} \end{bmatrix} + \begin{bmatrix} \mathbf{C}_s & -\mathbf{K}_c \\ \mathbf{K}_c^T & \mathbf{C}_f/\rho \end{bmatrix} \begin{bmatrix} \dot{\mathbf{v}} \\ \dot{\mathbf{p}} \end{bmatrix} + \begin{bmatrix} \mathbf{K}_s & \mathbf{0} \\ \mathbf{0} & \mathbf{K}_f/\rho \end{bmatrix} \begin{bmatrix} \mathbf{v} \\ \mathbf{p} \end{bmatrix} = \begin{bmatrix} \dot{\mathbf{f}}_s \\ \ddot{\mathbf{q}} \end{bmatrix}. \quad (3)$$

Equation (3) is recognized as a special case of the linear time-invariant rotor model

$$\mathbf{M}\ddot{\mathbf{u}} + (\mathbf{C} + \mathbf{G})\dot{\mathbf{u}} + (\mathbf{K} + \mathbf{N})\mathbf{u} = \mathbf{f}, \quad (4)$$

which reads

$$\begin{bmatrix} \mathbf{M}_x & \mathbf{0} \\ \mathbf{0} & \mathbf{M}_y \end{bmatrix} \begin{bmatrix} \ddot{\mathbf{x}} \\ \ddot{\mathbf{y}} \end{bmatrix} + \begin{bmatrix} \mathbf{C}_x & \mathbf{G}_0 \\ -\mathbf{G}_0^T & \mathbf{C}_y \end{bmatrix} \begin{bmatrix} \dot{\mathbf{x}} \\ \dot{\mathbf{y}} \end{bmatrix} + \begin{bmatrix} \mathbf{K}_x & \mathbf{0} \\ \mathbf{0} & \mathbf{K}_y \end{bmatrix} \begin{bmatrix} \mathbf{x} \\ \mathbf{y} \end{bmatrix} = \begin{bmatrix} \mathbf{f}_x \\ \mathbf{f}_y \end{bmatrix}. \quad (5)$$

The mass, damping, and stiffness matrix are partitioned into separate symmetric blocks \mathbf{M}_x , \mathbf{M}_y , \mathbf{C}_x , \mathbf{C}_y , \mathbf{K}_x , and \mathbf{K}_y , respectively; if bearing load directions coincide, this applies for the configurations summarized in Section 2. A skew-symmetric gyroscopic matrix \mathbf{G} is taken into account; in the following, \mathbf{G}_0 need not be symmetric. The rotordynamic model (5) is extended to include a skew-symmetric matrix

$$\mathbf{N} = \begin{bmatrix} \mathbf{0} & \mathbf{N}_0 \\ -\mathbf{N}_0^T & \mathbf{0} \end{bmatrix}, \quad (6)$$

where \mathbf{N}_0 need not be symmetric; this results in the model

$$\begin{bmatrix} \mathbf{M}_x & \mathbf{0} \\ \mathbf{0} & \mathbf{M}_y \end{bmatrix} \begin{bmatrix} \ddot{\mathbf{x}} \\ \ddot{\mathbf{y}} \end{bmatrix} + \begin{bmatrix} \mathbf{C}_x & \mathbf{G}_0 \\ -\mathbf{G}_0^T & \mathbf{C}_y \end{bmatrix} \begin{bmatrix} \dot{\mathbf{x}} \\ \dot{\mathbf{y}} \end{bmatrix} + \begin{bmatrix} \mathbf{K}_x & \mathbf{N}_0 \\ -\mathbf{N}_0^T & \mathbf{K}_y \end{bmatrix} \begin{bmatrix} \mathbf{x} \\ \mathbf{y} \end{bmatrix} = \begin{bmatrix} \mathbf{f}_x \\ \mathbf{f}_y \end{bmatrix} \quad (7)$$

under consideration.

4 Eigenvector relations

The right eigenvectors

$$\boldsymbol{\theta}_{rn} = \begin{bmatrix} \boldsymbol{\theta}_{xrn} \\ \boldsymbol{\theta}_{yrn} \end{bmatrix} \quad (8)$$

of equation (7) satisfy the equation

$$\begin{bmatrix} \lambda_n^2 \mathbf{M}_x + \lambda_n \mathbf{C}_x + \mathbf{K}_x & \lambda_n \mathbf{G}_0 + \mathbf{N}_0 \\ -\lambda_n \mathbf{G}_0^T - \mathbf{N}_0^T & \lambda_n^2 \mathbf{M}_y + \lambda_n \mathbf{C}_y + \mathbf{K}_y \end{bmatrix} \begin{bmatrix} \boldsymbol{\theta}_{xrn} \\ \boldsymbol{\theta}_{yrn} \end{bmatrix} = \mathbf{0} \quad (9)$$

with the n -th eigenvalue λ_n . This is equivalent to

$$\begin{bmatrix} \lambda_n^2 \mathbf{M}_x + \lambda_n \mathbf{C}_x + \mathbf{K}_x & -\lambda_n \mathbf{G}_0 - \mathbf{N}_0 \\ \lambda_n \mathbf{G}_0^T + \mathbf{N}_0^T & \lambda_n^2 \mathbf{M}_y + \lambda_n \mathbf{C}_y + \mathbf{K}_y \end{bmatrix} \begin{bmatrix} \boldsymbol{\theta}_{xrn} \\ -\boldsymbol{\theta}_{yrn} \end{bmatrix} = \mathbf{0}. \quad (10)$$

Transposing equation (10) leads to

$$\begin{bmatrix} \boldsymbol{\theta}_{xrn}^T & -\boldsymbol{\theta}_{yrn}^T \end{bmatrix} \begin{bmatrix} \lambda_n^2 \mathbf{M}_x + \lambda_n \mathbf{C}_x + \mathbf{K}_x & \lambda_n \mathbf{G}_0 + \mathbf{N}_0 \\ -\lambda_n \mathbf{G}_0^T - \mathbf{N}_0^T & \lambda_n^2 \mathbf{M}_y + \lambda_n \mathbf{C}_y + \mathbf{K}_y \end{bmatrix} = \mathbf{0}; \quad (11)$$

it follows that the left eigenvectors $\boldsymbol{\theta}_{ln}$ of equation (7) are related to the right eigenvectors by

$$\boldsymbol{\theta}_{ln} = \begin{bmatrix} \boldsymbol{\theta}_{xln} \\ \boldsymbol{\theta}_{yln} \end{bmatrix} = \begin{bmatrix} \boldsymbol{\theta}_{xrn} \\ -\boldsymbol{\theta}_{yrn} \end{bmatrix}. \quad (12)$$

5 Properties of the Frequency Response Matrix

The rotor model (7) is transferred to the frequency domain by taking the Laplace transform and setting the Laplace variable $s=i\omega$. The Laplace transforms of the vectors \mathbf{x} , \mathbf{y} , \mathbf{f}_x , and \mathbf{f}_y are denoted as \mathbf{X} , \mathbf{Y} , \mathbf{F}_x , and \mathbf{F}_y , respectively. From the frequency domain model

$$\begin{bmatrix} -\omega^2 \mathbf{M}_x + i\omega \mathbf{C}_x + \mathbf{K}_x & i\omega \mathbf{G}_0 + \mathbf{N}_0 \\ -i\omega \mathbf{G}_0^T - \mathbf{N}_0^T & -\omega^2 \mathbf{M}_y + i\omega \mathbf{C}_y + \mathbf{K}_y \end{bmatrix} \begin{bmatrix} \mathbf{X}(i\omega) \\ \mathbf{Y}(i\omega) \end{bmatrix} = \begin{bmatrix} \mathbf{F}_x(i\omega) \\ \mathbf{F}_y(i\omega) \end{bmatrix} \quad (13)$$

it can be seen that the displacement vector is related to the force vector by

$$\begin{bmatrix} \mathbf{X}(i\omega) \\ \mathbf{Y}(i\omega) \end{bmatrix} = \mathbf{H}(i\omega) \begin{bmatrix} \mathbf{F}_x(i\omega) \\ \mathbf{F}_y(i\omega) \end{bmatrix} \quad (14)$$

with the frequency response matrix

$$\mathbf{H}(i\omega) = \begin{bmatrix} \mathbf{H}_{xx}(i\omega) & \mathbf{H}_{xy}(i\omega) \\ \mathbf{H}_{yx}(i\omega) & \mathbf{H}_{yy}(i\omega) \end{bmatrix} = \begin{bmatrix} -\omega^2 \mathbf{M}_x + i\omega \mathbf{C}_x + \mathbf{K}_x & i\omega \mathbf{G}_0 + \mathbf{N}_0 \\ -i\omega \mathbf{G}_0^T - \mathbf{N}_0^T & -\omega^2 \mathbf{M}_y + i\omega \mathbf{C}_y + \mathbf{K}_y \end{bmatrix}^{-1}. \quad (15)$$

Equation (14) is equivalent to

$$\begin{bmatrix} \mathbf{X}(i\omega) \\ -\mathbf{Y}(i\omega) \end{bmatrix} = \begin{bmatrix} \mathbf{H}_{xx}(i\omega) & \mathbf{H}_{xy}(i\omega) \\ -\mathbf{H}_{yx}(i\omega) & -\mathbf{H}_{yy}(i\omega) \end{bmatrix} \begin{bmatrix} \mathbf{F}_x(i\omega) \\ \mathbf{F}_y(i\omega) \end{bmatrix}. \quad (16)$$

From equations (13) and (16), it follows that

$$\begin{bmatrix} \mathbf{H}_{xx}(i\omega) & \mathbf{H}_{xy}(i\omega) \\ -\mathbf{H}_{yx}(i\omega) & -\mathbf{H}_{yy}(i\omega) \end{bmatrix} = \begin{bmatrix} -\omega^2 \mathbf{M}_x + i\omega \mathbf{C}_x + \mathbf{K}_x & -i\omega \mathbf{G}_0 - \mathbf{N}_0 \\ -i\omega \mathbf{G}_0^T - \mathbf{N}_0^T & \omega^2 \mathbf{M}_y - i\omega \mathbf{C}_y - \mathbf{K}_y \end{bmatrix}^{-1}, \quad (17)$$

and this matrix is symmetric; this leads to the properties

$$\mathbf{H}_{xx}(i\omega) = \mathbf{H}_{xx}^T(i\omega), \quad (18)$$

$$\mathbf{H}_{yy}(i\omega) = \mathbf{H}_{yy}^T(i\omega), \quad (19)$$

and

$$\mathbf{H}_{yx}(i\omega) = -\mathbf{H}_{xy}^T(i\omega) \quad (20)$$

of the frequency response matrix $\mathbf{H}(i\omega)$.

Using equations (18), (19), and (20), each column of the frequency response matrix can be related to a row. For a column located in the left half of $\mathbf{H}(i\omega)$, the corresponding row is obtained from the transpose after changing the sign in the lower half of the column. For a column located in the right half of $\mathbf{H}(i\omega)$, the corresponding row is obtained from the transpose after changing the sign in the upper half of the column.

6 Modal Analysis

In terms of eigenvalues and eigenvectors, the elements of the frequency response matrix $\mathbf{H}(i\omega)$ are expressed as

$$H_{jk}(i\omega) = \sum_{n=1}^N \left(\frac{\theta_{rnj}\theta_{lnk}}{a_n(i\omega - \lambda_n)} + \frac{\bar{\theta}_{rnj}\bar{\theta}_{lnk}}{\bar{a}_n(i\omega - \bar{\lambda}_n)} \right), \quad j, k = 1, \dots, N, \quad (21)$$

in which θ_{rnj} is the j -th component of the right eigenvector $\mathbf{\theta}_{rn}$, θ_{lnk} is the k -th component of the left eigenvector $\mathbf{\theta}_{ln}$, a_n is a constant for each mode, and N is the number of degrees of freedom (Irretier, 1999); the bar above a symbol denotes the complex conjugate. Equation (21) shows that the right eigenvectors $\mathbf{\theta}_{rn}$ can be identified from the k -th column of $\mathbf{H}(i\omega)$ if the values of θ_{lnk}/a_n are selected in advance; the left eigenvectors $\mathbf{\theta}_{ln}$ can be identified from the j -th row of $\mathbf{H}(i\omega)$ after selecting the values of θ_{rnj}/a_n .

For rotors modelled by equation (7), the j -th row of $\mathbf{H}(i\omega)$ is obtained from the j -th column using the properties (18), (19), and (20). This means that the left eigenvectors can be identified from a column of the frequency response matrix, which only requires an excitation in one degree of freedom.

Alternatively, the left eigenvectors can be determined from the right eigenvectors using the relationship (12). If equation (12) is inserted into equation (21), the elements of $\mathbf{H}(i\omega)$ become

$$H_{abjk}(i\omega) = \sigma \sum_{n=1}^N \left(\frac{\theta_{arnj}\theta_{brnk}}{a_n(i\omega - \lambda_n)} + \frac{\bar{\theta}_{arnj}\bar{\theta}_{brnk}}{\bar{a}_n(i\omega - \bar{\lambda}_n)} \right), \quad a \in \{x, y\}, \quad b \in \{x, y\}, \quad j, k = 1, \dots, N/2, \quad (22)$$

$\sigma=1$ for $b=x$ and $\sigma=-1$ for $b=y$; θ_{xrnj} , θ_{xrnk} , θ_{yrnj} , and θ_{yrnk} are the j -th and k -th components of $\mathbf{\theta}_{xrn}$ and $\mathbf{\theta}_{yrn}$, respectively.

From equation (22), it follows that

$$H_{xxjk}(i\omega) = H_{xxkj}(i\omega), \quad (23)$$

$$H_{yyjk}(i\omega) = H_{yykj}(i\omega), \quad (24)$$

and

$$H_{yxjk}(i\omega) = -H_{xykj}(i\omega). \quad (25)$$

Thus, the properties (18), (19), and (20) of the frequency response matrix have been rederived, and it is obvious that they are also valid separately for each mode.

7 Numerical Example

To illustrate the theory, the example of a rigid rotor supported by two identical anisotropic bearings is taken from Lee and Joh (1993) and described by the coordinates used in this paper. A schematic view of the rotor is given in Figure 1.

The system submatrices appearing in equation (7) are given as

$$\mathbf{M}_x = \mathbf{M}_y = \frac{1}{L^2} \begin{bmatrix} mL_2^2 + I_t & mL_1L_2 - I_t \\ mL_1L_2 - I_t & mL_1^2 + I_t \end{bmatrix}, \quad (26)$$

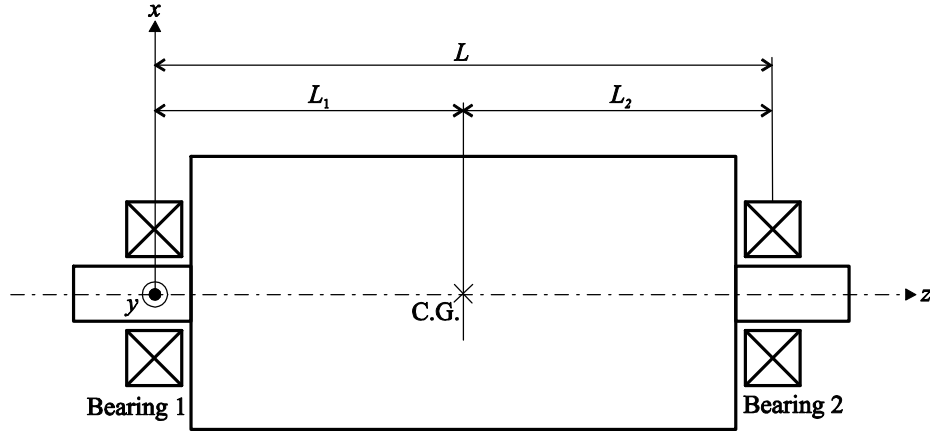


Figure 1. Rigid rotor-bearing system

$$\mathbf{C}_x = \begin{bmatrix} c_{xx} & 0 \\ 0 & c_{xx} \end{bmatrix}, \quad \mathbf{C}_y = \begin{bmatrix} c_{yy} & 0 \\ 0 & c_{yy} \end{bmatrix}, \quad (27)$$

$$\mathbf{K}_x = \begin{bmatrix} k_{xx} & 0 \\ 0 & k_{xx} \end{bmatrix}, \quad \mathbf{K}_y = \begin{bmatrix} k_{yy} & 0 \\ 0 & k_{yy} \end{bmatrix}, \quad (28)$$

$$\mathbf{G}_0 = \frac{\Omega}{L^2} \begin{bmatrix} I_p & -I_p \\ -I_p & I_p \end{bmatrix} + \begin{bmatrix} c_{xy} & 0 \\ 0 & c_{xy} \end{bmatrix}, \quad \text{and} \quad \mathbf{N}_0 = \begin{bmatrix} k_{xy} & 0 \\ 0 & k_{xy} \end{bmatrix}, \quad (29)$$

where m is the rotor mass, I_t and I_p are the transverse and polar mass moments of inertia about the centre of gravity of the rotor, Ω is the rotational speed, and the distances L , L_1 , and L_2 are depicted in Figure 1; c_{xx} , c_{xy} , c_{yx} , c_{yy} and k_{xx} , k_{xy} , k_{yx} , k_{yy} are the damping and stiffness coefficients of the bearings. Due to the fact that $c_{yx} = -c_{xy}$ and $k_{yx} = -k_{xy}$, the rotor under consideration complies with the model structure (7). For model parameters according to Table 1, the right and left eigenvalue problems are solved, and the resulting eigenvalues and eigenvectors are listed in Table 2. It is obvious that each pair of corresponding right and left eigenvectors satisfies the relationship (12). Moreover, the frequency response functions $H_{xy11}(i\omega)$ and $H_{yx11}(i\omega)$ are depicted in Figure 2 and apparently satisfy the property (25). For the rotor under consideration, all modal parameters can be identified exactly from one row or column of the frequency response matrix even though the bearings are not isotropic.

Table 1. Model parameters of the rigid rotor-bearing system.

m	8 kg
L_1/L	0.5
L_2/L	0.5
I_t/L^2	0.45 kg
I_p/L^2	0.15 kg
Ω	10 000 rpm
c_{xx}	300 Ns/m
c_{yy}	300 Ns/m
c_{xy}	20 Ns/m
k_{xx}	3 900 000 N/m
k_{yy}	4 100 000 N/m
k_{xy}	50 000 N/m

Table 2. Modal parameters of the rigid rotor-bearing system (complex conjugates not included).

mode	eigenvalue $\lambda_n(s^{-1})$	right eigenvector θ_{rn}	left eigenvector θ_{ln}
1 backward	$-38.9+988.0i$	1 1 $0.2524+0.1184i$ $0.2524+0.1184i$	1 1 $-0.2524-0.1184i$ $-0.2524-0.1184i$
1 forward	$-36.1+1010.5i$	1 1 $3.2220-1.5459i$ $3.2220-1.5459i$	1 1 $-3.2220+1.5459i$ $-3.2220+1.5459i$
2 backward	$-165.2+1922.1i$	1 -1 $-0.0011+0.8564i$ $0.0011-0.8564i$	1 -1 $0.0011-0.8564i$ $-0.0011+0.8564i$
2 forward	$-168.2+2297.1i$	1 -1 $-0.0012-1.1387i$ $0.0012+1.1387i$	1 -1 $0.0012+1.1387i$ $-0.0012-1.1387i$

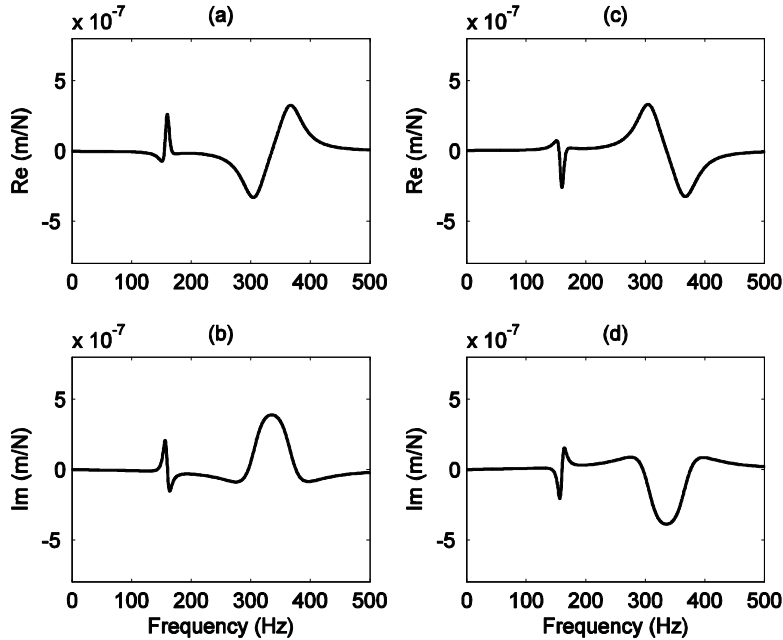


Figure 2. Selected frequency response functions of the rigid rotor-bearing system. (a): real part of $H_{xyII}(i\omega)$, (b): imaginary part of $H_{xyII}(i\omega)$, (c): real part of $H_{yxII}(i\omega)$, (d): imaginary part of $H_{yxII}(i\omega)$.

8 Conclusion

For rolling element and tilting pad bearings, the stiffness and damping matrix of the rotor are free from cross-coupling terms if bearing loads are confined to a coordinate plane through the rotor axis. Under these conditions, a simple relationship between right and left eigenvectors has been derived; the rows of the frequency response matrix have been related to its columns, and the elements of the frequency response matrix have been expressed in terms of eigenvalues and right eigenvectors. The results allow for advanced applications of modal testing even if the rotor can only be excited in one degree of freedom.

Acknowledgement

The author would like to thank Prof. Dr. Helmut Springer for his encouragement and advice.

References

Bucher, I.; Ewins, D.-J.: Modal analysis and testing of rotating structures. *Phil. Trans. R. Soc. Lond. A*, 359, (2001), 61-96.

Childs, D.-W.; Vannini, G.; Delgado, A.: Tilting-pad bearings: measured frequency characteristics of their rotordynamic coefficients. In: *Proc. Fortieth Turbomachinery Symposium* Houston, Texas, Sept. 12-15 (2011).

Dietl, P.: *Damping and Stiffness Characteristics of Rolling Element Bearings*. PhD Thesis, Vienna University of Technology, Vienna (1997).

Dimond, T.; Younan, A.; Allaire, P.: A review of tilting pad bearing theory. *International Journal of Rotating Machinery*, (2011), Article ID 908469, 23 pages, doi:10.1155/2011/908469.

Genta, G.: *Dynamics of rotating systems*. Springer, New York (2005).

Gutierrez-Wing, E.-S.: *Modal analysis of rotating machinery structures*. PhD Thesis, Imperial College, London (2003).

Irretier, H.: Mathematical foundations of experimental modal analysis in rotor dynamics. *Mechanical Systems and Signal Processing*, 13(2), (1999), 183–191.

Krämer, E.: *Dynamics of rotors and foundations*. Springer, Berlin (1993).

Lee, C.-W.: A complex modal testing theory for rotating machinery. *Mechanical Systems and Signal Processing*, 5(2), (1991), 119–137.

Lee, C.-W.; Joh, Y-D.: Theory of excitation methods and estimation of frequency response functions in complex modal testing of rotating machinery. *Mechanical Systems and Signal Processing*, 7(1), (1993), 57–74.

Meirovitch, L.: A new method for the solution of the eigenvalue problem for gyroscopic systems. *AIAA Journal*, 12(10), (1974), 1337-1342.

Meirovitch, L.; Ryland, G.: Response of slightly damped gyroscopic systems. *JSV*, 67(1), (1979), 1-19.

Nordmann, R.: Identification of the modal parameters of an elastic rotor with oil film bearings. *Transactions of the ASME – Journal of Vibration, Acoustics, Stress, and Reliability in Design* 106, (1984), 107–112.

Someya, T.: *Journal-Bearing Databook*. Springer, Berlin, Heidelberg (1989).

Wang, W.; Kirkhope, J.: New eigensolutions and modal analysis for gyroscopic/rotor systems, Part 1: Undamped systems. *JSV*, 175(2), (1994a), 159–170.

Wang, W.; Kirkhope, J.: New eigensolutions and modal analysis for gyroscopic/rotor systems, Part 2: Perturbation analysis for damped systems. *JSV*, 175(2), (1994b), 171–183.

Wyckaert, K.; Augusztinovicz, F.; Sas, P.: Vibro-acoustical modal analysis: reciprocity, model symmetry, and model validity. *The Journal of the Acoustical Society of America*, 100(5), (1996), 3172–3181.

Zhang, Q.; Lallement, G.; Fillod, R.: Relations between the right and left eigenvectors of non-symmetric structural models. Applications to rotors. *Mechanical Systems and Signal Processing*, 2(1), (1988), 97–103.

Address: Dr. Gudrun Mikota, Institute of Machine Design and Hydraulic Drives, Johannes Kepler University Linz, Altenbergerstrasse 69, A-4040 Linz, Austria
email: gudrun.mikota@jku.at

More Flexible Damping Systems for Blades and Vanes

A. Hartung, H.-P. Hackenberg, U. Retze

The blades and the vanes of aero engines are subject to very high thermo-mechanical loads. In some cases, an additional damping system is necessary to reach the lifetime goals. Commonly, damping systems based on energy dissipation due to friction are used, e.g. under platform dampers for blades and spring dampers for the vanes. These damping systems have some limitations: under platform dampers work well mostly for just one mode family, their effectiveness is limited relative to rotational speed (because of the associated contact forces) and is dependent on the excitation order. The spring dampers work well for more than one mode family but their effectiveness is limited concerning the available contact force (just one value). Additionally, the use of the spring dampers requires a significant, sometimes suboptimal design change of the vane cluster. In this paper, some alternative damping systems are introduced and analyzed. All these new systems offer additional possibilities for damping and give more design flexibility. Two of them: insert damping and rocking damping are also based on frictional energy dissipation. The third one, impulse mistuning, adopts a special kind of absorption and is based on the so called targeted energy transfer. The analytical results for the insert damping systems were presented previously in Borufka et al. (2009), while in this paper the experimental validation by shaker tests is shown. The rocking damping was not presented so far – to the knowledge of the authors. Impulse mistuning was first presented in: Hartung and Retze (2011) and Hartung et al. (2016). In this work, an overview of such damping systems and some additional information on the experimental validation of some impulse mistuning systems are presented.

1 Damping Systems for Blades and Vanes: State of the Art

As mentioned above, the blades and vanes of modern aero engines are subject to very high thermomechanical loads and in some cases an additional damping system is necessary to reach the life targets, before high cycle fatigue (HCF) damage occurs. The HCF damage could be caused by different kinds of vibrations: forced synchronous vibrations (SV), driven by resonances with excitation or engine orders (EO), forced non-synchronous vibrations (NSV) and self-excited non-synchronous vibrations (flutter). In Figure 1, a sketch of a Campbell diagram with all these kinds of vibrations from Krack et al. (2016) complemented by indication of excitation orders is plotted. In Figure 2, the measured Campbell diagram of a blade stage from a MTU test engine is shown. Different kinds of vibration are visible, however an example of NSV is not absolutely identified. All of this would be analyzed during the analytical development and during engine validation. The need for a damping system arises when one (or more) of types of vibration lead to an HCF problem. The state of the art of damping systems for the blade stages are under-platform dampers, for the vanes, respectively, vane clusters – damper-springs. Both types of designs are depicted in Figure 3. The acting principle of both damping system is energy dissipation due to friction. These damping systems could be designed to be very effective in damping of the (mostly one, sometimes two) mode shape(s) or mode family causing an HCF concern. Hereby only mode shapes with enough relative motion between the blade or vane and the damper can be damped effectively. Additionally, the dampers are designed for limited rotation speed intervals only – due to the fixed geometry and the fixed mass of the damper. Consequently, the limitations of the under-platform dampers are:

- Mode family (mostly just one)
- Rotation speed interval
- Excitation order

and the limitations of the spring-dampers:

- Mode family (mostly 1-2)
- Friction force (just one value)

The strategic aim of turbine makers is to invent and to integrate the damper design with significantly fewer limitations. In this paper, three different damping systems with reduced effectiveness' limitations than the state of the art dampers are analyzed.

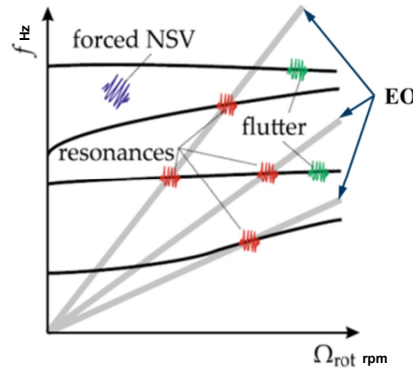


Figure 1. The schematic Campbell diagram from Krack et al. (2016) including excitation orders (EO)

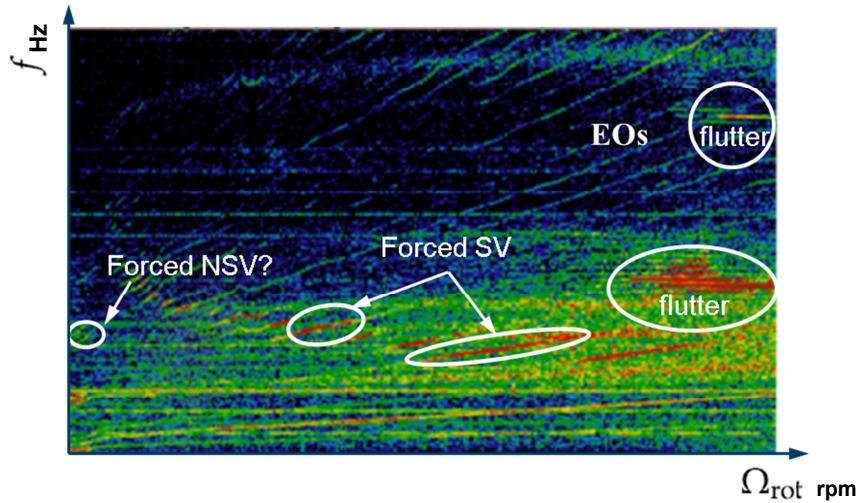


Figure 2. The measured Campbell diagram of a blade stage, from an MTU test aero engine

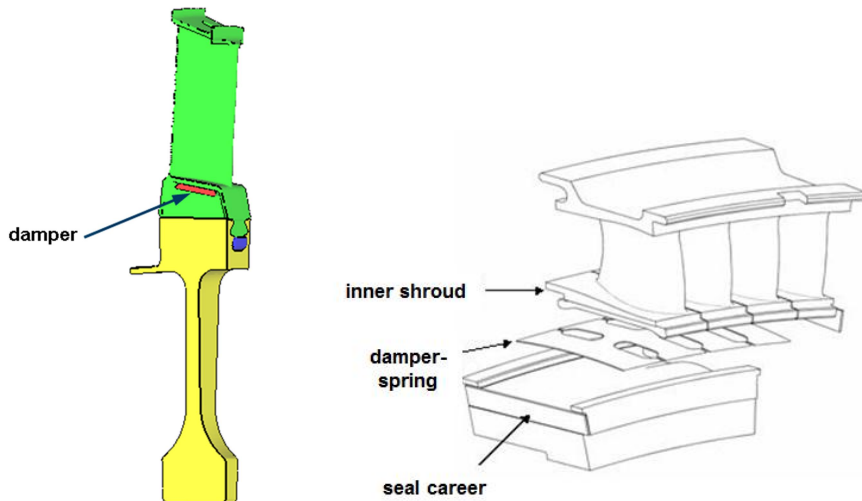


Figure 3. Examples of the common blade and vane damping systems – under-platform damper and damper-spring

2 Insert damping Systems

An insert damping system is a combination of a damping device and a cooling system which requires the use of hollow blades. For this reason, the insert damping system is independent of the excitation order. The idea of combining the damping and cooling system for hollow blades and vanes is not new. In Borufka et al. (2009), some design ideas from different patent applications were shown, followed by the presentation of the MTU design “Insert Damping System” with analytical results of the damping effectiveness. In the present paper, a brief overview of the most important topics from Borufka et al. (2009) will be given, supplemented with new experimental results.

The design idea of the insert damping system is shown in Figure 4. It entails complementing the cooling system “insert” with “pedestals”, which are in frictional contact with specific positions of the airfoil. These positions will be designed dependent on the resonant mode shapes. In Figure 5, this is indicated for two resonant mode shapes, first bending (1F) and first torsion mode (1T). During the resonance passage, the energy dissipation due to friction between pedestals and the airfoil leads to the reduction of the vibration stresses and avoidance of HCF damage.

The proof of the damping effectiveness for the design shown in Fig. 4 and 5 was given in Borufka et al. (2009) as well and is plotted in Figure 6. The amplitude reduction for the 1F mode was 40% and for the 1T mode 70%. The analysis was performed to engine conditions. Due to a moved static equilibrium, the curves in Figure 6 are not symmetric anymore. In the same paper, robustness of this design concerning friction coefficient and hence concerning contact conditions in general was proven.

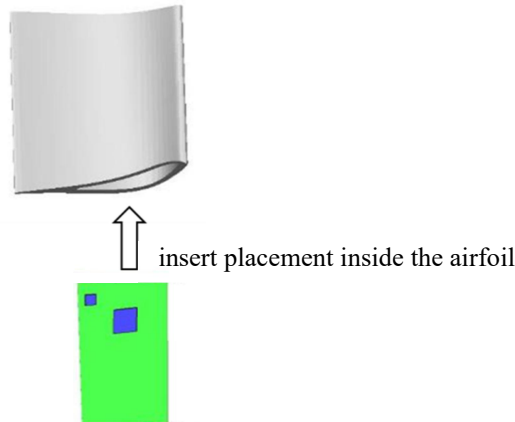


Figure 4. Design idea of the insert damping system: cooling system insert with “pedestals” from Borufka et al. (2009)

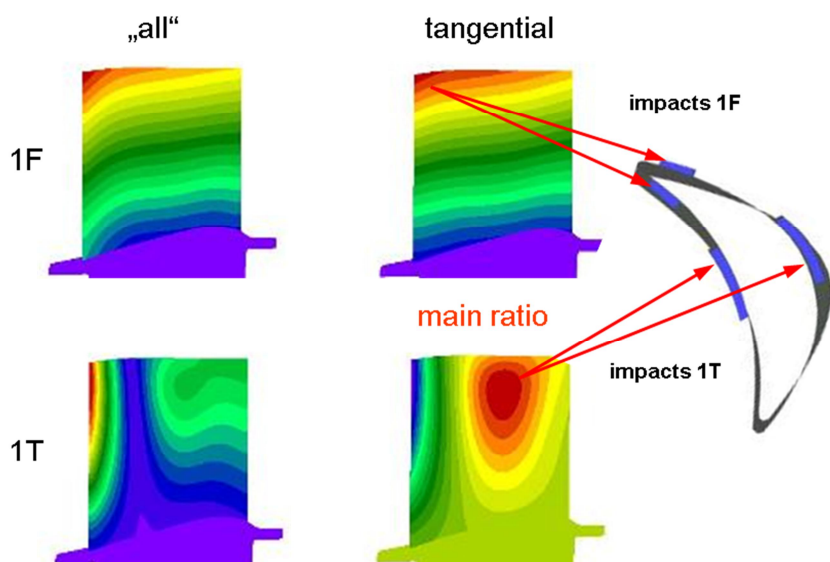


Figure 5. Design development of the insert damping system, Borufka et al. (2009)

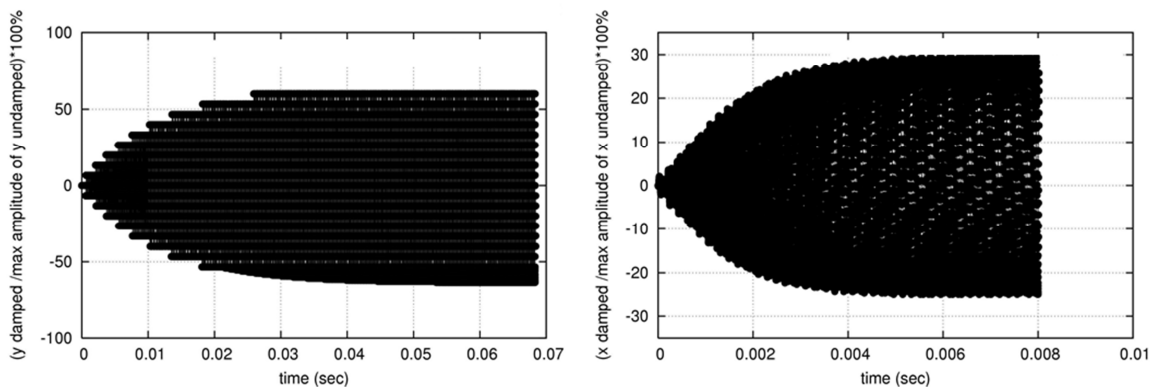


Figure 6. Proof of the damping effectiveness of the insert damping system, Borufka et al. (2009)

Recently, the experimental validation of the insert damping concept was performed at MTU Aero Engines. For this reason, a shaker test specimen was developed and manufactured. The specimen including design features (pedestal positioning) is shown in Figure 7. The blade root cannot be shown for confidentiality reasons. Because of the significant difference between laboratory and engine conditions, it was not possible to test exactly the same design as analyzed in Borufka et al. (2009). However, the test constitutes an appropriate concept validation. Just mode shape 1T was tested, the comparison of the measured and calculated mode shapes including the placement of the characteristic node for experimental vibration comparison is plotted in Figure 8. Additionally, the positioning of the substitute excitation for the linear plausibility proof is explained. The experimental results as measured forced response curves on this characteristic node with and without insert are plotted in Figure 9. Additionally to the measured curves, linear steady state dynamics calculations with measured equivalent linear damping ratios are depicted as well. The substitute excitation for the linear calculation was adjusted to the measurements without inserts. The measured amplitude reduction of 56% compared to the measurements without inserts confirm the possibility of high damping potential of the insert damping. The plausibility proof with the linear analysis (amplitude reduction 60%) proceeded successfully as well.

Summary of the conclusions concerning insert damping system:

- Independent on the excitation order
- Damping of more than one mode family simultaneously conditionally possible
- Robust concerning contact conditions
- Experimentally validated in a shaker test
- Flexibility concerning rotation speed is limited: it deals with one contact force similar to the state of the art damping systems

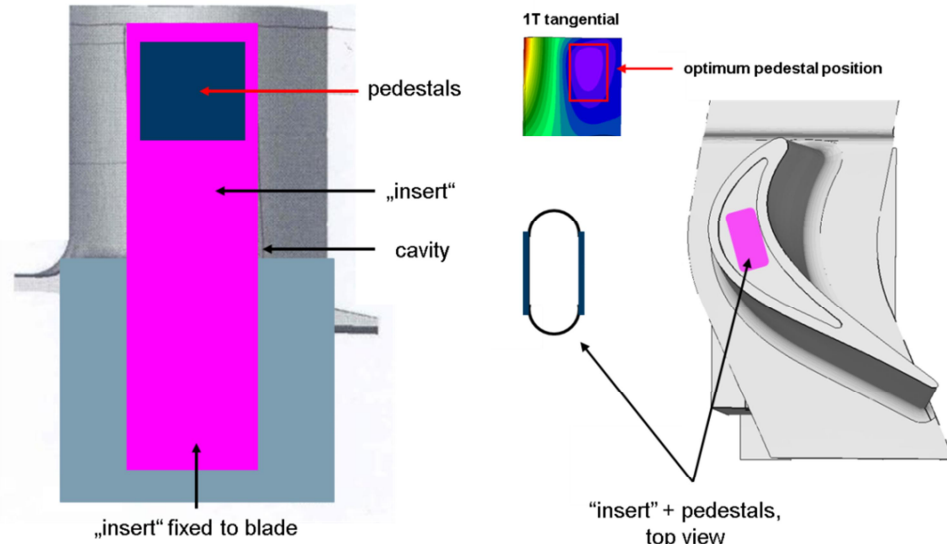


Figure 7. Specimen for the shaker test and explanation of the pedestals positioning

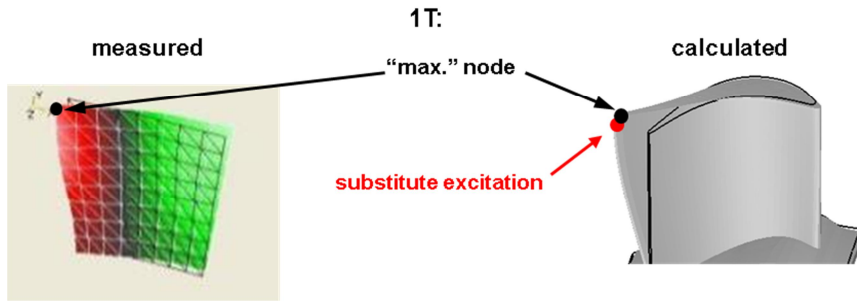


Figure 8. Measured and calculated mode shapes 1T and explanation of the characteristic node to comparison of the experimental results and linear proof of its plausibility as well as positioning for the substitute excitation in the numerical analysis

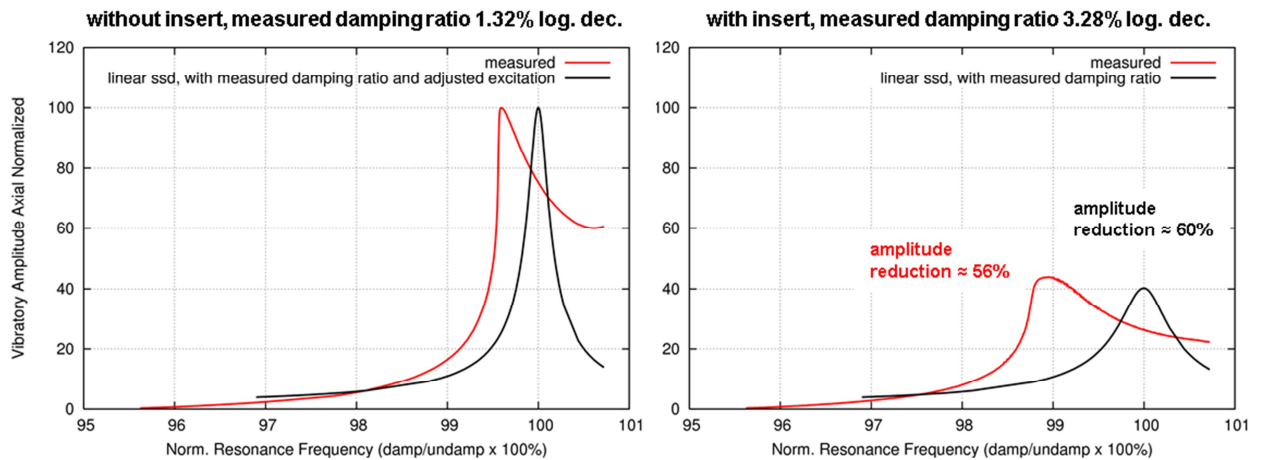


Figure 9. Measured and calculated results on the characteristic node

3 Rocking Damper

The second damping system, which is independent of the excitation order, is the rocking damper. This is only possible for blades with a “cover plate” as a special design feature. Cover plates are seals placed on the face side of the blades. Hence rocking dampers can only be used together with cover plates or similar features. The design of a rocking damper will not be shown in this paper, but two substitute models are analyzed in Erbts (2011). Here, two new damping systems are analyzed, the rocking damper being one of them. In the following, the most important results of this work are presented.

In Figure 10a, a sketch of dummy rocking damper with a dummy carrier is given (necessary to illustrate the boundary conditions on the damper because of the cover plate), Figure 10b shows a sketch of the assembly with a dummy blade, and Figure 10c the placement for a real blade.

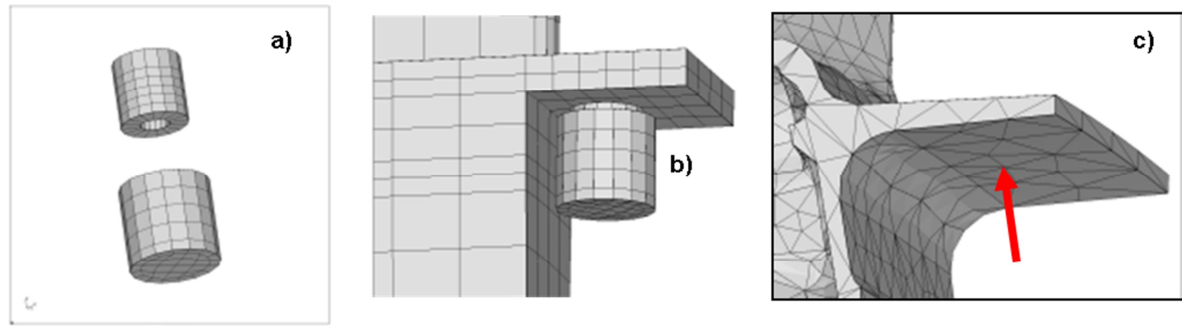


Figure 10. Geometrical features of the rocking damper derived from Erbts (2011). a) dummy damper and carrier, b) assembly of these dummy with a dummy blade, c) placement of the rocking damper for a real blade

In Erbts (2011) a real blade with substitute damper was analyzed, whereas two substitute models were analyzed, a lumped parameter model and a finite element model (in CalculiX) with a regularized contact formulation realized in a user-subroutine. The preparation of the lumped parameter model for the mode shape 1F free shroud is exemplarily explained in Figure 11.

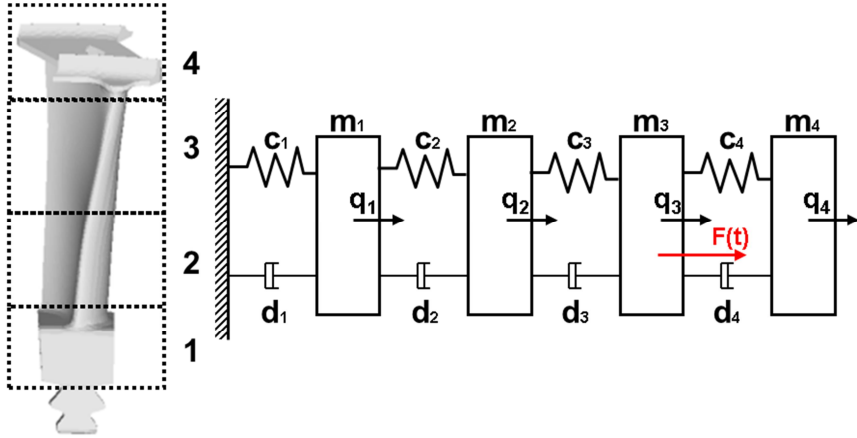


Figure 11. Lumped parameter model of the undamped blade, Erbts (2011)

The parameters shown in this Figure are:

c_k – substitute stiffness, derived from the relevant mode shape and eigen frequency,

d_k – substitute damping ratios, derived from the substitute stiffness,

q_k – generalized coordinates chosen concerning the dominant direction of the relevant mode shape,

$F(t)$ – substitute aero-elastic excitation force of the relevant resonance crossings, derived by forced response prediction or from testing.

In the simulations, harmonic excitation was assumed.

The modelling of the damper influence was proposed in Erbts (2011) as follows: In case of sticking damper conditions, the motion of the substitute lumped mass m_1 is suppressed:

$$q_1'' = q_1' = 0, \quad (1)$$

hence a three D.O.F. linear ordinary differential equations system with an additional algebraic condition for the contact force F_C to prove the end of sticking (whenever the contact force is larger than Coulomb's sliding friction force F_T) needs to be solved. In case of sliding, a four D.O.F linear ordinary differential equations system with the additional Coulomb friction force is to be solved. The condition for the end of the sliding becomes

$$q_1' = 0 \text{ and } F_C < F_T \quad (2)$$

Such lumped parameter models have to be prepared for each mode shape separately. The analysis with the lumped-parameter models were performed in the time domain until steady state conditions were reached. In Erbts (2011), two mode shapes, 1F and 1T, both with free shrouds, were analyzed.

The second substitute model, prepared and analyzed in Erbts (2011), was a standard FE model of the blade with a simple follow regularized contact formulation:

$$F_T = -\mu F_N \psi, \quad \psi = \begin{cases} -1, & \text{if } q'_T < -\varepsilon \\ q'_T/2\varepsilon & \text{if } -\varepsilon < q'_T < \varepsilon \\ 1, & \text{if } q'_T > \varepsilon \end{cases} \quad (3)$$

The analysis with the second model was also performed in the time domain but in difference to the lumped-parameter model as a transient resonance passage through the resonance using the approach described in Hartung (2010). Care was taken to ensure that the frequency sweep velocity is slow enough to obtain stationary amplitudes during transient passage.

Based on the simulation with both models, the diagrams in Figure 12 are provided. The diagrams contain just amplitudes of the simulations, normalized to the analysis without the damper.

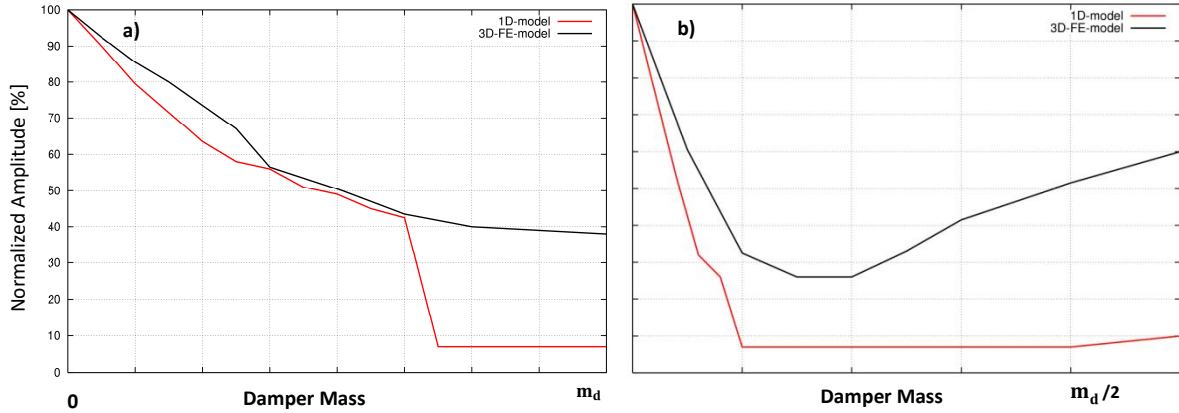


Figure 12. Normalized maximum amplitude over the rocking damper mass: a) 1F, b) 1T

The results show good agreements between 1D and 3D-FE-analysis for 1F until sticking. Discrepancies between 1D and 3D for 1T are related to the simple lumped parameter model. From the authors' point of view, these very different simulations give the numerical validation for the damping effectiveness of the rocking damping system. The finite element results in Figure 12 show that it is possible to damp simultaneously both mode shapes, 1F and 1T (Figure 13).

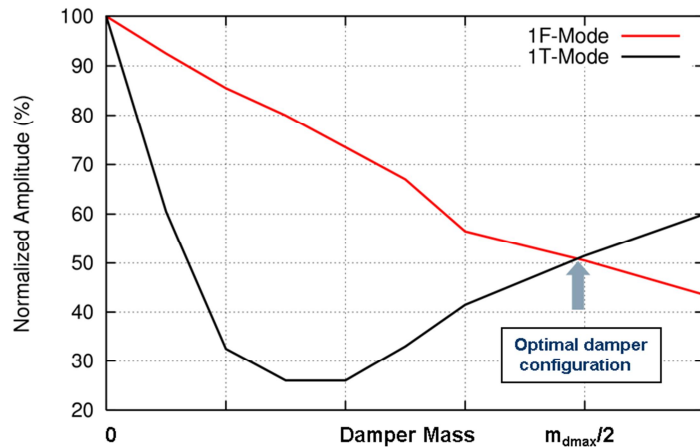


Figure 13. Evaluation of the optimal rocking damper configuration for simultaneously damping both mode shapes, 1F and 1T

For the analyzed blade, the evaluated damper mass is a realistic one – a rocking damper could be designed if necessary.

Summary of conclusions concerning rocking dampers:

- Independent of the excitation order
- Damping of more than one mode family simultaneously conditionally possible
- Robust concerning contact conditions
- Numerically validated on two different models
- Limited flexibility concerning rotation speed: it deals with one contact force similar to the state of the art damping systems

4 Impulse mistuning Systems

The idea of the Impulse Mistuning Systems goes back to the attempt to damp the blades and vanes by free moving bodies placed e.g. inside of the airfoils. The idea of the inside damping systems is not new generally,

some references are given in Borufka et al. (2009), Hartung and Retze (2011) and Hartung et al. (2016). To make a classification of the inside damping systems for blades and vanes, the Figure 14 is prepared.

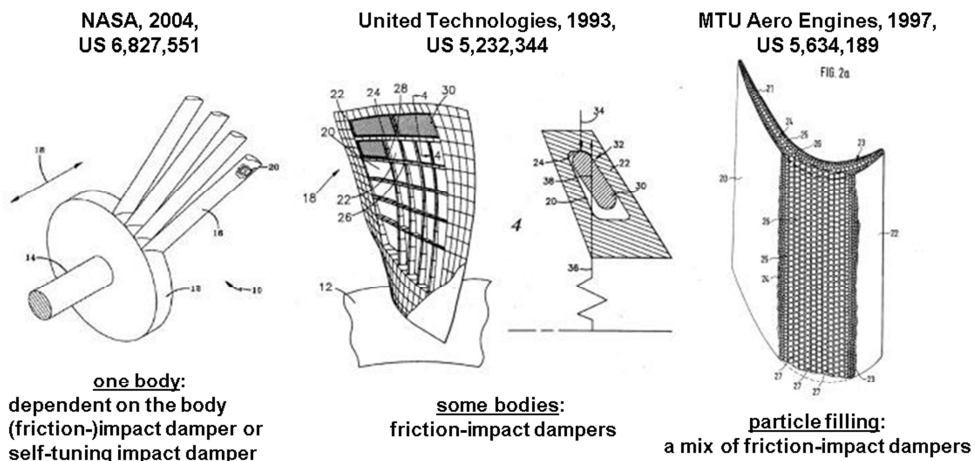


Figure 14. Some examples of inside, (friction)-impact based dampers from Borufka et al. (2009)

The most important features of the damping systems shown here are the geometry and the mass of the bodies, the number of bodies in a cavity and the geometry of the cavities. Dependent on all of this, the inside damping systems work as impact, friction-impact, particle or self-tuning impact dampers, as highlighted in Hartung and Retze (2011) and Hartung et al. (2016). In these papers was shown, that assumed only one body is placed in a cavity and for much smaller dimensions of the damping bodies and of the cavities another acting principle is active: mistuning of the resonance frequency due to impacts – “impulse mistuning”. Impulse mistuning could be also described as a special kind of vibration-impact nonlinear energy sinks (VI-NES) with a large capability of energy absorption and negligible contribution of energy dissipation. The mass ratio of such VI-NES to the main system is <1%. There are also some other types of Nonlinear Energy Sinks: e.g. friction or non-linear stiffness based. The acting of the Nonlinear Energy Sinks lead to Targeted Energy Transfer (TET): one-way directed transfer of energy from a primary subsystem to a nonlinear attachment. References and more explanations are given in Hartung et al. (2016). In difference to the energy dissipation based damping systems, the impulse mistuning systems work for a larger interval of rotation speed (for all speeds below a critical value) in case of blade and has no dependency on the contact pressure in case of vanes. Additionally, every mode shape with enough movement at the cavity will be damped, independent of the direction of the motion – more than one mode family could be damped. In Hartung et al. (2016) damping of two mode shapes for a turbine blade was presented: from analytical prediction until experimental validation in a rotated rig. The validation in an engine demonstrator was mentioned. A vane Impulse Mistuning System with five bodies (mistuners) for a vane was analyzed in Hartung et al. (2016) as well. In this case, the robustness of the mistuning system concerning masses of the bodies and the gaps between the mistuners as well as the cavity walls was analyzed analytically and proved experimentally. The damped vane mode shape in Hartung et al. (2016) was a “1E cluster” mode (Figure 15a). Beside the cluster mode shapes so-called airfoil mode shapes could be HCF-critical as well. Because of design features of the vane clusters it is not possible to damp the airfoil mode shapes with a friction based damping system. For such a mode shape, “1T-Airfoil”, experimental analysis of another vane cluster (Figure 15b) was performed at MTU recently and will be presented below for the first time. The test series consisted of five shaker tests of the vane cluster (Figure 15b): without dampers and with four impulse mistuning systems - two different designs of the impulse mistuning system with three different manufacturing approaches were tested. A special feature of the airfoil mode shapes is that a family of such mode shapes exist in the vicinity of each other instead a single resonance in case of the cluster mode shapes. So, first the identification of these was performed (Figure 16). Mode 3 is the most relevant for the engine. For this mode and the relevant excitation level, the highest amplitude reduction of 40% with one of the tested impulse mistuning systems was established (Figure 17). The second result of this test series is, that the impulse mistuning system produced with three different manufacturing technologies showed no significant difference in damping effectiveness.

Summary concerning Impulse Mistuning systems:

- Suitable for both, blades and vanes, respectively. vane clusters
- Action principle: frequency mistuning due to impulses, targeted energy transfer
- Independent on the excitation order
- Robustness concerning design parameters and production technologies proven

- Damping of more than one mode family simultaneously often possible
- Fully validated – including engine experiences, Hartung et al. (2016)
- A very large flexibility concerning the contact force

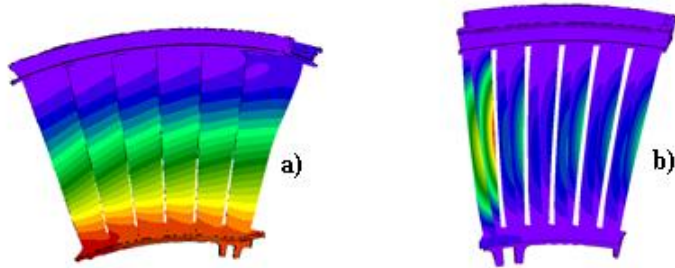


Figure 15. Analyzed vane cluster mode shapes a) “1E cluster”, Hartung et al. (2016), b) “1T airfoil”

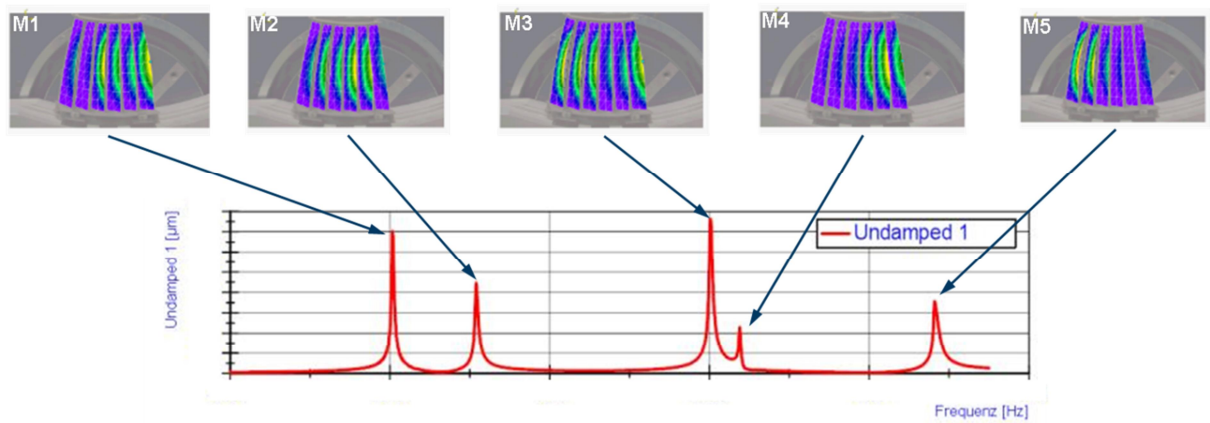


Figure 16. Measured and identified “1T airfoil” mode family

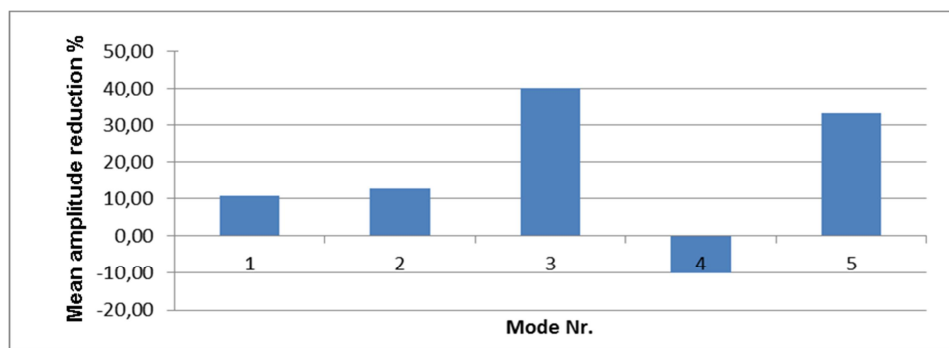


Figure 17. Measured mean amplitude reduction mode shape “1T airfoil” for the second impulse mistuning system averaged over all test samples manufactured using three different production technologies

5 Conclusions

Three different new damping systems independent of the excitation order are presented. All three systems are analyzed and validated using the different analytical and experimental methods. All three systems showed good capability of damping effectiveness. Insert and Rocking Dampers could be designed more flexible than under-platform dampers concerning simultaneously damping of more than one mode family but are limited concerning using for different rotation speeds. This restriction is of general quality because of the acting principle of energy dissipation due to friction. Impulse mistuning systems showed the highest effectiveness and flexibilities: concerning the rotation speed, mode families and production technologies.

Acknowledgments

The authors would like to thank MTU Aero Engines AG for the permission to publish this paper. The partial funding of the work through the Clean Sky Program of the European Commission is gratefully acknowledged. The authors also would like to thank all members of the “Impulse Mistuning” project team within the MTU Aero Engines AG and Patrick Erbts, former student of the Leibniz University of Hannover for the successful performed Master Thesis with MTU Aero Engines AG.

References

Borufka, H. P.; Arrieta, H. V.; Hartung, A.: Insert Damping of Hollow Airfoils. *Proceedings of the ASME Turbo Expo 2009*, (2009), GT2009-59976, Orlando, Florida, USA.

Erbts, P.: Modelling and analysis of two new damping systems for turbine blades. *Master Thesis*, (2011), Leibniz University of Hannover, Institute of Dynamics and Vibrations (unpublished).

Hartung, A.; Retze, U.: Multi-Body Damping of a Vane Cluster. *Proceedings of the ASME Turbo Expo 2011*, (2011), GT2011-45666, Vancouver, Canada.

Hartung, A.; Retze, U.; Hackenberg, H.-P.: Impulse Mistuning of Blades and Vanes. *Proceedings of the ASME Turbo Expo 2016*, (2016), GT2016-56433, Seoul, South Korea.

Hartung, A.: A numerical approach for the resonance passage computation. *Proceedings of the ASME Turbo Expo 2010*, (2010), GT2010-22051, Glasgow, UK.

Krack, M.; Salles, L.; Thouverez, F.: Vibration Prediction of Bladed Disks Coupled by Friction Joints. *Arch. Computat. Methods Eng.*, in press, (2016), pp. 1-48, Springer, DOI 10.1007/s11831-016-9183-2.

Address: MTU Aero Engines AG, Dachauer Str. 665, 80995 Munich, Germany
email: andreas.hartung@mtu.de

On Dynamics and Stability of the Automotive Engine Turbocharger Rotor Supported by the Electrodynanic Passive Magnetic Bearings

T. Szolc

In the paper dynamic investigations on the automotive turbocharger rotor-shaft supported on the electro-dynanic passive magnetic bearings (EDPMB) and on the traditional floating-ring journal bearings have been carried out using a computer model. The results of computations obtained for the two mutually compared kinds of suspension are demonstrated in the form of Campbell diagrams and amplitude-frequency characteristics. Here, the main attention is focused on resonant-free operation ability assured by the support on the EDPMBs. Moreover, conditions of stability for the support on the journal bearings and on the EDPMBs have been investigated by means of the eigenvalue analysis. There is studied an influence of skew-symmetrical dynamic properties of the both kinds of rotor-shaft suspensions caused by the bearing stiffness negative cross-coupling terms as well as by the gyroscopic effects which are particularly severe at turbocharger high rotational speeds.

1 Introduction

The turbocharger is now viewed as feasible option when looking for an output power increase in a broad variety of internal combustion reciprocating petrol- and diesel engines. At present, this device is frequently applied in passenger car engines subjected to the downsizing tendency. Despite of the fact that the modern turbochargers have reached a relatively high level of robustness and operational excellence, there are still observed various problems with floating-ring journal bearings commonly supporting rotor-shafts of these devices. Namely, the turbocharger rotor-shafts supported by this kind of bearings often indicate a tendency to self-excitations and sub-synchronous oscillations leading to instability (Schweizer (2009), Kamesh (2011), Koutsovasilis and Driot (2015), Göbel et al. (2015)). Turbocharger rotors with foil-air bearing show analogous problems like self-excitations which lead to instability, what is carried out in the studies of Bonello (2016). Since maximal rotational speeds of the relatively light-weight turbocharger rotors reach 200,000 rpm and more, their suspension on another touch-less and lubricant-free bearings seems to be very required. For this purpose passive magnetic bearings (PMB) could be particularly promising. Actually, during the last 10-15 years, by means of the newest achievements of electrical engineering, electronics and material technology, various kinds of passive magnetic bearings (PMB) have been developed to give a chance for broad applications for numerous cases of the high-speed rotating machines. These are: the permanent magnet magnetic bearings (PMMB), superconductor passive magnetic bearings (SCPMB) and the electrodynanic passive magnetic bearings (EDPMB) which seem to be very advantageous here. In order to generate levitation forces these kinds of passive magnetic bearings use conductors mounted on the shaft and rotating in a magnetic field created by permanent magnets built-in the stators embedded in bearing housings. Then, eddy-currents are induced in the conductors, which generate the Lorenz forces levitating the rotor-shaft. The physical fundamentals for a passive magnetic levitation together with conditions of its stable operation can be found in Filatov et al. (2002). In Lempke (2005), Amati et al. (2008) and in Falkowski (2016) the concept of radial EDPMBs has been developed theoretically and by Lempke (2005) tested experimentally for the small-size high-speed rotating systems. The results of comparative rotordynamic analyses performed for the industrial centrifugal compressor and for the single-spool gas turbine supported on the EDPMBs as well as on the classical oil-film journal- and rolling-element bearings were demonstrated in Szolc and Falkowski (2014). The passive magnetic suspensions have got more important advantages then the active magnetic bearings (AMB). Namely, the EDPMBs do not need any power supply, enable us resonant-free operation, have a simple structure and they are cheaper than the AMBs. According to the above, in this paper in order to indicate mechanical advantages of the turbocharger rotor-shaft support on the EDPMBs, a comparative rotor-dynamic analysis has been performed, where the obtained results of computations were confronted with the analogous findings determined for the same rotor-shaft suspended by the floating-ring journal bearings.

2 Modelling of the Turbocharger-Rotor-Shaft System

The object of considerations is a typical automotive engine turbocharger rotor-shaft shown in Figure 1a. This rotating element is originally supported on two floating-ring oil journal bearings (#1 and #2). Its full geometry, material constants, inertial parameters as well as the journal bearing dimensions are taken from Göbel et al. (2015). This rotating system is expected to operate within the rotational speed range of 0-210,000 rpm. It consists of the flexible stepped shaft of the total length 0.16 m with attached two heavy disks corresponding respectively to the turbine and compressor rotor. The considered rotor-shaft is characterized by the entire mass of 0.564 kg and by the bearing span equal to 0.05 m. Such a structure can be very representative for a broad variety of turbochargers applied in internal combustion piston engines. Thus, this rotor-shaft system was theoretically slightly adopted to run on the electrodynamic passive magnetic bearings regarded here as a perspective alternative.

2.1 Modelling of the Rotor-Shaft

In order to obtain sufficiently reliable results of theoretical calculations for the considered rotor-shaft system, the dynamic analysis will be performed by means of the one-dimensional hybrid structural model consisting of finite beam elements and discrete oscillators. The flexural beam elements represent successive cylindrical segments of the stepped rotor-shaft. With an accuracy that is sufficient for practical purposes the heavy turbine and compressor rotors are substituted by rigid bodies attached to the respective beam-element extreme cross-sections. Using such a model, the rotor-shaft geometry as well as its material properties can be described in an identical way as in an analogous classical finite element model of the same structure. However, in the hybrid model inertial-visco-elastic properties of its beam elements are not discretized, but they have been left as naturally distributed in a continuous way. Such a hybrid model of the turbocharger rotor-shaft is presented in Figure 1b.

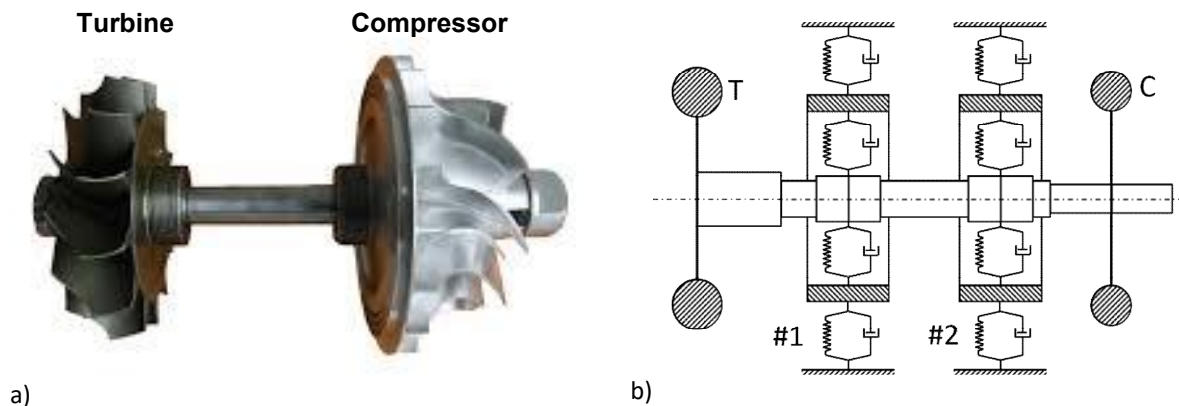


Figure 1: The automotive engine turbocharger rotor-shaft: the real object (a) and the hybrid model (b)

Here, each bearing support is represented by a dynamic oscillator of two degrees of freedom, where its rigid mass represents an inertia of the floating ring in the case of the journal bearing or an inertia of the stator elements in the case of the EDPMBs. Using such a model, apart from the magnetic field or oil-film interaction, also the visco-elastic properties of an embedding of both kinds of bearings in the turbocharger housings are taken into consideration. This bearing model makes possible to represent with a relatively high accuracy kinetostatic and dynamic anisotropic and anti-symmetric properties in the form of constant or variable stiffness and damping coefficients. The obtained in this way mutual combination of continuous finite elements together with discrete oscillators and rigid bodies according to the structure of the real object results in the hybrid mechanical model of the automotive turbocharger rotor-shaft system.

2.2 Modelling of the Electrodynamic Passive Magnetic Bearing

Here, dynamic modelling of the electrodynamic passive magnetic bearings reduces to determinations of their electromagnetic stiffness- and damping characteristics. For this purpose it is necessary to calculate the bearing global levitation force or the global radial ‘in-plane’ stiffness K regarded as a derivative of the Lorenz force with respect of the conductor-to-stator radial proximity (Lempke, 2005, Szolc and Falkowski, 2014, Falkowski, 2016). This target is usually achieved by computations carried out by means of advanced 3D finite element models of the electrodynamic bearing for various rotational speeds Ω or using the analytical-numerical method based on the Kirchhoff electrical circuit theory (Amati et al., 2008). All these approaches result in magnetic force and stiffness characteristics respectively very similar qualitatively to each other. Then, according to Lempke (2005), the main (rotor)- and cross-coupling stiffness components of the EDPMB can be determined for selected successive values of the rotor-shaft rotational speed by means of the following formulae:

$$\begin{aligned} k_{xx}(\Omega) &= k_{yy}(\Omega) = K(\Omega) \cos \theta, \\ k_{xy}(\Omega) &= K(\Omega) \sin \theta = -k_{yx}(\Omega), \end{aligned} \quad (1)$$

where $\theta = \text{arc tan}(R/\Omega L)$ is the so called ‘force angle’ expressed as a function of the magnetic bearing coil resistance R and inductance L . Nevertheless, for the need of numerical simulations and qualitative analyses the bearing main (rotor)- and cross-coupling stiffness values obtained for several successive rotational speed values can be approximated using the following continuous analytical functions:

$$\begin{aligned} k_{xx}(\Omega) &= k_{yy}(\Omega) = K_R \cdot f^\alpha \cos \left(\text{arc tan} \left(\frac{\beta}{f} \right) \right), \\ k_{xy}(\Omega) &= -k_{yx}(\Omega) = K_C \cdot f^\delta \sin \left(\text{arc tan} \left(\frac{\gamma}{f} \right) \right), \\ f &= \frac{\Omega}{2\pi}, \end{aligned} \quad (2)$$

where K_R , K_C , α , β , δ and γ are the proper fitting coefficients. In Figure 2a there are presented the rotor main- and cross-coupling stiffness characteristics determined using formulae (2) for the EDPMBs suspending the considered turbocharger rotor-shaft system within its entire operating rotational speed range. These plots have been obtained for $K_R=3.5 \cdot 10^4$ N/m, $K_C=6.32 \cdot 10^3$ N/m, $\alpha=0.05$, $\beta=270.0$, $\delta=0.3$ and $\gamma=270.0$ and they are

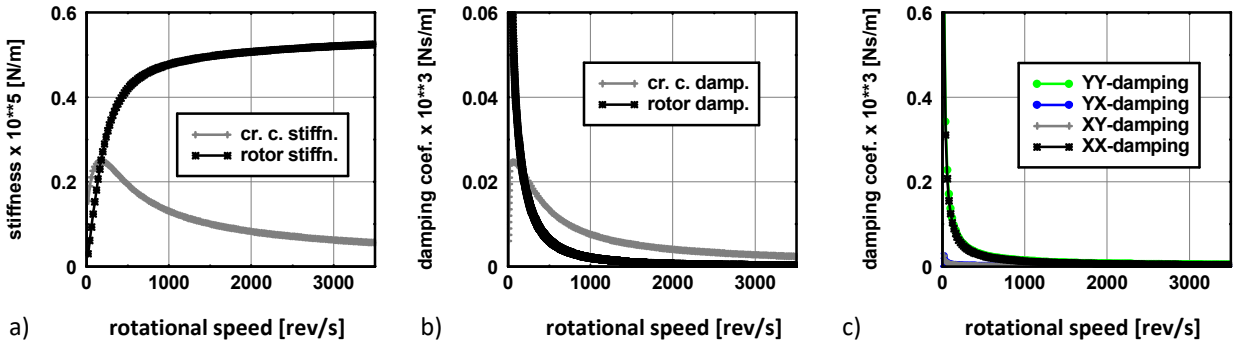


Figure 2: Stiffness (a) and damping (b) characteristics of the EDPMB, damping characteristics of the inner floating-ring journal bearing (c)

qualitatively identical with those obtained in Lempke (2005), Amati et al. (2008), Szolc and Falkowski (2014), Falkowski (2016) for high-speed rotor machines different than investigated here. For the listed fitting coefficient

values the static turbocharger rotor-shaft vertical displacement off-set in the bearing stators due to the gravitational forces does not exceed 0.11 mm. Then, according to Lempke (2005), Szolc and Falkowski (2014), damping coefficients of the EDPMB have been calculated by means of the following formulae:

$$\begin{aligned} d_{xx}(\Omega) &= d_{yy}(\Omega) = k_{xy}(\Omega) / \Omega, \\ d_{xy}(\Omega) &= -d_{yx}(\Omega) = k_{xx}(\Omega) / \Omega. \end{aligned} \quad (3)$$

The plots of the corresponding main- and cross-coupling damping coefficients for the considered EDPMB are presented in Figure 2b. It is to remark that the mutual skew-symmetry of the cross-coupling stiffness and damping coefficient components characterizing the EDPMBs has an essential influence on the levitation stability.

2.3 Modelling of the Floating-Ring Oil-Journal Bearing

A mathematical modelling of the oil-film interaction in the floating-ring journal bearings commonly reduces to a numerical solving of the Reynolds equations and determination of the oil pressure distributions (Schweizer (2009), Kamesh (2011), Koutsovassis and Driot (2015), Göbel et al. (2015)). Since a character of this interaction is usually non-linear, several associated phenomena as a self-excitation by oil whirl and whip or sub-synchronous oscillations can be taken into considerations. As it follows e.g. from Schweizer (2009), Kamesh (2011), Koutsovassis and Driot (2015), Göbel et al. (2015), such advanced investigations are often extensive enough to become their own separate studies. But here, the dynamic properties of the turbocharger suspension by the floating-ring journal bearings are going to be regarded as an approximate qualitative reference to the corresponding support on the EDPMBs. Thus, a linearized model of the floating-ring journal bearing has been assumed, where the stiffness and damping coefficients of the inner and outer bearing were determined according to Someya (1989) using the solutions of the Reynolds equations, as well. For great rotational speeds of the turbocharger rotor the respective Sommerfeld numbers of the inner and outer bearing are appropriately high. Therefore, for the admissible journal-to-bushing clearance values the resulting main- and cross-coupling stiffness coefficients are big enough to substitute them by the proper average values. Here, it turned out that the main stiffness components became ca. 13 times larger than the mean levitation stiffness realized by the assumed EDPMBs. According to Someya (1989), the corresponding coefficients of damping in the journal bearings hyperbolically decay with the shaft rotational speed Ω , as demonstrated by the plots in Figure 2c.

3 Mathematical Solution of the Problem

The complete mathematical formulation and solution for the hybrid models of rotor-shaft systems assumed in the way described above can be found e.g. in Szolc (2000). In these models flexural motion of cross-sections of each visco-elastic macro-element is governed by the partial differential equations derived using the Timoshenko or the Rayleigh rotating beam theory. In such equations there are contained gyroscopic forces mutually coupling rotor-shaft lateral vibrations in the vertical and horizontal plane. The analogous coupling effect caused by the system rotational speed dependent shaft material damping described using the standard body model is also taken into consideration. The solution for the lateral vibration analysis has been obtained using the analytical-computational approach demonstrated in details in Szolc (2000). In the considered case it is to emphasize that since, according to formulae (1), (2) and (3), the visco-elastic bearing support parameters are rotational speed dependent, the fundamental dynamic properties of the rotor-shaft, e.g. its natural frequencies, eigenfunctions, modal masses and others, also depend on the shaft rotational speed value Ω . Then, solving the differential eigenvalue problem for the orthogonal system obtained for the given Ω and an application of the Fourier solutions in the form of fast convergent series in orthogonal eigenfunctions lead to the set of modal equations

$$\mathbf{M}(\Omega) \cdot \ddot{\mathbf{r}}(t) + \mathbf{D}(\Omega) \cdot \dot{\mathbf{r}}(t) + \mathbf{K}(\Omega) \cdot \mathbf{r}(t) = \mathbf{F}(t, \Omega^2), \quad (4)$$

where:

$$\mathbf{D}(\Omega) = \mathbf{D}_0(\Omega) + \Omega \cdot \mathbf{D}_g(\Omega)$$

and

$$\mathbf{K}(\Omega) = \mathbf{K}_0(\Omega) + \mathbf{K}_b(\Omega) + \Omega \cdot \mathbf{K}_d(\Omega).$$

The symbols $\mathbf{M}(\Omega)$, $\mathbf{K}_0(\Omega)$ denote the diagonal modal mass and stiffness matrix, respectively, $\mathbf{D}_0(\Omega)$ is the non-symmetrical damping matrix and $\mathbf{D}_g(\Omega)$ denotes the skew-symmetrical matrix of gyroscopic effects. Skew- or non-symmetrical elastic properties of the bearings are described by matrix $\mathbf{K}_b(\Omega)$. Anti-symmetrical effects due to the standard body material damping model of the rotating shaft are expressed by the skew-symmetrical matrix $\mathbf{K}_d(\Omega)$ and $\mathbf{F}(t, \Omega^2)$ denotes the external excitation vector due to the unbalance and gravitational forces. On the one hand, for a given value of Ω all matrices are constant. But on the other hand, since visco-elastic properties of the bearing supports are rotational speed dependent, the successive lateral eigenforms and natural frequencies of the turbocharger rotor-shaft are also functions of Ω . Hence, according to the fundamentals of modal analysis, the elements of modal mass, stiffness and damping-gyroscopic matrices become rotational speed dependent, as well. The modal coordinate vector $\mathbf{r}(t)$ consists of the unknown time functions that occur in the Fourier solutions. The number of equations (4) corresponds to the number of lateral eigenmodes taken into consideration in the range of frequency of interest.

Since the main target of the realized study is an investigation of stability of the considered rotating system, its eigenvalue real parts are going to be regarded first as the fundamental measure of the asymptotic stability. In order to determine eigenvalues of the rotor-shaft dynamic model, it is convenient to transform its homogeneous modal motion equations (4) into analogous equations in modal state coordinates. Next, using for them the well-known exponential complex analytical solution one can obtain the standard complex eigenvalue problem. Then, the problem reduces to searching the eigenvalue imaginary and real parts expressed as functions of the shaft rotational speed Ω by means of the following matrix (Szolc et al., 2016):

$$\mathbf{H}(\Omega) = \begin{bmatrix} \mathbf{0} & \mathbf{I} \\ -\mathbf{M}^{-1}(\Omega) \cdot (\mathbf{K}_0(\Omega) + \mathbf{K}_b(\Omega) + \Omega \cdot \mathbf{K}_d(\Omega)) & -\mathbf{M}^{-1}(\Omega) \cdot (\mathbf{D}_0(\Omega) + \Omega \cdot \mathbf{D}_g(\Omega)) \end{bmatrix}. \quad (5)$$

where \mathbf{I} is the identity matrix.

It is to remark that the modal submatrix $\mathbf{D}_0(\Omega)$ containing the damping coefficients (see Eq. (3)) of the passive magnetic bearings is non-symmetrical. Moreover, in matrix $\mathbf{H}(\Omega)$ described by Eq. (5), in addition to the skew-symmetrical gyroscopic matrix $\mathbf{D}_g(\Omega)$, also the skew-symmetrical stiffness submatrices $\mathbf{K}_d(\Omega)$ and $\mathbf{K}_b(\Omega)$ occur. This fact can influence very essentially dynamic stability effects of the entire rotor-shaft system. Because matrix $\mathbf{H}(\Omega)$ is a non-symmetrical one, in order to determine effectively the complex eigenvalues it is necessary to reduce it to the Hessenberg form using the Hausholder transformation. Then, the final computation of the eigenvalue real and imaginary parts for each lateral eigenmode of the considered system is achieved by means of the commonly known QR algorithm.

Since the comparison of dynamic behaviours of the turbocharger rotor-shaft suspended by the floating-ring journal bearings and by the electro-dynamic passive magnetic bearings is going to be performed also for forced vibrations at steady-state operating conditions, constant values of the shaft rotational speeds Ω will be assumed. At the constant rotational speed Ω equations (4) are a system of linear ordinary differential equations with constant coefficients and harmonic external excitation due to residual unbalances. For the mentioned above harmonic and gravitational excitation with the respective amplitude modal components \mathbf{P} , \mathbf{Q} and \mathbf{R} , the induced steady-state vibrations are also harmonic with the same synchronous circular frequency Ω . Thus, the analytical solutions for the successive modal functions contained in vector $\mathbf{r}(t)$ can be assumed in an appropriate harmonic form. Then, by substituting them into (4), derived here for $\Omega=\text{const}$, one obtains the following systems of linear algebraic equations:

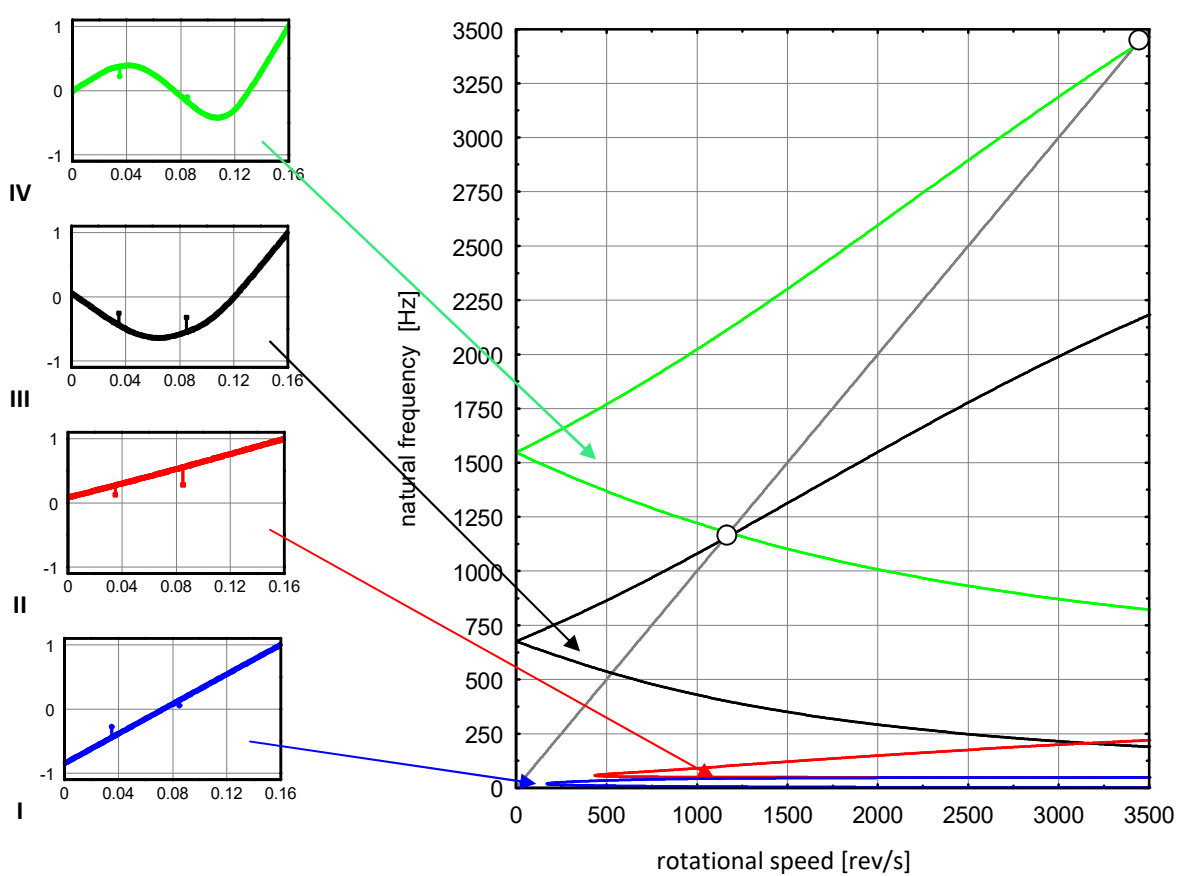
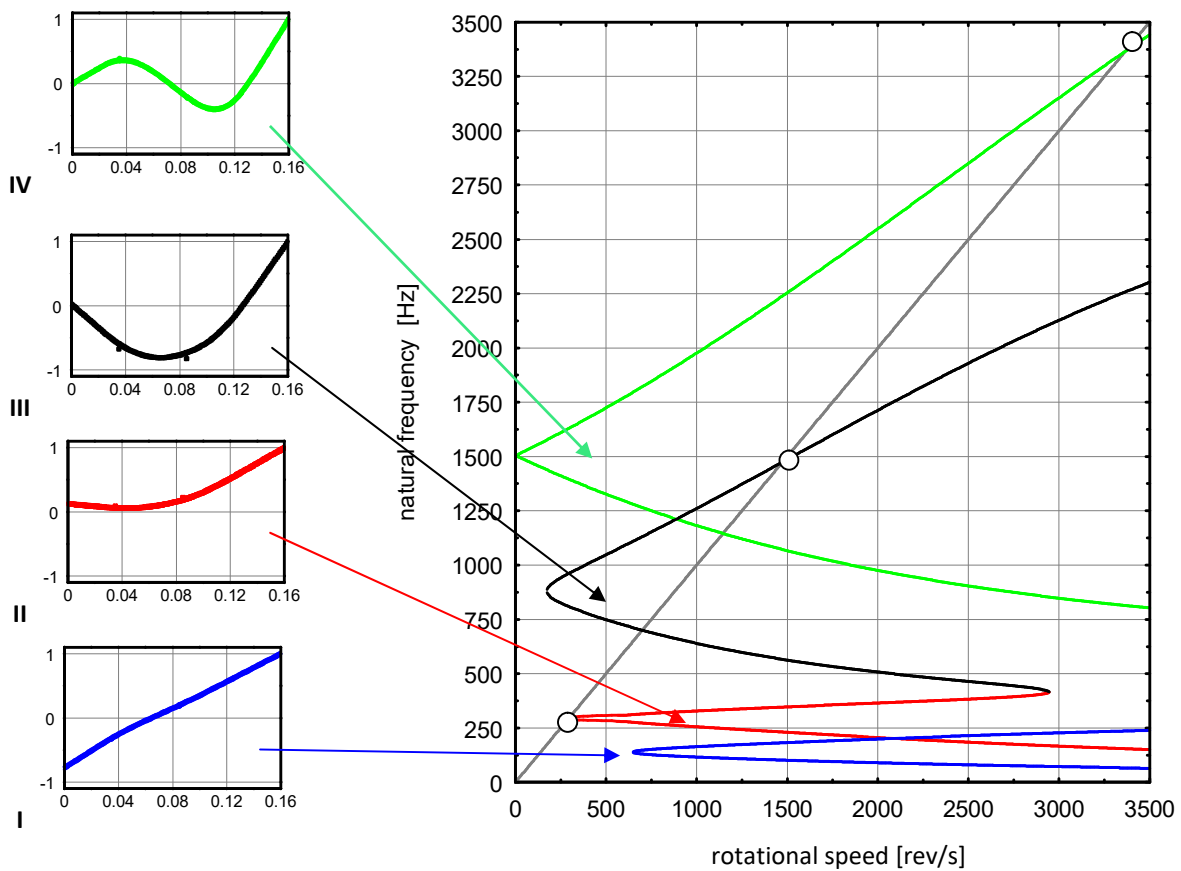
$$\begin{aligned} \mathbf{K}(\Omega) \cdot \mathbf{G} &= \mathbf{R}, \\ (\mathbf{K}(\Omega) - \Omega^2 \mathbf{M}(\Omega)) \cdot \mathbf{C} + \Omega \cdot \mathbf{D}(\Omega) \cdot \mathbf{S} &= \mathbf{P}(\Omega^2), \\ (\mathbf{K}(\Omega) - \Omega^2 \mathbf{M}(\Omega)) \cdot \mathbf{S} - \Omega \cdot \mathbf{D}(\Omega) \cdot \mathbf{C} &= \mathbf{Q}(\Omega^2), \end{aligned} \quad (6)$$

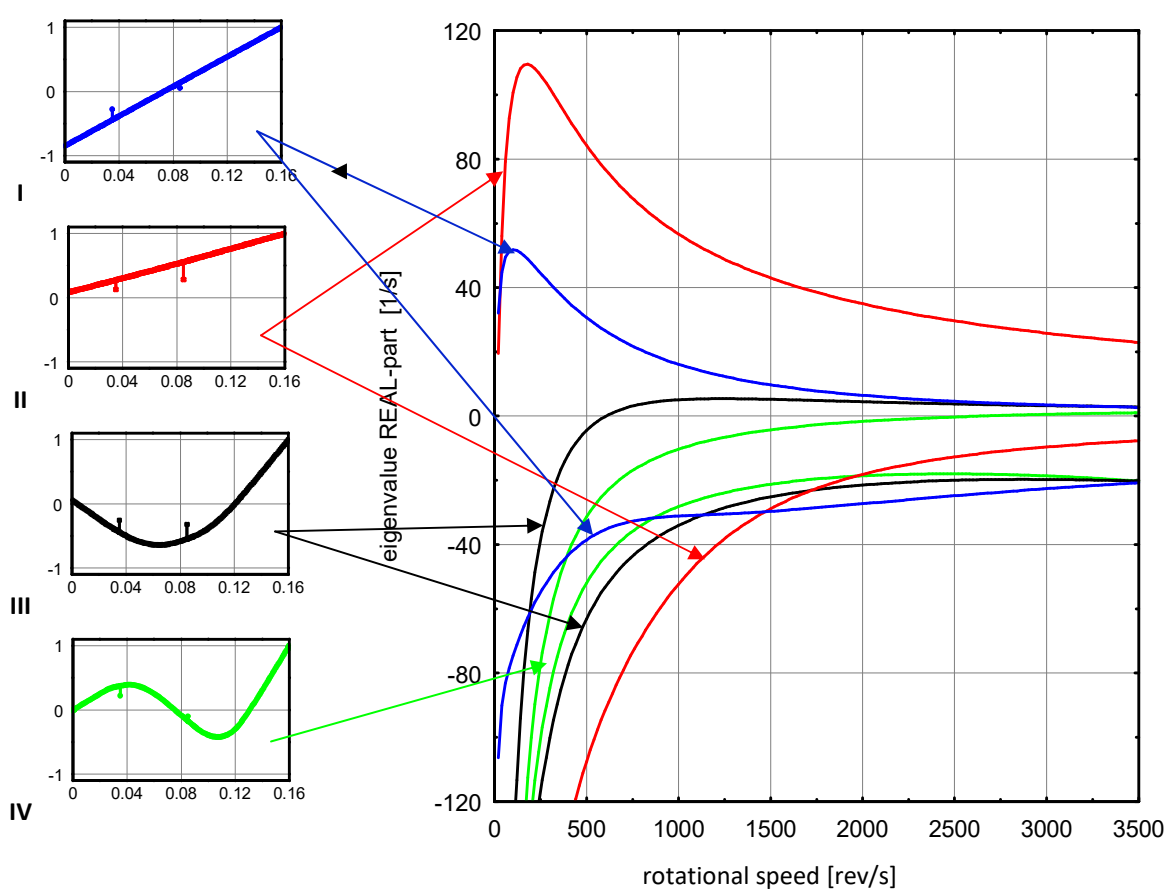
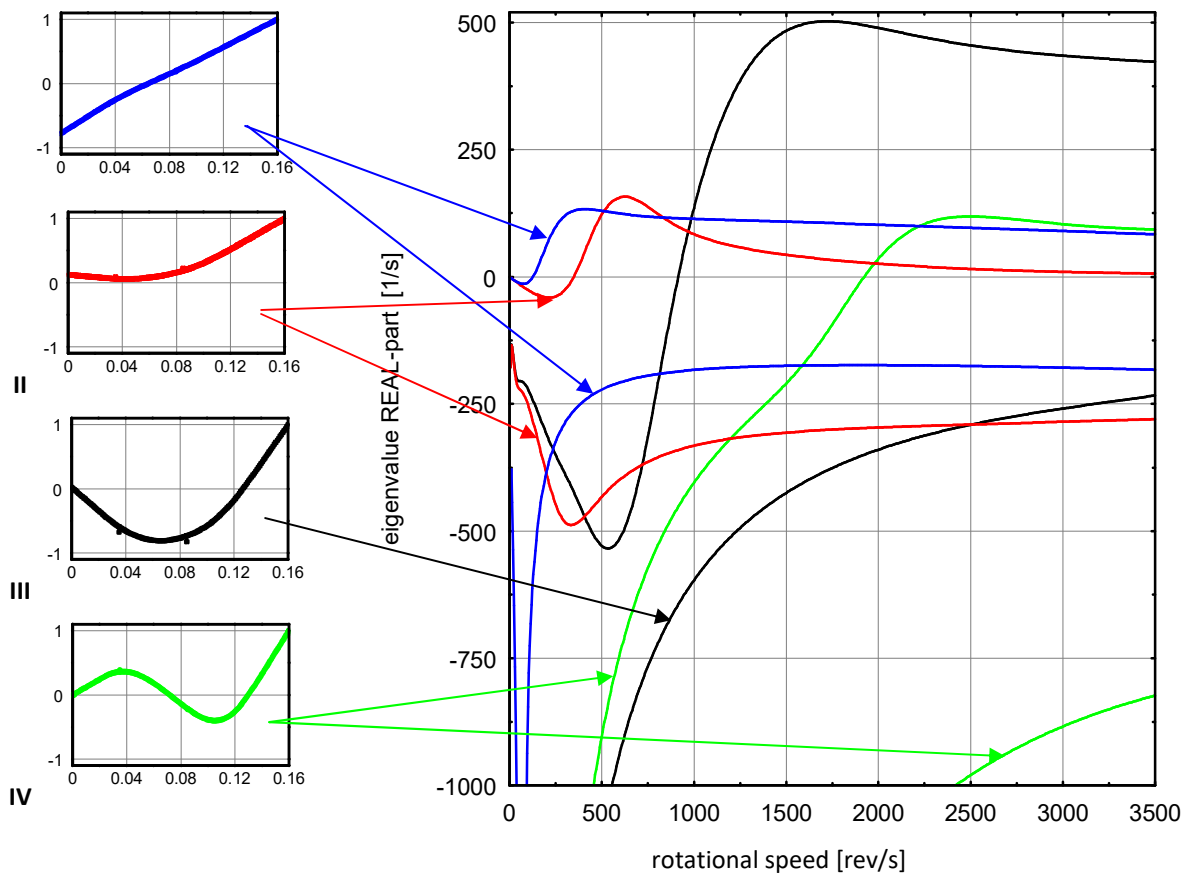
where vectors \mathbf{C} , \mathbf{S} contain respectively the modal cosine- and sine-components of forced vibration amplitudes and vector \mathbf{G} contains the modal components of the rotor-shaft static deflection due to the gravitational force. These equations are very easy to solve with respect of the unknown components of vectors \mathbf{C} , \mathbf{S} and \mathbf{G} .

4 Stability Analysis of the Turbocharger Rotor-Shaft System

Before investigations concerning the proper stability analysis, there is worth studying some fundamental dynamic properties of the considered turbocharger rotor-shaft-bearing systems in the form of the Campbell diagrams in the expected rotational frequency range 0-210,000 rpm which corresponds to 0-3500 rev/s. In Figure 3 there is presented the Campbell diagram for the turbocharger rotor suspended by the floating-ring journal bearings and in Figure 4 the analogous diagram for a support on the EDPMBs is shown. For a better clarity, on the left-hand sides of the both diagrams also the respective lateral eigenfunctions are depicted. Because of the relatively soft suspension by the EDPMBs towards the rotor-shaft flexibility, from among the fundamental lateral eigenforms one can distinguish first two similar to ‘rigid-body’ ones, see Figure 4. However, the harder support on the journal bearings results in almost all typical bending eigenmodes, as shown in Figure 3. In the considered synchronous external excitation frequency range 0-3500 Hz in the both cases of bearing support four lateral eigenforms of the turbocharger rotor-shaft have been determined, respectively with their backward and forward whirl branches. It is to emphasize that because of an influence of the significant negative cross-coupling stiffness components characterizing both the journal bearings as well as the EDPMBs, the fundamental first natural frequencies appear upon certain shaft rotational speed values, as shown in Figures 3 and 4. Due to his fact, in the case of the turbocharger rotor-shaft support on the journal bearings, the first critical speed coincides with the second eigenmode forward precession. Consequently, the third and the fourth critical speed coincide respectively with the third and fourth eigenmode forward precession, as marked using the small rings in Figure 3. However, from the analogous rings in Figure 4 it follows that in the case of the much “softer” suspension by the EDPMBs only two critical speeds are observed: namely with the forward whirls of the third and the fourth eigenmode. Moreover, in the case of journal bearing support, due to gyroscopic forces the second and the third eigenform tend to mutually coincide with the shaft rotational speed rise. Thus, the natural frequency of the second eigenmode forward whirl as well as the natural frequency of the third eigenmode backward whirl vanish together above ca. 2950 rev/s.

A dynamic stability analysis of the hybrid structural model of the considered turbocharger rotor-shaft system supported on the floating-ring journal bearings as well as on the electrodynamic passive magnetic bearings has been performed within the frequency range 0-6000 Hz containing its 6 lateral eigenforms. The investigations are carried out for the shaft material loss factor 0.002 and for the bearing visco-elastic characteristics depicted in Figure 2. Here, the eigenvalue imaginary and real parts are determined as rotational speed functions using matrix \mathbf{H} defined by Eq. (5). Because of a commonly low magnitude of steel shaft material damping as well as due to the relatively small damping coefficient values characterizing the both kind of bearings, particularly for bigger rotational speeds, see Figures 2b and 2c, the eigenvalue imaginary parts, playing a role of damped natural frequencies, almost overlay with the corresponding plots of undamped natural frequencies in the Campbell diagrams in Figures 3 and 4. Thus, for a better clarity they have not been presented here in a graphical form. In Figures 5 and 6, respectively for the turbocharger rotor-shaft support on the journal bearings and on the EDPMBs, there are demonstrated eigenvalue real parts. From the plots illustrated in these figures it follows that not every eigenvalue real parts are negative, what means that the both considered rotating systems pain a lack of stability. Namely, in the case of the journal-bearing support with abovementioned significant negative cross-coupling stiffness components the eigenvalue real parts corresponding to backward whirls of the first four eigenmodes are positive, particularly for greater rotational speeds, as shown in Figure 5. The suspension by the EDPMBs also results in the unstable backward whirls of the first four eigenmodes. But this instability is essentially severe for small rotational speeds in the cases of the first and the second eigenmode, see Figure 6, which follows from the visco-elastic properties of this kind of a magnetic support (Lempke, 2005, Amati et al., 2008, Szolc et al., 2016). It is to emphasize that this result has been obtained for a relatively hard structure of the EDPMB stators embedded in the turbocharger housing, i.e. in the so called ‘metal-to metal’ way. But for an appropriately flexible stator suspension in the housing, e.g. by means of a vulcanized rubber or polymer foil strip, as well as for a properly “soft” visco-elastic structure of the stators, a sufficient amount of passive damping can be introduced. Such damping results in almost complete stabilization of the rotor-shaft support on the EDPMBs, as indicate the system respective eigenvalue real parts presented in Figure 7. It is worth noting that in this way it was possible to stabilize the light-weight and high-speed turbocharger rotor without any specialized dampers, contrary to e.g. Amati et al. (2008) and Szolc et al. (2016), where for other rotors suspended by EDPMBs it had to be made.





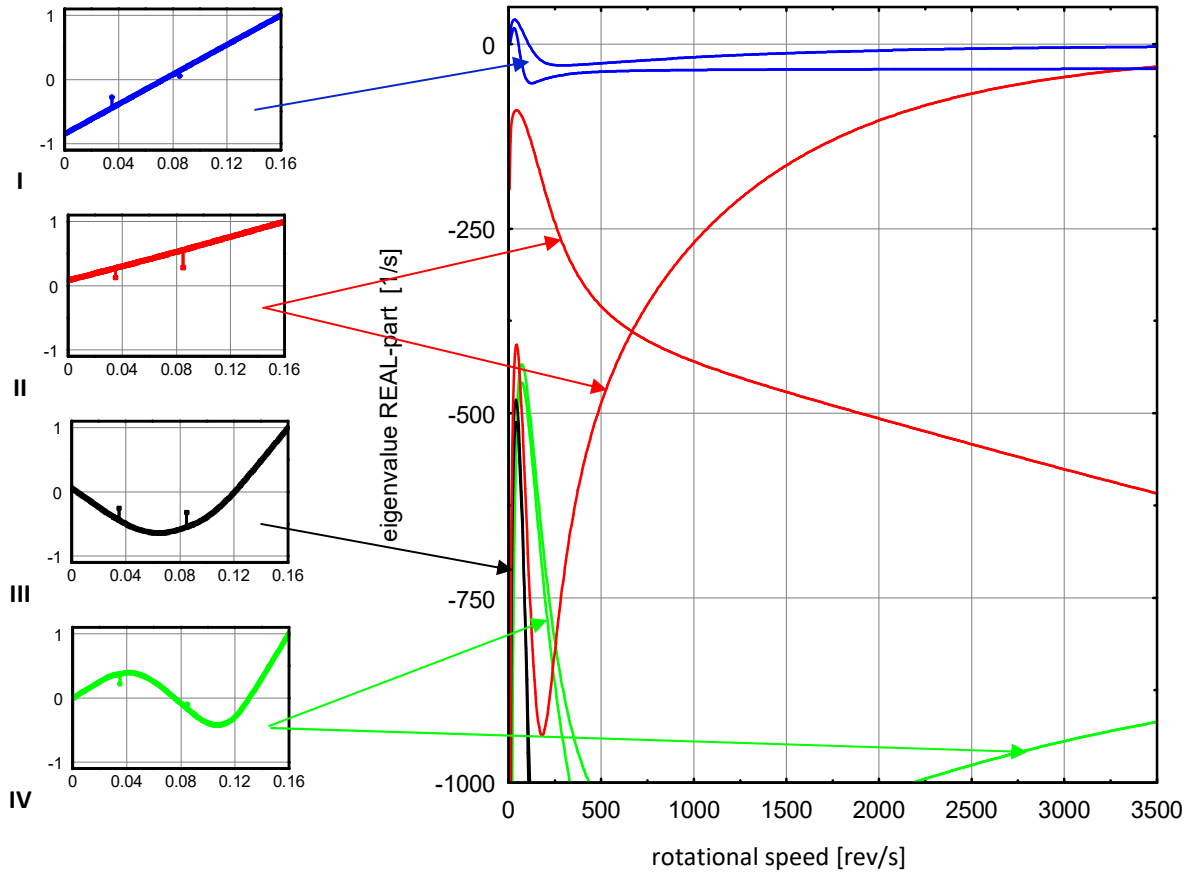


Figure 7: Eigenvalue real parts of the turbocharger rotor-shaft system “softly” supported on the EDPMBs

5 Forced Vibration Comparative Analysis

In addition to the comparison of eigenvibration properties of the turbocharger rotor-shaft supported on the floating-ring journal-bearings and on the EDPMBs, there are going to be compared also amplitude-frequency characteristics of the steady-state forced dynamic responses due to synchronous excitations caused by unavoidable residual unbalances. According to Göbel et al. (2015), $0.6 \cdot 10^{-6}$ kgm unbalance of the turbine rotor and $0.4 \cdot 10^{-6}$ kgm unbalance of the compressor rotor have been assumed. Here, two unbalance variants will be investigated, i.e. the commonly called “static unbalance”, when the turbine and compressor rotor unbalances are mutually oriented ‘in phase’, as well as the “dynamic unbalance”, for which these two unbalances are mutually oriented ‘in anti-phase’. In order to determine the amplitude-frequency characteristics Eqs. (6) had to be solved for the both mentioned above unbalance variants and for the turbocharger rotor-shaft system parameters representing the two considered kinds of bearing support within the expected rotational speed range 0-210,000 rpm corresponding to the harmonic synchronous excitation frequency band 0-3500 Hz.

Figures 8 and 9 demonstrate amplitude-frequency characteristics of the steady-state dynamic responses excited by the static unbalance of the rotor-shaft. In Figure 8 the lateral displacement amplitudes of the turbocharger rotors are depicted and in Figure 9 the bearing vertical reaction force amplitudes are plotted. In these figures the black lines correspond to the rotor-shaft location close to turbine rotor and the grey lines to that of the compressor one. In an identical way Figures 10 and 11 illustrate amplitude-frequency characteristics of the analogous dynamic responses excited by the dynamic unbalance of the rotor-shaft. Figures 8-11a correspond to the support on the EDPMBs and Figures 8-11b to that on the journal bearings regarded here as an approximate reference. From the obtained characteristics it follows that the visco-elastic properties of the rotor-shaft suspension by the EDPMBs result in the much smaller vibration displacements in the critical speed vicinity and in the almost unremarkable bearing force amplitudes in a comparison with the classical, original support on the journal bearings. As it follows from the Campbell diagram in Figure 4, the skew-symmetry of the EDPMBs significantly “shifts” the fundamental first two ‘rigid-body’ modes far away from a synchronous excitation

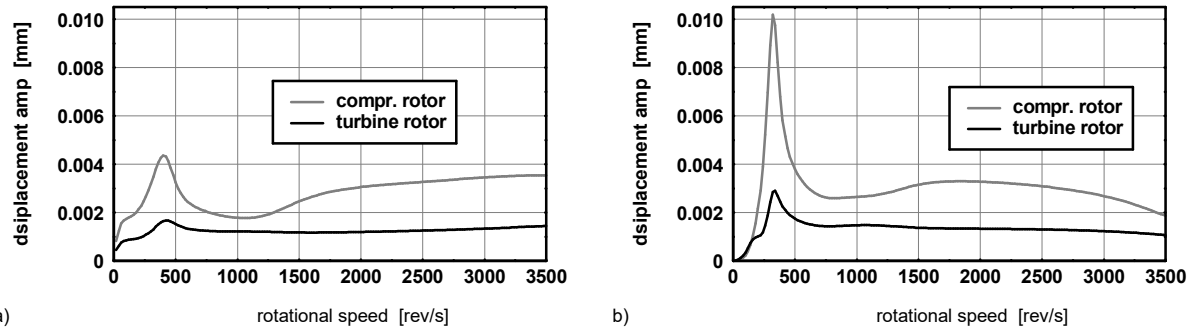


Figure 8: Displacement amplitude characteristics of the turbocharger rotor-shaft supported on the passive magnetic bearings (a) and on the journal bearings (b) obtained for the static residual unbalance

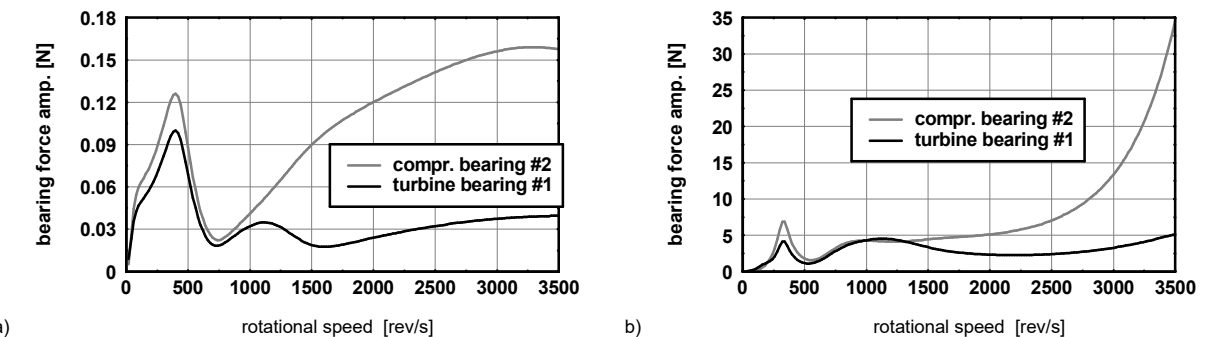


Figure 9: Bearing force amplitude characteristics of the turbocharger rotor-shaft supported on the passive magnetic bearings (a) and on the journal bearings (b) obtained for the static residual unbalance

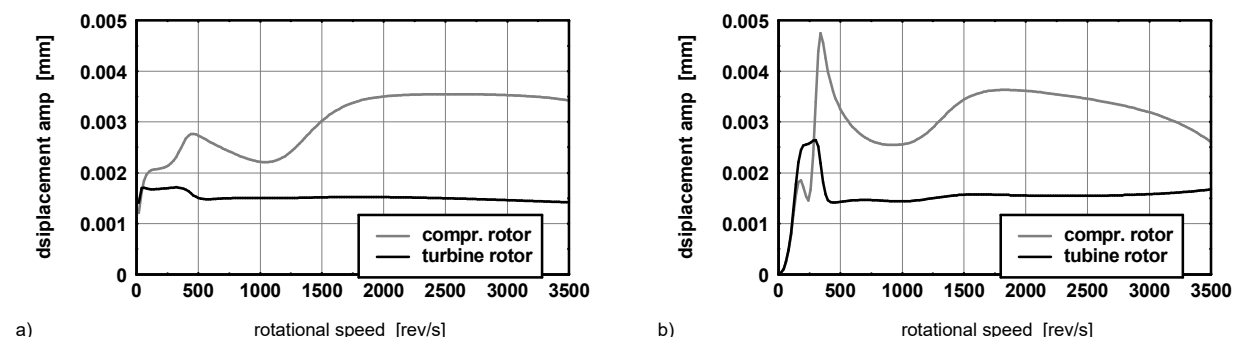


Figure 10: Displacement amplitude characteristics of the turbocharger rotor-shaft supported on the passive magnetic bearings (a) and on the journal bearings (b) obtained for the dynamic residual unbalance

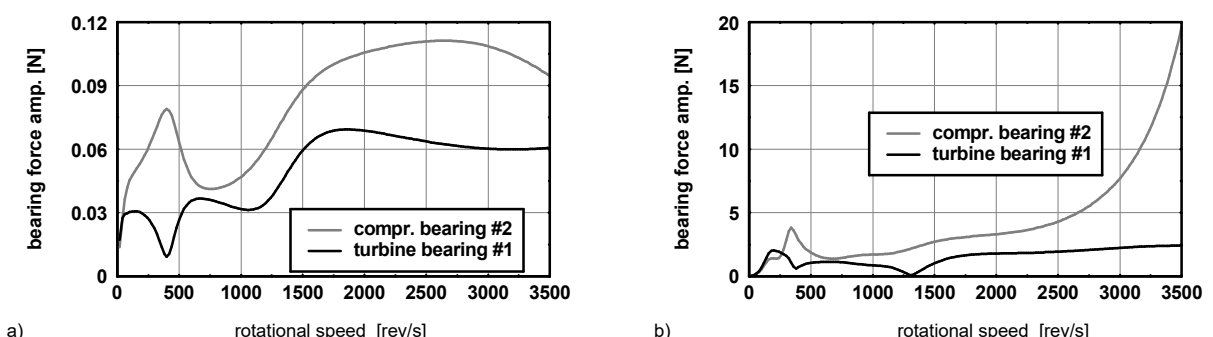


Figure 11: Bearing force amplitude characteristics of the turbocharger rotor-shaft supported on the passive magnetic bearings (a) and on the journal bearings (b) obtained for the dynamic residual unbalance

possibility. However, at the critical speeds marked in this figure resonances with the successive two ‘elastic’ modes can be rather hardly induced. Thus, the turbocharger rotor behaves as a typical overcritical, self-centring shaft, what actually results in the obtained very small dynamic reaction forces transmitted by the bearings. Here, some amplifications of lateral vibration amplitudes are observed only at ca. 450 rev/s, because of predominant damping force activity exceeding an interaction of the elastic forces at low rotational speeds. Such a dynamic behaviour has been indicated also in Amati et al. (2008) for this kind of bearings. The naturally ‘harder’ journal bearings are responsible not only for much greater vibration amplitudes, but at ca. 280 rev/s the severe resonance occurs as a result of the critical speed with the second eigenmode shown in Figure 3. Nevertheless, it is to remember that non-linear properties omitted in the simplified floating-ring journal bearing model assumed here can result in various additional oscillation components, oil whirl and whip effects and in other phenomena (Schweizer (2009), Kamesh (2011), Koutsovassis and Driot (2015), Göbel et al. (2015)). Hence, all the critical speeds discussed in this study are caused by the synchronous harmonic excitations, i.e. they arise from the linearized inertial-visco-elastic properties of the rotor-shaft-bearing models. Then, possible resonances occurring at these speeds are induced by external excitations due to unbalances, but neither by self-excitations associated with non-linear descriptions of the journal bearings nor with the EDPMBs which actually are linear in character.

6. Final Remarks and Preview

In the paper dynamic properties of the automotive turbocharger rotor-shaft supported on the electro-dynamic passive magnetic bearings (EDPMB) have been investigated. Here, the analogous suspension of this object by the floating-ring journal bearing, commonly applied till present, was regarded as a reference. Such a comparison has indicated essential advantages of the proposed kind of magnetic contact-free and lubrication-free support for the relatively light-weight turbocharger rotor-shafts rotating within very broad speed ranges. Moreover, a properly selected visco-elastic design of the EDPMB stators and their flexible embedding in the turbocharger housing can assure asymptotic stability of the considered rotor-shaft systems. Using such a simple mean, it was possible to introduce a sufficient magnitude of additional external damping into the vibrating rotor-shaft system in order to satisfy the Routh-Hurwitz stability criterion as well as to keep all its eigenvalue real parts always negative. Thus, it turned out that a suspension of relatively small and very quickly rotating automotive turbocharger rotor-shafts by the EDPMBs is particularly advantageous and perspective. Nevertheless, the main target of the introductory theoretical study presented here reduced to lateral vibration- and stability analyses. But in order to realize this idea in an engineering and industrial application many further investigations are required. First of all, this is an axial support in the form of a proper magnetic thrust bearing. Then, it will be necessary to design relatively simple and robust touch-down bearings. It can be expected that an application of the EDPMBs should not cause many problems in design of the turbocharger housing and shaft. Namely, a substitution of the lubricating oil supply system by properly embedded permanent magnets as well as an installation of the touch-down bearings do not seem to be particularly expensive and difficult. Consequently, the rotor-shaft journals should be easily substituted by conductor sleeves. Nevertheless, several thermal loading phenomena as well as many other problems hard to foresee now ought to be solved using an appropriate real prototype of the considered object.

References

Amati, N.; De Lépine, X.; Tonoli, A.: Modeling of electrodynamic bearings, *ASME Journal of Vibration and Acoustics*, Vol. 130, (2008), 061007-1–061007-9.

Bonello, P.: Simulations of the nonlinear dynamic response of a turbocharger on foil-air bearings with focus on unbalance excitation, Proc. of the 11th IMechE Int. Conference “*Vibrations in Rotating Machinery*” VIRM-11, September 2016, Manchester, UK (2016), 419–429.

Falkowski, K.: *Passive Magnetic Suspensions*, Military University of Technology Eds., Warsaw (2016).

Filatov, A. V.; Maslen, E. H.; Gillies, G. T.: Stability of an electrodynamic suspension, *Journal of Applied Physics*, Vol. 92, (2002), 3345–3353.

Göbel, S.; Daniel, Ch.; Woschke, E.; Strackeljan, J.: DoE basierte Sensitivitätsanalyse konstruktiver Lagerparameter eines gleitgelagerten Abgasturboladers, Proc. of the 11th Int. Tagung “*Schwingungen in rotierenden Maschinen*” (SiRM), Magdeburg, Germany, February 2015, Paper ID-55 (2015).

Kamesh, P.: *Oil-Whirl Instability in an Automotive Turbocharger*, University of Southampton Research Repository, Ph.D. Thesis (2011), <http://eprints.soton.ac.uk>.

Koutsovasilis, P.; Driot, N.: Turbocharger rotors with oil-film bearings: sensitivity and optimization analysis in virtual prototyping, Proc. of the 11th Int. Tagung "Schwingungen in rotierenden Maschinen" (SiRM), Magdeburg, Germany, February 2015, Paper ID-43 (2015).

Lempke, T. A.: *Design and Analysis of a Novel Low Loss Homopolar Electrodynamic Bearing*, Doctoral Thesis, KTH Electrical Engineering, Stockholm (2005).

Schweizer, B.: Vibrations and bifurcations of turbocharger rotors, Proc. of the 8th Int. Tagung "Schwingungen in rotierenden Maschinen" (SiRM), Vienna, Austria, February 2009, Paper ID-23 (2009).

Someya, T.: *Journal-Bearing Databook*, Springer-Verlag Berlin, Heidelberg, New York (1989).

Szolc, T.: On the discrete-continuous modeling of rotor systems for the analysis of coupled lateral-torsional vibrations, *International Journal of Rotating Machinery*, 6(2), (2000), 135–149.

Szolc, T.; Falkowski, K.: Dynamic analysis of the high-speed flexible rotors supported on the electrodynamic passive magnetic bearings, *Mechanisms and Machine Science*, Springer Verlag, Vol. 21 Part XI, (2014), 1489–1500.

Szolc, T.; Falkowski, K.; Henzel, M.; Kurnyta-Mazurek, P.: Passive and active stabilization of the electrodynamic magnetic bearings supporting high-speed rotors, Proc. of the 11th IMechE Int. Conf. "Vibrations in Rotating Machinery" VIRM-11, September 2016, Manchester, UK, (2016), 721–731.

Address: Tomasz Szolc, Institute of Fundamental Technological Research, Polish Academy of Sciences,
ul. Pawińskiego 5B, 02-106 Warsaw, Poland
email: tszolc@ippt.pan.pl

On the Importance of Frictional Energy Dissipation in the Prevention of Undesirable Self-Excited Vibrations in Gas Foil Bearing Rotor Systems

T. Leister, C. Baum, W. Seemann

In this contribution, a nonlinear and fully coupled fluid–structure–rotor interaction model of a gas foil bearing rotor system is presented. Aiming at the reduction of undesirable self-excited vibrations, many common bearing designs feature a compliant and slightly movable multi-part foil structure inside the lubrication gap. The present paper discusses the general impact of frictional energy dissipation within the foil structure by adding equivalent viscous damping to the widespread simple elastic foundation model. For the computational analysis, the PDEs describing the fluid pressure distribution and the foil structure deformation field are spatially discretized using finite difference schemes. After suitable nondimensionalization of the resulting system of nonlinear ODEs, a corresponding state-space representation is deduced. Using numerical simulation tools, the stability of equilibrium points and the occurrence of self-excited vibrations are addressed and possible bifurcation scenarios are discussed. Summing up all results, frictional energy dissipation proves to be of crucial importance with regard to the reduction or prevention of undesirable self-excited vibrations in gas foil bearing rotor systems.

1 Introduction and Motivation

Gas foil bearings (GFBs) are an upcoming and promising oil-free technology in modern high-speed rotating machinery. Relying on a thin gas film building up an aerodynamic, load-carrying lubrication wedge, such bearings are self-acting and do not require any external pressurization. Most notably, due to the absence of solid-to-solid contact between the airborne rotor journal and the bearing sleeve, excessively low wear and power loss can be achieved (Heshmat et al., 1983). During the last few decades, the potential of GFBs has been widely confirmed by a great number of successful applications in air cycle machines of commercial aircraft (Howard et al., 2007). Lately, in particular as a result of insurmountable speed, temperature, and weight limitations of conventional rolling-element bearings, novel concepts of oil-free turbochargers (Howard, 1999) and oil-free rotorcraft propulsion engines (Howard et al., 2010) are gaining more and more interest.

Most of the considered rotating machinery is supposed to reach and to maintain a stable operating point after completing the run-up. However, as a result of the highly nonlinear bearing forces induced by the pressurized fluid, the existing equilibrium points of GFB rotor systems tend to become unstable for higher rotational speeds. Subsequently, undesirable self-excited vibrations with comparatively large amplitudes may occur (Bonello and Pham, 2014; Hoffmann et al., 2014; Baum et al., 2015a). For this reason, many common bearing designs feature a compliant and slightly movable multi-part foil structure inside the lubrication gap. By dissipating a certain amount of energy via dry sliding friction mechanisms (Peng and Carpino, 1993; Howard et al., 2001), this countermeasure is supposed to reduce the vibrational amplitudes or, as the ultimate goal, to prevent the occurrence of self-excited vibrations in the first place.

In currently conducted research on GFBs, sophisticated models and reliable numerical tools are of major interest with regard to the complexity and costliness of experimental investigations. As the classical mathematical model, based on the assumption of a full fluid film lubrication regime, the fluid pressurization is usually described by the Reynolds equation for compressible ideal gases (Reynolds, 1886; Szeri, 2010). With regard to the foil structure, many recent publications discuss complex FE models with or without considering frictional effects (Le Lez et al., 2007; San Andrés and Kim, 2008). In most cases, however, such models do not capture the true coupled nature of fluid–structure–rotor interaction (Bou-Saïd et al., 2008; Bonello and Pham, 2014) and thus prove to be inapplicable when it comes to a transient analysis of the system's nonlinear dynamic response. The main objective of the present paper is a systematic investigation of the general impact of energy dissipation within the foil structure. To this effect, a nonlinear and fully coupled model considering equivalent viscous damping

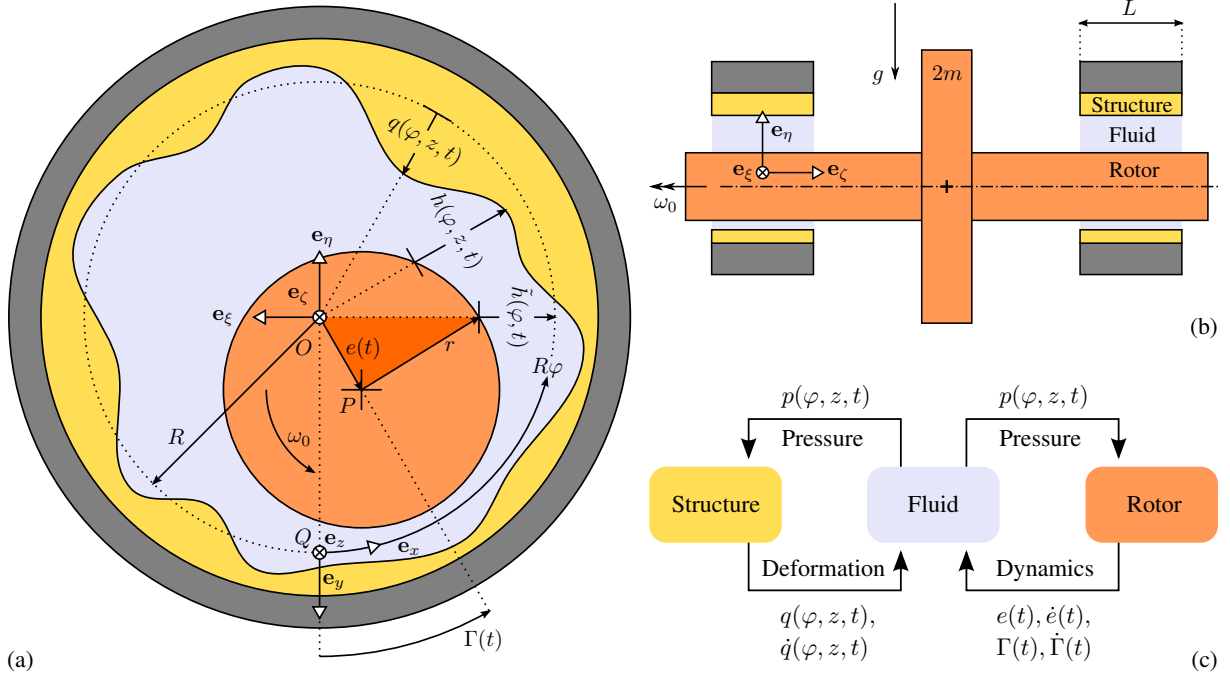


Figure 1. Schematic sketches (with greatly magnified lubrication gap) showing the fluid–structure–rotor model: (a) front view of the rotor journal inside the GFB model, (b) side view of the rotor model mounted on two GFBs, (c) interaction chart of the three fully coupled submodels.

is presented in a way which bears some basic resemblance to a recent contribution by Bonello and Pham (2014). Using numerical simulation tools, the essential question to be answered is whether and to what extent frictional energy dissipation is beneficial with regard to the reduction or prevention of undesirable self-excited vibrations.

2 Theory and Modeling

2.1 Fluid–Structure–Rotor Interaction

In the considered GFB rotor system, the pressurized fluid inside the lubrication gap is supposed to interact strongly with both the compliant foil structure and the movable rotor shaft (Bonello and Pham, 2014; Baum et al., 2015a; Leister et al., 2016a). In this regard, a realistic analysis of the system’s nonlinear dynamic response requires an interconnected simulation approach in which all parts of the model are fully coupled to each other and in which all governing equations are solved simultaneously (Bonello and Pham, 2014; Baum et al., 2015a; Leister et al., 2016a). As depicted by the schematic sketches in Figure 1a (front view) and in Figure 1b (side view), the comprehensive overall model presented in this paper essentially comprises three submodels: an aerodynamic fluid model (colored in blue), a dissipative foil structure model (colored in yellow), and a turbomachine rotor model (colored in orange).

The basic bearing geometry is described by the axial length L of the bearing sleeve and by the inner radius R of the undeformed foil structure. Depending on the outer radius r of the rotor journal inside the bearing, the nominal height of the gas-filled lubrication gap is characterized in terms of a small radial clearance parameter

$$C = R - r, \quad 0 < C/R \ll 1. \quad (1)$$

Given the small clearance assumption in Equation (1), the curvature of the lubrication gap and any radial dependence of the fluid properties can be neglected. Thus, the boundary value problem for the gas pressure calculation is henceforth considered on a two-dimensional, rectangular domain. Altogether, introducing a characteristic time scale T , we define a tuple of nondimensional independent variables $(\varphi, Z, \tau) = (x/R, z/L, t/T)$. The arising nondimensional time derivative is denoted by $(\square)' = d(\square)/d\tau$ for better legibility of the following equations.

The fluid–structure–rotor interaction chart in Figure 1c visualizes the coupling mechanisms between the three submodels. Defined in relation to the constant ambient pressure p_0 , the nondimensional pressure field $P(\varphi, Z, \tau) = p(\varphi, ZL, \tau T)/p_0$ represents the load acting upon the foil structure. Moreover, the same pressure distribution induces

a bearing force which supports the rotor. On the other hand, the pressurization of the fluid is influenced by the dynamics of both the foil structure and the rotor. For this reason, considering the nominal radial clearance C from Equation (1), we introduce the nondimensional foil structure deformation field $Q(\varphi, Z, \tau) = q(\varphi, ZL, \tau T)/C$, the nondimensional rotor journal eccentricity $\varepsilon(\tau) = e(\tau T)/C$, and the nondimensional rotor journal attitude angle $\gamma(\tau) = \Gamma(\tau T)$. Due to squeeze effects which are discussed later, a transient coupling mechanism must also account for the respective time derivatives $Q'(\varphi, Z, \tau)$, $\varepsilon'(\tau)$, and $\gamma'(\tau)$.

2.2 Aerodynamic Fluid Model

It is obvious from the sketch in Figure 1a that the effective fluid film thickness $h(\varphi, z, t)$ depends on the nominal lubrication gap clearance, the foil structure deformation field, and the position of the rotor journal, which is assumed to be perfectly aligned with the bearing. By applying the law of cosines to the highlighted orange triangle and after linearization with respect to the rotor journal eccentricity, we find the nondimensional expression

$$H(\varphi, Z, \tau) = \frac{h(\varphi, ZL, \tau T)}{C} = \underbrace{1}_{\text{Clearance}} - \underbrace{\varepsilon(\tau) \cos[\varphi - \gamma(\tau)]}_{\text{Rotor position}} - \underbrace{Q(\varphi, Z, \tau)}_{\text{Structure deformation}} \quad (2)$$

and the corresponding nondimensional time derivative

$$H'(\varphi, Z, \tau) = -\varepsilon'(\tau) \cos[\varphi - \gamma(\tau)] - \varepsilon(\tau) \gamma'(\tau) \sin[\varphi - \gamma(\tau)] - Q'(\varphi, Z, \tau). \quad (3)$$

The considered bearing is supposed to operate within the full fluid film lubrication regime, such that a minimum fluid film thickness larger than the surrounding surface roughnesses is sustained at any time. In this case, the lubricant pressure is governed by a generalized form of the classical Reynolds equation which is applicable for compressible fluids (Reynolds, 1886; Szeri, 2010). Under isothermal conditions with a constant viscosity μ_0 and under the assumption of the ideal gas law, we obtain the nondimensional partial differential equation (PDE)

$$\left\{ \begin{array}{c} \text{Expansion} \\ P' \end{array} \right\} H + P \left\{ \begin{array}{c} \text{Rotor squeeze} \\ -\varepsilon'(\tau) \cos[\varphi - \gamma(\tau)] - \varepsilon(\tau) \gamma'(\tau) \sin[\varphi - \gamma(\tau)] \\ -Q' \end{array} \right\} = \frac{\partial}{\partial \tau} [PH] = \frac{1}{2} \left\{ \begin{array}{c} \text{Poiseuille} \\ \frac{\partial}{\partial \varphi} \left[PH^3 \frac{\partial P}{\partial \varphi} \right] + \kappa^2 \frac{\partial}{\partial Z} \left[PH^3 \frac{\partial P}{\partial Z} \right] \\ -\Lambda \frac{\partial}{\partial \varphi} [PH] \\ \text{Couette} \end{array} \right\}, \quad (4)$$

which involves the fluid film thickness from Equation (2) and the corresponding time derivative from Equation (3). In the above stated PDE, a nondimensional bearing geometry parameter $\kappa = R/L$ and the nondimensional bearing number $\Lambda = 6\mu_0\omega_0/p_0(R/C)^2$ arise, the latter corresponding to the angular velocity $\omega_0 = 2\pi n_0$ of the rotor. Moreover, with regard to transient run-up and coast-down simulations, it is convenient to adopt a characteristic time scale T for the overall problem which does not depend on the rotor speed, giving $\tau = t/T = t/[6\mu_0/p_0(R/C)^2]$. According to Hamrock (1991), the pressurization described by the Reynolds equation results from four basic mechanisms, which are subsequently referred to as Poiseuille flow, Couette flow, fluid expansion, and squeeze flow. With regard to the modeled fluid–structure–rotor interaction, it should be emphasized that the latter can be subdivided into a transient foil structure squeeze flow and a transient rotor journal squeeze flow.

In axial direction, the lubrication gap is open to the atmosphere, imposing ambient pressure $P_0 = 1$ at $Z = \pm 1/2$. With regard to the circumferential direction, however, different concepts can be found in recent literature. A first common approach (see, e.g., San Andrés and Kim, 2010) suggests that the fluid is supplied with ambient pressure through the foil fixation gap (see Figure 2) at a certain angular position $\varphi = \varphi_0$. In this case, the Reynolds equation can be considered on a rectangular domain with four Dirichlet boundaries. A second common approach (see, e.g., Bin Hassan and Bonello, 2017) neglects the foil fixation gap and considers the Reynolds equation on a cylindrical domain with only two Dirichlet boundaries, supposing in addition circumferential periodicity of the fluid properties and of the respective gradients. The present study is based on the second approach with the objective of obtaining generic results which are independent of φ_0 .

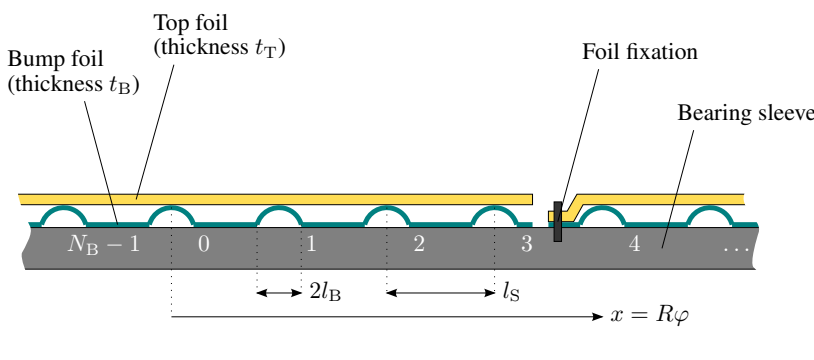


Figure 2. Schematic sketch showing the foil structure configuration (bump foil and top foil) of a typical first generation bump-type GFB.

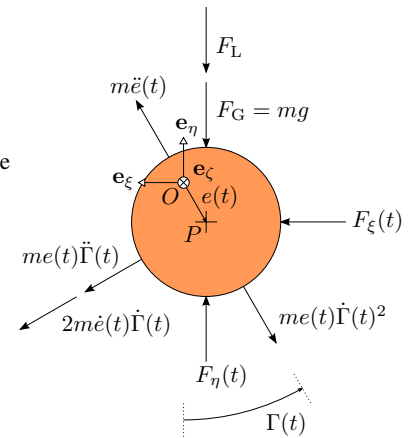


Figure 3. Free body diagram with all the forces acting on the rotor journal.

2.3 Dissipative Foil Structure Model

The schematic sketch in Figure 2 depicts the foil structure configuration which is typically used in first generation bump-type GFBs. It is composed of a thin, corrugated bump foil with N_B bumps (thickness t_B , bump width $2l_B$, bump distance $l_S = 2\pi R/N_B$, Young's modulus E_B , Poisson's ratio ν_B) and a thin, smooth top foil (thickness t_T , Young's modulus E_T , Poisson's ratio ν_T). With the exception of the foil fixation, relative motion and local detachment between the compliant bump foil, the compliant top foil, and the bearing sleeve are possible. Hence, a realistic structure model is supposed to consider not only the foil deformation, but also the energy dissipation caused by dry sliding friction. Earlier experimental works have reported relatively small deformation gradients in axial direction (Ruscitto et al., 1978), confirming that the foil structure can be represented in good approximation by plane 1D models (San Andrés and Kim, 2008) loaded by the axially averaged pressure

$$\bar{P}(\varphi, \tau) = \int_{-\frac{1}{2}}^{+\frac{1}{2}} P(\varphi, Z, \tau) \, dZ. \quad (5)$$

The classical 2D simple elastic foundation model, sometimes referred to as the Winkler foundation model and firstly applied to GFBs by Heshmat et al. (1983), is not applicable for rotor journal eccentricities $\varepsilon(\tau) \geq 1$ as it predicts non-physical contact at the open bearing edges resulting from the prevailing ambient pressure. However, this issue can be avoided by using a slightly modified 1D simple elastic foundation model respecting the aforementioned assumption of small deformation gradients in axial direction (Baum et al., 2015a; Leister et al., 2016a). In this case, since it is supposed to be uniform along the Z -axis, the elastic deformation $\bar{Q}_e(\varphi, \tau)$ depends directly on the averaged pressure from Equation (5) and is obtained by the algebraic expression

$$K_W \bar{Q}_e(\varphi, \tau) = -[\bar{P}(\varphi, \tau) - 1]. \quad (6)$$

According to Walowitz and Anno (1975), the bumps can be approximated by means of a simple beam model, giving the nondimensional foundation stiffness $K_W = E_B C / [2(1 - \nu_B^2) \rho_0 l_S] (t_B/l_B)^3$. Even though the elastic foundation model is completely uncoupled in circumferential direction and does not account for local stiffness variations, no important inaccuracy is expected to result from this simplification (Leister et al., 2016a). Under certain conditions, however, the analytical expression K_W tends to underestimate the real structural stiffness (Larsen et al., 2014). Using Equations (5) and (6), the fluid–structure interaction via film thickness and structure squeeze in Equation (4) is described by

$$\bar{Q}_e(\varphi, \tau) = -K_W^{-1} \left[\int_{-\frac{1}{2}}^{+\frac{1}{2}} P(\varphi, Z, \tau) \, dZ - 1 \right], \quad (7)$$

$$\bar{Q}'_e(\varphi, \tau) = -K_W^{-1} \left[\int_{-\frac{1}{2}}^{+\frac{1}{2}} P(\varphi, Z, \tau) \, dZ \right]' = -K_W^{-1} \underbrace{\int_{-\frac{1}{2}}^{+\frac{1}{2}} P'(\varphi, Z, \tau) \, dZ}_{(*)}. \quad (8)$$

Since the Reynolds equation must be solved for the fluid expansion $P'(\varphi, Z, \tau)$ in order to obtain a state-space form, it should be noted that the evaluation of the integral (\star) requires a special treatment upon substitution of Equation (8) into Equation (4). This can be achieved by approximating (\star) using a numerical integration method, which leads to a finite sum of discrete fluid expansion values. The resulting Reynolds equation being linear with respect to the spatially discretized fluid expansion, the state-space form is found by an inverse matrix operation. In this context, it must be stressed that (\star) cannot be neglected if one is interested in a strongly coupled overall model.

As already mentioned, the dominating energy dissipation mechanism is attributed to dry sliding friction. However, according to a proposition by Peng and Carpino (1993), the assumption of equivalent viscous damping reveals to be a useful approximation. Therefore, in addition to the nondimensional stiffness parameter K_W , the nondimensional damping parameter D_W is introduced. Based on the elastic foundation model from Equation (6), an extended viscoelastic foundation model for the deformation $\bar{Q}_v(\varphi, \tau)$ is stated by the ordinary differential equation (ODE)

$$D_W \bar{Q}'_v(\varphi, \tau) + K_W \bar{Q}_v(\varphi, \tau) = -[\bar{P}(\varphi, \tau) - 1]. \quad (9)$$

Knowing that Equation (9) is a differential equation rather than an algebraic equation, it is convenient to consider henceforth the foil structure deformation field $\bar{Q}_v(\varphi, \tau)$ as a state variable with the corresponding state equation

$$\bar{Q}'_v(\varphi, \tau) = -D_W^{-1} \left[K_W \bar{Q}_v(\varphi, \tau) + \int_{-\frac{1}{2}}^{+\frac{1}{2}} P(\varphi, Z, \tau) dZ - 1 \right]. \quad (10)$$

Most notably, in contrast to Equation (8) for the elastic model, the integral (\star) does not appear anymore, thus allowing for a simplified evaluation of the Reynolds equation despite the structure model being more comprehensive.

2.4 Turbomachine Rotor Model

As the present study is focused on gaining a basic understanding of energy dissipation inside the bearing, we consider a simple horizontal rigid rotor of mass $2m$ without unbalance, which is symmetrically mounted on two GFBs. In this case, an additional static load $2F_L$ is equivalent to a modified gravitational acceleration $g + F_L/m$. Integrating the gas pressure acting on each of the rotor journals, we obtain the nondimensional bearing force vector

$$\mathbf{f}(\tau) = \begin{bmatrix} f_\xi(\tau) \\ f_\eta(\tau) \end{bmatrix}_{\{\mathbf{e}_\xi, \mathbf{e}_\eta\}} = \frac{1}{p_0 R L} \begin{bmatrix} F_\xi(\tau T) \\ F_\eta(\tau T) \end{bmatrix}_{\{\mathbf{e}_\xi, \mathbf{e}_\eta\}} = \int_{-\frac{1}{2}}^{+\frac{1}{2}} \int_0^{2\pi} P(\varphi, Z, \tau) \begin{bmatrix} \sin \varphi \\ \cos \varphi \end{bmatrix}_{\{\mathbf{e}_\xi, \mathbf{e}_\eta\}} d\varphi dZ. \quad (11)$$

With the nondimensional rotor mass parameter $M = p_0/(36\mu_0^2 L)(C/R)^5 m$ and the modified gravity parameter $G = 36\mu_0^2/(p_0^2 R)(R/C)^5(g + F_L/m)$, the free body diagram in Figure 3 yields the equations of motion

$$\left. \begin{aligned} \varepsilon''(\tau) - \varepsilon(\tau)\gamma'(\tau)^2 - G \cos \gamma(\tau) + \frac{1}{M} [f_\xi(\tau) \sin \gamma(\tau) + f_\eta(\tau) \cos \gamma(\tau)] \\ \varepsilon(\tau)\gamma''(\tau) + 2\varepsilon'(\tau)\gamma'(\tau) + G \sin \gamma(\tau) + \frac{1}{M} [f_\xi(\tau) \cos \gamma(\tau) - f_\eta(\tau) \sin \gamma(\tau)] \end{aligned} \right\} = 0. \quad (12)$$

2.5 State-Space Representation

The domain of the lubrication gap is discretized using a uniform computational grid with $N_\varphi \times N_Z$ grid points. Defining discrete pressure values $P_{i,j}(\tau)$ for the Reynolds equation as well as discrete displacement values $\bar{Q}_i(\tau)$ for the viscoelastic foundation model, we obtain the nondimensional discrete state vector

$$\begin{bmatrix} \mathbf{s}_F(\tau) \\ \mathbf{s}_S(\tau) \\ \mathbf{s}_R(\tau) \end{bmatrix} = \begin{bmatrix} \text{Fluid state } \mathbf{s}_F^\top(\tau) \\ \text{Structure state } \mathbf{s}_S^\top(\tau) \\ \text{Rotor state } \mathbf{s}_R^\top(\tau) \end{bmatrix}^\top = \begin{bmatrix} P_{0,1}(\tau) \dots P_{N_\varphi-2, N_Z-2}(\tau) \\ \bar{Q}_0(\tau) \dots \bar{Q}_{N_\varphi-2}(\tau) \\ \varepsilon(\tau) \varepsilon'(\tau) \gamma(\tau) \gamma'(\tau) \end{bmatrix}^\top = \mathbf{s}(\tau) \in \mathbb{R}^{(N_\varphi-1)(N_Z-2)+(N_\varphi-1)+4} = \mathbb{R}^n, \quad (13)$$

which will not contain any structure displacement values if the purely elastic foundation model is considered. For the right-hand side \mathbf{k} of the state equation system, depending on the structure model, we use either Equation (8) or (10). Moreover, a state-space form of Equation (12) is stated for the rotor. With regard to the fluid model, we solve Equation (4) for $P'(\varphi, Z, \tau)$ and discretize all spatial derivatives by means of a finite difference scheme. The bearing number Λ being the bifurcation parameter, we obtain the nonlinear autonomous first-order ODE system

$$\mathbf{s}'(\tau) = \begin{bmatrix} \mathbf{s}_F(\tau) \\ \mathbf{s}_S(\tau) \\ \mathbf{s}_R(\tau) \end{bmatrix}' = \mathbf{k} \left\{ \begin{bmatrix} \mathbf{s}_F(\tau) \\ \mathbf{s}_S(\tau) \\ \mathbf{s}_R(\tau) \end{bmatrix}, \Lambda \right\} = \mathbf{k} \{ \mathbf{s}(\tau), \Lambda \}, \quad \mathbf{k}: \mathbb{R}^n \times \mathbb{R} \rightarrow \mathbb{R}^n. \quad (14)$$

Table 1. Parameters used for the numerical simulations.

Parameter	Symbol	Value
Axial bearing width	L	38.10 mm
Bearing radius	R	19.05 mm
Lubrication gap clearance	C	50 μm
Ambient pressure	p_0	1013.25 hPa
Dynamic viscosity	μ_0	1.85×10^{-5} Ns/m ²
Rotational speed	n_0	36 000 min ⁻¹
Rotor mass	$2m$	2×185 g
Gravity	g	9.81 m/s ²
External load	$2F_L$	2×20.25 N
Number of bumps	N_B	26
Bump width	$2l_B$	2×1.778 mm
Foil thickness	t_B, t_T	101.6 μm
Young's modulus	E_B, E_T	214 GPa
Poisson's number	ν_B, ν_T	0.29

3 Results and Discussion

3.1 Model Parameters

The numerical results presented hereafter are based on data of a typical first generation bump-type GFB, which is referred to in a great number of both experimental and numerical investigations (Ruscitto et al., 1978; Peng and Khonsari, 2004; San Andrés and Kim, 2008), thus allowing the authors to validate their code against the literature. According to the definitions in the preceding sections, a nondimensional parameter set is deduced from the dimensional values in Table 1. In doing so, one must be aware of the uncertainty which might arise from the empirically estimated value $C = 50 \mu\text{m}$ describing the poorly known lubrication gap clearance (Peng and Khonsari, 2004; Leister et al., 2016b). For the numerical analysis, we use $N_\varphi \times N_Z = 79 \times 7$ grid points, which is sufficient for a grid-independent solution if local stiffness variations of the foil structure are not taken into account (Leister et al., 2016a).

As known from the literature (see, e.g., Thomson, 1996), the equivalent viscous damping can be assessed by opposing the viscoelastic model to a Coulomb friction model (coefficient μ_C) and by equilibrating the respective amounts of energy dissipated during one cycle of a characteristic sinusoidal displacement $\hat{q} \sin(\omega t)$. With the choice of reasonable parameter values and the assumption of a normal force induced by a characteristic pressure p , we obtain the order-of-magnitude estimate

$$D_W = \overbrace{\frac{4}{\pi}}^{=O(1)} \overbrace{\mu_C}^{=O(0.1)} \overbrace{\frac{C}{\hat{q}}}^{=O(1)} \overbrace{\frac{\omega_0}{\omega}}^{=O(1)} \overbrace{\frac{p}{p_0}}^{=O(10)} \overbrace{\Lambda^{-1}}^{=O(1)} = O(1). \quad (15)$$

3.2 Stabilization of Stationary Operating Points

In the first part of the analysis, we investigate the capability of frictional energy dissipation to prevent the occurrence of self-excited vibrations in the first place. Mathematically speaking, we are interested in stationary solutions $\mathbf{s}(\tau) = \mathbf{s}_0$ of Equation (14) for which the overall system state remains unchanged as time elapses. For this purpose, the nonlinear algebraic equation system $\mathbf{k}\{\mathbf{s}_0, \Lambda\} = \mathbf{0}$ is solved for \mathbf{s}_0 using a Newton–Raphson method with an adequate initial guess. Locally, by virtue of the Hartman–Grobman theorem, the stability of these equilibrium points can be assessed by a consideration of the corresponding linearized problem. Thus, we calculate the eigenvalues λ_i of the numerically approximated Jacobian $\mathbf{J}_K|_{\mathbf{s}(\tau)=\mathbf{s}_0, \Lambda}$. With the condition $\max_{\lambda_i} \Re(\lambda_i) < 0$ for asymptotic stability, the critical bearing number $\Lambda = \Lambda_c$ can be estimated using a numerical continuation method. From a practical point of view, the existence of a stability threshold suggests that no stable stationary operating point of the GFB rotor system is possible anymore if some critical rotor speed is exceeded.

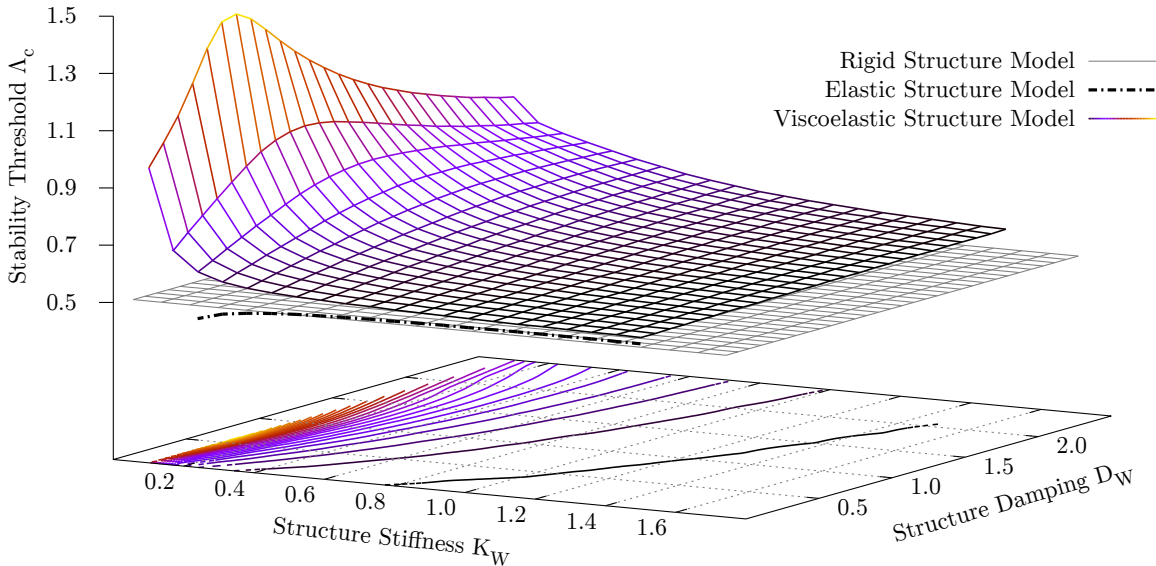


Figure 4. Stability diagram showing the critical bearing number depending on foil structure stiffness and damping.

In the stability diagram in Figure 4, the black chain-dotted line visualizes the critical bearing number for the elastic structure model as a function of the structure stiffness K_W . As a reference, the gray surface indicates the critical bearing number which is found for a rigid bearing with the same parameters but without any structural deformation. When comparing the results found with the elastic model and the results found with the rigid model, a slightly stabilizing effect due to the foil structure deformation can be observed for stiffnesses $K_W > 0.4$, which is in accordance with earlier works by the authors (Baum et al., 2015a; Leister et al., 2016b). On the other hand, if the stiffness is excessively low, the overall system is destabilized to such an extent that no stable equilibrium point at all can be found.

For the viscoelastic model, the multicolored surface in Figure 4 visualizes the critical bearing number as a function of the structure stiffness K_W and the structure damping D_W , both of them influencing the eigenvalues. In contrast to the elastic model, much larger critical bearing numbers are predicted, in particular for low stiffnesses. As shown in the diagram, a specific optimum damping value which maximizes the critical bearing number is associated to each stiffness value. When the stiffness is increased, the optimum damping is also shifted toward higher values.

Thus, we conclude that energy dissipation within the foil structure has the potential to stabilize stationary operating points of the GFB rotor system and, if the dissipation rate is chosen appropriately, to prevent the occurrence of undesirable self-excited vibrations in the first place.

3.3 Nonlinear Dynamic Response of the System during Run-Up and Coast-Down

Despite the stabilizing effect of frictional energy dissipation, the occurrence of self-excited vibrations can only be shifted toward higher rotational speeds and is never completely avoidable. In order to gain a basic understanding of the dynamic response of the GFB rotor system, a typical machine run-up and coast-down scenario is simulated in this part of the analysis. According to the first plot in Figure 5, the rotational speed is varied linearly during $\tau_{\max} = 50\,000$ ($t_{\max} = 50$ s) from $\Lambda_1 = 0.500$ ($n_1 = 30\,000\, \text{min}^{-1}$) to $\Lambda_2 = 0.833$ ($n_2 = 50\,000\, \text{min}^{-1}$) and back. The numerical time integration of Equation (14) is performed using a trapezoidal-type scheme in order to avoid numerical damping.

The second and the third plot in Figure 5 show the horizontal position of the rotor journal $\xi(\tau)$ as a red signal envelope curve and the vertical position of the rotor journal $\eta(\tau)$ as a blue signal envelope curve. In each of the plots, the solid lines correspond to the viscoelastic structure model and the chain-dotted lines correspond to the rigid structure model. Beyond the critical bearing number, no further stationary solution is stable and the onset of self-excited vibrations can be observed. In accordance with the eigenvalue analysis above, the critical bearing number is significantly higher for the viscoelastic model compared to the rigid model. During the coast-down, the self-excited vibrations collapse only at a subcritical bearing number and the resulting asymmetry of the curves suggests that a certain range of bearing numbers exists where both stationary and periodic solutions are stable. This

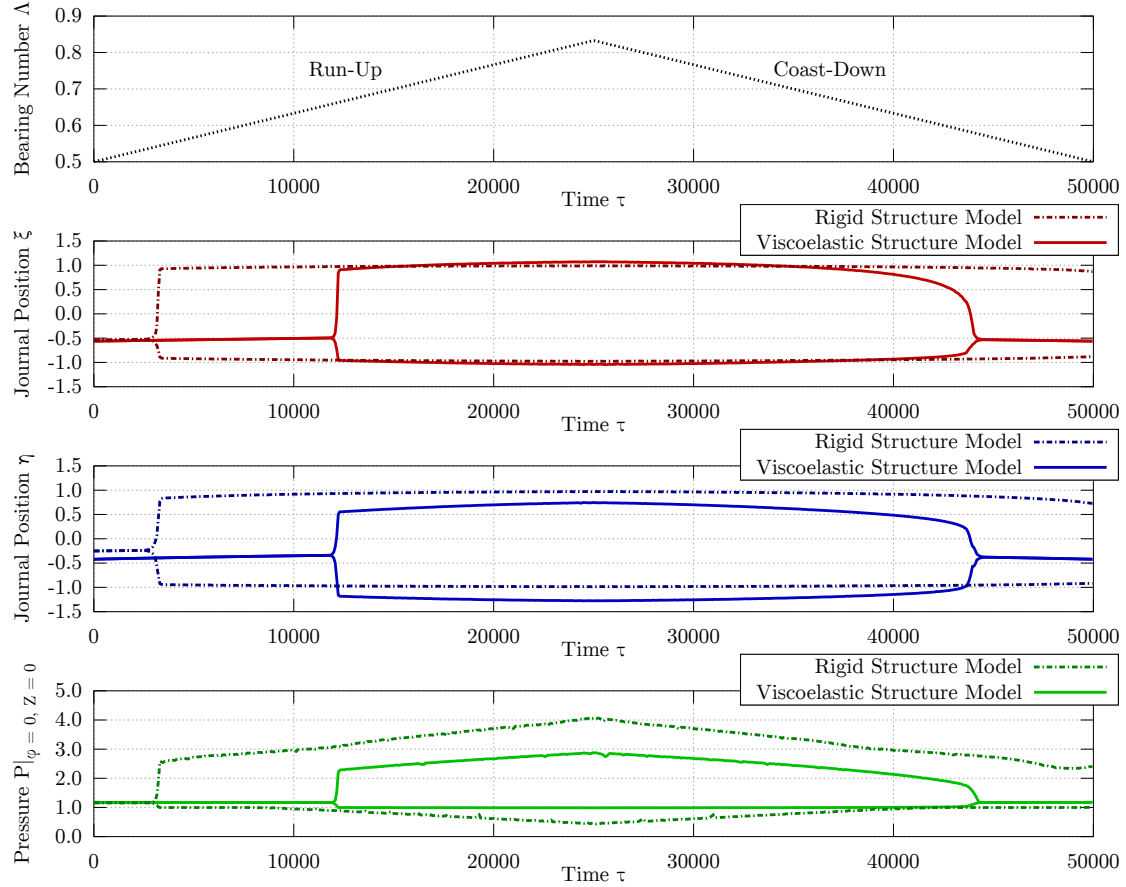


Figure 5. Signal envelopes of rotor journal position and fluid pressure during run-up and coast-down.

is a characteristic property of dynamic systems in which a subcritical Poincaré–Andronov–Hopf bifurcation and a subsequent fold bifurcation of cycles occur (Baum et al., 2015a,b). Most notably, the vertical rotor journal vibrations with the viscoelastic model exhibit smaller amplitudes than the rigid model predicts. Moreover, the absolute positions are shifted vertically because of the foil structure deformation, which allows for positions with $|\xi(\tau)| \geq 1$ and/or $|\eta(\tau)| \geq 1$.

The fourth plot in Figure 5 shows, at an exemplary point, the pressure $P(0, 0, \tau)$ as a green signal envelope curve. The arising oscillation is similar to the rotor journal position oscillations. It should be noted that each of the discrete pressure values could be considered as a vibrating subsystem. For the viscoelastic model, the pressure peaks are significantly lower than for the rigid model as a result of the foil structure deformation. Most notably, in contrast to the rigid model, this result shows that almost no underpressure with $P(\varphi, Z, \tau) < P_0$ is predicted by the viscoelastic model. Assuming the top foil to be lifted up until ambient pressure is reached, underpressure is forbidden in most of the available literature using a boundary condition originally proposed by Heshmat et al. (1983). However, according to the present investigation, this assumption seems to be redundant if an appropriate structure model is utilized, knowing that the top foil lift-off could also be limited by a counteracting structural stiffness.

Altogether, we conclude that frictional energy dissipation does not only increase the critical bearing number but has also the potential to reduce the amplitudes of self-excited vibrations if these cannot be avoided.

3.4 Amplitude Reduction of Self-Excited Vibrations

In the last part of the analysis, we investigate the aforementioned capability of frictional energy dissipation to reduce the amplitudes of self-excited vibrations if their occurrence cannot be prevented in the first place. Thus, we are now interested in limit cycles, i.e., periodic solutions $\mathbf{s}(\tau) = \mathbf{s}_p(\tau)$ of Equation (14) which verify the conditions

$$\mathbf{s}_p'(\tau) = \mathbf{k} \{ \mathbf{s}_p(\tau), \Lambda \}, \quad \mathbf{s}_p(\tau) = \mathbf{s}_p(\tau + \mathcal{T}). \quad (16)$$

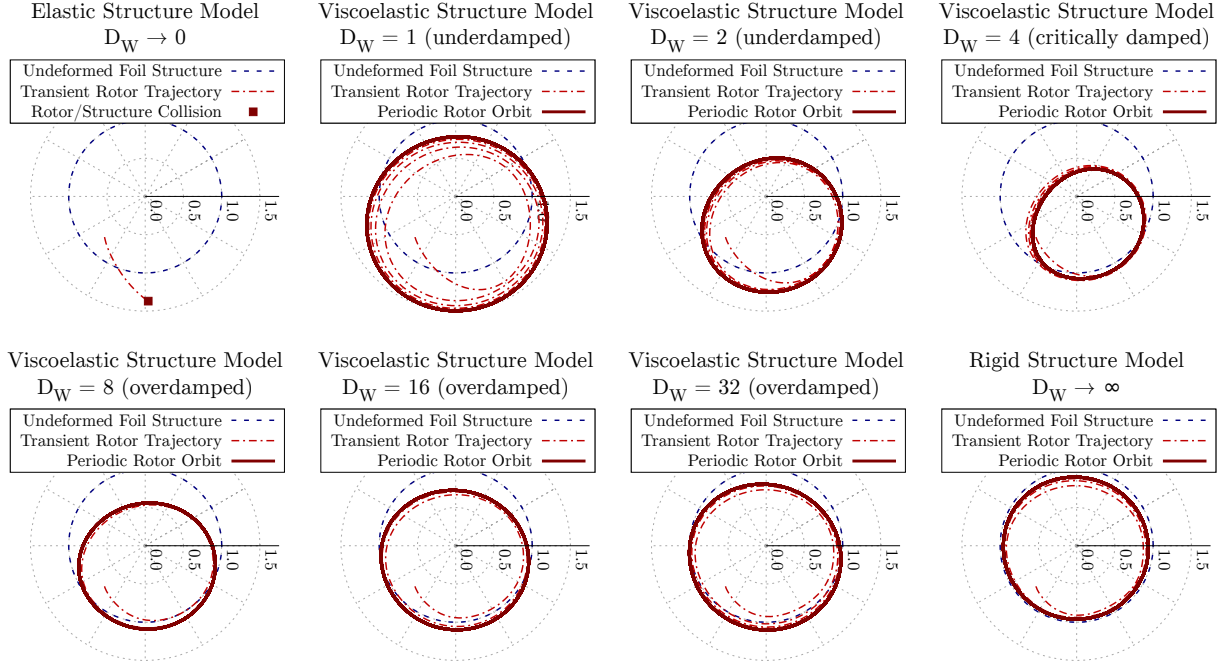


Figure 6. Periodic rotor journal orbits (self-excited vibrations) with increasing foil structure damping.

Choosing a moderate stiffness $K_W = 1$ and maintaining the rotational speed $\Lambda_0 = 0.600$ ($n_0 = 36\,000\, \text{min}^{-1}$), the influence of a varying damping parameter D_W is investigated in Figure 6. The chain-dotted red lines show rotor journal trajectories, which result in stable periodic orbits highlighted by thicker solid red lines. With the elastic structure model, no stable periodic orbit can be observed in the numerical simulation because the rotor journal is predicted to collide with the excessively deformed top foil. However, stable periodic orbits can be reproduced as expected when considering the viscoelastic structure model. With weak damping $D_W < 4$, the arising vibrations exhibit relatively large amplitudes with rotor journal eccentricities $\varepsilon(\tau) > 1$. These amplitudes are reduced with increasing damping coefficient, the optimum being equal to the critical damping $D_W \approx 4$, which has already been identified with regard to the stability of stationary equilibrium points. With strong damping $D_W > 4$, the rotor journal eccentricities fall back to $\varepsilon(\tau) \approx 1$. In accordance with a proposition by Le Lez et al. (2007), we conclude that there is an optimum damping which ensures to dissipate the maximum energy possible per cycle.

In Figure 7, some of the periodic solutions are compared in the frequency domain by means of an FFT analysis, yielding characteristic subsynchronous whirling frequencies with $2\pi/\mathcal{T} \approx \Lambda/2$. According to a heuristic explanation given by Genta (2009), the observed whirling speeds are directly correlated with the circumferential fluid velocity, which is the superposition of a Poiseuille flow and a Couette flow. Dominated by the triangular velocity profile of the Couette flow, the average circumferential fluid velocity is found to be approximately equal to half the peripheral rotor journal speed. Due to a decelerating influence of the Poiseuille flow, which is typically growing with increasing fluid film thickness, whirling motions at rather small eccentricities may actually occur with distinctly lower whirling speeds. In accordance with this expectation, the results of the FFT analysis reveal that not only the amplitudes but also the frequencies are minimized when considering the critically damped viscoelastic structure model. Altogether, it can be concluded that energy dissipation strongly affects subsynchronous whirling phenomena and thus must be considered carefully in realistic simulations.

4 Conclusion and Perspective

The nonlinear GFB rotor model presented in this paper has been developed with the aim of capturing the true coupled nature of fluid–structure–rotor interaction phenomena. As the present study is focused on gaining a basic understanding of frictional energy dissipation inside the bearing, a rather simple structure model based on a viscoelastic foundation is utilized. It has been shown that damping stabilizes stationary operating points and that the occurrence of self-excited vibrations may be prevented if an adequate dissipation rate is ensured. Moreover, it has been shown that vibrational amplitudes can be reduced significantly by means of frictional energy dissipation. Summing up all results, frictional energy dissipation proves to be of crucial importance with regard to the reduction or prevention of undesirable self-excited vibrations in GFB rotor systems.

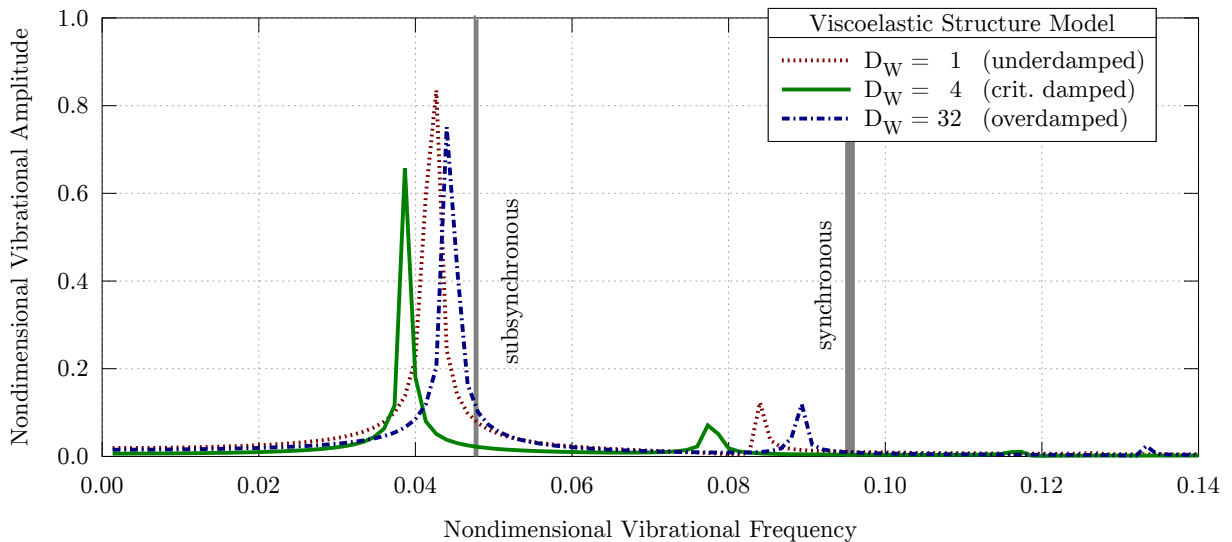


Figure 7. FFT analysis of an underdamped, a critically damped, and an overdamped GFB rotor system.

Future work will aim at the development of a more sophisticated dry sliding friction model considering stick-slip transitions and interaction mechanisms between the bumps. Moreover, the fluid model will be extended with regard to thermal effects and more realistic rotor models will be integrated into the simulation, knowing that many practical issues caused by subsynchronous vibrations are directly related to heavy loading conditions and rotor unbalance.

References

Baum, C.; Hetzler, H.; Seemann, W.: On the stability of balanced rigid rotors in air foil bearings. In: *Proceedings of the SIRM 2015*, Magdeburg, Germany (2015a).

Baum, C.; Leister, T.; Seemann, W.: Foil air bearing rotor interaction – Bifurcation analysis of a Laval rotor. In: *Proceedings of the EUROMECH Colloquium 573*, Lyon, France (2015b).

Bin Hassan, M. F.; Bonello, P.: A neural network identification technique for a foil-air bearing under variable speed conditions and its application to unbalance response analysis. *Journal of Tribology*, 139, 2, (2017).

Bonello, P.; Pham, H. M.: The efficient computation of the nonlinear dynamic response of a foil-air bearing rotor system. *Journal of Sound and Vibration*, 333, 15, (2014), 3459–3478.

Bou-Saïd, B.; Grau, G.; Iordanoff, I.: On nonlinear rotor dynamic effects of aerodynamic bearings with simple flexible rotors. *Journal of Engineering for Gas Turbines and Power*, 130, 1, (2008).

Genta, G.: *Vibration Dynamics and Control*. Springer, New York, United States of America (2009).

Hamrock, B. J.: *Fundamentals of Fluid Film Lubrication (NASA Reference Publication 1255)*. National Aeronautics and Space Administration, United States of America (1991).

Heshmat, H.; Walowitz, J. A.; Pinkus, O.: Analysis of gas-lubricated foil journal bearings. *Journal of Lubrication Technology*, 105, 4, (1983), 647–655.

Hoffmann, R.; Pronobis, T.; Liebich, R.: Non-linear stability analysis of a modified gas foil bearing structure. In: *Proceedings of the 9th IFToMM International Conference on Rotor Dynamics*, Milan, Italy (2014).

Howard, S. A.: Rotordynamics and design methods of an oil-free turbocharger. Tech. Rep. NASA CR-208689, National Aeronautics and Space Administration, United States of America (1999).

Howard, S. A.; Bruckner, R. J.; DellaCorte, C.; Radil, K. C.: Gas foil bearing technology advancements for closed Brayton cycle turbines. Tech. Rep. NASA TM-214470, National Aeronautics and Space Administration, United States of America (2007).

Howard, S. A.; Bruckner, R. J.; Radil, K. C.: Advancements toward oil-free rotorcraft propulsion. Tech. Rep. NASA TM-216094, National Aeronautics and Space Administration, United States of America (2010).

Howard, S. A.; DellaCorte, C.; Valco, M. J.; Prahl, J. M.; Heshmat, H.: Dynamic stiffness and damping characteristics of a high-temperature air foil journal bearing. *Tribology Transactions*, 44, 4, (2001), 657–663.

Larsen, J. S.; Varela, A. C.; Santos, I. F.: Numerical and experimental investigation of bump foil mechanical behaviour. *Tribology International*, 74, (2014), 46–56.

Le Lez, S.; Arghir, M.; Frêne, J.: Static and dynamic characterization of a bump-type foil bearing structure. *Journal of Tribology*, 129, 1, (2007), 75–83.

Leister, T.; Baum, C.; Seemann, W.: Computational analysis of foil air journal bearings using a runtime-efficient segmented foil model. In: *Proceedings of the ISROMAC 2016*, Honolulu, United States of America (2016a).

Leister, T.; Baum, C.; Seemann, W.: Sensitivity of computational rotor dynamics towards the empirically estimated lubrication gap clearance of foil air journal bearings. *Proc. Appl. Math. Mech.*, 16, 1, (2016b), 285–286.

Peng, J.-P.; Carpino, M.: Calculation of stiffness and damping coefficients for elastically supported gas foil bearings. *Journal of Tribology*, 115, 1, (1993), 20–27.

Peng, Z. C.; Khonsari, M. M.: Hydrodynamic analysis of compliant foil bearings with compressible air flow. *Journal of Tribology*, 126, 3, (2004), 542–546.

Reynolds, O.: On the theory of lubrication and its application to Mr. Beauchamp Tower's experiments, including an experimental determination of the viscosity of olive oil. *Philosophical Transactions of the Royal Society of London*, 177, (1886), 157–234.

Ruscitto, D.; McCormick, J.; Gray, S.: Hydrodynamic air lubricated compliant surface bearing for an automotive gas turbine engine, I – Journal bearing performance. Tech. Rep. NASA CR-135368, National Aeronautics and Space Administration, United States of America (1978).

San Andrés, L.; Kim, T. H.: Analysis of gas foil bearings integrating FE top foil models. *Tribology International*, 42, 1, (2008), 111–120.

San Andrés, L.; Kim, T. H.: Thermohydrodynamic analysis of bump type gas foil bearings: A model anchored to test data. *Journal of Engineering for Gas Turbines and Power*, 132, 4, (2010).

Szeri, A. Z.: *Fluid film lubrication*. Cambridge University Press, Cambridge, United Kingdom, 2nd edn. (2010).

Thomson, W.: *Theory of Vibration with Applications*. CRC Press, Boca Raton, United States of America, 4th edn. (1996).

Walowitz, J. A.; Anno, J. N.: *Modern developments in lubrication mechanics*. Applied Science Publishers, London, United Kingdom (1975).

Address: Institute of Engineering Mechanics, Karlsruhe Institute of Technology, Kaiserstr. 10, D-76131 Karlsruhe
 e-mail: {tim.leister, christoph.baum, wolfgang.seemann}@kit.edu

On the Incorporation of Friction Into a Simultaneously Coupled Time Domain Model of a Rigid Rotor Supported by Air Foil Bearings

Sebastian von Osmanski, Jon S. Larsen, Ilmar F. Santos

Despite decades of research, the dynamics of air foil bearings (AFBs) are not yet fully captured by any model, suggesting that the fundamental mechanisms of the AFB and their relative merits are not yet fully understood. The recent years have seen promising results from nonlinear time domain models, allowing the dynamic pressure-compliance interaction and the unsteady terms of the compressible Reynolds equation to be considered.

By including the simple elastic foundation model (SEFM) in a fully coupled simultaneous time integration, the dynamics of a rotor supported by industrial AFBs have previously been modelled by the authors, leading to good agreement with experimental results. In this paper, the authors investigate the substitution of the SEFM for a new foil structure model which is based on directly measurable quantities and includes frictional energy dissipation in the foil structure. An important finding is that the incorporation of a friction model into the global model cannot be reconciled with a simultaneous time solution without the inclusion of the foil inertia. The resulting AFB model allows the effects of friction on AFB performance to be directly examined and leads to the questioning of friction's role and its significance to the operation of AFBs.

Nomenclature

AFB	Air Foil Bearing	h, \tilde{h}	Film height, $\tilde{h} = h/C$
CG	Center of Gravity	h_b	Bump foil height
DAE	Differential/Algebraic Equation	h_c, \tilde{h}_c	Film height (compliant), $\tilde{h}_c = h_c/C$
DOF	Degree of Freedom	h_r, \tilde{h}_r	Film height (rigid), $\tilde{h}_r = h_r/C$
FE	Finite Element	h_s, \tilde{h}_s	Slope height, $\tilde{h}_s = h_s/C$
ODE	Ordinary Differential Equation	k	Stiffness
SEFM	Simple Elastic Foundation Model	k_{j,d_j}	Truss stiffness and damping, $j \in \{1, 1b, 2, 3, 3b, 4\}$
(\cdot)	Time derivative, $d^2/d\tau^2$	l_0	Bump half length
(\cdot)	Time derivative, $d/d\tau$	l_1, l_2	Distance from CG to bearings
$\nabla \cdot$	Divergence	l_3, l_4	Distance from CG to discs
∇	Gradient, $\nabla = \{\partial/\partial\theta, \partial/\partial\tilde{z}\}$	m	Mass
A, B	Bearings	p, \tilde{p}	Film pressure, $\tilde{p} = p/p_a$
C	Radial clearance	p_a	Ambient pressure
E_b	Young's modulus of bump foil material	t	Physical time
E_t	Young's modulus of top foil material	t_b	Thickness of bump foil
I	Mass moment of inertia	t_t	Thickness of top foil
L, \tilde{L}	Bearing length, $\tilde{L} = L/R$	v_r	Relative sliding velocity
N_p	Number of bearing pads	x, y, z, \tilde{z}	Cartesian coordinates, $\tilde{z} = z/R$
R	Journal radius	x_j	Generalised degree of freedom
R_b	Bump radius of curvature	x_j	Relative displacement
S	Compressibility number, $S = 6\mu\omega/p_a (R/C)^2$	α	Bearing position, $\alpha = A, B$
S_b	Bump foil pitch	γ	Friction function smoothing parameter
W, \tilde{W}	Static load components, $\tilde{W} = 1/(p_a R^2)W$	μ	Dynamic viscosity
\tilde{p}_m	Nondimensional mean axial pressure	μ_f	Coefficient of friction
e, ε	Journal eccentricity components, $\varepsilon = e/C$	ν_b	Poisson's ratio of bump foil material
f_N	Normal force function	ν_t	Poisson's ratio of top foil material
f_μ	Friction force	ω	Angular speed of journal
f_{μ_f}	Friction coefficient smoothing function		

ψ	Film state variable (nondimensional), $\psi = \tilde{p}\tilde{h}$	Ψ	Film state vector
ρ_b	Density of bump foil material	$\tilde{\mathbf{p}}$	Pressure vector
ρ_t	Density of top foil material	$\boldsymbol{\varepsilon}$	Eccentricity vector, $\{\varepsilon_{Ax}, \varepsilon_{Ay}, \varepsilon_{Bx}, \varepsilon_{By}\}^T$
τ	Dimensionless time, $\tau = \omega t$	\mathbf{f}_μ	Vector of friction forces
θ	Circumferential angle	\mathbf{f}_p	Vector of pressure forces
θ'	Curvilinear coordinate, $\theta' = \theta R$	$\mathbf{g}()$	Nonlinear vector function
θ_0	Bump half angle	\mathbf{r}	Residual vector
θ_j	Truss transmission angle, θ_d or θ_{db}	\mathbf{x}	Foil displacement vector
θ_l	First pad leading edge angle	\mathbf{y}	Global state vector
θ_s	Inlet slope extend	$\mathbf{z}_1, \mathbf{z}_2$	Rotor state vectors, $\mathbf{z}_1 = \boldsymbol{\varepsilon}$, $\mathbf{z}_2 = \mathbf{z}_1$
θ_t	First pad trailing edge angle	$\mathbf{0}$	Zero matrix
$\tilde{\theta}$	Dimensionless circumferential coordinate, $\tilde{\theta} = \theta'/R = \theta$	$\mathbf{A}_f, \tilde{\mathbf{A}}_f$	Foil structure system matrix
ζ	Damping ratio	$\mathbf{D}_f, \tilde{\mathbf{D}}_f$	Foil structure damping matrix
$\tilde{\mathbf{u}}$	Foil structure state space vector, $\tilde{\mathbf{u}} = \{\tilde{\mathbf{x}}^T, \dot{\tilde{\mathbf{x}}}^T\}^T$	$\mathbf{G}_r, \tilde{\mathbf{G}}_r$	Rotor gyroscopic matrix, $\tilde{\mathbf{G}}_r = \omega^2 C/(p_a R^2) \mathbf{G}_r$
$\mathbf{f}, \tilde{\mathbf{f}}$	Bearing force vector, $\mathbf{f} = \{\mathbf{f}_A^T, \mathbf{f}_B^T\}^T, \tilde{\mathbf{f}} = 1/(p_a R^2) \mathbf{f}$	\mathbf{I}	Identity matrix
$\mathbf{f}_{ub}, \tilde{\mathbf{f}}_{ub}$	Unbalance force, $\tilde{\mathbf{f}}_{ub} = 1/(p_a R^2) \mathbf{f}_{ub}$	$\mathbf{K}_f, \tilde{\mathbf{K}}_f$	Foil structure stiffness matrix
\mathbf{s}	Advection vector, $\mathbf{s} = \{S, 0\}^T$	$\mathbf{M}_f, \tilde{\mathbf{M}}_f$	Foil structure mass matrix
$\mathbf{w}, \tilde{\mathbf{w}}$	Load vector, $\tilde{\mathbf{w}} = 1/(p_a R^2) \mathbf{w}$	$\mathbf{M}_r, \tilde{\mathbf{M}}_r$	Rotor mass matrix, $\tilde{\mathbf{M}}_r = \omega^2 C/(p_a R^2) \mathbf{M}_r$
		Γ	Fluidity matrix
		(\cdot)	Nondimensional quantity

1 Introduction

Practical application of gas lubrication appeared in the mid-1950s driven by its attractiveness to several emerging technologies and facilitated by improved experimental equipment together with the development of computerised numerical methods (Powell, 1970). The first gas bearings with compliant inner surfaces appeared in the mid-1960s and the air foil bearing (AFB) was introduced industrially by Garret AiResearch in 1969 (Agrawal, 1997). The AFB offers several advantages compared to conventional rigid gas bearings, and it is a key component in NASA's efforts towards creating a completely oil-free turbine engine (NASA, 2001). NASA is interested in the AFB technology's weight-saving potentials in rotorcrafts and its high-temperature capabilities, but AFBs also present an environmentally friendly alternative in many applications of oil-lubricated high-speed rotating machinery.

The compliant nature of AFBs does, however, complicate the modelling of its dynamic characteristics and is capable of introducing undesirable nonlinear features. As the performance of AFB supported rotor-bearing systems is often limited by nonlinear phenomena, such as sub-synchronous vibrations driven by unbalance, reliable means for predicting the response are an essential prerequisite for further spread of the technology.

The majority of the literature on AFB modelling rests on the original contributions by Heshmat et al. (1983b,a), who introduced the simple elastic foundation model (SEFM). The original SEFM, as well as the refined version by Peng and Carpino (1993), was applied in a perturbation method framework introduced by Lund (1968) and hence relied on a linearisation of the reaction forces to effectively replace the bearing and fluid film with a spring-dashpot system. Such analyses are inherently restricted to an assumed small-amplitude periodic motion (Bonello and Pham, 2009), and recent work (Larsen et al., 2016) additionally suggests an inadequacy in the applied Taylor series expansion of the pressure field. Another commonality shared throughout much of the literature is equivalent viscous models for the energy dissipation in the compliant structure. This approximation is pivotal since sliding friction in the foil structure is widely assumed to constitute a major source of damping (Agrawal, 1997; San Andrs and Kim, 2007; Howard and San Andrs, 2011; Le Lez et al., 2009) and hence to be essential in the workings of the AFB.

Nonlinear time domain integration circumvents the limitations of the perturbation techniques and provides a basis for the incorporation of foil structure models without the assumption of viscous dissipation. Applying different foil structure models, but based on a decoupling of the fluid, rotor and foil structure equations, time domain models have been presented by for example Lee et al. (2009); Le Lez et al. (2009); Hoffmann et al. (2015). This approach introduces a demand for very small time steps and temporal convergence studies, which has been overcome using simultaneous formulations (Bonello and Pham, 2014b,a; Larsen and Santos, 2015; Larsen et al., 2015b). Several promising results have been presented from these simultaneous models, but they are, however, still relying on the SEFM and hence on the assumption of viscous dissipation.

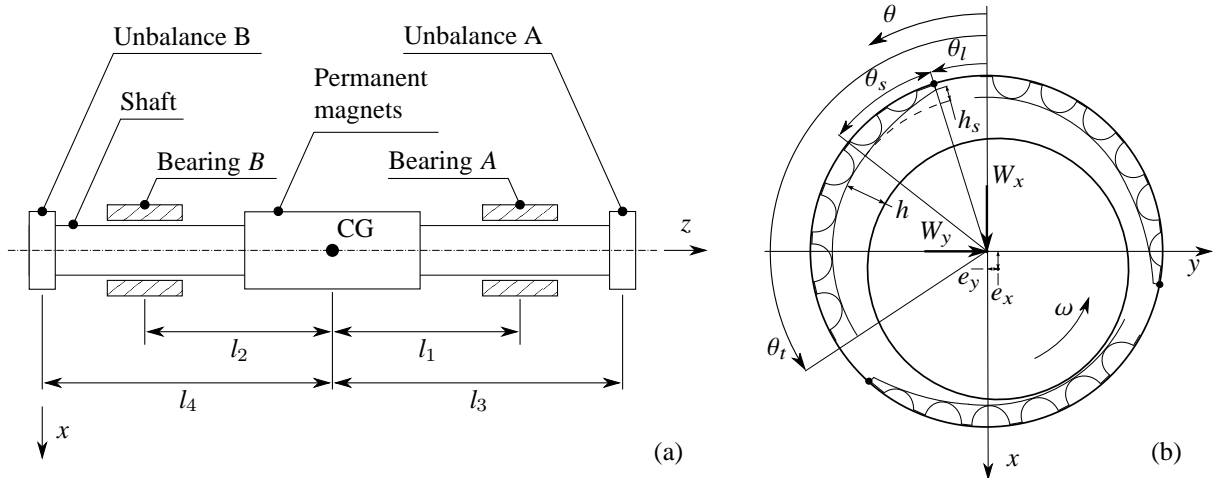


Figure 1: Schematics and nomenclature of a rigid rotor supported by AFBs: (a) shaft, bearings and rotor discs for unbalance masses; and (b) detailed view of the bearing geometry.

In recent work by the authors (von Osmanski et al., 2017), a fully coupled simultaneously formulated AFB model including friction has been presented. The current work provides additional discussions on the necessity of foil mass inclusion and an assessment of three effects related to friction: (a) displacement of the static equilibrium; (b) introduction of a dynamic foil stiffness; and (c) dissipation of energy through sliding friction.

2 The Rotor–Bearing System

The presented model and the derived considerations are based on a test rig previously presented and described by the authors (Larsen et al., 2015a,b; Larsen and Santos, 2015; Larsen et al., 2016; von Osmanski et al., 2017). The rig comprises a near-symmetrical hollow rotor supported by two identical second generation Siemens AFBs as sketched in Fig. 1a. The illustrated permanent magnets are part of the electrical drive capable of rotating the shaft to approximately 30 kRPM and the discs at each of the shaft's extremities allow unbalance mass to be added. As observed from the AFB geometry (Fig. 1b), the foil structure is segmented into three pads fixed to the bearing housing at their leading edges. The dimensions and mechanical properties as used throughout this paper are listed in Table 1.

3 Mathematical Model of the Rotor and the Fluid Film

As the dynamics of the support structure is not considered, modelling of the rotor-bearing system requires three domains to be assessed: the rotor, the fluid film and the compliant structure of the AFBs. This paper concerns mainly the latter of these, hence only a brief exposition of the applied rotor and fluid film models will be made.

The operational range of the rig is limited by the electrical drive to 30 kRPM, while the lowest free-free natural frequency of the assembled shaft is found to be approximately 1050 Hz, hence a rigid shaft model is deemed adequate. This gives a four degrees of freedom (DOFs) model which is considered a system of first order ordinary differential equations (ODEs) as

$$\begin{Bmatrix} \dot{\mathbf{z}}_1 \\ \dot{\mathbf{z}}_2 \end{Bmatrix} = \begin{Bmatrix} \mathbf{0} & \mathbf{I} \\ \mathbf{0} & \tilde{\mathbf{M}}_r^{-1} \tilde{\mathbf{G}}_r \end{Bmatrix} \begin{Bmatrix} \mathbf{z}_1 \\ \mathbf{z}_2 \end{Bmatrix} + \begin{Bmatrix} \mathbf{0} \\ \tilde{\mathbf{M}}_r^{-1} (\tilde{\mathbf{w}} - \tilde{\mathbf{f}} + \tilde{\mathbf{f}}_{ub}) \end{Bmatrix}, \quad (1)$$

where the state vectors hold the rotor displacements and velocities at the bearing positions as

$$\mathbf{z}_1 = \mathbf{\hat{e}} = \{\mathcal{E}_{Ax}, \mathcal{E}_{Ay}, \mathcal{E}_{Bx}, \mathcal{E}_{By}\}^T \quad \text{and} \quad \mathbf{z}_2 = \mathbf{\hat{z}}_1 = \mathbf{\hat{e}}. \quad (2)$$

The system matrix contains the dimensionless mass and gyroscopic matrices of the rotor, \tilde{M}_r and \tilde{G}_r , while \tilde{w} , \tilde{f} and \tilde{f}_{ub} represent the static load, integrated fluid film reaction forces and unbalance forces, respectively.

The fluid film formed between the shaft and compliant inner surface of the AFBs is assumed to be governed by the

Table 1: Geometry, material properties and operating conditions of the Siemens AFB test rig.

Shaft assembly				
Bearing A to CG, l_1	201.1 mm	Mass, $m = m_x = m_y$		21.1166 kg
Bearing B to CG, l_2	197.9 mm	Polar moment of inertia, I_{zz}		30.079×10^{-3} kg m ²
Unbalance A to CG, l_3	287.2 mm	Transverse moment of inertia, $I_{xx} = I_{yy}$		525.166×10^{-3} kg m ²
Unbalance B to CG, l_4	304.0 mm			
Bearing configuration				
Bearing radius, R	33.50 mm	First pad leading edge, θ_l		30°
Bearing length, L	53.00 mm	First pad trailing edge, θ_t		145°
Radial clearance, C	40 μm	Slope extend, θ_s		30°
Number of pads, N_p	3	Slope height, h_s		50 μm
Fluid properties				
Viscosity, μ	1.95×10^{-5} Pa s	Ambient pressure, p_a		1×10^5 Pa
Bump foil properties				
Bump foil thickness, t_b	0.13 mm	Bump foil pitch, S_b		7.00 mm
Bump foil half length, l_0	3.43 mm	Bump foil height, h_b		1.15 mm
Young's modulus E_b	207 GPa	Poisson's ratio, ν_b		0.3
Radius of curvature, R_b	5.7 mm	Coefficient of friction, μ_f		0.05
Density, ρ_b	8280 kg/m ³	Bump half angle, θ_0		37°
Top foil properties				
Top foil thickness, t_t	0.254 mm	Poisson's ratio, ν_t		0.3
Young's modulus E_t	2.07×10^{11} Pa	Density, ρ_t		8280 kg/m ³

isothermal, compressible, transient Reynolds equation:

$$\nabla \cdot (\tilde{p} \tilde{h}^3 \nabla \tilde{p}) = \nabla \cdot (\tilde{p} \tilde{h}) \mathbf{s} + 2S \frac{d}{d\tau} (\tilde{p} \tilde{h}), \quad (3)$$

where $S = 6\mu\omega/p_a (R/C)^2$ is the compressibility number, $\mathbf{s} = \{S, 0\}^T$ is the advection vector and the film height \tilde{h} is divided into a rigid and a compliant contribution as first suggested by Heshmat et al. (1983b):

$$\tilde{h} = \tilde{h}_r(\varepsilon_x, \varepsilon_y, \tilde{\theta}) + \tilde{h}_c. \quad (4)$$

The rigid contribution \tilde{h}_r depends on the initial undeformed bearing geometry as illustrated in Fig. 1b and is given by e.g. von Osmanski et al. (2017), while the compliant contribution \tilde{h}_c is treated in the following sections.

Following a partial substitution of ψ for $\tilde{p} \tilde{h}$ as introduced in Bonello and Pham (2014a,b), the fluid film partial differential equation Eq. (3) is spatially discretised using a finite element (FE) scheme. This gives a system of nonlinear ODEs in the film state variable time derivative vector $\dot{\psi}_\alpha$ for each bearing $\alpha = A, B$

$$\Gamma_\alpha \dot{\psi}_\alpha = \mathbf{r}_\alpha(\psi_\alpha, \dot{\psi}_\alpha), \quad (5)$$

where the fluidity matrix Γ_α is constant for a given angular velocity, while the residual vector \mathbf{r}_α depends on both the pressures, the film heights and the film heights' temporal derivatives.

4 Modelling of the Foil Structure

In the first time domain model presented by Larsen et al. (2015b); Larsen and Santos (2015) as well as in the presented models by Bonello and Pham (2014a,b), the compliant height contribution \tilde{h}_c in Eq. (4) is supplied using the SEFM. This is numerically efficient, but implies that (a) the foil structure's energy dissipation is modelled as being viscous using an equivalent rotor-speed based loss factor; (b) the stiffness is linear and independent of both deformation and frequency; and (c) neighbouring points in the foil are assumed to deform independently. Other authors, such as Hoffmann et al. (2015); San Andrs and Kim (2009), have applied the SEFM merely to the underlying bump foil structure while incorporating more comprehensive models for the top foil. In this case, the top foil's bending stiffness couples the deflections of neighbouring points, but any bump–bump interaction effects are still neglected. An objective of the present work has hence been to discard the SEFM entirely in favour of a more general foil structure model. This model should facilitate the inclusion of friction, allow for a simultaneous solution of the equation system and be sufficiently efficient to permit time integration.

4.1 Friction Models

Sliding friction in the foil structure is widely assumed to be an important mechanism in AFBs (Agrawal, 1997; San Andrs and Kim, 2007; Howard and San Andrs, 2011; Le Lez et al., 2009); consequently, a friction model is included in the present work. Time integration of friction phenomena is difficult due to the nonlinear behaviour of the friction force near zero velocity and/or zero normal force. The potentially applicable friction models available in the literature can be roughly divided into three categories: stick-slip bookkeeping with alternating boundary conditions (Tariku and Rogers, 2001; Lee et al., 2009; Le Lez et al., 2007), nonlinear springs with moving reference points (Larsen et al., 2014) and continuous dynamic friction approximations (Oden and Martins, 1985; Makkar et al., 2005; Le Lez et al., 2008; Petrov and Ewins, 2003).

The stick-slip bookkeeping models introduce a differentiation between static and dynamic friction regimes in which either a boundary condition or a dynamic friction force is applied. These models hence rely on a continuous evaluation of the stick/slip states, and the abrupt changes inevitably caused by the change of state pose a challenge to numerical stability due to non-smooth, or even discontinuous, reaction and friction forces.

A friction model relying on nonlinear springs with moving reference points has also been suggested (Larsen et al., 2014) and shown to perform well in a quasi-static setting. The model handles the classical issue of determining the friction force at zero velocity, but has proven difficult to apply in a time domain framework due to the requirement of instantaneous detection of direction shifts.

The friction model applied in the current work belongs to the group of continuous dynamic friction approximations. These are based on expressions for the friction force f_μ of the form

$$f_\mu = f_N f_{\mu_f}(v_r), \quad (6)$$

where f_N is the normal force function and $f_{\mu_f}(v_r)$ is a smooth function of the sliding velocity v_r approximating the sign function. In the literature, various different functions can be found serving as sign approximations, including the inverse tangent, fractions similar to $v_r/(\gamma + |v_r|)$ and the hyperbolic tangent. The latter is used in the present as

$$f_{\mu_f}(v_r) = \mu_f \tanh(\gamma v_r), \quad (7)$$

where μ_f is a dynamic coefficient of friction and γ is a smoothing parameter controlling the slope near $v_r = 0$ and hence the level of approximation. As it can be seen, Eq. (7) provides no distinction between static and dynamic friction, but this could be achieved using the extended version given by Makkar et al. (2005).

Note that while the particular choice of friction model and smoothing function is debatable, an important point is that all of the assessed approaches share the common characteristic of velocity dependency. This is, to the best knowledge of the authors, the case for all existing and suitable friction models.

4.2 Structural Models

The compliant structure of the Siemens AFB consists of a bump foil and a top foil. For the present purpose, a simple one dimensional Bernoulli–Euler beam model is utilised for the top foil, as the main point of attention is the supporting bump foil structure. This approach leaves out any axial film height variations, but this has been shown to be a reasonable assumption (San Andrs and Kim, 2009).

For modelling of the bump foil, a straightforward plane FE approach requires several thousand DOFs per bump (Larsen et al., 2014), and is hence precluded from time integration purposes. A model reduction technique could possibly be applied, but here an efficient equivalent model by Le Lez et al. (2007) is used instead. In this model, the bump foil is represented using bar elements forming a simple truss with member stiffness coefficients $k_1, k_2, k_3, k_4, k_{1b}, k_{3b}$ and force transmission angles θ_d, θ_{db} . These coefficients are calculated from 33 analytical expressions given by Le Lez et al. (2007) based on Castigliano’s second theorem, and their values for the present geometry are given by von Osmanski et al. (2017).

In Table 2, the effective radial stiffness of the truss model for a nine-bump foil strip with dimensions from Table 1 is compared to results from a plane FE model based on a very accurate replication of the actual foil geometry. To emphasise the significance of the boundary condition at the foil–housing contacts, results are included for both rolling and pinned supports at this interface. The truss coefficients from Le Lez et al. (2007) are based

on the case of rolling supports, meaning that the bumps are allowed to slide circumferentially with no frictional resistance. Considering that the widely used expression by Walowitz and Anno (1975) predicts a uniform stiffness of 0.88 GN/m^3 , the observed agreement between the truss and plane FE models is very good. If the foil-housing contacts are pinned, i.e. restrained from circumferential sliding, the effective truss stiffness is increased more than fivefold, while the plane FE model stiffness increases at least tenfold. A similar stiffening was observed by Feng and Kaneko (2010) and should be kept in mind as the two cases correspond to the extreme cases of zero friction and permanent sticking, respectively.

Table 2: Effective radial stiffness (for a uniform pressure) resulting from the truss model compared to a plane FE model for the two cases of (frictionless) rolling and pinned housing contact nodes.

Condition	Model	Effective normal stiffness for each bump [GN/m ³]								
		1	2	3	4	5	6	7	8	9
Sliding	Truss model	3.4	3.2	3.3	3.2	3.2	3.3	3.1	3.7	1.7
	Plane FE model	2.4	3.6	3.2	3.3	3.3	3.3	3.1	4.5	1.6
Pinned	Truss model	19.8	19.8	19.8	19.8	19.8	19.8	19.8	19.8	11.0
	Plane FE model	42.5	43.6	43.7	43.8	43.8	43.8	43.7	43.3	40.5

The truss model is formulated as a static model, meaning that it is governed by a system of algebraic equations. Coupling any (quasi-) static model directly to the differential equations governing the fluid film and the velocity dependent friction model gives rise to certain issues. These become evident if considering the simple mechanical system sketched in Fig. 2. It comprises a single point mass supported by four massless springs affected by a friction force in a configuration similar to the bump foil truss model. Writing out the governing equations in first order form, the following system can be obtained:

$$\begin{Bmatrix} 0 \\ 0 \\ 0 \\ \dot{x}_4 \\ \ddot{x}_4 \end{Bmatrix} = \begin{bmatrix} 2kc_\theta^2 & 0 & -kc_\theta^2 & 0 & 0 \\ 0 & k(3-2c_\theta^2) & kc_\theta s_\theta & -k & 0 \\ -kc_\theta^2 & kc_\theta s_\theta & kc_\theta^2 + k & 0 & 0 \\ 0 & 0 & 0 & 0 & 1 \\ 0 & k/m & 0 & -k/m & 0 \end{bmatrix} \begin{Bmatrix} x_1 \\ x_2 \\ x_3 \\ x_4 \\ \dot{x}_4 \end{Bmatrix} - \begin{Bmatrix} 0 \\ 0 \\ \frac{f_N(x_1, x_2, x_3) f_{\mu_f}(\dot{x}_3)}{0} \\ 0 \\ 0 \end{Bmatrix} \quad \text{where } \begin{aligned} c_\theta &= \cos \theta_d, \\ s_\theta &= \sin \theta_d. \end{aligned} \quad (8)$$

If friction is discarded, the upper three rows of Eq. (8) governing the massless truss are purely algebraic and hence provide neither velocities nor accelerations. Together with the two differential equations governing the point mass, this constitutes a system of semi-explicit differential/algebraic equations (DAEs). The DAEs represent a superset of the ODEs and are, in general, more troublesome since no guarantees on solution uniqueness or existence can be given as is the case for ODEs (see Poulsen et al. (2002); Petzold (1982)). Without friction, Eq. (8) is nevertheless very easy to solve. It could be condensed and solved as two first order ODEs, or it could be solved as is using a DAE solver.

Introducing friction, the solution of Eq. (8) becomes considerably more troublesome since the velocity required to determine the orientation and size of the friction force is not available. Obviously, this could be reconstructed using information from previous time steps using finite difference, but this would violate the requirement for a simultaneous formulation and reintroduce the demand for temporal convergence studies. In the case of a strictly positive normal force, the system could be considered as an implicit ODE (or DAE), but for any reasonable approximation to the sign function, this system is too stiff for practical purposes. In the actual AFB model, the case of zero normal force, implying zero friction force for any sliding velocity, would furthermore have to be spanned leaving the very structure of the equation system state dependent.

From a physical point of view, the fundamental issue is the lack of inertia to smooth out the displacements caused by the rapidly changing friction forces in the vicinity of zero sliding velocity. As a remedy, it is therefore natural to introduce the foil mass, even though this is per se insignificant to the overall rotordynamic response. Lumping the bump foil mass onto the truss structure (giving a diagonal mass matrix) the equations are remoulded from algebraic to differential with sliding velocities directly available. Coupling the obtained bump foil differential equations to the (also dynamic) Bernoulli–Euler beam top foil model and the friction model, the overall foil structure is assembled as visualised in Fig. 3. Notice that viscous dampers have also been introduced in the truss. These are principally undesired as a main objective is to model frictional instead of viscous dissipation, but a slight structural damping has proven numerically necessary due to the very high natural frequencies in the foil ranging up to around 500 kHz. The frequency range of interest for the rotordynamic response goes to around 500 Hz, and is hence well separated from the first natural frequency of the foil structure at around 2 kHz. This allows a proportional damping,

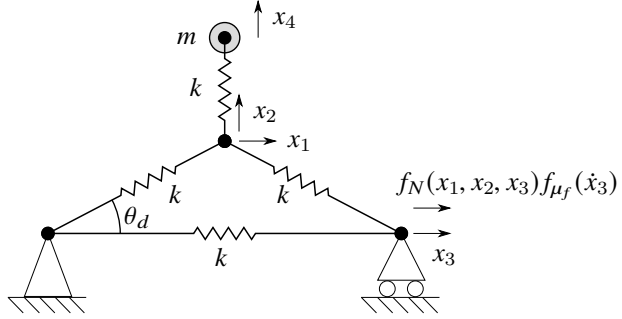


Figure 2: Mechanical system illustrating the challenges of using a massless foil model. It comprises a point mass (governed by a second order differential equation) supported by a massless truss (governed by four algebraic equations) subject to a friction force.

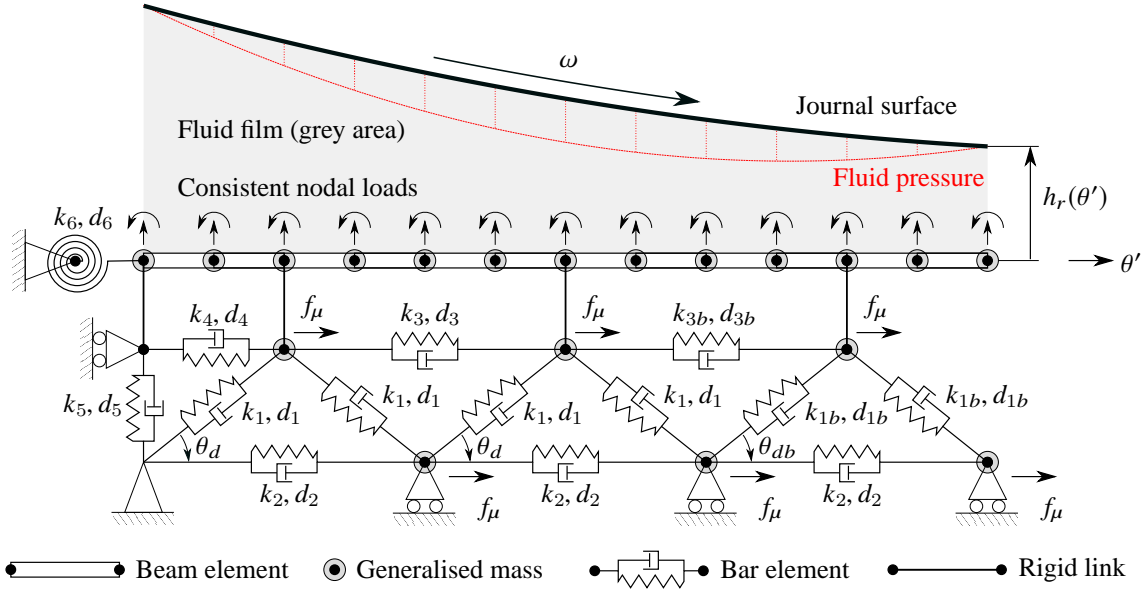


Figure 3: Illustration of the foil structure model for three bumps interacting with the journal through the generated fluid film (grey area). k_j, d_j denote the truss element stiffness and damping, while θ_j are the transmission angles and f_μ represents the friction forces. Notice that the last bump uses different coefficients than the remaining ones.

providing a damping ratio of $\zeta = 0.001$ at 500 Hz, to be introduced to effectively dampen out the foil structure dynamics while leaving the dynamics of interest virtually unaffected.

Collecting the DOFs of the foil structure for each bearing $\alpha = A, B$ into the foil state vector $\tilde{\mathbf{u}}_\alpha$, the system of first order nonlinear ODEs governing the structure in Fig. 3 can be written as

$$\dot{\tilde{\mathbf{u}}}_\alpha = \underbrace{\tilde{\mathbf{A}}_f}_{\begin{bmatrix} \mathbf{0} & \mathbf{I} \\ -\tilde{\mathbf{M}}_f^{-1}\tilde{\mathbf{K}}_f & -\tilde{\mathbf{M}}_f^{-1}\tilde{\mathbf{D}}_f \end{bmatrix}} \tilde{\mathbf{u}}_\alpha + \left\{ \tilde{\mathbf{M}}_f^{-1} (\mathbf{f}_\mu (\tilde{\mathbf{u}}_\alpha, \dot{\tilde{\mathbf{u}}}_\alpha, \tilde{\mathbf{p}}_\alpha) + \mathbf{f}_p (\tilde{\mathbf{p}}_\alpha)) \right\}, \quad (9)$$

where $\tilde{\mathbf{M}}_f$, $\tilde{\mathbf{D}}_f$ and $\tilde{\mathbf{K}}_f$ are the mass, (proportional-) damping and stiffness matrices of the foil structure, respectively. The vector function \mathbf{f}_μ represents the friction forces at the contact nodes given from Eq. (6) and the vector function \mathbf{f}_p represents the work equivalent nodal loads on the top foil stemming from the fluid film pressure $\tilde{\mathbf{p}}_\alpha$.

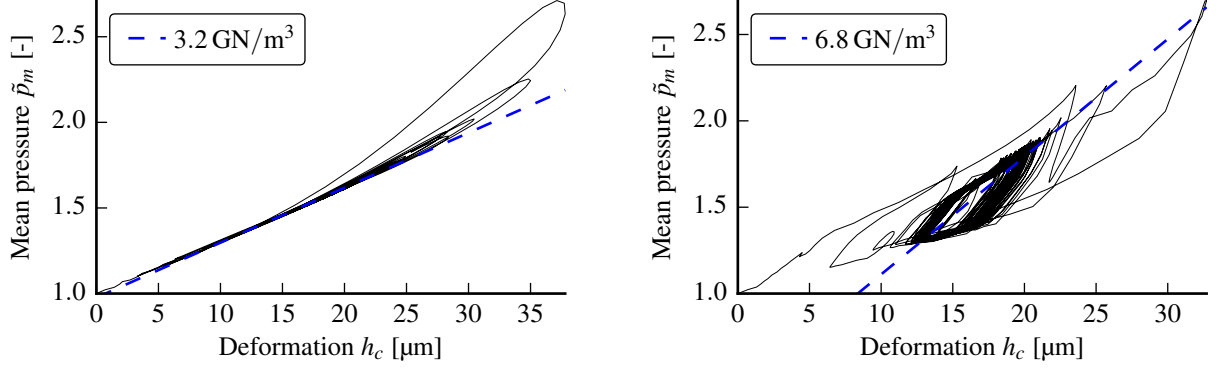


Figure 4: Hysteresis curves at the summit of bump three in the second pad segment ($\theta = 180^\circ$) for 0.5 s of simulation from a rotor drop from the centre with (left) and without (right) friction. The dashed lines are fits to the last 0.125 s and indicate the local effective foil stiffness.

5 Structure of the Assembled Equation System

The three sets of first order ODEs representing the rotor, fluid and foil structure domains given from Eq. (1), Eq. (5) and Eq. (9) are now coupled. For this purpose, the global state vector

$$\mathbf{y} = \{ \Psi_A^T \ \Psi_B^T \ \tilde{\mathbf{u}}_A^T \ \tilde{\mathbf{u}}_B^T \ \mathbf{z}_1^T \ \mathbf{z}_2^T \}^T, \quad (10)$$

is introduced, using which a single system of nonlinear first order ODEs can be written as

$$\begin{Bmatrix} \dot{\Psi}_A \\ \dot{\Psi}_B \\ \dot{\tilde{\mathbf{u}}}_A \\ \dot{\tilde{\mathbf{u}}}_B \\ \dot{\mathbf{z}}_1 \\ \dot{\mathbf{z}}_2 \end{Bmatrix} = \begin{bmatrix} 0 & \dots & \dots & \dots & 0 \\ \vdots & \dots & \dots & \dots & \vdots \\ \vdots & \vdots & \tilde{\mathbf{A}}_f & \mathbf{0} & \dots \\ \vdots & \vdots & \mathbf{0} & \tilde{\mathbf{A}}_f & \vdots \\ \vdots & \vdots & \dots & \mathbf{0} & \mathbf{I} \\ \mathbf{0} & \dots & \dots & \mathbf{0} & \tilde{\mathbf{M}}_r^{-1} \tilde{\mathbf{G}}_r & \mathbf{0} \end{bmatrix} \begin{Bmatrix} \Psi_A \\ \Psi_B \\ \tilde{\mathbf{u}}_A \\ \tilde{\mathbf{u}}_B \\ \mathbf{z}_1 \\ \mathbf{z}_2 \end{Bmatrix} + \begin{Bmatrix} \mathbf{g}_{\dot{\Psi}_A}(\Psi_A, \mathbf{z}_1, \mathbf{z}_2, \tilde{\mathbf{u}}_A) \\ \mathbf{g}_{\dot{\Psi}_B}(\Psi_B, \mathbf{z}_1, \mathbf{z}_2, \tilde{\mathbf{u}}_B) \\ \mathbf{g}_{\dot{\tilde{\mathbf{u}}}_A}(\Psi_A, \mathbf{z}_1, \tilde{\mathbf{u}}_A, \dot{\tilde{\mathbf{u}}}_A) \\ \mathbf{g}_{\dot{\tilde{\mathbf{u}}}_B}(\Psi_B, \mathbf{z}_1, \tilde{\mathbf{u}}_B, \dot{\tilde{\mathbf{u}}}_B) \\ \mathbf{0} \\ \tilde{\mathbf{M}}_r^{-1}(\tilde{\mathbf{w}} - \tilde{\mathbf{f}} + \tilde{\mathbf{f}}_{ub}) \end{Bmatrix}. \quad (11)$$

The nonlinear functions $\mathbf{g}_{\dot{\Psi}_\alpha}$ on the right hand side of the upper equations representing the fluid film are defined from Eq. (5), while those in the midmost rows representing the foil structure, $\mathbf{g}_{\dot{\tilde{\mathbf{u}}}_\alpha}$, are given as the nonlinear part of Eq. (9).

It should be noted that the numerical time integration of the coupled equation system given from Eq. (11) is a nontrivial task. To make the presented foil model extension practically feasible, considerable prior optimisation of the SEFM based time integration code has been necessary. Through these efforts, the SEFM based simulation times has been reduced from days to minutes; but with the new foil structure, especially the friction model, the relevant simulations nevertheless take in the order of 24 hours to complete.

6 Results & Discussion

To provide insight into the behaviour of the foil model and the influence of friction, a rotor drop from the bearing centres with a high level of unbalance at 20 kRPM is simulated for 0.5 s with and without friction. In Fig. 4, the mean axial pressure \tilde{p}_m is plotted as a function of the top foil deformation h_c at $\theta = 180^\circ$. This point is in the heaviest loaded region and coincident with the summit of bump three in the second pad. Setting γ to zero, effectively deactivating the friction model, the foil behaves linearly and no friction-induced hysteresis is present. Fitting a line to the last 125 ms reveals a local stiffness of 3.2 GN/m³, which is very close to the statically obtained values from Table 2. Activating the friction model using $\gamma = 10^4$, a hysteresis loop opens up and the fit now gives a line passing diagonally through the hysteresis loop indicating an increase in effective stiffness to 6.8 GN/m³.

In Fig. 5, the vertical eccentricity ratio in bearing A is plotted during the first and last 40 ms of the rotor drop simulation both with and without friction. In the transient part, the inclusion of friction lowers the displacement

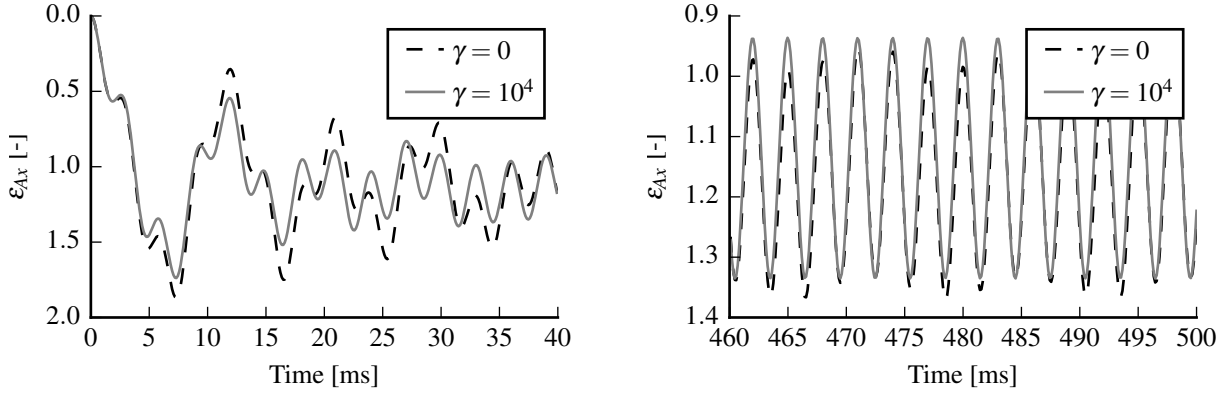


Figure 5: Vertical eccentricity ratio ε_{Ax} with friction ($\gamma = 10^4$) and without ($\gamma = 0$) friction. The first 40 ms after the rotor drop are shown to the left, while the final 40 ms, where steady state has set in, are shown to the right.

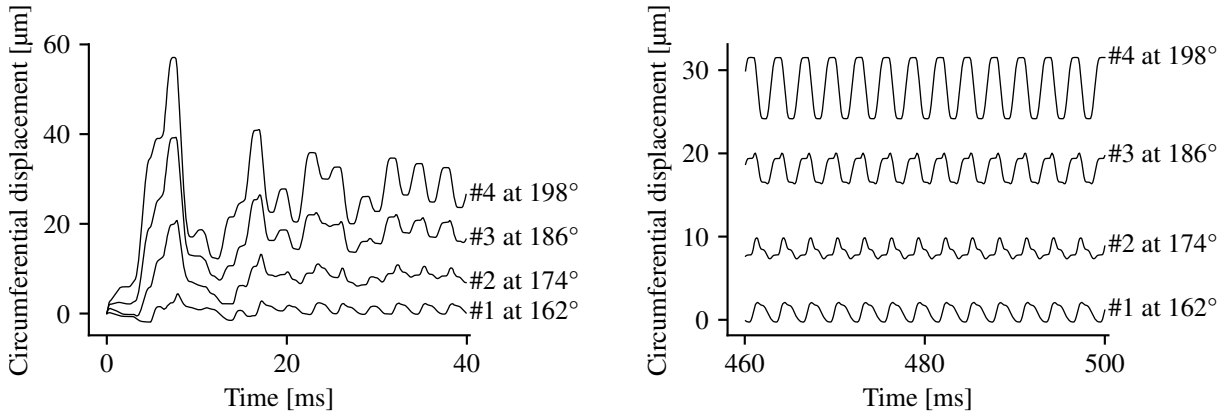


Figure 6: Circumferential displacement, i.e. sliding, of the bump foil–housing contact nodes of the four leading bumps in pad segment two. The left plot shows the first 40 ms after the rotor drop, while the right plot shows the final 40 ms of the simulation where steady state has been reached.

amplitudes, but almost identical steady states are eventually reached. This indicates that the equilibrium position is determined by the structural stiffness alone. This is in the order of 3–4 GN/m³ and hence much lower than the equivalent SEFM stiffness of 9 GN/m³ used by Larsen and Santos (2015). The value of 9 GN/m³ was based on a number of "engineering assumptions" and was intended by Larsen and Santos (2015) to represent the dynamic foil stiffness, but as the applied model made no distinction between static and dynamic behaviour, this resulted in equilibrium points lying much higher than those obtained from the present model. If the effective static stiffness of the foil structure is in fact closer to 9 GN/m³, as suggested by the agreement to experimental results, the foil structure must, at least partly, be sticking.

Fig. 6 shows the circumferential sliding displacement for the first four bump foil–housing contact nodes in the second pad during the first and last 40 ms. The presence of friction is evident in both plots from the characteristic flattened peaks and valleys related to the sign change of the friction forces. As both the mean displacements and the dynamic displacement amplitudes increase along the pad (this is also true for the remaining five bumps), the frictional energy dissipation will be largest for the bumps closest to the trailing edge.

The original motivation for introducing a friction model was twofold: (a) to circumvent the requirement for an empirically determined and constant equivalent stiffness; and (b) to avoid the inclusion of an empirical mechanical loss factor. It is evident from Fig. 4 that the friction model provides damping and that it increases the effective dynamic stiffness. It has, however, also been shown that the friction induced dynamic stiffness does not affect the equilibrium position. This means that the present AFB model results in steady state rotor eccentricities determined solely by the structural foil stiffness, while its dynamic characteristics at this equilibrium are influenced by friction. The effect is sketched in Fig. 7, where the left plot shows the radial deflection of a bump subjected to the load profile shown to the right. When loading up, point "A" is reached tracking the upper edge of the global hysteresis loop, where the effective stiffness is that of the sliding structure plus a frictional contribution. Ramping down the load, a line parallel to the right edge of the global loop is tracked to point "B" while the direction of sliding

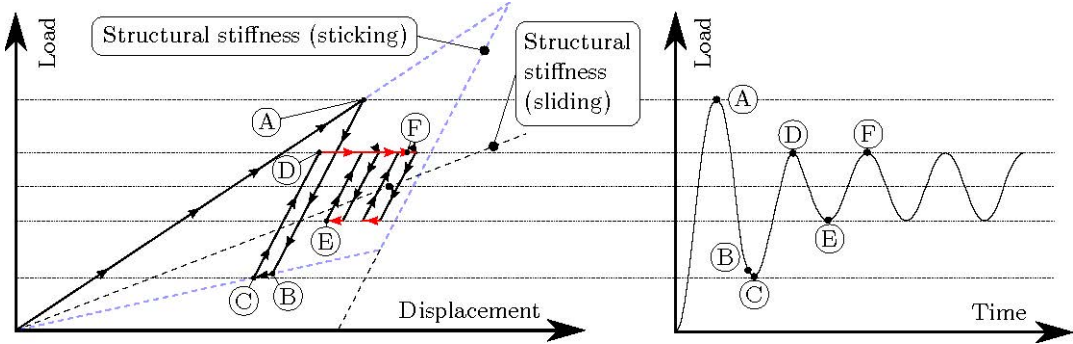


Figure 7: Sketch of the frictional drift present for the dynamic friction model. The right plot depicts a hypothetical load profile applied to a single bump and the left plot is the resulting displacement.

and hence the frictional force is reversed. Ideally, the effective stiffness is here close to that of a pinned bump, as no sliding should occur while the friction force changes direction. Note that the friction force crosses zero and changes direction as the dashed line indicating the sliding bump stiffness is crossed. Further decreasing the load from "B", the global hysteresis loop is tracked until "C" while the contact slides. Increasing the load to "D", the same stiffness as between "A" and "B" is experienced, but as the load is lowered from "D" towards "E", a frictional force sign change is required without any sliding. This is not possible for the dynamic friction model, meaning that the contact point will drift towards the frictionless equilibrium for each sign change made within the global loop. These drifts are marked in red in the plot (the short horizontal arrows) and even though their magnitude is dependent on the smoothing parameter, point "F" will eventually be reached. At this point, the oscillations take place around the same equilibrium as would have been reached without friction.

7 Conclusion

The paper has presented an alternative foil structure model for AFB simulation based on a truss representation of the bump foil originally proposed by Le Lez et al. (2007). The top foil is added using a simple one dimensional Bernoulli–Euler beam and a dynamic friction approximation is included to model frictional energy dissipation at the top foil–bump foil and bump foil–bearing housing interfaces. The usually applied foil structure models are static, i.e. represented by algebraic equations, but it is argued that the combination of a simultaneous solution in time and a friction model requires the inclusion of the foil inertia. This is achieved by augmenting the bump foil truss and top foil beam elements with lumped masses and subsequently to eliminate the entailed very high natural frequencies using stiffness proportional damping.

The new foil structure model is coupled to a nonlinear time domain model of a rigid shaft supported by two AFBs as a replacement for the SEFM. This allows the SEFM's inherent assumptions of viscous dissipation, constant stiffness and decoupled neighbouring points to be abandoned, and the empirically determined equivalent stiffness and loss coefficients of the SEFM can be replaced by directly measurable quantities.

The numerical results from the coupled model demonstrates that energy is dissipated by the friction model and that an increased effective dynamic stiffness is introduced. It is, however, evident that the dynamic stiffness caused by friction does not affect the obtained steady state position in the current model. This is reasonable considering the applied dynamic friction approximation, as this is not capable of representing true sticking and hence will allow net sliding until the equilibrium position dictated by the structural stiffness is reached. This is interesting, as the equivalent SEFM stiffness used by Larsen and Santos (2015) to obtain unbalance responses in very good agreement to experimental results, was based on the dynamic foil structure stiffness. In the SEFM, no distinction is made between the static structural stiffness and the friction induced dynamic stiffness, meaning that much higher foil compliances and rotor eccentricities are obtained using the new model than was the case using the SEFM (Larsen and Santos, 2015).

The agreement to experimental results achieved using the SEFM, with a constant equivalent stiffness much higher than that of a sliding bump foil structure, suggests that sticking is in fact a prevalent state. This would imply that the orbits predicted using the new foil structure model are too low-lying and, most importantly, that frictional dissipation is not as significant as generally assumed.

References

Agrawal, G. L.: Foil air/gas bearing technology - an overview. In: *ASME 1997 International Gas Turbine and Aeroengine Congress and Exhibition*, page 347, ASME (1997).

Bonello, P.; Pham, H. M.: A receptance harmonic balance technique for the computation of the vibration of a whole aero-engine model with nonlinear bearings. *Journal of Sound and Vibration*, 324, 1-2, (2009), 221–242.

Bonello, P.; Pham, H. M.: The efficient computation of the nonlinear dynamic response of a foilair bearing rotor system. *Journal of Sound and Vibration*, 333, 15, (2014a), 3459–3478.

Bonello, P.; Pham, H. M.: Nonlinear dynamic analysis of high speed oil-free turbomachinery with focus on stability and self-excited vibration. *Transactions of the ASME, Journal of Tribology*, 136, 4, (2014b), 041705.

Feng, K.; Kaneko, S.: Analytical model of bump-type foil bearings using a link-spring structure and a finite-element shell model. *Journal of Tribology*, 132, 2, (2010), 021706.

Heshmat, H.; Walowitz, J. A.; Pinkus, O.: Analysis of gas lubricated compliant thrust bearings. *Journal of Lubrication Technology*, 105, 4, (1983a), 638.

Heshmat, H.; Walowitz, J. A.; Pinkus, O.: Analysis of gas-lubricated foil journal bearings. *Journal of Lubrication Technology*, 105, 4, (1983b), 647–655.

Hoffmann, R.; Pronobis, T.; Liebich, R.: Non-linear stability analysis of a modified gas foil bearing structure. In: *Proceedings of the 9th IFTOMM International Conference on Rotor Dynamics*, pages 1259–1276 (2015).

Howard, S. A.; San Andrs, L.: A new analysis tool assessment for rotordynamic modeling of gas foil bearings. *Journal of Engineering for Gas Turbines and Power*, 133, 2, (2011), 022505.

Larsen, J. S.; Hansen, A. J.; Santos, I. F.: Experimental and theoretical analysis of a rigid rotor supported by air foil bearings. *Mechanics & Industry*, 16, 1, (2015a), 106.

Larsen, J. S.; Nielsen, B. B.; Santos, I.: On the numerical simulation of nonlinear transient behavior of compliant air foil bearings. In: *Proceedings of the 11. International Conference on Schwingungen in Rotierenden Maschinen (SIRM2015)*, Magdeburg, Germany (23-25 February 2015b).

Larsen, J. S.; Santos, I. F.: On the nonlinear steady-state response of rigid rotors supported by air foil bearingstheory and experiments. *Journal of Sound and Vibration*, 346, (2015), 284–297.

Larsen, J. S.; Santos, I. F.; von Osmanski, S.: Stability of rigid rotors supported by air foil bearings: Comparison of two fundamental approaches. *Journal of Sound and Vibration*, 381, (2016), 179–191.

Larsen, J. S.; Varela, A. C.; Santos, I. F.: Numerical and experimental investigation of bump foil mechanical behaviour. *Tribology International*, 74, (2014), 46–56.

Le Lez, S.; Arghir, M.; Frene, J.: A new bump-type foil bearing structure analytical model. *Journal of Engineering for Gas Turbines and Power*, 129, 4, (2007), 1047–1057.

Le Lez, S.; Arghir, M.; Frene, J.: A dynamic model for dissipative structures used in bump-type foil bearings. *Tribology transactions*, 52, 1, (2008), 36–46.

Le Lez, S.; Arghir, M.; Frene, J.: Nonlinear numerical prediction of gas foil bearing stability and unbalanced response. *Journal of Engineering for Gas Turbines and Power*, 131, 1, (2009), 012503.

Lee, D.-H.; Kim, Y.-C.; Kim, K.-W.: The dynamic performance analysis of foil journal bearings considering coulomb friction: Rotating unbalance response. *Tribology Transactions*, 52, 2, (2009), 146–156.

Lund, J. W.: Calculation of stiffness and damping properties of gas bearings. *Journal of Lubrication Technology*, 90, 4, (1968), 793–803.

Makkar, C.; Dixon, W. E.; Sawyer, W. G.; Hu, G.: A new continuously differentiable friction model for control systems design. In: *Proceedings of the 2005 IEEE/ASME International Conference on Advanced Intelligent Mechatronics*, pages 600–605, IEEE, Monterey, California, USA (2005).

NASA: Creating a turbomachinery revolution: Research at Glenn enables an oil-free turbine engine, FS-2001-07-014-GRC (2001).

Oden, J. T.; Martins, J. A. C.: Models and computational methods for dynamic friction phenomena. *Computer Methods in Applied Mechanics and Engineering*, 52, 1, (1985), 527–634.

Peng, J. P.; Carpino, M.: Calculation of stiffness and damping coefficients for elastically supported gas foil bearings. *Journal of Tribology*, 115, 1, (1993), 20–27.

Petrov, E. P.; Ewins, D. J.: Generic friction models for time-domain vibration analysis of bladed discs. *American Society of Mechanical Engineers, International Gas Turbine Institute, Turbo Expo (Publication) IGTI*, 4, (2003), 223–233.

Petzold, L.: Differential/algebraic equations are not ODE's. *SIAM Journal on Scientific and Statistical Computing*, 3, 3, (1982), 367–384.

Poulsen, M. Z.; Thomsen, P. G.; Houbak, N.: *Structural analysis of DAEs*. Ph.D. thesis, Technical University of Denmark, Lyngby, Denmark (9 2002).

Powell, J. W.: A review of progress in gas lubrication. *Review of Physics in Technology*, 1, 2, (1970), 96–129.

San Andrs, L.; Kim, T. H.: Improvements to the analysis of gas foil bearings: Integration of top foil 1d and 2d structural models. In: *ASME Turbo Expo 2007: Power for Land, Sea, and Air*, vol. 5, pages 779–789, International Gas Turbine Institute, ASME, Montreal, Canada (2007).

San Andrs, L.; Kim, T. H.: Analysis of gas foil bearings integrating FE top foil models. *Tribology International*, 42, 1, (2009), 111–120.

Tariku, F. A.; Rogers, R. J.: Improved dynamic friction models for simulation of one-dimensional and two-dimensional stick-slip motion. *Journal of Tribology – Transactions of the ASME*, 123, 4, (2001), 661–669.

von Osmanski, S.; Larsen, J. S.; Santos, I. F.: A fully coupled air foil bearing model considering friction - theory & experiment. *Journal of Sound and Vibration*, 400, (2017), 660–679.

Walowitz, J. A.; Anno, J. N.: *Modern developments in lubrication mechanics*. Applied Science Publishers London (1975).

Address: Department of Mechanical Engineering, Technical University of Denmark, 2800, Kgs. Lyngby, Denmark
 E-mail addresses: asvosc@mek.dtu.dk (S. von Osmanski), josla@mek.dtu.dk (J.S. Larsen) and ifss@mek.dtu.dk (I.F. Santos)

Practical Approach for Solving Vibrations of Large Turbine and Generator Rotors - Reconciling the Discord between Theory and Practice

Z. Racic, M. Racic

The purpose of this paper is to illustrate a different perspective in viewing and solving vibration problems in large rotating machines regarding the commonly seen discord between theoretical predictions of dynamic behavior, especially the standard predicted and expected "fixes" to many vibration problems, versus observed operation in practice when unexpected vibration problems still remain or arise anew. The paper will also discuss the key root causes behind this discord with regard to large turbine and generators rotors, and behind unexpected or unexplainable vibration in operation, usually after a major outage. In short, the primary cause in a substantial portion of such cases is the presence of "significant", axially distributed mass eccentricities inherent to individual rotors, or compound eccentricities from misaligned rotors or bearings. These cases require a different approach versus the methodology traditionally utilized for diagnosing and resolving "unbalance responses" in general, on a variety of rotating machines of different sizes and operating speeds. The paper also presents and describes an improved rotor balancing approach when dealing with such cases. These problems should be ideally resolved in service shops, and when balancing significantly eccentric rotors in balancing facilities, it is necessary to apply a new balancing method using $2N+1$ balancing planes, where "N" is the highest mode reached in operation.

1 Introduction

Over many years of consulting work, the authors have recognized that at any number of power plants, turbine-generator rotor vibration problems continue sometimes for years without an effective resolution, despite the best efforts of OEMs and plant engineers and other consultants to solve them. It is likely that most practicing engineers working in this area of rotordynamics and vibration have encountered special cases where the machine appears unaware of the theoretical behavior it is supposed to adhere to. Likewise, the suspected root causes and proposed solutions predicted by standard theory do not always reliably resolve the turbine-generator vibration problems at hand. In a lot of these cases, any excessive discord between predicted and actual measured behavior is written off as "nonlinearity" or as due to unknowable external variables. Subsequently, an educated series of what become essentially trial-and-error solutions (particularly field balancing) are usually attempted until finally a combination arises that creates a tolerably running machine.

However, through many years of focusing on troubleshooting these kinds of special cases, it is evident that a good majority of these situations actually do tend to follow a regular and predictable pattern of root cause, and can be treated with a reliable framework of solutions - if the observed symptoms are properly recognized and understood. The root cause of "unexplainable" vibrations is almost always the presence of distributed mass eccentricity in the rotor train. This includes distributed eccentricity on individual rotors (such as a rotor bow, or skewed generator retaining rings, etc.), and includes induced eccentricity within an overall rotor train (such as from bearing or coupling misalignment, off-square couplings, etc.).

The largest point of discord arises when interpreting high measured rotor vibration as resonant modal excitation (or "unbalance response"), and likewise attempting to resolve it by balancing, when the real root cause is actually distributed mass eccentricity. Distributed mass eccentricity is commonly and often erroneously considered as a particular subset of unbalance. However, there are subtle but crucial differences in rotor behavior and in the approach and viewpoint needed to recognize and address distributed eccentricity versus typical unbalance. First, it is important to distinguish between the definitions of "unbalance" and "eccentricity".

"Unbalance" as addressed in this paper can be considered as any axially-localized mass that produces net-asymmetric centrifugal force when under rotation, but that doesn't otherwise statically shift the mean mass center axis of the rotor (such as the effect of a chipped blade, or variance in blade static moment weight). "Unbalance"

forces can act as a source of excitation of resonant responses at system critical speeds, creating whirling (an enlarged shaft orbit) when passing through the critical(s), but it doesn't otherwise affect the rotation or orientation of the rotor in its bearings. It is important to remember that any resonant modal response requires a sufficient force to act as a source of excitation, or otherwise the rotor will pass through its system critical speed regions without a visible increase in the shaft orbit amplitude (or so-called high vibration).

"Distributed mass eccentricity" produces the same excitation effects as unbalance, but with the important added effect that it also statically shifts the mean mass center axis of the rotor relative to the rotor's geometric axis. This means that there is a net parallel offset and/or skew (depending on axial eccentricity distribution) between the rotor's geometric centerline axis and the actual mean mass axis (the "amount" of eccentricity), which itself is constant regardless of the rotor's modal deformation. The geometric axis refers to the line connecting the concentric journal centers, based on the rigid shape of the rotor, and is the line through which torque is applied. If the rotor dynamically and elastically bends at high speed or under resonance, both the geometric axis and the mass axis would equally distort along with the elastic bent shape of the rotor. The threshold of relevance (by practical experience) when the amount of mass eccentricity can be considered "significant" enough to have an effect is generally around ~ 0.05 mm (~ 0.002 inches). (Note, by the author's interpretation, ISO 1940-1, for class G2.5 rotors, gives a more conservative value at 0.025 mm (0.001 inches) based on modal mass at the system fundamental harmonic frequency.)

The rotor's mass axis itself can also be thought of in two separate ways. One way would represent the intrinsic rotor mass eccentricity of the stationary rotor. This is essentially the curving line connecting the radial mass center of every "slice" of the rotor, and would never change with speed. The second way would be to additionally incorporate any induced modal bending of the rotor (which would be speed dependent), and create a straight line through the centers of the modal masses of the purely rigid segments (or elements) of the rotor. The latter can be referred to as the "modal mass axis".

The key consideration when dealing with significant mass eccentricity is the recognition that every object if free and unconstrained has a natural tendency to rotate about its center of mass (by conservation of angular momentum). Any object rotating in this manner is perfectly balanced, and would produce no forces against any constraint holding it in space. Likewise, any object not rotating about its center of mass must be forced into maintaining this "unnatural" state by an imposed constraint, and will produce cyclic forces against its constraint with each revolution. For horizontal rotors, the applicable constraints are the rotor bearings and the force of gravity holding the journals in the bearings at the points of contact. In multi-rotor trains, adjacent rotors/couplings also act as constraints.

When dealing with a rotor with significant mass eccentricity, the rotor's natural tendency is to rotate about its mean mass axis, which incorporates any eccentricity. However, the rotor is constrained by gravity in its bearings and is forced to spin about its principal rotation axis defined by the line connecting its journal centers, assuming the journals are concentric. Likewise, torque is applied concentrically to the rotor about this same principal rotation axis, either transferred concentrically through an adjacent coupling or via turbine blades. The net result is the rotor being maintained in a forced unnatural state of non-centroidal rotation. This requires a perpetual force to be applied by and against the constraints (bearings), as a force-pair to the reactive centrifugal force being generated by the mass eccentricity of the rotating rotor. Unlike "unbalance", which produces enough centrifugal force only to excite the resonant modal responses at the critical speed regions, the reactive centrifugal force from distributed mass eccentricity is sufficient to affect the rotor motion through much of the speed range, in a manner proportional to increasing speed. These responses would be considered the "rigid modes" of the rotor (lateral translational and conical or "rocking"). These rigid modes are entirely dependent on the presence of mass eccentricity and its axial distribution, and cannot and should not be treated in the same manner as resonant modal excitation from "unbalance".

Generally speaking, the traditional theoretical-based approaches to resolving rotor vibration tend to focus on unbalance as fundamental, and on mass eccentricity as secondary or as simply another form of the same thing. However, by experience, whenever distributed mass eccentricity is present on a rotor or within a rotor train, it must be recognized and resolved as the fundamental problem before dealing with any modal excitation from unbalance. This applies equally to rotor trains installed in the field and to individual rotors on a balancing machine in the shop. It could be argued that recognizing these differences (and evaluating the presence of eccentricity) is actually the most relevant and critical when balancing a rotor with significant mass eccentricity in a high-speed balancing facility, prior to installation in the field. Furthermore, it is also crucial to distinguish that a rotor with significant mass eccentricity behaves differently at speeds below the fundamental system critical speed (first critical) and at speeds above it.

2 Common Points of Discord between Theory and Practice

In a wider sense, the differences between the classical interpretation of unbalance and the focus on eccentricity presented here originate in the application of rotor condition **assumptions** used within theoretical rotordynamics for predictive modeling purposes and to simplify mathematical modeling. This is not to point out a problem with modern classical rotordynamics theory, which is well proven in its general predictive ability. Rather the discord arises with the practical means of application of the theory to troubleshooting and diagnosing problems within operating machines, and in creating practical solutions to remedy these problems. This can occur when applying assumptions regarding often-unverified real-life rotor conditions, when the rotors do not adhere to the boundary conditions and assumptions required within the theory (namely rotor concentricity/symmetry). This applies especially to the measurement and evaluation of 1x and 2x rotor eccentricity, as well as coupling perpendicularity, journal concentricity and issues arising from bearing misalignment.

2.1 Rotor Reference Frames and Axes

Generally speaking, the standard theoretical models upon which rotor vibration behavior (and subsequently rotor balancing) is understood assume a concentric rotor, with added static and dynamic "unbalances" that are reduced to point masses. For an otherwise concentric rotor, this approach is accurate, and creates no issues. For eccentric rotors, it can lead to problems. Distinguishing unbalance and eccentricity becomes important when recognizing rotor behavior within the speed region of the fundamental system harmonic frequency (first critical speed); namely the rotor's center of rotation switches from a forced centering around the journal (geometric) axis to a natural re-centering and re-orientation around its mass axis. As previously described, when significant eccentricity is present, there are two initial reference axes of note within the rotor itself: the journal (geometric) axis about which the rotor is constrained within its bearings, and the true mean mass axis that governs the rotor's natural tendency of rotation.

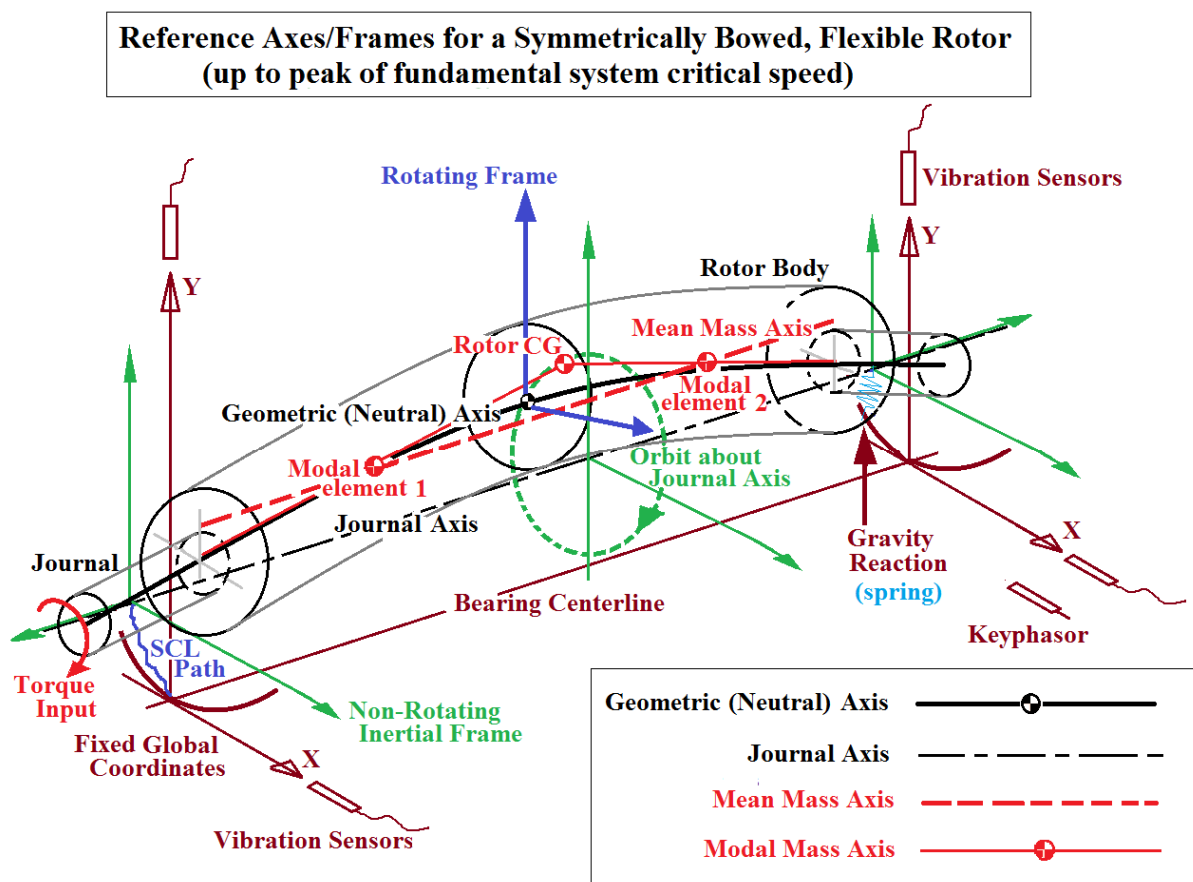


Figure 1. Reference coordinates and axes within an eccentric/bowed rotor

Note that when in dynamic motion, there are five relevant axes or frames of reference: 1) the stationary global coordinates that represent the standstill rotor shaft centerline position within each bearing (the proximity sensors remain fixed to this reference), 2) the non-rotating but slowly shifting "inertial frame" representing the "static" axis line connecting the rotor shaft centerline at each bearing through all speeds (the "virtual" center points of the shaft orbit), 3) the "geometric axis" or neutral axis representing the concentric geometric centerline of each radial "slice" of the rotor through which torque is applied and transferred (including dynamic bending), 4) the "journal axis" which represents the line connecting the journal centers not including any dynamic bending (this can also be called the principal rotational axis), and 5) the mass axis as previously described. When the rotor exhibits only rigid-mode behavior (no dynamic or resonant bending), the "geometric axis" and "journal axis" are coincident. When the rotor is in motion, the geometric axis (transmitting torque), journal axis and the mass axis (and the resulting forces in reference to these axes) are most easily recognized and described within a rotating reference frame (Figure 1).

Below the first system critical speed peak, the rotor maintains its forced constrained rotation about its journal axis. This leads to the increasing rotor forces and whirling seen while accelerating toward the critical speed peak, as net centrifugal force arises from any eccentric mass. Upon passing the critical speed peak and at higher speeds, the rotor achieves a new mode of rotation self-centered about its mean mass axis, to the extent that bearing clearances allow, in accordance with its natural tendency to rotate about its center of mass, based on its eccentricity distribution.

2.2 Points of Discord within Applied Rotor Balancing

Balancers often carry and apply a number of common theoretical modeling assumptions to practical shop and field balancing practices that can lead to unrecognized errors and create problems in the field. One of the points of discord with traditional theory (or modeling) relative to real-life rotor balancing is the consistent focus on only a single axis of rotation for all speeds and conditions, generally based on the stationary global coordinates. A second is the assumption that all balancing performed both below or above the first critical speed is equivalent. This overlooks the switch in rotation axes through the first critical speed region, and therefore implicitly assumes that the journal axis remains the sole reference frame for all speeds, and that all measured dynamic rotor vibration amplitudes at all speeds are caused by unbalance relative to this reference axis. The balancers then focus their efforts on resolving only dynamic modal displacement responses observed and measured at the journals (at the bearings as points of constraint). The rotor is assumed to bend or deflect at any speed by centrifugal force(s) acting radially out from the "inertial frame" axis line. Therefore, this approach diminishes the relevance the shaft centerline path and recognition of speed-dependent rigid mode responses as indicators of unresolved mass eccentricity.

A similar understanding can be applied within assembled rotor trains as a whole, where bearing misalignment can lead to induced bows in flexible rotors when the couplings of adjacent non-parallel rotors are pulled and bolted together. This situation is quite commonly seen, particularly when rotor coupling faces are unknowingly off-square, but still used to set the bearing alignment via standard 16-point coupling gap and rim measurements. The off-square couplings combined with resulting misaligned bearings lead to induced "static" bows within the rotor train and unexpected vibration in operation, often seen as shaft whirling at outboard bearings or as seal rubs as the rotors attempt to "naturally" self-align under increasing inertia and applied torque in accordance with the overall mass axis of the rotor train. Attempts to field-balance such a condition believing it to be rooted in "unbalance" are not often successful, and can actually create larger long-term problems or damages within the rotor train due to imposing additional internal cyclic bending moments and corresponding axial forces on the rotors.

Shop balancers also often neglect the relevance of the self-orientation of the "inertial frame" which represents the natural shift or skew in space (within bearing clearances) of the principal rotation axis, dependent on the distribution of mass eccentricity (observable in the shaft centerline path). When significant eccentricity is present, balancers will inadvertently balance an eccentric rotor about its mass axis when at speeds above the first critical speed region. This can still lead to a very well-balanced rotor when it is spinning unconstrained and solo in the balancing facility. The problem arises upon installation in the field when this rotor is installed within a rotor train and constrained by adjacent rotors to maintain rotation about its journal axis even above its individual fundamental critical speed.

The balance weights that were placed in the shop during the balancing process above the critical speed region (relative the self-orientation governed by the rotor's mass axis) now create an unbalanced condition in the field.

The rotor will still naturally tend to self-align to its mass axis, but if constrained against doing so, it will require increasing forces proportional to speed to maintain that "unnatural" state of rotation. Upon the assembly and restart of a unit in a power plant following a major outage, this can frequently lead to unexpected or stubborn vibration with a rotor that was supposedly "balanced" in the shop. These forces will be reflected as either high dynamic vibration amplitudes where the rotor has clearance to whirl, high bearing seismic forces or high bearing metal operating temperatures where the bearings constrain such motion, or will be absorbed in more flexible rotors as internal cyclic bending. Such internal bending can create hidden damage over time, especially in generator rotor materials and other assembly components.

The primary focus in balancing should first be the evaluation of mass eccentricity on every rotor. If 1x evaluated eccentricity near 0.050mm (~0.002 inches) or greater is seen, then the balancer's focus needs to be placed on the often-overlooked overall static asymmetry of the mass axis of the rotor relative to its journal axis, and on rigid-mode behavior at speeds below the fundamental system critical speed range up to the critical speed peak amplitude. The rigid modes of the rotor must be addressed and "balanced" first at "pseudo high speed" (Ehrich, 1993) to avoid the source of unexpected dynamic behavior (the change in rotational axis and self-centering of the rotor) when the rotor is accelerated to speed at and above the fundamental system resonance velocity (1st critical speed).

Another important area of consideration in balancing is the axial distribution of correction weights. In standard balancing methods, the first critical speed response is addressed first, and is usually compensated with a single weight placed at the midplane (N-method) (Bishop, 1972). In flexible rotors with significant eccentricity, this type of correction for the first critical response results in a too-concentrated weight, and acts to bow and distort the rotor around the midplane. In effect, the balancer is inadvertently attempting to push and bend the rotor's geometric axis to align the journal centers to coincide with the rotor's mass axis. This results in deforming the rotor and introduces internal cyclic bending moments within the rotor body. This can be particularly problematic for longer term operation of generator rotors, which can experience premature fatigue in internal insulation and windings, leading to electrical shorts and other damage. Also, corresponding axial forces generated from this cyclic bending may create forced or resonant excitation of free standing turbine blades.

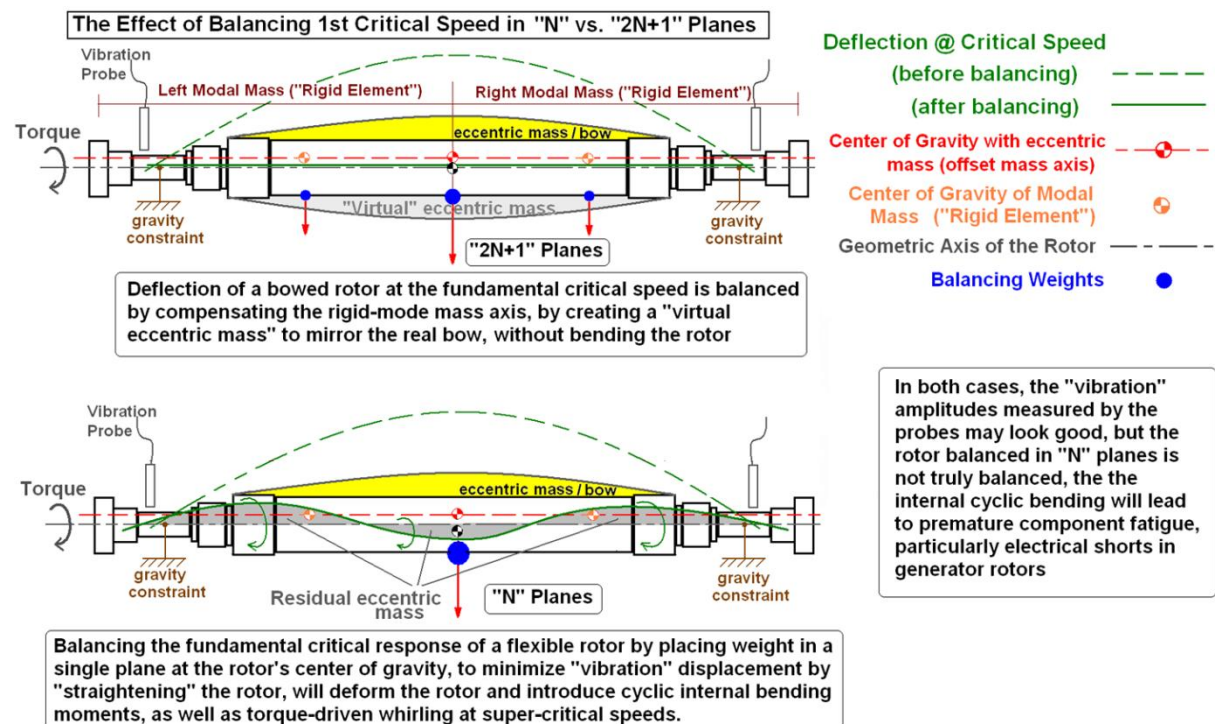


Figure 2. Comparison of post-balancing condition between balancing in N (bottom) and 2N+1 (top) planes

When balancing rotors with mass eccentricity distributed across a sizeable portion of the rotor body (any permanent bow or distributed asymmetry on the rotor between the bearings), the rigid-mode eccentricities need to be statically compensated around the principal rotational axis by mirroring the eccentricity distribution without otherwise bending or distorting the rotor (Figure 2). In a balancing facility, this must be performed at rotational speeds at or below the fundamental critical speed of the rotor-bearing system, restoring the symmetry of the rotor about its journal axis and eliminating the rotor's rigid-mode responses. This is necessary to prevent the rotor from switching its center of rotation to the mean mass axis once above the critical speed. To achieve

this goal for significantly eccentric rotors, it is necessary to follow a new balancing method using $2N+1$ balancing planes (similar to a patented method applied in practice by GE (Ehrich, 1993), where "N" is the highest mode of the rotor within its designed operating speed range). This also means that the rigid modes of a bowed rotor must be balanced at minimum in three balancing planes (Racic, 2014a).

2.3 A Look at Real Rotor Behavior

To better conceptually define the idea meant by "rigid mode" behavior in this paper, consider the motion of a bowed flexible rotor at higher speed which is undergoing some amount of induced elastic bending while in some orbital lateral translation or pivotal rocking motion. We can conceptually dissociate this total rotor motion into two parts, a rigid component and a flexible component. The "rigid-mode" component of the motion is representative of the dynamic motion of the rotor in its innate bowed shape. This is generally limited to motion of the journals within the oil film of hydrodynamic bearings. The flexible or elastic-bending component is representative of any superimposed bending deviation of the rotor from its innate shape. The rigid-mode rotor motion is tied purely to any distributed mass eccentricity on the rotor and to its effect on the position and skew of the rotor's mean mass axis relative to its inertial frame.

The elastic-bending component is tied to the centrifugal force generated at any given speed by any points of "unbalance" on the rotor. This can additionally include the centrifugal force generated by distributed mass eccentricity, and also includes any amplified harmonic modal responses from resonant excitation. There is some conceptual overlap in this visualization, in that mass eccentricity both affects the static symmetry of the rotor, and can act as unbalance generating a centrifugal force to induce bending deflection of a constrained rotor (Racic, 2014b). In diagnosing the cause of observed vibration and in identifying an ideal balancing solution, the rigid-mode behavior should be viewed and treated as fundamental, and the elastic-bending component should be secondary.

It has been experimentally shown (Zhyvotov, 2011) that in a torque-driven rotor at speeds below its first system critical speed peak, its mass center axis (intrinsic rotor mass eccentricity) is synchronously rotating around its geometric axis. Above the first system critical speed, the rotor's geometric axis is rotating around its mass axis. These rotations are referenced within the rotor body itself, best viewed in a rotating reference frame centered within the rotor body. At the same time, the rotor's geometric axis is laterally translating (essentially synchronously) in an orbit around the rotor's principal rotational axis (the straight line connecting the journal centers). This is best referenced from the non-rotating "inertial frame" represented by the shaft centerline position at each bearing (the "virtual" center of each orbit).

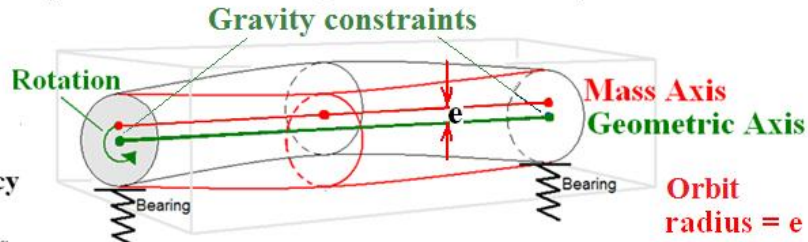
When an eccentric rotor is rotating at speeds below its system critical speed range, it behaves as in the upper image shown in Figure 3, since the rotor journals are held and constrained by gravity in their bearings. Above the peak of the first critical speed range, the rotor's natural tendency is to rotate around its mass axis, as shown in the lower image in Figure 3. When rotors are unconstrained, rotated in free space, or rotated vertically, (e.g. like a spinning top, or vertical hydro-turbine-generators or other vertical machines), the natural tendency of rotation would resemble the lower figure at any speed and always naturally self-center around its mass axis.

We want a bowed rotor to still spin balanced about its geometric axis at all speeds...

Like this:

However,

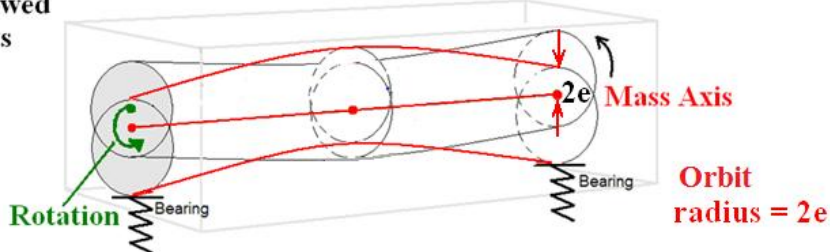
Any rotor's natural tendency is to rotate about its actual center of mass axis, which is offset due to eccentricity



When coupled, this natural tendency is constrained. This produces forces and vibration.

Natural tendency of a bowed rotor is to rotate about its center of mass axis.

Like this:



(produces very high bearing forces if bearing clearances are insufficient to allow the increased displacement)

Figure 3. The natural behavior tendency of bowed rotors (top) and (bottom) the first critical speed

For a better understanding of real life vibration problems the combined turbine-generator rotor-bearing system can be thought of as comprising two interconnected equilibriums, one being the non-rotating "static" equilibrium between the shaft and the bearing (best viewed in an inertial reference frame), and the other being the rotating "quasi-dynamic" equilibrium of the forces in the spinning rotor itself (best viewed in a rotating, non-inertial reference frame). These equilibriums are "cross coupled" (Figure 4) and affect each other, and instability in one can produce instability in the other. The non-rotating, "static" equilibrium of the rotor position in the bearings remains generally stable (only following the shaft centerline path). It is held by gravity load which is constant, and oil hydrodynamic forces which govern the rotor's elevation in the bearings. The rotating "dynamic" equilibrium remains referenced to the geometric center of the shaft or its neutral centerline.

The dynamic forces originating from rotor rotation/orbit are vectorially summed with the static forces from the static equilibrium in the bearings. The net summation then governs the position and orientation and stability of the rotor in its bearings. In an eccentric rotor, the internal moments and forces dynamically generated by any eccentric mass (tangential forces in particular) will at some sufficient speed govern the rotor's orientation in "search" of its static bearing equilibrium. If gravity loading on a bearing is low, these forces can potentially create subsynchronous rotor instabilities.

Cross Coupling of Forces and Bearing Stability Threshold for an Accelerating Flexible Rotor-Bearing System

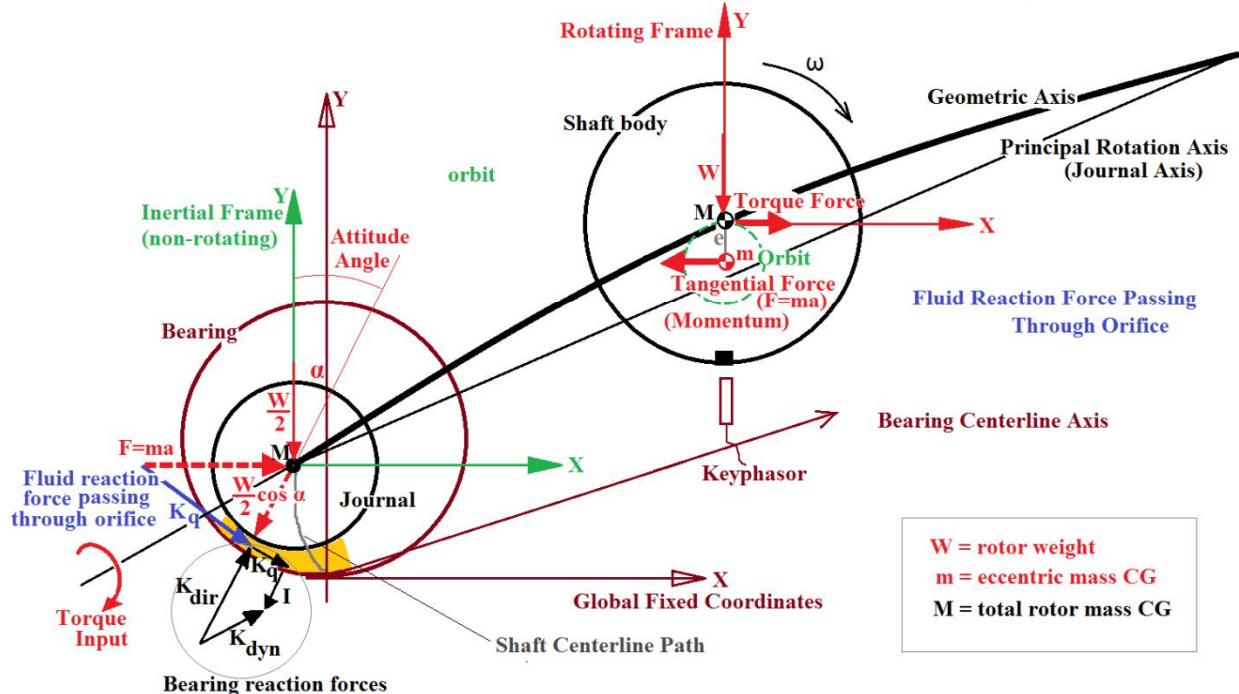


Figure 4. Cross coupling between "static" and "dynamic" forces during rotation under torque, the static best viewed in an inertial reference frame (left) and the dynamic in a rotating reference frame (right)

The real generated vibration of a flexible rotor is not a single simple motion and is not truly as modeled by a linear mass-spring-damper analogue, since the "vibration" of the rotor itself is really a predominantly synchronous translational motion in an orbit, without any real cyclic bending oscillation of the shaft itself (if the orbit is circular). That said, there still is a standard radial oscillatory component within the total rotor-bearing system response at the bearings (points of gravity constraint) "seen" by vibration sensors located in a global (fixed) reference frame. Although a "vibrating" rotor is really undergoing a combination of synchronous rotations, its bearing support (the oil film primarily, but also the shell, housing and pedestal) can be viewed as a linear, non-rotating spring under a "static" rotor gravity load. This load is in a line of action matching the attitude angle of the rotor in the bearing, and is summed with the cyclic dynamic load from the translation orbit.

3. Rotor Balancing - Modified Approach for Bowed and Eccentric Rotors

The key requirement of the rotor itself for balancing when any significant eccentricity is present is that the rotor must have at least three balancing planes, two endplanes and a midplane. If a rotor has more "significant" body runout ($>0.050\text{mm}$, or > 0.002 inches, 0-peak), but only has two balancing planes on the ends, then a third plane, either a machined grove or bolt-holes must be added at the midplane. If attempting balancing in the endplanes only, it can be practically guaranteed that the rotor will cause problems in the field after shop balancing, even if the vibration amplitudes in a balancing facility look successful. If a third, center balancing plane cannot be added due to material conditions or potential thermal stresses, then the only chance of good operation in the field is to remove the eccentricity in the shop either by machining the full rotor to a new centerline, by "truing" the centers, or by thermal straightening, to bring the rotor body runout under a threshold of 0.025mm (0.001 inches), as referenced to the journals (Hidalgo and Racic, 2009).

Historically, there have been numerous proposals and experiments of balancing in three planes, but they have not yet been raised to a level of general acceptance by industry or academia to become scientifically approved as necessary for balancing large turbine-generator rotors, at least as far as the service industry is concerned (Federn, 1957; Kellenberger, 1967; Zorzi et al, 1979). To have a proper and effective way of balancing and resolving the system responses of a flexible, bowed or eccentric rotor, there was a need to develop a new balancing method (Racic, 2014a). This balancing method is a hybrid of rigid-mode balancing combined with the standard influence coefficient method, and is based on displacement readings, though it could also be applied based on

measuring and vanishing bearing reaction forces (Ehrich, 1993). To account for rotor flexibility, this balancing method is based on the inverse of a particular Finite Element modeling requirement. In the FE modeling of rotors, the minimum number of nodes of modal elements required in the model to ensure that no rotor modes are missed in calculation works out to $2N+1$ (Chen and Gunter, 2005).

This correlates to the minimum number of axial divisions (or balancing planes) required to divide a rotor by to ensure that each resulting division or modal element will then behave sufficiently as a rigid beam through the full speed range. A well known idea in balancing is that any purely rigid rotor can be fully balanced in any two balancing planes. By taking a flexible rotor and dividing it using $2N+1$ divisions (nodal points) as in the FE model, each resulting division or element can be assured to behave as a fully rigid beam, with a defined number of constraints. As a result, each element can be properly balanced as a rigid beam in two planes. The inner planes shared by two neighboring elements are essentially used twice (Figure 5).

This means that any correction weights for a flexible rotor passing through the first system critical speed must initially be placed simultaneously in three balancing planes, symmetrically axially distributed (often 50% in the midplane, and 25% at each end-plane, at least as a starting point). This can be considered as solving the so-called "static" component of the rotor response, effectively compensating the translational rigid mode. When dealing with a more flexible rotor operating above its second mode ($N=2$), five planes may be used to compensate for the mode seen at the second harmonic frequency. This second mode is a result of an axially asymmetric position of the net center of mass of the rotor. It is usually a combination of rigid-mode rocking (which increases in amplitude proportional to speed once above the first critical speed range) plus the resonant bending response at the second harmonic frequency of the rotor. This second-mode response can be potentially resolved in three planes by axially redistributing the initial static correction used for the first (lateral) rigid-mode response without adding any additional correction masses. In cases of a second mode for more slender, flexible rotors, the proper axial redistribution may have to be spread among five balancing planes, and determined with additional trial runs with pairs of weights to obtain additional influence coefficients for proper redistribution. The weights given by a "single" influence coefficient calculation (from a pair of equivalent forces) are placed simultaneously as a pair within each end of a single modal element.

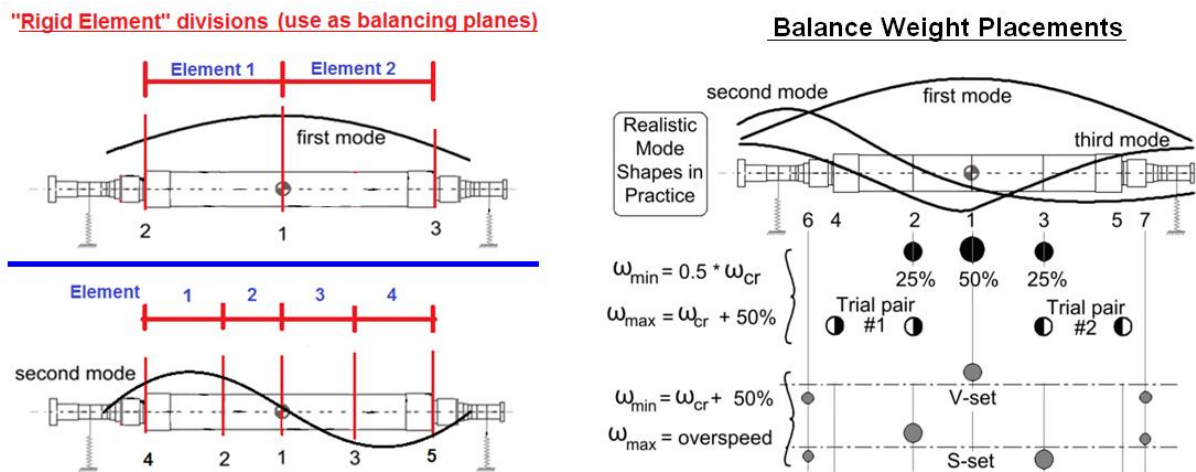


Figure 5. Representation of rotor element divisions and weight placements in the $2N+1$ plane balancing method

This axial redistribution is optimized through trial runs as necessary until all dynamic cyclic reaction forces in the bearings are vanished (Ehrich, 1993), or displacements are minimized to the magnitude of the initial indicated runout. This latter procedure is not performed at the actual speed of the second critical resonant response, but rather at a "quasi-high speed" not more than up to 50% above the first critical speed (Racic, 2014a).

If a very flexible rotor (such as newer types of large generator rotors) operates at or above its first flexural mode, or its so-called third critical, then the final trim balancing to achieve desired amplitude limit values in operation is determined using modal influence coefficients, but in this stage is run and measured at operating speed. It is even better to balance at rotor overspeed to assure a well-balanced condition when placed in the field, where different bearings and support stiffness may alter the relative response and speed of the third critical. The trial weight sets must be placed following the well known modal balancing weight distributions, where the sum of the

forces and sum of the moments of the weight distribution is zero, so as not to disturb the already corrected rigid-mode solution by inadvertently altering the corrected net mass axis of the rotor (Kellenberger, 1972).

Utilizing the 2N+1 plane balancing method is beneficial for balancing any rotor, but it is absolutely necessary when balancing any large flexible rotor with "significant" residual eccentricity or bowing. Overall, it is essential that the rigid mode responses are resolved first at lower speeds, before even considering balancing at higher critical speeds (Schneider, 2006). Because this balancing procedure is done mostly at lower speeds, the author of the initial iteration of this approach, (Ehrich, 1993) named it "Pseudo-High Speed Balancing." The modified and improved balancing method described in this paper has therefore been named similarly as the "Quasi-High Speed Balancing Method" (Racic, 2014a).

As a result of using this axial distribution of balancing weights, any rotor will maintain its inherent shape, even if it is bowed, without any distortion during operation, which can be termed as running "dynamically straight", i.e. with minimum residual error (Giordano and Zorzi, 1985). This prevents any internal cyclic bending moments, which can be a problem with generator rotors especially, and prevents high cyclic forces being transmitted into the bearings, which often happens when standard balancing methods are applied to flexible and eccentric rotors in the balancing facility, or when balancing an assembled rotor train in the field. The rotor also remains balanced about and naturally spinning and orbiting about its journal axis at all speeds, and behaves as if it were concentric, since now the journal axis is coincident with the resultant of the inherent mass axis and dynamic mass axis from balancing weights. The most important factor is that this method restores symmetry to the rotor about its journal axis connecting the coupling and journal centers, which is the line that the rotor is constrained to run about in the field when coupled to adjacent rotors. The final balance weight distribution (and their generated force vectors) will approximately mirror the distribution of mass eccentricity on the rotor.

4 Conclusion

It is important to review the assumptions used to create the common theoretical understanding and predictions of general rotordynamics behavior, and to recognize the rotor conditions and areas in practical rotor behavior and balancing that diverge from those assumptions in order to more accurately identify root causes and effective solutions to vibration problems with rotors in operation. Of course, the effects of resonances, damping and stiffness in the design of the system are still of great importance when dealing with external forces acting on rotors in operation, and these are generally well-studied and optimized by design engineers. However, many "unexpected" vibration problems have little to do with the common areas of focus (resonances and typical unbalance, damping and "instability") but rather are rooted in the presence of mass eccentricities and the rigid-mode behavior of the rotor, which is the true cause of the majority of synchronous vibration problems.

The recognition of the change of rotational axes during the balancing process as a rotor is accelerated through the fundamental system critical speed explains why the rigid-mode eccentricities of a rotor body need to be fully corrected in a balancing facility at rotational speeds at or below the fundamental critical speed of the rotor-bearing system. This means that all eccentricity is statically compensated around the principal rotational axis, restoring rigid mode symmetry of the rotor. It also shows why certain defects that can introduce eccentricity in operation (e.g. static runouts of couplings and journals) must be fully resolved by machining prior to balancing.

It has been found by practical experience on multiple occasions that verification and correction of journal and coupling runouts (eccentricities), and utilizing the Quasi-High Speed Balancing Method using 2N+1 balancing planes in the shop prevents and solves the majority of potential vibration problems at start up after a planned outage, and practically eliminates the need for field balancing of turbine-generators at start-ups after a major outage.

Based on discussions with plant managers and service shops, the estimated prevalence of flexible turbine and generator rotors with significant distributed mass eccentricities in the rotor service industry has statistically risen to over 20 percent of serviced rotors. This fact should require that current shop and balancing methods be amended to first include mandatory specific measurement and mathematical 1x and 2x evaluation of rotor and coupling runouts, including the correction of coupling deviations by machining prior to balancing, and that rotors should be balanced by the new 2N+1 plane balancing method (Racic, 2014a). Additionally, the allowable residual eccentricities stated in ISO-1940-1 for rigid rotors should be further applied to the concept of "modal elements" described in this paper, referenced to the rotor/bearing system fundamental critical speed.

References

Bishop R.E.D., Parkinson A.G. On the use of balancing machine for flexible rotors. *J Eng Ind*, 94, (1972), 561– 572.

Chen, W. J.; Gunter, E. J.: *Introduction to Dynamics of Rotor- Bearing Systems*. Eigen Technologies, RODYN Vibration Analysis Inc., (2005).

Ehrich, F. F.: *Balancing Method and Product*. General Electric Company, assignee. Patent US 5214585 A. 25 May 1993, (1993).

Federn K.: *Fundamentals of Systematic Vibration Elimination from Rotors with Elastic Shafts*, VDI Ber., (1957).

Giordano, J.; Zorzi, E.: *HPOTP Low-Speed Flexible Rotor Balancing*. Prepared for NASA Marshall Space Flight Center, by MTI, doc # 85TR28, (1985).

Hidalgo, J.; Racic, Z.: *Diagnosis and Treatment of Bowed, Misaligned, and Eccentric Rotor Trains*. Proc. of ASME 2009 IDETC/CIE, San Diego, CA, USA, (2009).

Kellenberger, W.: *Should a Flexible Rotor be Balanced in N or N+2 Planes?*. ASME Journal of Engineering for Industry, 94, No 2. (1972).

Racic, Z.; Hidalgo, J.: *Practical Balancing of Flexible Rotors for Power Generation*. Proc. of ASME DECT/CIE, Las Vegas, Nevada, USA. (2007).

Racic, Z.; Racic, M.: *Development of a New Balancing Approach for Significantly Eccentric or Bowed Rotors*. Mechan. Machine Science, 21, Paolo Pennacchi(Ed): Proceedings of the 9th IFToMM International Conference on Rotor Dynamics, Milan, Italy, (2014a).

Racic, Z.; Racic, M.: *Behavior of Eccentric Rotors through the Critical Speed Range*. Mechan. Machine Science, 21, Paolo Pennacchi(Ed): Proceedings of the 9th IFToMM International Conference on Rotor Dynamics, Milan, Italy, (2014b).

Schneider, H.: *Balancing and Beyond*, Shenck Ro-Tec Gmbh, (2006).

Zhyvotov A.Y.: *Resonance effect, critical and resonance velocities*. 13th world congress in mechanism and machine science, Guanajuato, Mexico, (2011).

Address: Z. Racic, M. Racic, 1370 S 74th St, West Allis, WI, USA 53214
email: mzracic@gmail.com

Reduced Order Modeling of Mistuned Bladed Disks under Rotation

S. Willeke, L. Panning-von Scheidt, J. Wallaschek

In this paper, a substructure-based reduced order model for mistuned bladed disks is extended to account for the effect of rotational-dependent dynamic properties. To reduce the overall size of the structural model, successive transformations to reduced modal subspaces of smaller dimension are performed by means of a fixed-interface Component Mode Synthesis, a Wave-Based Substructuring, and a Secondary Modal Truncation. Since the three-dimensionally shaped rotor blades tend to untwist under the influence of centrifugal forces, the modal reduction bases may undergo significant changes for different speeds of rotation. To prevent the necessity of identifying individual modal subspaces for each operating point and a repetitious passing through the full reduction process, a multi-model formulation is used to obtain a parameterized reduced order model in terms of rotational speed. The accuracy of this approach is assessed by comparison with full finite element models for various steady operating conditions. In terms of computational solution time, the proposed approach outperforms the finite element calculation by 90%. Finally, numerical results are presented addressing the mitigating influence of constant and variable rotational speeds on the amplitude amplification of mistuned bladed disks.

1 Introduction

During operation, the rotating bladed disks in turbomachines are exposed to large static and dynamic stresses. While static loads mainly arise from centrifugal forces and thermal strains, fluctuating gas pressures and rotor imbalances lead to forced vibrations. In particular, the periodic motion of the rotor blading through the irregular wake pattern downstream the stator vanes is known as a major source of forced excitation. Besides this synchronous stimulus, unsteady flow phenomena like aeroelastic flutter may cause self-excited blade vibrations of asynchronous type. The response of the structural components to these forcing mechanisms is in turn affected by the rotational motion. For instance, the static stresses stemming from centrifugal forces change the frequency characteristic of the rotating structure. In addition, small imperfections caused by the manufacturing process break the cyclic symmetry of the bladed disk and lead to a local concentration of vibrational energy. This mistuning may cause increased blade vibration amplitudes which in turn lead to an elevated risk of high-cycle fatigue. To efficiently predict this amplitude amplification in the turbomachinery design process, *Reduced Order Models* (ROM) of the full annulus are applied.

A numerical comparison between the mistuned vibrations of a transonic shrouded fan at 8,000 rpm and at rotor rest is presented in Moyroud et al. (2002). It is concluded from simulations that the stiffening effect of the rotational motion mitigates stiffness perturbations between the blades and reduces the overall sensitivity to mistuning. To approximate the evolution of mistuning under the influence of rotation, a simplified prediction method is proposed by Feiner (2002) and by Feiner and Griffin (2004). In combination with the *Fundamental Mistuning Model* (FMM), it is used to predict the response of an integrally bladed compressor disk at 40,000 rpm. A similar method for the approximation of the mistuned blade stiffness under rotation is described by Nipkau (2011) based on an SDOF-approach. Its application in numerical studies of a high pressure compressor blisk indicates a reduced effect of mistuning under rotation. Experimental measurements of a mistuned centrifugal impeller by Maywald et al. (2009) show no significant influence of rotation on mistuning for a speed range from 10,000 rpm to 19,000 rpm. A reduced multi-model approach that allows to consider mistuning under rotation is presented by Balmès (1996), Sternchüss and Balmès (2008), and Sternchüss (2009).

The present paper focuses on the extension of a substructure-based reduced order approach described in Hohl et al. (2009) by the multi-model formulation proposed in Balmès (1996), Sternchüss and Balmès (2008), and Sternchüss (2009). To this end, the modal subspaces of each reduction step are enriched by additional modes at various operating points in the analyzed range of rotational speeds. In addition, the effect of stiffness variation by centrifugal forces on the associated natural frequencies is incorporated by a second-order polynomial in the structural stiffness matrix (Sternchüss, 2009).

In order to predict the forced response of a mistuned bladed disk at an angular frequency ω , the following equation of motion at the rotational speed Ω is solved:

$$[-\omega^2 \mathbf{M} + i\omega \mathbf{C}_v(\Omega) + i\mathbf{C}_s(\Omega) + \mathbf{K}(\Omega)] \hat{\mathbf{u}} = \hat{\mathbf{f}}_e. \quad (1)$$

Since the present study is focused on modeling the interacting effects of centrifugal stiffness variations and structural mistuning, any gyroscopic effects in Eq. (1) are neglected. Proportional and structural damping \mathbf{C}_v and \mathbf{C}_s are considered in terms of the mass matrix \mathbf{M} and the stiffness matrix \mathbf{K} ,

$$\mathbf{C}_v(\Omega) = \alpha \mathbf{M} + \beta \mathbf{K}(\Omega) \quad \text{and} \quad \mathbf{C}_s(\Omega) = d_0 \mathbf{K}(\Omega). \quad (2)$$

The vectors $\hat{\mathbf{u}}$ and $\hat{\mathbf{f}}_e$ denote the displacement and forcing amplitudes of each blade k respectively,

$$\mathbf{u} = \hat{\mathbf{u}} e^{i(\omega t + \phi_u)} \quad \text{and} \quad \mathbf{f}_e = \hat{\mathbf{f}}_e e^{i(\omega t + \phi_e)} \quad \text{where} \quad \phi_{e,k} = \frac{2\pi}{N} \text{EO}(k-1) \quad \text{for} \quad k = 1, 2, \dots, N. \quad (3)$$

In case of synchronous excitation mechanisms, the angular forcing frequency ω is expressed in terms of the *Engine Order* (EO) and the rotational speed Ω as

$$\omega = \text{EO} \cdot \Omega. \quad (4)$$

Depending on the finite element discretization of the structure, the vector $\hat{\mathbf{u}}$ may contain numerous degrees of freedom. To reduce the computational effort for solving Eq. (1), the problem is projected to modal subspaces of gradually smaller dimensions.

2 Reduced Order Modeling of mistuned bladed Disks

In this section, the substructure-based reduction technique presented by Hohl et al. (2009) is summarized prior to addressing its multi-model extension. The reduction steps include a *Component Mode Synthesis* (CMS), a *Wave-Based Substructuring* (WBS), and a *Secondary Modal Truncation* (SMT).

2.1 Component Mode Synthesis

Based on the finite element representation of a single segment, the bladed disk is partitioned into a cyclic symmetric disk and the mistuned blading components. By distinguishing degrees of freedom along the blade-disk-interface boundary Γ from the internal domain Ξ , the matrix \mathbf{Z} related to a component s (i.e. either a blade or the disk) at operating point $n \in \mathbb{N}$ is described by,

$$\mathbf{Z}^{(s,n)} = \begin{bmatrix} \mathbf{Z}_{\Gamma\Gamma}^{(s,n)} & \mathbf{Z}_{\Gamma\Xi}^{(s,n)} \\ \mathbf{Z}_{\Xi\Gamma}^{(s,n)} & \mathbf{Z}_{\Xi\Xi}^{(s,n)} \end{bmatrix} \quad \text{where} \quad \mathbf{Z}^{(s,n)} = \mathbf{M}^{(\text{blade})}, \mathbf{M}^{(\text{disk})}, \mathbf{K}^{(\text{blade},n)}(\Omega), \mathbf{K}^{(\text{disk},n)}(\Omega). \quad (5)$$

In the following simulations, the parameter n refers to different rotational speeds of the bladed disk. To verify the extended modeling approach, a speed range from 0 rpm up to 15,000 rpm is chosen. The samples for the stiffness matrix $\mathbf{K}^{(s,n)}$ are taken at rotational speeds of 0 rpm ($n = 0$), 6,000 rpm ($n = 1$), and 12,000 rpm ($n = 2$, see section 4). This range of the parameter Ω is wide enough to induce distinct changes in eigenfrequencies and eigenvectors by stress stiffening and spin softening.

According to the fixed-interface approach by Craig and Bampton (1968), the vibrational displacement of each component is approximated by a set of dynamic *component modes* $\Phi^{(s,n)}$ related to the eigenvalues along the diagonal of the spectral matrix $\Lambda^{(s,n)}$ and static *constraint modes* $\Psi^{(s,n)}$,

$$\mathbf{K}_{\Xi\Xi}^{(s,n)} \Phi^{(s,n)} = \mathbf{M}_{\Xi\Xi} \Phi^{(s,n)} \Lambda^{(s,n)} \quad \text{and} \quad \Psi^{(s,n)} = -\mathbf{K}_{\Xi\Xi}^{(s,n)-1} \mathbf{K}_{\Xi\Gamma}^{(s,n)}. \quad (6)$$

By reducing the amount of retained component modes $\Phi^{(s,n)}$ in the transformation matrix $\mathbf{T}_{\text{cms}}^{(s,n)}$, a low order modal representation for each component s is obtained,

$$\begin{pmatrix} \mathbf{u}_{\Gamma}^{(s,n)} \\ \mathbf{u}_{\Xi}^{(s,n)} \end{pmatrix} = \mathbf{T}_{\text{cms}}^{(s,n)} \begin{pmatrix} \mathbf{u}_{\Gamma}^{(s,n)} \\ \boldsymbol{\eta}^{(s,n)} \end{pmatrix} \quad \text{where} \quad \mathbf{T}_{\text{cms}}^{(s,n)} = \begin{bmatrix} \mathbf{I} & \mathbf{0} \\ \boldsymbol{\Psi}^{(s,n)} & \Phi^{(s,n)} \end{bmatrix}. \quad (7)$$

Subsequent to the transformation in Eq. (7), the disk and blading are reassembled along the interface Γ yielding a reduced order model of the completely bladed disk. Mode-specific frequency mistuning is directly applied to the reduced spectral matrix of each blade.

At this point it should be noted that the transformation matrix $\mathbf{T}_{\text{cms}}^{(s,n)}$ in Eq. (7) includes mode sets $\Phi^{(s,n)}$ and $\Psi^{(s,n)}$ which in turn are dependent on the stiffness matrix $\mathbf{K}^{(s,n)}$. Since a change in rotational speed Ω leads to a stiffness variation, the eigenproblem in Eq. (6) has to be solved for each operating point n .

2.2 Wave-Based Substructuring

After the CMS transformation, the internal displacement $\mathbf{u}_\Xi^{(s,n)}$ is represented by a reduced amount of generalized coordinates $\boldsymbol{\eta}^{(s,n)}$. The amount of interface degrees of freedom $\mathbf{u}_\Gamma^{(s,n)}$, however, remains unreduced in the model. Therefore, a limited modal basis $\mathbf{W}^{(n)}$ of orthogonal displacement *waves* along the blade-disk-boundary is extracted from a modal analysis of the tuned CMS-reduced blisk model,

$$\begin{pmatrix} \mathbf{u}_\Gamma \\ \mathbf{u}_\Xi \end{pmatrix} = \begin{bmatrix} \mathbf{I} & \mathbf{0} \\ \boldsymbol{\Psi}^{(n)} & \boldsymbol{\Phi}^{(n)} \end{bmatrix} \mathbf{T}_{\text{wbs}}^{(n)} \begin{pmatrix} \boldsymbol{\xi}^{(n)} \\ \boldsymbol{\eta}^{(n)} \end{pmatrix} \quad \text{where} \quad \mathbf{T}_{\text{wbs}}^{(n)} = \begin{bmatrix} \mathbf{W}^{(n)} & \mathbf{0} \\ \mathbf{0} & \mathbf{I} \end{bmatrix}. \quad (8)$$

The orthonormalization of the interface modes $\boldsymbol{\Phi}^{(n)}$ is achieved by a *Singular Value Decomposition* (SVD) as described by Donders (2008) and Hohl et al. (2009),

$$\boldsymbol{\Phi}^{(n)} = \mathbf{Q}^{(n)} \boldsymbol{\Sigma}^{(n)} \mathbf{V}^{(n)\text{T}} \quad \text{and} \quad \mathbf{W}^{(n)} = \left\{ \mathbf{q}_i^{(n)} \right\} \quad \text{for} \quad \sigma_i^{(n)} \geq \sigma_{\text{tol}}^{(n)}. \quad (9)$$

The symbol $\boldsymbol{\Sigma}^{(n)}$ denotes a rectangular matrix, while $\mathbf{Q}^{(n)}$ and $\mathbf{V}^{(n)\text{T}}$ depict unitary matrices formed column-wise by the left-singular and right-singular eigenvectors of the matrix $\boldsymbol{\Phi}^{(n)}$. Each column $\mathbf{q}_i^{(n)}$ of the matrix $\mathbf{Q}^{(n)}$ represents an orthogonal basis function and is associated to a singular value $\sigma_i^{(n)}$. Based on a tolerance $\sigma_{\text{tol}}^{(n)}$, the amount of column vectors is reduced and the wave basis $\mathbf{W}^{(n)}$ is obtained (see section 3.5). Again, the matrix $\mathbf{T}_{\text{wbs}}^{(n)}$ in Eq. (8) depends on the operating point n and has to be adapted to each rotational speed Ω .

2.3 Secondary Modal Truncation

The last reduction step is based on a modal analysis of the CMS/WBS-reduced model (superscript $*$). By retaining a limited set of blisk modes $\boldsymbol{\Phi}^{(n)*}$ in the matrix $\mathbf{T}_{\text{smt}}^{(n)}$, the transformation to the final modal subspace is achieved,

$$\mathbf{u}_{\text{cms,wbs}}^{(n)} = \mathbf{T}_{\text{smt}}^{(n)} \boldsymbol{\eta}^{(n)} \quad \text{where} \quad \mathbf{T}_{\text{smt}}^{(n)} = \boldsymbol{\Phi}^{(n)} \quad \text{and} \quad \mathbf{K}^{(n)} \boldsymbol{\Phi}^{(n)*} = \mathbf{M} \boldsymbol{\Phi}^{(n)*} \boldsymbol{\Lambda}^{(n)*}. \quad (10)$$

As outlined in the preceding sections, the *Secondary Modal Truncation* (SMT) in Eq. (10) requires repetitive modal analyses at each operating point n .

3 Multi-model Extension

To account for the rotation-induced variation of the mode shapes, the modal bases for the CMS, WBS, and SMT transformation have to be adapted to each operating point of interest. In order to avoid a repetitious passing through the full reduction process for each rotational speed, the modal bases are enriched by mode samples at various operating points. For this purpose, each reduction step is reformulated in terms of a multi-model approach proposed by Balmès (1996), Sternchüss and Balmès (2008), and Sternchüss (2009). In summary, the procedure comprises the following steps:

1. Enrich the modal basis by adding mode samples at various operating points in the relevant speed range.
2. Orthonormalize the enriched modal basis by means of a Singular Value Decomposition.
3. Reduce the dimension of the orthonormal basis by retaining a limited subset of relevant modes.

Following these general steps, the detailed reformulation of the CMS, WBS, and SMT transformation is outlined in the following sections. To account for the stiffness variation by centrifugal forces, a second-order approximation of the reduced stiffness matrix is applied.

3.1 Interpolation of the Stiffness Matrix

Besides the change in mode shapes, the change of the structural eigenfrequencies has to be taken into account. The eigenfrequencies of a rotating bladed disk may either increase (*stress stiffening*) or decrease (*spin softening*)

with rotational speed. To this end, the following interpolation of the reduced spectral matrix \mathbf{K}_{rom} is applied (Sternchüss, 2009),

$$\mathbf{K}_{\text{rom}}(\Omega) = \sum_{n=0}^2 \Omega^{2n} \mathbf{P}_{\text{rom}}^{(n)} = \mathbf{P}_{\text{rom}}^{(0)} + \Omega^2 \mathbf{P}_{\text{rom}}^{(1)} + \Omega^4 \mathbf{P}_{\text{rom}}^{(2)}. \quad (11)$$

In the present study, a fourth-order polynomial in rotational speed Ω (upper limit $n_{\text{max}} = 2$) is sufficient to represent both stiffening and softening effects. The coefficient matrices $\mathbf{P}_{\text{rom}}^{(n)}$ are obtained from three samples of reduced stiffness matrices $\mathbf{K}_{\text{rom}}^{(n)}$ at various rotational speeds Ω . In combination with the enriched reduction bases presented in the following sections, the interpolation in Eq. (11) allows an efficient vibration prediction at constant and variable rotational speed. It should be noted that this interpolation may be performed at any reduction level. Since the reduced stiffness matrix features the smallest dimension after CMS, WBS, and SMT transformation, the interpolation is preferably performed at this final stage of the reduction process.

3.2 Extended Component Mode Synthesis

According to section 2.1, the enriched CMS basis is formed by dynamic component modes $\Phi^{(s,n)}$ and static constraint modes $\Psi^{(s,n)}$ at various operating points. With respect to the second order polynomial in Eq. (11), three sets of modal samples are used,

$$\mathbf{T}_{\text{cms}}^{(s)} = \begin{bmatrix} \mathbf{I} & \mathbf{0} & \mathbf{I} & \mathbf{0} & \mathbf{I} & \mathbf{0} \\ \Psi^{(s,0)} & \Phi^{(s,0)} & \Psi^{(s,1)} & \Phi^{(s,1)} & \Psi^{(s,2)} & \Phi^{(s,2)} \end{bmatrix}. \quad (12)$$

Relating the additional static modes to a reference modal set $\Psi^{(s,0)}$, the transformation matrix $\tilde{\mathbf{T}}_{\text{cms}}^{(s)}$ becomes,

$$\begin{aligned} \tilde{\mathbf{T}}_{\text{cms}}^{(s)} &= \begin{bmatrix} \tilde{\mathbf{T}}_{\text{i}}^{(s)} & \tilde{\mathbf{T}}_{\text{m}}^{(s)} \end{bmatrix} \quad \text{where} \quad \tilde{\mathbf{T}}_{\text{i}}^{(s)} = \begin{bmatrix} \mathbf{I} \\ \Psi^{(s,0)} \end{bmatrix} \quad \text{and} \\ \tilde{\mathbf{T}}_{\text{m}}^{(s)} &= \begin{bmatrix} \mathbf{0} & \mathbf{0} & \mathbf{0} & \mathbf{0} & \mathbf{0} & \mathbf{0} \\ \Psi^{(s,1)} - \Psi^{(s,0)} & \Psi^{(s,2)} - \Psi^{(s,0)} & \Phi^{(s,0)} & \Phi^{(s,1)} & \Phi^{(s,2)} \end{bmatrix}. \end{aligned} \quad (13)$$

Next, the obtained modal basis is orthonormalized by a Singular Value Decomposition and reduced by retaining only modes associated to singular values above a tolerance $\sigma_{\text{tol}}^{(s)}$,

$$\tilde{\mathbf{T}}_{\text{m}}^{(s)} = \mathbf{Q}^{(s)} \boldsymbol{\Sigma}^{(s)} \mathbf{V}^{(s)\text{T}} \quad \text{and} \quad \tilde{\mathbf{T}}_{\text{m,red}}^{(s)} = \left\{ \mathbf{q}_i^{(s)} \right\} \quad \text{for} \quad \sigma_i^{(s)} \geq \sigma_{\text{tol}}^{(s)}. \quad (14)$$

A synthesis of the reduced basis $\tilde{\mathbf{T}}_{\text{m,red}}^{(s)}$ and its reference $\tilde{\mathbf{T}}_{\text{i}}^{(s)}$ leads to the enriched transformation matrix $\tilde{\mathbf{T}}_{\text{cms,red}}^{(s)}$,

$$\tilde{\mathbf{T}}_{\text{cms,red}}^{(s)} = \begin{bmatrix} \tilde{\mathbf{T}}_{\text{i}}^{(s)} & \tilde{\mathbf{T}}_{\text{m,red}}^{(s)} \end{bmatrix}. \quad (15)$$

3.3 Extended Wave-Based Substructuring

Enriching the set of interface waves in Eq. (8) with samples at different rotational speeds

$$\mathbf{T}_{\text{wbs}} = \begin{bmatrix} \mathbf{W}^{(0)} & \mathbf{0} & \mathbf{W}^{(1)} & \mathbf{0} & \mathbf{W}^{(2)} & \mathbf{0} \\ \mathbf{0} & \mathbf{I} & \mathbf{0} & \mathbf{I} & \mathbf{0} & \mathbf{I} \end{bmatrix} \quad (16)$$

and performing the rearrangement

$$\tilde{\mathbf{T}}_{\text{wbs}} = [\tilde{\mathbf{T}}_{\text{m}} \quad \tilde{\mathbf{T}}_{\text{i}}] \quad \text{where} \quad \tilde{\mathbf{T}}_{\text{m}} = \begin{bmatrix} \mathbf{W}^{(0)} & \mathbf{W}^{(1)} & \mathbf{W}^{(2)} \\ \mathbf{0} & \mathbf{0} & \mathbf{0} \end{bmatrix} \quad \text{and} \quad \tilde{\mathbf{T}}_{\text{i}} = \begin{bmatrix} \mathbf{0} \\ \mathbf{I} \end{bmatrix} \quad (17)$$

yields the reduced WBS matrix $\tilde{\mathbf{T}}_{\text{wbs,red}}$,

$$\tilde{\mathbf{T}}_{\text{wbs,red}} = [\tilde{\mathbf{T}}_{\text{m,red}} \quad \tilde{\mathbf{T}}_{\text{i}}] \quad \text{where} \quad \tilde{\mathbf{T}}_{\text{m}} = \mathbf{Q} \boldsymbol{\Sigma} \mathbf{V}^{\text{T}} \quad \text{and} \quad \tilde{\mathbf{T}}_{\text{m,red}} = \left\{ \mathbf{q}_i \right\} \quad \text{for} \quad \sigma_i \geq \sigma_{\text{tol}}. \quad (18)$$

3.4 Extended Secondary Modal Truncation

Modal analyses of the reduced blisk model at three different rotational speeds provide the SMT basis

$$\mathbf{T}_{\text{smt}} = \begin{bmatrix} \Phi^{(0)*} & \Phi^{(1)*} & \Phi^{(2)*} \end{bmatrix} \quad \text{where} \quad \tilde{\mathbf{T}}_{\text{smt}} = \tilde{\mathbf{T}}_{\text{m}} \quad (19)$$

which is orthonormalized and reduced to form the enriched SMT matrix $\tilde{\mathbf{T}}_{\text{smt,red}}$,

$$\tilde{\mathbf{T}}_{\text{smt,red}} = \tilde{\mathbf{T}}_{\text{m,red}} \quad \text{where} \quad \tilde{\mathbf{T}}_{\text{m}} = \mathbf{Q} \mathbf{\Sigma} \mathbf{V}^T \quad \text{and} \quad \tilde{\mathbf{T}}_{\text{m,red}} = \{\mathbf{q}_i\} \quad \text{for} \quad \sigma_i \geq \sigma_{\text{tol}}. \quad (20)$$

3.5 Singular Value Tolerance

To illustrate the feasible range of the parameter σ_{tol} , the singular values for a bladed disk at different rotational speeds Ω are analyzed. The effect of choosing a specific tolerance is assessed in terms of the maximum relative difference $\Delta f_{\text{rel,max}}$ of the lowest 100 eigenfrequencies f_i between the reduced and full finite element model,

$$\Delta f_{\text{rel,max}} = \max \left\{ \frac{f_{\text{rom},i} - f_{\text{full},i}}{f_{\text{full},i}} \right\}. \quad (21)$$

In the following, the singular values $\sigma_i^{(n)}$ of the interface waves in Eq. (9) are presented. For simplicity, the values $\tilde{\sigma}_i^{(n)}$ are normalized with respect to the largest singular value $\sigma_1^{(n)}$,

$$\tilde{\sigma}_i^{(n)} = \frac{\sigma_i^{(n)}}{\sigma_1^{(n)}}. \quad (22)$$

Despite different operating points n , a similar decrease of the singular values for the analyzed rotational speeds of 0 rpm, 6,000 rpm, and 12,000 rpm is shown in Fig. 1. Consequently, a common tolerance $\tilde{\sigma}_{\text{tol}}^{(n)} = 0.1$ is chosen for all three angular velocities. Exemplary values for some tolerance levels are listed in Tab. 1.

Table 1: Maximum relative frequency difference $\Delta f_{\text{rel,max}}$ between ROM and FEA as a function of the normalized singular value tolerance $\tilde{\sigma}_{\text{tol}}^{(n)}$

Tolerance $\tilde{\sigma}_{\text{tol}}^{(n)}$	Interface waves i	Max. frequency difference $\Delta f_{\text{rel,max}}$
0.1	100 waves	< 2%
0.3	75 waves	< 5%
0.7	20 waves	< 10%

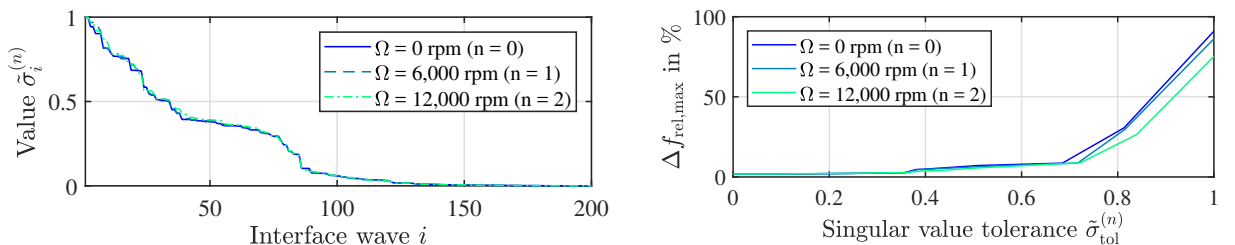


Figure 1: Normalized singular values $\tilde{\sigma}$ of the interface waves (left) and maximum frequency difference $\Delta f_{\text{rel,max}}$ between the FEA and ROM with various tolerances $\tilde{\sigma}_{\text{tol}}^{(n)}$ for the first 100 tuned blisk modes (right) at constant rotational speeds Ω of 0 rpm, 6,000 rpm, and 12,000 rpm

4 Comparison with the Full Model

To assess the accuracy of the reformulated modeling approach, the reduced order model of a sample blisk comprising ten bladed segments is compared to its full finite element representation. First, an appropriate discretization of the blisk by finite elements has to be chosen by comparing the results obtained from successively refined meshes. Since this study is focused on modeling the evolution of dynamic properties under rotation, the relative change $\Delta f_{\text{rpm},k}$ of the eigenfrequency f_k in the speed range from $\Omega_{\min} = 0$ rpm up to $\Omega_{\max} = 15,000$ rpm is chosen as a convergence criterion between the meshes,

$$\Delta f_{\text{rpm},k} = \left\| \frac{f_k(\Omega_{\max}) - f_k(\Omega_{\min})}{f_k(\Omega_{\min})} \right\|. \quad (23)$$

The results of the mesh convergence study in Fig. 2 indicate that the maximum frequency change $\Delta f_{\text{rpm},k}^{\max}$ of about 70% in the analyzed speed range is well predicted by meshes with at least 5,000 *degrees of freedom* (dof). A detailed study of 10 mode families with two nodal diameters shows that the maximum frequency change $\Delta f_{\text{rpm},k}^{\text{ND}2}$ is related to the first mode family. In view of the computational expense to solve the unreduced finite element model, a medium mesh size with 9,300 dof is chosen for the subsequent model verification.

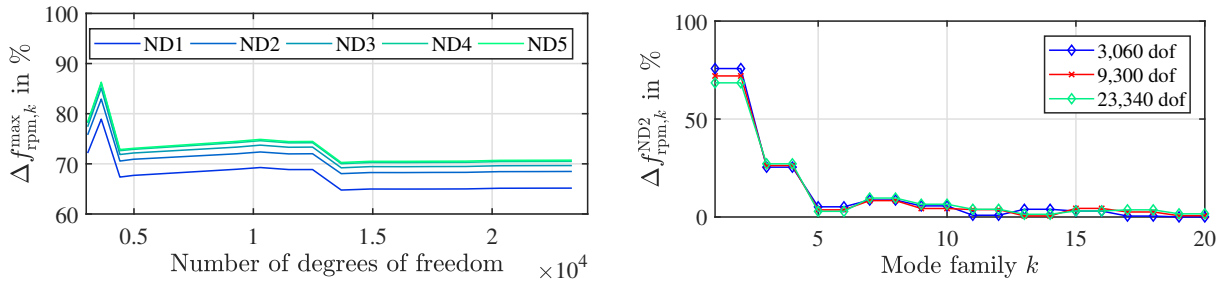


Figure 2: Relative change $\Delta f_{\text{rpm},k}$ of eigenfrequencies in the rotational speed range from 0 rpm to 15,000 rpm for different finite element meshes and various nodal diameters ND

The comparison between the reduced and full model in Fig. 3 is performed at different steady operating points with constant rotational speeds. The reduced order approximation is based on three samples of prestressed stiffness matrices at speeds Ω of 0 rpm, 6,000 rpm, and 12,000 rpm. The number of retained modes in the enriched CMS, WBS, and SMT bases is listed in Tab. 2. Prior to addressing a mistuned configuration under rotation, the tuned dynamics of the blisk are discussed. In conclusion, the effectiveness of the presented approach in terms of computational time saving is highlighted.

Table 2: Parameters of the reduced order model

CMS	WBS	SMT
10 modes per blade / 10 modes per harm. index	200 waves	100 blisk modes

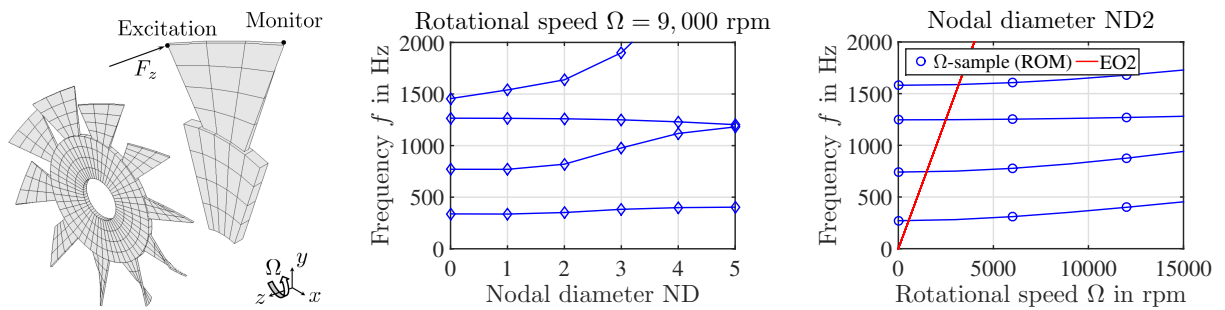


Figure 3: Finite element model, nodal diameter diagram, and ND2-Campbell diagram of the tuned blisk (stiffness samples for ROM taken at constant rotational speeds Ω of 0 rpm, 6,000 rpm, and 12,000 rpm)

4.1 Tuned Blisk under constant Rotation

First, the mode shape approximation by enriched CMS, WBS, and SMT bases is evaluated in terms of the *Modal Assurance Criterion* (MAC) presented by Allemand and Brown (1982). The interpolation of the reduced stiffness matrix within a limited range of rotational speeds is rated by means of the relative eigenfrequency difference Δf_{rel} between the reduced and full finite element model,

$$\text{MAC}_{i,j} = \frac{|\Phi_{\text{rom},i}^T \Psi_{\text{full},j}|^2}{\Phi_{\text{rom},i}^T \Phi_{\text{rom},i} \Psi_{\text{full},j}^T \Psi_{\text{full},j}} \quad \text{and} \quad \Delta f_{\text{rel},i} = \frac{f_{\text{from},i} - f_{\text{full},i}}{f_{\text{full},i}}. \quad (24)$$

Since slight frequency differences between the full and reduced order models may lead to a different order of the associated mode shapes i , the resulting modal assurance criterion $\text{MAC}_{i,i}$ undergoes abrupt changes between maximum and minimum values. This circumstance is illustrated by a progressively increasing scatter of large MAC values for higher modes in the contour plot of Fig. 4.

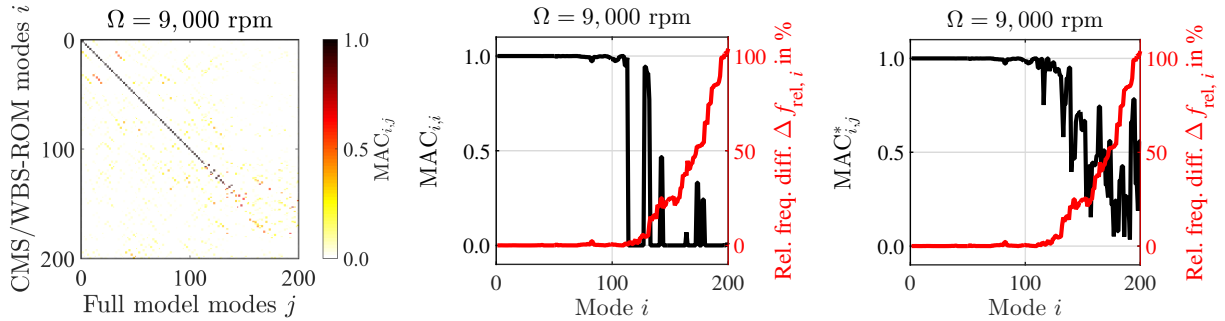


Figure 4: Modal assurance criteria and relative frequency differences of the tuned blisk for a constant rotational speed of 9,000 rpm

Consequently, a modified criterion $\text{MAC}_{i,j}^*$ is defined which yields a gradually decreasing mode correlation for increasing frequency deviations in Fig. 4,

$$\text{MAC}_{i,j}^* = \max_j \left\{ \frac{|\Phi_{\text{rom},i}^T \Psi_{\text{full},j}|^2}{\Phi_{\text{rom},i}^T \Phi_{\text{rom},i} \Psi_{\text{full},j}^T \Psi_{\text{full},j}} \right\}. \quad (25)$$

The accuracy of the parameterized multi-model formulation is assessed at the sample speeds of 0 rpm, 6,000 rpm, and 12,000 rpm as well as intermediate and extended speeds of 3,000 rpm, 9,000 rpm, and 15,000 rpm. A MAC level above 0.96 and a relative frequency difference below 1% for the first 110 modes in Fig. 5 demonstrates the accurate approximation of free blisk vibrations at different rotational speeds by the reduced order model. While this decent approximation is expected for operating points which are included as stiffness samples in the model, the good correlation at intermediate and extrapolated rotation speeds demonstrates the validity of the underlying stiffness interpolation in Eq. (11) and the multi-model extension.

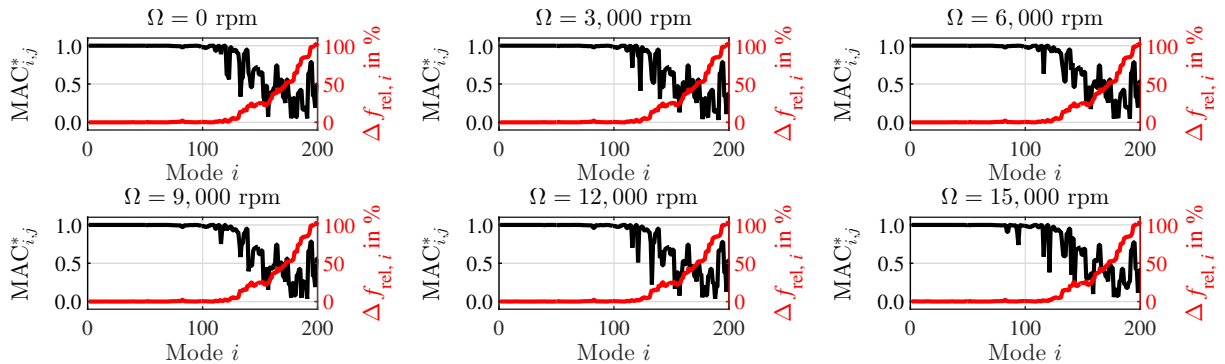


Figure 5: Modal assurance criteria and relative frequency differences of the tuned blisk for constant rotational speeds ranging from 0 rpm to 15,000 rpm

This conclusion is substantiated by the excellent agreement of the forced EO2 response of the full and reduced blisk models at a rotor speed of 9,000 rpm in Fig. 6. The depicted amplitude \hat{u}^* is normalized with respect to the maximum displacement of the tuned blisk at rotor standstill. To illustrate the stiffening effect on the forced response, an amplitude comparison for various rotational speeds is provided in Fig. 7. Again, the amplitudes of the full and reduced order models match well in the analyzed range of frequencies and rotational speeds. A detailed view of the stiffening effect on the resonance of the first flapwise bending mode is provided in Fig. 7.

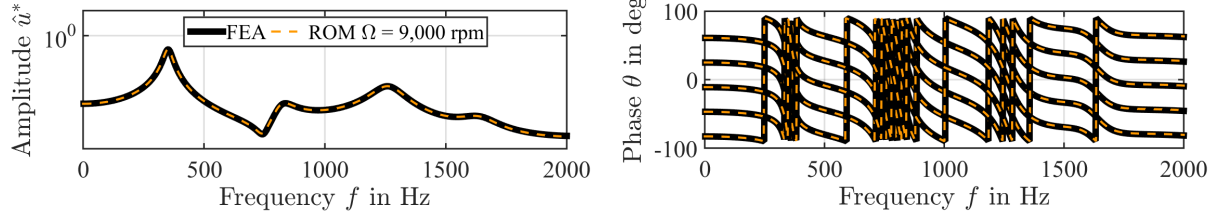


Figure 6: Forced EO2 response of the reduced and full finite element models of the tuned blisk for a constant rotational speed Ω of 9,000 rpm

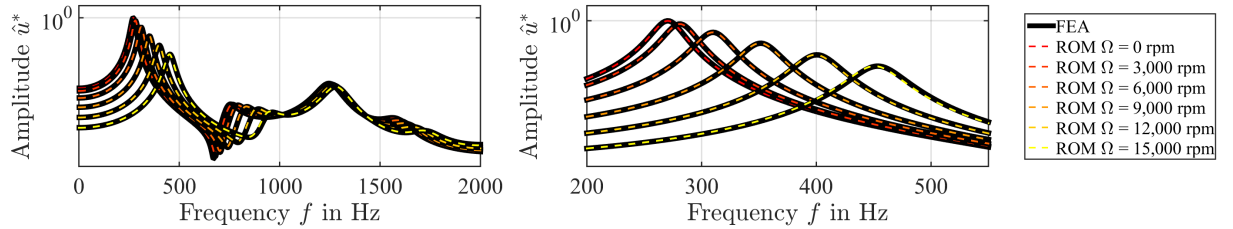


Figure 7: Forced EO2 response of the reduced and full finite element models of the tuned blisk for constant rotational speeds Ω ranging from 0 rpm to 15,000 rpm

4.2 Mistuned Blisk under constant Rotation

To assess the accuracy of the reduced order prediction for mistuned bladed disks, the stiffness of each blade k is multiplied by an individual mistuning factor κ_k in Tab. 3. It should be noted that this frequency mistuning is applied to the blading at rotor standstill. Consequently, the ratios of tuned and mistuned blade frequencies may change for various operating points. In the presented reduced order model, this evolution of mistuning factors with a variable speed Ω is covered by considering the reduced stiffness matrices of each individual blade at three different rotational speeds and applying the interpolation in Eq. (11).

A comparison between the full and reduced models by means of a mistuned EO2 response at 9,000 rpm is presented in Fig. 8. Again, an excellent agreement in terms of amplitude and phase approximation is highlighted. The accuracy of the reduced order model for various rotational speeds ranging from 0 rpm to 15,000 rpm is demonstrated in Fig. 9.

Table 3: Frequency mistuning factors of the blisk at rotor standstill ($\Omega = 0$ rpm)

Blade k	1	2	3	4	5	6	7	8	9	10
κ_k	0.84	0.98	1.05	0.81	1.49	1.05	1.12	0.52	1.41	1.12

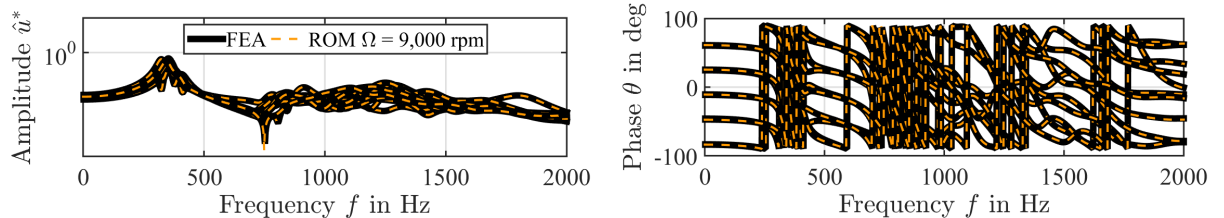


Figure 8: Forced EO2 response of the reduced and full finite element models of the mistuned blisk for a constant rotational speed Ω of 9,000 rpm

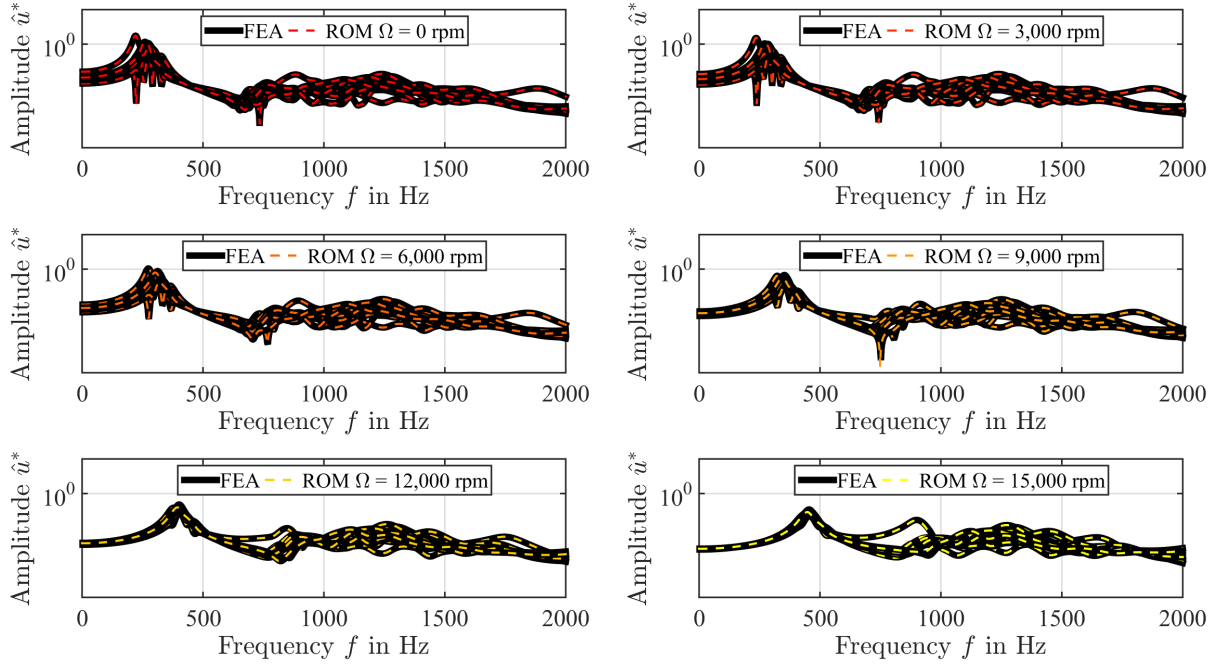


Figure 9: Forced EO2 response of the reduced and full finite element models of the mistuned blisk for constant rotational speeds Ω ranging from 0 rpm to 15,000 rpm

4.3 Computational Time Saving

To highlight the effectiveness of the presented approach, the computational times required for the forced response analysis of the previously introduced blisk sample are shown in Fig. 10. The computational setup used for all simulations is summarized in Tab. 4. First, the time t_{FEA} required for solving the full finite element model is compared to the overall computation time $t_{\text{ROM, total}}$ of the reduced order model (including the model reduction as well as the solution process). This direct comparison demonstrates that the reduced order approach outperforms the full model by a factor of almost four (saving 73% of computational time).

In addition, the amount $t_{\text{ROM, reduction}}$ of 48 s indicates that the reduction process takes up more than half of the overall computation time $t_{\text{ROM, total}}$ of 77 s. Since the model reduction has to be performed just once prior to the actual solution process, the reduced order approach provides a computational saving of 90% for the forced response prediction in comparison to the full finite element model.

Table 4: Computational setup used for all simulations

Operating system	CPU	RAM
Windows 7 Professional (64 Bit)	Intel Core i5-4590 (3.3 GHz)	16 GB

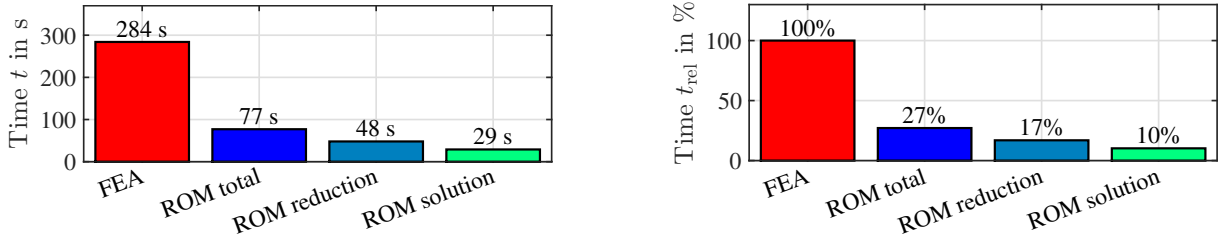


Figure 10: Comparison of the computational time required for a mistuned forced response prediction (1,000 frequency samples per response curve) by the full finite element model and the reduced order approach

5 Analysis of Blisks under variable Rotation

Besides the vibration prediction for various constant operating points, the presented model allows the analysis of bladed disks at variable speeds of rotation. In the following, the resonance of the first flapwise bending mode for a synchronous stimulus according to Eq. (4) is analyzed. Since each frequency f is related to a specific rotational speed Ω via the engine order EO, the structural properties are adapted to each operating point in the analyzed frequency range according to Eq. (11). It should be noted that despite the variation of rotor speed, the response at each frequency is assumed as a steady operating state and no transient run-up or coast-down effects are considered. In Fig. 11, the forced response of the tuned blisk under variable rotor speed (indicated by the tilted line) is compared to its amplitudes at constant rotation for the engine orders EO2, EO6, and EO10. It becomes clear that the frequencies at the crossings of the synchronous response (tilted line) and the amplitudes at constant rotation meet the condition in Eq. (4) according to the specific engine order. For example, the amplitude response at 15,000 rpm (corresponding to $\Omega = 250$ Hz) is crossed by the variable EO2 response at a frequency f of 500 Hz. In addition, the stiffening effect modeled by Eq. (11) is identifiable as an increase of the resonance frequency with growing rotor speed.

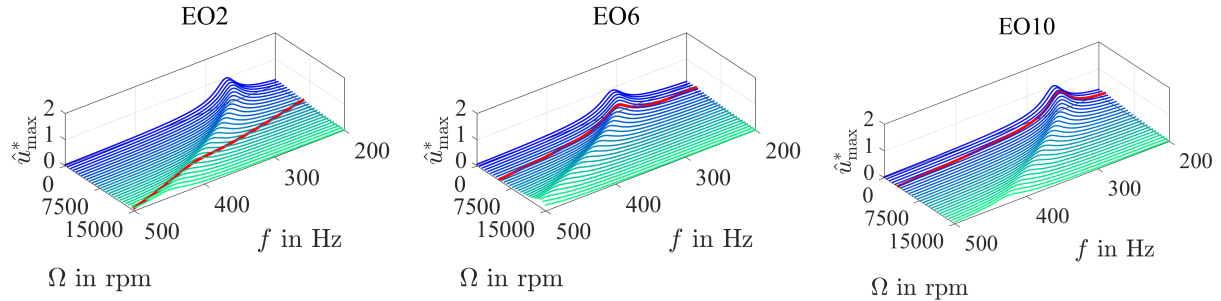


Figure 11: Forced response of the tuned reduced order model for constant and variable rotational speeds (tilted line)

A comparison between the forced EO2, EO6, and EO10 responses of a mistuned blisk (see Tab. 3) under variable rotation and its responses at constant rotational speed is shown in Fig. 12. For simplicity, the mistuned response is depicted in terms of the overall envelope of the maximum amplitudes. Again, the response crossings for variable and constant rotational speeds meet the relation in Eq. (4).

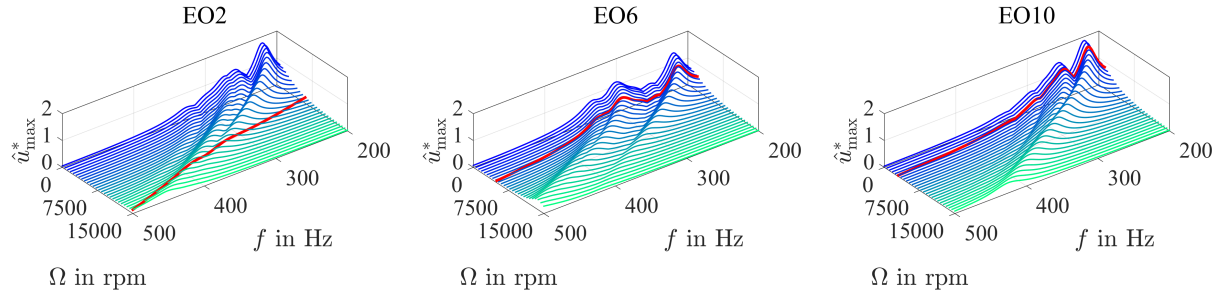


Figure 12: Maximum amplitudes of the mistuned reduced model for constant and variable rotor speeds (tilted line)

To study the effect of constant and variable rotor speed Ω on the amplification of mistuned vibrations, the following ratio between the maximum amplitude of the tuned (superscript ^{tu}) and mistuned blisk (superscript ^{mt}) is defined:

$$a_\Omega = \frac{\hat{u}_\Omega^{\text{mt,max}}}{\hat{u}_\Omega^{\text{tu,max}}} \quad (26)$$

While the maximum amplitude ratio at constant rotational speed is obtained by division of the amplitude maxima along the response curves aligned with the frequency abscissa f in Fig. 11 and Fig. 12, the amplification factor a_Ω under variable rotation results from the ratio of the tilted response curves in mentioned figures. It should be noted that the frequency range which is considered for the determination of the maximum amplitudes $\hat{u}_\Omega^{\text{max}}$ under variable rotation depends on the actual rotor speed Ω and the analyzed engine order EO through Eq. (4). Consequently, the analysis of EO1 is limited to excitation frequencies below 250 Hz since this value corresponds to the upper limit of the rotational speed range ($\Omega = 15,000$ rpm) validated in section 4.

The corresponding amplification factors for engine orders EO1 to EO10 are depicted in Fig. 13. It is indicated that the amplitude amplification ratios for all analyzed engine orders at constant rotor speed tend to decrease for an increase in Ω . This result is in accordance with the mitigation effect of rotation on mistuning reported by Moyroud et al. (2002) and Nipkau (2011).

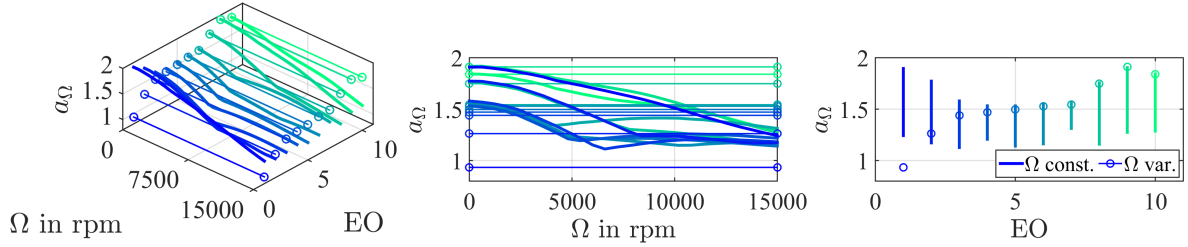


Figure 13: Amplitude amplification of the mistuned reduced order model for constant and variable rotational speed

In comparison, the maximum amplitude amplification for engine orders EO5 to EO10 under variable rotor speed (indicated by circles in Fig. 13) is of the same order as the ratios at constant rotational speed. For EO1 to EO4 the assumption of constant rotational speed leads to an overprediction of the mistuning effect. This result can be traced back to Eq. (4), Fig. 11, and Fig. 12: Since the synchronous stimulus response (tilted line) approaches the response at rotor rest ($\Omega = 0$ rpm, line aligned with frequency axis) for large EO levels, the amplitude amplification for an increasing engine order converges towards the corresponding maximum value at rotor standstill.

6 Summary and future Work

The extension of a reduced order model to account for the rotational speed dependence of mistuned bladed disk dynamics has been presented. By usage of a multi-model formulation presented in Balmès (1996), Sternchüss and Balmès (2008), and Sternchüss (2009), the reformulated substructural approach allows efficient blade vibration predictions at constant and variable rotor speeds. The accuracy of the model has been demonstrated in terms of modal assurance criteria, relative frequency differences, and a forced response comparison. Comparing the computational times for solving the reduced model and the full finite element representation of a mistuned blisk reveals a time saving of 90%. The applicability of the proposed approach has been shown by the study of a mistuned bladed disk at various rotational speeds. The analyses indicate that the rotational motion has a mitigating effect on the amplitude amplification caused by mistuning.

In future work, the evolution of the speed-dependent mistuning coefficients will be incorporated in the presented model. Finally, the numerically predicted response may be compared to experimental measurements in an operating turbomachinery test rig.

Acknowledgments

This work was supported by the German Research Foundation (DFG) and the Research Association for Combustion Engines (FVV) e.V. within the framework of the co-funded project “Mistuning of bladed disks with aerodynamic and structural coupling”.

References

- Allemand, R. J.; Brown, D. L.: A Correlation Coefficient for Modal Vector Analysis. In: *Proceedings of the 1st International Modal Analysis Conference*, pages 110–116 (1982).
- Balmès, E.: Parametric families of reduced finite element models. Theory and applications. In: *Mechanical Systems and Signal Processing*, vol. 10(4), pages 381–394 (1996).
- Craig, R. R.; Bampton, M. C. C.: Coupling of Substructures for Dynamic Analysis. *AIAA Journal*, , 6, (1968), 1313–1319.
- Donders, S.: *Computer-aided engineering methodologies for robust automotive NVH design*. Ph.D. thesis, KU Leuven, Leuven (2008).
- Feiner, D. M.: *A Fundamental Model of Mistuning for Forced Response Prediction and System Identification*. Ph.D. thesis, Carnegie Mellon University, Pittsburgh (2002).

Feiner, D. M.; Griffin, J. H.: Mistuning Identification of Bladed Disks Using a Fundamental Mistuning Model - Part I: Theory. *ASME J. Turbomach.*, 126(1), (2004), 150–158.

Hohl, A.; Siewert, C.; Panning, L.; Wallaschek, J.: A Substructure Based Reduced Order Model for Mistuned Bladed Disks. In: *ASME 2009 International Design Engineering Technical Conferences and Computers and Information in Engineering Conference*, pages 899–906 (2009).

Maywald, T.; Beirow, B.; Heinrich, C. R.; Kühhorn, A.: Vacuum Spin Test Series of a Turbine Impeller With Focus on Mistuning and Damping by Comparing Tip Timing and Strain Gauge Results. In: *ASME Turbo Expo 2015: Turbine Technical Conference and Exposition, GT2015-42649* (2009).

Moyroud, F.; Fransson, T.; Jacquet-Richardet, G.: A Comparison of Two Finite Element Reduction Techniques for Mistuned Bladed Disks. *ASME J. Eng. Gas Turbines Power*, 124(4), (2002), 942–952.

Nipkau, J.: *Analysis of Mistuned Blisk Vibrations Using a Surrogate Lumped Mass Model with Aerodynamic Influences*. Ph.D. thesis, Brandenburgische Technische Universität Cottbus, Cottbus (2011).

Sternchüss, A.: *Multi-level parametric reduced order models of rotating bladed disk assemblies*. Ph.D. thesis, École Centrale Paris, Paris (2009).

Sternchüss, A.; Balmès, E.: On the reduction of quasi-cyclic disks with variable rotation speeds. In: *International Conference on Advanced Acoustics and Vibration Engineering*, pages 3925–3939 (2008).

Address: Institute of Dynamics and Vibration Research, Leibniz Universität Hannover, 30167 Hannover, Germany
email: willeke@ids.uni-hannover.de

Rotordynamic Computation of a Permanent-Magnetic excited Synchronous Machine due to Electromagnetic Force Excitation

M. Clappier, L. Gaul

For the acoustical computation of electromagnetic noise, it is very important to consider both, the rotor and stator vibrations of the electrical machine. Rotor vibrations can be transmitted as structure-borne sound to connected systems which might be excited at their resonances and radiate airborne sound. In order to predict the dynamical behaviour of complex electrical machine rotors (such like rotors of permanent-magnetic excited synchronous machines) in frequency domain, finite element (FE) computations can be efficiently applied using rotating coordinates. Hereby, it has to be taken into account that rotor vibrations are mainly influenced by stiffness and damping of the built-in laminated stacks and mechanical joints. Therefore, a FE model of the rotor is required which takes these parameters into account. In order to obtain the material properties, two experimental set-ups are considered. On the one hand, a generic lap joint is considered to determine the stiffness and damping of mechanical joints. On the other hand, a test rig for laminated stacks is presented which allows for the determination of direction-dependent stiffness and damping of laminated stacks by a shear and dilatation test. All identified parameters are included into the FE model. Thereby, local stiffness and damping of mechanical joints are modelled by so-called thin-layer elements. In order to prove the quality of the rotor FE model, a numerical modal analysis without considering rotor spin speed is carried out and compared to experimental results. Electromagnetic force densities are computed in the air gap of the electrical machine using an electromagnetic FE model. To cover different FE meshes of the mechanical and electromagnetic model, a method is presented which allows for converting force densities into equivalent nodal forces on the rotor surface. These excitation forces are used to compute electromagnetically caused rotor vibrations dependent on rotor spin speed by a frequency domain rotor dynamic analysis.

1 Introduction and Aim of this Work

Acoustical noise of electrical machines is made up of three different types of sources: electromagnetically, mechanically and aerodynamically excited vibrations/noise (Gieras et al., 2006). Electromagnetically caused vibrations result from electromagnetic forces in the air gap between rotor and stator (Gieras et al., 2006). These forces are mainly affected by the magnetic design and operational conditions of the electrical machine. Mechanically caused vibrations are e.g. due to rotor dynamic loads, bearing defects or tolerances and shaft misalignments (Gieras et al., 2006). Aerodynamic noise normally occurs due to the noise of cooling fans (Gieras et al., 2006). For totally enclosed and water-cooled machine housings, the last type of source does not occur. For acoustical computations both, vibrations of the stator housing as well as rotor vibrations must be taken into account in order to model all structure-borne and airborne sound paths. Especially rotor vibrations can be transmitted to connected systems where airborne sound can be radiated additional to the sound radiated by the electrical machine housing.

The acoustical behavior of electrical machines has already been considered in many publications. Most of them are only related to vibrations and sound radiation of the machine housing caused by electromagnetic force excitation on stator teeth (with/without eccentricity effects), cf. (Dupont et al., 2014) and (Shiohata et al., 2011). Only in few works the rotor is included as additional component into the structural finite element (FE) model (see Humbert et al. (2012), McCloskey et al. (2014) and Pellerey et al. (2012)) and magnetic forces are applied on the rotor (see McCloskey et al. (2014) and Pellerey et al. (2012)).

So far, no publication has been found by the authors which considers the numerical computation of rotor dynamics due to distributed electromagnetic forces on the laminated stack (obtained from magnetic FE analysis) using structural three-dimensional (3D) solid FEs. Available works are based on either analytical rotordynamic models with one or a few degrees of freedom or FE models built up by beam elements, cf. (Arkkio et al., 2010), (Pellerey et al., 2012) and named references in (Pellerey et al., 2012). Therefore, this work is concentrated on 3D FE rotordynamic analysis in order to examine electromagnetically caused rotor vibrations.

As application case, the rotor of a permanent-magnetic excited synchronous machine (PMSM) is considered which consists of many single electrical sheets stacked together and positioned between two balancing discs onto the rotor shaft, see Figure 1. Thereby, the laminated rotor stack is pre-tensioned by both balancing discs.

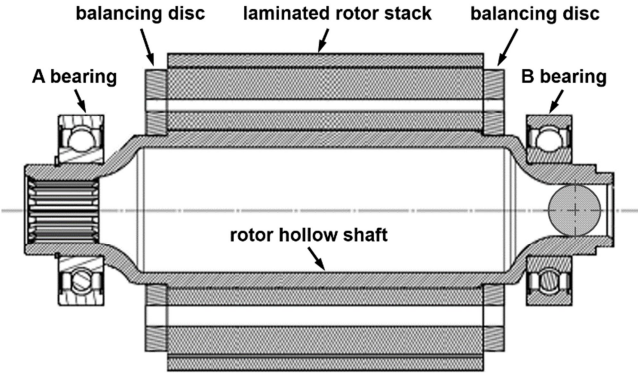


Figure 1. Rotor cross section of the considered PMSM rotor, cf. (Clappier and Gaul, 2016)

In order to carry out rotordynamic computations, it is very important to know the direction-dependent stiffness and structural damping of the laminated stack because both parameters mainly influence the dynamical behavior of the rotor. Normally, both quantities are unknown and estimated numerically via model updating, cf. (Gieras et al., 2006) for stators. The axial stiffness can also be determined load-dependent by a static compression test (Siegl, 1981). A detailed overview about literature and available approaches is given in (Clappier and Gaul, 2015). However, none of the named methods allows for the determination of structural damping and direction-dependent stiffness using only one experimental set-up.

In this paper, an experimental set-up is presented which allows for the determination of the direction-dependent stiffness and structural damping of laminated rotor stacks for certain pre-stress conditions using a shear and dilatation test. Based on these parameters, a FE model of the rotor is created. Thereby, so-called thin-layer elements (TLEs) are used to take the dynamics of several mechanical interfaces into account, cf. (Desai et al., 1984), (Gaul et al., 2011) and (Gaul and Schmidt, 2014). The computed eigenfrequencies, mode shapes and modal damping factors of the rotor (without spin speed) are compared to results of an experimental modal analysis (EMA). Finally, rotordynamic analyses are carried out to compute the response due to electromagnetic force excitation with and without taking dynamical rotor eccentricity into account. Thereby, a new method is presented to transform airgap forces from a two-dimensional (2D) electromagnetic computation onto a 3D structural mechanic FE mesh.

2 Experimental Determination of the Properties of Mechanical Joints and Laminated Rotor Stacks

2.1 Stiffness and Structural Damping of Mechanical Joints

Figure 2(a) depicts the experimental set-up of the considered generic lap joint (Gaul et al., 2015). Thereby, two masses m_1 and m_2 are supported by two thin wires at their center of gravity (Bograd et al., 2008).

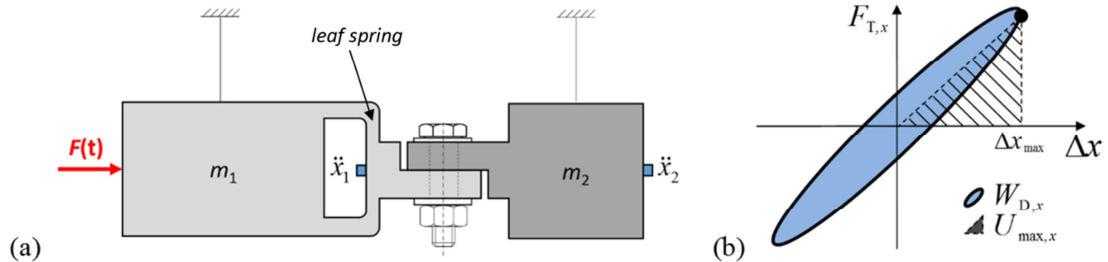


Figure 2. (a) Generic lap joint and (b) damping hysteresis, cf. (Bograd et al., 2008), (Gaul et al., 2016), (Gaul et al., 2011), (Gaul et al., 2015) and (Gaul et al., 1997)

Both masses are connected by a screw connection on a lap joint in order to define a certain interface contact pressure. Mass m_1 is excited harmonically with a certain excitation frequency and amplitude by an

electromagnetic shaker, cf. (Bograd et al., 2008) and (Gaul et al., 2015). Because of the leaf spring attached to mass m_1 , a longitudinal system resonance is excited allowing to evaluate the structural damping of the mechanical joint up to high tangential forces (Bograd et al., 2008), (Gaul et al., 2015). When the set-up is in steady-state, the accelerations \ddot{x}_1 and \ddot{x}_2 of both masses are measured by two accelerometers (Bograd et al., 2008), (Gaul et al., 2015). Twice integration of both acceleration signals with respect to the time leads to the displacement signals x_1 and x_2 , from which the relative displacement $\Delta x = x_1 - x_2$ can be computed (Bograd et al., 2008). Plotting the transmitted tangential force $F_{T,x} = m_2 \cdot \ddot{x}_2$ in the mechanical interface representing the inertia force of mass m_2 versus the relative displacement Δx leads to a hysteresis (Figure 2(b)), from which the tangential joint stiffness k_T and structural damping loss factor η can be derived by equations given in (1), see (Bograd et al., 2008), (Gaul et al., 2011) and (Gaul et al., 2015). Thereby, $W_{D,x}$ and $U_{\max,x}$ are the dissipated damping energy and the maximum stored potential energy ((Bograd et al., 2008), (Gaul et al., 2011) and (Gaul et al., 2015)).

$$k_T = \frac{F_{T,x}(\Delta x_{\max})}{\Delta x_{\max}} \quad , \quad \eta = \frac{W_{D,x}}{2\pi \cdot U_{\max,x}} \quad (1)$$

As it is shown in (Clappier et al., 2015b) and (Gaul et al., 2015), the joint damping loss factor strongly depends on the relative displacement, tangential force $F_{T,x}$ and normal force. Thus, this load dependency must be taken into account in FE models for applications with inhomogeneous contact pressure distributions, cf. (Clappier et al., 2015b) and (Gaul et al., 2016).

2.2 Stiffness and Structural Damping of Laminated Rotor Stacks

In (Clappier and Gaul, 2015), (Clappier et al., 2015a) and (Clappier and Gaul, 2016), a measurement set-up is presented for the determination of the direction-dependent stiffness and structural damping of arbitrarily shaped laminated structures. The experimental idea goes back to Crandall et al. (1971). The measurement concept is transferred and enhanced for measurements on laminated rotor stacks. A brief description of the measurement principle is given in the following according to Figure 3.

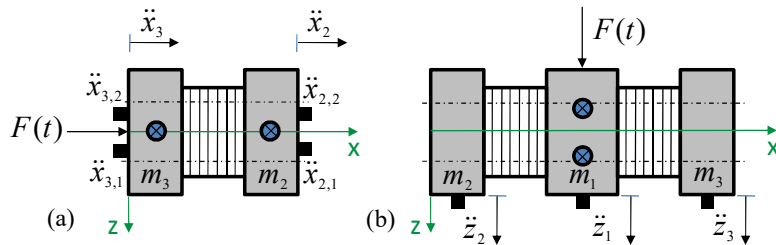


Figure 3. Measurement set-up for laminated rotor stacks. (a) Dilatation test and (b) shear test (Clappier et al., 2015a)

In order to determine the axial stiffness and structural damping of a laminated rotor stack, a dilatation test is applied (see Figure 3(a)) whereas a shear test is used for the determination of shear stiffness and structural damping (Figure 3(b)). Thereby, the measurement and evaluation idea is quite similar. In both configurations, one test specimen is axially pre-tensioned between two adjacent steel plates by screw connections (chain lines in Figure 3(a,b)). Thus, certain rotor prestress conditions can be considered. The masses of the steel plates (including the mass of the test specimen in distributed form) are denoted according to Figure 3(a,b) by m_1 , m_2 and m_3 . Both set-ups are supported at the metal plates by two thin wires as indicated by the crossed circular symbols. In order to examine the dissipative effects of the laminated stack, both set-ups are excited harmonically by an electromagnetic shaker. Thereby, the excitation direction differs by 90° . When the set-ups are in steady-state, the excitation force and acceleration of each metal plate are measured by a force sensor and accelerometers. Then, the relative displacement $\Delta x = x_3 - x_2$ (dilatation test) and $\Delta z_i = z_1 - z_i$ with $i = 2, 3$ (shear test) can be calculated by integrating the acceleration signals twice with respect to the time and subtracting them from each other. Plotting the transmitted normal force $F_{T,x} = m_2 \cdot \ddot{x}_2$ (index “ T ” denotes “transmitted”) versus the relative displacement Δx (dilatation test) or $F_{T,z,i} = m_i \cdot \ddot{z}_i$ versus Δz_i with $i = 2, 3$ (shear test) leads to a hysteresis curve, cf. (Gaul and Schmidt, 2014) and Figure 2(b). Based on this hysteresis, the structural damping loss factors η_x (dilatation test) and $\eta_{z,i}$ (shear test) can be computed using the equations given in (2). Thereby, the dissipative damping energy $W_{D,x}$ or $W_{D,z,i}$ (from the dilatation or shear test) is divided by 2π times the corresponding maximum stored potential energy $U_{\max,x}$ or $U_{\max,z,i}$, cf. (Bograd et al., 2008) and (Gaul and Schmidt, 2014).

$$\eta_x = \frac{W_{D,x}}{2\pi \cdot U_{\max,x}} \quad , \quad \eta_{z,i} = \frac{W_{D,z,i}}{2\pi \cdot U_{\max,z,i}} \quad , \quad i = 2, 3 \quad (2)$$

The normal stiffness of the laminated stack for a certain pre-load F_N can be derived by the slope of the hysteresis, cf. (Gaul and Schmidt, 2014). The Young's modulus E can be computed using the normal stiffness k_x , initial thickness h_0 and cross section A of the test specimen. The shear modulus G is attained analogously using the shear stiffness $k_{z,i}$ (Gaul and Schmidt, 2014), see equations in (3). Further details can be found in (Clappier and Gaul, 2015) and (Clappier et al., 2015a).

$$E(F_N) = \frac{k_x(F_N) \cdot h_0}{A} \quad , \quad G_i(F_N) = \frac{k_{z,i}(F_N) \cdot h_0}{A} \quad , \quad i = 2, 3 \quad (3)$$

3 Finite Element Computation of electromagnetically caused Rotor Vibrations

3.1 Mechanical Finite Element Model of the Electrical Machine Rotor

The FE model of the rotor is created in ABAQUSTM, cf. (Clappier and Gaul, 2016). Figure 4(a) shows the FE model which consists of the laminated stack, rotor shaft, inner bearing rings and two balancing discs. The geometry is slightly simplified to reduce the number of finite elements. The mesh is created as a complete conform FE mesh using mainly linear brick elements with incompatible modes and a few linear wedge elements.

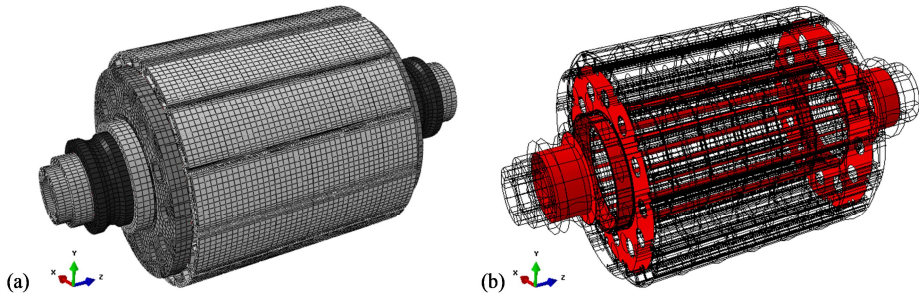


Figure 4. FE rotor model. (a) Mesh, (b) mechanical interfaces modelled by thin-layer elements (Clappier and Gaul, 2016)

Figure 4(b) depicts all mechanical interfaces. At these interfaces, so-called thin-layer elements are inserted to incorporate the joint stiffness and damping, cf. (Bograd et al., 2008) and (Gaul and Schmidt, 2014). Here, the TLEs are represented by linear brick elements with a small thickness to length ratio which can be as low as 1:1000, see (Bograd et al., 2008) and (Gaul and Schmidt, 2014). The dynamical behavior of each mechanical interface is described by one thin layer (TL) using a linearized orthotropic material model (cf. Section 3.2) (Bograd et al., 2008). All TLEs in one thin layer get the same stiffness and damping properties which can be identified experimentally on a generic lap joint (Gaul et al., 2011). In general, joint properties are load-dependent, cf. (Clappier et al., 2015b), (Gaul et al., 2016) and (Gaul et al., 2015). However, for applications with homogeneous contact pressure distributions at the interfaces, a homogenized parametrization of the TLEs can be efficiently applied (Bograd et al., 2008), (Clappier et al., 2015b). Otherwise, a load-dependent parametrization of the TLEs is necessary, see (Clappier et al., 2015b) and (Gaul et al., 2016). Figure 5 shows that the application requirement of a homogeneous contact pressure is fulfilled for the considered rotor. Due to the homogeneous contact pressure on the laminated stack in the set-up of Section 2.2 (Clappier and Gaul, 2015), the rotor application is well-suited for further investigations.

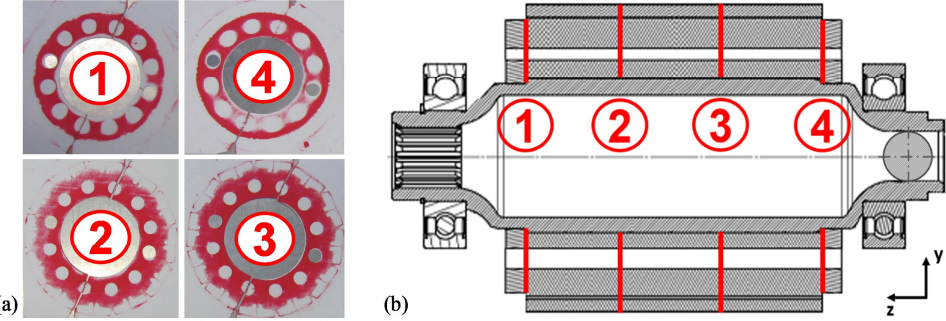


Figure 5. (a) Contact pressure measured via Fujifilm Prescale films at (b) different rotor positions (Clappier and Gaul, 2016)

3.2 Numerical Modal Analysis without Rotor Spin Speed

In order to prove the quality of the FE model, a numerical modal analysis (NMA) without boundary conditions and inner bearing rings is done. The equation of motion for free undamped vibrations

$$M \cdot \ddot{x} + K \cdot x = 0 \quad (4)$$

is transformed into the frequency domain by assuming time harmonic vibrations. This leads to the following eigenvalue problem (cf. Dassault Systèmes Simulia Corp. (2014))

$$(\alpha_k^2 \cdot M + K) \cdot \phi_k = 0. \quad (5)$$

M is the mass matrix, K the real-valued stiffness matrix, x the displacement vector and \ddot{x} the acceleration vector of the whole system. α_k and ϕ_k are the purely imaginary eigenvalue and real-valued eigenvector of mode k , respectively. Because the structural damping of mechanical joints, materials and laminated stacks can be considered to be frequency-independent in a wide frequency range ((Bograd et al., 2008), (Clappier and Gaul, 2015) and (Gaul et al., 2011)), the model of constant hysteretic damping can be efficiently applied to describe the damping of the system by a complex stiffness matrix K^* (cf. (Bograd et al., 2008), (Clappier et al., 2015a) and (Gaul and Schmidt, 2014))

$$K^* = K + j \cdot \left[\sum_{c=1}^{N_c} K_c \cdot \eta_c + \sum_{i=1}^{N_i} K_i \cdot \eta_i \right] \quad (6)$$

The first term of K^* represents the real-valued system stiffness matrix. The second and third terms are imaginary terms and represent the material and joint damping of all mechanical components (index c) and interfaces (index i). The last two terms are built-up by a summation over all products of the real-valued component or interface stiffness matrix (K_c , K_i) and its corresponding structural damping loss factor η_c or η_i . Values for η_c (excepted for the laminated rotor stack) and η_i are taken from (Gaul et al., 2011). Substituting K in equation (5) by K^* leads to a complex eigenvalue problem with complex eigenvalues and eigenvectors (Bograd et al., 2008). These are different from those of equation (5).

The joint stiffness of each interface is modeled by an orthotropic elasticity matrix D_i , cf. (Bograd et al., 2008) and (Gaul and Schmidt, 2014).

$$D_i = \begin{bmatrix} 0 & 0 & 0 & 0 & 0 & 0 \\ 0 & 0 & 0 & 0 & 0 & 0 \\ & D_{33} & 0 & 0 & 0 & 0 \\ & 0 & 0 & 0 & 0 & 0 \\ \text{sym.} & & D_{55} & 0 & & \\ & & & D_{66} & & \end{bmatrix} \quad (7)$$

The values of D_i are chosen according to Figure 6(a) such that the normal and tangential behavior of the joint is represented. The normal contact stiffness D_{33} is chosen to be 10...50% of the Young's modulus of the contacting materials, cf. (Netzmann, 2013). The shear moduli D_{55}, D_{66} are equal in their magnitudes and can be computed by equation (8) based on the contact area A and tangential stiffness k_T (both from the generic lap joint) and the TLE thickness h (Bograd et al., 2008). Thereby, the elasticity law for shear is used by assuming only small deformations $\gamma \ll 1$ (Figure 6(a), cf. (Bograd et al., 2008)). Data for k_T are taken from (Gaul et al., 2011).

$$D_{55} = D_{66} = \frac{k_T \cdot A}{h} \quad (8)$$

For physical reasons, all other diagonal terms of D_i should be zero. However, for numerical reasons values nearly zero are chosen (Bograd et al., 2008). Because of the interface geometries, it is necessary to use local Cartesian coordinates for one part of the TLEs and local cylindrical coordinates for the other part. In the case of using cylindrical coordinates, the diagonal terms of D_i have to be re-sorted.

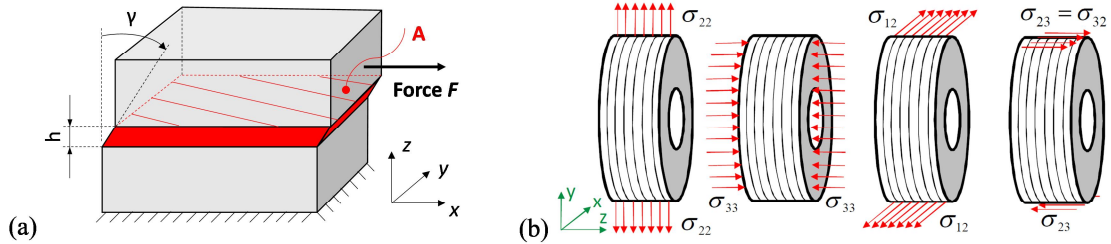


Figure 6. (a) Deformed thin-layer element (Bograd et al., 2008), (Clappier and Gaul, 2016), (b) illustration of laminated rotor stack properties (Clappier et al., 2015a)

The loss factor η_c , Young's modulus E_t in axial direction and shear modulus G_t of the laminated rotor stack can be obtained from measurement results of a dilatation and shear test which are carried out at a pre-stress condition corresponding to the rotor pre-stress condition. In order to define the component stiffness matrix K_c of the laminated stack, a transversely isotropic material model is used (Clappier et al., 2015a). The inverse of the elasticity matrix D_c is shown in equation (9), cf. (Clappier et al., 2015a) and (Dassault Systèmes Simulia Corp., 2014).

$$\varepsilon_c = D_c^{-1} \cdot \sigma_c$$

$$\begin{bmatrix} \varepsilon_{11} \\ \varepsilon_{22} \\ \varepsilon_{33} \\ 2 \cdot \varepsilon_{12} \\ 2 \cdot \varepsilon_{13} \\ 2 \cdot \varepsilon_{23} \end{bmatrix} = \begin{bmatrix} 1/E_p & -v_p/E_p & -v_{tp}/E_t & 0 & 0 & 0 \\ -v_p/E_p & 1/E_p & -v_{tp}/E_t & 0 & 0 & 0 \\ -v_{pt}/E_p & -v_{pt}/E_p & 1/E_t & 0 & 0 & 0 \\ 0 & 0 & 0 & 1/G_p & 0 & 0 \\ 0 & 0 & 0 & 0 & 1/G_t & 0 \\ 0 & 0 & 0 & 0 & 0 & 1/G_t \end{bmatrix} \begin{bmatrix} \sigma_{11} \\ \sigma_{22} \\ \sigma_{33} \\ \sigma_{12} \\ \sigma_{13} \\ \sigma_{23} \end{bmatrix} \quad (9)$$

ε_c , σ_c , E and G are the strain vector, stress vector, Young's modulus and shear modulus (Dassault Systèmes Simulia Corp., 2014), respectively. The indices t and p denote 'transverse' and 'in-plane' (Dassault Systèmes Simulia Corp., 2014). While E_t and G_t can be identified experimentally, all other quantities are given by the properties of a single electrical sheet, see (Clappier et al., 2015a). This becomes clearer by the illustrations in Figure 6(b). Further details are given in (Clappier et al., 2015a).

3.3 Rotor Dynamics Simulation

In this section, rotordynamic computations are done dependent on rotor spin speed. Thereby, further matrices in the equation of motion must be taken into account. Because of the asymmetric rotor geometry, rotordynamic analyses are carried out meaningfully in rotational coordinates fixed to the rotor, see (Friswell et al., 2012), (Genta, 2005) and (Vollan and Komzsik, 2012). Thus, the rotor stiffness matrix stays constant in time for a fixed rotor speed, cf. (Friswell et al., 2012). According to (Genta, 2005) and (Vollan and Komzsik, 2012), the equation of motion in the rotating coordinate system is given by

$$M \cdot \ddot{g} + (D + 2\Omega \cdot C) \cdot \dot{g} + (K - \Omega^2 \cdot Z + \Omega^2 \cdot K_G + \Omega \cdot K_D) \cdot g = F(t) \quad (10)$$

Thereby, M represents the general mass matrix, D the viscous damping matrix, C the gyroscopic matrix containing Coriolis effects, K the general stiffness matrix, Z the centrifugal matrix, K_G the geometric stiffness matrix, K_D the circulatory matrix, g the displacement vector, \ddot{g} the acceleration vector and $F(t)$ the excitation force vector in rotating coordinates. In this work, the viscous damping matrix D (containing internal and external damping described by a viscous model) is not applied. Therefore, the matrix K_D also drops out. Internal damping is included by the complex stiffness matrix (see equation (6)). External damping is not considered because of the generally small damping of ball bearings (Gasch et al., 2006). For ball bearings, a (transversely) isotropic elastic bearing model is assumed for simplicity. In general, the bearing stiffness is different in vertical and horizontal direction, see (Gasch et al., 2006) and (Krämer, 1993). The radial bearing stiffness k_B is computed by equation (11) (Krämer, 1993) as a function of rotor spin speed dependent on the occurring unbalance forces (which act in the planes of both balancing discs), gravity force and speed-dependent external application forces. Thereby, z , d and F are the number of ball elements, ball diameter and bearing force. The bearing stiffness is included by connector elements in ABAQUS (Dassault Systèmes Simulia Corp., 2014) representing a “spring” stiffness which is incorporated into K during FE matrix assembling process. The bearing A is modeled to be axially rigid (using either a displacement boundary condition or a very high connector stiffness) and the bearing B without axial connector stiffness.

$$k_B = 1.3 \cdot z^{2/3} \cdot d^{1/3} \cdot F^{1/3} \quad [N/\mu m] \quad (11)$$

3.4 Computation of Electromagnetic Forces

For the computation of electromagnetic airgap forces and torque at a certain operational point of the electrical machine, a 2D magnetic FE model is built up (cf. also (Arkkio et al., 2010), (Funieru and Binder, 2014) or (Pellerey et al., 2012)) using the software FEMAG (Reichert, 2011). Thereby, it is assumed that both, stator and rotor are of equal axial length and perfectly aligned to each other (in axial direction). In addition, it is assumed that no noteworthy axial forces occur in the airgap. Figure 7(a) depicts the created and used FE model which is a full model over 360° in order to examine the effects of dynamical rotor eccentricities. The considered PMSM has six pole pairs, 36 stator teeth and three phases.

In order to compute the magnetic force densities, a fine FE mesh is required in the airgap (cf. (Humbert et al., 2012) and (Reichert, 2011)) to attain sufficient computation accuracy. It is also recommended to use rectangular finite elements of equal size along the circumference for better accuracy, see (Cai et al., 2001), (Funieru and Binder, 2014) and (Reichert, 2011). In this work, first-order rectangular elements are used (Reichert, 2011) to mesh the airgap. Thereby, a mesh of equidistant increments of 0.25° is created along the circumference. For meshing rotor and stator first-order triangular elements are used. Rotor movement is modelled by the moving band technique, see (Funieru and Binder, 2014). Hereby, the airgap is remeshed for each rotor position after a rotational step (Funieru and Binder, 2014). For the computation of electromagnetic force densities in the airgap, different methods are discussed in literature, like Maxwell stress tensor, virtual work / co-energy method, Coulomb virtual work or Arkkio method, cf. (Cai et al., 2001), (Funieru and Binder, 2014), (Gieras and Wing, 2002), (Popescu, 2006) and (Wang et al., 2008). In this work, radial and tangential force densities are calculated using FEMAG based on Maxwell stress tensor (Reichert, 2011). This method is the most popular one and commonly used for excitation force computations in vibro-acoustic analyses of electrical machines, see (Funieru and Binder, 2014), (Gieras and Wing, 2002) and (Popescu, 2006).

During FE computation, the magnetic vector potential \vec{A} is solved for all FE nodes as primary field variable, see (Gieras and Wing, 2002) and (Wang et al., 2008). Thereby, only the normal/radial flux density is satisfying continuity at the interface of different media/materials (e.g. interface air/iron) (Cai et al., 2001). Because of discontinuous tangential flux densities at the interface (see (Gieras and Wing, 2002) and (Popescu, 2006)), the global torque and local force densities are evaluated in this work on a circular path in the middle of the airgap, see Figure 7(b). This procedure is also recommended by other authors (Cai et al., 2001), (Funieru and Binder, 2014), FEMAG (Reichert, 2011) and (Wang et al., 2008). Furthermore, three FE layers of squared first-order rectangular FEs are used to mesh the airgap, cf. Figure 7(b) and (Cai et al., 2001), (Funieru and Binder, 2014), (Reichert, 2011), (Wang et al., 2008). The layer in the middle is used to apply the moving band technique (Funieru and Binder, 2014).

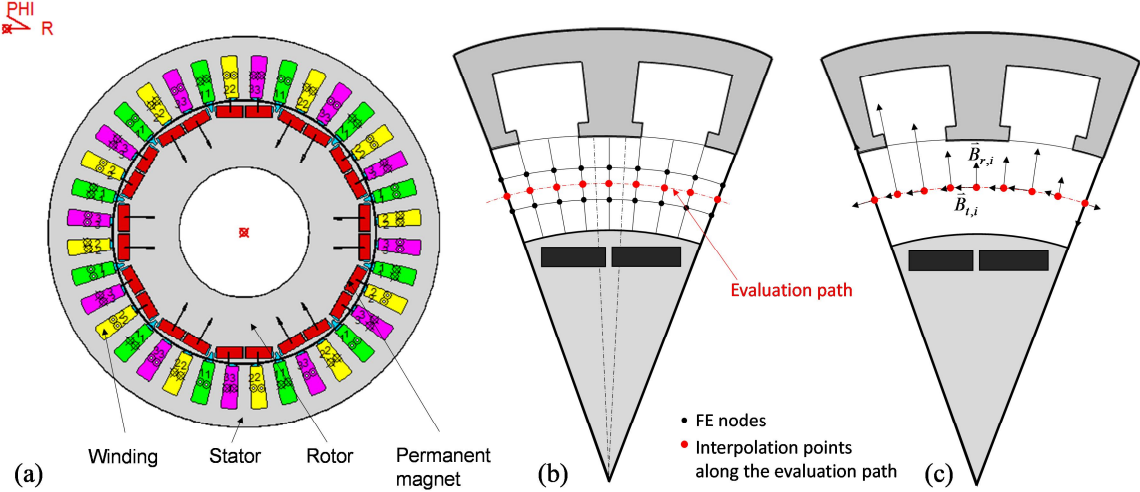


Figure 7. (a) 2D electromagnetic model (FE mesh not depicted because of the fine resolution), (b) evaluation path, (c) flux densities along evaluation path

Based on the magnetic vector potential \vec{A} in the airgap (which only has one z-component in 2D, cf. Geras and Wing (2002)), the magnetic flux density \vec{B} is evaluated by

$$\vec{B} = \text{rot}(\vec{A}) \quad (12)$$

(Geras and Wing, 2002) for all finite elements along the circular evaluation path. Due to the used linear elements, the 2D magnetic flux density vector has constant components within an element, see (Geras and Wing, 2002) and (Popescu, 2006). From these values, the radial and tangential flux densities are interpolated at the interpolation points (feedback FEMAG support) on the evaluation path (cf. PLT1-file), Figure 7(c). Based on radial and tangential flux densities (B_r, B_t) at the interpolation nodes and magnetic permeability of air μ_0 , the radial and tangential force densities (p_r, p_t) can be computed by the equations in (13) using Maxwell Stress Tensor, see (Cai et al., 2001), (Geras and Wing, 2002) and (Humbert et al., 2012).

$$p_r = \frac{1}{2\mu_0} \cdot (B_r^2 - B_t^2) \quad , \quad p_t = \frac{1}{\mu_0} \cdot B_r \cdot B_t \quad (13)$$

Physically, the computed force densities in the airgap middle represent stresses which cause attraction or repulsion forces between rotor and stator. In mechanics, stresses are internal quantities that describe the internal loading of a material and are therefore not visible without any body cuts. To deal with that issue and make the “internal” airgap forces “visible”, a “magnetic-mechanical coupling element” is introduced, see Figure 8(a,b).

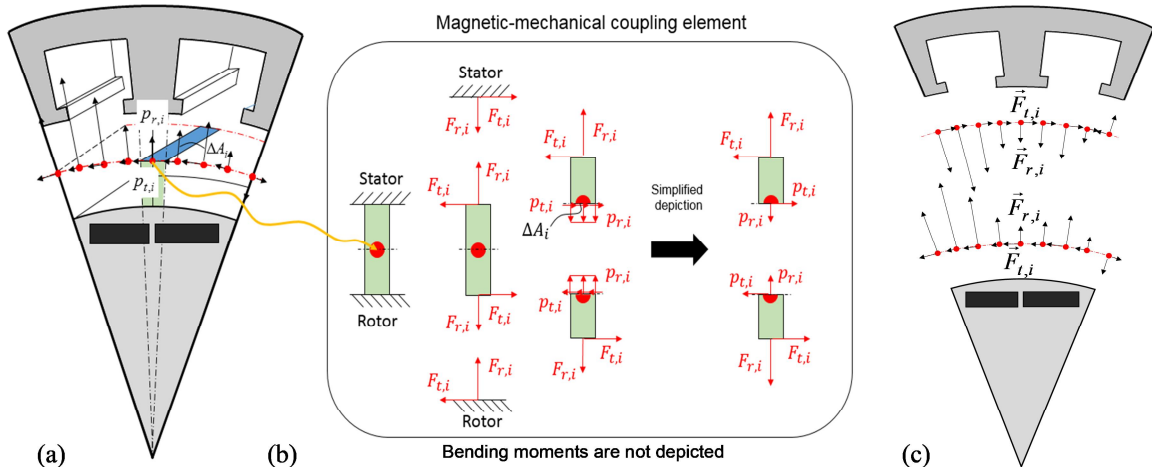


Figure 8. (a) Force density distribution, (b) magnetic-mechanical coupling element and (c) stator and rotor orientated “internal” airgap forces

This coupling element represents a mechanical stress element between the rotor and stator surfaces and includes the computed electromagnetic force density as internal load, see Figure 8(b). Thus, this model enables to interpret physically actio-reactio forces in the airgap (between rotor and stator) by means of internal forces which can be computed along the evaluation path (Figure 8(c)) through multiplication of force densities with the corresponding action area, Figure 8(a,c). The sum of rotor and stator oriented internal airgap forces Figure 8(c) have to be zero.

In order to carry out vibro-acoustic computations, the “internal” rotor and stator forces have to be transformed from the airgap middle onto the rotor and stator surfaces where they physically act. Thus, the internal forces become active forces on the mechanical structure. The applied transformation process is presented exemplarily for “internal” forces acting at one interpolation point i on the evaluation path, see Figure 9(a). Firstly, rotor oriented radial forces are moved along their action line onto the rotor surface. Secondly, the tangential forces are moved parallel to their force action line onto the rotor surface. In order to yield the same force conditions after parallel translation of tangential forces, an additional moment has to be added, see Figure 9(b). The superscript “LS” denotes the location in the airgap middle while “Sz” and “Ra” characterize forces on stator teeth and rotor surface.

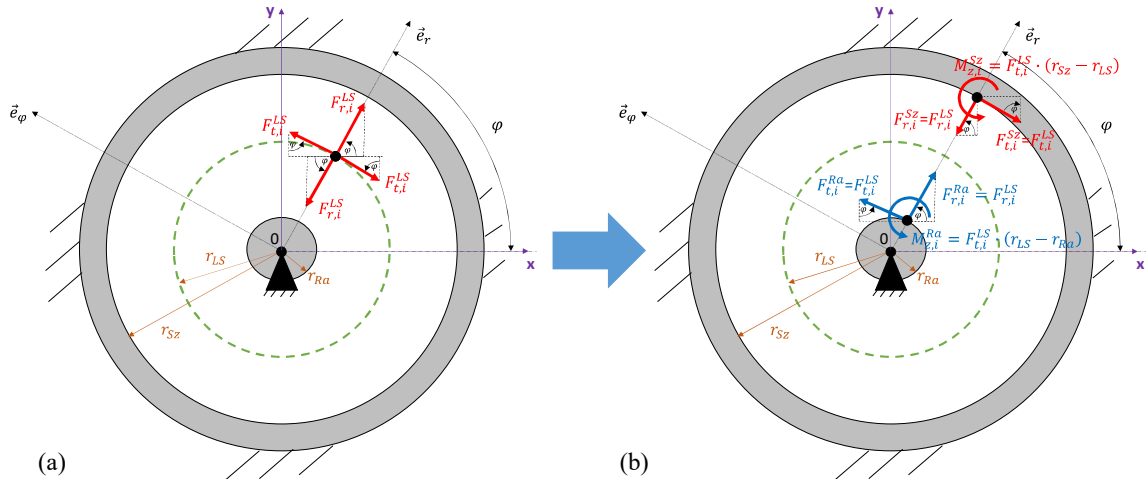


Figure 9. Transformation of internal “airgap forces” (a) into rotor and stator surface forces (b)

This procedure is done on both sides, for the rotor and stator. However, the focus of this paper is given to rotor dynamics and the corresponding excitation forces. Therefore, the process describing the transformation of surface forces into nodal forces for the structural FE model is only explained for the rotor side. At any rate, the same procedure can also be applied on stator side. However, the force transformation step into the rotating coordinate system is not required to examine stator or housing vibrations.

For reasons of computational accuracy and efficiency, the electromagnetic FE mesh is usually designed much finer (due to the considered small airgap) as the vibro-acoustic FE model, cf. (Humbert et al., 2012). To carry out rotor dynamic computations, the transformed rotor surface forces (Figure 10(a)) have to be summarized in a suited way at the nodes of the mechanical rotor FE model. Firstly, all moments $M_{z,i}^{Ra}$ in Figure 10(a) are replaced by equivalent tangential force pairs which are summarized with the already given tangential loads in Figure 10(a). Secondly, all radial and modified tangential rotor surface forces are transformed into the rotating coordinate system (Figure 10(b)) which is used for rotor dynamics computation. Lastly, all rotor surface forces within equidistant angular distances are summarized as resultant components at the surface FE nodes of the rotor model taking equivalent force pairs into account (Figure 10(c)).

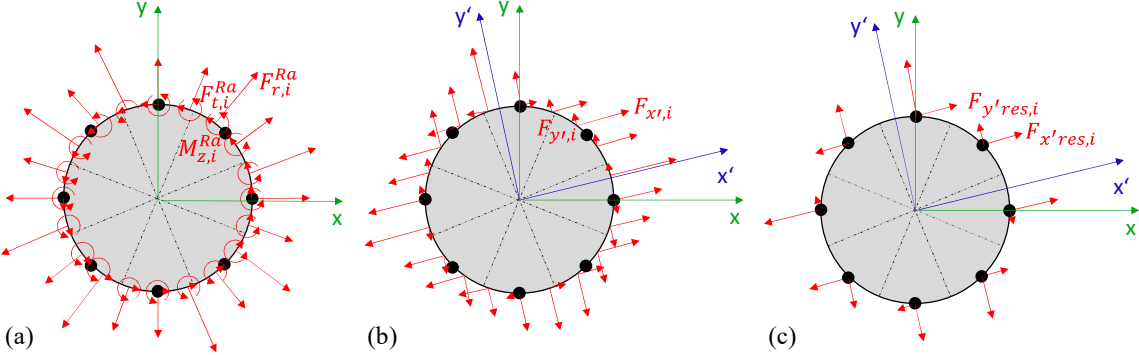


Figure 10. Rotor surface loads in (a) stationary coordinates (x,y), (b) in rotating coordinates (x',y') and (c) summarized rotor forces acting on FE nodes of the structural model

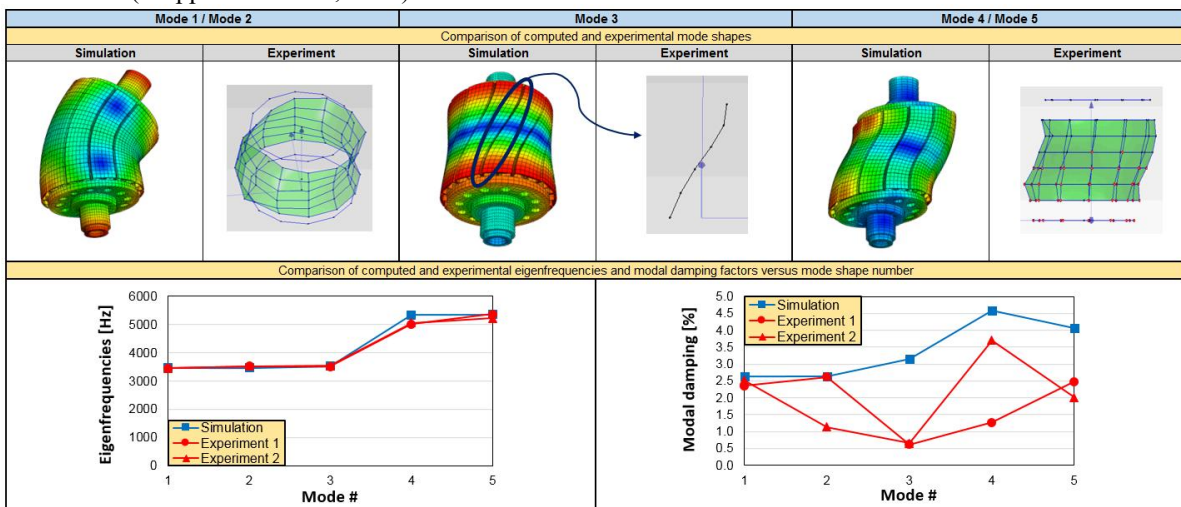
The FE mesh of the rotor is extruded in the region of the laminated stack. Thus, the transformed resultant nodal forces (see Figure 10(c)) can be equally distributed along FE nodes in axial direction for mapping on a 3D structural FE mesh. In other words, the resultant force at one angular position (Figure 10(c)) is divided by the number of corresponding axial nodes at this position. Thus, all nodal forces are equal in magnitude and direction at one angular position (cf. (Pellerey et al., 2012) and (Shiohata et al., 2011)). The advantage of the proposed force transformation algorithm is the conservation of resulting torque as well as radial and tangential forces (originally obtained in the middle of the air gap), even after the transformation what is in contrast to available projection methods, like given in (Dupont et al., 2014).

4 Computational Results

4.1 Numerical Modal Analysis without considering Rotor Spin Speed

Table 1 shows the results of a NMA and EMA for two equivalent built-up rotors. A good agreement for the first five eigenfrequencies and mode shapes can be obtained. The experimental grid is fine enough to resolve all considered modes reliably. The modal damping of the first two modes is also predicted quite well but the prediction error increases at higher frequencies. However, the ‘general’ trend (except mode 3) is predicted correctly.

Table 1. Comparison of numerical and experimental rotor eigenfrequencies, mode shapes and damping
(Clappier and Gaul, 2016)



4.2 Rotordynamic Vibration Response due to Electromagnetic Force Excitation

In general, magnetic forces consist of many time and spatial harmonics (Gieras et al., 2006). Figure 11 shows for example the vibration response (in rotating coordinates) due to electromagnetic force excitation (on the laminated stack) for the 36th time harmonic order ($k=36$) without and with dynamical rotor eccentricity ϵ_d . The

magnetic forces of the 36th time harmonic order are obtained by a one-dimensional fast Fourier transformation (FFT) of the nodal rotor surface forces. Without rotor eccentricity, the radial forces acting on the rotor cancel itself and only a torsional excitation occurs (Figure 11(a)). With eccentricity, a resultant radial force, the so-called unbalanced magnetic pull (UMP) (Friswell et al., 2012), occurs in addition to the torsional excitation leading to a superimposed radial rotor deflection. Thus, the rotordynamic response has to be determined within acoustical computations of electrical machines because the vibrations are transmitted to connected systems and the motor housing where undesirable sound can be caused.

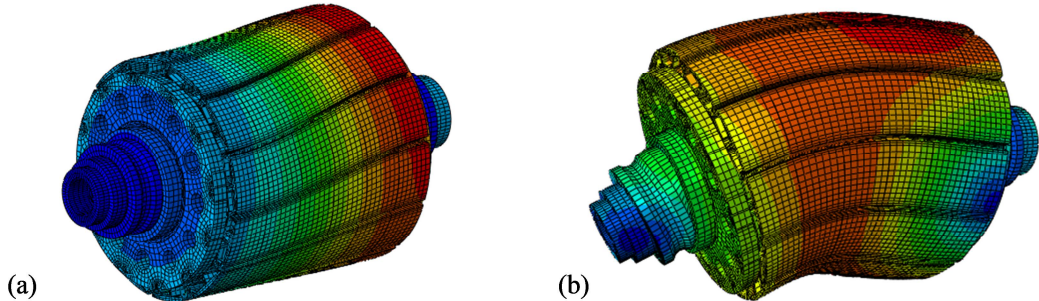


Figure 11. Rotor vibration response due to electromagnetic forces for time harmonic order $k = 36$ in rotating coordinates for dynamical rotor eccentricity (a) $\varepsilon_d = 0$ mm and (b) $\varepsilon_d = 0.25$ mm (Clappier and Gaul, 2016)

5 Conclusions and Outlook

Stator housing and rotordynamic vibrations must be taken both into account if acoustical computations of electrical machines are carried out. Especially rotor vibrations can be transmitted to connected systems of the powertrain and affect its overall acoustical behavior. Therefore, a finite element model of the rotor is presented in order to predict rotordynamic responses. The material properties of the laminated rotor stack are determined experimentally and incorporated by a transversely isotropic material model. Mechanical joints are modeled by thin-layer elements and damping by the model of constant hysteretic damping. A numerical modal analysis leads to a good agreement with the experiment. Furthermore, rotordynamic responses due to electromagnetic force excitation with and without dynamical rotor eccentricity are examined. Thereby, a new method is presented to transform the magnetic forces from a 2D electromagnetic onto a 3D mechanical finite element mesh.

References

Arkkio, A.; Nepal, B.R.; Sinervo, A.: Electromechanical interaction in a synchronous reluctance machine. In: *Proc. of SPEEDAM 2010*, IEEE, Pisa, Italy, June 14-16, (2010), 501-506.

Bograd, S.; Schmidt, A.; Gaul, L.: Joint Damping Prediction by Thin Layer Elements. In: *Proc. of IMAC XXVI: A Conference and Exposition on Structural Dynamics*, Orlando, USA, February 4-7, (2008).

Cai, W.; Pillay, P.; Reichert, K.: Accurate computation of electromagnetic forces in switched reluctance motors. In: *Proc. of 5-th ICEMS 2001*, IEEE, Shenyang, China, August 18-20, (2001), 1065-1071.

Clappier, M.; Gaul, L.: Experimental Investigation of Structural Damping of Laminated Stacks of Electrical Machine Rotors. In: P. Pennacchi, ed., *Mechanisms and Machine Science*, Vol. 21, *Proceedings of the 9th IFTOMM International Conference on Rotor Dynamics*, Springer, (2015), 613-624.

Clappier, M.; Gaul, L.; Westkämper, E.: Experimental Determination of Material Properties in Stacking Direction of Laminated Stacks belonging to Electrical Machine Rotors using a Dilatation Test. In: *Proc. of the 22nd International Congress on Sound and Vibration*, Florence, Italy, July 12-16, (2015a).

Clappier, M.; Ehrlich C; Gaul, L.: Linearized Joint Damping Model for Assembled Structures with Inhomogeneous Contact Pressure using Thin-Layer Elements. In: *Proc. of the 22nd International Congress on Sound and Vibration*, Florence, Italy, July 12-16, (2015b).

Clappier, M.; Gaul, L.: Frequency Domain Dynamic Simulation of an Electrical Machine Rotor. In: *Proc. of the 23rd International Congress on Sound and Vibration*, Athens, Greece, July 10-14, (2016).

Crandall, S.H.; Kurzweil, L.G.; Nigam, A.K.: On the Measurement of Poisson's Ratio for Modeling Clay. *Journal of Experimental Mechanics*, 11(9), (1971), 402-407.

Dassault Systèmes Simulia Corp.: *Abaqus Documentation, Abaqus Analysis User's Guide and Abaqus Theory Guide*. Release 6.14, Providence, RI, USA, (2014).

Desai, C. S.; Zaman, M. M.; Lightner, J. G.; Siriwardane, H. J.: Thin-layer element for interfaces and joints, *International Journal for Numerical and Analytical Methods in Geomechanics*, 8, (1984), 19-43.

Dupont, J. B.; Aydoun, R.; Bouvet, P.: Simulation of the noise radiated by an automotive electric motor: influence of the motor defects. *SAE Int. J. Alt. Power*, 3(2), (2014), 310-320.

Friswell, M.; Penny, J.E.T.; Garvey, S.D.; Lees A.W.: *Dynamics of Rotating Machines*. Cambridge University Press, New York, (2010, reprinted 2012).

Funieru, B.; Binder, A.: 3D numerical calculation method of electrical machines with time efficient air gap coupling and stabilized torque and force calculation. In: *Proc. ICEM2014*, Berlin, Sept. 3-5, (2014), 954-960.

Gasch, R.; Nordmann, R.; Pfützner, H.: *Rotordynamik*. 2. Auflage, Springer, Berlin, (2006).

Gaul, L.; Lenz, J.: Nonlinear dynamics of structures assembled with bolted joints. *Acta Mechanica*, 125, (1997), 169-181.

Gaul, L.; Clappier, M.; Einbock, S.: Frequency Domain Structural Dynamic Simulation of an Electrical Machine Housing. In: *Proc. of the 23rd Int. Congress on Sound and Vibration*, Athens, July 10-14, (2016).

Gaul, L.; Schmidt, A.; Bograd, S.: *Modellierung von Werkstoff- und Fügestellendämpfung in der FEM*. FVV-Vorhaben 984, Heft 940, (2011).

Gaul, L.; Hanss, M.; Schmidt, A.; Ehrlich, C.: *Modellierung von Werkstoff- und Fügestellendämpfung in der FEM unter Berücksichtigung von Unsicherheiten*. FVV-Vorhaben 1119, Heft R572, (2015).

Gaul, L.; Schmidt, A.: Experimental Identification and Simulation of Rotor Damping. In: *Proc. of IMAC XXXII: A Conference & Exposition on Structural Dynamics*, Orlando, USA, February 3-6, (2014).

Genta, G.: *Dynamics of Rotating Systems*. Springer, New York, (2005).

Gieras, J.F.; Wang, C.; Lai, J.C.: *Noise of Polyphase Electric Motors*. CRC Press, Boca Raton, (2006).

Gieras, J.F.; Wing, M.: *Permanent Magnet Motor Technology*. Dekker, New York, (2002).

Humbert, L.; Pellerey, P.; Cristaudo, S.: Electromagnetic and structural coupled simulation to investigate NVH behavior of an electrical automotive powertrain. *SAE Int. J. Alt. Power*, 1(2), (2012), 395-404.

Krämer, E.: *Dynamics of Rotors and Foundations*. Springer, Berlin, (1993).

McCloskey, A.; Arrasate, X.; Almandoz, G.; Hernandez, X.; Salgado, O.: Vibro-acoustic finite element analysis of a permanent magnet synchronous machine. In: *Proc. of 9th EURODYN*. Porto, Portugal, (2014), 3321-3328.

Netzmann, H.D.: *NVH-Akustik-Berechnung am Motorrad-Motor unter Berücksichtigung unsicherer Modelparameter*. PhD thesis, University of Stuttgart, Der Andere Verlag, Uelversbüll, (2013).

Pellerey, P.; Lanfranchi, V.; Friedrich, G.: Numerical simulations of rotor dynamic eccentricity effects on synchronous machine vibrations for full run up. In: *Proc. of ICEM2012*, Marseille, September 2-5, (2012), 3008-3014.

Popescu, M.: Prediction of the electromagnetic torque in synchronous machines through Maxwell stress harmonic filter (HFT) method. *Journal Electrical Engineering*, 89(2), (2006), 117-125.

Reichert, K.: *FEMAG Benutzer-Anleitung*. ETH Zürich, Zürich, (2011).

Shiohata, K.; Kusama, R.; Ohtsu, S.; Iwatsubo, T.: The study on electromagnetic force induced vibration and noise from a normal and an eccentric universal motors. In: *Proc. of PIERS*, Marrakesh, Morocco, March 20-23, (2011), 1654-1660.

Siegl, G.: Das Biegeschwingungsverhalten von Rotoren, die mit Blechpaketen besetzt sind. PhD thesis, TU Berlin, Berlin, (1981).

Vollan, A.; Komzsik, L.: *Computational Techniques of Rotor Dynamics with the Finite Element Method*. CRC Press, Boca Raton, (2012).

Wang, L.; Cheung, R.W.; Ma, Z.; Ruan, J.; Peng, Y.: Finite-element analysis of unbalanced magnetic pull in a large hydro-generator under practical operations. *IEEE Trans. on Mag.*, 44(6), (2008), 1558-1561.

Graduate School of Excellence advanced Manufacturing Engineering in Stuttgart (GSaME), University of Stuttgart, 70569, Stuttgart, Germany
marcel.clappier@gsame.uni-stuttgart.de

Institute for Nonlinear Mechanics (INM), Research Group Prof. Gaul, University of Stuttgart, 70569, Stuttgart, Germany
lothar.gaul@inm.uni-stuttgart.de

Selected operational Problems of high-speed Rotors supported by Gas Foil Bearings

G. Żywica, P. Bagiński, J. Kiciński

In this paper, several issues related to the operation of gas foil bearings were discussed. The description of the foil bearings' operation was performed, with a special focus on the following issues: the friction processes taking place between the bearing elements together with the friction-generated heat, the appropriate selection of structural and coating materials, ensuring the bearing preload, and the vibration amplitudes in run-up and rundown of the rotor. The operational problems discussed are supplemented with practical examples. A very thorough understanding of the issues at stake makes it possible to specify more precisely the potential areas of application for foil bearings and take into account their operational properties in the contemplated implementations.

1 Introduction

With the development of high-speed fluid-flow machinery, there is a growing need for innovative bearing systems. Foil bearings are ideally suited for such applications as they allow stable and high-speed operation of the rotors at elevated temperatures (Agrawal, 1997; Bonello and Pham, 2014a). They do not require an external lubrication system to be applied for their proper functioning, even under such conditions. Excellent dynamic properties of foil bearings are achieved by using additional elastic-damping elements (usually made of thin metal foils in which a properly modified surface layer is of particular significance). Such bearings have many advantages that make them the preferred option for fluid-flow machines such as gas and vapour microturbines, compressors or expanders (Agrawal, 1997; Bruckner, 2010; DellaCorte, 1997). In their typical applications foil bearings are used to damp vibration, even at high rotational speeds, which is far more difficult to accomplish using gas bearings with high radial rigidity. This results from the fact that the vibration-damping element in such bearings is a specially shaped set of foils which, during operation, interact with each other and with the internal surface of the bush (Bonello, 2014b; Larsen and Santos, 2013; Żywica et al. 2016c). Therefore, a very important issue is the selection of the appropriate shape and thickness of the top and bump foils (Hoffmann et al., 2014; Kim et al., 2009; Larsen et al., 2014). Classical gas bearings operating at high rotational speeds support their loads solely on a thin layer of gas, the vibration-damping properties of which are rather poor. This disadvantage of classical gas bearings is not present in foil gas bearings.

Obviously, foil bearings also have some disadvantages which render them unsuitable for some types of rotating machinery. As foil bearings are still a long way from widespread use, their availability is limited. They are usually manufactured on request and have to be adapted to the actual conditions of use. As the experience gained by the authors of this article has shown, such bearings are also the origin of operational problems that have been reported in the scientific literature only rarely until today. Chief among these problems are wear of the mating surfaces, high starting torque and significant journal displacements occurring during speed and load changes. Many engineers and scientists all over the world constantly work to eliminate as many of these problems as possible, and the subsequent generations of foil bearings are characterized by better and better load capacities (Agrawal, 1997; Heshmat et al., 2005). In general, significant attention is placed on optimization of bearing design and tribological issues, including the selection of suitable constructional and functional materials. Sliding layers in foil bearings may be made of different metals including metal-ceramic composites and plastics (DellaCorte, 1997; Żywica et al., 2016b). Based on the literature review and the authors' experience, it can be concluded that in the case of bearings operating at low temperatures the best results are achieved by using soft sliding coatings for top foils which come into contact with a hard and wear-resistant journal (Kiciński and Żywica, 2014; Żywica et al., 2016b). When bearings are exposed to high temperatures (above 200°C) metal-ceramic composites are often used (DellaCorte, 1997; Jahanmir et al., 2009).

A foil bearing is a mechanical system, the modelling of which is extremely difficult. A model of such a bearing has to take into account several physical phenomena such as non-linear deformations of thin foils having a complex geometry, friction and wear processes on the contact surfaces, heat exchange, thermal deformations, flow-related phenomena taking place within the lubricating gap and fluid-structure interactions (Kozanecki et al. 2011; Źywica et al., 2016c). Therefore, in this case, computational models have limited reliability and are usually used only at the initial design stage. In practice, this means that each manufactured foil bearing goes through a series of tests before application in a target machine. This is done on specially designed test rigs, allowing simulating real operating conditions (DellaCorte, 1997; Tkacz et al., 2015). An effective implementation of foil bearings requires a lot of experience and long-lasting pre-implementation tests during which the bearings operate under extreme conditions, i.e. they are subjected to maximum loads at various rotational speeds. All the problems discussed herein were encountered by the authors of this article in the process of developing and testing new foil bearings. It is worth familiarising yourself with the issues covered here because the knowledge about them should facilitate the elaboration of new bearing systems and their implementation.

2 Temperature Distribution and Wear in Foil Bearings

The experimental research was carried out for the foil bearing consisting of a single top foil and three bump foils. The photo showing all parts of the disassembled bearing is presented in Figure 1. The journal diameter is 34 mm and the bush width 40 mm. The foils were manufactured using sheet metals with 0.1 mm thickness and are made of a nickel-chromium alloy (Inconel). The top foil is coated on one side with the coating made of a synthetic polymer (PTFE) that has supreme sliding properties. The molybdenum-coated bearing journal (made of steel) is plasma sprayed. The foil was profiled by cold forming and the journal surface was subjected to grinding in order to achieve the surface roughness average of 0.63 Ra. The bearing bush (made of bronze) has been prepared in such a way that it can be mounted on a bearing support and the temperature can be measured in 12 locations inside the bearing. Thermocouples were inserted into the bearing through gaps and holes in the bush; all of them operated at a sampling rate of 128 Hz.

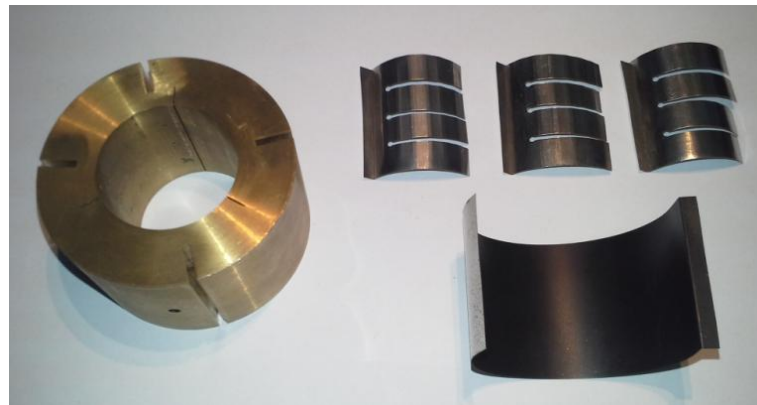


Figure 1. Parts of the foil bearing prepared for assembling

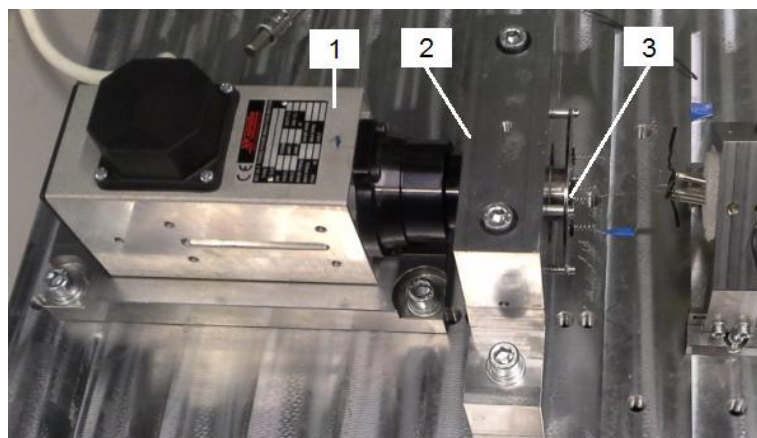


Figure 2. Foil bearing test rig (1 – electro-spindle, 2 – bearing support, 3 – journal)

The experimental studies were carried out on the test rig at the IMP PAN in Gdańsk. The test rig is adapted to testing multi-supported rotors, but only one bearing support was used for this research. The journal of the tested bearing was mounted directly on the electro-spindle shaft. A picture of the test rig is shown in Figure 2. The maximum rotational speed of the electro-spindle is 24,000 rpm. All parts of the test rig were fixed to a solid steel plate, which was equipped with anti-vibration rubber pads. The planned experimental research consisted in increasing the journal's speed up to 15,000 rpm within 55 seconds and then maintaining the same speed until the thermal equilibrium of the bearing node is reached. The operating temperature of a foil bearing is a very good diagnostic symptom since in the case of improper bearing operation its value rapidly increases (Żywica et al., 2016b).

The temperature values measured in the central part of the bearing during its start-up are presented in Figure 3, taking into consideration the circumferential positions of the measurement points. The highest temperature occurred at the lower part of the bearing (200°) and was 59°C . The lowest temperature increase was observed at the upper part of the bearing (20°), where the temperature was 25°C . The temperature values measured by the thermocouples positioned at 90° and at 290° were 52°C and 31°C , respectively. The temperature increases at different parts of the top foil are between 5°C and 39°C , during time duration as small as 55 seconds.

The highest temperature rise in the lower part of the bearing resulted from the movement of the journal in the direction of the lower part of the bearing support, as in the case of a bearing subjected to heavy loads. The differences between the temperatures measured at three different locations situated on the same angular position of the bush were small and did not exceed 2°C . For this reason, only the measurement results relating to the centrally located thermocouple are presented.

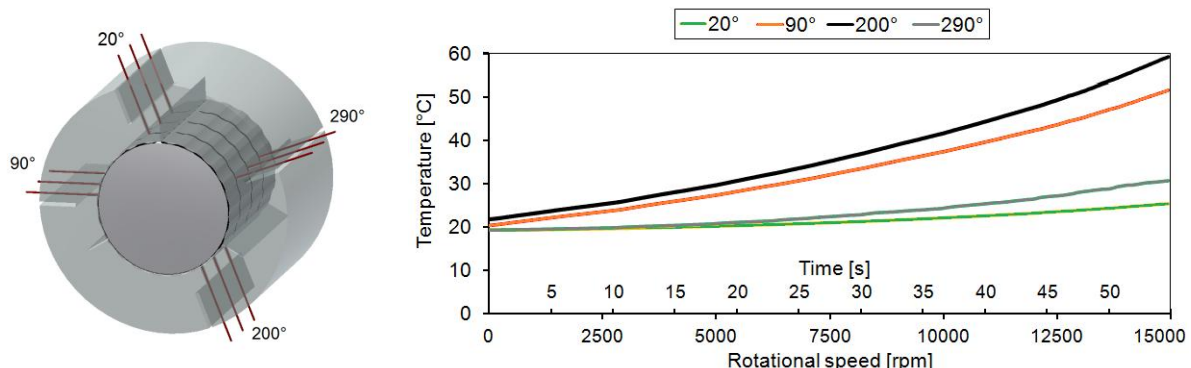


Figure 3. Thermocouples' location (left) and measured temperature of the central part of the foil bearing during acceleration of the rotor (right)

Operating the rotor at 15,000 rpm resulted in further rises in temperature, especially in the lower part of the bearing. During operation of the foil bearing, the temperature differences between various measuring points distributed circumferentially in the bush continued to increase. Despite the expected stabilization of the bearing temperature, its temperature was still rising and – after ca. 300 seconds of operation – reached very high values. The top foil had the temperature of 130°C and 60°C at its lower and upper part, respectively.

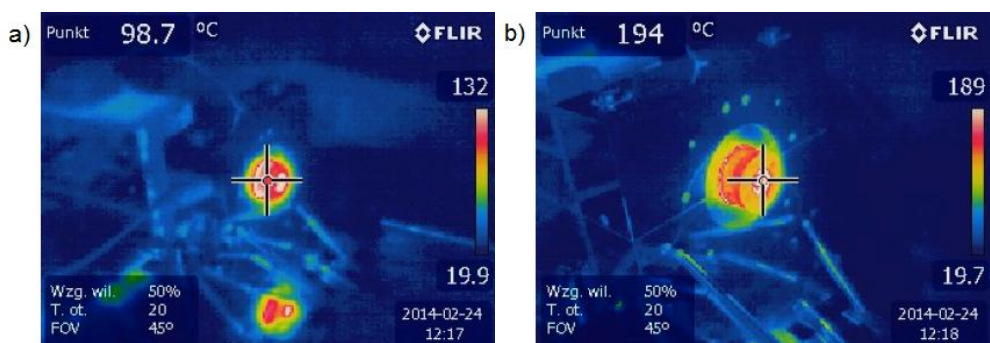


Figure 4. Foil bearing temperature measured using a thermal imaging camera: a – temperature on the external part of the journal, b – temperature in the journal opening

The temperatures of other parts of the bearing were measured using an infrared camera. The results of these measurements are presented in Figure 4. The shaft temperature measured on its cylindrical surface (near the bearing) was around 100 °C. However, the highest temperature value (about 200 °C) was observed in the shaft's hole. Given that there was a serious risk of rapid damage to the bearing, the electro-spindle was stopped. The thermal resistance of the coating covering the top foil was defined by the manufacturer at approx. 200 °C. Its damage may have led to a direct contact between the two raw surfaces not adjusted to such operation. That situation could be dangerous for the bearing and test rig, including electro-spindle.

The bearing was then disassembled in order to evaluate the technical condition of its components. A quick visual inspection of the top foil revealed that it sustained permanent damage at several locations (Figure 5). In those locations in which the top foil was supported by the bump foil, the slide coating was ground down, which caused the friction between the journal and the top foil's construction material. This is why so high operating temperatures had been recorded. The technical condition of the bearing made its further operation impossible. Since the slide coating was ground down only at the lower part of the bearing, it can be said that the reason for this was the journal and bush eccentricities. The deliberate movement of the journal towards the bush caused that the bearing became overloaded. Some skewing of the journal and bush was also observed. Under such conditions, a lubricating film did not form itself in the lower part of the bearing and the journal and top foil surfaces were not properly separated. Only the material covering the surface of the top foil was ground down because it has lower thermal resistance and hardness than the molybdenum coating of the journal.



Figure 5. Damage of the sliding surface in the top foil

The analysis of the results obtained from the research showed that the bearing was not operating properly in the test run configuration applied. Accordingly, the bearing load had to be reduced to increase its lifespan. In order to reduce the bearing load in this system, the precise alignment of the electro-spindle shaft and the bush should be carried out. A similar effect can be achieved by using the so-called floating bush bearing, in which the bush position is adjusted to actual operating conditions. The implementation of this type of solutions is rare and one of the preconditions for this to happen is a small bearing load. When it comes to foil bearings testing, it may be observed, however, that sometimes there is a rapid wear of the sliding layer covering the foils, despite the relatively high compliance of the set of foils. Therefore, one cannot exclude the need to precisely align a rotor supported by foil bearings before running any tests.

Another important issue is the appropriate selection of both structural and sliding materials. In the case discussed above, the sliding layer of the top foil was made of a soft polymer and it was in contact with the journal covered with molybdenum layer. Although this pair of materials successfully underwent testing with lower loads, the test discussed herein resulted in a significant damage to the sliding material. This was caused by too high level of bearing load and the problem of forming a gaseous lubricating film. The bearing operation under such conditions led to a sharp rise in temperature to a level at which the sliding layer no longer possessed its sliding properties. This was obviously followed by an almost immediate wear of this layer.

An interesting result of this work is the observation of a substantial increase in the journal temperature, while there was a relatively low increase in the temperatures of the bush and the bearing support. This was indicative of the problem with a poor heat transfer from the sliding surface of the bearing towards the bush. The thorough analysis of this issue by using a numerical model has demonstrated that the problem is mainly linked to the bearing structure, and more precisely to the small cross-section of the bump foil (Żywica et al., 2016a). The thin bump foil separating the top foil from the bush forms a barrier for heat flow towards the bush. This causes fast

heating of both the top foil and the journal. It should be borne in mind that a local temperature rise in a foil bearing can lead to a rapid wear of the sliding layer and a bearing itself. Furthermore, it can happen as the result of even temporary overloads.

3 Vibrations of the Rotor with Foil Bearings

Sets of foils, which are the structural components of foil bearings, improve dynamical properties of the rotors supported by such bearings. In classical gas bearings consisting of a journal and a bush (which are both rigid components), the gaseous lubricating film is the only vibration-damping element, which, at high relative speeds between the sliding surfaces, forms a thin and rigid layer separating a journal and a bush from each other. Such a construction has very limited vibration-damping abilities. The addition of an elastic-damping element between a journal and a bush makes it possible to obtain more desirable dynamic properties. The change of the properties of a set of foils can be carried out by the careful selection of foils geometry and their constructional materials, so as to achieve a stable operation of the rotor-bearings system at high rotational speeds and at different loads.

Experience with foil bearings so far showed that the rotors supported by such bearings are characterized by a reliable operation, even at very high rotational speeds (Bonello, 2014; Bruckner, 2010). In general, this matched what our expectations were. Foil gas bearings also have some drawbacks compared to classical gas bearings, among which the most important are the following: high vibration levels at some speeds and shift of the critical speed towards lower values. These drawbacks mean that serious operational problems might arise in certain foil bearing configurations. This is of particular relevance for microturbines' constructions aiming at decreasing the gaps above vanes in such a way as to improve total efficiency by reducing energy losses. Similar problems we can encounter when designing bearing systems for high-speed electric generators in which there are very small gaps between the rotor and the stator. In such systems, the application of foil bearings may not be able to make up for losses resulting from lower efficiency of the machine and/or its shorter life span, because when the machine operates under extreme conditions, the damage to its rotating elements, and as a consequence of that, damage to the machine itself is likely to happen.

In this part of the article were presented the results of research aimed at the determination of vibration amplitudes at different rotational speeds of the rotor. Additionally, we conducted the analysis of the impact of ambient temperature on the operation of the rotor supported by two foil bearings. The rotor is propelled by the electro-spindle and rotation of the spindle shaft is conveyed by the coupling (Figure 6). The electro-spindle and bearing supports rest on a steel plate. The smooth rotor (shaft without any disc) is made of stainless steel. The rotor diameter is 34 mm, its length is 435 mm and the distance between the bearings is 245 mm. In order to protect the shaft against wear, the bearing journals were coated with chromium oxides and then grinded. The characteristic of the foil bearings was discussed in the previous part of this article. The elevated temperature was obtained by the use of the so-called heat gun (which acted as a hot air blower) and the infrared illuminators shown in Figure 6. In order to check the system's vibrations at different temperatures and for the whole range of rotational speeds, the measurements were conducted during the run-up of the rotor, increasing its speed up to 24,000 rpm at a constant acceleration.

The measurement results obtained for both room and elevated operation temperatures are presented in Figure 7 and Figure 8, respectively. In these graphs, the resonance area can be clearly identified, which occurred around a rotational speed of 8,000 rpm. The analysis of the results shows that the change in ambient temperature of the system resulted in a change of the resonant speed. When the bearing operated at room temperature (approx. 25°C), the highest vibration amplitudes were observed at a rotational speed of around 8,400 rpm. After the temperature was increased to 100°C, the highest vibration amplitudes were recorded at approx. 7,800 rpm. The decrease of the resonant speed can be explained by a higher compliance of the bearing's foils when operating at an elevated temperature. In this context, attention must also be given to the increase in the maximum vibration amplitude levels in both bearings. Looking at Figure 7 and Figure 8, it can be observed that the maximum peak-to-peak vibration amplitude, relating to a horizontal direction, changes from 0.18 to 0.28 mm for bearing number 1 and from 0.09 to 0.13 mm for bearing number 2. Similar differences can be observed as regards the vibration amplitudes in the vertical direction recorded in bearing number 1. However, the maximum vibration level in bearing number 2, measured in the vertical direction, was less dependent on the ambient temperature level.

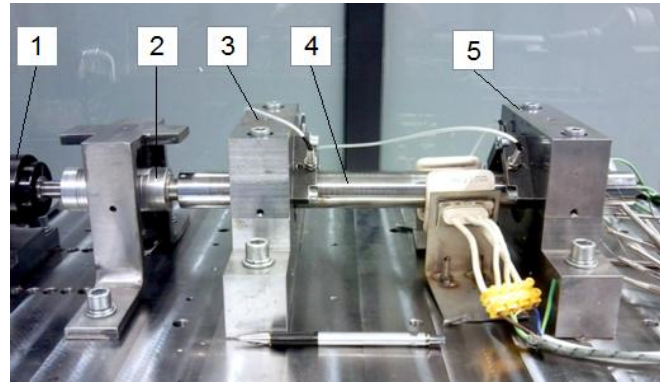


Figure 6. Configuration of the test rig for the rotor with two foil bearings (1 – electro-spindle, 2 – coupling, 3 – bearing support no. 1, 4 – shaft, 5 – bearing support no. 2)

At lower and higher rotational speeds (outside the resonance range), the rotor supported by foil bearings was characterized by a stable operation and the maximum vibration level did not exceed a few dozen micrometres. There was no increase in the vibration level or any signs of unstable operation, even at maximum speed (24,000 rpm). Thus, it can be concluded that independently of ambient temperatures, a very stable operation of the rotor–bearings system has been achieved, under the condition that the current rotational speed remains outside the resonance area of the rotor. In the case of a real machine having a similar rotor–bearings system, it is apparent that only the speeds above the resonant speed (i.e. from approximately 12,000 rpm) could be taken into consideration for determining the operating speed range. A stable gaseous lubricating film did not form itself in any of the bearings operating below the rotational speed of 8,000 rpm. A continuous and reliable operation in this speed range would, therefore, be impossible.

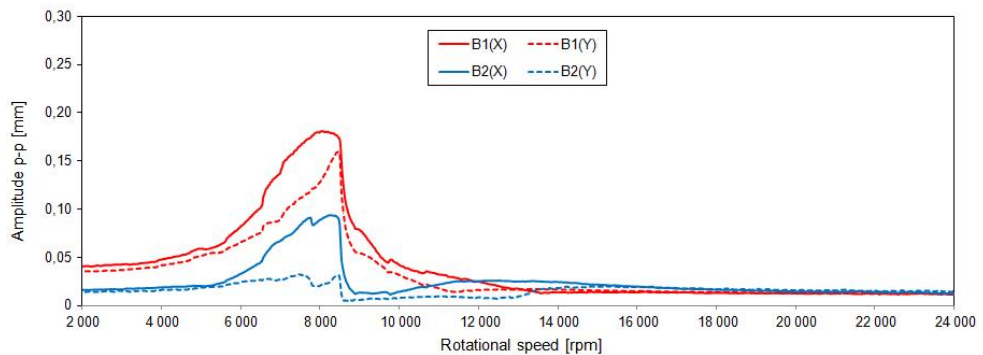


Figure 7. Peak-to-peak vibration amplitude of the shaft vs. rotational speed at 25°C (B1 – bearing no. 1, B2 – bearing no. 2, X – horizontal direction, Y – vertical direction)

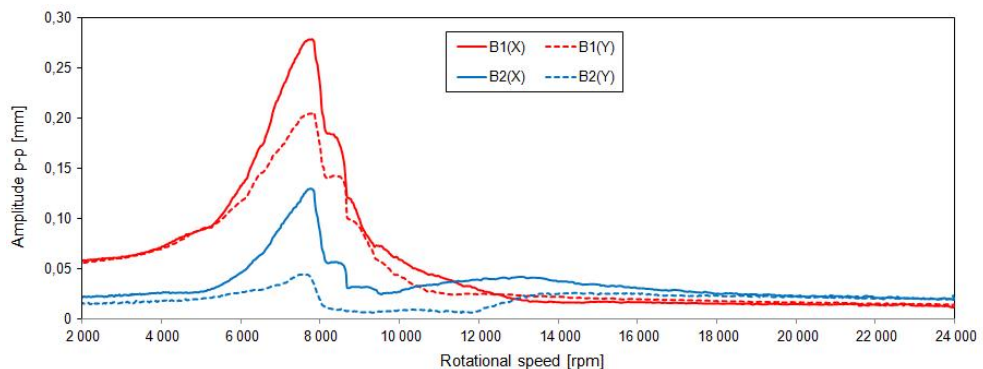


Figure 8. Peak-to-peak vibration amplitude of the shaft vs. rotational speed at 100°C (B1 – bearing no. 1, B2 – bearing no. 2, X – horizontal direction, Y – vertical direction)

The obtained results show that the amplitudes of peak-to-peak vibrations were at a level of 0.3 mm under the least favourable operating conditions. It means that radial displacement of the bearing reached a level of 0.15 mm. For microturbines used in power engineering systems, such a high level of radial vibration is not acceptable on the ground that there are very small radial clearances near the seals and in a blade system. When both the shaft

and the disks have small diameters the radial clearance is usually below 0.1 mm (Kiciński and Żywica, 2014; Tkacz et al., 2015), and it depends on the flow system of a turbine (axial-flow, radial-flow or diagonal-flow turbine). In such a machine, the use of foil bearings would be likely to lead to a number of negative consequences (e.g. damage to the rotor or the seal during the first start-up). In the case in which axial foil bearings would be used, these side effects are even more likely to occur, since, in such bearings, the axial displacements caused by a load change can have even higher values than that of the lateral foil bearing types.

In order to avoid the above-mentioned problems, we would like to present a few approaches we use in our research. One such approach is the design of bearings equipped with a set of foils that is very compact and very rigid. However, this often comes at the cost of worsening vibration-damping properties. It is also possible to design flow systems in such a way, that they are more clearance resistant (but only with respect to the preferred directions). Such an effect may be obtained, for example, in axial-flow microturbines in which the blade tips are connected by a ring, which rotates inside a casing. This creates higher clearance at the ring's location, but it does not cause considerable losses since the ring is protected from the working medium flow. It is clear that the application of foil bearings in such machines requires a lot of interference in the construction of a machine embodying our idea.

4 Conclusion

The article discusses the selected issues related to the application of gas foil bearings in modern fluid-flow machinery. Compared to conventional gas bearings, foil gas bearings stand out through their ability to operate at very high rotational speeds and the lack of external lubrication system. However, their application must be preceded by a detailed analysis of a particular machine, i.e. the machine itself must be adapted to the operation with such a bearing system. The main problems existing in foil gas bearings that must be taken into account during the selection process are the following: low load capacity, poor overload resistance, high vibration levels at some speeds, large impact of ambient temperature on the bearing's operational characteristics, a very high dimensional accuracy and assembly accuracy must be maintained. The issues presented on the pages of this article relate to many problems connected with the operation of foil gas bearings. However, they are still spoken of as a bearing system of the future whose best days are still to come.

The first case study concerns the wear of a foil bearing that happened very fast and was caused by the overload which occurred as the result of a wrong position of the bush in relation to the journal. In such operating conditions, there occurred a rapid rise in temperature and the damage to the sliding layer on the top foil. The foil bearing could not be operated any longer because the top foil was so damaged that it was clear that it required replacement. The second case study is focused on the assessment of the impact of temperature and rotational speed on the vibration amplitudes of the rotor supported by foil bearings. Its results show that high vibration levels observed at some rotational speeds can cause the rubbing between the rotating and stationary bearing elements, and as a consequence of that, the damage to the machine itself is very likely to happen.

The authors of the article want to point out that the examples provided do not cover all operational problems related to foil bearing applications. It is also worth mentioning that when designing a foil bearing, manufacturing technology for foils should be developed. It must also be remembered that a proper operation of the rotor at high speeds requires the use of an initial clamp, which unfortunately impedes the run-up. The presented case studies aim to provide an accurate picture of the scale and type of the problems, which may be encountered by all those who want to design and construct fluid-flow machines equipped with foil bearings.

Acknowledgement

The research was carried out within the framework of the project PBS1/A6/6/2012, entitled "Application of thermoelectric materials in order to improve thermal stability of bearing systems intended for high-speed rotors", financed by the National Centre for Research and Development in Poland.

References

Agrawal, G. L.: Foil air/gas bearing technology - an overview. *ASME Paper*, (1997), No. 97-GT-347.

Bonello, P. P.; Pham, H. M.: Nonlinear dynamic analysis of high speed oil-free turbomachinery with focus on stability and self-excited vibration. *ASME Journal of Tribology*, 136(4), (2014a), 041705-10.

Bonello, P. P.; Pham, H. M.: The efficient computation of the nonlinear dynamic response of a foil-air bearing rotor system. *Journal of Sound and Vibration*, 333, (2014b), 3459-3478.

Bruckner, R. J.: An assessment of gas foil bearing scalability and the potential benefits to civilian turbofan engines. *Proceedings of ASME Turbo Expo 2010*, Glasgow, UK, June 14-18, (2010), GT2010-22118.

DellaCorte, C.: A new foil air bearing test rig for use to 700 °C and 70,000 rpm. *Technical Report NASA* No. TM-107405, Washington (USA), (1997).

DellaCorte, C.: Oil-free shaft support system rotordynamics: past, present and future challenges and opportunities. *Mechanical Systems and Signal Processing*, 29, (2012), 67-76.

Heshmat, H.; Hryniwicz, P.; Walton II, J. F.; Willis, J. P.; Jahanmir, S.; DellaCorte C.: Low-friction wear-resistant coatings for high-temperature foil bearings, *Tribology International*, 38, (2005), 1059-1075.

Hoffmann, R.; Pronobis, T.; Liebich, R.: The impact of modified corrugated bump structures on the rotor dynamic performance of gas foil bearings. *Proceedings of ASME Turbo Expo 2014*, Dusseldorf, Germany, June 16-20, (2014), GT2014-25636.

Jahanmir, S.; Heshmat, H.; Heshmat, C.: Assessment of tribological coatings for foil bearing applications. *Tribology Transactions*, 52(2), (2009), 231-242.

Kiciński, J.; Żywica, G.: *Steam microturbines in distributed cogeneration*. Springer, Cham (2014).

Kim, T.; Breedlove, A. W.; San Andrés, L.: Characterization of a foil bearing structure at increasing temperatures: static load and dynamic force performance. *ASME Journal of Tribology*, 131(4), (2009), 041703-9.

Kozanecki, Z.; Kiciński, J.; Żywica, G.: Numerical model of the high speed rotors supported on variable geometry bearings, *IUTAM Symposium on emerging trends in rotor dynamics*, New Delhi, India, (2011), 217-227.

Larsen, J. S.; Alejandro, C. V.; Ilmar, F. S.: Numerical and experimental investigation of bump foil mechanical behaviour. *Tribology International*, 74, (2014), 46-56.

Larsen J. S.; Santos, I.: Compliant foil journal bearings – Investigation of dynamic properties. *SIRM 2013 - 10th International Conference on Vibrations in Rotating Machines*, Berlin, Germany, February 25-27, (2013).

Tkacz, E.; Kozanecka, D.; Kozanecki, Z.; Łagodziński, J.: Oil-free bearing development for high-speed turbomachinery in distributed energy systems – dynamic and environmental evaluation. *Open Engineering*, 3, (2015), 343-348.

Żywica, G.; Bagiński, P.; Andrearczyk, A.: Analysis of thermal damage in the high-speed foil bearing. *12th International Conference Mechatronic Systems and Materials MSM'2016*, Białystok, Poland, July 3-8, (2016a) 101.

Żywica, G.; Bagiński, P.; Banaszek, S.: Experimental studies on foil bearing with a sliding coating made of synthetic material. *ASME Journal of Tribology*, 138(1), (2016b), 011301-10.

Żywica, G.; Kiciński, J.; Bagiński, P.: The static and dynamic performance analysis of the foil bearing structure. *Journal of Vibration Engineering & Technologies*, 4(3), (2016c), 213-220.

Address: Grzegorz Żywica (Ph.D., Eng.), Paweł Bagiński (M.Sc., Eng), Prof. Jan Kiciński (D.Sc., Eng.)
 Institute of Fluid Flow Machinery, Polish Academy of Sciences, 80-231 Gdańsk, Fiszera 14, Poland
 email: gzywica@imp.gda.pl, pbaginski@imp.gda.pl, kic@imp.gda.pl

Simple Electromagnetic Motor Model for Torsional Analysis of Variable Speed Drives with an Induction Motor

T. P. Holopainen, A. Arkkio

Torsional vibrations must be considered in the design of all high-power drive-trains including an induction motor. Electromagnetic (EM) field in the air gap of an induction motor generates additional magnetic stiffness and damping between the rotor and stator. The inclusion of these magnetic effects is limited by the availability of simple and portable motor models. The main aim of this paper is to introduce a motor model including the speed and torque variation. The presented model is based on the linearization of the common space-vector models of induction motors. The parameters of this model are identified for the rated operating condition. This motor model can be extended to include variable speed and torque operation. The numerical results demonstrate that this model describes accurately the magnetic effects over the large speed and torque range. In addition, the numerical results demonstrate the significance of magnetic stiffness and damping in variable speed motor-driven compressors with a soft coupling.

1 Introduction

Induction motors rotate process machines by converting electric energy to mechanical work. The power is transmitted by a drive train including couplings and optional gears and branches. An essential part of the drive train design is the torsional vibration analysis. This analysis requires the inertia and stiffness data of all the drive train components with loading and damping parameters.

Increasing power density, together with increasing demands of reliability of industrial systems, has led to the increased requirements of calculation accuracy. With motor driven reciprocating compressors, this has resulted in the inclusion of magnetic stiffness and damping in torsional analysis (Anon., 2015). Due to this need, simple models, based on the motor characteristic data, have been presented for the evaluation of these magnetic parameters; see Knop (2012) and Hauptmann et al. (2013). These models are based on the space-vector theory, developed to describe the steady-state and transient motor behaviour, and used for the evaluation of magnetic stiffness and damping, see Concordia (1952), Jordan et al. (1979, 1980), Shaltou (1994) and Brunelli et al. (2015). Space-vector models, or the simplified versions of them, are well suited for the torsional analysis of drive trains. Using these models, the parameters required to describe the magnetic stiffness and damping can be calculated in advance by the motor manufacturer and submitted to the suppliers, e.g. compressor manufacturer, responsible for the drive train design.

Simultaneously, numerical methods have been increasingly applied for the analysis of induction motors. This trend has been expanded also to the determination of magnetic stiffness and damping parameters (Repo 2008) and the effect of these has been evaluated in calculation examples of actual drive trains (Holopainen et al. 2010).

The accuracy and modelling capability of numerical models exceeds clearly the potential of space-vector models. However, the accuracy is only one, though significant, requirement of feasible models for torsional analyses. A remarkable shortcoming of numerical models is the portability. The numerical models are usually non-linear and the application requires the integration of particular codes for electromagnetic fields. Thus, the portability of numerical motor models is poor, or at least limited. By contrast, the space-vector model is simple and the number of model parameters is small, and thus, the portability excellent.

The main aim of this paper is to introduce a simple linearized motor model including the speed and torque variation. The second aim is to show the significance of the magnetic stiffness and damping particularly in motor-driven reciprocating compressors with a soft coupling.

This paper is based strongly on the methods and findings of two previous papers, see Arkkio et al. (2016) and Holopainen et al. (2016). The paper starts by reviewing the linearization of the space-vector model in the operating point. Next, the inclusion of the speed and torque variation is presented. These two parameters define the steady-state operation of an induction motor. After this, the developed models are applied for a 3.7 MW induction motor. The obtained magnetic stiffness and damping values are compared to the results calculated numerically by a refined finite element (FE) method with time-stepping analysis. Finally, the motor model is applied to evaluate the magnetic effects on a reciprocating compressor drive train. All the calculations are carried out with a steady-state sinusoidal voltage supply of the motor. Thus, all the effects induced by the frequency converter control are neglected and the scope is restricted purely to the motor.

2 Methods

2.1 Space-vector Model of Induction Motor

A single-cage space-vector model for an induction motor written in a reference frame rotating at the synchronous angular speed ω_s is

$$\begin{aligned}\underline{u}_s &= R_s \underline{i}_s + \frac{d\underline{\psi}_s}{dt} + j\omega_s \underline{\psi}_s \\ 0 &= R_r \underline{i}_r + \frac{d\underline{\psi}_r}{dt} + j(\omega_s - \omega) \underline{\psi}_r \\ T_e &= \frac{3}{2} p \text{Im}(\underline{\psi}_s^* \underline{i}_s)\end{aligned}\tag{1}$$

where \underline{u}_s , \underline{i}_s and $\underline{\psi}_s$ are the space vectors of stator voltage, stator current and stator flux linkage, \underline{i}_r and $\underline{\psi}_r$ are the space vectors of rotor current and rotor flux linkage, R_s is the stator resistance, R_r is the rotor resistance, ω is the angular speed of the rotor, p is the number of pole pairs, j is the imaginary unit, and asterisk denotes complex conjugation. The angular speeds are given in electrical radians, i.e. $\omega = p\Omega$, where Ω is the mechanical rotational speed.

The linear relation between the flux linkages and currents is

$$\begin{aligned}\underline{\psi}_s &= L_s \underline{i}_s + L_m \underline{i}_r \\ \underline{\psi}_r &= L_m \underline{i}_s + L_r \underline{i}_r\end{aligned}\tag{2}$$

where L_s and L_r are the self-inductances of the stator and rotor windings and L_m is the mutual inductance between them.

2.2 Linearization of Space-vector Model in Operation Point

The system of equations (1) is non-linear because of the product of angular speed and rotor flux linkage in the second equation. In addition, the electromagnetic torque in the third equation is non-linear due to the product of stator flux linkage and stator current. However, the torsional vibrations are manifested by small oscillations around the equilibrium point. Thus, the calculation of torsional vibrations can be carried out by linearizing the equations at the operation point. The linearized system of equations in the synchronously rotating reference frame is (Arkkio et al. 2016)

$$\begin{aligned}\Delta \underline{u}_s &= R_s \Delta \underline{i}_s + L_s \frac{d\Delta \underline{i}_s}{dt} + j\omega_s L_s \Delta \underline{i}_s + L_m \frac{d\Delta \underline{i}_r}{dt} + j\omega_s L_m \Delta \underline{i}_r \\ 0 &= R_r \Delta \underline{i}_r + L_m \frac{d\Delta \underline{i}_s}{dt} + j(\omega_s - \omega_0) L_m \Delta \underline{i}_s + L_r \frac{d\Delta \underline{i}_r}{dt} + \\ &\quad + j(\omega_s - \omega_0) L_r \Delta \underline{i}_r - j(L_m \underline{i}_{s0} + L_r \underline{i}_{r0}) \Delta \omega \\ \Delta T_e &= \frac{3}{2} p L_m \text{Im}(\underline{i}_{r0}^* \Delta \underline{i}_s + \underline{i}_{s0} \Delta \underline{i}_r^*)\end{aligned}\tag{3}$$

where the currents have been chosen as the free variables, Δ denotes a small variation from the steady state value, i.e. a linearized variable, and \underline{i}_{s0} , \underline{i}_{r0} and ω_0 are the steady-state stator current, rotor current and angular speed.

The resistance and inductance parameters of the non-linear and linearized space-vector models, (1) and (3), were obtained from a time-harmonic FE analysis (Repo et al. 2006). A non-linear effective permeability of operating point was used to get the parameters to calculate the steady-state currents of equation (1). A differential permeability was used to get the linearized parameters for equation (3).

2.3 Improved Space-vector Models

The simple space-vector model of equations (1) and (3) can be improved to include skin effect of rotor bars by increasing the number of rotor branches. Figure 1 shows a steady-state equivalent circuit having three rotor branches or cages. The corresponding dynamic space-vector model is (Arkkio et al. 2016)

$$\begin{aligned}
 \underline{u}_s &= R_s \underline{i}_s + \frac{d\Psi_s}{dt} + j\omega_k \underline{\Psi}_s \\
 0 &= R_r \underline{i}_r + \frac{d\Psi_r}{dt} + j(\omega_s - \omega) \underline{\Psi}_r \\
 0 &= R_q \underline{i}_q + \frac{d\Psi_q}{dt} + j(\omega_s - \omega) \underline{\Psi}_q \\
 0 &= R_p \underline{i}_p + \frac{d\Psi_p}{dt} + j(\omega_s - \omega) \underline{\Psi}_p \\
 T_e &= \frac{3}{2} p \text{Im}(\underline{\Psi}_s^* \underline{i}_s)
 \end{aligned} \tag{4}$$

where subscripts q and p refer to the second and third rotor branches. A double- and triple-cage linearized model can be constructed in a similar way as the single-cage model above. Again, the resistance and inductance parameters were obtained from a time-harmonic FE analysis (Repo et al. 2006)

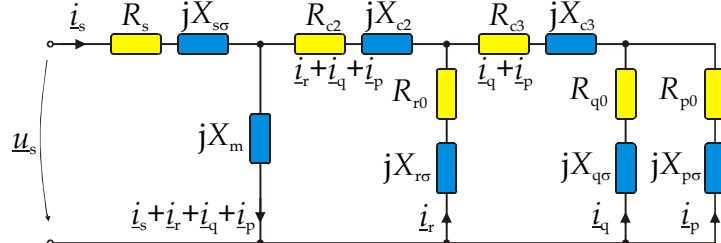


Figure 1. Steady-state space-vector equivalent circuit with three rotor branches (Arkkio et al. 2016)

The number of real-valued parameters, i.e. original and linearized model resistances and inductances, is 10, 18 and 26 in single-cage, double-cage and triple-cage models, respectively. The number of complex-valued variables, i.e. electromagnetic degrees-of-freedom, is 2, 3 and 4 in single-cage, double-cage and triple-cage models, respectively. Because the number of variables in a typical FE model used for the identification of parameters is thousands, the reduction grade is remarkable.

2.4 Variable Speed and Torque Operation

A large share of the new motors is used in variable speed applications. In these applications the motor speed and torque is adjusted according to process requirements. A common approach is to keep the fundamental flux of the machine constant independently of the actual speed and torque. This means that the supply voltage is directly proportional to the supply frequency up to the field weakening point, which is often above the maximum speed. It can be mentioned that modern frequency controllers may adjust the torque based on the feedback. However, all the calculations of this paper are carried out with a steady-state sinusoidal voltage supply of the motor, and thus, all the effects induced by the frequency converter control are neglected.

In this paper, the model parameters, i.e. inductances and resistances, are identified for the rated operating condition. These model parameters are extended to an arbitrary speed and torque by adjusting first the supply voltage according to the constant flux approach

$$\underline{u}_s = \frac{\omega_s}{\omega_{s,\text{rat}}} \cdot \underline{u}_{s,\text{rat}} \quad (5)$$

where the subscript “rat” refers to the rated values. The rotational speed and torque are connected by the slip of the rotor with respect to the rotating magnetic field

$$s = (\omega_s - \omega_0)/\omega_s \quad (6)$$

This slip must be solved iteratively from the non-linear equation (1) using the pre-set values of speed and torque. In addition, the inductances of the linearized model, equation (3), must be divided by the synchronous speed ratio $\omega_s/\omega_{s,\text{rat}}$. All other parameters of the non-linear and linearized models remain unchanged.

2.5 Calculation of magnetic Stiffness and Damping

The analytical expression for the frequency response function for the single-cage space-vector model is obtained from equation (3) by replacing the small variations by phasor variables of oscillation frequency ω_d and solving the relation between the torque and rotation angle of the rotor.

The magnetic stiffness k_m and damping coefficients d_m can be associated with the real and imaginary parts of the frequency response function $\underline{G}_{\text{frf}}$

$$\begin{aligned} k_m &= -\text{Re}[\underline{G}_{\text{frf}}(\omega_d)] \\ d_m &= -\text{Im}[\underline{G}_{\text{frf}}(\omega_d)]/\omega_d \end{aligned} \quad (7)$$

where ω_d is the angular frequency of oscillation.

2.6 Reference results by Finite Element Analysis (FEA)

In the 2D FEA models, the magnetic field in the core region of the motor is assumed to be two-dimensional. End-winding impedances are added to the circuit equations of the windings to approximatively model the 3D end-winding fields. The field and circuit equations are discretized and solved together (Arkkio 1990). Moving-band technique in the air gap of the machine is used for rotating the rotor (Davat et al. 1985). The torque is computed using Coulomb’s method (Coulomb 1983). The resistive losses of the windings were included in the model when solving the field equations within FEA.

The frequency response function was needed for the reference result. Two time-stepping simulations in steady-state are used. In the first one, the rotor is rotated at a constant speed. In the second one, the rotation speed is forced to oscillate at a frequency ω_d and small amplitude around the constant speed of the first simulation. The results of the two simulations, particularly the electromagnetic torque and the rotation angle of the rotor, are subtracted from each other. The component varying at frequency ω_d is extracted from the torque and rotation angle differences by complex Fourier analysis, and finally, the complex value of the frequency response function at frequency ω_d is obtained by dividing the Fourier components of the torque and rotation angle. This process was repeated at about 30 different excitation frequencies between 10 Hz and 100 Hz to collect data for the comparison of the analytically and numerically obtained frequency response functions.

Another way to get the frequency response function numerically is to excite the machine by a single pulse in the rotation angle (Repo 2008). In this way, all the interesting frequencies can be obtained from two simulations, one with the pulse and another one without it. This method is applied to obtain the reference results for the variable speed and torque comparison.

3 Results

3.1 Magnetic stiffness and damping

A 3.7 MW induction motor is used in all the calculation examples. The main parameters of this motor are shown in Table 1.

Table 1. Rated parameters of the example motor.

Parameter	Value	Unit
Power	3551	kW
Frequency	60	Hz
Speed	895.3	rpm
Number of poles	8	
Connection	star	
Voltage	4000	V
Current	620	A
Rated torque	37.88	kNm
Breakdown torque	82.71	kNm

Figure 2 shows the magnetic stiffness and damping calculated by an analytic formula presented by Hauptmann et al. (2013), by single- and triple-cage models with parameters based only on the non-linear models, and FEA results. The FEA results are assumed to be most accurate and will be used here and later as reference values. In this case, the analytic equation underestimates the EM stiffness and damping and neglects the effects close to the supply frequency. Similarly, all the cage models underestimate the EM stiffness and damping. The triple-cage model gives the best prediction.

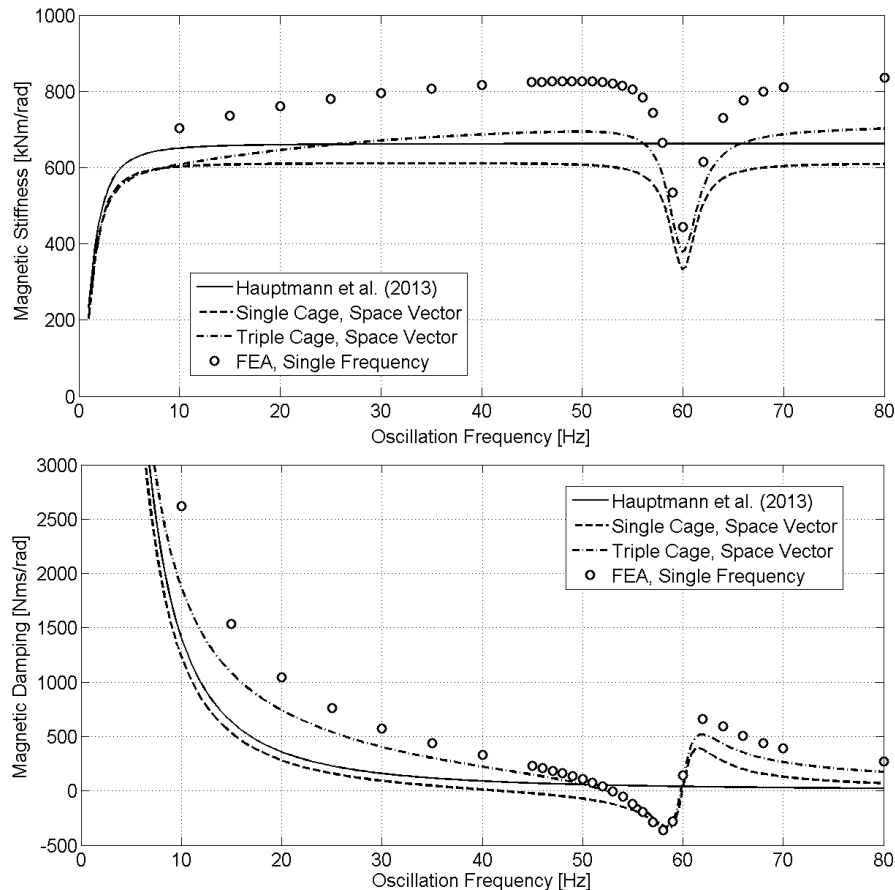


Figure 2. Magnetic stiffness and damping in rated operating condition with non-linear model parameters in cage models.

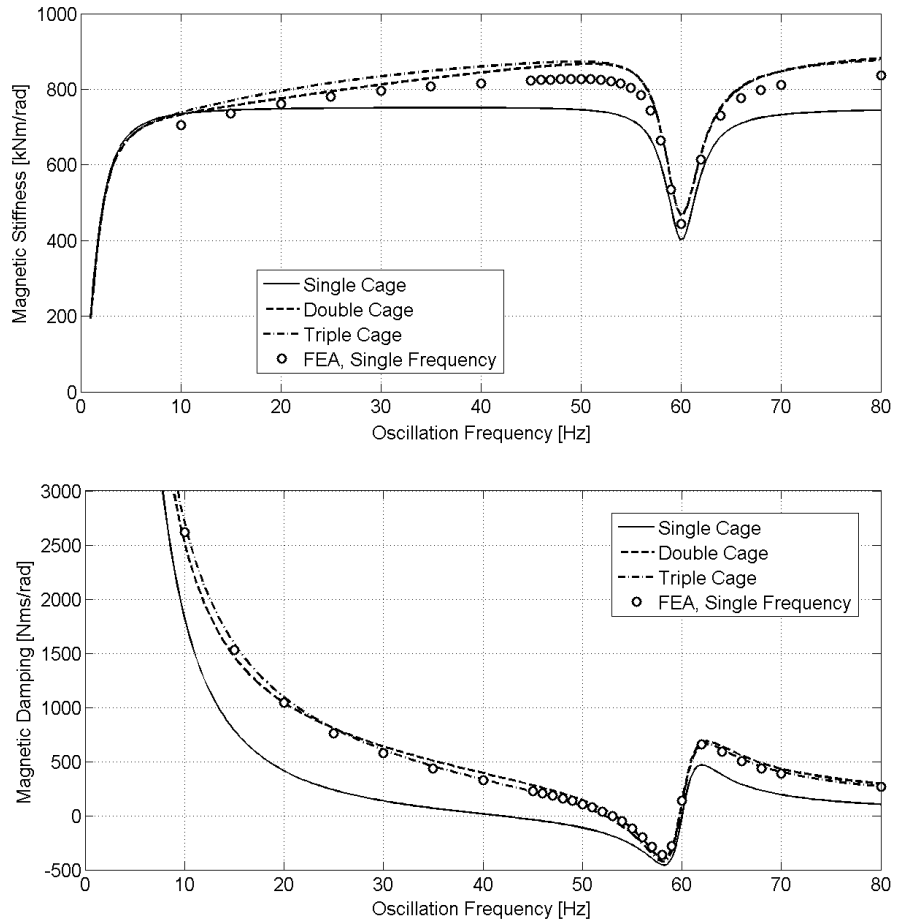


Figure 3. Magnetic stiffness and damping in rated operating condition with linearized space-vector model.

Figure 3 shows the magnetic torsional stiffness and damping in the rated operating condition calculated by linearized space-vector models and by FEA. The parameters of the space-vector models are identified for the slip frequency 1.2 Hz (Holopainen et al. 2016). As can be seen the single-cage model underestimates the stiffness and damping. In the contrary, the double- and triple-cage models overestimate somewhat the stiffness and predict the damping accurately. The difference between the double- and triple-cage models is small.

3.2 Effect of Speed and Torque

The synchronous speed range of the example motor in the variable speed operation is 450 – 900 rpm. This corresponds roughly to the supply frequency range 30 – 60 Hz. The field weakening point of this motor is at 60 Hz and the load torque of reciprocating compressors depends on the process medium and pressure ratio, and is independent of the speed. Thus, it is assumed that the torque varies between 50 – 100 % of the rated torque. Table 2 shows the calculation points. These points are the corner points of the speed-torque domain. However, for simplicity the calculation points are defined by the supply frequency and electric power. The slip, torque and speed values in table 2 are calculated by iteration during the space-vector and FEA solutions.

Figure 4 shows the magnetic stiffness and damping for these four operating points calculated by the linearized triple-cage space-vector model. It can be clearly seen that both the speed and torque affects the magnetic parameters.

Figure 5 shows the same information in the form of the complex frequency response functions (FRFs) between the torque and rotor oscillation, see equation (5). In this figure, the FRFs are plotted as functions of the relative oscillation frequency. This presentation format gives a better overview of the speed and torque effect on the magnetic stiffness and damping. It can be seen that the effect of speed (50% reduction) is slightly larger than the effect of torque (50% reduction). In addition, it can be seen that the change of torque changes the real part of the FRF, i.e. magnetic stiffness, but leaves the imaginary part of FRF, i.e. magnetic damping, almost intact.

Table 2. Calculated operation points of the example motor used in FEA.

Case	Freq.	Power	Space-Vector Model			FEA		
			Slip [%]	Torque [kNm]	Speed [rpm]	Slip [%]	Torque [kNm]	Speed [rpm]
1	60	3729	0.546	39.78	895.1	0.543	39.78	895.1
2	60	1864	0.257	19.83	897.7	0.259	19.83	897.7
3	30	1864	1.114	40.01	445.0	1.108	40.00	445.0
4	30	932	0.518	19.88	447.7	0.521	19.88	447.7

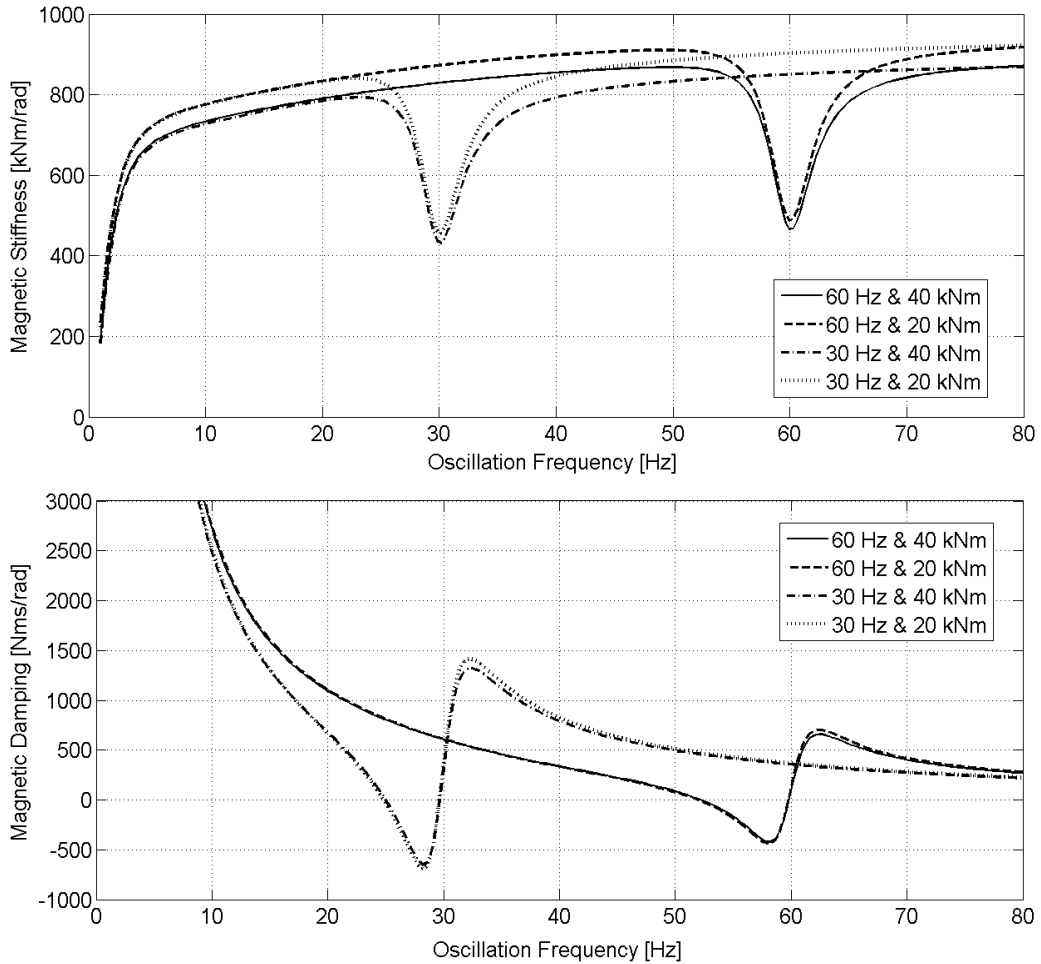


Figure 4. Magnetic stiffness and damping calculated by the linearized triple-cage space-vector model.

Figure 6 shows the corresponding frequency response functions for the example motor calculated by the FEM in time domain and the pulse method (Repo 2008). It can be concluded that the behaviour of the linearized space-vector model (Figure 5) and the FE model (Figure 6) correlates well over the whole speed range.

3.3 Motor driven reciprocating Compressor

The example motor drives a reciprocating compressor. The drive train consists of the following components: Motor, flexible coupling, flywheel and reciprocating four-cylinder compressor. This compressor can be used in direct-on-line operation with constant speed 895 rpm and in variable speed operation (450 – 900 rpm) supplied by a frequency converter. The mechanical drive train was modelled with 26 inertias with connecting torsional stiffness elements. The viscous damping was added to the motor and compressor cylinder locations. The damping induced by the flexible coupling was neglected due to the missing input data.

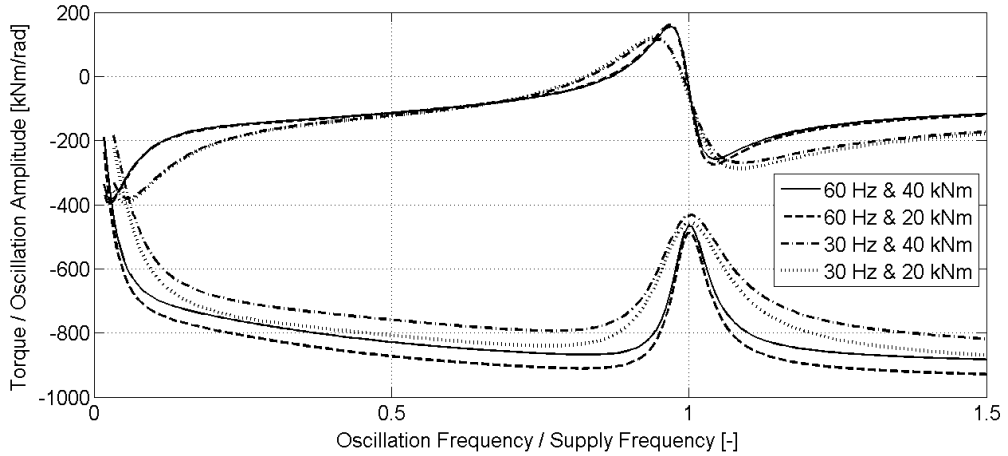


Figure 5. Frequency response function between the magnetic torque and rotor oscillation calculated by the linearized space-vector model. The real parts of the complex valued functions are below and the imaginary parts are up.

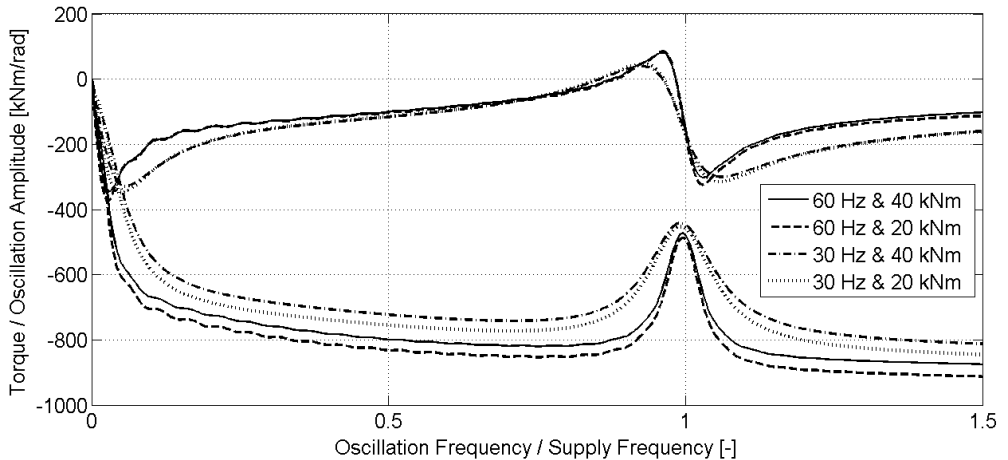


Figure 6. Frequency response function between the magnetic torque and rotor oscillation calculated by the FEA. The real parts of the complex valued functions are below and the imaginary parts are up.

Table 3 shows the natural frequency and damping ratio for the lowest modes without and with magnetic effects. The calculations are carried out by adding the magnetic stiffness and damping to the mechanical model. The calculation was carried out iteratively in order to use the magnetic stiffness and damping values corresponding to the natural frequencies. The first mode without magnetic effects is the rigid body mode. The main deformation of the second mode occurs in the flexible coupling. The third mode is an internal mode of the coupling, and in the fourth mode the flywheel and the compressor line are in the opposite phase without angular displacement of the motor.

Table 3 shows that the electromagnetic interaction increases clearly the natural frequency and damping ratio of the two first modes. The effect on modes 3 and 4 is negligible. This is logical due to the modal amplitudes of the modes 1 and 2 in contrast to the amplitudes of the modes 3 and 4.

Due to the variation of supply frequency, the magnetic stiffness and damping changes though the torque is assumed to be constant. Figure 7 shows the natural frequency and damping ratio of the two lowest modes as a function of the motor speed. In addition, the first and second order excitations are shown in this Campbell diagram. It can be seen that the natural frequency and damping ratios are only slightly dependent on the speed above 300 rpm. Below that speed the effects of the supply frequency on the second mode are clearly visible. Actually, the damping factor is negative in the speed range 140 – 190 rpm. The second mode crosses the first order excitation frequency at about 600 rpm. The response of the system on this torsional critical speed depends on the first order excitation amplitude and the total damping. In this case the damping factor is predicted to be

8.6%. The amount of damping provided by the electromagnetic system is significant compared to the mechanical damping (Table 3).

Table 3. Natural frequency and damping ratio for the four lowest modes without and with electromagnetic coupling at rated operation.

Mode	Magnetic Effects			
	Without		With	
	f [Hz]	ζ [-]	f [Hz]	ζ [-]
1	0.00	0.00	4.14	10.09
2	6.35	1.60	10.03	8.63
3	37.27	0.01	37.29	0.02
4	130.29	0.92	130.29	0.92

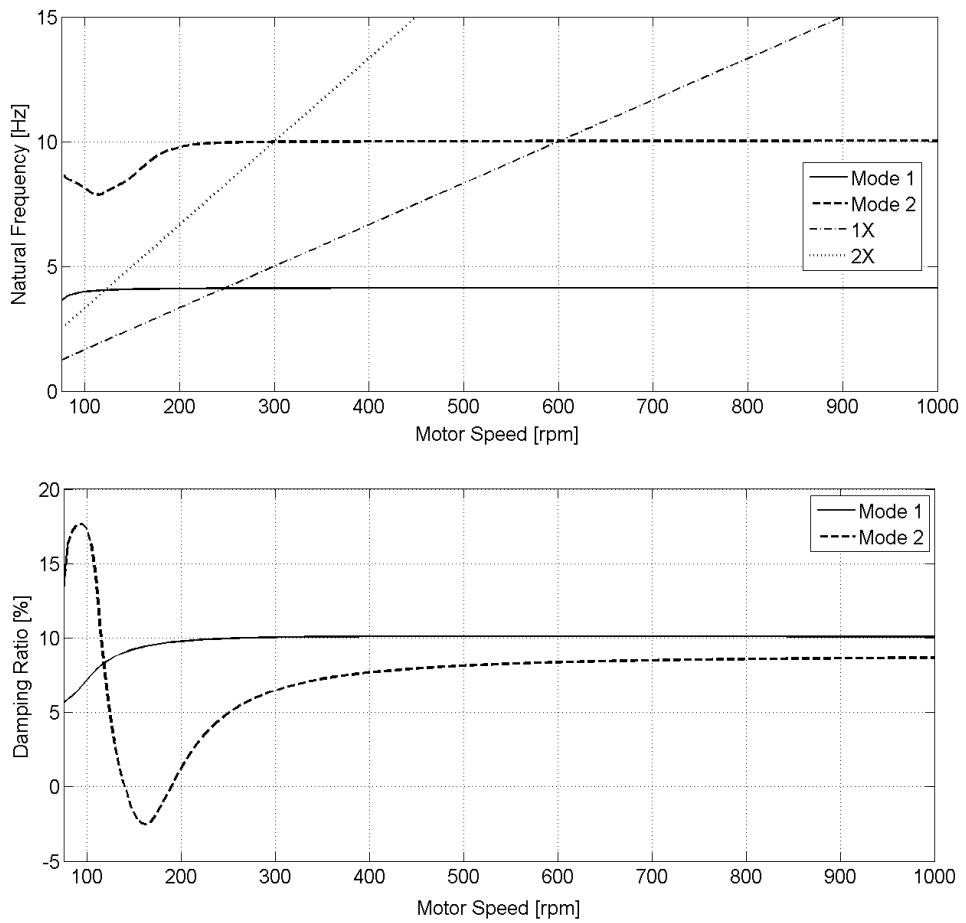


Figure 7. Natural frequency and damping ratio of the motor compressor train.

4 Discussion and Conclusions

The obtained results show that the linearized space-vector models can be used to predict the magnetic stiffness and damping of induction motors. Particularly, the prediction capability of the double- and triple-cage models in the rated operating condition is good. However, there seems to be a difference in magnetic stiffness compared to the FEA results. The triple-cage model yields about 5% higher stiffness values than the FEA. The origin of this discrepancy is not known.

The parameters of the presented non-linear and linearized space-vector models are obtained from the time-harmonic FEA. The number of parameters is 10, 18 and 26 in single-cage, double-cage and triple-cage models,

respectively. Because the number of variables in a typical FE model, used for the identification of parameters, is thousands, the reduction grade is remarkable. More importantly, the space-vector model is portable to be a part of standard torsional analyses without direct coupling to solvers of electromagnetic fields.

The calculation results indicate that the space-vector model can be extended to variable speed and torque operation. The results of the simple three-cage model are well compatible to the results obtained by the non-linear FEA in the time domain.

The calculation example for a reciprocating compressor train shows that the inclusion of magnetic effects is significant with flexible coupling. This follows from the two effects: The magnetic stiffness increases the natural frequencies and the magnetic damping decreases the oscillation amplitudes of torsional modes. The magnetic damping is particularly advantageous and can be exploited in the design of torsional drive trains.

The calculations were carried out with a steady-state sinusoidal voltage supply of the motor. Thus, all the effects induced by the frequency converter control are neglected and the scope is restricted purely to the motor.

References

Anon.: Guideline and recommended practice for control of torsional vibrations in direct-driven separable reciprocating compressors. *Gas Machinery Research Council, ACI Services*, (2015).

Arkkio, A.: Finite element analysis of cage induction motors fed by static frequency converters. *IEEE Trans. Magnetics*, 26, (1990), 551-554.

Arkkio, A.; Holopainen, T. P.: Space-vector models for torsional vibration of cage induction motors. *IEEE Trans. on Industry Applications*, 52, (2016), 2988-2995.

Brunelli, M.; Fusi, A.; Grasso, F.; Pasteur, F.; Ussi, A.: Torsional vibration analysis of reciprocating compressor trains driven by induction motors. In *Proc. 9th Int. Conf. on Compressors and their Systems*, London, UK, Sept.7-9, (2015), 10 p.

Concordia, C.: Induction motor damping and synchronizing torques. *AIEE Trans. Power Apparatus and Systems*, 71, (1952), 364-366.

Coulomb, J. L.: A methodology for the determination of global electromechanical quantities from a finite element analysis and its application to the evaluation of magnetic forces, torques and stiffness. *IEEE Trans. Magnetics*, 19, (1983), 2514-2519.

Davat, B.; Ren, Z.; Lajoie-Mazenc, M.: The movement in field modeling, *IEEE Trans. Magnetics*, 21, (1985), 2296-2298.

Hauptmann, E.; Howes, B.; Eckert, B.: The influence on torsional vibration analysis of electromagnetic effects across an induction motor air gap. In *Proc. GMRC Gas Machinery Conf.* Albuquerque, New Mexico, Oct. 6-9, (2013), 11 p.

Holopainen, T. P.; Repo, A.-K.; Järvinen, J.: Electromechanical interaction in torsional vibrations of drive train systems including an electrical machine. In *Proc. 8th IFTOMM Int. Conf. Rotordynamics*. Seoul, Korea, Sept 12-15, (2010) 8 p.

Holopainen, T. P.; Liukkonen, O. J.; Arkkio, A.: Portable induction motor model for torsional vibration analysis of drive train systems. In *Proc. 11th Int. Conf. on Vibrations in Rotating Machinery*. Manchester, UK, Sept. 13-15, (2016), 141-151.

Jordan, H.; Müller, J.; Seinsch, H. O.: Über elektromagnetische und mechanische Ausgleichsvorgänge bei Drehstromantrieben. *Wiss. Ber. AEGTELEFUNKEN*, 52, (1979), 263-270.

Jordan, H.; Müller, J.; Seinsch, H. O.: Über das Verhalten von Drehstromasynchronmotoren in drehelastischen Antrieben. *Wiss. Ber. AEGTELEFUNKEN*, 53, (1980), 102-110.

Knop, G.: The importance of motor dynamics in reciprocating compressor drives. In *Proc. 8th Conf. EFRC*. Düsseldorf, Germany, Sept. 27-28, (2012), 10 p.

Repo, A.-K.: *Numerical impulse response tests to identify dynamic induction-machine models*. Dissertation, Helsinki University of Technology, Finland, (2008).

Repo, A.-K.; Niemenmaa, A.; Arkkio, A.: Estimating circuit models for a deep-bar induction motor using time harmonic finite element analysis. In *Proc 17th Int. Conf. on Electrical Machines*, Chania, Greece, Sept. 2-5, (2006), 6 p.

Shaltout, A. A.: Analysis of torsional torques in starting of large squirrel cage induction motors. *IEEE Trans. Energy Convers.* 9, (1994), 135-142.

Address: Timo P. Holopainen, ABB Oy, P.O. Box 186, FI-00381 Helsinki, Finland

email: timo.holopainen@fi.abb.com

Antero Arkkio, Aalto University, P.O. Box 15500, FI-00076 Aalto, Finland

antero.arkkio@aalto.fi

Prediction of Instability in Rotor-Seal Systems using Forward Whirl Magnetic Bearing Excitation

C. Wagner¹, W. Tsunoda², O. Matsushita³, T. Berninger¹, T. Thümmel¹, D. Rixen¹

To separate different fluids and pressure levels in high-speed turbomachinery or pumps, mostly contactless seals are used. The leakage flow inside the seal gap applies forces to the vibrating rotor system in deflectional and tangential directions, that are dependent on the rotational speed. Above a speed limit, mainly tangential seal forces can lead to self-excited vibrations and, ultimately, rotor instability. This is similar to the “oil whip” phenomenon in journal bearings. To predict the speed limit, two methods are shown and compared: Simulations based on the bulk flow assumptions and an experimental method. To demonstrate the application, a test rig is used. The experimental method uses measured transfer functions, utilizing an active magnetic bearing for forward whirl excitation in the safe operational range. The speed limit can be predicted by analyzing and extrapolating the vibrational behavior of the rotor-seal system.

1 Introduction

Seals in pumps or compressors are used to minimize leakage flow between areas of different pressure levels. Due to the high rotational and relative speeds between rotor and stator in modern turbomachinery, mostly contactless seals like labyrinth, floating ring or gap seals are used. The seal clearance causes a fluid flow through the gap. For an eccentric rotor position, the fluid flow distribution in the gap becomes unsymmetrical and leads to forces on the rotor. These can be modeled similar to additional stiffness, damping and inertia coefficients. The critical speeds can be clearly differentiated compared to the dry rotor ones. This makes dry calculations of the dynamic behavior, like natural frequencies or damping, useless for real operating conditions. The seal gap shown in fig. 1 provides the source of the acting forces, according to Gasch et al. (2006) and Childs (1993).

1. Force pressure velocity relation

The relation between a fluid velocity v and the static pressure is provided by BERNOULLI's equation:

$$p_s = p_t - p_d = p_t - \frac{1}{2} \rho v^2 \quad (1)$$

With the total pressure p_t , the dynamic pressure p_d and the static pressure p_s , which acts on the surface. The integration of the pressure distribution p_s across the rotor surface leads to the acting forces \vec{F} :

$$\vec{F} = \int_A p_s dA \quad (2)$$

2. Restoring force

The restoring LOMAKIN force \vec{F}_L acts against the rotor deflection. It is developed by the axial fluid velocity \vec{u} , which is a pressure-driven POISEUILLE flow, Black and Jenssen (1969). For an eccentric rotor position, the axial fluid flow velocity \vec{u} is higher at the expanded side because of the lower wall-friction influence. This leads to a lower static pressure p_s and a restoring, stiffening force \vec{F}_L , see fig. 1 left. At the seal's entrance, the inlet pressure loss increases this effect and causes the kink of p_s .

3. Destabilizing, deflecting force

Fluid flow in circumferential direction \vec{v} creates the BERNOULLI force \vec{F}_B , which acts in the direction of the rotor eccentricity. The flow is driven by the rotor rotation and evolves into a COUETTE flow for higher seal lengths. Because of mass conservation, the flow speed becomes higher in the narrowed area. This induces a deflecting, destabilizing force \vec{F}_B , see fig. 1 right.

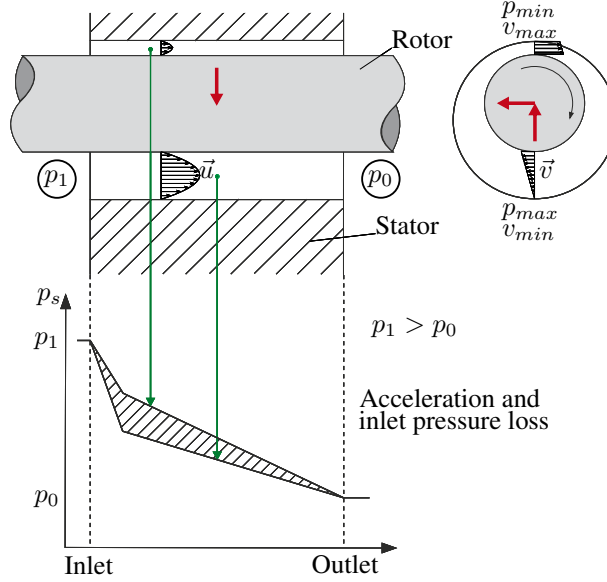


Figure 1: Contactless annular seal, pressure drop and reaction forces, Gasch et al. (2006)

4. Tangential Force

The tangential forces \vec{F}_T pose the highest risk to self-excited rotor vibrations. They act like skew symmetric parts in the stiffness matrix and can induce a rotor instability, similar to the “oil whip” phenomenon in journal bearings, Muszynska (1986). The forces are created by shear stresses between the fluid and the wall, as well as the pressure distribution at the narrowed area of the eccentric rotor.

For a rotordynamic analysis, seals are commonly modeled as a spring-mass-damper system using rotordynamic seal coefficients:

$$-\vec{h}_s = \begin{bmatrix} m_{xx} & 0 \\ 0 & m_{yy} \end{bmatrix} \ddot{\vec{q}} + \begin{bmatrix} c_{xx} & c_{xy} \\ c_{yx} & c_{yy} \end{bmatrix} \dot{\vec{q}} + \begin{bmatrix} k_{xx} & k_{xy} \\ k_{yx} & k_{yy} \end{bmatrix} \vec{q} \quad (3)$$

$\vec{q} = (x \ y)^T$ is the cross deflection (bending) of the rotor, \vec{h}_s is the seal force using the seal coefficients m , c and k for added mass, the fluid’s inertia, damping and stiffness with cross-coupled parts. The cross coupling in the mass matrix is neglected. For the rotordynamic analysis, the various geometries and types of seals are simplified to a plain annular seal.

To calculate critical speeds, vibration amplitudes and rotor instability at the design phase of the machine, validated seal simulation models and experimental methods for component testing are needed. Therefore, two approaches are shown below. The applied simulation models are based on the bulk flow theory and use simplifications made by Black and Jenssen (1969) and Childs (1983) to solve the fluid equations.

To examine the rotordynamic influence of liquid annular seals at the test rig, the authors apply a modern stability diagnosis method that uses measurements in an uncritical speed range to predict the onset speed of instability. The methodology’s origin is the experimental stability diagnosis of oil-film-bearing rotor systems, well described in Matsushita and Fujiwara (2014) and Tsunoda et al. (2016). Here, this method is applied to a flexible rotor with rigid ball-bearing support with plain annular seals. The phenomenology of rotor instability is similar to the journal bearing case. The experimental methodology uses an active magnetic bearing (AMB) as an actuator to excite the rotor system. Other investigations using AMB excitation in rotor-seal systems, mainly for coefficient determination, are Kwanka (1999), Gaszner (2015) or Wagner et al. (2016). Another solution for identifying the seal is a levitating AMB-supported rotor, like Zutavern (2006).

In contrast to those, the presented methodology predicts the onset speed of instability to determine the safe operational range of the machinery, using measurements that can be done in the real machine in an uncritical range.

2 Modeling

Here, we provide a brief introduction to the used seal and rotor models. The description of the self-excited rotor vibration phenomenon is based on the work of Muszynska (1986) and Bently et al. (2002). A reduced LAVAL rotor model, according to Gasch et al. (2006), provides the basis to show the model coupling and the seal-rotor behavior.

2.1 Rotor Model

The LAVAL rotor model with a flexible, massless shaft and a symmetrical arranged disk is shown in fig. 2, according to Gasch et al. (2006). The Index I indicates the inertial frame. The disk's center of mass S is displaced by the

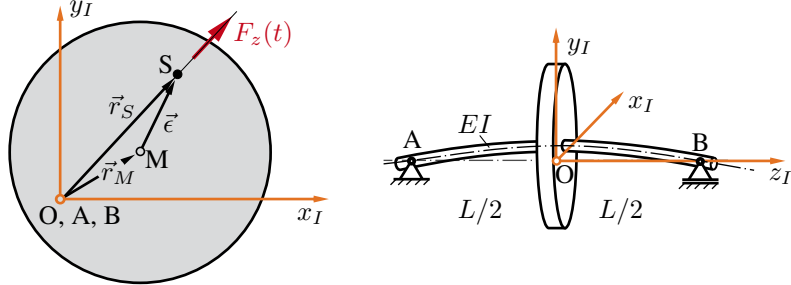


Figure 2: LAVAL rotor model, parametrization to Thümmel et al. (2015) and Roßner (2015)

eccentricity \vec{e} from the geometric center M . The coordinate $q = \vec{r}_M$ is the position of M according to the inertial bearing connection line A-B. Substituting $\vec{r}_S = \vec{r}_M + \vec{e}$, the dynamic equilibrium of the rotor can be written with mass m_r and stiffness (bearing and shaft) k_r :

$$\mathbf{M}\ddot{\vec{q}} = \sum_i \vec{F}_i = -\mathbf{K}\vec{q} + \vec{h} \quad (4)$$

$$\begin{bmatrix} m_r & 0 \\ 0 & m_r \end{bmatrix} \ddot{\vec{q}} + \begin{bmatrix} k_r & 0 \\ 0 & k_r \end{bmatrix} \vec{q} = \vec{h} \quad (5)$$

Using $\vec{h} = \vec{h}_u + \vec{h}_e + \vec{h}_s \dots$ (unbalance, external forces, seal forces, etc.) as equivalent forces. The unbalance force with rotational angular frequency Ω of the rotor results in:

$$\vec{h}_u = m_r \vec{e} \Omega^2 \begin{pmatrix} \cos(\Omega t) \\ \sin(\Omega t) \end{pmatrix} \quad (6)$$

The rotor's natural angular frequency is $\omega_{crit} = \sqrt{\frac{k_r}{m_r}}$, its critical speed.

2.2 Seal model

The seal is coupled to the rotor system using forces \vec{h}_s , eq. (3) and fig. 3. As mentioned in the introduction, the rotordynamic seal coefficients are calculated using models and simplifications of the bulk flow theory according to Black and Childs.

Black developed a simple model considering the pressure gradient and the squeeze film. The wall friction is modeled using a constant friction loss factor for both, rotor and stator. Assuming a constant circumferential fluid velocity and neglecting the inertia terms are further simplifications of this model.

Child's model differs in formulating a more complete bulk flow model. The use of semi empirical shear stress formulations for both walls gives the possibility to model different surfaces for rotor and stator (e.g. for damper seals). The fluid's inertia is taken into account to develop the circumferential velocity of the fluid element proceeding along the seal. Further, the inlet swirl (rotational fluid velocity at the seal entrance, see Diewald and Nordmann (1989)) whereas a full developed COUETTE flow is assumed here (due to the long retention time at the rotor surface ahead the seal entrance in our test rig). The detailed description of the theory and the solving process of the fluid equations is well written in Black and Jenssen (1969) and Childs (1983).

The coupled rotor-seal equation of motion is:

$$\begin{bmatrix} m_r + m_{xx} & 0 \\ 0 & m_r + m_{yy} \end{bmatrix} \ddot{\vec{q}} + \begin{bmatrix} c_{xx} & c_{xy} \\ c_{yx} & c_{yy} \end{bmatrix} \dot{\vec{q}} + \begin{bmatrix} k_r + k_{xx} & k_{xy} \\ k_{yx} & k_r + k_{yy} \end{bmatrix} \vec{q} = \vec{h} \quad (7)$$

It is simplified with the assumption of an isotropic, centered rotor using: $M = m_r + m_{xx} = m_r + m_{yy}$, $C = c_{xx} = c_{yy}$, $c = c_{xy} = -c_{yx}$, $K = k_r + k_{xx} = k_r + k_{yy}$ and $k = k_{xy} = -k_{yx}$, (Gasch et al. (2006), p.468 ff.), eq. (7) becomes:

$$\begin{bmatrix} M & 0 \\ 0 & M \end{bmatrix} \ddot{\vec{q}} + \begin{bmatrix} C & c \\ -c & C \end{bmatrix} \dot{\vec{q}} + \begin{bmatrix} K & k \\ -k & K \end{bmatrix} \vec{q} = \vec{h} \quad (8)$$

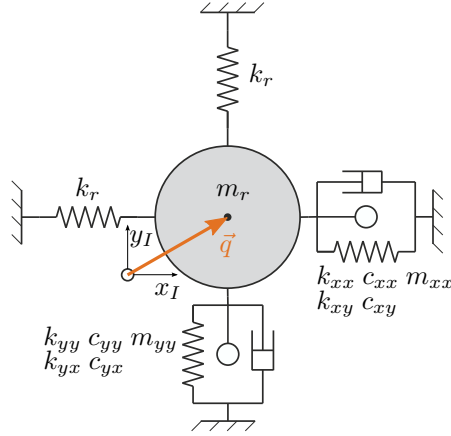


Figure 3: Simplified model: Laval rotor coupled to seals

We substitute \vec{q} and \vec{h} with complex coordinates $z = x + jy$ and $F_z = h_x + jh_y$:

$$F_z = M\ddot{z} + C\dot{z} + Kz - j(c\dot{z} + kz) \quad (9)$$

This equation is used to describe the dynamic behavior of the coupled, isotropic Laval rotor system.

3 Rotor Instability

A linear oscillation system becomes unstable if the real part of the eigenvalues of the equation of motion becomes positive. The seal coefficients, and eq. (9), are dependent on rotational speed. An eigenvalue analysis of the system for stability analysis is common; $z = \hat{z}e^{\lambda t}$ and $F_z = 0$ are used:

$$M\lambda^2 + C\lambda + K - j(c\lambda + k) = 0 \quad (10)$$

with the eigenvalues $\lambda = \delta + j\omega$:

$$M(\delta + j\omega)^2 + C(\delta + j\omega) + K - j(c(\delta + j\omega) + k) = 0 \quad (11)$$

Instability occurs for $\delta > 0$. This leads to an unstable rotor vibration at the system's first natural frequency. The onset speed of instability is determined at the transition of negative (stable) to positive (unstable) real part δ . At this point, $\delta = 0$ follows:

$$-M\omega^2 + c\omega + K + j(C\omega - k) = 0 \quad (12)$$

Separated into real and imaginary parts:

$$-M\omega^2 + c\omega + K = 0 \quad (\text{quadratic curve}) \quad \wedge \quad C\omega - k = 0 \quad (\text{linear curve}) \quad (13)$$

If both parts of eq. (13) are simultaneously satisfied, so the quadratic and linear curve have a crossing point, the onset speed of instability is reached. Because of the rotational speed dependency of the seal coefficients, this occurs above the speed limit n_{limit} . If the solution for eq. (13) can be found at a stable and safe operating condition, a prediction of n_{limit} is possible. This experimental estimation is done at the test rig and shown in the chapters below.

4 Test Rig: Description and experimental Methodology

The used test rig is shown in fig. 4. It consists of a flexible shaft ⑨ with a mass disk, the seal rotor ② and two stiff ball-bearings ⑥, driven by a servo motor ⑧. The two seals ①, clearance s , are symmetrically arranged to an injection ring ③ in the middle. The fluid is injected and flows through the gaps into the environment. An active magnetic bearing ④ is used as an actuator to excite the system at determined frequencies and whirls. The rotor's movement is detected by two eddy-current sensors ⑤ in the disk's center plain. The seal forces are measured by a piezo dynamometer ⑦ under the seal stator. Furthermore, the fluid temperature, pressure, fluid volume flow and torque are recorded. The dimensions, fluid parameters and operation conditions of the test rig are summarized by

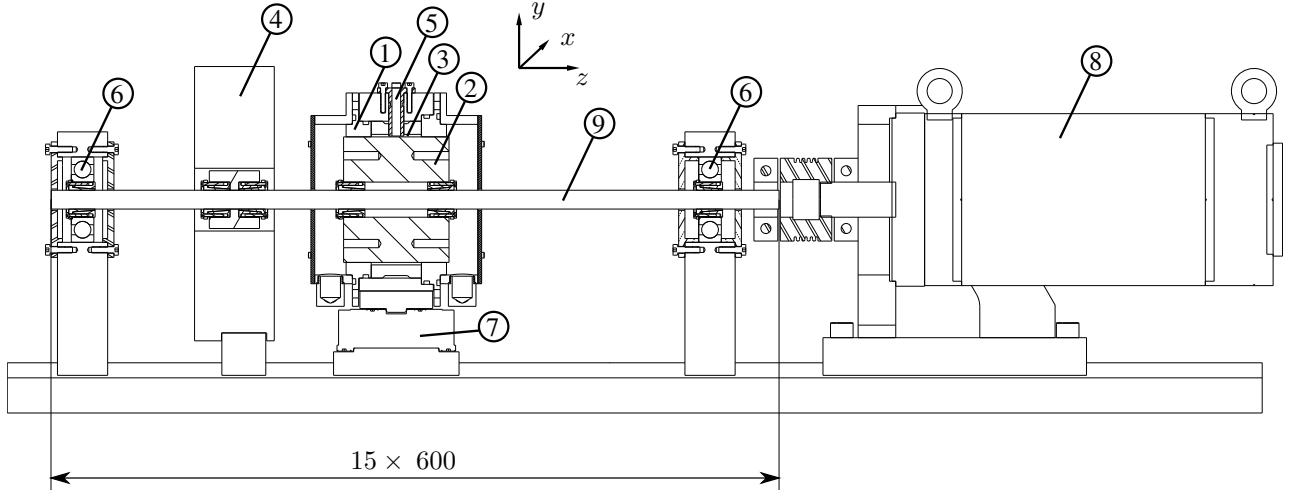


Figure 4: Seal test rig, Wagner et al. (2016)

Table 1: Test rig and fluid parameters

Name	Description	Value
s	clearance seals	0.17 mm
s_i	clearance injection ring	2 mm
n	rot. speed	0 – 6000 rpm
Ω	unbalance angular frequency	1/s
l	seal length	20 mm
l_i	length injection ring	40 mm
Δp	pressure drop at the seal	$2 \cdot 10^5$ Pa
ν	kinematic viscosity at 40°C	$4.05 \cdot 10^{-2}$ Pa · s
ρ	density at 40°C	880 kg/m ³
d	diameter seal rotor	0.1 m
m_r	mass disk	5 kg
k_r	shaft stiffness	$2.93 \cdot 10^5$ N/m
ω_0	“dry” 1.natural frequency	38.6 Hz

table 1.

Figure 5 shows the run-up response of the rotor-seal system. Compared to the seal-less system, whose behavior is like an ideal LAVAL rotor, the seal dominates the system dynamics. The unbalance response looks like an overdamped system with a first natural frequency at about half the rotational speed. Due to this, the rotor is always in an overcritical range.

This measurement result shows a strong rotational speed depending of the first natural frequency, induced by the rotational speed dependency of the rotordynamic seal coefficients $m(n), c(n), k(n)$.

5 Prediction of Rotor Instability

To predict the speed limit at the instability, two methods are shown. The first one uses the eigenvalue calculation of simulated seal coefficients. The second one is an experimental method, which uses a separation, a Co-QUAD analysis, and a zero-crossing search of the measured frequency response function $G(\omega)$ at stable operating points.

5.1 Simulation: Eigenvalue Analysis

Using the coupled equation of motion (7) and simulated seal coefficients, the eigenvalues $\lambda = \delta \pm j\omega$ can be calculated for a stability analysis according to the rotational speed. Figure 6 shows the plots of the eigenvalues of

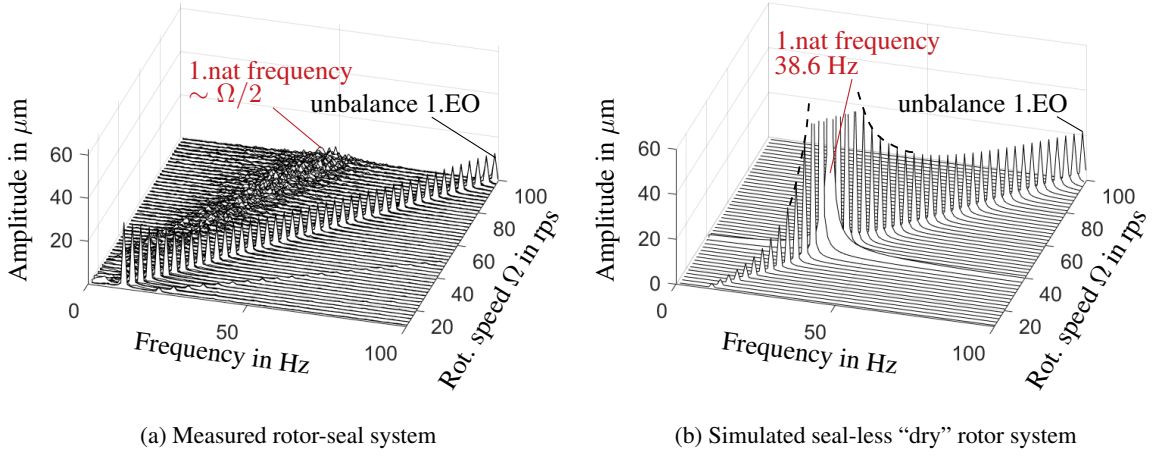


Figure 5: 3D-Campbell diagram of the test rig

the system for two implemented simulation models, Black and Jenssen (1969) and Childs (1983) model. The zero crossing of the real part δ detects the onset speed of instability to $n_{limit} = [160 \text{ and } 124] \text{ rps}$ for the two models. The imaginary part, the natural frequency, shows a strong rotational speed dependency, like the measurement in fig. 5. It is about $\Omega/2$ at the stability limit. The simulation results are just used for verification of the experimental

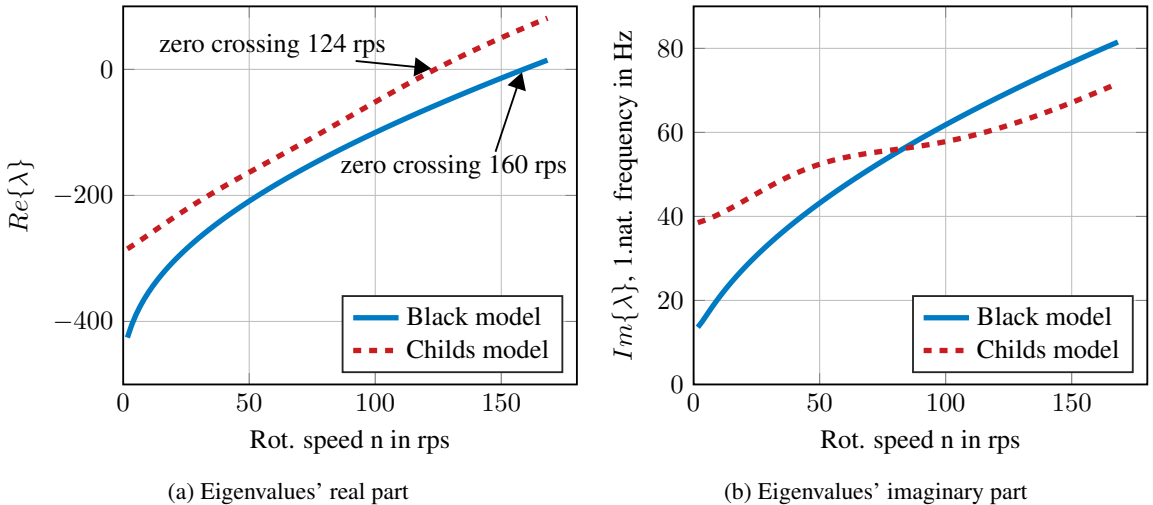


Figure 6: Eigenvalue analysis of the simulated rotor-seal system

methodology. At this point, the test rig cannot reach the instability due to rotational speed restrictions.

5.2 Experimental Methodology: Co-Quad Analysis

Using the measured rotor displacement in frequency domain $\hat{z}(\omega)$, rotor response, and the exciting force (forward whirl with AMB) $\hat{F}_z(\omega)$, the transfer function (TF) $G(\omega)$ can be calculated according to the model eq. (9):

$$G(\omega) = \frac{\hat{z}}{\hat{F}_z} = \frac{1}{-M\omega^2 + c\omega + K + j(C\omega - k)} \quad (14)$$

Separated into real and imaginary parts, in Co-QUAD form:

$$Re\{G(\omega)\} = \frac{-M\omega^2 + c\omega + K}{(-M\omega^2 + c\omega + K)^2 - (C\omega - k)^2} \quad (15)$$

$$Im\{G(\omega)\} = \frac{-C\omega + k}{(-M\omega^2 + c\omega + K)^2 - (C\omega - k)^2} \quad (16)$$

The plots of the measured TF separated into real and imaginary parts are shown in fig. 7. The solution for eq. (13) is the zero crossing of both parts, $(Re\{G(\omega)\})$ and $Im\{G(\omega)\}$, at the same frequency ω . At this point, the denominator of eq. (14) becomes zero, so the amplitude \hat{z} arises and the instability occurs.

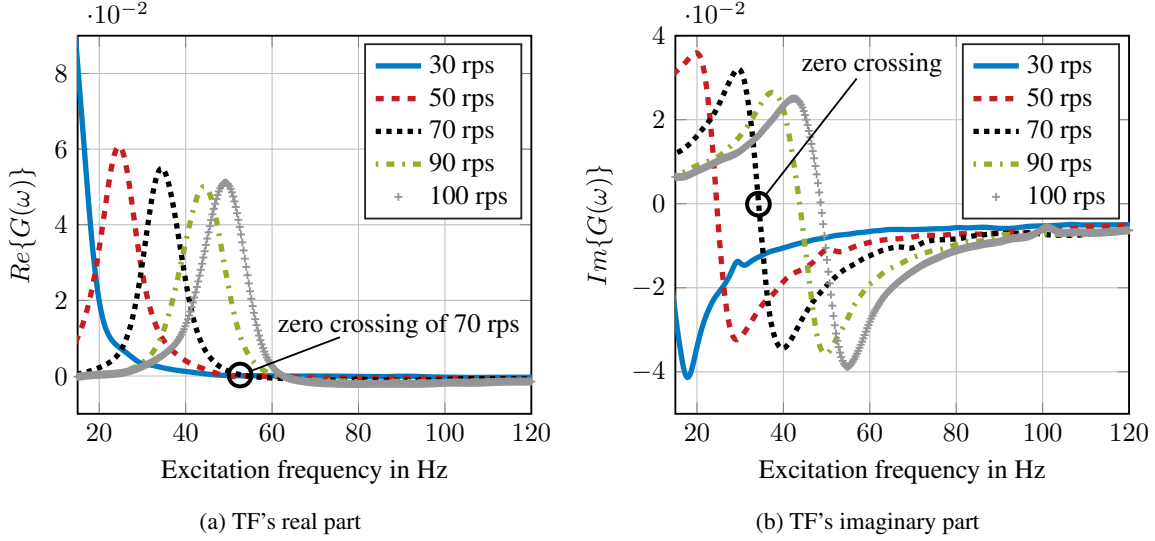


Figure 7: Measured TF $G(\omega)$ of the test rig as a CO-QUAD plot

Therefore, at constant rotational speed n , the system becomes excited in a forward whirl direction with AMB at several frequencies ω and the TF $G(\omega)$ is calculated using discrete Fourier transformation. Then, the zero crossing of the real and imaginary parts at every rotational speed must be found. These zero-crossing frequencies show almost linear behavior according to the rotational speed, see fig. 8. The zero-crossing points of the real part are the undamped natural frequency and are nearly constant. The imaginary ones increase linearly with the rotational speed.

This occurs because the tangential forces, the cross-coupled parts in the stiffness matrix, are responsible for the instability. These forces are created by shear stresses between the fluid and the wall, depending on the velocities in circumferential direction, which are almost linear to the rotational speed (COUETTE flow assumption).

When both curves cross, the denominator of eq. (14) becomes zero, eq. (13) is fulfilled and the instability occurs. A linear fit of the graphs with extrapolation, using the least squares method, provides the crossing, and the instability can be predicted to $n_{limit} = 122$ rps.

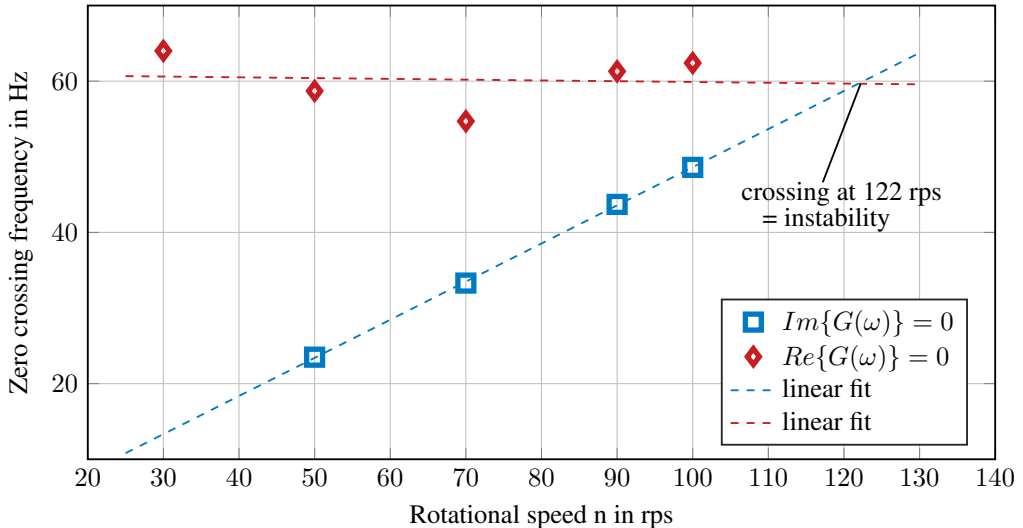


Figure 8: Zero crossing of the real and imaginary parts of the measured TF $G(\omega)$ and prediction of stability limit using linear fit and extrapolation

6 Conclusion

This article examines the influence of contactless seals on rotor systems. The rotor instability phenomenon as well as a simulative and an experimental methodology to predict the speed limit are shown. The experimental prediction method uses transfer function measurements, curve fitting and extrapolation at a safe, low-speed range. The measured transfer functions at several rotating speeds are separated into real and imaginary parts and a Co-QUAD analysis is done to identify the zero crossing frequencies. Plotting the zero points of the real and imaginary parts according to the rotational speed, one can predict the onset speed of instability. The comparison between the simulation and the experimental-based prediction shows 24% for the Black simulation model and 1.6% discrepancy for the Childs. Future works will include increasing the test rig's rotational speed until instability as well as the validation of the simulation model and the experimental prediction methodology.

7 Acknowledgment

This project is supported by the Ludwig Bölkow Campus and the Bavarian State. The good cooperation between the partners within the research project is well appreciated.

References

Bently, D. E.; Hatch, C. T.; Grissom, B.: *Fundamentals of rotating machinery diagnostics*. Bently Pressurized Bearing Press (2002).

Black, H.; Jenssen, D.: *Dynamic Hybrid Bearing Characteristics of Annular Controlled Leakage Seals*. Proceedings of the Institution of Mechanical Engineers; SAGE Publications Sage UK, London, England (1969).

Childs, D. W.: Dynamic Analysis of Turbulent Annular Seals Based On Hirs' Lubrication Equation. *ASME, Lubrication Technology*, 105, (1983), 429–436.

Childs, D. W.: *Turbomachinery Rotordynamics*. Wiley-Interscience, Dallas, TX, USA (1993).

Diewald, W.; Nordmann, R.: Dynamic Analysis of Centrifugal Pump Rotors With Fluid-Mechanical Interactions. *Journal of Vibration Acoustics Stress and Reliability in Design*, 111, 4, (1989), 370.

Gasch, R.; Nordmann, R.; Pfützner, H.: *Rotordynamik*. Springer (2006).

Gaszner, M.: *Rotordynamische Charakterisierung von Dichtungssystemen zur Anwendung in Kraftwerksturbinen*. Ph.D. thesis, Technical University of Munich (2015).

Kwanka, K.: *Dynamic Coefficients of Stepped Labyrinth Gas Seals*, vol. 122. Journal of Engineering for Gas Turbines and Power (1999).

Matsushita, O.; Fujiwara, H.: *Rotordynamics in HIL and Vibrational diagnostic technics*. v_BASE forum, Tokyo, Japan (2014).

Muszynska, A.: *Whirl and whip-Rotor/bearing stability problems*, vol. 110. Journal of Sound and Vibration (1986).

Roßner, M.: *Modellbasiertes Monitoring von Rotoren mit mehreren gleichzeitigen Fehlern*. Ph.D. thesis, Technical University of Munich (2015).

Thümmel, T.; Roßner, M.; Ulbrich, H.; Rixen, D.: *Unterscheidung verschiedener Fehlerarten beim modellbasierten Monitoring*. Proceedings SIRM2015 - 11. Internationale Tagung Schwingungen in Rotierenden Maschinen (2015).

Tsunoda, W.; Hijikata, W.; Shinshi, T.; Fujiwara, H.; Matsushita, O.: *Diagnostic experiments for stability of rotor-oil film bearing systems using radial magnetic bearing excitation*. Vibrations in Rotating Machinery (VIRM 11) Conference, Manchester, UK. (2016).

Wagner, C.; Berninger, T.; Thümmel, T.; Rixen, D.: *Rotordynamic Effects in Turbopumps for Space Propulsion Systems - First Minimal Models and Experimental Validation*. Space Propulsion 2016 Conference, 3AF, Rome, Italy (2016).

Zutavern, Z. S.: *Identification of Rotordynamic Forces in a Flexible Rotor System Using Magnetic Bearings Identification of Rotordynamic Forces in a Flexible Rotor System Using Magnetic Bearings*. Ph.D. thesis, Texas (2006).

Address: ¹ Chair of Applied Mechanics, Technical University of Munich, Boltzmannstr. 15, 85748 Garching
email: {c.wagner, t.berninger, thuemmel, rixen}@tum.de

² Department of Mechanical Engineering, Tokyo Institute of Technology, 4259, Nagatsuta-cho, Midori-ku, 226-8503 Yokohama, Japan
email: tsunoda.w.aa@m.titech.ac.jp

³ Department of Mechanical Engineering, National Defense Academy, 1-10-20 Hashirimizu, 239-8686 Yokosuka, Japan
email: osami@tiger.odn.ne.jp

Stability Analysis of parameter-excited linear Vibration Systems with Time Delay, using the Example of a Sheetfed Offset Printing Press

S. Neeb, N. Norrick

This article describes stability studies on parameter-excited linear vibration systems with time delay. A method for stability analysis is presented. Therefore, the transcendental transmission element of the time delay e^{-st} is approximated as an all-pass element with the rational transfer function by means of the so-called Padé approximation. The system can be represented in the state space and the methods of the Floquet theory can also be applied to the system with approximated time delay. The process can be implemented without great effort in a standardized simulation environment such as MATLAB/SIMULINK, whereby existing models and methods can be reused. The suitability of the method is shown in the well-known example of the Mathieu differential equation with time delay. Variations between different solvers and approximation orders are described. An extended view and the transfer to an industrial application take place with the example of the drive of a sheetfed offset printing machine. The relevant vibration system is represented by an oscillator with several degrees of freedom. The belt, which couples the degrees of freedom of the drive motor and the machine, leads to a periodic (harmonic) parameter excitation of the system due to its inhomogeneous nature. The speed and position control of the drive motor (PI controller) is associated with a time delay, resulting in a system of the type described above.

1 Introduction

Sheetfed offset printing machines print individual sheets of paper that are picked up from a pile in the feeder and placed on a pile after they have passed through the machine. At present, production speeds of up to 18,000 sheets/hour (corresponding to 5 sheets/second) can be achieved. The Heidelberg Speedmaster XL162-6 + L is a modern large-format press (sheet format up to 1,210 mm x 1,620 mm) with six printing units and a varnishing unit.

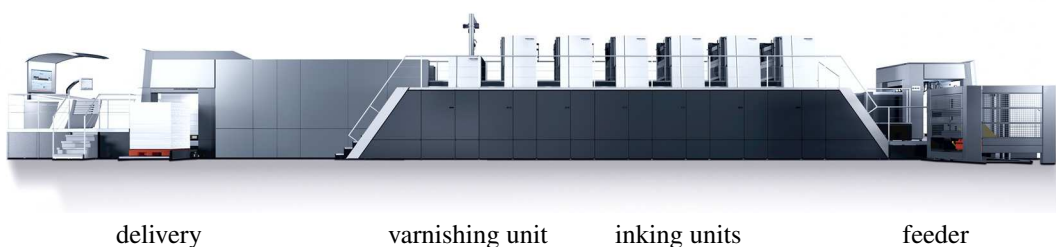


Figure 1: Heidelberg Speedmaster XL162-6 + L sheetfed offset printing press with six inking units and one varnishing unit. The paper sheets pass through the machine from the feeder (right) to the delivery (left).

The hand-over of sheets within the machine takes place by an interconnection of cylinders. The individual cylinders are equipped with grippers which hold the sheet on the cylinder. During the transfer of the sheet from one to the next cylinder, the grippers open and close at defined times. The grippers are controlled by cam drives. All cylinders are coupled by a continuous gear train, which is connected to the electric drive motor by means of a belt drive. The drive control of the machine takes place via a controller with P and I components, which is implemented on a central control unit.

The printing quality is essentially influenced by the position of the individual color separations relative to one another, the so-called register (Kipphan, 2000). Deviations in the position of a few μm result in recognizable color shifts and thus also in a reduction in print quality. Vibrations of the drive train result in relative motions of the

cylinders which then also affect the register. The frequencies and the order of the machine vibrations are also found in the register fluctuation on the sheet.

In operation, the machine is excited by a variety of interfering mechanisms to vibrate. In addition to the reaction moments of the cam mechanisms for the control of the grippers, torque fluctuations from the inking unit, tolerance-related residual moments of the cylinders and moments from the belt drive of the main drive arise. As drive belts, ribbed belts are used, which are constructed from a material composite. Due to manufacturing tolerances, the mechanical parameters of the belt fluctuate over the length of the belt, causing the drive train to vibrate (Langer, 2013; Dresig and Fidlin, 2013). With respect to printing machines, such vibrations were examined by Messer (2012). Furthermore, it is known from the experience that in many cases the time delay in the control units can not be neglected. The time delay has an effect on the machine vibrations such as negative damping.

In order to gain a better understanding of the acting effects as a result of excitation by the belt drive, a model is built, which makes it possible to study the machine vibrations including the parametric system excitation and time delay. This article focuses on the stability analysis of the system. The modeling and evaluation are realized in the program environment of MATLAB/SIMULINK.

The investigations are carried out on a sheetfed offset printing machine Heidelberg Speedmaster XL162-6 + L, as shown in Fig. 1.

2 Basic System Modeling

Mechanical systems, whose descriptive parameters are time-dependent, are important in many technical applications. The fluctuations in the mechanical parameters of the drive belt described in the previous section can also be modeled by time-dependent system coefficients (see also Messer (2012) or Dresig and Holzweißig (2011)). Further examples of this can be found in the case of unevenly translated mechanisms, rotors, gear transmissions, and other fast-running traction drives (Dresig and Holzweißig, 2011; Dresig and Fidlin, 2013). In the present case of the main drive of a sheetfed offset printing press, preliminary investigations were presented in Messer (2012).

As part of the heteronomous vibrational systems, systems with time-dependent coefficients are referred to as parameter-excited or rheonomous systems (Deutsches Institut für Normung e.V., 2000). They can be represented in their general form as a $2N$ -dimensional Ordinary Differential Equation (ODE) system with time-dependent coefficients

$$\dot{\mathbf{y}}(t) = \mathbf{A}(t)\mathbf{y}(t). \quad (1)$$

Hierin, $\mathbf{A}(t) \in \mathbb{R}^{2N \times 2N}$ is the system matrix and $\mathbf{y}(t) \in \mathbb{R}^{2N}$ the state vector.

By means of an additional time delay τ , occurring for example, in the case of closed-loop systems for which the time delay in the information processing system can not be neglected, Eq. (1) expands with the system matrix $\mathbf{B}(t) \in \mathbb{R}^{2N \times 2N}$ to

$$\dot{\mathbf{y}}(t) = \mathbf{A}(t)\mathbf{y}(t) + \mathbf{B}(t)\mathbf{y}(t - \tau). \quad (2)$$

Systems with time delay are represented by Delayed Differential Equations (DDE). In the case of an assumed periodic time dependency, it also holds that

$$\mathbf{A}(t) = \mathbf{A}(t + T) \quad \text{and} \quad \mathbf{B}(t) = \mathbf{B}(t + T). \quad (3)$$

The investigation of the stability is an important point in the study of the above mentioned applications. In the case of heteronomous ODEs, as occur in the mechanical systems mentioned, the parameter excitation can cause the system to have destabilizing resonances (e.g. Dohnal (2012); Dresig and Holzweißig (2011) or Gasch and Knothe (1989)). They can be calculated according to

$$\omega_n^{k,l} = \frac{|\omega_k \pm \omega_l|}{n}, \quad k, l = 1, 2, \dots \quad (4)$$

Here, ω_k and ω_l denote the k th and l th eigenfrequencies of the time invariant system, and n the order of the

resonance. It is called parameter resonance for $k = l$ and of parameter combination resonances for $k \neq l$.

In the case of autonomous DDEs as they can be found for example in controlled systems, the time delay results in a phase shift, which increases continuously with increasing frequency and can cause instability (Lunze, 2012).

3 Stability Analysis Methods

The stability studies of parameter-excited systems without a time delay Eq.(1), ie of heteronomous ODEs, can be carried out with the help of the so-called Floquet theory (see, e.g. Dohnal (2012); Gasch and Knothe (1989) or Tagawa (1967)). Based on a set of $2N$ linearly independent initial conditions $\mathbf{y}(0)_1, \mathbf{y}(0)_2, \dots, \mathbf{y}(0)_{2N}$, the monodromy matrix $\Phi(T, t_0 = 0)$ is obtained by numerical integration of the system equations (1) over the period T . Based on the eigenvalues μ_n of the monodromy matrix, the stability of the system can be carried out. The system is asymptotically stable if all $2N$ eigenvalues of the monodromy matrix are less than one in amount, and thus lie inside the unit circle in the complex plane.

For autonomous DDEs, see Eq. (2) with $(\mathbf{A}(t), \mathbf{B}(t)) = (\mathbf{A}_0, \mathbf{B}_0)(\text{const})$, the stability statement can be made in analogy to autonomous ODEs, see Eq. (1) with $\mathbf{A}(t) = \mathbf{A}_0(\text{const})$, by means of the eigenvalues of the characteristic equation (Gu and Niculescu, 2003; Wu et al., 2010). The stability is asymptotically given if all eigenvalues λ_n have a negative real part and thus lie in the left half-plane of the complex plane. In contrast to autonomous ODEs, for autonomous DDEs, the characteristic equation $\det(\lambda \mathbf{I} - \mathbf{A}_0 - \mathbf{B}_0 e^{-\lambda \tau})$ is a transcendental equation, which has an infinite number of solutions because of the term $e^{-\lambda \tau}$. For a numerical stability analysis, it is necessary to find a suitable approximation for $e^{-\lambda \tau}$ to obtain a finite number of solutions. Thus, in control engineering, rational functions are often used (Lunze, 2012). One possible way to get a suitable model is the so-called Padé approximation (see, e.g. Lam and Chung (1992); Lam (1996); Baratchart et al. (1995)). In Gu and Niculescu (2003), a comprehensive overview of further procedures and the handling of time delay in the context of stability considerations and the control of systems is given (see also Sipahi and Olgac (2006); Sipahi et al. (2011) or Wu et al. (2010)). The functionalities that MATLAB offers in handling systems with time delays are explained in Gumussoy et al. (2012).

In the case of heteronomous DDEs the Floquet theory can be extended, the result is a monodromy operator of infinite dimension (Insperger and Stépán, 2003; Tweten et al., 2012). The stability of heteronomous DDEs can be determined by various highly efficient discretization methods, which have been developed in recent years. The general objective of the discretization methods is to approximate the monodromy operator of infinite dimension by a monodromy matrix of finite dimensions. The semi-discretization method develops the DDE into a system of piecewise autonomous ODE (Insperger and Stépán, 2002a, 2004; Insperger et al., 2004). The so-called temporal finite element method and, in particular, the transition to the so-called spectral element method are presented in Khasawneh and Mann (2011), see also (Khasawneh et al., 2010; Tweten et al., 2012; Ahsan et al., 2015a) or (Ahsan et al., 2015b). While the temporal finite element method is a piecewise approximation of the DDE that has the full flexibility of a spatial finite element method, the so-called collocation method is a global approximation over the DDE domain (Khasawneh et al., 2010), see also (Khasawneh and Mann, 2011; Tweten et al., 2012; Butcher and Bobrenkov, 2009) or (Breda et al., 2015).

The described methods for the stability analysis of heteronomous DDEs are numerically highly efficient, but they are also complex and usually only to be implemented with some effort in an existing methodology. In the industrial context it is necessary to use standardized methods and simulation environments. MATLAB/SIMULINK is such a simulation environment. There is the possibility to model systems by graphical blocks. MATLAB/SIMULINK is used in particular for time domain simulation and for controller design. If a mechanical system and its controller is already modeled in MATLAB/SIMULINK, it is desirable to be able to carry out further investigations, such as the stability analysis, also in this simulation environment. For this reason, a method for stability analysis on heteronomous DDEs is presented in this thesis, which can be integrated into the existing methodology under MATLAB/SIMULINK without much effort.

In the method described here, the time delay is approximated by a rational function (see also (Lunze, 2012)). Thus the heteronomous DDE (2) becomes a heteronomous ODE

$$\dot{\mathbf{y}}(t) = \mathbf{A}(t)\mathbf{y}(t) + \mathbf{B}(t)\mathbf{C}_0\mathbf{y}(t), \quad (5)$$

where the approximated properties of the time delay are represented by \mathbf{C}_0 . The dimension of the system increases as a result of the approximation in Eq. (1) or Eq. (2). The stability of the so approximated system can then be

determined for various parameter combinations according to the above-described Floquet theory.

The so-called Padé approximation is a common method for obtaining a suitable approximation of the propagation delay (see, e.g. Lam and Chung (1992); Lam (1996); Baratchart et al. (1995)). By applying the Laplace transformation, the time delayed function $\mathbf{y}(t - \tau)$ can be converted into the frequency domain

$$\mathcal{L}\{\mathbf{y}(t - \tau)\} = \mathbf{Y}(s) e^{-s\tau}. \quad (6)$$

The aim of the approach is the approximation of the transcendental element $e^{-s\tau}$ by a rational function of the type

$$R_{K,L}(s\tau) = P_{K,L}(s\tau)/Q_{K,L}(s\tau), \quad \text{with} \quad \deg P_{K,L} = K, \quad \deg Q_{K,L} = L. \quad (7)$$

This is a Padé approximation of the type (K,L) . According to e.g. Baratchart et al. (1995), explicit formulations are available for the numerator polynomial $P_{K,L}(s\tau)$ and the denominator polynomial $Q_{K,L}(s\tau)$ with

$$P_{K,L}(s\tau) = \sum_{m=0}^K \frac{(K+L-m)! K!}{(K+L)! m! (K-m)!} (-s\tau)^m, \quad Q_{K,L}(s\tau) = \sum_{m=0}^L \frac{(K+L-m)! L!}{(K+L)! m! (L-m)!} (s\tau)^m. \quad (8)$$

If the time delay is approximated in this way, Eq. (5) has the dimension $2N + L$ and the above-described steps can be applied to perform the stability study on heteronomous ODE according to the Floquet theory. The monodromy matrix $\Phi(T, t_0 = 0)$ returns $2N + L$ eigenvalues μ_n , by which the stability statement is made. This approach can also be found in Tagawa (1967).

The described method is implemented in MATLAB/SIMULINK. In order to prove its suitability, stability studies are carried out on a known example, the delayed Mathieu differential equation. Furthermore, various numerical solvers and approximation orders are examined.

As a further application example, the transfer to the sheetfed offset printing machine Heidelberg Speedmaster XL162-6 + L described in section 1 is carried out. The influence of various parameters, which in particular concern the control of the machine, is investigated.

4 Examples

4.1 Delayed Mathieu Differential Equation

The delayed Mathieu differential equation is one of the simplest equations, which maps the two properties of the parameter excitation and the time delay, and still has a practical relevance (Stépán and Insperger, 2006)

$$\ddot{q}(t) + a_1 \dot{q}(t) + (a_2 + a_3 \cos(\Omega t)) q(t) = b q(t - \tau). \quad (9)$$

This differential equation can be interpreted as the system equation of a mechanical oscillator with one degree of freedom and position control.

On the left side of this DDE are the system parameters; a_1 is the damping and a_2 and a_3 are the mean value and the amplitude of the harmonic stiffness, respectively. On the right is the controller parameter b , which amplifies the τ delayed signal. For various combinations of the coefficients a_1 , a_2 , a_3 and b , there are analytical and numerical solutions in the literature. Therefore, this example is excellent for verifying the applicability of the method described in section 3.

4.1.1 System with Parameter Excitation, without Time Delay ($a_3 \neq 0, b = 0$) (heteronomous ODE)

The stability map of Eq. (9) with $b = 0$ has been calculated for the first time by Strutt and Ince. Representations can be found, for example, in Insperger and Stépán (2002b); Magnus and Popp (1997) or Klotter (1978), where Klotter (1978) as well as Magnus and Popp (1997) provide detailed technical discussions.

The following Fig. 2 shows the computed stability map, stable areas are marked 'S' herein.

Since the system (9) does not have a delay time with $b = 0$, a Padé approximation is not performed. The MATLAB/SIMULINK block to approximate the time delay is a constant of the magnitude one after Eq. (7) and Eq. (8).

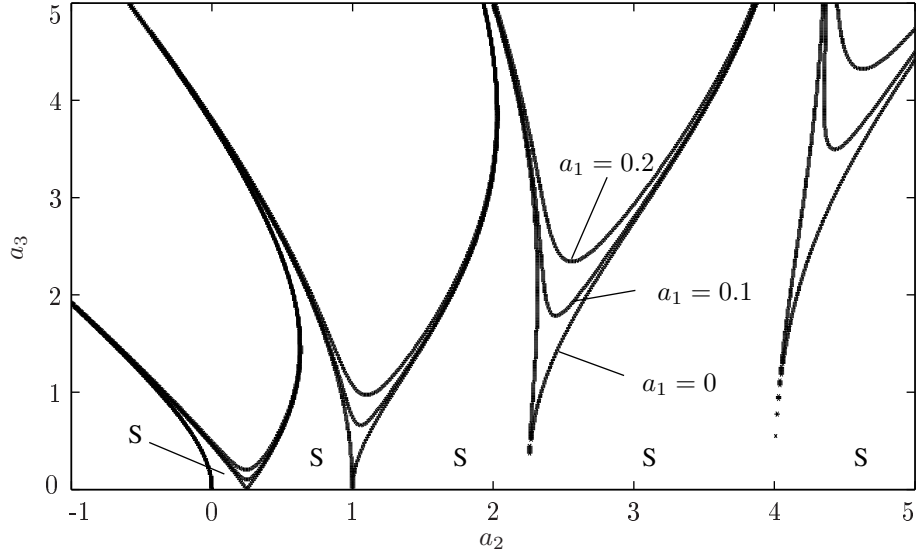


Figure 2: Stability map in the (a_2, a_3) -plane with $b = 0$ for $\Omega = 1$, $\tau = 2\pi$, Padé type $(0, 0)$, solver `ode23tb`.

The accordance of the results shown in Fig. 2 with those found in the literature (Insperger and Stépán (2002b); Magnus and Popp (1997) or Klotter (1978)) is good. Only the narrow slopes of the unstable areas at $a_2 = 2.25$ and $a_2 = 4$ are not found through to the abscissa.

Since the stability maps are determined by numerical integration, the quality of the result is partly dependent on the solver used. MATLAB/SIMULINK offers two classes of solvers, with constant step size and with variable step size. Compared with constant-step solvers, variable-step equilibrators provide greater stability, whereas the cost per unit of time to be calculated is usually greater (The Mathworks, Inc., 2008). Fig. 3 shows a comparison of a section of the stability map shown in Fig. 2 for various solvers.

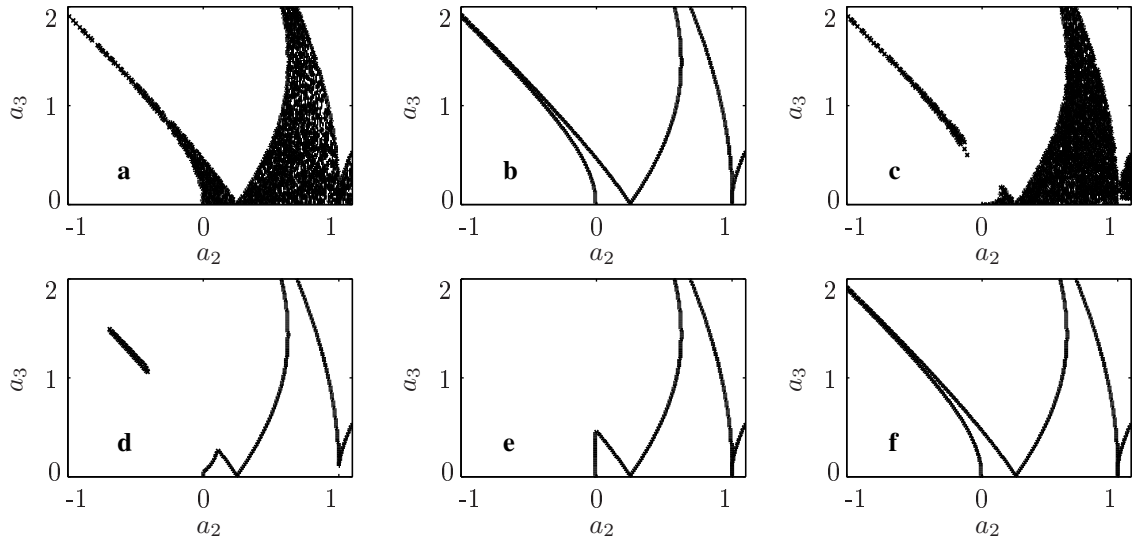


Figure 3: Stability map in the (a_2, a_3) -plane with $b = 0$ for $\Omega = 1$, $\tau = 2\pi$, Padé type $(0, 0)$, solver: **a)** `ode45`, **b)** `ode23`, **c)** `ode113`, **d)** `ode15s`, **e)** `ode23t`, **f)** `ode23tb`.

There are clear differences in the results shown in Fig. 3. The solvers `ode23` and `ode23tb` provide the best results

as can be seen clearly. The maximum time step, which the solver is limited to, also has a strong influence on the quality of the results. A reduction of the maximum time step leads to better results, an increase to poorer results. The results shown in Fig. 3 are generated with a maximum time step size of $5 \cdot 10^{-4} T$, where T is the cycle time. Since the solvers ode23 and ode23tb perform equally well, with respect to robustness of results against higher time steps and computational time, and both provide slight numerical damping, the decision is arbitrary. Therefore, the simulations are performed using the equation solver ode23tb. The special features of the individual solvers can be found in the MATLAB/SIMULINK help (The Mathworks, Inc., 2008).

4.1.2 System without Parameter Excitation, with Time Delay ($a_3 = 0, b \neq 0$) (autonomous DDE)

An autonomous oscillator with time delay follows from Eq. (9) if $a_3 = 0$ is set. In this case, the stability map is shown in the (a_2, b) -plane. For an undamped oscillator with $a_1 = 0$, there is an analytical solution after Insperger and Stépán (2002b). The boundary curves of the stability map are straight lines that have the slope ± 1 for $\Omega = 1$ and $\tau = 2\pi$. They intersect the abscissa in the points $(p/2)^2$, $(p = 1, 2, \dots)$.

The numerical solution according to the described method with a Padé approximation of the time delay of the type (10, 10) is shown in Fig. 4.

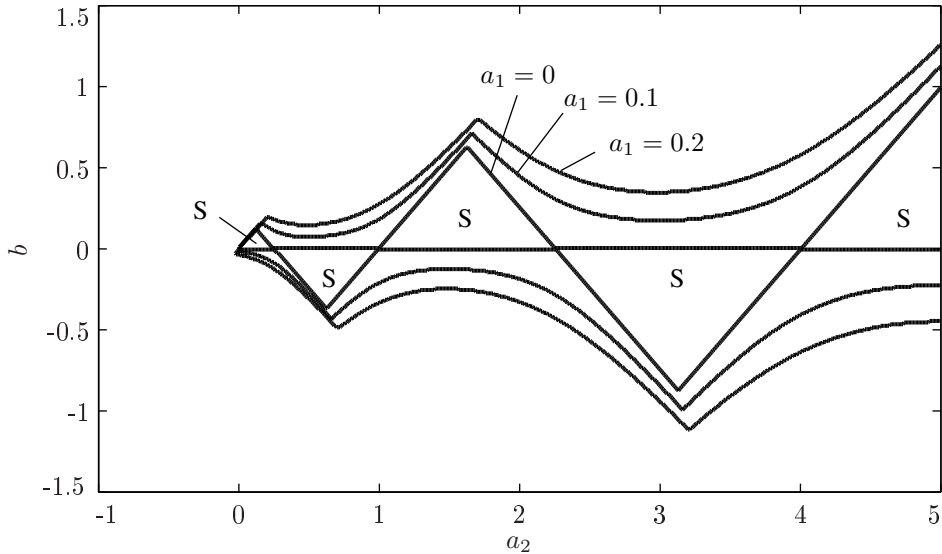


Figure 4: Stability map in the (a_2, b) -plane with $a_3 = 0$ for $\Omega = 1, \tau = 2\pi$, Padé type (10, 10), solver ode23tb.

The stability map in the (a_2, b) -plane clearly shows the described properties of the analytical solution for $a_1 = 0$. The boundary curves with the slope ± 1 intersect the abscissa as mentioned in the points $(p/2)^2$, $(p = 1, 2, \dots)$, see also the solution in the (a_2, a_3) -plane (Fig. 2).

The quality of the approach of approximating the transcendental function $e^{-s\tau}$ with the Padé approximation, described by Eq. (8) and Eq. (7), is strongly dependent on the order of the approximation, i.e. the type. For this example, the Padé approximations converge from type (10, 10), see also Fig. 5.

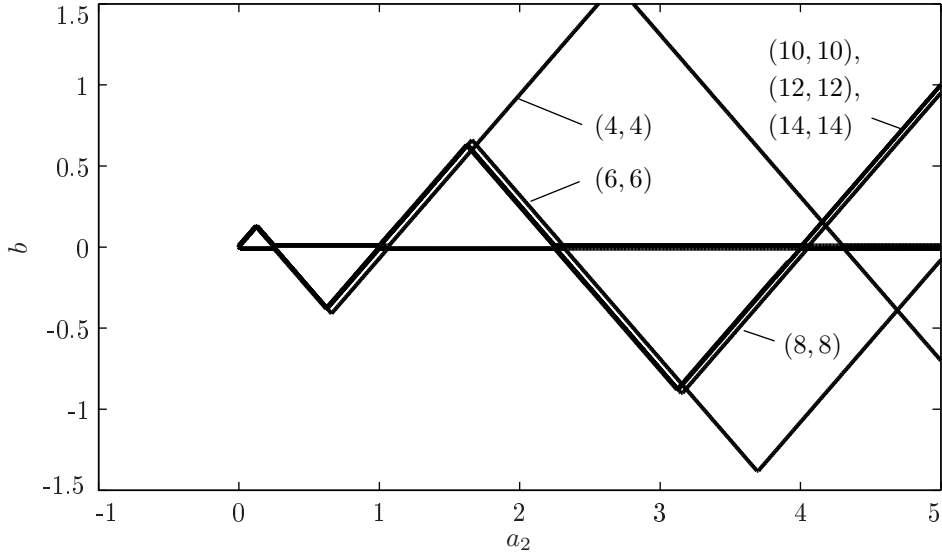


Figure 5: Stability map in the (a_2, b) -plane with $a_3 = 0$ for $\Omega = 1$, $\tau = 2\pi$, Padé type see marking, solver ode23tb.

4.1.3 System with Parameter Excitation, with Time Delay ($a_3 \neq 0, b \neq 0$) (heteronomous DDE)

The generalization or the combination of the two previous cases represents the solution of the heteronomous DDE. Therefore, both parameters a_3 and b are not equal to zero. In Fig. 6 the solutions for various values a_3 are shown in the (a_2, b) -plane. Again, the consistency with already published data is very good (e.g. Insperger and Stépán (2003)).

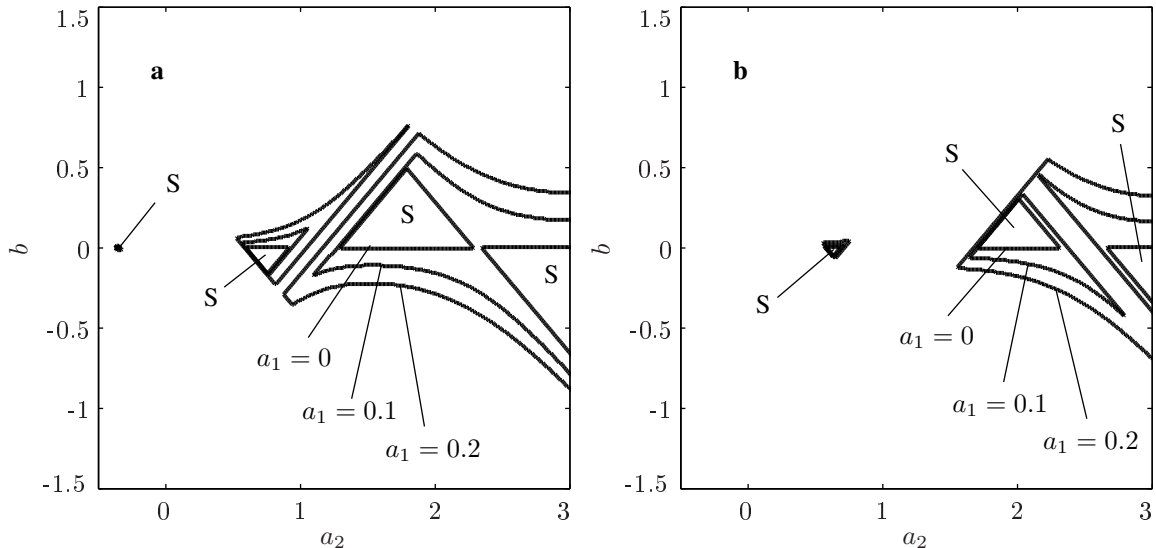


Figure 6: Stability map in the (a_2, b) -plane with **a**) $a_3 = 1$, **b**) $a_3 = 2$ for $\Omega = 1$, $\tau = 2\pi$, Padé type (10,10), solver ode23tb.

For all of the cases described above, the data obtained with the described method very well agree with known and published data. The approach of approximating the transcendental function $e^{-s\tau}$ with a rational function, the so-called Padé approximation, can thus be applied to convert a heteronomous DDE into a heteronomous ODE. The stability of this heteronomous ODE can then be determined by applying the Floquet theory. The procedure can easily

be integrated into the simulation environment of MATLAB/SIMULINK and thus represents a process that can be implemented in an industrial context.

4.2 Sheetfed Offset Printing Machine (system with N degrees of freedom)

The actual focus of the investigations is, as described above, on the stability analysis of the drive of the Heidelberg Speedmaster XL162-6 + L sheetfed offset printing press. This is a sheetfed offset printing machine with six printing units and a varnishing unit. In the course of modeling, the MATLAB/SIMULINK model of the actual printing press is reduced to an oscillator with two modal degrees of freedom, ie the rigid-body mode an the first flexible mode, and then coupled to the drive. The system equation

$$\mathbf{M}_S \ddot{\mathbf{q}}(t) + \mathbf{D}_S \dot{\mathbf{q}}(t) + (\mathbf{K}_S + \epsilon \cos(\Omega_{PE} t) \mathbf{K}_{PE}) \mathbf{q}(t) = \mathbf{G}_I \dot{\mathbf{q}}(t - \tau) + \mathbf{G}_P \mathbf{q}(t - \tau) \quad (10)$$

contains with \mathbf{M}_S , \mathbf{D}_S and \mathbf{K}_S the mass, damping and stiffness matrices of the mechanical system. In addition, $\epsilon \cos(\Omega_{PE} t) \mathbf{K}_{PE}$ describes the parameter excitation and $\mathbf{G}_I \dot{\mathbf{q}}(t - \tau) + \mathbf{G}_P \mathbf{q}(t - \tau)$ is the time delayed speed and position control. For the parameter excitation \mathbf{K}_{PE} is the stiffness matrix of the drive belt and $\epsilon \cos(\Omega_{PE} t)$ describes the harmonic oscillation of the belt stiffness. For the control matrices, it is furthermore limited that they are composed of scalar gain factors g_I and g_P as well as coupling matrices \mathbf{T}_I and \mathbf{T}_P which contain only zeros and ones

$$\mathbf{G}_I = g_I \mathbf{T}_I, \quad \mathbf{G}_P = g_P \mathbf{T}_P. \quad (11)$$

Eq. (10) can be easily converted into Eq. (2) and by applying the Padé approximation it can be converted further into Eq. (5).

The result of the stability consideration by varying the machine speed ν and the relative variation of the belt stiffness ϵ for various gains of the speed control g_I and time delays τ is shown in Fig. 7.

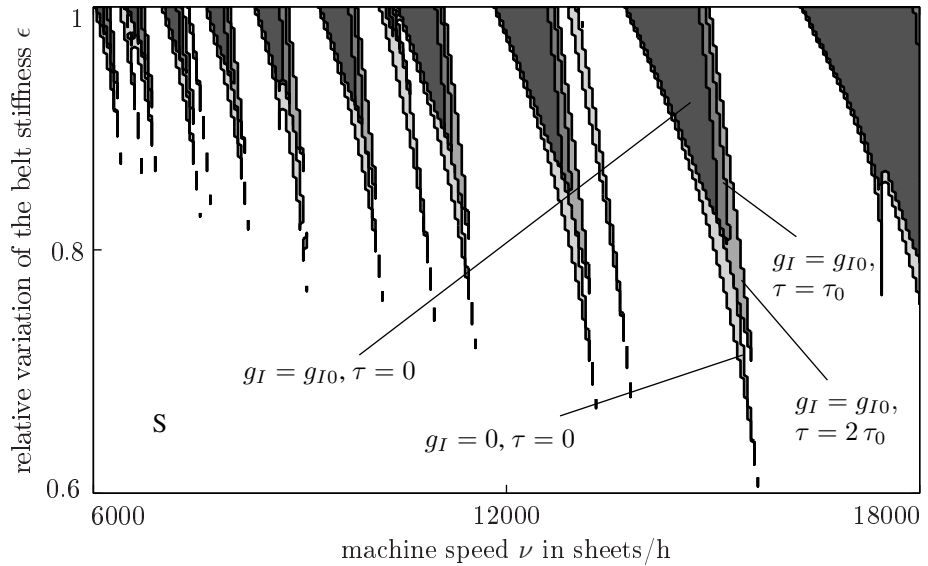


Figure 7: Stability map in the (ν, ϵ) -plane with $\Omega_{PE} = \Omega_{PE0}$, $g_p = g_{P0}$, $\tau = \tau_0$, Padé type (10, 10), solver ode23tb.

It can be seen that the system can be stabilized by the additional damping due to the speed-proportional regulation. The system with $g_I = 0$ and $\tau = 0$ serves as a reference. The time delay principally acts as a negative damping, which can be clearly seen by the increase in the unstable ranges as a result of an increasing time delay. Furthermore, the time delay still shows a different effect, the unstable areas are slightly shifted towards the higher machine speeds compared to the reference system. Overall, it can also be seen that instability occurs only at very large amplitudes of the parameter excitation ($\epsilon > 0.6$).

5 Summary and Conclusions

In this thesis, a method has been proposed which allows heteronomous DDEs to be converted into heteronomous ODEs via the Padé approximation. The heteronomous ODEs can be modeled without great effort in a standardized simulation environment such as MATLAB/SIMULINK. Using the Floquet theory, the stability maps can be calculated by numerical integration of the system equations. The suitability of the method was shown in the well-known example of the delayed Mathieu differential equation. Differences and influences of various solvers and approximation orders were investigated and illustrated. Finally, the transfer of the method to a practical example was carried out and the stability behavior of a sheetfed offset printing press was examined. The tests were carried out as a function of the machine speed and the relative variation of the stiffness of the drive belt for various system configurations. It is shown that time delay increases the unstable areas of the stability map because it has the effect of a negative damping.

References

Ahsan, Z.; Sadath, A.; Uchida, T.; Vyasarayani, P., C. Galerkin approximations with embedded boundary conditions for retarded delay differential equations. *Mathematical and Computer Modelling of Dynamical Systems*, 21, 6, (2015a), 560–572.

Ahsan, Z.; Uchida, T.; Vyasarayani, P., C. Galerkin-arnoldi algorithm for stability analysis of time-periodic delay differential equations. *ASME Journal of Nonlinear Dynamics*, 82, 4.

Baratchart, L.; Saff, B., E. Wielonsky, F.: Rational interpolation of the exponential function. *Canadian Journal of Mathematics*, 47, 6, (1995), 1181–1147.

Breda, D.; Maset, S.; Vermiglio, R.: *Stability of Linear Delay Equations*. Springer-Verlag, Heidelberg, Dodrecht, London, New York (2015).

Butcher, A., E. Bobrenkov, A., O. The chebyshev spectral continuous time approximation for periodic delay differential equations. In: *Proceedings of IDETC/CIE 2009 the ASME 2009 International Design Engineering Technical Conferences & Computers and Information in Engineering Conference*, San Diego, USA (2009).

Deutsches Institut für Normung e.V.: *DIN 1311-1: Schwingungen und schwingungsfähige Systeme. Teil 1: Grundbegriffe, Einteilung* (in German). Berlin (Feb. 2000).

Dohnal, F.: *A contribution to the mitigation of transient vibrations. Parametric anti-resonance: theory, experiment and interpretation*. Habil., Technische Universität Darmstadt (2012).

Dresig, H.; Fidlin, A.: *Schwingungen mechanischer Antriebssysteme* (in German). Springer-Verlag, Heidelberg, Dodrecht, London, New York, 3 edn. (2013).

Dresig, H.; Holzweißig, F.: *Maschinendynamik* (in German). Springer-Verlag, Heidelberg, Dodrecht, London, New York, 10 edn. (2011).

Gasch, R.; Knothe, K.: *Strukturdynamik* (in German), vol. 2. Springer-Verlag, Berlin, Heidelberg, New York (1989).

Gu, K.; Niculescu, S.-I.: Survey on recent results in the stability and control of time-delay systems. *Transactions of ASME, Journal of Dynamic Systems, Measurement, and Control*, 125, 2, (2003), 158–165.

Gumussoy, S.; Eryilmaz, B.; Gahinet, P.: Working with time-delay systems in matlab. In: *Proceedings of the 10-th IFAC Workshop on Time Delay Systems*, Boston, USA (2012).

Insperger, T.; Stépán, G.: Semi-discretization method for delayed systems. *International Journal for Numerical Methods in Engineering*, 55, (2002a), 503–518.

Insperger, T.; Stépán, G.: Stability chart for the delayed mathieu equation. In: *Mathematical, Physical and Engineering Sciences*, 458, pages 1989–1998 (2002b).

Insperger, T.; Stépán, G.: Stability of the damped mathieu equation with time delay. *Transactions of ASME, Journal of Dynamic Systems, Measurement, and Control*, 125, (2003), 166–171.

Insperger, T.; Stépán, G.: Updated semi-discretization method for periodic delay-differential equations with discrete delay. *International Journal for Numerical Methods in Engineering*, 61, (2004), 117–141.

Insperger, T.; Stépán, G.; Turi, J.: Comparison of zeroth- and first-order semi-discretizations for the delayed mathieu equation. In: *Proceedings of the 43rd IEEE Conference on Decision and Control*, Atlantis, Bahamas (2004).

Khasawneh, A., F. Mann, P., B. A spectral element approach for the stability of delay systems. *International Journal for Numerical Methods in Engineering*, 87, (2011), 566–592.

Khasawneh, A., F. Mann, P., B. Butcher, A., E. Comparison between collocation methods and spectral element approach for the stability of periodic delay systems. In: *Proceedings of the 9th IFAC Workshop on Time Delay Systems*, Prag, Czech Republic (2010).

Kipphan, H.: *Handbuch der Printmedien: Technologien und Produktionsverfahren* (in German). Springer-Verlag, Berlin, Heidelberg, New York (2000).

Klotter, K.: *Technische Schwingungslehre* (in German), vol. 1 of 3. Springer-Verlag, Berlin, Heidelberg, New York (1978).

Lam, J.: Model reduction of delay systems using pade approximants. *International Journal of Control*, 52, 2, (1996), 377–391.

Lam, J.; Chung, W., K. Error bounds for padé approximations of e^{-z} on the imaginary axis. *Journal of Approximation Theory*, 69, (1992), 222–230.

Langer, P.: Bestimmung der Übertragungsgüte von Riementrieben (in German). *VDI-Berichte*, 2197, (2013), 129–140.

Lunze, J.: *Regelungstechnik* (in German), vol. 1 of 9. Springer-Verlag, Heidelberg, Dodrecht, London, New York (2012).

Magnus, K.; Popp, K.: *Schwingungen: eine Einführung in physikalische Grundlagen und die theoretische Behandlung von Schwingungsproblemen* (in German). B. G. Teubner, Stuttgart, 5 edn. (1997).

Messer, M.: Parametrically excited torsional vibrations in a sheet-fed offset printing machine. In: *Book of abstracts of the EUROMECH 532 – 1st International Colloquium on Time-periodic Systems, Current trends in theory and application.*, Darmstadt, Germany (2012).

Sipahi, R.; Niculescu, S.-I.; Abdallah, T., C. Michiels, W.; Gu, K.: Stability and stabilization of systems with time delay. *IEEE control systems*, 31, 1, (2011), 38–65.

Sipahi, R.; Olgac, N.: Stability robustness of retarded lti systems with single delay and exhaustive determination of their imaginary spectra. *SIAM Journal on Control and Optimization*, 45, 5, (2006), 1680–1696.

Stépán, G.; Insperger, T.: Stability of time-periodic and delayed systems – a route to act-and-wait control. *Annual Reviews in Control*, 30, 2, (2006), 159–168.

Tagawa, R.: A numerical method for stability analysis of time-varying linear systems with periodic coefficients. In: *Memoirs of the Faculty of Engineering*, vol. 12, pages 33–48, Hokkaido University (1967).

The Mathworks, Inc.: *MATLAB version 7.8.0.347 (R2008a)*. Natick, Massachusetts, USA (2008).

Tweten, J., D. Lipp, M., G. Khasaweneh, A., F. Mann, P., B. On the comparison of semi-analytical methods for the stability analysis of delay differential equations. *Journal of Sound and Vibration*, 331, (2012), 4057–4071.

Wu, M.; He, Y.; She, J.-H.: *Stability Analysis and Robust Control of Time-Delay Systems*. Springer-Verlag, Heidelberg, Dodrecht, London, New York (2010).

Address: Steffen Neeb, Heidelberger Druckmaschinen AG, Alte Eppelheimer Str. 26, 69115 Heidelberg, Germany
email: steffen.neeb@heidelberg.com

Study of the Influence of a Delayed Yielding Phenomenon in Magnetorheological Damping Devices on the Vibration Attenuation of a Jeffcott Rotor

J. Zapoměl, P. Ferfecki

A frequently used technological solution for attenuation of lateral oscillations of rotating machines consists in inserting damping devices between the rotor and its stationary part. To achieve their optimum performance, their damping effect must be controllable. This is enabled by magnetorheological squeeze film dampers. As resistance against the flow of magnetorheological liquids depends on magnetic induction, the change of magnetic flux passing through the lubricating film enables to control the damping effect. The developed mathematical model of a magnetorheological squeeze film damper is based on assumptions of the classical theory of lubrication. The oil is represented by bilinear material. The pressure distribution in the damper gap is described by the modified Reynolds equation. The dependence of the stationary value of the yielding shear stress on magnetic induction is approximated by a power function. Its dependence on time is governed by a convolution integral, which enables to take into account that the yielding shear stress depends not only on the instant value of magnetic induction but also on its history in the past. In cavitated regions it is considered that the yielding shear stress drops to zero. The developed mathematical model of the damper was implemented in the computational procedures for analysis of lateral vibrations of a flexibly supported Jeffcott rotor loaded by the disc unbalance. The carried out simulations showed that the rising value of the delayed yielding time constant reduces the damping effect. The development of a novel model of a magnetorheological squeeze film damper based on representing the lubricating oil by bilinear material taking into account the delayed yielding phenomenon, its implementation into the procedures for analysis of oscillations of rotating machines, increasing their computational stability, and learning more on the effect of magnetorheological damping devices on behaviour of flexible rotors are the principal contributions of this article.

1 Introduction

The unbalance of rotating machines produces their lateral oscillation. A frequently used technological solution for its attenuation consists in inserting damping devices between the rotor and its stationary part. To achieve their optimum performance, their damping effect must be controllable. This is enabled by magnetorheological squeeze film dampers. The magnetorheological oils belong to the category of fluids with a yielding shear stress. The flow occurs only in those areas in which the shear stress exceeds a limit value - the yielding shear stress. In regions, called a core, where the shear stress is lower the magnetorheological oil behaves as solid matter.

The principles of work of magnetorheological dampers and practical experience with their applications are reported in a number of publications (Gong et al, 2014; Aravindhan and Gupta, 2006; Carmignani et al., 2006). The mathematical model of a squeeze film magnetorheological damper, in which the lubricant is represented by Bingham material, is reported in (Zapoměl et al., 2012; Zapoměl and Ferfecki, 2010). The modelling of magnetorheological oil by bilinear material (Zapoměl et al., 2016b) arrives at increase of stability of the computational procedures, in which the mathematical model of the magnetorheological squeeze film damper is implemented.

In this paper, the mathematical model of a magnetorheological squeeze film damper developed in Zapoměl et al., 2016b has been extended. The model was completed with the phenomenon of the delayed yielding which takes into account the time history of magnetic induction on the yielding shear stress magnitude. Unlike of Zapoměl and Ferfecki, 2016a, the new mathematical model was implemented into computational procedures for investigation of lateral vibrations of flexible rotors.

The implementation of the delayed yielding phenomenon in the mathematical model of a magnetorheological squeeze film damper, its application into the computational procedures for analysis of vibrations of flexible rotors, increase of their numerical stability, and learning more on the effect of magnetorheological damping devices on the oscillations attenuation of flexible rotors are the principal contributions of this article.

2 A Novel Model of a Magnetorheological Squeeze Film Damper

The main parts of a magnetorheological squeeze film damper (Figure 1) are two concentric rings between which there is a layer of magnetorheological oil. The inner ring is coupled with the shaft through a rolling element bearing and with the damper housing by a squirrel cage spring. Lateral vibration of the shaft squeezes the oil film, which produces the damping effect. Magnetic flux generated in the damper coils passes through the lubricant and as its resistance against the flow depends on magnetic induction the change of the applied current changes the damping force.

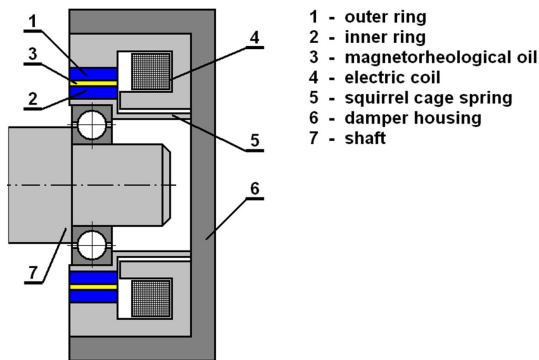


Figure 1. MR squeeze film damper

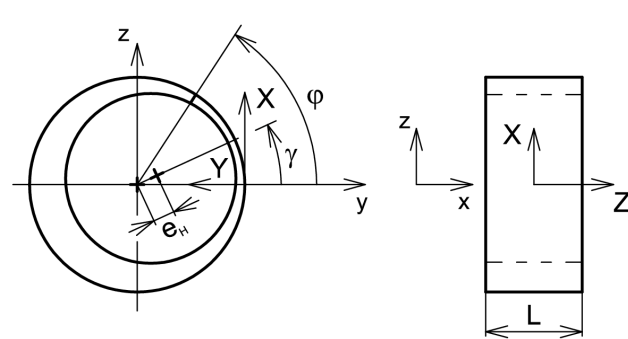


Figure 2. The damper coordinate system

The developed mathematical model of the damper is based on assumptions of the classical theory of lubrication. The magnetorheological oil is represented by bilinear material the yielding shear stress of which is a function of magnetic induction. In addition it is assumed that both the geometric and design parameters of the damper make it possible to consider it as short (Childs, 1993; Hori, 2006).

The pressure distribution in the full oil film is governed by the Reynolds equation (1) - (2) adapted for bilinear material (Zapoměl et al., 2016b)

$$\frac{\partial}{\partial Z} \left(\frac{1}{\eta_c} h^3 p' \right) = 12 \dot{h}, \quad \text{for } 0 \leq Z \leq Z_c, \quad (1)$$

$$\frac{\partial}{\partial Z} \left[\frac{1}{\eta} \left(h^3 p' + 3h^2 \tau_y + 8 \frac{\tau_c^3}{p'^2} - 12 \frac{\tau_y \tau_c^2}{p'^2} \right) - \frac{8}{\eta_c} \frac{\tau_c^3}{p'^2} \right] = 12 \dot{h}, \quad \text{for } \dot{h} < 0, \quad Z > Z_c, \quad (2)$$

$$Z_c = -\frac{\tau_c h^2}{6\eta_c h}, \quad (3)$$

$$p'_c = -\frac{2\tau_c}{h}. \quad (4)$$

p is the pressure, p' stands for the pressure gradient in the axial direction, Z is the axial coordinate perpendicular to the axes X , Y and defining position in the oil film (Figure 2), h is the film thickness, τ_y is the yielding shear stress, τ_c is the shear stress at the core border, η_c , η are the dynamic viscosities of the oil inside and outside the core area, respectively, Z_c defines the axial coordinate of the location where the core touches the rings surfaces, p'_c denotes the pressure gradient in the axial direction at that location Z_c , and (\cdot) denotes the first derivative with respect to time.

The thickness of the lubricating film depends on the position of the inner damper ring relative to the outer one (Hori, 2006).

$$h = c - e_H \cos(\varphi - \gamma). \quad (5)$$

c is the width of the gap between the inner and outer rings of the damper, e_H is eccentricity of the rotor journal centre, φ is the circumferential coordinate, and γ is the position angle of the line of centres (Figure 2).

In that part of the damper gap where the oil film thickness rises with time a cavitation is assumed. The pressure of the medium in cavitated areas is considered to remain constant and equal to the pressure in the ambient space.

The y and z components of the magnetorheological damping forces F_{mry} , F_{mrz} are calculated by integration of the pressure distribution p_d which takes into account different pressure profiles in noncavitated and cavitated regions

$$F_{mry} = -2R \int_0^{\frac{L}{2}} \int_0^{2\pi} p_d \cos\varphi \, d\varphi \, dZ, \quad (6)$$

$$F_{mrz} = -2R \int_0^{\frac{L}{2}} \int_0^{2\pi} p_d \sin\varphi \, d\varphi \, dZ. \quad (7)$$

R is the mean radius of the damper gap, L is the damper length and φ is the circumferential coordinate (Figure 2).

Based on experiments, dependence of the stationary value of the yielding shear stress on magnetic induction is approximated by a power function

$$\tau_y = k_y B^{n_y}. \quad (8)$$

B is magnetic induction and k_y and n_y are material constants of the magnetorheological oil.

Due to the physical substance, the yielding shear stress of magnetorheological fluids depends not only on the instant value of magnetic induction but also on its history in the past. This time dependence is described by a convolution integral, which is consequently transformed to the differential form

$$\dot{\tau}_y \dot{\tau}_y + \tau_y = k_y B^{n_y}. \quad (9)$$

T_y is the delayed yielding time constant, which expresses the rapidity of the change of the yielding shear stress on the change of magnetic induction. In cavitated regions it is considered that the yielding shear stress becomes zero there.

In the developed mathematical model the damper housing is considered to be composed of a series of meridian segments and each segment is considered to be a divided core of an electromagnet with the gap filled by magnetorheological oil. This enables to determine magnetic induction as a function of the applied current and thickness of the oil film at any location in the oil film around the damper circumference

$$B = k_B \mu_0 \mu_r \frac{I}{h}. \quad (10)$$

μ_0 , μ_r are the vacuum and relative permeabilities of the magnetorheological oil, respectively, I is the applied current, k_B is the design parameter that is defined as a product of the number of the coil turns and the magnetic efficiency. More details on its determination can be found in Ferfecki et al., 2017.

3 The Computational Model of the Studied Rotor

The investigated rotor (Figure 3) consists of a flexible shaft and of one rigid disc. At both its ends it is coupled with the stationary part by two magnetorheological squeeze film dampers. The rotor rotates at a constant angular speed, is loaded by its weight and excited by the disc unbalance. The squirrel cage springs of both dampers are pre-bent to be eliminated their deflection caused by the rotor weight. The whole system can be considered as symmetric relative to the disc middle plane.

The task was to study the effect of the delayed yielding phenomenon on performance of magnetorheological damping devices and on attenuation of vibrations of flexible rotors.

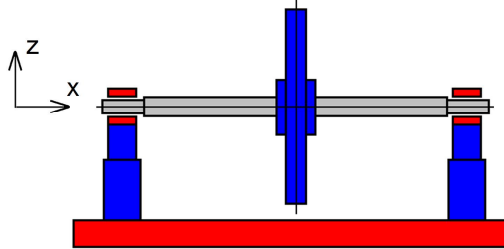


Figure 3. Scheme of the investigated rotor system

The rotor is implemented in the computational model by a Jeffcott one and the magnetorheological squeeze film dampers are represented by linear springs and nonlinear force couplings. With respect to the system symmetry, the lateral vibration of the rotor is governed by a set of four differential equations

$$m\ddot{y} + (b_p + b_M)\dot{y} - b_M\dot{y}_B + k_S y - k_S y_B + \dot{g}b_M z - \dot{g}b_M z_B = m e_T \dot{\vartheta}^2 \cos \vartheta, \quad (11)$$

$$m\ddot{z} + (b_p + b_M)\dot{z} - b_M\dot{z}_B + k_S z - k_S z_B - \dot{g}b_M y + \dot{g}b_M y_B = m e_T \dot{\vartheta}^2 \sin \vartheta - mg, \quad (12)$$

$$-b_M\dot{y} + b_M\dot{y}_B - k_S y + (k_S + 2k_B)y_B - \dot{g}b_M z + \dot{g}b_M z_B = 2F_{mry}, \quad (13)$$

$$-b_M\dot{z} + b_M\dot{z}_B - k_S z + (k_S + 2k_B)z_B + \dot{g}b_M y - \dot{g}b_M y_B = 2F_{mrz}. \quad (14)$$

m is the disc mass, k_S is the stiffness of the shaft, k_B is the stiffness of each squirrel cage spring, b_p and b_M are the linear viscous coefficients related to the rotor environmental and material damping, e_T is the eccentricity of the disc centre of gravity, g is the gravity acceleration, y , z , y_B , z_B are displacements of the disc and shaft journal centres in the horizontal and vertical directions, ϑ is the angle of the rotor rotation and (\cdot) denotes the second derivative with respect to time.

The solution of the governing equations was obtained by application of a numerical time integration method based on the Adams-Moulton one.

4 The Results of the Computational Simulations

The main technological parameters of the investigated rotor are: 250 kg the mass of the disc, 20 MN/m the bending stiffness of the shaft, 600 Ns/m is the shaft material viscous damping coefficient (material damping), 10 Ns/m the disc viscous damping coefficient (external damping), 15 kgmm the disc unbalance, 5 MN/m the stiffness of each squirrel cage spring, 0.3 Pas the oil viscosity (if not effected by a magnetic field), 150 mm the mean diameter of the damper gap, 50 mm the damper land length, 0.8 mm the width of damper clearance, 60 the damper design parameter, $5, 10, 000 \text{ PaT}^{-1.1}$, 1.1 the oil relative permeability and the proportional and exponential constants, respectively. The rotor turns at constant angular speed of 150 rad/s.

A simple dynamical analysis shows that the resonance frequencies of the rotor system related to the cases when the dampers exhibit no damping (e.g. no magnetorheological oil is supplied to the dampers) and when they work

in the overdamped regime are 163 and 283 rad/s, respectively. It implies the rotor operates below the first critical speed.

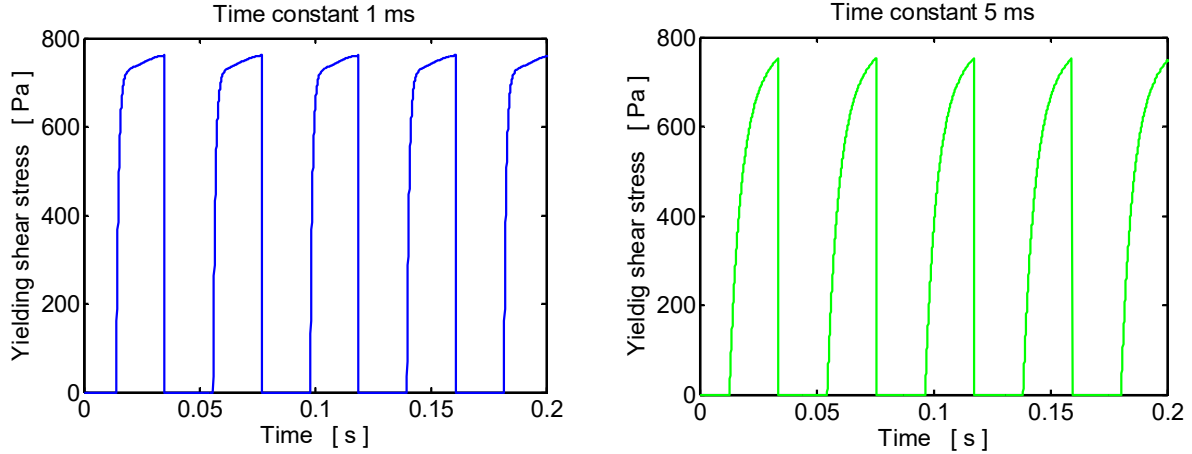


Figure 4. Time history of the yielding shear stress

Time history of the yielding shear stress for the current of 0.2 A and two delayed yielding time constants (1 ms and 5 ms) referred to the specified location on the damper circumference are depicted in Figure 4. The results show that rising magnitude of the delayed yielding time constant makes the response of the oil on the change of the magnetic field slower and slightly reduces the maximum value of the yielding shear stress. During the time periods when the cavitation takes place at the investigated location the yielding shear stress drops to zero.

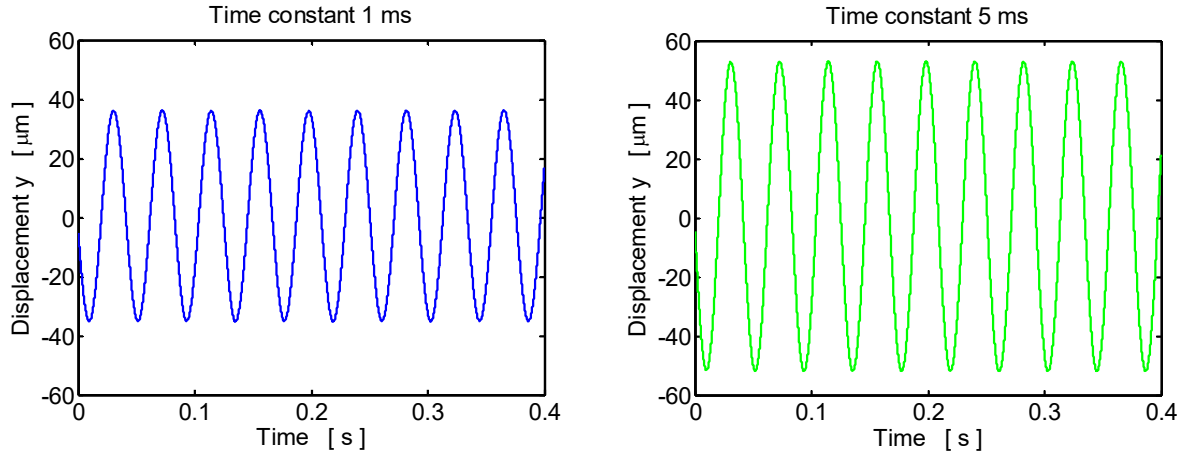


Figure 5. Time history of the disc displacement in the horizontal direction (time constants 1 ms, 5 ms)

Time histories of the disc centre displacement in the horizontal direction are depicted in Figure 5 for two magnitudes of the time constant (1 ms, 5 ms). The analysis of the results shows that higher value of the time constant increases amplitude of the oscillations. It implies it reduces the damping effect.

The steady state orbits of the disc centre for the applied current of 0.2 A and for two values of the time constant 1 ms and 5 ms are drawn in Figure 6. The trajectories are circular which is caused by prestressing the squirrel cage springs. The weight of the disc shifts the orbits in the vertical direction. The results show that higher value of the time constant reduces the damping effect and increases amplitude of the disc vibration.

The steady state trajectories of the rotor journal centre are drawn in Figure 7 for two values of the delayed yielding time constants of 1 ms and 5 ms and for the applied current of 0.2 A. Rising magnitude of the time constant arrives at increase of the orbit size.

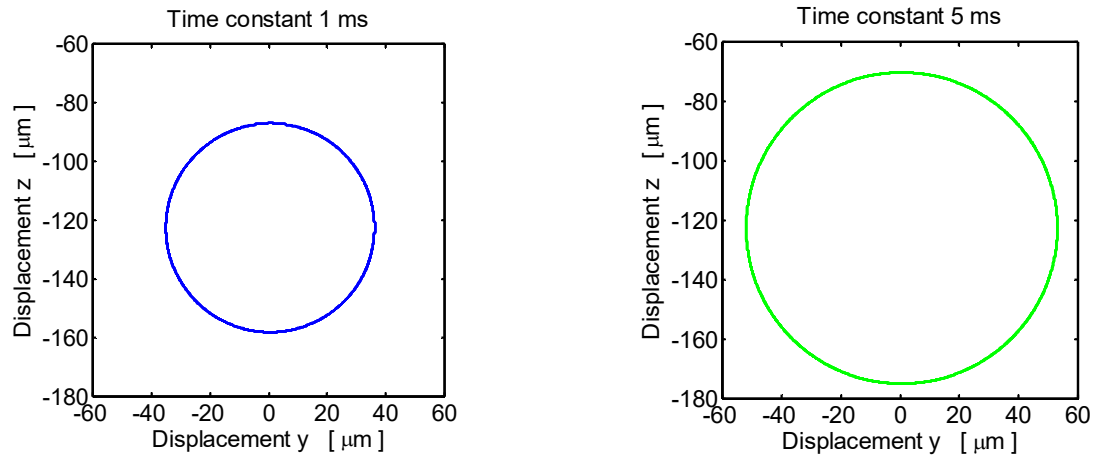


Figure 6. Steady state orbits of the disc centre (time constants 1 ms, 6 ms)

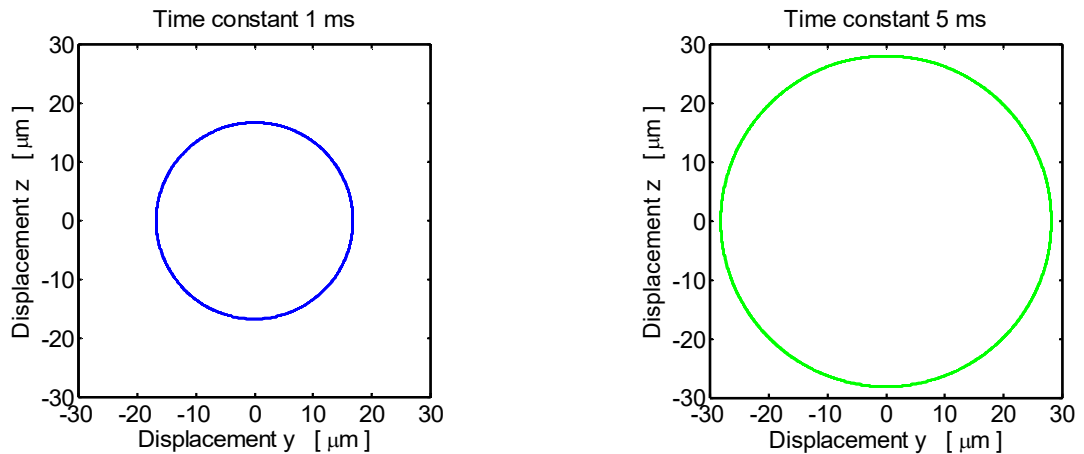


Figure 7. Steady state orbits of the rotor journal centre (time constants 1 ms, 5 ms)

5 Conclusion

This paper presents a new mathematical model of a short magnetorheological squeeze film damper for rotordynamic applications in which the delayed yielding phenomenon is implemented. The model is based on assumptions of the classical theory of lubrication. The oil is represented by bilinear material. The pressure distribution in the full oil film in the damper gap is governed by the adapted Reynolds equation. The dependence of the stationary value of the yielding shear stress on magnetic induction is approximated by a power function and its dependence on time by a convolution integral. The developed mathematical model of the magnetorheological damper was implemented in the computational procedures for investigating lateral vibrations of flexible rotors. The results of the simulations show that rising magnitude of the delayed yielding time constant reduces rapidity of the response of the magnetorheological oil on the change of a magnetic field which arrives at reduction of the damping effect. The implementation of the delayed yielding phenomenon in the mathematical model of a magnetorheological squeeze film damper, its implementation into the computational procedures for analysis of lateral vibrations of flexible rotors, the increase of their numerical stability due to representing the magnetorheological oil by bilinear material, and learning more on the effect of magnetorheological damping devices on behaviour of flexible rotors are the principal contributions of this article.

Acknowledgement

The research work reported in this article was made possible by the projects 15-06621S (Czech Science Foundation) and LQ1602 (IT4Innovations excellence in science). The support is highly acknowledged.

References

Aravindhan, T. S.; Gupta, K.: Application of magnetorheological fluid dampers to rotor vibration control. *Adv. Vib. Eng.*, 5, (2006), 369-380.

Carmignani, C.; Forte, P.; Rustighi, E.: Design of a novel magneto-rheological squeeze-film damper. *Smart Mater. Struct.*, 15, (2006), 164-170.

Childs, D.: *Turbomachinery Rotordynamics: Phenomena, Modelling, and Analysis*. John Wiley & Sons, New York, Chichester (1993).

Hori, Y.: *Hydrodynamic Lubrication*. Springer-Verlag, Tokyo, Berlin (2006).

Ferfecki, P.; Zapoměl, J.; Kozánek, J.: Analysis of the vibration attenuation of rotors supported by magnetorheological squeeze film dampers as a multiphysical finite element problem. *Adv. in Eng. Soft.*, 104, (2017), 1-11.

Gong, X.; Ruan, X.; Xuan, S.; Yan, Q.; Deng, H.: Magnetorheological damper working in squeeze model. *Adv. Vib. Eng.*, 6, (2014), 410158.

Zapoměl, J.; Ferfecki, P.: Mathematical modelling of a long squeeze film magnetorheological damper for rotor systems. *Model. Optim. Phys. Syst.*, 9, (2010), 97-100.

Zapoměl, J.; Ferfecki, P.; Forte, P.: A computational investigation of the transient response of an unbalanced rigid rotor flexibly supported and damped by short magnetorheological squeeze film dampers. *Smart Mater. Struct.*, 21, (2012), 105011.

Zapoměl, J.; Ferfecki, P.: The transient vibration attenuation of rotors damped by magnetorheological dampers utilizing bilinear material and the delayed yielding phenomenon to model the lubricating oil, In: *Proceedings of the conference VIRM 11 - Vibrations in Rotating Machinery*, Manchester, Great Britain, pages 647-657 (2016a).

Zapoměl, J.; Ferfecki, P.; Kozánek, J.: Modelling of magnetorheological squeeze film dampers for vibration suppression of rigid rotors. *Int. J. Mech. Sci.*, (2016b), In Press, <http://doi.org/10.1016/j.ijmecsci.2016.11.009>.

Address:

Jaroslav Zapoměl, Department of Dynamics and Vibration, Institute of Thermomechanics, Dolejškova 1402/5, 182 00 Prague 8, Czech Republic, email: zapomel@it.cas.cz

Jaroslav Zapoměl, Department of Applied Mechanics, VŠB-Technical University of Ostrava, 17. listopadu 15/2172, 708 33 Ostrava Poruba, Czech Republic, email: jaroslav.zapomel@vsb.cz

Petr Ferfecki, IT4Innovations National Supercomputing Center, VŠB-Technical University of Ostrava, Studentská 6231/1B, 708 33 Ostrava Poruba, Czech Republic, email: petr.ferfecki@vsb.cz

Petr Ferfecki, Department of Applied Mechanics, VŠB-Technical University of Ostrava, 17. listopadu 15/2172, 708 33 Ostrava Poruba, Czech Republic, email: petr.ferfecki@vsb.cz

The Effect of Field Damping on Rotordynamics of Non-salient Pole Generators

F. Boy, H. Hetzler

This paper investigates the influence of magnetic field damping on lateral shaft oscillations of non-salient pole generators. Field damping is caused by compensating currents affecting the magnitude and orientation of the magnetic field and resulting lateral forces. These currents can either occur in especially constructed devices, like a damper cage, or simply in the core material as eddy currents. While damper windings are used to reduce torsional shaft vibrations by generating an asynchronous damper torque, this survey reveals that in contrary to intuition, the field damping in general may cause self-excited lateral shaft oscillations leading to noise emission and reliability issues. It is shown that the effect is strongly dependent upon the machine type and the nominal rotational speed compared to the critical speed. The applied approach is analytical taking into account arbitrary lateral rotor motion in the context of linear rotordynamics.

1 Introduction

The main purpose of an electric generator is the conversion of mechanical to electrical power. To do so an electromechanical torque is transmitted by a rotating magnetic field which originates from currents flowing in the stator and rotor windings and from compensating currents in damper windings or the core material, respectively. However, the magnetic field also causes reluctance stresses at the air gap surface. Especially when the rotor runs eccentrically in the stator bore, these stresses are unbalanced, causing unbalanced magnetic forces. The most important one, pointing towards the direction of the smallest air gap is denoted as unbalanced magnetic pull (UMP) and has been studied extensively in the past century, as summarised for example by Kaehne (1963). However, in view of rotordynamics and the evolution of lateral shaft oscillations, especially the force component perpendicular to the UMP plays an important role due to the fact that it can feed and remove comparably large amounts of energy to and from the orbital motion of the rotor. Effects influencing the perpendicular force component have been investigated mainly in asynchronous machines due to the fact that squirrel cage rotors cause strong perpendicular forces (Früchtenicht, 1982). Furthermore, there are a lot of additional influences changing the amplitude and direction of the magnetic force. Among them are effects due to parallel paths in the windings, as investigated by Burakov (2006), magnetic homopolar fluxes (Belmans, 1987) and saturation (Arkkio, 2000).

Damper windings are another interesting example affecting the force. Usually, their purpose is to reduce torsional shaft vibrations (Jordan, 1970). However, as shown by Dorell et al. (2011) for asynchronous machines and by Wallin et al. (2013) for salient pole generators, damper windings may also change the direction of the lateral electromagnetic forces.

This study discusses the influence of field damping on the rotordynamics of non-salient pole generators as a similar question to the studies mentioned above. The machines being considered here, usually run at higher speeds, making effects due to dynamic rotor eccentricity more relevant. While only some of them actually possess damper windings, field damping as a general qualitative phenomenon, might also be caused by eddy currents in the rotor core material resulting in an analogous effects.

This study extends existing surveys by Kellenberger (1966) and the authors (Boy, 2016), which found that the forces and thus the rotordynamics of turbogenerators are strongly dependent on the load condition. In the present work, it is shown, that field damping might cause self-excited lateral shaft oscillations at higher rotational speeds. Their dependency on the machine design, occurring homopolar flux and load condition will be outlined.

The applied modelling approach is an analytical one. Solving the combined electro-mechanical problem by space vector theory and assuming stationary speed of operation, the forces of electromagnetic origin are derived for an arbitrary orbital motion of the rotor. With this information a stability analysis of the steady state, indicating the occurrence of self-excited oscillations is carried out. All symbols introduced subsequently are explained in the text.

Additionally a nomenclature is given in the appendix.

2 Model

Investigating electrical machine rotordynamics involves the solution of three subproblems (Fig. 1): The current flowing in the electrical circuits are sources to the magnetic field in the air gap of the machine. The changing magnetic flux in return induces voltage into these circuits. Furthermore the magnetic field exerts forces on the rotor of the machine, while the rotor motion in return distorts the air gap domain and thus affects the magnetic field.

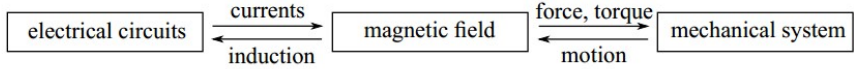


Figure 1. Electro-mechanical machine model involving three subproblems.

2.1 Assumptions and Kinematics

To analytically solve the magnetic field problem several assumptions have to be made. Both stator and rotor shall be perfectly aligned cylinders (radii r_1 (stator) and r_2 (rotor)). The material shall be infinitely permeable, allowing to restrict the consideration to the air gap domain but excluding saturation effects. The problem shall be two-dimensional, neglecting axial boundary effects and corresponding stray losses. The actual windings in the slots are replaced by current sheets a_1 and a_2 for the stator (index 1) and the rotor (index 2) respectively. This simplification is permissible according to the field equivalence principle for sufficiently smooth surfaces, as it is the case in non-salient pole machines. The involved compensating currents shall be represented by currents in damper windings (index D), realised comparable to the squirrel cage of an induction machine with N_D bars, which are continuously connected by conducting rings at the axial ends of the rotor. Corrections in the air gap width due to slotting or in the winding factors due to skewed damper bars etc. are left out here, as the study is concerned with qualitative effects.

Fig. 2 shows an overview of the field domain and the involved kinematics. For the description of the problem several frames of reference are introduced: A cartesian inertial frame of reference $\mathcal{K}_1 = [O, \{\vec{e}_{x_1}, \vec{e}_{y_1}, \vec{e}_{z_1}\}]$, one where the x -axis is pointing towards the direction of eccentricity (smallest air gap), denoted as $\mathcal{K} = [O, \{\vec{e}_x, \vec{e}_y, \vec{e}_z\}]$ and one, identified by $\mathcal{K}_2 = [O, \{\vec{e}_{x_2}, \vec{e}_{y_2}, \vec{e}_{z_2}\}]$, where the x -axis shall be aligned with a distinct pole axis of the rotor. Analogous to these coordinate systems, cylindrical systems $\mathcal{Z}_1, \mathcal{Z}$ and \mathcal{Z}_2 are defined. The magnetic field problem in the air gap Ω will be stated in cylindrical coordinates, with the radial coordinate r and corresponding angles $\theta_1 = \theta + \gamma = \theta_2 + \vartheta$.

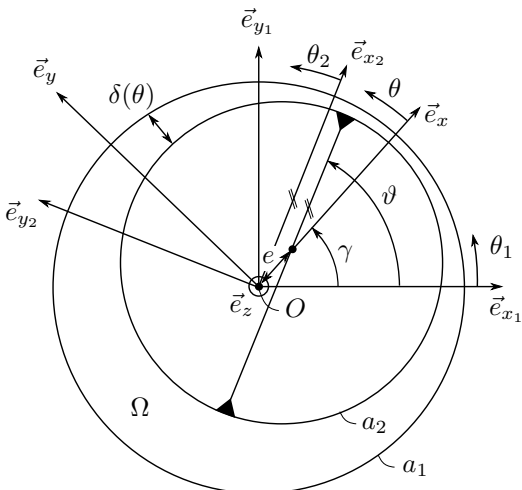


Figure 2. Kinematics and field domain.

The rotor position can either be described by polar (e, γ) , or cartesian coordinates (x_1, y_1) , (x, y) and (x_2, y_2) in the different frames of reference. The absolute angular orientation of the rotor is described by the angle ϑ . Note that all angles θ_i (with some index i) represent spatial coordinates, while γ and ϑ are discrete mechanical coordinates. Later on, different electrical angles φ_k will be introduced. They transform with $\varphi_k = p\vartheta_k$ to a corresponding mechanical angle ϑ_k .

With the kinematic definitions and physical simplifications stated before and assuming that the mean air gap width $\delta_m = r_1 - r_2$ is small compared to the rotor radius $(\varepsilon = \frac{\delta_m}{r_2} \ll 1)$, it can be shown that the magnetic field of order $\mathcal{O}(1)$ is orientated straight radially neglecting terms of higher order $\mathcal{O}(\varepsilon)$.

Due to circumferential periodicity the one dimensional magnetic flux density can be written as a Fourier series

$$B = B_0 + \sum_{\nu=1}^{\infty} \underbrace{\hat{B}_{\nu} \cos(\nu\theta_2 - \varphi_{B\nu})}_{B_{\nu}} = B_0 + \sum_{\nu=1}^{\infty} \operatorname{Re} \left\{ \underline{B}_{\nu} e^{-j\nu\theta_2} \right\}, \quad (1)$$

here expressed in the frame of reference \mathcal{Z}_2 , corotating with the rotor. In this equation each harmonic resembles a rotating field wave of different circumferential velocity. In eq. (1) complex notation was introduced, where j is the imaginary unit and $\underline{B}_{\nu} = \hat{B}_{\nu} e^{j\varphi_{B\nu}}$ represents the complex amplitude of the ν -th field harmonic. Here and further on underlining shall indicate complex variables \underline{A} and overlining their complex conjugate \overline{A} . In the context of this work only the fundamental wave of order p (where p is the number of pole pairs) and the eccentricity waves of order $p \pm 1$ are regarded. This assumption is justified in machines with a sufficiently well arranged winding design.

Deriving an approximate solution to the magnetic field (which means finding $B_0, \hat{B}_p, \hat{B}_{p \pm 1}$ and $\varphi_{Bp}, \varphi_{Bp \pm 1}$) presumes solving of the voltage equations of the equivalent electrical circuits. These circuits are a representative phase of the stator and a representative mesh of the damper cage. To derive the induced voltages, it has to be considered that the field waves of order ν induces alternating voltages of different frequency in the stator windings (index 1) and damper cage (index D) respectively. Thus, the voltage in an equivalent circuit (see e.g. Jordan (1970)) can be written as

$$u_i(t) = \sum_{\nu=1}^{\infty} \hat{u}_{i\nu} \cos(\omega_{i\nu} t + \varphi_{i\nu}) = \sum_{\nu=1}^{\infty} \operatorname{Re} \left\{ \sqrt{2} \underline{U}_{i\nu} e^{j\omega_{i\nu} t} \right\} \quad (2)$$

where $i = (1, D)$ is an index and $\underline{U}_{i\nu} = \frac{\sqrt{2}}{2} \hat{u}_{i\nu} e^{j\varphi_{i\nu}}$ is the complex phasors of the ν -th voltage harmonic. The frequencies are related by $\omega_{D\nu} = s_{\nu} \omega_{1\nu}$. In synchronous operation the slip is $s_p = s = 0$ and the higher field harmonic slips become $s_{p \pm 1} = 1 - \frac{p \pm 1}{p} (1 - s) = \mp \frac{1}{p}$. As the currents in the mentioned circuits are caused by these voltages, they can be expressed similarly. Each order of these AC quantities can be treated separately balancing only the complex phasors, which will be done subsequently.

2.2 Fundamental Field Harmonics

The voltage equations of order p are

$$\underline{U}_{1p} = (R_{1p} + j\omega L_{1p}) \underline{I}_{1p} + \underline{U}_{12p} \quad (\text{stator}), \quad (3)$$

$$0 = (R_{Dp} + j\omega L_{Dp}) \underline{I}_{Dp} \Rightarrow \underline{I}_{Dp} = 0, \quad (\text{damper cage}). \quad (4)$$

Here $\underline{U}_{1p} = U_{1p}$ is the phasor of the supply voltage, which shall be aligned with the real axis without loss of generality. The phasor of the synchronous generated voltage in eq. (3) is $\underline{U}_{12p} = U_{12p} e^{j\varphi_{12p}}$, with the effective value U_{12p} and the polar wheel angle φ_{12p} . Note that there is no mutual induction of order p between the rotating field and the damper cage, as they are assumed to move synchronously ($s = 0$).

Inserting \underline{U}_{12p} into eq. (3), neglecting the resistive component (as usual for larger machines (Jordan, 1970)) and solving for \underline{I}_{1p} yields

$$\underline{I}_{1p} = -j \frac{U_{1p}}{\omega L_{1p}} + j \frac{U_{12p}}{\omega L_{1p}} e^{j\varphi_{12p}}. \quad (5)$$

The fundamental field harmonic is

$$B_p = \frac{\mu_0}{\delta_m} \operatorname{Re} \left\{ k_{1p} \underline{I}_{1p} e^{j(\omega t - p\theta_1)} + k_{2p} i_2 e^{-jp\theta_2} \right\}, \quad (6)$$

where μ_0 is the magnetic constant, k_{1p} and k_{2p} are constants depending on the machine geometry and winding design and i_2 is the DC excitation current. Transforming to corotating coordinates \mathcal{Z}_2 using $\theta_1 = \theta_2 + \vartheta$, with $p\vartheta = \omega t - \frac{\pi}{2} + \varphi_{12p}$, inserting \underline{I}_{1p} from eq. (5) and regarding $k_{2p}i_2 = k_{1p} \frac{U_{12p}}{\omega L_{1p}}$ finally results in

$$B_p = \frac{\mu_0}{\delta_m} \operatorname{Re} \left\{ k_{1p} \frac{U_1}{\omega L_1} e^{-j\varphi_{12p}} e^{-jp\theta_2} \right\}, \quad (7)$$

where it is easy to identify the complex phasor $\underline{B}_p = \hat{B}_p e^{j\varphi_{Bp}} = \frac{\mu_0}{\delta_m} k_{1p} \frac{U_1}{\omega L_1} e^{-j\varphi_{12p}}$

2.3 Eccentricity Field Harmonics

The voltage equations of order $p \pm 1$ are

$$0 = (R_{1p\pm 1} + j\omega L_{1p\pm 1}) \underline{I}_{1p\pm 1} \Rightarrow \underline{I}_{1p\pm 1} = 0 \quad (\text{stator}), \quad (8)$$

$$0 = (R_{Dp\pm 1} + j s_{p\pm 1} \omega L_{Dp\pm 1}) \underline{I}_{Dp\pm 1} + \underline{U}_{21Dp\pm 1} \quad (\text{damper cage}). \quad (9)$$

Here it is assumed that the field waves of order $p \pm 1$ cannot induce voltage into the stator phases, which is the case for integer-slot windings without parallel branches (Tüxen, 1941). The induced voltages $\underline{U}_{21p\pm 1}$ originate from the eccentricity fields and have to be calculated subsequently. Therefore a closer look at the formation of these harmonics shall be taken here.

As it is well known, the eccentricity field harmonics arise from the multiplication of the magnetic excitation with the air gap permeance $\Lambda(\theta) = \frac{\mu_0}{\delta(\theta)} = \frac{\mu_0}{\delta_m} \left(1 + \frac{e}{\delta_m} \cos \theta \right) + \mathcal{O}(\varepsilon)$ (Frohne, 1968), where $\delta(\theta)$ is the actual air gap width at a certain circumferential position θ as shown in Fig. 2. Again, higher order terms were neglected. Multiplying with the fundamental magnetic excitation one obtains

$$\Lambda(\theta) k_{1p} \frac{U_1}{\omega L_{1p}} \cos(p\theta_2 + \varphi_{12p}) = \hat{B}_p \left(\cos(p\theta_2 - \varphi_{Bp}) + \frac{1}{2} \frac{e}{\delta_m} \cos((p \pm 1)\theta_2 + \varphi_{12p} \pm (\vartheta - \gamma)) \right), \quad (10)$$

where $\theta = \theta_2 + (\vartheta - \gamma)$ has been inserted. In complex notation these field components read

$$\hat{B}_p \operatorname{Re} \left\{ e^{-j(p\theta_2 + \varphi_{12p})} + \frac{1}{2} \frac{e}{\delta_m} e^{\mp j(\vartheta + \gamma)} e^{-j((p \pm 1)\theta_2 + \varphi_{12p})} \right\}. \quad (11)$$

Here it is possible to identify the phasor $\underline{z}_2^\pm = x_2 \pm jy_2 = e^{\mp j(\vartheta - \gamma)}$, representing the rotor orbit position within the corotating frame of reference (compare Fig. 2). Obviously, the components of the eccentricity field harmonics shown in eq. (11) cause the mutual induced voltage in the damper cage, which is calculated by

$$u_{21Dp\pm 1} = \frac{d\Psi_{21Dp\pm 1}}{dt} = \frac{1}{2} \hat{B}_p \int_{\mathcal{M}} \frac{\partial}{\partial t} \operatorname{Re} \left\{ \frac{\underline{z}_2^\pm}{\delta_m} e^{-j(p \pm 1)\theta_2 + \varphi_{12p}} \right\} dS, \quad (12)$$

where $\Psi_{21Dp\pm 1}$ is the linked flux of the field components of order $p \pm 1$, caused by eccentricity into a representative damper mesh surface \mathcal{M} . Note that the second part of this equation refers to the moving frame of reference. Due to the fact that the damper cage mesh represents a moving surface, the Helmholtz transport theorem (see e.g. Rothwell (2008)) has to be applied. In this case the component proportional to the rotor orbital motion (motion of the damper cage surface) is of order $\mathcal{O}(\varepsilon)$ and therefore neglected here.

Evaluating eq. (12) results in the voltage phasor

$$\underline{U}_{21Dp\pm 1} = \frac{1}{2} \hat{B}_p k_{Dp\pm 1} \frac{\dot{\underline{z}}_2^\pm}{\delta_m} e^{-j\varphi_{12p}}, \quad (13)$$

where $k_{Dp\pm 1}$ is a constant similar to k_{1p} and k_{2p} , depending on the machine geometry and damper cage design. At this point a major drawback modelling the electrical voltages and currents as pure AC quantities shall be pointed out: considering eq. (13) it is found that the voltage phasor depends on the time derivative of the rotor orbital

motion \dot{z}_2^\pm . This result contradicts the model assumption of a harmonic time dependency and would only be permissible, if the time rate of change of \dot{z}_2^\pm would be small compared to the frequency of $u_{21Dp\pm 1}$, what might not be the case.

Nevertheless, inserting the result into the damper cage voltage equation (9) and solving for the current phasors $\underline{I}_{Dp\pm 1}$ yields

$$\underline{I}_{Dp\pm 1} = -\frac{js_{p\pm 1}}{\beta + js_{p\pm 1}} \frac{\underline{U}_{21Dp\pm 1}}{js_{p\pm 1}\omega L_{Dp\pm 1}}. \quad (14)$$

Here the resistance to reactance ratio $\beta = \frac{R_{Dp\pm 1}}{\omega L_{Dp\pm 1}}$ for the damper cage has been introduced as it is usually done in literature (Früchtenicht (1982), Jordan (1969)) and the complex number $-\frac{js_{p\pm 1}}{\beta + js_{p\pm 1}} = (a_{p\pm 1} - 1) + jb_{p\pm 1}$ is identified as the complex field damping factor.

Finally, the field component of the eccentricity harmonics, caused by the damper cage reads

$$\frac{\mu_0}{\delta_m} \text{Re} \left\{ k_{Dp\pm 1} \underline{I}_{Dp\pm 1} e^{-j(p\pm 1)\theta_2} \right\} = -\frac{1}{2} \hat{B}_p \text{Re} \left\{ \frac{1}{\beta + js_{p\pm 1}} \frac{1}{\omega} \frac{\dot{z}_2^\pm}{\delta_m} e^{-j((p\pm 1)\theta_2 + \varphi_{12p})} \right\}. \quad (15)$$

Adding this result to the eccentricity harmonics, caused by the air gap permeance (eq. (11)) results in

$$B_{p\pm 1} = \frac{1}{2} \hat{B}_p \text{Re} \left\{ \left(\frac{\dot{z}_2^\pm}{\delta_m} - \frac{1}{\beta + js_{p\pm 1}} \frac{1}{\omega} \frac{\dot{z}_2^\pm}{\delta_m} \right) e^{-j\varphi_{12p}} e^{-j(p\pm 1)\theta_2} \right\}. \quad (16)$$

With this result also the complex amplitudes $B_{p\pm 1} = \hat{B}_{p\pm 1} e^{j\varphi_{Bp\pm 1}} = \frac{1}{2} \hat{B}_p \left(\frac{\dot{z}_2^\pm}{\delta_m} - \frac{1}{\beta + js_{p\pm 1}} \frac{1}{\omega} \frac{\dot{z}_2^\pm}{\delta_m} \right) e^{-j\varphi_{12p}}$ are known.

Considering eq. (1) for the magnetic field only B_0 is left undetermined until now. As mentioned before it results in a homopolar flux in 2-pole machines and can be calculated as proposed by Belmans (1987). Assuming maximum homopolar flux leading to maximum electromagnetic forces, a worst case scenario considering rotordynamics will be investigated in this work. This assumption leads to $B_0 = 0$ completing the derivation of the magnetic field formula.

2.4 Electromagnetic Forces

The electromagnetic forces can be calculated using the Maxwell stress tensor (Rothwell, 2008). For the sake of simplicity, stress is integrated over the stator surface here. As higher order terms have been neglected (resulting in a straight radial flux density) the force formula reads

$$\vec{F}_2 = -\vec{F}_1 = F_{x_2} \vec{e}_{x_2} + F_{y_2} \vec{e}_{y_2} = \frac{1}{2\mu_0} \int_{\partial\Omega_1} B^2 \vec{e}_r dS. \quad (17)$$

The calculation will be carried out in the rotor fixed frame of reference, where $\vec{e}_r = \cos \theta_2 \vec{e}_{x_2} + \sin \theta_2 \vec{e}_{y_2}$ and $dS = r_1 \ell d\theta_2$ with the effective length ℓ of the air gap.

Calculating the force components F_{x_2} and F_{y_2} involves some algebra and has to be done individually for the cases $p > 1$ (machines with more than two poles) and $p = 1$ (2-pole machines). As it is usual in rotordynamics (Gasch, 2006), matrix notation will be used further on. In this context, a matrix M is displayed in bold letters.

In the first case ($p > 1$) one finds

$$\begin{bmatrix} F_{x_2} \\ F_{y_2} \end{bmatrix} = \begin{bmatrix} \text{Re} \{ \underline{B}_p \overline{\underline{B}}_{p\pm 1} \} \\ \text{Im} \{ \mp \underline{B}_p \overline{\underline{B}}_{p\pm 1} \} \end{bmatrix} \quad \text{and} \quad \begin{bmatrix} F_{x_2} \\ F_{y_2} \end{bmatrix} = \begin{bmatrix} \text{Re} \{ \underline{B}_p \overline{\underline{B}}_{p\pm 1} + \underline{B}_p \underline{B}_{p-1} \} \\ \text{Im} \{ \mp \underline{B}_p \overline{\underline{B}}_{p\pm 1} + \underline{B}_p \underline{B}_{p-1} \} \end{bmatrix} \quad (18)$$

in the second case ($p = 1$). Here, the field wave of order $\nu = p - 1 = 0$ is homopolar, creating additional force components. Note that the value of p for $p = 1$ is not inserted for the sake of comparability here and in the following considerations.

Evaluating the expressions in eqs. (18) respectively yields

$$\begin{bmatrix} F_{x_2} \\ F_{y_2} \end{bmatrix} = \underbrace{c_{\text{elm}} \mathbf{I} \begin{bmatrix} x_2 \\ y_2 \end{bmatrix}}_{\mathbf{F}_{\text{UMP}}} - \underbrace{\frac{c_{\text{elm}}}{\omega} \mathbf{P}_1 \begin{bmatrix} \dot{x}_2 \\ \dot{y}_2 \end{bmatrix}}_{\mathbf{F}_{\text{FD}}}, \quad (19)$$

in the first case ($p > 1$), where FD stands for field damping and where \mathbf{I} is the identity matrix and

$$\mathbf{P}_1 = \frac{1}{2} \begin{bmatrix} \frac{\beta}{\beta^2 + s_{p+1}^2} + \frac{\beta}{\beta^2 + s_{p-1}^2} & \left(\frac{s_{p+1}}{\beta^2 + s_{p+1}^2} - \frac{s_{p-1}}{\beta^2 + s_{p-1}^2} \right) \\ - \left(\frac{s_{p+1}}{\beta^2 + s_{p+1}^2} - \frac{s_{p-1}}{\beta^2 + s_{p-1}^2} \right) & \frac{\beta}{\beta^2 + s_{p+1}^2} + \frac{\beta}{\beta^2 + s_{p-1}^2} \end{bmatrix}. \quad (20)$$

In the second case ($p = 1$) the result is

$$\begin{bmatrix} F_{x_2} \\ F_{y_2} \end{bmatrix} = \underbrace{c_{\text{elm}} (\mathbf{I} + \mathbf{T}) \begin{bmatrix} x_2 \\ y_2 \end{bmatrix}}_{\mathbf{F}_{\text{UMP}}} - \underbrace{\frac{c_{\text{elm}}}{\omega} (\mathbf{P}_1 + \mathbf{P}_2 \mathbf{T}) \begin{bmatrix} \dot{x}_2 \\ \dot{y}_2 \end{bmatrix}}_{\mathbf{F}_{\text{FD}}} \quad (21)$$

with

$$\mathbf{T} = \frac{1}{2} \begin{bmatrix} \cos(2\varphi_{12p}) & -\sin(2\varphi_{12p}) \\ -\sin(2\varphi_{12p}) & -\cos(2\varphi_{12p}) \end{bmatrix} \quad \text{and} \quad \mathbf{P}_2 = \begin{bmatrix} \frac{\beta}{\beta^2 + s_{p-1}^2} & \frac{s_{p-1}}{\beta^2 + s_{p-1}^2} \\ -\frac{s_{p-1}}{\beta^2 + s_{p-1}^2} & \frac{\beta}{\beta^2 + s_{p-1}^2} \end{bmatrix}. \quad (22)$$

The electromagnetic spring constant in eqs. (19) and (21) is $c_{\text{elm}} = \frac{\pi r_1 \ell \hat{B}_p^2}{2\mu_0 \delta_m}$. There are additional forces proportional to the rotor orbit velocity, which had not been considered in earlier works: these forces originate from field damping. As they are due to induction and as the voltage equations have been solved for the induced currents explicitly the forces usually proportional to the currents are now proportional to the rotor orbit velocity.

Components on the main diagonal can be considered as inner damping (compare Gasch (2006)), as the coefficients in \mathbf{P}_1 and \mathbf{P}_2 are positive. Components at the secondary diagonal correspond to gyroscopic effects relative to the moving frame of reference. As it is well known from classical rotordynamics, inner damping is a typical source of self-excited oscillations and in fact it is the only possible source here.

2.5 Rotor Model

The mechanical system is modelled as a classical Laval-rotor (Jeffcott-rotor). With this model one mode shape of the generator system can be depicted and analysed dynamically. The basic assumptions are that the rotor consists of a massless elastic shaft (isotropic stiffness c) supported by isotropic rigid bearings with a circular rigid disk on it. The centre of inertia S shall be eccentric causing imbalance. Combined with the forces of electromagnetic origin the equations of motion read

$$\begin{bmatrix} m & 0 \\ 0 & m \end{bmatrix} \begin{bmatrix} \ddot{x}_2 \\ \ddot{y}_2 \end{bmatrix} + \begin{bmatrix} d + d_i & -2m\Omega \\ 2m\Omega & d + d_i \end{bmatrix} \begin{bmatrix} \dot{x}_2 \\ \dot{y}_2 \end{bmatrix} + \begin{bmatrix} c_x - m\Omega^2 & -d\Omega \\ d\Omega & c_y - m\Omega^2 \end{bmatrix} \begin{bmatrix} x_2 \\ y_2 \end{bmatrix} = m\Omega^2 \begin{bmatrix} e_{Sx} \\ e_{Sy} \end{bmatrix} + \begin{bmatrix} F_{x_2} \\ F_{y_2} \end{bmatrix} \quad (23)$$

in the rotor fixed corotating frame of reference. Here $\Omega = \frac{\omega}{p}$ is the synchronous angular velocity of the rotor and m is the rotor mass. In eq. (23) two different kinds of mechanical damping are introduced: one damping force $\mathbf{F}_D = -d\dot{x}_1$, proportional to the inertial orbital velocity \dot{x}_1 of the rotor and another force $F_{D_i} = -d_i \dot{x}_2$, proportional to the orbital velocity \dot{x}_2 of the rotor relative to the corotating frame of reference. While the first damping force accounts for air friction etc., the second one is due to internal friction, e.g. at joints on the rotor. The mechanical spring constants c_x (along a certain pole axis) and c_y (perpendicular to that) are equal in machines with more than two poles ($c_x = c_y$ if $p > 1$) and different in machines with two poles ($c_x \neq c_y$ if $p = 1$), due to the rotor construction (Gasch, 2006). The values $(e_{Sx}, e_{Sy}) = \text{const.}$ are the positional coordinates of the centre of inertia in the rotor fixed frame of reference.

In the following the parameters and variables

$$\begin{aligned}\omega_0 &= \sqrt{\frac{c}{m}}, \quad \tau = \omega_0 t, \quad \eta = \frac{\Omega}{\omega_0} = \frac{\omega}{p\omega_0}, \quad D = \frac{d}{2m\omega_0}, \\ D_i &= \frac{d_i}{2m\omega_0}, \quad c = \frac{c_x + c_y}{2}, \quad \kappa = \frac{c_x - c_y}{c_x + c_y}, \quad \zeta = \frac{c_{elm}}{c},\end{aligned}$$

are introduced. In this context ω_0 is the angular eigenfrequency of the corresponding undamped system without electromechanical forces, τ is a dimensionless timescale, D and D_i are mechanical damping ratios, c is the mean spring constant and κ is a measure for the noncircularity of the rotor shaft. This parameter is $\kappa = 0$ for machines with more than two poles ($p > 1$), and $\kappa \neq 0$ for 2-pole machines ($p = 1$). The parameters η and ζ will be explained below. Using these definitions eqs. (23) transform to

$$\begin{bmatrix} x_2'' \\ y_2'' \end{bmatrix} + \begin{bmatrix} 2(D + D_i) & -2\eta \\ 2\eta & 2(D + D_i) \end{bmatrix} \begin{bmatrix} x_2' \\ y_2' \end{bmatrix} + \begin{bmatrix} 1 + \kappa - \eta^2 & -2D\eta \\ 2D\eta & 1 - \kappa - \eta^2 \end{bmatrix} \begin{bmatrix} x_2 \\ y_2 \end{bmatrix} - \frac{\zeta}{c_{elm}} \begin{bmatrix} F_{x_2} \\ F_{y_2} \end{bmatrix} = \eta^2 \begin{bmatrix} e_{Sx} \\ e_{Sy} \end{bmatrix} \quad (24)$$

where $()'$ indicates the derivative with respect to the nondimensional time τ . The factor $\zeta = \frac{c_{elm}}{c}$ represents the relative strength of the electromagnetic forces, which are dependent on the electromagnetic machine design. Its order of magnitude is usually below 10%. Additionally the term $\frac{1}{\omega}$ in eqs. (19) and (21) becomes $\frac{1}{p\eta} = \frac{\omega_0}{\omega}$. Here η is the mechanical speed of rotation compared to the critical speed of the system. Usually machines running far below this critical speed ($\eta = 1$) are denoted as rigid shaft machines, while the ones running above it are known as soft mounted (Dawson, 1983).

3 Results

Eq. (24) is an inhomogenous system of two ODEs of second order with constant coefficients for the orbital motion $\mathbf{q} = [x_2 \ y_2]^\top$ of the rotor. Its solution is described by a homogenous- and an inhomogenous part (\mathbf{q}_h and \mathbf{q}_p). The latter one represents the steady state solution, when free oscillations have vanished. In view of electromechanically excited oscillations especially the question of self-excited oscillations is of great interest (Früchtenicht, 1982). Therefore in this section a stability analysis will be carried out posing the question under which circumstances free oscillations (homogenous solution) of exponentially rising amplitude may occur. Therefore an ansatz of the kind $\mathbf{q}_h = \mathbf{q} - \mathbf{q}_p = \mathbf{r}e^{\lambda\tau}$, where λ is an eigenvalue and \mathbf{r} is a corresponding eigenvector, is made and the characteristic polynomial in λ is derived. Applying Hurwitz' criterion (see e.g. Merkin (2012)) inequalities for the stability of the steady state can be found. These expressions describe regions in the parameter space where free oscillations decay (stable steady state) or rise (unstable steady state).

Before presenting stability maps a short view on relevant system parameters shall be given: Besides the mechanical parameters η , κ and D and D_i , there are three electromagnetic parameters: ζ , φ_{12p} and β . The parameter ζ for the relative strength of the electromagnetic forces has already been explained. As it turns out in the following, its influence on the stability is quite significant. Furthermore the electrical torque angle φ_{12p} and the resistance to reactance ratio β play a role in this context. For generators the torque angle is in between $\varphi_{12p} = 0$ (no load) and $\varphi_{12p} = \frac{\pi}{2}$ (critical load). Despite that it will not exceed $\frac{\pi}{4}$ under normal load conditions. The resistance to reactance ratio β has an order of magnitude of $\mathcal{O}(10^{-1})$. As the influence of the mechanical parameters D and κ is known, their values are set to $D = 0.002$ (weak damping) and $\kappa = 0.1$ in the case of 2-pole machines. The influence of all other parameters will be shown subsequently.

Fig. 3 shows two basic stability maps plotting the regions of stable and unstable states in the parameter space. In the figure the force parameter ζ is plotted against the specific rotational speed η for a 4-pole machine (Fig. 3 (a)) and a 2-pole machine (Fig. 3 (b)) considering homopolar fluxes, respectively. Each map shows stable regions in white and unstable states in grey for a basic parameter configuration. Note that changing the specific rotational speed $\eta = \frac{\Omega}{\omega_0}$ does not mean changing to the absolute running speed of the machine, which is fix and given by $\Omega = \frac{\omega}{p}$, but changing the critical speed ω_0 relative to Ω . Thus in Fig. 3 different machine designs are compared.

Analysing the stability behaviour different aspects raise the attention: As a first point both maps show an unstable region at high rotational speeds and high electromagnetic forces. In both cases one finds, that the higher the nominal rotational speed compared to the critical speed, the more likely it seems to be, that a stable state becomes unstable. As a major difference, 2-pole machines (Fig. 3 (b)) have two additional regions of unstable states. One narrow region around the critical speed ($\eta = 1$), which corresponds to the one found in earlier works (Kellenberger (1966), Boy (2015)) and one at very low running speeds and low values of ζ . The region around $\eta = 1$ originates

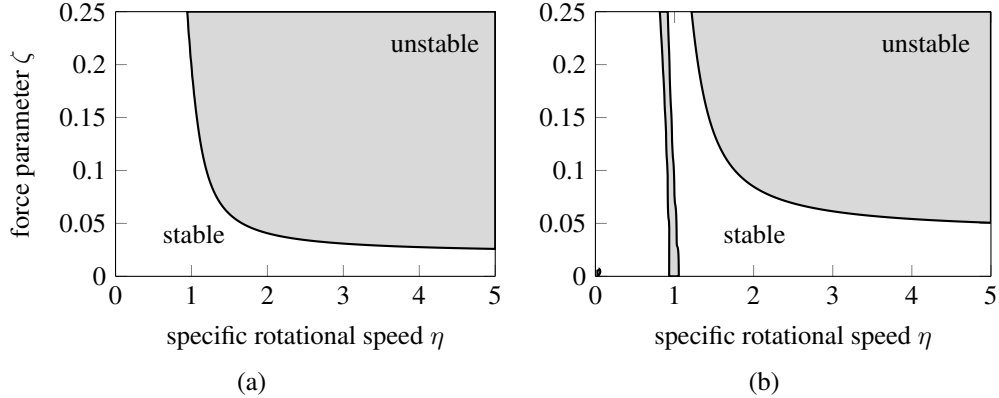


Figure 3. Stability map for the steady state of a 4-pole (a) and a 2-pole machine (b).

Here $D = 0.002$, $D_i = 0$, $\varphi_{12p} = \frac{\pi}{8}$ and $\beta = 0.1$ were chosen.

from the shaft noncircularity. Fig. 3 (b) shows that it is affected by the electromagnetic forces, as the critical speed is reduced with higher values of ζ . The second additional region is very small and seems not to be relevant for normal operational conditions. It originates from homopolar fluxes.

As stated before additional forces due to field damping can be compared to inner mechanical damping. To analyse their effect, consider Fig. 4, which shows a classical stability map considering the influence of inner mechanical damping for the example of a 4-pole machine. Here the damping ratio $\frac{D}{D_i}$ is plotted against the specific rotational speed η . From literature (Gasch, 2006) it is known, that in presence of inner damping, a certain critical speed depending on the damping ratio exists. Introducing electromagnetic forces to the system changes this map significantly, as indicated by dashed lines in the map. These lines show the stability border, if the resistance to reactance ratio β is increased from 0 by 0.025 to 0.1. Here it becomes obvious, that field damping may reduce the stability of the steady state. However, it should be noted here that the shown effect becomes weaker, if the mechanical damping forces become stronger compared to the electromagnetic forces.

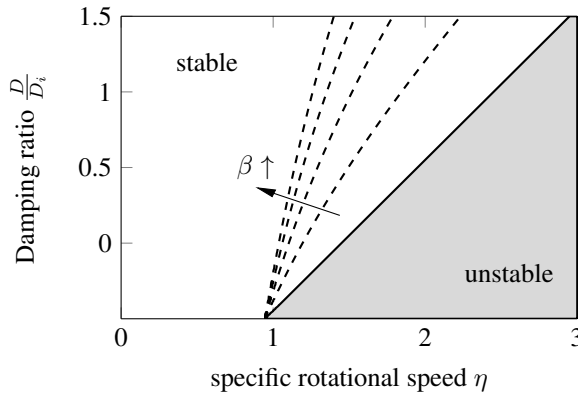


Figure 4. Stability map for the steady state of a 4-pole machine comparing the mechanical and inner Damping varying β from 0 by 0.025 to 0.1. All remaining parameters are chosen according to Fig. 3.

Having discussed the basic stability behaviour, a short view on parameter influence shall be taken as a last point of this section. For the sake of brevity these results are not shown explicitly, but simply explained.

Rising the number of pole pairs moves the stability border (critical speed in Fig. 3) towards lower values of η . This fact shows that self-excited oscillations become more likely in machines with a higher number of pole pairs. Although this model is not well suited for non-salient pole generators (which have even more magnetic poles), they might be even more sensitive to such oscillations.

Considering the stability conditions derived from Hurwitz' criterion one finds that the load condition (torque angle φ_{12p}) does not affect generators with more than two magnetic poles. However, in 2-pole machines when homopolar fluxes are present the picture changes. While in this case the narrow region of unstable states around $\eta = 1$ (Fig. 3 (b)) grows with increasing torque angle, the border of critical speeds for the region caused by field damping is slightly shifted towards higher rotational speeds. Furthermore the small region at very low speeds becomes larger.

4 Summary and Conclusions

Within this contribution the effect of field damping on lateral rotordynamics of non-salient pole generators has been investigated. The implemented electro-mechanical model comprises the electrical circuits of the stator and the rotor, as well as a damper cage, an approximation to the involved magnetic field problem and a Laval-rotor (Jeffcott-rotor). It has been shown that the currents flowing in the damper cage are affected by the orbital motion of the rotor and that there is a back coupling via electromagnetic forces exerted by the magnetic field. The mathematical structure of these forces is similar to inner mechanical damping and depends on the rotational speed of the machine, the machine design in general and the electrical properties of the damper cage. The survey has clarified that self-excited oscillations might occur in machines operating under high nominal rotational speeds compared to their critical speed. The stability behaviour is different for 2-pole machines and ones with a higher number of pole pairs due to the occurring homopolar fluxes in the first case.

In future surveys it would be sensible to reconsider the modelling in detail. At the one hand side, a major model contradiction concerning the assumptions of AC voltages in the damper cage has been found and at the other hand side effects like saturation should not be neglected. As a further point the model should be validated by more detailed numerical simulations and practical experiments.

Recently the authors pointed out, that rotational disturbances (e.g. hunting) may also significantly influence the steady state stability (Boy, 2016). A combined investigation of field damping and these effects could also be considered.

References

- [1] Arkkio, A. et al. (2000): Electromagnetic force on a whirling cage rotor. *IEE Proceedings-Electric Power Applications*, **147**, pp. 353–360.
- [2] Belmans, R. and Vandenput, A. and Geysen, W. (1987): Calculation of the flux density and the unbalanced pull in 2-pole induction machines. *Electr. Eng. (Archiv für Elektrotechnik)*, **70**, pp. 151–161.
- [3] Boy, F. and Hetzler, H. (2015): Rotordynamics of two-pole turbogenerators with refined modelling of the unbalanced magnetic pull. *Proc. Appl. Math. Mech.*, **15**, pp. 243–244.
- [4] Boy, F. and Hetzler, H., Ph. Schäfer (2016): On the rotordynamical stability of synchronous electric machinery considering different load cases and operating conditions. *Proc. ISMA 2016*, pp. 837–849.
- [5] Burakov, A. and Arkkio, A. (2006): Low-order parametric force model for eccentric-rotor electrical machine with parallel connections in stator winding. *IEE Proceedings-Electric Power Applications, IET*, **153**, pp. 592–600.
- [6] Dawson, R. and Eis, R. (1983): Specifying and designing flexible shaft electrical machines. *IEEE transactions on industry applications*, **6**, pp. 985–995.
- [7] Dorrell, D.-G. et al. (2011): Damper windings in induction machines for reduction of unbalanced magnetic pull and bearing wear. *2011 IEEE Energy Conversion Congress and Exposition*, **49**, pp. 1612–1619.
- [8] Frohne, H. (1968): Über den einseitigen magnetischen Zug in Drehfeldmaschinen. *Electr. Eng. (Archiv für Elektrotechnik)*, **51**, pp. 300–308.
- [9] Früchtenicht, J. (1982): Exzentrizitätsfelder als Ursache von Laufinstabilitäten bei Asynchronmaschinen. *Electr. Eng. (Archiv für Elektrotechnik)*, **65**, pp. 271–281.
- [10] Gasch, R. and Nordmann, R. and Prützner H. (2006): *Rotordynamik*. Springer-Verlag, Berlin Heidelberg.
- [11] Jordan, H. and Weis, M. (1970): *Synchronmaschinen I*. Vieweg & Sohn, Braunschweig.
- [12] Jordan, H. and Weis, M. (1969): *Asynchronmaschinen*. Springer Fachmedien, Wiesbaden.
- [13] Kaehne, P. (1963): Unbalanced Magnetic Pull in Rotating Electric Machines: Survey of Published Work. *ERA Report*, **142**.
- [14] Kellenberger, W. (1966): Der magnetische Zug in Turbogenerator-Rotoren als Ursache einer Instabilität des mechanischen Laufes. *Electr. Eng. (Archiv für Elektrotechnik)*, **50**, pp. 253–265.
- [15] Merkin, D. (2012): *Introduction to the Theory of Stability*. Springer Science & Business Media, New York.

[16] Rothwell, E.-J. and Michael J.-C. (2008): *Electromagnetics*. CRC press, Boca Raton.

[17] Tüxen, E. (1941): Das Oberwellenverhalten mehrphasiger Wechselstromwicklungen. Jahrbuch d. AEG-Forschung, **78**.

[18] Wallin, M. and Bladh, J. and Lundind, U. (2013): Damper winding influence on unbalanced magnetic pull in salient pole generators with rotor eccentricity. IEEE Transactions on Magnetics, **49**, pp. 5158–5165.

Nomenclature

r_1	stator radius	a_1	current sheet stator
r_2	rotor radius	a_2	current sheet rotor
\mathcal{K}	cartesian coordinate system	N_D	number of damper cage bars
\mathcal{Z}	cylindrical coordinate system	φ_k	electrical phase angle
$\vec{e}_x, \vec{e}_y, \vec{e}_z$	cartesian basis vectors	p	number of pole pairs
$\vec{e}_r, \vec{e}_\theta, \vec{e}_z$	cylindrical basis vectors	ν	number of field harmonic
r, θ, z	cylindrical coordinates	$\varepsilon = \frac{\delta_m}{r_2}$	small parameter
e	rotor eccentricity	B	magnetic flux density
γ	rotor eccentricity phase angle	j	imiginary unit
ϑ	rotor angle	\underline{A}	complex quantity
$\delta(\theta)$	actual air gap width at angle θ	$\underline{\underline{A}}$	complex conjugate
Ω	air gap region	$u(t)$	voltage
$\partial\Omega$	air gap region boundary	\underline{U}	voltage phasor (particular solution)
\mathcal{M}	representative damper cage mesh	$\underline{i}(t)$	current
μ_0	magnetic field constant	\underline{I}	current phasor (particular solution)
k	machine winding parameter	ω_ν	angular frequency of ν -th harmonic
$\Lambda(\theta)$	air gap permeance at angle θ	s_ν	slip of ν -th harmonic
\underline{z}^\pm	rotor eccentricity phasor	ω	supply angular frequency
Ψ	flux linkage	R	resistance
\vec{F}_1	force acting on the stator	L	inductivity
\vec{F}_2	force acting on the rotor	β	specific resistance of damper cage
ℓ	effective air gap length	S	center of inertia
\mathbf{I}	unity matrix	$\frac{\omega}{p}$	synchronous angular frequency
$\mathbf{P}_1, \mathbf{P}_2$	force matrix damper cage	ω_0	angular eigenfreq. (undamped system)
\mathbf{T}	transformation matrix (homopolar flux)	η	specific rotor speed
c_{elm}	electromagnetic stiffness constant	κ	noncircularity parameter
c	mechanical stiffness constant	ζ	specific electromagnetic stiffness
c_x	mechanical stiffness constant (x-direction)	τ	nondimensional time
c_x	mechanical stiffness constant (y-direction)	$(\cdot)'$	nondimensional time derivative
m	rotor mass	\mathbf{q}	mechanical position matrix
d	external damping constant	\mathbf{q}_h	homogenous solution
D	specific external damping constant	\mathbf{q}_p	particular solution
d_i	internal damping constant	λ	eigenvalue
D_i	specific internal damping constant	\mathbf{r}	eigenvector

On Behavior of a Double Rotor HAWT with a Differential Planet Gear

E. Shalimova, L. Klimina, K.-H. Lin

The mathematical model of a double disk horizontal axis wind turbine is constructed. The turbine has two propellers (actuator disks). One propeller is rigidly connected to a carrier of a planet gear, the other is rigidly connected to an external ring of the same planet gear. A rotor of an electrical generator is rigidly connected to a sun of the planet gear. The generator is included into a local electrical circuit with several consumers. The quasi-steady model of aerodynamic action is used. The electromechanical torque acting on the rotor of generator is assumed to be a linear function of an angular speed of the rotor. Existence and stability of steady motions are studied. Analysis of characteristics of steady motions such as angular speed of each propeller and mechanical power trapped from the flow is performed. A control strategy is suggested.

1 Introduction

Experimental tests and mathematical modeling have proved that using of two contra-rotating propellers in the construction of a horizontal axis wind turbine (HAWT) improves its aerodynamic characteristics (Jung et al., 2005; Shen et al., 2007; Farthing, 2010; Lee et al., 2012). Corresponding models of turbine aerodynamics are well-developed (see Hansen (2015)). But only in few of them the influence on the turbine dynamics produced by the interaction between mechanical and electrical parts of the HAWT is taken into account. Such an interaction is very essential for a so-called small-scale turbine with the generator connected to a local electrical circuit. Changes of electrical load influence such turbines greatly. In particular, the hysteresis of a trapped power with respect to increase/decrease of electrical load appears. This fact was shown for a classical (one propeller) HAWT in the frames of closed mathematical model by Dosaev et al. (2009).

In the current paper it is supposed that the generator of the double disk HAWT is connected to a local electrical circuit. The closed dynamical model with taking into account electromechanical interaction in the system is constructed. One of the parameters of the model is responsible for the value of external resistance in the circuit, so it describes the load from consumers upon the HAWT.

A special type of a double disk HAWT is studied: Propellers are installed at two rings of a differential planet gear (DPG), a rotor of a generator is connected to the third ring of the gear. Thus, the dynamics of the system essentially differs from that of a classical double disk HAWT, for which one propeller is joined to a rotor of a generator and the other is joined to a stator.

The evident advantage of using the DPG is that the relative angular speed of the rotor of the generator can be much higher than the relative angular speed of one propeller with respect to the other. Moreover, the DPG offers more options for additional control devices.

2 Description of the Mechanical System

The mechanical system includes two propellers. The front propeller is rigidly joined to the carrier of a DPG, the second propeller is rigidly joined to the external ring of the DPG (Figure 1). The front propeller is supposed to produce good torque at high tip speed ratio (to be leading at a regular mode of the operation). The back propeller is supposed to produce rather good torque at low tip speed ratio (to be leading at a starting stage of the operation). A rotor of a generator is rigidly joined to the sun gear of the DPG. The generator is connected to a local electrical circuit with a changeable external resistance.

Assume that r_c, r_s, r_r, r_p are the radii of corresponding rings, J_c, J_r, J_s, J_p are the central moments of inertia

of rigid bodies “front propeller + carrier”, “back propeller + external ring”, “sun + rotor”, each planet, m_p is the mass of each planet.

Suppose that there is no slipping between elements of DPG. Then the mechanical system has two degrees of freedom.

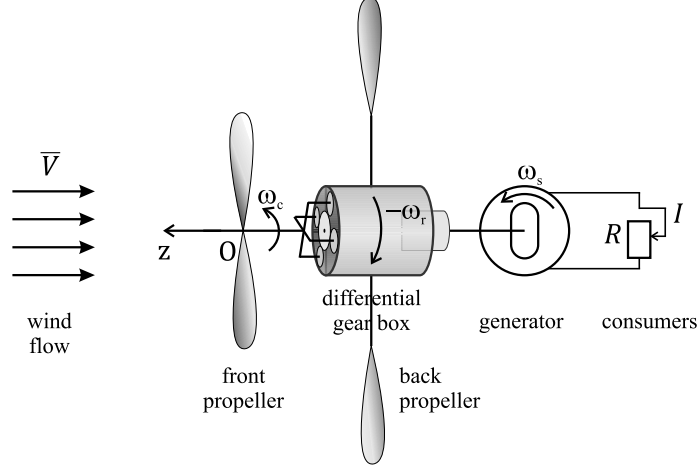


Figure 1. A general scheme of the system.

2.1 Model of External Forces

Assume that each propeller is under an aerodynamic action of an upcoming wind flow of a speed V , and the rotor of the generator is influenced by an electromagnetic field presenting between the rotor and the stator. Let us use the following model (similar to Dosaev et al. (2009, 2015)) for corresponding torques: Aerodynamic torques T_c , T_r and electromagnetic torque T_s with respect to the axis of rotation.

$$\begin{aligned} T_c &= 0.5\rho SbV^2 f_c(\lambda), & \lambda &= b\omega_c V^{-1}, \\ T_r &= 0.5\rho SdV^2 f_r(\eta), & \eta &= d\omega_r V^{-1}, \\ T_s &= -c^2 \omega_s (R+r)^{-1}, \end{aligned} \quad (1)$$

where ω_c , ω_s , ω_r , are the angular speeds of the carrier, the sun, and the external ring of the DPG, b is the radius of the front propeller, d is the radius of the back propeller, S is the characteristic area of each propeller, ρ is the air density, λ and η are the tip speed ratio of the front and back propeller respectively, c is the coefficient of electromechanical interaction (responsible for conversion of mechanical energy into electrical energy), r is the inner resistance of the generator, R is its external resistance. $f_c(\lambda)$, $f_r(\eta)$ are dimensionless functions of an aerodynamic torque.

Examples of functions $f_c(\lambda)$, $f_r(\eta)$ are represented in the Figure 2. The qualitative behavior of these functions for $\lambda > 0$ and $\eta < 0$ respectively corresponds to results of experimental tests (see Dosaev et al. (2009)). Parts of the curves, for which $\lambda < 0$ and $\eta > 0$ respectively, correspond to non-desirable direction of the propeller rotation. It is supposed that in these cases the aerodynamic torque increases or decreases exponentially. Thus, the functions $f_c(\lambda)$, $f_r(\eta)$ are continuous, but not differentiable at $\lambda = 0$ and $\eta = 0$ respectively (Figure 2).

Further qualitative results are valid for a wide class of functions. For the front propeller, the product $\omega_c T_c$ is positive for $\lambda \in (0, \lambda_1)$ and for $\lambda \in (\lambda_2, \lambda_3)$. For the back propeller, the product $\omega_r T_r$ is positive for $\eta \in (\eta_1, 0)$. The maximum absolute value of aerodynamic torque for the front propeller is larger than that for the back one. Thus, if the front propeller starts from zero angular speed, it can not reach its optimal angular speed without external help. On the other hand, if the back propeller works alone, it can not produce as high torque as the maximum torque of the front one.

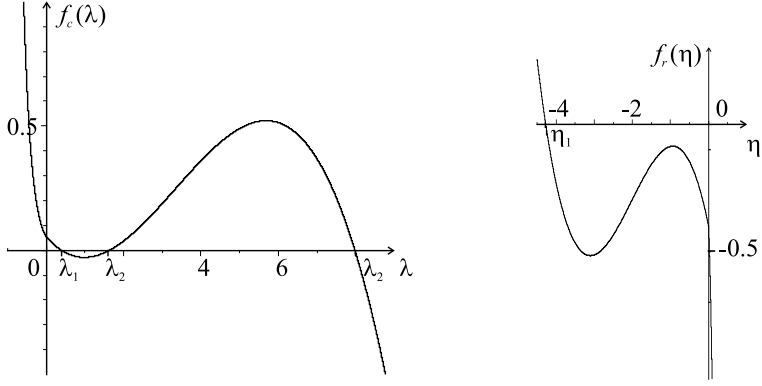


Figure 2. Dimensionless aerodynamic torques (on the same scale).

In further calculations it is assumed for simplicity that $b = d$ (the radius of the front propeller is equal to the radius of the back propeller).

3 Dynamical Equations and Statement of the Problem

Dynamical equations for a single-propeller HAWT with a DPG were derived in Dosaev et al. (2009). These equations can be easily modified for the case of two propellers, taking into account the relations (1). The obtained equations for a double rotor HAWT are as follows:

$$\begin{aligned}\lambda' &= a(A_2 + A_3)f_c(\lambda) + kA_3f_r(\eta) - pa^{-1}A_2\lambda + pk^{-1}A_2\eta; \\ \eta' &= kf_c(\lambda) + k^2(a^{-1}A_3 + A_1)f_r(\eta) + pka^{-1}A_1\lambda + pA_1\eta,\end{aligned}\quad (2)$$

where

$$\begin{aligned}p &= \frac{c^2}{2(R+r)\rho Sb^2V}, \quad a = \frac{r_s}{4r_c}, \quad k = \frac{a}{1-2a}, \\ A_1 &= \frac{r_c}{Jr_s}\rho Sb^3\left(\frac{r_r r_p}{2r_c r_s}J_c + \frac{2r_c r_r r_p}{r_s}m_p - \frac{2r_c r_r}{r_s r_p}J_p\right), \\ A_2 &= \frac{r_c}{Jr_s}\rho Sb^3\left(\frac{r_p}{2r_r}J_r + \frac{r_r}{r_p}J_p\right), \\ A_3 &= \frac{r_c}{Jr_s}\rho Sb^3\left(\frac{r_r r_p}{2r_s^2}J_r + \frac{r_p}{r_p}J_p\right), \\ J &= \frac{r_p r_r J_c J_s}{4r_s^2} + \frac{r_p J_c J_r}{4r_r} + \frac{r_c^2 r_p J_s J_r}{r_s^2 r_r} + \frac{r_r J_c J_p}{r_p} + \frac{r_c^2 r_r J_s J_p}{r_s^2 r_p} + \frac{r_c^2 J_r J_p}{r_r r_p} + \frac{r_c^2 r_r J_s m_p r_p^2}{r_s^2 r_p} + \\ &+ \frac{r_c^2 J_r m_p r_p^2}{r_r r_p} + \frac{4r_c^2 r_r J_p m_p r_p^2}{r_p^3}.\end{aligned}$$

All listed parameters are positive values. Parameter p is responsible for the electrical load in the circuit and for the wind speed, parameters A_1 , A_2 , A_3 , J are responsible for geometrical and inertia properties of the system.

Stable steady solutions of the system (2) correspond to operation modes of the wind turbine.

The task is to describe these steady solutions depending on parameters of the model, especially with respect to the parameter p . This parameter is responsible for the changeable conditions of operation such as the wind speed and the external resistance (e.g. if there are no consumers in the circuit, p is zero). The other parameters of the model for a particular wind turbine are fixed. Another task is to design a control strategy that allows reaching the operation mode with maximal trapped power.

4 Operation Modes

Each steady solution (λ^*, η^*) of the system (2) satisfies the following equations:

$$\begin{aligned}\lambda' &= a(A_2 + A_3)f_c(\lambda) + kA_3f_r(\eta) - pa^{-1}A_2\lambda + pk^{-1}A_2\eta = 0; \\ \eta' &= kf_c(\lambda) + k^2(a^{-1}A_3 + A_1)f_r(\eta) + pka^{-1}A_1\lambda + pA_1\eta = 0.\end{aligned}\quad (3)$$

Equations (3) define two curves: $\lambda' = 0$ and $\eta' = 0$. These curves divide the plane $\{\lambda, \eta\}$ into domains with determined signs of λ' and η' . Thus the direction of the trajectory $(\lambda(\tau), \eta(\tau))$ is determined in each domain. This is enough to find steady points and check their stability.

An example is shown in the Figure 3. The curve “1” is given by $\{\lambda' = 0\}$, the curve “2” is given by $\{\eta' = 0\}$; the arrows represent qualitative direction of trajectories in corresponding domains; black points correspond to attracting steady solutions, white points correspond to repelling steady solutions. The picture was constructed numerically for the following values of the parameters: $a = 0.125$, $A_1 = 3.7$, $A_2 = 2.8$, $A_3 = 3.4$, and $p = 0.0008$.

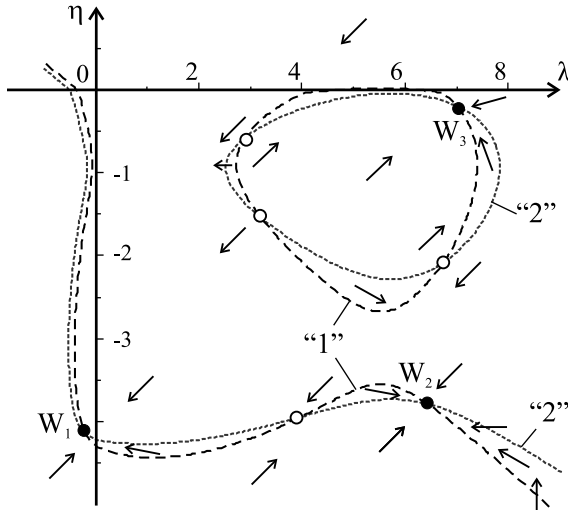


Figure 3. An example of location of steady points in the plane $\{\lambda, \eta\}$.

In our example the system possesses three attracting steady states: $W_i, i = 1, 2, 3$ (Figure 3).

In the operation mode corresponding to W_1 both propellers rotate in the same direction. The rotation speed of the back propeller is high, and the rotation speed of the front propeller is close to zero. In the operation mode corresponding to W_2 the propellers rotate in opposite directions with a rather high speed. In the operation mode corresponding to W_3 the propellers rotate in opposite directions, the speed of the front propeller is high, the speed of the back propeller is close to zero.

An attracting steady regime is preferable for practical applications, if a corresponding value $(\omega_c T_c + \omega_r T_r)$ of mechanical power taken from the flow is the largest. For the case shown in Figure 3, such a regime corresponds to the steady point $W_2 = \{\lambda^* = 6.4, \eta^* = -3.7\}$. Notice, that maximal value of $\lambda f_c(\lambda)$ could be reached for $\lambda = 6.2$, and maximal value of $\eta f_r(\eta)$ corresponds to $\eta = -3.4$. Thus, in the operation mode corresponding to the point W_2 , the power produced by both propellers is near the maximum. The value $p = 0.0008$ is chosen for the purpose to get closer to the maximum power taken from the flow.

5 Discussion and Control Strategy

The following problem is to reach a preferable operation mode from the starting state of the turbine, i.e. $\{\lambda = 0, \eta = 0\}$. For a single propeller small-scale HAWT, this problem can be solved by disconnecting consumers at the stage of starting the turbine (Dosaev et al. (2009)). Consumers are to be connected when the turbine reaches a rather high speed. This approach is suitable for a HAWT with aerodynamic torque function qualitatively similar to the function f_r in Figure 2 (the equation $f_r(\eta) = 0$ has only one root). But if the only propeller of a HAWT is qualitatively similar to the front propeller, no high angular speed can be expected without additional starter.

In our double disk system, the back propeller acts as a starter for the front one. Still from the Figure 3 one can notice that the point $\{0, 0\}$ doesn't belong to the domain of attraction of the preferable steady state W_2 .

The following control strategy bringing the system to a preferable operation mode is proposed:

Step 1. The external load coefficient p is set to zero, that means the consumers are disconnected from the circuit of the generator. (This first step is similar to the case of a single propeller HAWT.) The system will go to the steady

state with small λ and rather high η (see Figure 4). All parameters of the model in Figure 4 are similar to those in Figure 3 except the value of external load coefficient p . Thus, Figure 4 characterizes the behavior of the same turbine for disconnected electrical load.

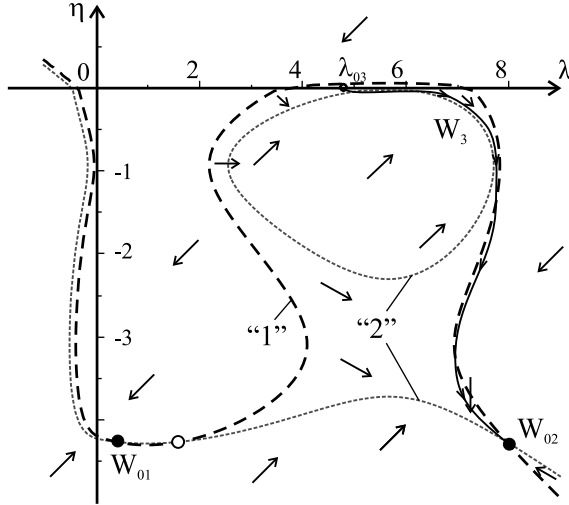


Figure 4. An example of location of steady points for $p = 0$. Solid line shows an example of a trajectory.

From zero initial conditions, the system approaches the attracting steady state W_{01} , that is approximately $\{0.4, -4.3\}$ in our example. If we just connect the desirable electrical load ($p = 0.0008$), the task will not be fulfilled, because the point W_{01} is not in the domain of attraction of W_2 (but in the domain of attraction of the state W_1). So additional step of control switching is needed.

Step 2. Let p be zero and the system be already in the state W_{01} . Apply the brake torque to the external ring. Here we assume that the brake system can be applied to any ring of the DPG, and it stops the corresponding ring very quickly. Additionally, assume that the moment of inertia of the sun ring is much higher than the moment of inertia of the carrier. So when the brake stops the external ring, the angular speed ω_s of the sun remains almost constant. Neglect small deviations of ω_s , and write down the kinematic relation ($\omega_s r_s = 2\omega_c r_c - \omega_r r_r$) before and after applying the brake:

$$\begin{aligned}\omega_{s01} r_s &= 2\omega_{c01} r_c - \omega_{r01} r_r, \\ \omega_{s01} r_s &= 2\omega_{c03} r_c.\end{aligned}\tag{4}$$

From equations (4) we obtain that the angular speed of the carrier after the second control intervention will be $\omega_{c03} = \omega_{c01} - 0.5\omega_{r01} r_r / r_c$. In our example $r_r / r_c = 2$. So we obtain: $\lambda_{03} = \lambda_{01} - \eta_{01} \approx 0.4 + 4.3 = 4.7$. Notice that for $\lambda \approx 4.7$, as well as for $\eta = 0$, the aerodynamic torque acting upon the corresponding propeller is accelerating (with respect to desirable direction of rotation). In our example for the case $p = 0$, the point $\{\lambda_{03}, 0\} \approx \{4.7, 0\}$ is in the domain of attraction of the point $W_{02} \approx \{8, -4.3\}$ (Figure 4). So after the system comes close to the state $\{\lambda_{03}, 0\}$ we switch off the brake, allowing the external ring to move free. Then the system moves from the state $\{\lambda_{03}, 0\}$ to the state W_{02} .

Step 3. Now the system is in the state W_{02} . Connect electrical load, making the desirable value $p = 0.0008$. For $p = 0.0008$, the point W_{02} is in the domain of attraction of the desirable steady point W_2 . The task is fulfilled.

It is noticeable that for the classical double disk contra-rotating HAWT, for which one propeller is joined to a rotor of a generator and the other is joined to a stator, and no DPG is used, the problem of accelerating one propeller using another one has not such an easy solution. In that case there is no option for a brake to transmit the energy of rotation of one propeller into the energy of contra-rotation of the other without special additional mechanism.

Thus, we confirmed one of the advantages of a DPG, that is to offer useful control options for reaching the desirable operation modes.

6 Conclusions

In this paper the closed dynamical model of a double propeller contra-rotating HAWT with a DPG is introduced. Torsional behavior of the system under external loading is discussed. Steady operation modes are studied with respect to a certain example of the configuration of the system. By this example it is shown that the system possesses an operation mode for which mechanical power produced by each propeller is close to its maximum. To obtain such an operation mode certain conditions on parameters of the model should be fulfilled.

It is the common situation, that the domain of attraction of this desirable operation mode does not include the initial state of the system with zero angular speeds of both propellers. Due to this fact, the special control strategy that makes the system reach desirable operation mode is constructed. This strategy involves two control actions: Disconnection/connection of consumers in the local electrical circuit of the generator and switching on/off of the brake applied to the external ring of the DPG. It was shown on the example, that this strategy provides the desirable result.

References

Dosaev, M.; Holub, A.; Klimina, L.: Preferable operation modes of a wind turbine with a differential planetary gearbox. *Mech. Mach. Sci.*, 25, (2015), 545–552.

Dosaev, M.; Lin, C.-H.; Lu, W.-L.; Samsonov, V.; Selyutskii, Y.: A qualitative analysis of the steady modes of operation of small wind power generators. *J. Appl. Math. Mech.*, 73(3), (2009), 259 – 263.

Farthing, S.: Robustly optimal contra-rotating hawt. *Wind Engineering*, 34(6), (2010), 733–742.

Hansen, M.: *Aerodynamics of Wind Turbines*. Routledge, London and New York (2015).

Jung, S.; No, T.-S.; Ryu, K.-W.: Aerodynamic performance prediction of a 30kw counter-rotating wind turbine system. *Renew. Energy*, 30(5), (2005), 631–644.

Lee, S.; Kim, H.; Son, E.; Lee, S.: Effects of design parameters on aerodynamic performance of a counter-rotating wind turbine. *Renew. Energy*, 42, (2012), 140–144.

Shen, W.; Zakkam, V.; Sorensen, J.; Appa, K.: Analysis of counter-rotating wind turbines. *Journal of Physics: Conference Series*, 75(1), (2007), 1–9.

Address: 1, Michurinckiy prospect, Moscow, 119192, Russia
email: ekateryna-shalimova@yandex.ru, klimina@imec.msu.ru

Transient Run-Up Simulations of Rotors in Journal Bearings Considering Mass-Conserving Cavitation Approaches

G. Nowald, R. Schmoll, B. Schweizer

The influence of mass-conserving cavitation modeling approaches on the stability of rotors in journal bearings is investigated. The model consists of a rotor represented by a flexible multibody system and the bearings discretized with finite elements. An approach for the pressure-dependent mixture density and mixture viscosity is made. Due to this mass-conserving cavitation approach, the Reynolds equation becomes explicitly time-dependent. Both subsystems – the multibody system for the rotor and the finite element system for the bearings – are coupled by means of an explicit co-simulation approach. Two different axial boundary conditions for the bearings are considered, namely a bearing submerged in an oil bath and an oil film free to air. The differences are studied in a stationary simulation. Then, the results of transient run-up simulations of a Jeffcott rotor and a turbocharger are discussed.

1 Introduction

Rotors supported in journal bearings are nonlinear systems, which are prone to subsynchronous oscillations and oil-whirl/whip instabilities, see e.g. Khonsari and Booser (2008); Szeri (2011). Especially lightweight rotors with high rotation speeds – such as turbochargers – are characterized by subsynchronous oscillations, see for instance Schweizer (2010). Numerical run-up simulations can be used to predict and to optimize the behavior of highly nonlinear rotor systems. Usually, complex phenomena in the bearings – such as cavitation – are neglected in order to reduce calculation times.

Cavitation in dynamic journal bearings occurs due to the limited ability of fluid lubricants to support tensile stresses. The lubricant film ruptures locally, resulting in a cavity filled with gas and/or vapor, see e.g. Braun and Hannon (2010); Dowson and Taylor (1979). Simple approaches to model cavitation are the well-known half-Sommerfeld (Gümbel) or Reynolds boundary conditions, see Dowson and Taylor (1979); Khonsari and Booser (2008); Szeri (2011). These approaches yield satisfactory results under stationary conditions and high bearing loads, see e.g. Dowson and Taylor (1979), yet they do not take into account the conservation of mass.

The more sophisticated Jakobsson-Floberg-Olsson (JFO) boundary condition, ref. Floberg (1974), considers a mass-conserving 2-phase flow. This boundary condition yields a complimentary problem: In the fully developed film region, the pressure is unknown, while in the cavitated region – where the bearing gap is partially filled with gas/vapor – the fluid fraction is unknown and the pressure is assumed to be equal to ambient pressure.

The cavitation algorithm of Elrod (1981), combines two separate differential equations – one for the cavitated region and one for the fully developed fluid film – into one single equation by means of a switch function. Since the area of the cavity is not known a-priori, the switch function has to be updated repeatedly, yielding large calculation times for transient run-up simulations. Furthermore, the type of the partial differential equation changes over the spatial coordinates, which may result in numerical difficulties.

To handle the complimentary problem more efficiently, some modifications of the Elrod algorithm have been proposed. Shi and Paranjpe (2002), introduced a universal variable, which incorporates the pressure and the fluid fraction. Alakhramsing et al. (2015), replaced the switch function by Boolean expressions of the universal variable. Nitzschke et al. (2016), proposed the smoothing of the switch function to reduce the mesh solution.

In this contribution, a modified Reynolds equation introduced in ref. Nowald et al. (2016) is used to study the influence of mass-conserving cavitation on the transient dynamic behavior and the stability threshold of rotor systems. The complementary problem and the use of a switch function are avoided by introducing a pressure-dependent fluid fraction. This yields a single differential equation for the unknown pressure, which is valid for both the cavitated region and the fully developed fluid film. This enables a straightforward solution of the Reynolds equation in a FEM package, which is well suited for complicated geometries and boundary conditions, see e.g. Dahmen and Reusken (2006); Shi and Paranjpe (2002). A co-simulation scheme, see Schmoll (2015), permits a simple coupling of the bearing model with different rotor models, implemented in a multibody software. Compared to a monolithic

model, the co-simulation approach allows the modeling of the subsystems with specialized software tools.

2 Numerical Rotor-bearing Model

In this section, the numerical model used for the transient run-up simulations is described. The model consists of a rotor and a bearing model, which are coupled by means of an explicit co-simulation approach.

2.1 Rotor Model

The turbocharger shown in figure 1 is modelled in the commercial multibody software (MBS) MSC Adams. The compressor and turbine wheel are assumed rigid bodies and are connected with a flexible shaft. Unbalance masses are considered at the compressor and at the turbine wheel. The forces from the journal bearings act on the shaft as externally applied forces. The rotor is kinematically driven: the rotor-speed is linearly increased from 0 up to a rotation speed of f_{max} during the simulation time T_{sim} .

The rotor system is represented by a nonlinear differential algebraic equation system, which has the following structure, see Shabana (2013),

$$\mathbf{M}(\mathbf{q})\ddot{\mathbf{q}} = \mathbf{f}(\mathbf{q}, \dot{\mathbf{q}}, t, \mathbf{u}_{MBS}) - \mathbf{G}^T(\mathbf{q}, t)\boldsymbol{\lambda}, \quad \mathbf{0} = \mathbf{g}(\mathbf{q}, t), \quad \mathbf{y}_{MBS} = \mathbf{y}_{MBS}(\mathbf{q}, \dot{\mathbf{q}}). \quad (1)$$

In the above equation, $\mathbf{M}(\mathbf{q})$ terms the mass matrix. The vectors collecting the generalized coordinates and the generalized velocities are denoted by \mathbf{q} and $\dot{\mathbf{q}}$, respectively. The vector \mathbf{f} contains the applied, gyroscopic and elastic forces. The bearing forces/torques in the lubricant films are collected in the multibody input vector \mathbf{u}_{MBS} , which is provided by the bearing model.

The algebraic constraint equations are summarized in the vector \mathbf{g} . The resulting constraint forces are $-\mathbf{G}^T(\mathbf{q}, t)\boldsymbol{\lambda}$ with the Jacobian $\mathbf{G}^T(\mathbf{q}, t) = \partial \mathbf{g} / \partial \mathbf{q}$ and the vector of Lagrange multipliers $\boldsymbol{\lambda}$, see Shabana (2013). The term $\mathbf{y}_{MBS}(\mathbf{q}, \dot{\mathbf{q}})$ indicates the output vector of the multibody system, containing the relevant kinematical quantities for the lubricant films, which are transferred to the bearing model.

2.2 Bearing Model

The dynamic forces in the journal bearings are calculated by integration of the pressure field $p(\phi, \bar{z}, t)$ in the lubricant film, which results from the displacement and the velocity of the rotor journal with respect to the bearing shell. The compressible Reynolds equation is used for the calculation of $p(\phi, \bar{z}, t)$, see e.g. Khonsari and Booser (2008); Szeri (2011), which reads

$$\frac{\psi^2}{6} \frac{\partial}{\partial \phi} \left[\frac{\rho}{\eta} H^3 \frac{\partial p}{\partial \phi} \right] + \left(\frac{R}{B} \right)^2 \frac{\psi^2}{6} \frac{\partial}{\partial \bar{z}} \left[\frac{\rho}{\eta} H^3 \frac{\partial p}{\partial \bar{z}} \right] = \omega \frac{\partial(\rho H)}{\partial \phi} + 2 \frac{d(\rho H)}{dt}, \quad (2)$$

with the circumferential coordinate ϕ and the axial dimensionless coordinate \bar{z} . The bearing has the radius R , the axial width B and the nominal relative gap size ψ . $H(\phi, \bar{z}, t)$ is the dimensionless gap function, ω denotes the

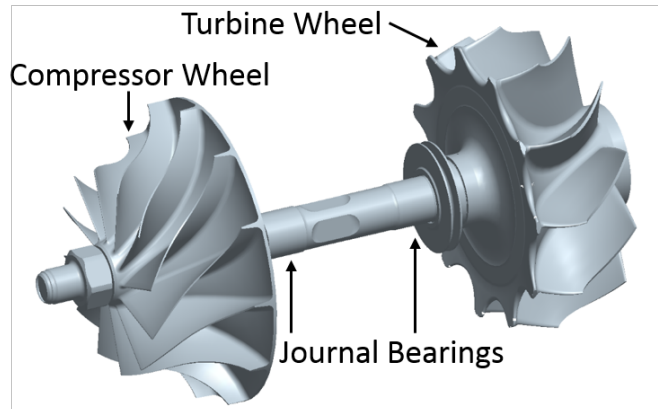


Figure 1. Turbocharger rotor

angular velocity of the rotor. ρ and η are the density and the viscosity of the lubricant, respectively.

A 2-phase cavitation approach is implemented which assumes a compressible mixture flow with mixture density ρ and mixture viscosity η . Since the mass of gas/vapor is negligible compared to the mass of the lubricant, the fluid fraction ϑ in the cavitated region is approximately equal to the density ratio, $\vartheta = \rho/\rho_0$, with the lubricant density ρ_0 , see Bartel (2010). Kumar and Booker (1991), proposed a proportional relation for the mixture viscosity

$$\vartheta = \frac{\rho}{\rho_0} = \frac{\eta}{\eta_0}, \quad (3)$$

where η_0 is the lubricant viscosity. In literature, a complementary problem is usually considered: in the fully developed film region, $\vartheta = 1$ and the pressure p is unknown, while in the cavitated film region p equals the atmospheric pressure p_0 and ϑ is unknown, see e.g. Kumar and Booker (1991); Alakhramsing et al. (2015); Nitzschke et al. (2016). In these approaches, a pressure-dependent switch function is used to determine for each discretized node separately, whether the fluid film is fully developed or cavitated.

Here, a pressure-dependent approach is made for the fluid fraction ϑ . For the fully developed fluid film, $p \geq p_0$ and $\vartheta = 1$, while for the cavitated film region $p < p_0$ and $\vartheta \rightarrow 0$. Thus, in the cavitated film region both p and ϑ can change to fulfill the Reynolds equation. A steep gradient $\partial\vartheta(p)/\partial p$ at $p \approx p_0$ causes the pressure p to only drop slightly below p_0 in the cavitated region, since the mixture density ρ is immediately reduced. A smoothed step function is used for $\vartheta(p)$, see figure 2.

Inserting equation (3) into (2) and assuming that the fluid fraction ϑ is pressure-dependent yields

$$-2H \frac{\partial\vartheta}{\partial p} \frac{dp}{dt} + \frac{\psi^2}{6\eta_0} \frac{\partial}{\partial\phi} \left[H^3 \frac{\partial p}{\partial\phi} \right] + \left(\frac{R}{B} \right)^2 \frac{\psi^2}{6\eta_0} \frac{\partial}{\partial\bar{z}} \left[H^3 \frac{\partial p}{\partial\bar{z}} \right] - \omega H \frac{\partial\vartheta}{\partial p} \frac{\partial p}{\partial\phi} = \vartheta \left[\omega \frac{\partial H}{\partial\phi} + 2 \frac{dH}{dt} \right]. \quad (4)$$

Note that equation (4) explicitly depends on time t . Since $\vartheta(p)$ is a known function, the derivative $\partial\vartheta(p)/\partial p$ can be calculated a-priori. Equation (4) is discretized with the commercial finite element software Comsol Multiphysics. The solution is stabilized by an artificial diffusion approach, see e.g. Kuzmin (2010).

The smoothing of Elrods switch function proposed in Nitzschke et al. (2016) smears the boundary between the fully developed fluid film region and the cavitated region. The smoothed switch function and the ansatz for the fluid fraction ϑ used in this contribution are both pressure-dependent and have a similar shape. However, they have different meanings: While the fluid fraction ϑ changes the compressibility of the lubricant-gas/vapor-mixture, the switch function changes the type of the differential equation. Furthermore, the switch function combines two independent differential equations for easier treatment, while equation (4) is a single differential equation for the mixture pressure, valid in both the fully developed fluid film region and the cavitated region.

For the solution of equation (4), axial boundary conditions of the pressure distribution $p(\phi, \bar{z}, t)$ in the fluid film are required. A simple and widely used assumption is constant ambient pressure p_0 , i.e.

$$p(\phi, \bar{z} = 0, t) = p(\phi, \bar{z} = 1, t) = p_0. \quad (5)$$

With the use of a Dirichlet boundary condition, the axial pressure gradient $\partial p/\partial\bar{z}$ is not specified. For classical cavitation models, the pressure p is never below ambient pressure p_0 and thus the lubricant is always flowing out of the bearing gap. Note that due to the assumption of a mixture flow, the pressure p can drop below ambient pressure

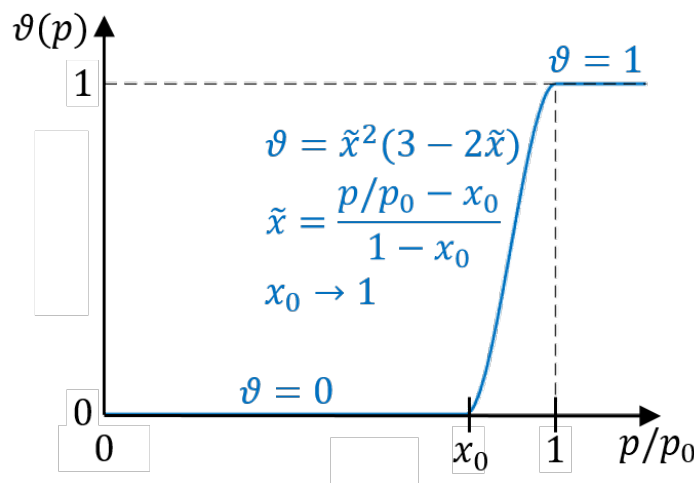


Figure 2. Pressure-dependent fluid fraction ϑ .

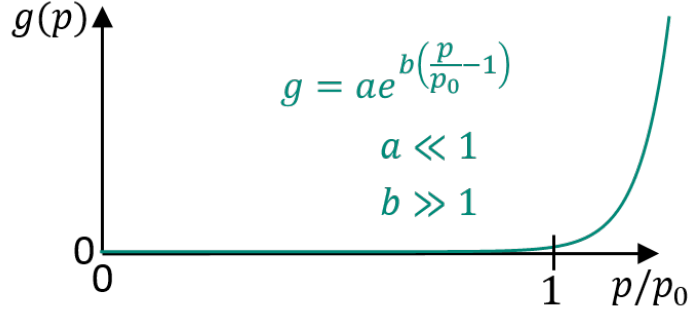


Figure 3. Penalty function $g(p)$ used for axial boundary condition (6).

p_0 , which results in a lubricant flow from the surrounding into the gap. Thus, the axial boundary condition (5) describes a bearing, which is completely submerged in an oil bath.

More common in applications of journal bearings are lubricant films, which are free to air at their axial boundaries. Here, the lubricant can only flow from the bearing gap to the surrounding. To prevent flow in the other direction, the pressure gradient $\partial p / \partial \bar{z}$ has to be 0 for $p < p_0$. This is achieved by applying a Neumann boundary condition, which incorporates a pressure dependent penalty function g :

$$\left(\frac{R}{B}\right)^2 \frac{\psi^2}{6\eta_0} \left[H^3 \frac{\partial p}{\partial \bar{z}} \right]_{\phi, \bar{z}=0, t} = g(p), \quad \left(\frac{R}{B}\right)^2 \frac{\psi^2}{6\eta_0} \left[H^3 \frac{\partial p}{\partial \bar{z}} \right]_{\phi, \bar{z}=1, t} = -g(p) \quad (6)$$

The shape of the chosen penalty function $g(p)$ is shown in Figure 3. For $p \leq p_0$, the axial flow is nearly zero, which is determined by the parameter a . The flow increases sharply for $p > p_0$, which is adjusted with the parameter b . The nonlinear equation system resulting from the discretization of equation (4) is solved by an iterative Newton method. A high axial outflow lowers the pressure p at the axial boundaries of the fully developed fluid film during the solution process until $p \approx p_0$. Then the axial outflow suddenly diminishes according to Figure 3. It has been found that $a=0.01$ and $b=100$ yield consistent results while still enabling a stable solution.

Equation (4) cannot be solved by only defining Neumann boundary conditions. This problem is solved by incorporating an inlet boundary condition with a prescribed feeding pressure p_{inlet} , see section 3.

2.3 Co-simulation Approach

The rotor-bearing system is decomposed by means of a force/displacement coupling approach, see e.g. Schmoll (2015); Schweizer et al. (2015). The MBS and the FEM software are coupled with an in-house interface using an explicit co-simulation approach, see Schweizer et al. (2015). Since commercial solvers usually do not give the possibility to save the current solver state and to repeat a time step, more stable implicit co-simulation techniques, see e.g. Schweizer et al. (2015), cannot be used. Figure 4 shows the schematic procedure of the sequential Gauss-Seidel master-slave scheme used in this paper. For simplicity, the subsystems are shown with only one output each,

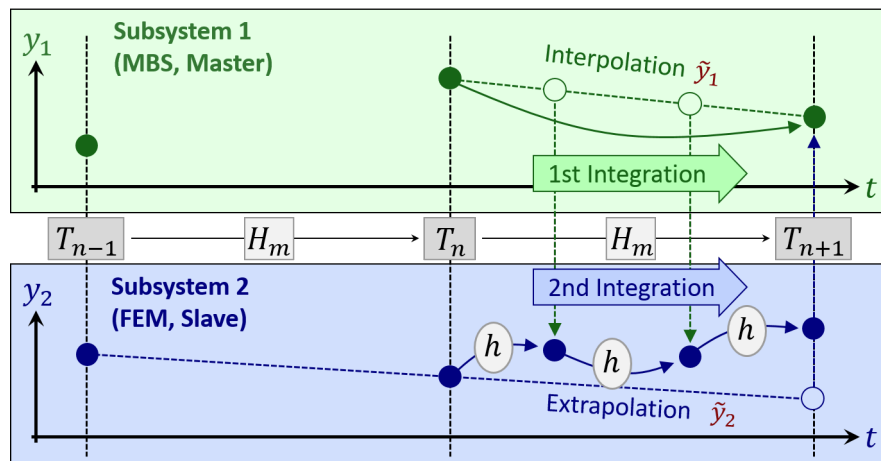


Figure 4. Explicit co-simulation approach: sequential Gauss-Seidel scheme.

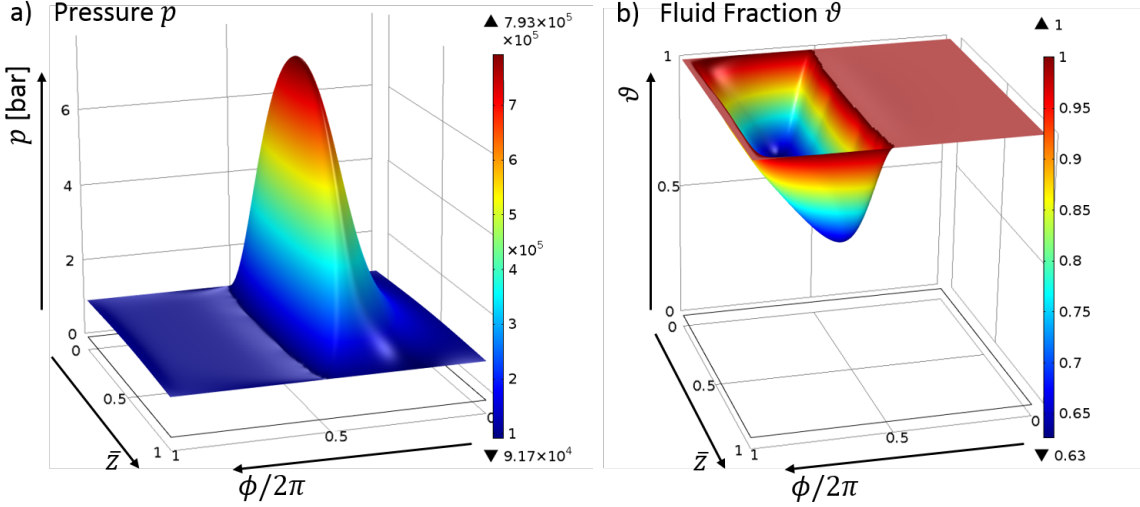


Figure 5. Stationary results for the bearing submerged in an oil bath, see eq. (5).

namely y_1 and y_2 . Firstly, subsystem 1 (master) is solved with the macro-time step H_m . At the time point T_{n+1} , the output y_2 from the second subsystem is required. Therefore, an approximation \tilde{y}_2 is carried out by applying appropriate extrapolation techniques for the output vector y_2 using the previous results. Then, subsystem 2 (slave) is solved with micro-time steps $h \leq H_m$. The required outputs y_1 from the first subsystem are approximated by the interpolation polynomial \tilde{y}_1 . Generally, Lagrange-polynomials are used for the extra- and interpolation. In this paper, both subsystems are solved using BDF-methods with variable time step size and variable integration order. In contrast to the parallel Jacobi-scheme used in Nowald et al. (2016), the subsystems have to be solved sequentially here. However, the bearing model has a substantially higher calculation time and requires smaller time steps to achieve an accurate solution, reducing the advantage of a parallel implementation. Note that the sequential Gauss-Seidel scheme usually exhibits a better stability behavior compared to the parallel Jacobi scheme, see Schmoll (2015).

3 Simulation Results

In this section, simulation results obtained with the 2-phase cavitation model are shown. Firstly, stationary calculations are performed to show the influence of the different applied axial boundary conditions. Then, results of transient run-up simulations of a Jeffcott rotor and of a heavy turbocharger with single oil films are discussed.

3.1 Influence of axial Boundary Conditions under stationary operating Conditions

Equation (4) is solved with constant kinematic input variables to study the influence of the two different axial boundary conditions (5) and (6) on the pressure distribution and the shape of the cavitating region. The shaft is considered to have a rotation speed of $\omega = 100$ Hz and a relative bearing eccentricity of $\varepsilon = 0.7$. The function H is minimal at $\phi = \pi$. The bearing parameters are $B/R = 1.6$, $\psi = 2.8\%$ and $\eta_0 = 12$ mPas. The dimensionless, developed fluid film geometry is discretized using 40×40 quadratic elements and parabolic shape functions.

Firstly, the results with the Dirichlet boundary condition (5) are shown in Figure 5. A periodic condition is used for the boundaries $\phi = 0$ and $\phi = 2\pi$, see Figure 6 a). The pressure in the fully developed fluid film region is not influenced significantly by the mass-conserving cavitation approach. Note that the ambient pressure is $p_0 = 1$ bar and that the pressure p is slightly below ambient pressure in the divergent part of the lubricant film gap. This yields a flow from the surrounding into the region of the divergent gap.

The fluid fraction ϑ represented in Figure 5 b) shows the change of the mixture properties in the lubricant film. In the convergent part of the gap, $\vartheta = 1$, i.e. the mixture density ρ and mixture viscosity η equal the properties of pure lubricant at ambient conditions, which is expected in the fully developed fluid film region. In the cavitating region, ϑ drops below 1. Since an oil bath is assumed for the axial boundary condition, the fluid fraction is 1 at the axial boundaries.

Secondly, results with the Neumann boundary condition (6) are shown in Figure 7. An axial feeding groove with an opening angle of $\theta_{\text{gap}} = 15^\circ$ is considered at $\phi = 0 = 2\pi$. A constant pressure $p_{\text{inlet}} = p_0$ is applied at the boundaries $\phi = \theta_{\text{gap}}/2$ and $\phi = 2\pi - \theta_{\text{gap}}/2$, see Figure 6 b). The pressure profile in Figure 7 a) resembles the

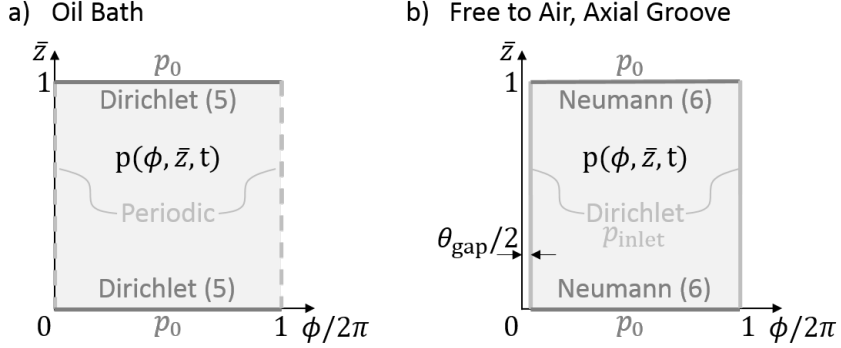


Figure 6. Pressure boundary conditions for the test cases.

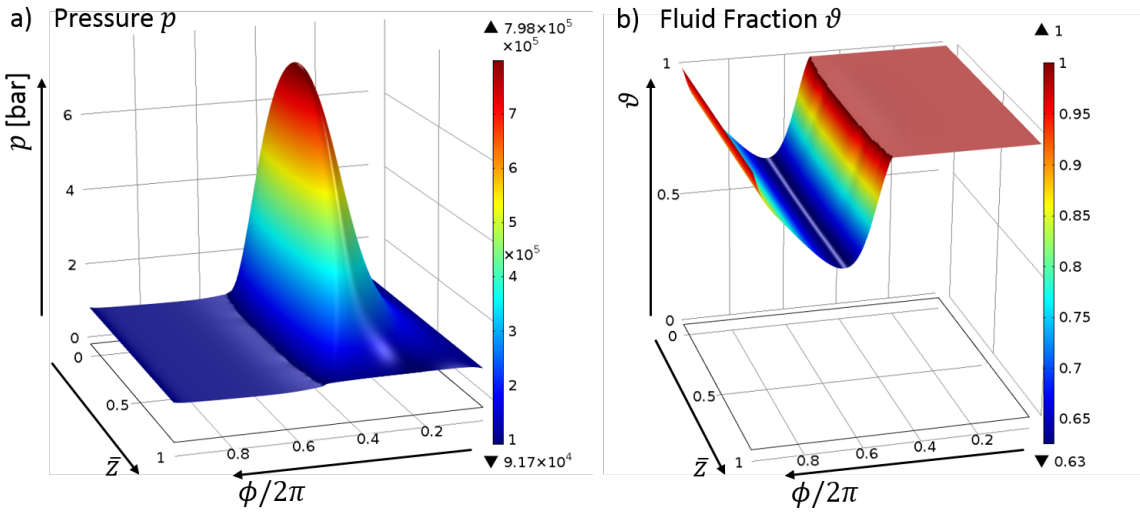


Figure 7. Stationary results for the bearing free to air, see eq. (6).

pressure distribution in Figure 5 a) in the convergent part of the gap. The difference of the maximum pressures is 0.6%. In the divergent part of the gap, the pressure also drops slightly below ambient pressure p_0 . The same minimal pressure is obtained for both boundary conditions. Note that in this case, the pressure is also below ambient pressure at the axial boundaries, resulting in a zero pressure gradient in axial direction. Hence, lubricant is not flowing at the axial boundary into the divergent part of the gap. This can also be seen in the fluid fraction ϑ shown in Figure 7 b), which also drops below 1 at the axial boundaries. The cavitated area is open to the surrounding.

3.2 Transient run-up Simulation of a Jeffcott Rotor

Transient run-up simulations of a symmetric Jeffcott rotor have been performed to study the influence of the cavitation model on the stability of the rotor-bearing system and to investigate the differences between the two different axial boundary conditions (5) and (6). The rotor has a mass of 6 kg and an unbalance of 3 gmm. The stiffness of the shaft is 4000 N/mm and the internal shaft damping is 0.1 Ns/m. External, linear viscous damping of 500 Ns/m has been applied on the center of mass of the rotor in order to enable passing through the subsynchronous oscillations. Results with low external damping have been presented in Nowald et al. (2016). The bearing parameters and the discretization are the same as in section 3.1. In the case that the bearings are free to air, axial feeding grooves with an opening angle of ϑ_{gap} and a constant feeding pressure $p_{\text{inlet}} = p_0$ are considered at the top of the bearing shells, see Figure 6 b). The rotor-speed is increased linearly from 0 to 800 Hz in 2 s.

Figure 8 shows the dimensionless eccentricity $\varepsilon(t)$ of the journal. At approximately 640 ms, the system with half-Sommerfeld cavitation boundary condition becomes unstable (oil whirl) and the journal eccentricity rises. Due to the high external damping, the eccentricity stays moderate, until the subsynchronous oscillations vanish at 1400 ms, leaving only synchronous oscillations due to unbalance.

Both simulations with the cavitation approach according to equation (4) have the onset of the oil whirl at lower rotation speeds and show higher eccentricities. The eccentricities of all three models are almost identical up to the

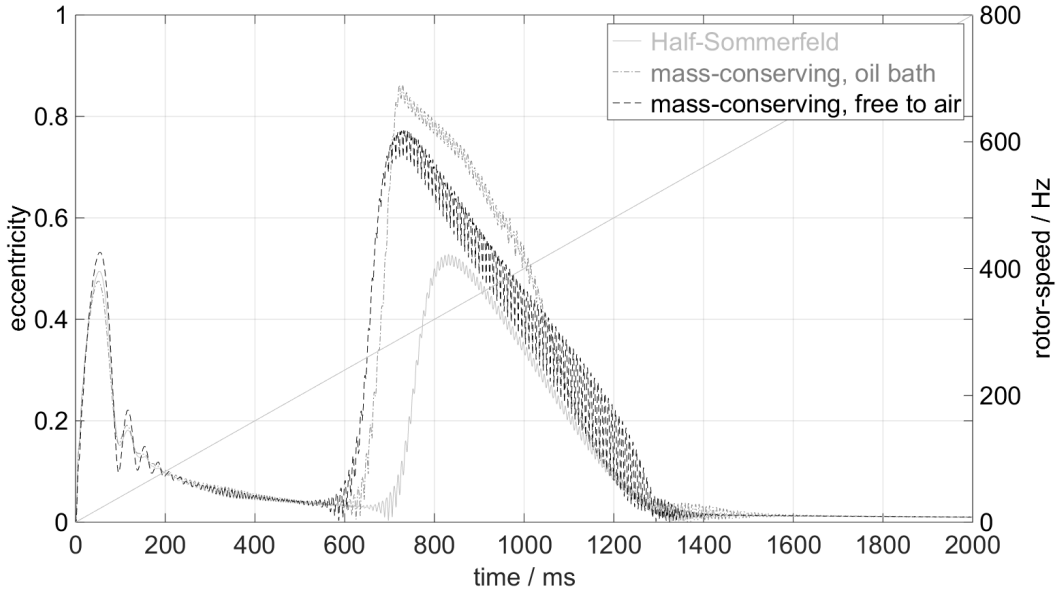


Figure 8. Run-up of a Jeffcott rotor with high external damping: journal eccentricity $\varepsilon(t)$.

onset of the oil whirl region. For all three cavitation models, the subsynchronous oscillations vanish at approximately the same rotor speed of 560 Hz.

The calculation time for one micro-step h of equation (4) using FEM discretization is approx. 10 ms on a standard desktop PC (Intel i7 processor). In the above example, the calculation time for one run-up simulation is approx. 20–30 h, depending on the number of microsteps the BDF-method takes.

3.3 Transient run-up Simulation of a Turbocharger Rotor

Now, run-up simulations with a heavy turbocharger in single oil film bearings are performed. The weight and unbalance of the rotor are the same as for the Jeffcott rotor. No external damping is applied. The bearing parameters and the discretization are equal to the corresponding parameters in the previous sections. The rotor-speed is increased linearly from 0 to 105 Hz in 7 s.

Figure 9 shows the dimensionless eccentricity $\varepsilon(t)$ of the rotor journal at the compressor-side, Figure 10 the dimensionless eccentricity $\varepsilon(t)$ at the turbine-side. Since no floating-ring bearings are considered here and no

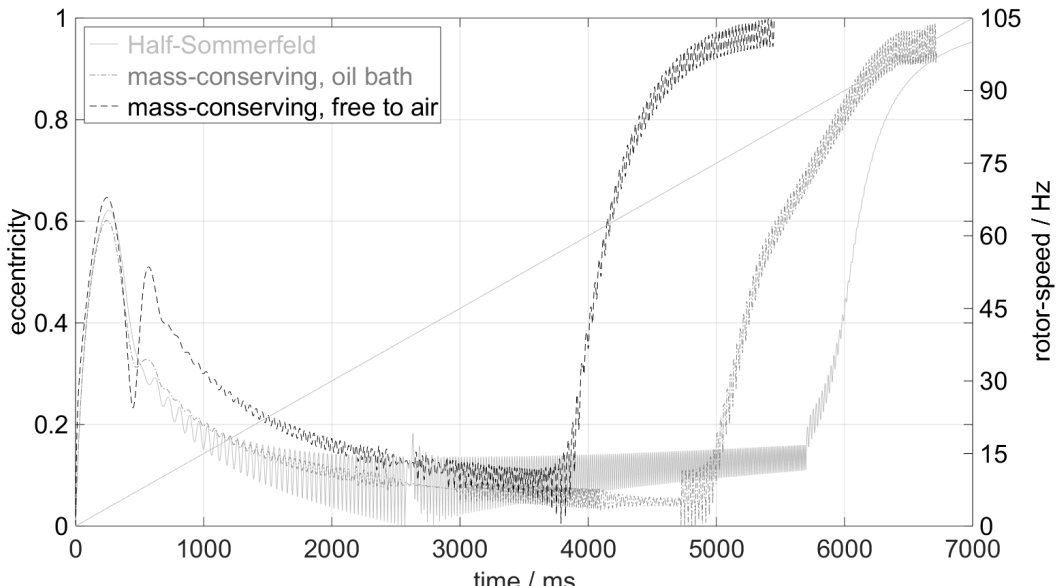


Figure 9. Run-up of a turbocharger rotor: journal eccentricity $\varepsilon(t)$ on compressor-side.

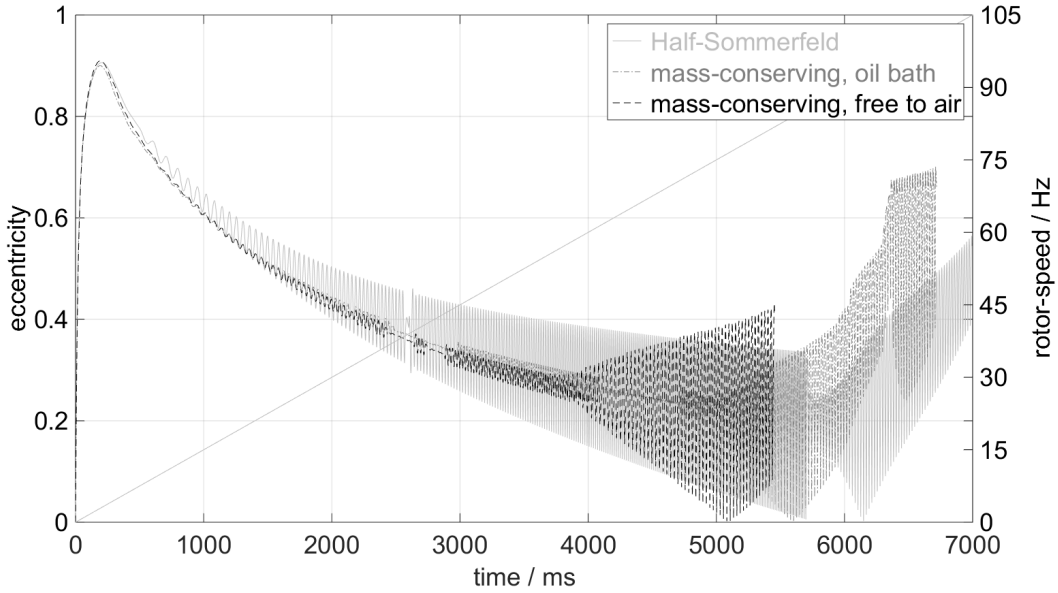


Figure 10. Run-up of a turbocharger rotor: journal eccentricity $\varepsilon(t)$ on turbine-side.

external damping is applied, the onset of the oil whirl region is reached at a low rotation speed and the eccentricities in the bearings become very large, preventing operation at higher rotation speeds. As for the Jeffcott rotor, the onset of the oil whirl is predicted at lower rotational speeds when the 2-phase cavitation approach is considered. The eccentricities of the three models are similar up to the onset of the oil whirl region. The whirl on the compressor-side is more pronounced due to the higher weight of the turbine wheel, which applies a higher load on the turbine-side journal.

4 Conclusion

In this contribution, transient run-up simulations have been performed to study the effect of mass-conserving cavitation algorithms on rotors in journal bearings. A modified Reynolds equation, which is based on a pressure-dependent density and viscosity, has been obtained. Compared to more sophisticated cavitation models, this straightforward approach can be implemented very easily within a FEM implementation. The rotor models, described as multibody systems, are coupled to the bearing model using an explicit co-simulation approach.

For the axial boundary conditions of the lubricant films, two cases have been considered. It has been found that the classical prescribed pressure (Dirichlet boundary condition) corresponds to a bearing, which is completely submerged in oil. This is due to the fact that with the current cavitation approach, also pressure values below the ambient pressure are possible, resulting in a lubricant flow from the surrounding into the divergent part of the bearing gap. In many practical applications, the lubricant films are axially free to air. Thus, a second boundary condition was implemented, which makes use of a penalty function to prevent flow into the cavitating region. The two boundary conditions have been compared. While the pressure in the fully developed lubricant film is very similar for both approaches, differences in the divergent part of the bearing gap and in the shape of the cavitating area have been observed.

Finally, transient run-up simulations have been performed to study the influence of the cavitation approach on the stability of the rotor bearing system. A symmetric Jeffcott rotor and an asymmetric heavy turbocharger with single oil films have been investigated. For both rotors, the models that considered mass-conserving cavitation predicted the onset of instability at a lower rotation speed than models using the classical half-Sommerfeld cavitation approach. For rotational speeds below the threshold of instability, all three models showed good agreement with the half-Sommerfeld cavitation approach.

Current work is focused on the extension of the model to rotors in floating-ring bearings.

References

Alakhramsing, S.; van Ostayen, R.; Eling, R.: Thermo-hydrodynamic analysis of a plain journal bearing on the basis of a new mass conserving cavitation algorithm. *Lubricants*, 3, 2, (2015), 256–280.

Bartel, D.: *Simulation von Tribosystemen: Grundlagen und Anwendungen*. Vieweg+Teubner research, Vieweg Verlag, Friedrich & Sohn Verlagsgesellschaft mbH (2010).

Braun, M.; Hannon, W.: Cavitation formation and modelling for fluid film bearings: a review. *Proceedings of the Institution of Mechanical Engineers, Part J: Journal of Engineering Tribology*, 224, 9, (2010), 839–863.

Dahmen, W.; Reusken, A.: *Numerik für Ingenieure und Naturwissenschaftler*. Springer-Verlag (2006).

Dowson, D.; Taylor, C.: Cavitation in bearings. *Annual Review of Fluid Mechanics*, 11, 1, (1979), 35–65.

Elrod, H.: A cavitation algorithm. *Journal of Lubrication Technology*, 103, 3, (1981), 350–354.

Floberg, L.: Cavitation boundary conditions with regard to the number of streamers and tensile strength of the liquid. *Cavitation and related phenomena in lubrication*, pages 31–36.

Khonsari, M.; Booser, E.: *Applied Tribology: Bearing Design and Lubrication*. Tribology in Practice Series, Wiley (2008).

Kumar, A.; Booker, J.: A finite element cavitation algorithm. *Journal of Tribology*, 113, 2-4, (1991), 276.

Kuzmin, D.: A guide to numerical methods for transport equations. *Lecture, Friedrich-Alexander-Universität Erlangen-Nürnberg*.

Nitzschke, S.; Woschke, E.; Schmicker, D.; Strackeljan, J.: Regularised cavitation algorithm for use in transient rotordynamic analysis. *International Journal of Mechanical Sciences*, 113, (2016), 175–183.

Nowald, G.; Schmoll, R.; Schweizer, B.: Influence of fluid film cavitation effects on the stability of rotors in journal bearings. In: *VIRM 11 – Vibrations in Rotating Machinery, Manchester, United Kingdom, September 13th–15th* (2016).

Schmoll, R.: *Co-Simulation und Solverkopplung: Analyse komplexer multiphysikalischer Systeme*. Ph.D. thesis, Universität Kassel (2015).

Schweizer, B.: Dynamics and stability of turbocharger rotors. *Archive of Applied Mechanics*, 80, 9, (2010), 1017–1043.

Schweizer, B.; Li, P.; Lu, D.: Explicit and implicit cosimulation methods: Stability and convergence analysis for different solver coupling approaches. *Journal of Computational and Nonlinear Dynamics*, 10, 5, (2015), 051007.

Shabana, A.: *Dynamics of multibody systems*. Cambridge university press (2013).

Shi, F.; Paranjpe, R.: An implicit finite element cavitation algorithm. *Computer Modeling in Engineering and Sciences*, 3, 4, (2002), 507–516.

Szeri, A.: *Fluid Film Lubrication*. Cambridge University Press (2011).

Address: Institut für Angewandte Dynamik, Technische Universität Darmstadt, 64287, Darmstadt, Deutschland
email: nowald@ad.tu-darmstadt.de

Turbocharger Dynamic Analysis: Advanced Design Simulation in Time Domain Using CFD Predicted Thermal Boundary Conditions

S. Bukovnik, G. Offner, A. Diemath, L. Smolik

Small changes of surface temperature, clearance and bearing profile can significantly change stiffness and damping characteristics of slider bearings. This may influence dynamics and in case of turbochargers the rotor radial deflection. Noise, Vibration, Harshness (NVH) or durability issues like rotor colliding with housing may be implied as a consequence.

This paper presents a new methodology for dynamic turbocharger investigation. It considers multi-body dynamics (MBD) of flexible rotor and housing structures coupled with elasto-hydrodynamics (EHD) of the inner and outer oil film. The energy equation for calculation of oil film temperature is considered in EHD using thermal boundary condition obtained from 3D computational fluid dynamics (CFD) simulation. Typical targets for CFD simulation within the turbocharger development process are flow and thermal investigation as well as specifically providing accurate thermal boundary condition for thermo-mechanical fatigue analysis. For this purpose CFD analysis considers a fully coupled fluid-structure interaction. However, the same CFD model can be used to provide the required boundary conditions for dynamic analysis as well. The bearing profiles under thermal load are derived from Finite Element (FEM) analysis based on same thermal boundary conditions.

The authors demonstrate the application of the methodology for a typical turbocharger design study applied for heavy-duty engines with full floating bushings that have radial bore connections between inner and outer oil films. The rotor operating speed reaches up to 110 krpm. Dynamic simulation results with nominal clearance and temperature are compared with the results obtained when CFD and FEM predicted boundary conditions are used. Based on results for the oil film pressure and flow through each oil film as well as flow between inner and outer oil film a valid conclusion about the rotor dynamic behaviour, bearing mechanical and thermal loads can be made. The presented methodology proves to be a next level approach in prediction of turbocharger simulation in the development process.

1 Introduction

In recent years the number of turbo charged combustion engines has dramatically increased. Turbocharger manufacturers are required to provide the optimized designs of turbochargers for a variety of combustion engines, which means a large effort for design optimization and testing is necessary. Simulation tools can be used to speed up the design and optimization process and reduce its cost and time. There are existing simulation approaches which can be used for the detailed dynamic analysis of the turbocharger behaviour. Such refined simulation approaches consider effects of rotor flexibility, unbalance distribution, gyroscopic effects, interaction of the oil films and structure and even coupling of inner and outer oil film for the full floating bushings design. However, to obtain accurate results a detailed information about the oil property in the bearings, especially the oil viscosity is needed. Oil viscosity is typically assumed as constant which is based on the assumed temperature. Alternatively measured oil temperature can be used for determination of oil viscosity. When temperature is measured this is typically done at the location where oil enters the turbocharger housing and not in the oil film. As turbochargers can operate at very high temperatures, the heat that spreads from the turbine side through the structure to the oil film might influence the temperature of the oil. In addition, due to the rotation of the rotor and floating bushing, heat is generated in the oil film due to viscous friction. This heat is dissipated to the surrounding structure but it also heats up the oil film. AVL EXCITE™ offers the possibility to consider the energy equation of the oil film in combination with its elasto-hydrodynamics. With this approach it is possible to consider the correct temperature distribution within the oil film and by this a correct oil viscosity over time.

Boundary condition for the oil film energy equation is structure temperature. This temperature is not uniform. It is strongly influenced by the heat coming from the turbine side and by cooling effects of the cold air at the compressor side. A typical temperature distribution in the turbocharger housing is shown in Figure 1.

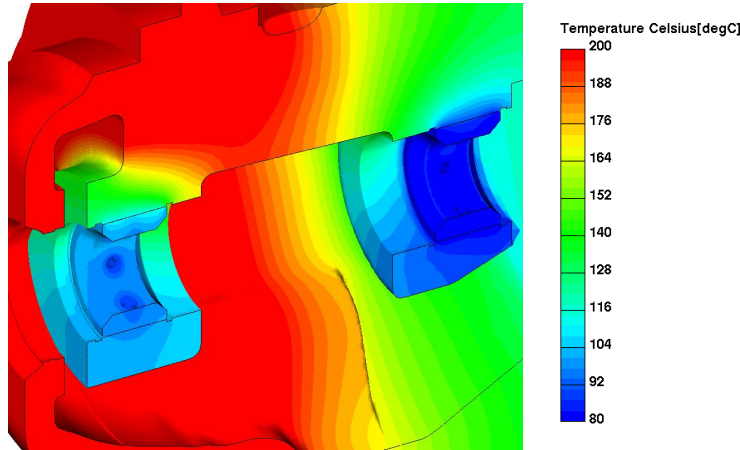


Figure 1. Typical temperature distribution in turbocharger housing

The consideration of the structure temperature distribution, is also done based on results of preliminary CFD calculation. Interacting surfaces of the turbocharger housing and floating bushing as well as floating bushing and the rotor are typically assumed as perfect cylinders in dynamic simulation. Under high temperature load, especially at the turbine side, thermal deformation of the structure is not uniform due to the unsymmetrical geometry of the turbocharger housing as well as the unsymmetrical temperature distribution in the housing structure. The deviation of the shape from the perfect cylinder at bearing surfaces can be several microns which is already a relevant percentage of the clearance and which therefore must not be neglected in order to be able to predict accurate oil film pressure distributions. This deviation can be considered in the dynamic simulation model as deviations of the cylindrical shape in radial direction, which can be defined as a surface map. Such maps can be obtained as a result of thermal structure analysis performed using FEM. The thermal boundary conditions for the FEM calculations are structure temperatures which again are obtained from CFD calculation.

2 Turbocharger used for this Investigation

The turbocharger used to demonstrate the methodology in this paper is the existing design applied for heavy-duty engines with full floating bushings that have 6 radial bore connections that connect outer and inner oil films. The rotor is axially supported with axial bearings close to the compressor wheel. Axial motion of the floating bushings is supported by the two circlips per floating bushing that are mounted in the housing.

The housing of the turbocharger is made of steel. The compressor wheel is made of aluminium and the rotor shaft and the turbine wheel are made of steel as well. The total rotor mass is about 1 kg of which the compressor wheel is about 0.19 kg and the turbine wheel is 0.56 kg. Unbalance is applied at both wheels, at wheel nose and wheel back separately. The level of unbalance is 0.6 to 0.8 gmm at the wheel nose and 0.9 to 1.3 gmm at the wheel back. The rotor operating speed reaches up to 110 krpm. The oil used in this turbocharger is SAE 10W-40. It is supplied in both outer oil films via a bore in the housing. The oil supply pressure is 3 bar, while the assumed temperature of the supplied oil is 90 degC.

3 CFD Simulation Model

This section briefly describes the fluid dynamics and conjugate heat transfer as part of the general multi-physics approach, which is implemented in the commercial CFD code AVL FIRE™, Basara et al. (2009) and AVL List (2017). In this multi-material approach, temperatures and local heat transfer coefficients on domain interfaces are exchanged after each iteration step considering implicitly coupled fluid and structure domains. Hence, the temperature distribution within the structural part of the turbocharger is also obtained from the steady CFD simulation. The steady CFD simulation for the highest exhaust gas temperature and exhaust gas flow is selected in order to obtain the highest possible structure temperature and by this the worst conditions for the oil films. The methodology is based on the fully conservative finite-volume method adopted for unstructured meshes which can contain computational cells of any shape. All dependent variables, such as momentum, pressure, density, turbulence kinetic energy, dissipation rate, and total enthalpy / temperature are calculated at the cell center. For fluid parts, such as gas flow in the turbine and compressor domains, the Reynolds-Averaged Navier-Stokes

(RANS) equations are used for numerical simulations. The rotational motion of the compressor and the turbine is modelled via the method of moving reference frame (MRF), Luo et al. (1994). The simulation mesh, which is used for the multi-material simulation, counts in total 7.17 million polyhedral cells. The entire mesh consists of 15 domains, whereas 13 domains are solid materials of various material properties, as shown in Figure 2, and the remaining two domains contain the calculated gas flow for exhaust gas residual (EGR) from the turbine side and air from the compressor side.

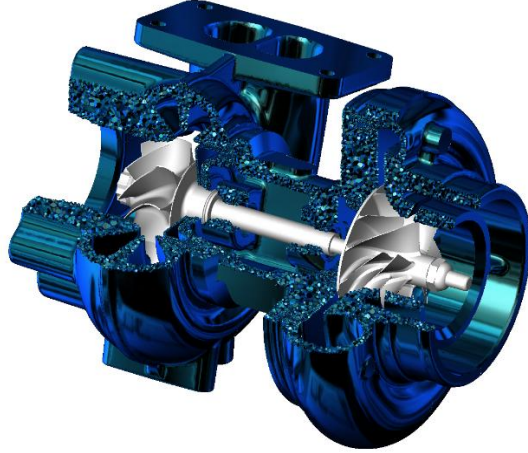


Figure 2. Structural parts of multi-material simulation model.

Figure 3 left displays the temperature field for the entire structural part gathered for the exemplary operating point at 80.7 krpm rotor speed. The corresponding temperature in an axial cross section of the flow field and structural part in the turbine section is shown in the right picture of Figure 3.

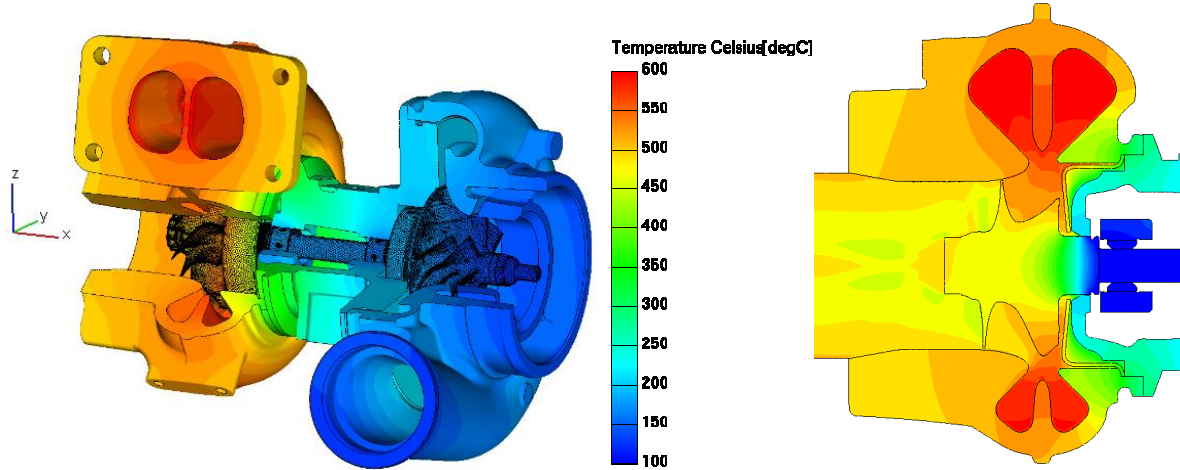


Figure 3. Temperature distribution in entire structure (left) and in a fluid/structure turbine cross section (right).

CFD simulations are typically done for a flow and thermal investigation as well as for providing accurate thermal boundary condition for thermo-mechanical fatigue analysis. In the investigation shown in this paper the condition with the hottest structure observed during CFD analysis is used as a boundary condition for the dynamics investigation. Structure deformed shape under the thermal load obtained from CFD is computed using FEM as shown in Figure 4. The FEM results in the figure are enlarged by a factor of 300.

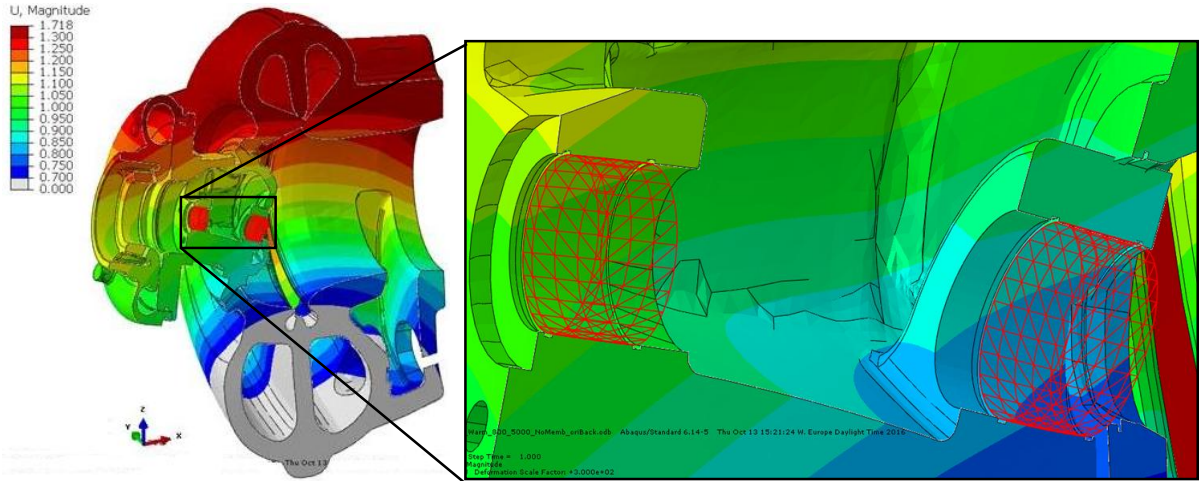


Figure 4. Turbocharger housing (left) and zoomed into the area of bearings (right) under thermal deformation.

4 Dynamic Simulation Model

Figure 5 shows a schematic representation of the turbocharger simulation model, which is used in this paper. The major components, which need to be considered, are housing and rotor that are considered as flexible bodies, which itself is supported by two bearings. Each bearing consists of an inner and an outer oil film and a floating bushing that is also a flexible body. Inner and outer oil films are connected via six drillings in the bushing, respectively. The according mathematical sub-models will be briefly introduced in the following sections. For more details of the sub-models as well as their coupling, refer to Offner (2013). During simulation, the coupled sub-models are solved in time domain using numerical time integration.

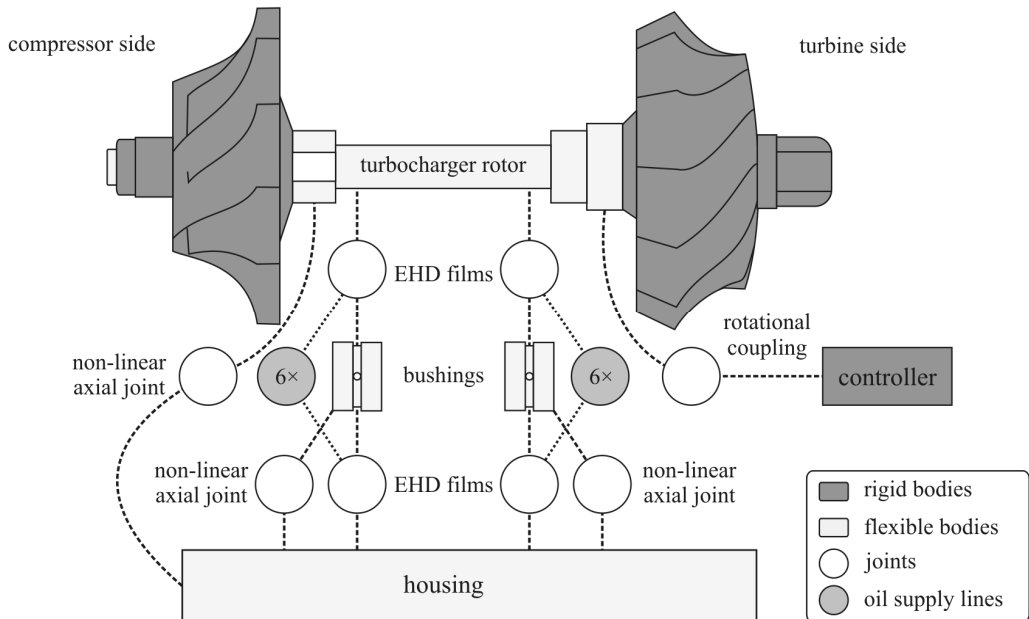


Figure 5. Schematic representation of the AVL EXCITE™ simulation model of the investigated turbocharger

Structural Components

Each structural component is represented by a body, which is modelled according to the floating frame of reference formulation (FFoR), see Offner (2011) for details. The formulation allows to distinguish global motion and local elastic deformation. Accordingly, the equations of motion for a structured flexible body, Parikyan et al. (2001), read

$$\begin{aligned}
\mathbf{M} \cdot \ddot{\mathbf{q}} + \mathbf{D} \cdot \dot{\mathbf{q}} + \mathbf{K} \cdot \mathbf{q} &= \mathbf{f}^* + \mathbf{f}^a + \mathbf{f}^{gyros} - \mathbf{f}^{rbAcc} \\
\mathbf{S}(\boldsymbol{\theta}_B) \cdot \dot{\boldsymbol{\theta}}_B &= \boldsymbol{\omega} \\
\boldsymbol{\theta}_B^T \cdot \boldsymbol{\theta}_B &= 1 \\
\mathbf{r}(\mathbf{q}) &= \mathbf{0}
\end{aligned} \tag{1}$$

This differential algebraic equation system describes the global motion and local vibrational behaviour of a flexible body and is solved with respect to the vector of unknowns, which reads

$$\mathbf{z} = (\mathbf{x}_B^T, \boldsymbol{\theta}_B^T, \dot{\mathbf{x}}_B^T, \boldsymbol{\omega}^T, \mathbf{q}^T, \dot{\mathbf{q}}^T)^T \tag{2}$$

and which considers the global position and orientation coordinates ($\mathbf{x}_B \in \mathfrak{R}^3$ and $\boldsymbol{\theta}_B \in \mathfrak{R}^4$), the velocity vectors $\boldsymbol{\omega} \in \mathfrak{R}^3$ and $\dot{\mathbf{x}}_B \in \mathfrak{R}^3$ as well as the generalized displacement vector \mathbf{q} and its first time derivative. \mathbf{q} represents the elastic deformations of the total body, considering a space discretization with N nodes

$$\mathbf{q} = (\mathbf{q}_1^T, \mathbf{q}_2^T, \dots, \mathbf{q}_N^T)^T. \tag{3}$$

The vector of local displacements \mathbf{q}_i of any node i consists of

$$\mathbf{q}_i = \begin{pmatrix} \mathbf{u}_i \\ \boldsymbol{\phi}_i \end{pmatrix} = (u_{i,1}, u_{i,2}, u_{i,3}, \varphi_{i,1}, \varphi_{i,2}, \varphi_{i,3})^T, \tag{4}$$

with the translatorial displacement components $u_{i,1}$, $u_{i,2}$ and $u_{i,3}$ and the rotational displacement components $\varphi_{i,1}$, $\varphi_{i,2}$ and $\varphi_{i,3}$.

The matrices \mathbf{M} , \mathbf{D} and \mathbf{K} are the time invariant mass, damping and stiffness matrix, which can be generated in a pre-processing step using commercial FEM software. The right-hand side of the ordinary differential equation sums up acting body forces. It contains inertia, external and joint forces. The inertia forces \mathbf{f}^{gyros} and \mathbf{f}^{rbAcc} result from the global motion of the body and denote the rigid body acceleration forces and the gyroscopic forces, respectively. External forces like axial or radial forces at the compressor or turbine wheel are considered in the vector \mathbf{f}^a . Those forces are given functions over time and can, for instance, be obtained by preceding measurement or pre-calculation. Forces, which occur due to contact to other component surfaces as for instance those in radial slider bearings, are considered in \mathbf{f}^* .

$\boldsymbol{\theta}_B$ are quaternions representing the orientation of the body coordinate system with respect to the inertial coordinate system. The quaternion normalization condition $\boldsymbol{\theta}_B^T \cdot \boldsymbol{\theta}_B = 1$ must hold. The matrix $\mathbf{S}(\boldsymbol{\theta}_B)$ is used to transform the time derivative of the Euler parameters into the vector of the body's global angular velocities $\boldsymbol{\omega}$. For distinguishing gross and local motions, a reference condition is given by the last equation $\mathbf{r}(\mathbf{q}) = \mathbf{0}$, which considers

$$\mathbf{r}(\mathbf{q}) = \begin{pmatrix} \mathbf{r}_1(\mathbf{q}) \\ \mathbf{r}_2(\mathbf{q}) \end{pmatrix} = \begin{pmatrix} \sum_{i=1}^N \mathbf{m}_i \cdot \mathbf{u}_i \\ \sum_{i=1}^N \mathbf{m}_i \cdot \mathbf{A}_{c_i} \cdot \mathbf{u}_i + \mathbf{I}_i \cdot \boldsymbol{\phi}_i \end{pmatrix}. \tag{5}$$

\mathbf{A}_{c_i} is a skew symmetric matrix operator, which is applied to the position vector \mathbf{c}_i of node i , reading

$$\mathbf{A}_{c_i} = \begin{pmatrix} 0 & -c_{i,3} & c_{i,2} \\ c_{i,3} & 0 & -c_{i,1} \\ -c_{i,2} & c_{i,1} & 0 \end{pmatrix}. \tag{6}$$

m_i and \mathbf{I}_i denote mass and tensor of inertia of any node i . Equation (5) is motivated by the assumption that local deformation have to remain as small as possible which assures the validity of the linearization used for linear elasticity theory.

Equation (1) is used in case of rotor but also in case of both floating bushings. As the housing body performs no global motion, equation (1) reduces to the dynamic ordinary differential equation in this case. For further details on the differential algebraic equation but also its solution algorithms refer to Drab et al. (2009).

Oil Film in Radial Slider Bearings

The hydrodynamic contacts are represented by an averaged Reynolds equation, which, formulated with respect to the outer sliding body coordinate system, reads

$$-\frac{\partial}{\partial x} \left(\frac{\theta \cdot \varphi_x \cdot h^3}{12\eta} \frac{\partial p}{\partial x} \right) - \frac{\partial}{\partial z} \left(\frac{\theta \cdot \varphi_z \cdot h^3}{12\eta} \frac{\partial p}{\partial z} \right) + \frac{u_i - u_o}{2} \frac{\partial (\tilde{h}_T + \sigma \cdot \varphi_s) \cdot \theta}{\partial \bar{x}} + \frac{\partial (\tilde{h}_T \cdot \theta)}{\partial t} = 0 \quad (7)$$

$h = h(x, z, t)$ represents the nominal clearance gap height between the two sliding surfaces. h is measured in y coordinates and considers the deformed shape of the structure under the thermal load, see Figure 4. x , y and z are the circumferential, the radial and the axial direction of the bearing. θ is the fill ratio, so the percentage of h , which is filled with oil. The surfaces slide with a velocity of u_i and u_o in x direction. i and o denote the surface of the inner and outer sliding body, respectively. These are the journal and the bushing surface in case of the inner oil film and the bushing and the housing in case of the outer oil film. η is the dynamic viscosity of the lubricant, which may depend on the lubricant's temperature T . The oil film temperature distribution of the lubricant is calculated by an averaged formulation of the energy equation. Bearing shell and journal structure temperatures are based on the three-dimensional heat conduction equation. Pre-calculated temperature boundary conditions (Figure 3) are considered at the surface of the inner and at the outer sliding body. See Lorenz (2015) for further details.

Equation (7) considers flow factors φ_x , φ_z and φ_s obtained according to Patir and Cheng (1978), assuming Gaussian distributed surface heights. σ is a composite roughness value, which can be computed from the standard deviation of the clearance height of the two sliding surfaces σ_i and σ_o via $\sigma = \sqrt{\sigma_i^2 + \sigma_o^2}$. The local oil film thickness h_T considers random roughness amplitudes with respect to the mean shape of the surfaces, respectively, where $h_T = h + \delta_i + \delta_o$ and \tilde{h}_T is the local mean value of h_T assuming Gaussian distribution.

Equation (7) is solved with respect to the hydrodynamic pressure p in lubricated areas and with respect to the oil vapour fraction θ in cavitation areas. Bushing drillings and therefore couplings between inner and outer oil film are considered in terms of boundary conditions. The pressure in the boundary condition is obtained employing oil supply line model in each drilling, Offner et al. (2013). In each drilling the oil is assumed to be incompressible with isothermal viscosity. The flow in each drilling is described by a steady state 1D Euler equation, i.e. Bernoulli equation. Fictitious force effects, which result from the motion of the bushing, and cavitation effects in the line are also considered.

In order to consider physical metal to metal contact, a local asperity pressure is computed in dry and mixed lubricated contact areas. The model developed by Greenwood and Tripp (1970-1971), is applied for that purpose.

5 Dynamic Results

Simulations are performed for constant speeds from 10 krpm up to 110 krpm every 10 krpm. Alternatively, rotor run-up for the same speed range is possible as a single calculation. Constant rotor speeds approach is selected due to available processors so that all speeds could run in parallel and the results are available in the shorter time. During the transient simulation viscous friction in oil films acts on rotor and floating bushings and influence their rotational speed. The speed of the floating bushings changes depending on the balance of the friction forces from the inner and the outer oil film. An initial speed of the rotor and floating bushings needs to be defined in terms of initial conditions. As these structural initial conditions typically are inaccurate, a number of rotor rotations are

required until the rotational speed of the floating bushings becomes stable. Therefore, the calculations are performed for up to 360 rotor rotations to ensure stable floating bushing speeds.

In the case of a turbocharger rotor that rotates at high speeds the dominant forces are implied by unbalances of the rotor wheels.

For each speed case two dynamic calculations are performed, the first one considers a perfect cylindrical shape of the bore, with nominal hot clearance and considering constant oil viscosity based on the assumed oil film temperature. This case is in further text referenced as nominal case. The second case considers a deformed housing shape (FEM) under thermal load and with CFD pre-calculated surface temperatures of the housing, rotor and floating bushings. In the second case viscosity is changing depending on the oil film temperature that is determined by solving energy equation for the oil film. An example of floating bushing temperatures that are used as boundary conditions are shown in the Figure 7.

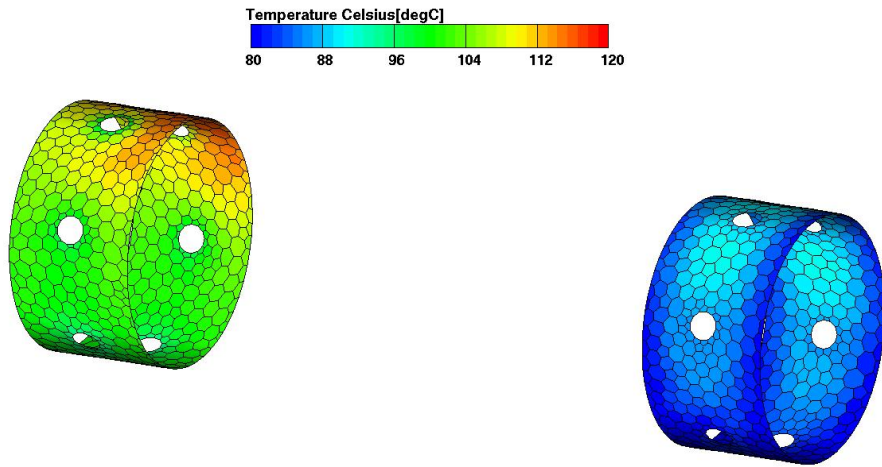


Figure 7. Floating bushing temperature used as boundary conditions for energy equation of the outer oil film

Oil Temperature

Oil film temperatures over speed are depicted in Figure 8. An assumed constant temperature of 90 degC for each oil film is shown in the same diagram with calculated temperatures, maximum and minimum that appear in the oil film for the dynamic simulation using CFD pre-calculated temperature distribution. During the simulation with consideration of energy equation in the oil film, the hydrodynamic friction in the oil film heats up the oil. Depending on the temperature difference of the oil film and the surrounding structure the heat is transferred from the oil to the structure or vice versa. It can be seen that oil film temperatures differ significantly from the assumptions made in the nominal case. In the outer oil film at the compressor side the assumption is relatively good as the obtained temperatures are ranging between 85 and 95 degC. At the outer film at turbine side temperatures are in a range of 105 to 115 degC. This is mainly due to the hotter housing structure that heats up the oil in the film. For the inner oil film the temperatures are much higher than assumed especially at the higher speed due to the oil heat up from the viscous friction. The results demonstrate that it is not possible to assume an accurate constant temperature that could be applied for the complete speed range of the turbocharger.

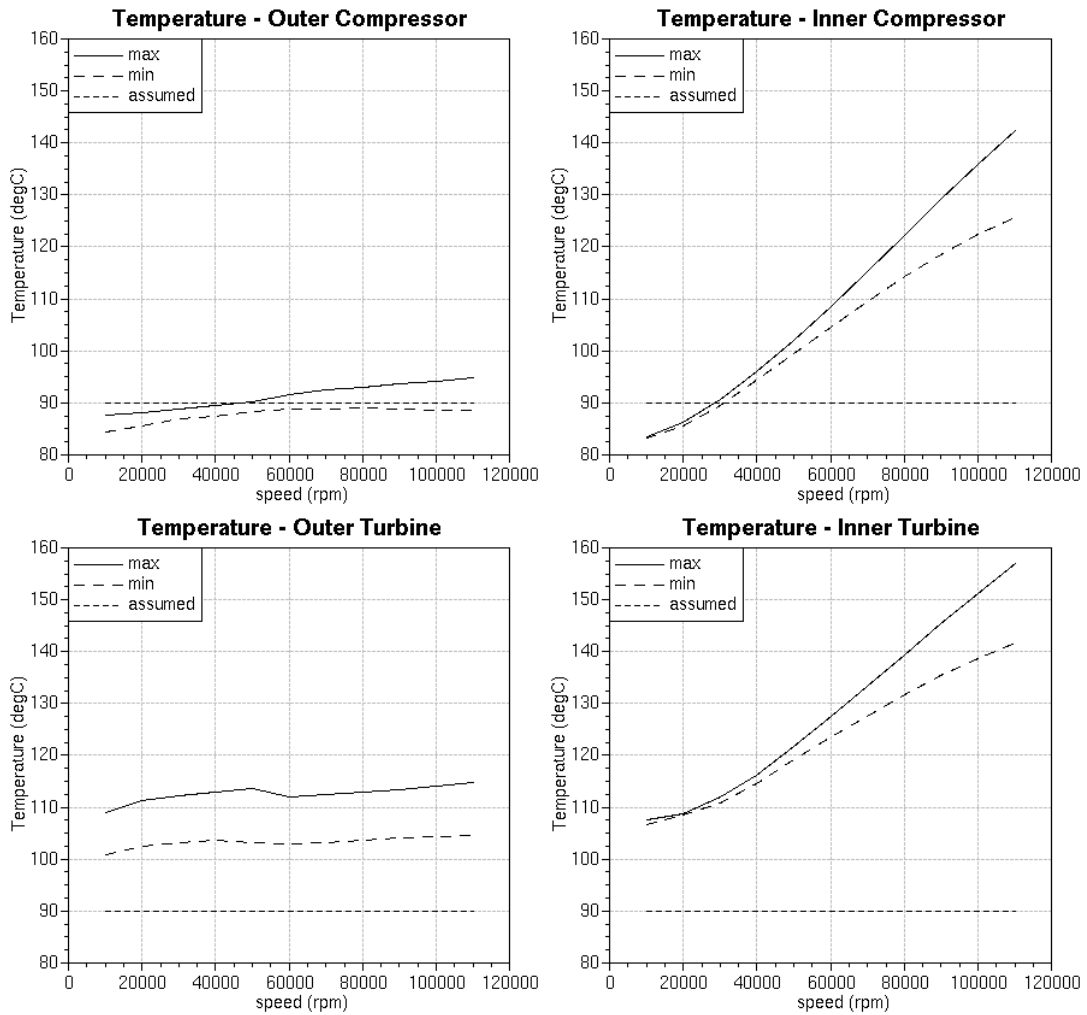


Figure 8. Oil film temperatures over speed: assumed constant temperature versus calculated minimum and maximum temperature using CFD and FEM pre-calculated boundary conditions

Oil Viscosity

Oil viscosity changes during the rotor operation depending mainly on temperature. The dependence on pressure and shear rate is assumed to be negligible in the present study. Results for maximum and minimum oil viscosity in each oil film over speed are shown in the Figure 9. It can be seen that at the compressor side outer film viscosity is relatively similar to the assumed value. For the inner film at the compressor side it is similar only for the lower speeds range. At the turbine side the assumed viscosity is significantly higher than the real one obtained in the simulation, which follows the previous conclusion that assumed temperature is too low at the turbine side.

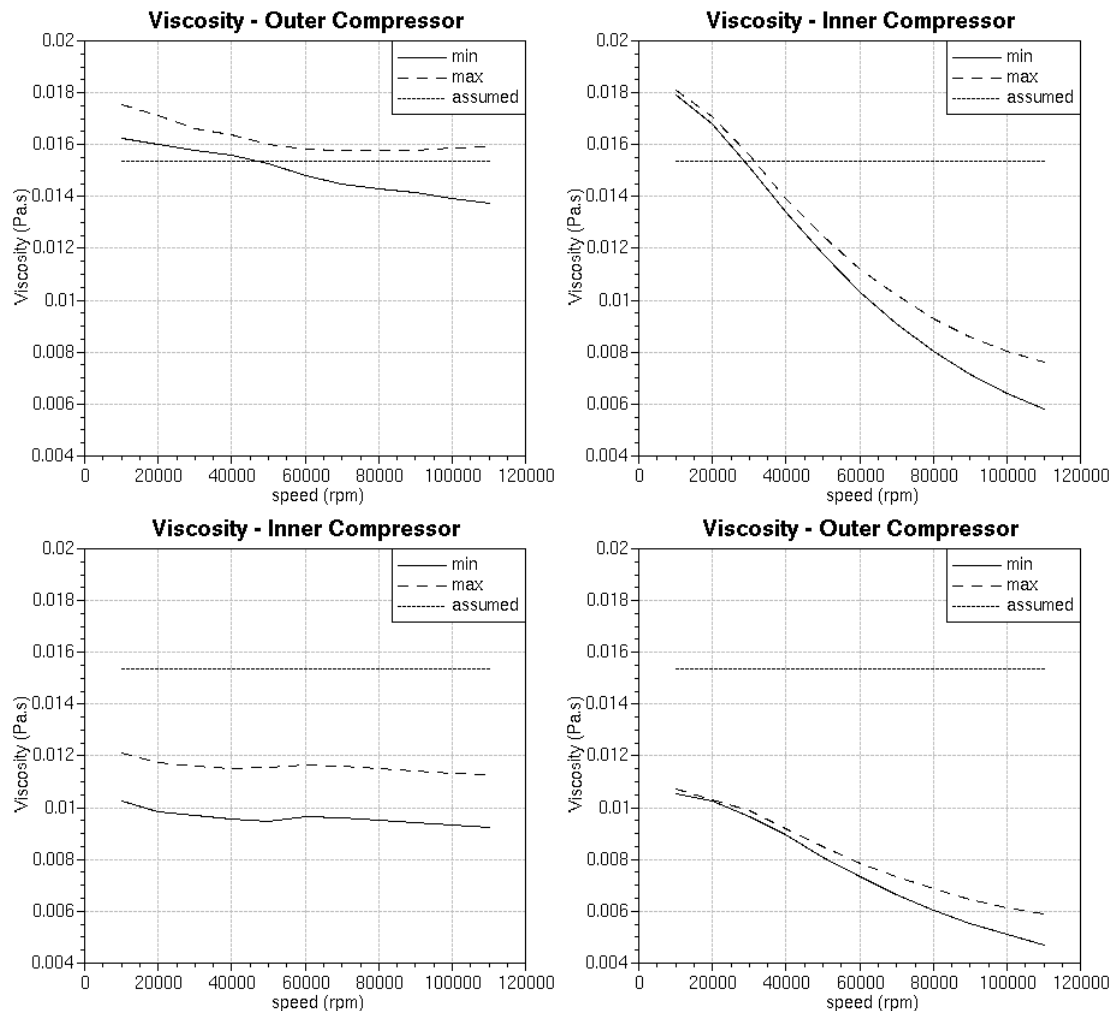


Figure 9. Dynamic viscosity in oil films over speed: constant viscosity (assumed) versus calculated minimum and maximum viscosity using CFD and FEM pre-calculates boundary conditions

Speeds of the Floating Bushings

Floating bushing rotational speeds are a further result of the dynamic simulation. Floating bushings rotate under the influence of viscous friction in oil film. Pressure, fill ratio and temperature and by this also viscosity in the oil films dynamically changes. This implies changing friction load on the floating bushing which leads to dynamically changing floating bushing speeds. Nevertheless, the mean speed of the floating bushing stabilizes after a few seconds. The mean floating bushing speeds over the rotor speeds are shown for both simulation cases in Figure 10. Solid line curves show the results for the nominal case with assumed temperature while the dashed line curves show the results for the CFD and FEM pre-calculated boundary conditions. The speed of the floating bushings are very similar in the lower rotor speed range and differ significantly in the higher speed range for the case with CFD and FEM pre-calculated boundary conditions. This is mainly influenced by lower viscosity in the inner oil films. Another influence is the lower clearance at outer oil films due to the higher temperature at the turbine side. The material of the floating bushing has higher thermal expansion compared to the housing. This means the floating bushing expands more and by this reduces the outer oil film clearance.

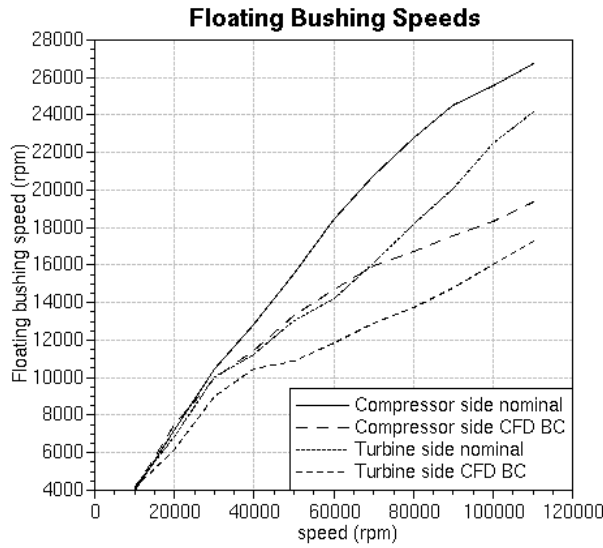


Figure 10. Rotational speed of floating bushings at compressor and turbine for nominal case with assumed temperature versus case with CFD and FEM pre- calculated temperature

Displacement at the Compressor Nut

Typical results, which also can be measured, are displacements of the rotor nut. The result for the maximum and minimum displacement in vertical direction Z with respect to the housing coordinate system and the frequency content of this displacement is shown in Figure 11 for nominal simulation and in Figure 12 for the simulation that uses CFD and FEM pre-calculated boundary conditions. In both cases significant vibrations are of lower sub-harmonic while the first order vibrations are only slightly visible. There is a strong difference between the cases with nominal and pre-calculated boundary conditions. The amplitude of motion is significantly smaller in case of using CFD and FEM pre-calculated boundary conditions. This is influenced mainly by lower clearance at the outer bearing especially at the turbine side. At higher temperature, floating bushings will have higher expansion due to the material with higher expansion coefficient compared to the housing material which will result in smaller clearance at outer oil films.

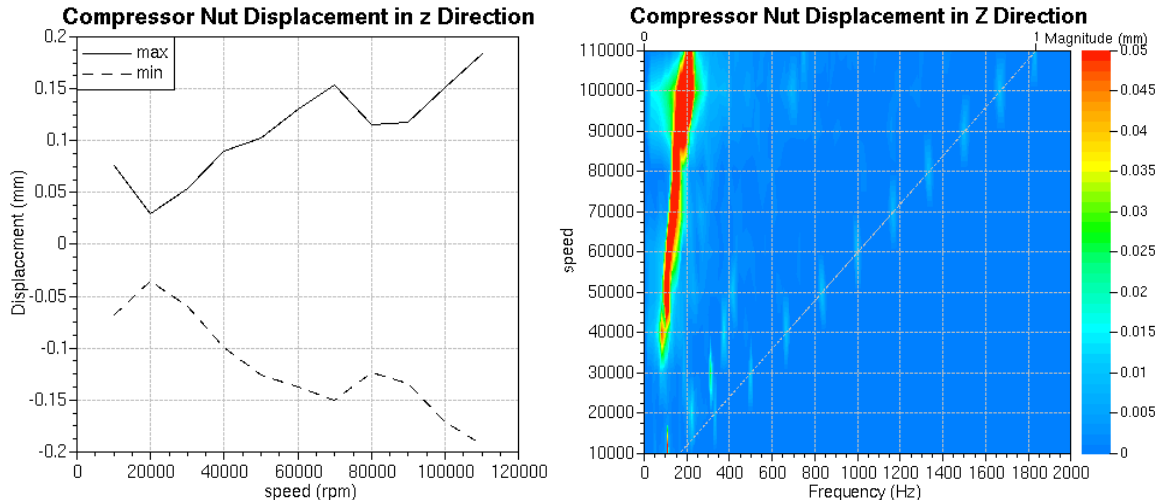


Figure 11. Maximum and minimum nut displacement in vertical direction Z for the nominal case over speed (left) and over speed (rpm) and frequency (right)

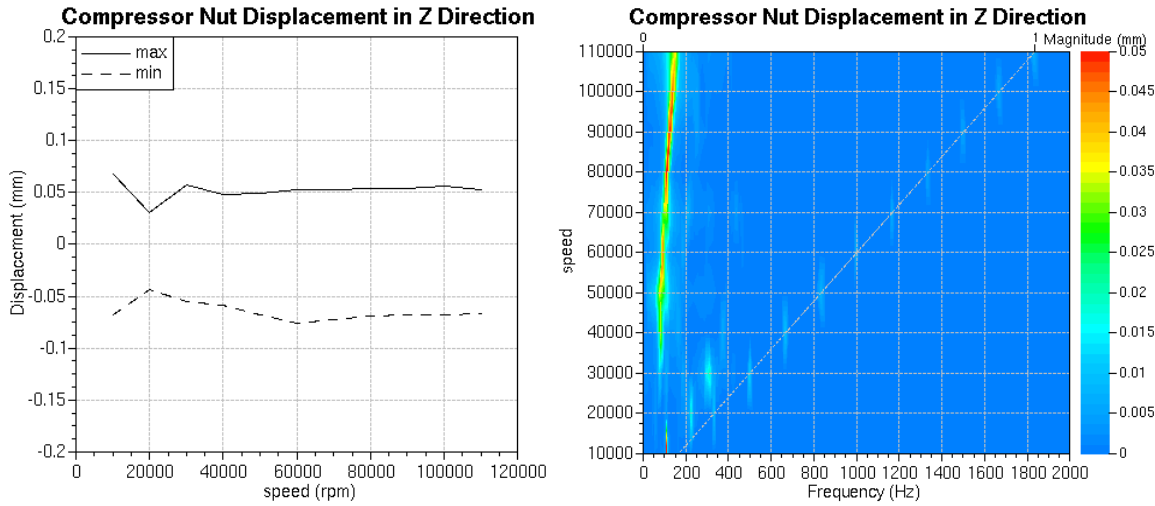


Figure 12. Maximum and minimum nut displacement in vertical direction Z for simulation with CFD and FEM pre-calculated boundary conditions over speed (left) and over speed (rpm) and frequency (right)

Similar observations can be made when looking at the orbital paths of the nut, Figure 13. Orbital paths for the nominal case and results for the case with CFD and FEM pre-calculated boundary conditions are depicted in the upper and the lower part of the figure, respectively. In case of CFD and FEM pre-calculated boundary conditions much smaller orbital paths at the nut can be observed which is influenced by smaller outer oil film clearance.

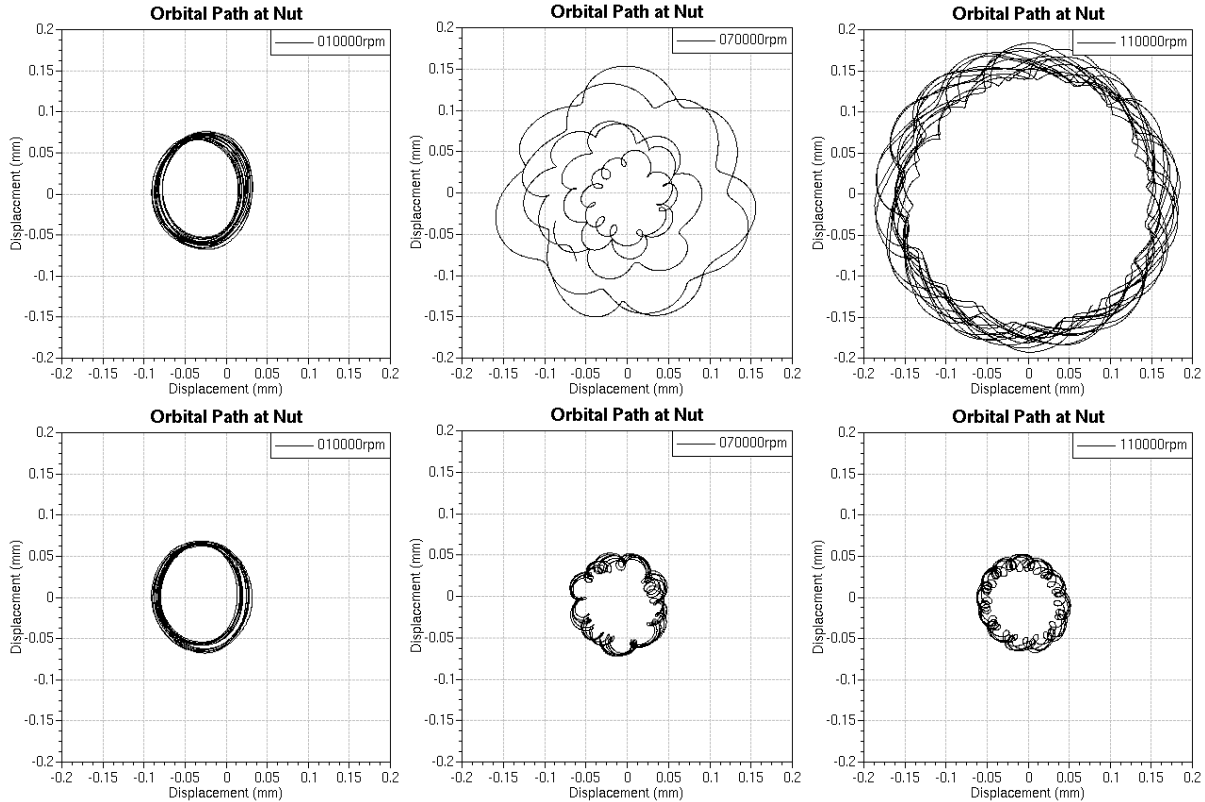


Figure 13. Orbital path at compressor nut for speed cases 10, 70 and 110 krpm: constant (top) versus variable (bottom) temperature boundary conditions

Force in the Bearings

The frequency content of the bearing forces is shown in Figure 14. The upper part of the figure depicts results for the nominal case and the lower part presents results for the case with CFD and FEM pre-calculated boundary conditions. It can be seen that the frequency content is similar for both cases. The large vibration amplitudes,

which can be observed for the compressor nut in the low frequency sub-harmonic, are also present in the bearing forces. But unlike the nut vibration, where sub-harmonic is dominant, in the bearing forces, also the first order shows large amplitudes especially at higher speeds. The bearing forces are in general smaller in amplitude, up to 100 N at outer oil film, for the case with CFD and FEM pre-calculated boundary conditions.

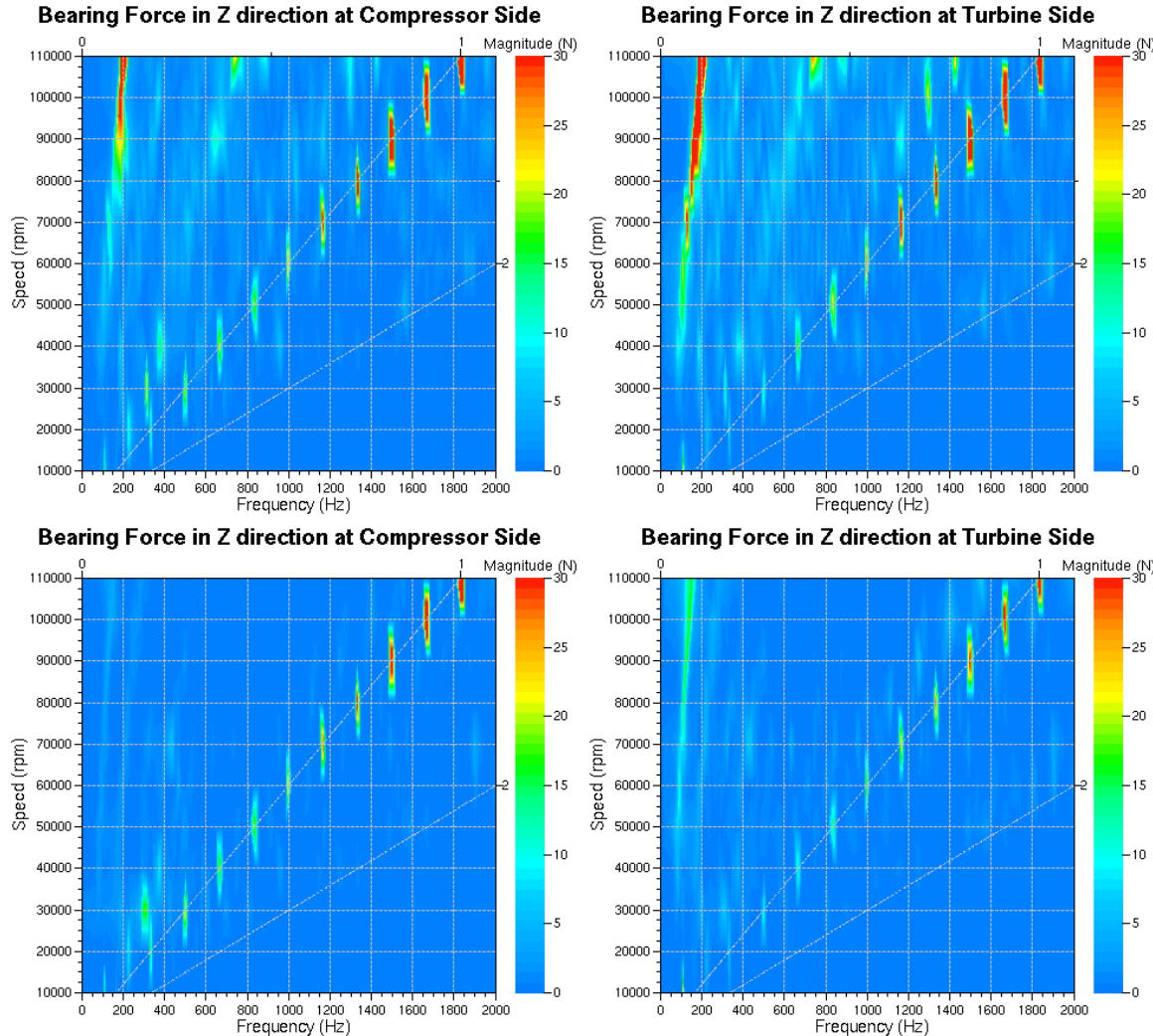


Figure 14. Bearing forces over speed and frequency for nominal case with assumed temperature (upper diagrams) versus case with CFD and FEM pre-calculated temperature (lower diagrams)

6 Conclusion

The paper shows a methodology in which it is possible to use accurately calculated oil film temperatures and according pre-calculated temperature boundary conditions for the dynamics simulation of a turbocharger. This proves to be mandatory in order to be able to compute reliable dynamic results in the complete speed range. The paper also shows the capabilities of modern simulation tools for turbocharger applications. The same method could be applied for semi-floating bushing turbocharger design.

For full floating bushing designs, where several hundred rotor rotations are necessary to obtain steady floating bushing speeds, the drawback of the approach is long calculation time per speed, which is in the range of 2 to 24 hours per speed. Alternative to the constant rotor speeds a run-up simulation using the same simulation approach can also be an option. Such a single simulation would cover the complete rotor speed range, but would last even longer. For performing investigation shown in this paper enough processor power was available to perform constant rotor speed calculations in parallel and obtain shorter simulation time then when running a single run-up calculation.

References

Basara B., v. d. Meer A. J. and Diemath A.: Numerical simulation of fluid flow and conjugate heat transfer in a matrix of surface-mounted cubes: Evaluation of different modelling approaches; *Turbulence, Heat and Mass Transfer 6*; K. Hanjalic, Y. Nagano and S. Jakirlic (Editors), *Begell House, Inc.*, (2009).

AVL AST, AVL FIRETM CFD Solver Users Guide, AVL List GmbH, Graz, (2017).

Luo J. Y., Issa R. I., Gosman A. D.: Prediction of impeller induced flows in mixing vessels using multiple frames of reference, *I. Chem. E. Symposium Series*, 136, (1994), 549–556.

Offner G.: Friction Power Loss Simulation of Internal Combustion Engines Considering Mixed Lubricated Radial Slider, Axial Slider and Piston to Liner Contacts, *Tribology Transactions*, 56, (2013) 503–515.

Drab C. B., Engl H., Haslinger J. R., Offner G., Pfau R. U. and Zulehner W.: Dynamic simulation of crankshaft multibody systems, *Journal of Multibody System Dynamics*, vol. 22(2), (2009), 133–144.

Offner G.: Modelling of Condensed Flexible Bodies Considering Non-linear Inertia Effects resulting from Gross Motions, *Proceedings of the Institution of Mechanical Engineers (IMechE), Part K: Journal of Multi-body Dynamics*, 225(3), (2011), 204–219.

Lorenz N., Offner G. and Knaus O.: Fast thermo-elasto-hydrodynamic modelling approach for mixed lubricated journal bearings in internal combustion engines, *Proceedings of the Institution of Mechanical Engineers (IMechE), Part J: Journal of Engineering Tribology*, 229(8), (2015), 962–976.

Offner G., Diwoky F., Schweiger C., Baier W.: Coupled Oil Film Lubricated Contact Simulation for ICEs, *Proceedings of the Institution of Mechanical Engineers (IMechE), Part J, Journal of Engineering Tribology*, 227(5), (2013), 447–458.

Parikyan T., Resch T., Priebsch H. H.: Structured Model of Crankshaft in the Simulation of Engine Dynamics with AVL EXCITETM, *Proceedings of the ASME 2001 Fall Technical Conference*, 2001-ICE-435, ICE 37-3, Chicago, September 23rd–26th, (2001).

Greenwood J. A., Tripp J. H.: The Contact of Two Nominally Flat Rough Surfaces, *Proceedings of the Institution of Mechanical Engineers (IMechE), Journal of Mechanical Engineering Science*, (1970-1971).

Patir N., Cheng H. S.: An average flow model for determining effects of three dimensional roughness on partial hydrodynamic lubrication, *Journal of Lubrication Technology*, 100(1), 12–17, (1978).

Address:

Advanced Simulation Technology, AVL List GmbH,
Hans-List-Platz 1, 8020, Graz, Austria
Saša Bukovnik, sasa.bukovnik@avl.com
Günter Offner, guenter.offner@avl.com
Andreas Diemath, andreas.diemath@avl.com

Department of Mechanics, University of West Bohemia,
Technicka 8, 306 14 Pilsen, Czech Republic
Luboš Smolík carlist@ntis.zcu.cz

Vibration Signal Analysis for the Lifetime-Prediction and Failure Detection of Future Turbofan Components

N. Mokhtari, M. Grzeszkowski, C. Gühmann

Planetary gearbox and hydrodynamic journal bearings (HJB) are going to be integrated in future turbofan engines. This paper presents the results of applied methods to detect failures of these components. At first, failure detection requirements are derived by using system engineering techniques. In consideration of the identified failures theoretical assumptions are discussed and subsequently verified. Vibration and acoustic emission (AE) sensors seem promising to detect failures in an early stage. To prove the theoretical considerations experiments are carried out on test benches.

Tooth flank damage of a planet gear in a planetary gearbox design is investigated. High demands are placed on the signal processing due to design-related amplitude modulation effects. Vibrations are measured using acceleration and AE sensors, which are mounted on the ring gear. The investigated failure type leads to excitation of non-stationary AE signals. It is proposed that the AE signals have a cyclostationary characteristic. Using cyclostationary-based processing techniques the signal's hidden periodicities can be revealed. A separated analysis of each planet and evaluation of the envelope spectrum finally allows the detection of this failure type.

Instead of roller bearings, HJB can be integrated in planet gears. The most essential damaging mechanism for HJB is wear as a result of mixed or boundary friction. These friction states are caused by conditions like Start/Stop Cycles, insufficient oil supply, overload or oil contamination. The accumulated intensity and duration of friction can be a measure of the remaining useful lifetime (RUL). To estimate the RUL friction has to be differentiated regarding the intensity. AE technology is a promising method to detect friction in HJB. Therefore, AE signals of the mentioned conditions are acquired. Due to rotating planet gears there is no possibility to place AE sensors directly on the surface of HJB.

Finally suitable features for both components are extracted from the processed signals. Their separation efficiency with respect to the failure types is evaluated.

1 Introduction

1.1 Planetary Gearbox

Planetary gearboxes are frequently used in applications where high power densities are in great demand, such as wind power plants and helicopter drivelines. Furthermore, future technologies of geared turbofans in civil aviation will also use a planetary gearbox in the drivetrain to reduce the fans speed and to increase the turbines speed. This leads to an increase of turbine efficiency and a reduction of noise, because the fan and the low-pressure turbine operate in their optimum working point. With the use of a gearbox further maintenance actions are required to ensure a reliable detection of gearbox faults due to wear and gear defects at an early stage. Therefore customers are interested in planning a condition-based maintenance in addition to time scheduled maintenance.

The main fault types in planetary gearboxes are tooth cracks in the dedendum (Reimche et al., 2007; Mohammed and Rantatalo, 2016), tooth break (Yoon et al., 2014) and carrier cracks (Ompusunggu et al., 2014; Blunt and Keller, 2006). To prevent the gearbox from a total failure, cracks and intense wear have to be detected in an early stage. A majority of the faults can be detected by acquiring the gear vibrations or the acoustic emission (AE) of the gearbox components. The disadvantages of these kind of signals are the complex signal structure and modulation effects due to the planet rotations, which lead to high requirements on the diagnostic methods (McFadden and

Smith, 1985). The sensor signatures which are related to a fault case can then only be detected and explored with the use of extensive signal processing methods.

During the gear meshing the time-variant tooth stiffness leads to excitation of acoustic waves in the sun gear, planet gears and the ring gear (Vicuna, 2009). This phenomenon represents the main excitation source for the gearbox vibrations, which can be measured with accelerometers located on the gearbox housing or the ring gear. Furthermore the planets cause an elongation of the ring gear in radial direction. This effect, on the other hand, can be measured using sensors which are sensitive to strain like strain gauges or fiber-optic sensors (Hoffmann et al., 2007).

This contribution presents a method for the diagnosis of planet gear cracks. Due to the rotation of the planet gears, signal processing methods are presented, which estimate the planets position for an efficient feature extraction process. The developed fault detection methods form a possible basis for the development of further techniques for the failure detection in planet bearings.

1.2 Hydrodynamic Journal Bearing

As described roller bearings are used in planetary gearboxes to reduce friction between pins and planets and to allow only the desired direction of movement. Instead of roller bearings, hydrodynamic journal bearings (HJB) can be integrated in planets. For this type of bearing a continuous oil supply is needed. Because of the eccentric position of the pin in the journal bearing and simultaneously relative movement of these components, the oil pressure is in equilibrium with the outer bearing load, so that a supporting oil film is formed. This supporting oil film separates the pins surface and journal bearings surface, so that only fluid friction can occur (Deters, 2014). This condition prevents mixed friction and solid friction, which are not desired. Mixed friction and solid friction cause wear, which is the most essential damaging mechanism for HJB (Albers and Dickerhof, 2010; Albers et al., 2012).

HJBs have many advantages over roller bearings. On the one hand, HJBs are non-sensitive against impact load, high oscillations and vibrations, and on the other hand, they have a simple structure, a very low noise level and are more suitable for high speeds compared to roller bearings. HJBs also have disadvantages. At low speed levels, machine shut down, lack of lubrication, overload or contamination, mixed or solid friction is generated between the journal bearing and pin (Kelm, 2009). Friction, which evokes wear, reduces the lifetime of HJB's and causes fatal failures. To prevent negative impact on product reliability, which causes high maintenance costs and downtime, the HJB's condition has to be known. One possibility to record friction is to use AE Technology. This method promises many advantages in terms of sensitivity to friction and failures compared to normal vibration measurements (Raharjo, 2013; Al-Ghamd and Mba, 2006). With suitable evaluation methods of the acquired AE signal and calculation tools the intensity and duration of mixed friction can be determined. This information can then be used to develop a remaining useful lifetime model.

2 Planetary Gearbox

2.1 Test Bench

The test bench (see Figure 1), which is being used for the planetary gearbox condition diagnosis measurements consists of a drive motor with a nominal torque of 320 Ncm at 3000 rpm. The maximum speed is limited to 3000 rpm. The torque is simulated by a magnetic powder brake with a maximum of 1 kW brake power. The driven gearbox consists of one planetary gear unit with a sun gear (50 teeth), three planets (35 teeth) and a fixed ring gear (120 teeth). These are spur-toothed gears with an 20 pressure angle. The planetary gear has a transmission ratio of 3.4 and a module of 1.5.

During tests, the vibration signals from a piezoelectric acceleration sensor mounted on the ring gear were acquired. Additionally, an AE sensor from PZT material (lead zirconate titanate) was mounted on the ring gear front side to measure high frequency AE signals resulting from tooth meshing. Centrifugal forces, which act on the ring gear when a planet gear passes the sensor, lead to low-frequency radial strain of the ring gear which is also acquired with the AE sensor. The sensor signals from a tachometer and a torquemeter installed on the output shaft were also

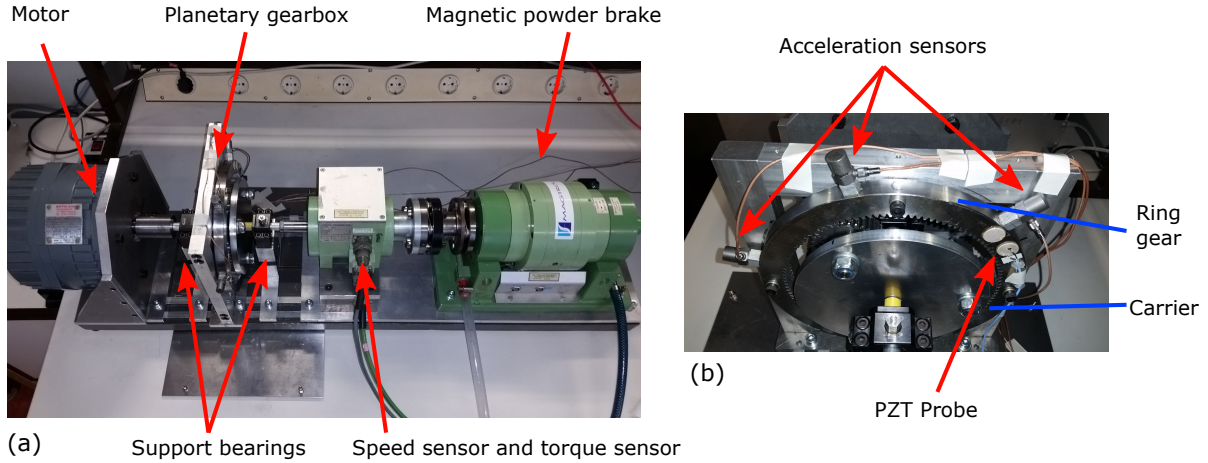


Figure 1: Planetary gearbox subscale test rig: (a) Motor-powered test bench, (b) Applied sensors at the planetary gearbox

acquired. The mentioned signals were sampled with a sampling frequency of 50 kHz to an extent of about 140 revolutions of the carrier.

2.2 Experimental Procedure

The proposed test campaign tests were carried out at different conditions of failure, driving speed and applied torque. The defined gearbox tests are listed in Table 1. To simulate a faulty gearbox a tooth crack with different crack depths at one defined planet gear were artificially inserted. The damage was inserted at the tooth root area at an angle of 30° related to the normal of tooth crest. A damaged tooth with the deepest crack is shown in Figure 2. As shown in Table 1, 45 test-runs were performed for every gearbox, whereas two gearboxes initially in a good condition were used in this test campaign.



Figure 2: Artificially cracked planet tooth

Table 1: Overview of the PG experiments

Parameter	Range
Sun speed	300 rpm, 512 rpm, 670 rpm
Torque	0 Ncm, 250 Ncm, 500 Ncm
Condition	Gearbox in good condition, 0.4 mm crack, 0.8 mm crack, 1.2 mm crack, 2.4 mm crack
Fault type	Artificial planet gear crack

2.3 Signal Processing Methods

To extract features for gear state estimations, two different kinds of features are investigated: Global features, which are calculated over the total carrier revolution and local features, derived from time windowed vibration signals, corresponding to specific gear teeth being in contact. The applied signal processing techniques are summarized in Figure 3.

Firstly, the vibration sensor signals and AE sensor signals were resampled using the speed sensor signal for every test-run with specific speed, torque and crack depth. The resampling process is used to reduce a smearing of the spectral lines in the FFT spectrum, which arise from speed fluctuations of the motor. Resampling is also required for the following order analysis, where speed-independent feature-carrying sidebands are gathered for the feature extraction process. Here especially the meshing order sidebands are recovered and extracted for further calculations, because of the impact a cracked planet tooth has on the amplitude modulation process (Shan et al., 1999).

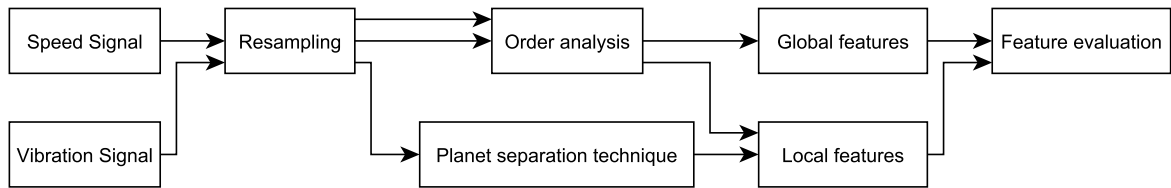


Figure 3: Signal processing

2.3.1 Planet-Separation

In previous investigations (McFadden and Smith, 1985) it could be observed that the level of the measured vibrations reaches a peak value when the planet is closest to the acceleration sensor. As a result of this observations McFadden (McFadden, 1991) developed a method to average the vibration signals of the individual planet gears and the sun gear through windowing the time period, where a planet passes the acceleration sensor. The idea of this method is integrated in this work, to enhance the sensitivity of features to planet cracks.

To use this differential planet diagnosis method through windowing the time signals, the teeth on the planet gear should be meshing with the same teeth on the ring gear near the sensor for every considered window. This state of the appropriate kinematic values is reached periodically every N_c carrier revolutions forming a period length of $T_p = N_c \cdot T_c$, where T_c is the period of one carrier revolution. Therefore, a synchronization of the vibration signals between the test-runs was realized. The sensor signals were synchronized through correlation analysis between the vibration signals of two different test-runs with same speed and torque but different gear failure conditions. This calculation is possible, because of the unequal planet load sharing due to manufacturing and assembling errors. Afterwards the signals are averaged over one state period T_p , to separate the vibration signature of the individual fixed-axis gears from the total vibration of the gearbox.

After the synchronization process the center point of the window functions, where one planet is closest to the sensor, has to be defined. For this purpose the displacement sensor signal from the PZT probe (see Figure 1b) is evaluated. The displacement sensor acquires the radial strain on the ring gear when the planets pass the displacement sensor. Investigations showed, that this sensor is more sensitive to radial strain through planet passing, than the acceleration sensors mounted on the ring gear's circumferential side.

With the processed displacement signal the equally spaced center points of the window function $w(t)$ can be gathered and multiplied with the vibration sensor signal $x(t)$ (see Figure 4). The resulting sensor signals $x_w(t, n)$ correspond to the vibrations at specific meshing points between teeth on the planet gears and teeth on the ring gear (Elia et al., 2013):

$$x_w(t, n) = x(t) \cdot w\left(t - n \cdot \frac{T_c}{N_p}\right). \quad (1)$$

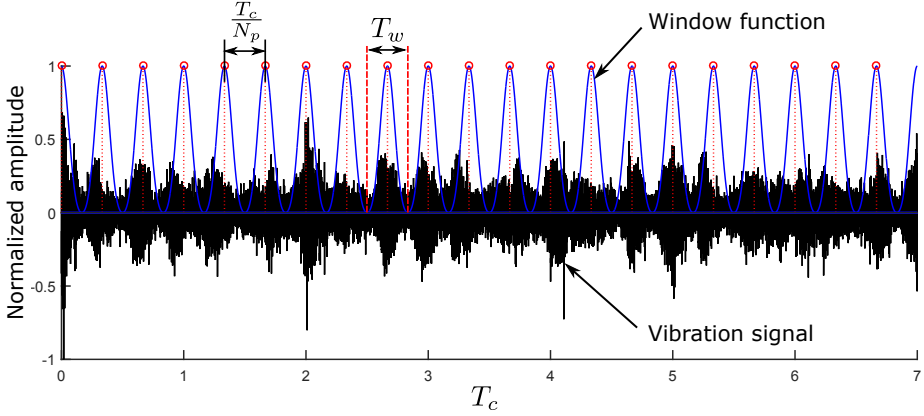


Figure 4: Windowed vibration signal

The value N_p represents the number of planets. The window width T_w has to be chosen appropriately to include all planet teeth of interest on one hand, and on the other to ensure an isolated planet tooth crack detection. It could be claimed that with rising state period T_p a smaller window size can be used. Afterwards local features can be extracted from the windowed sensor signals.

2.4 Results and Interpretation

An evaluation of the extracted global features root mean square (RMS), crest factor, peak value, standard deviation, skewness, kurtosis and the zero-order figure of merit parameter (FM0) (Vecer et al., 2005) showed, that there are no exploitable global features which correlate with the depth of the planet tooth crack. Only the feature FM0 showed negligible increased values with increasing crack depth at 670 rpm sun gear speed and a load of 500 Ncm.

The local features were calculated within every windowed time signal for the 3 planet gears. To find the correlations between specific feature values and the gearbox fault conditions the covariance matrices of the planet-specific features were calculated for a given motor speed and load. In Figure 5 two features (peak value and FM0-value) are shown for measurements at 300 rpm sun gear speed which seems to correlate with an increasing tooth crack depth.

To understand the relations between the feature values and the crack propagation further investigations have to be done in future work to finally estimate the gearbox condition. Because the time windowed extraction of local features seems to be a promising method, the condition of every single tooth pair should be monitored speed- and torque-independent by means of AE signal analysis. Therefore tooth meshing patterns generated from AE measurements will be analyzed using methods of classification. The methods should enable a discrimination between different time-windowed tooth meshing pairs utilizing manufacturing and assembling errors. This would allow the assignment of time-windowed features from same tooth meshing pairs of different measurements.

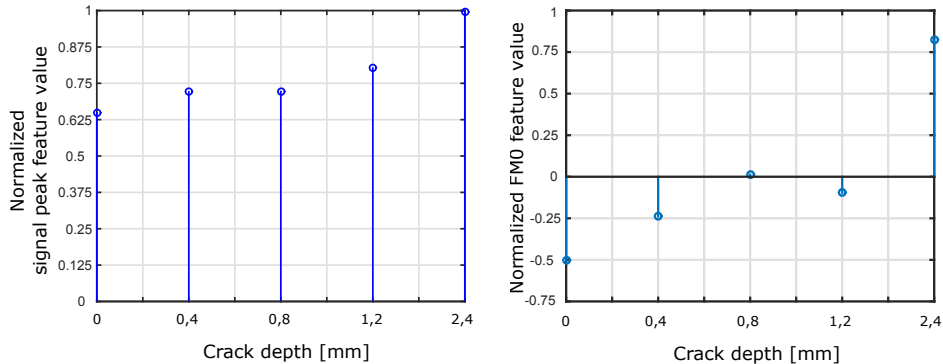


Figure 5: Feature values for measurements at 300 rpm sun gear speed

3 Hydrodynamic Journal Bearing

3.1 AE Technology

AEs are elastic waves that are generated by suddenly released elastic energy e.g. due to material deformation or damage. In addition, friction also generates AE, which is then transferred within the material or on the surface and can be detected by a sensor. From the molecular lattice theory point of view, AEs are generated as follows (Huang et al., 2007): If two surfaces rub against each other the molecule moves from a stable lower state to an unstable upper state. The energy generated during this process accumulates until a maximum is reached. After reaching this state, the molecule slips to the adjacent lower state to reach a new stable state. In this dislocation and slip process the molecule releases energy. One part of the strain energy propagates from the internal to the surface in form of elastic stress waves. The frequency ranges between infrasonic and ultrasonic range (typically between 30kHz - 2MHz). An AE sensor consists of a PZT, which works at its resonance frequency range to reach maximum sensitivity.

3.2 Subscale Journal Bearing Test Rig

Figure 6 shows the journal bearing test rig at which all tests were carried out. A Mattke servomotor drives the shaft. Two supporting roller bearings are located at the left and right side of the journal bearing. Two nylon strips are applied between the shaft and the supporting bearings to mostly reduce interfering signals. A Festo pneumatic cylinder provides the load for the journal bearing. The journal bearing consists of a bearing bush, which is made of the actual bearing material and a bearing back to prevent dilatation. The bearing back is made of two parts, which can be fixed with screws, to replace the journal bearing easily. A gear pump transports oil through a drilling, which is located on the lower part of the bearing back.

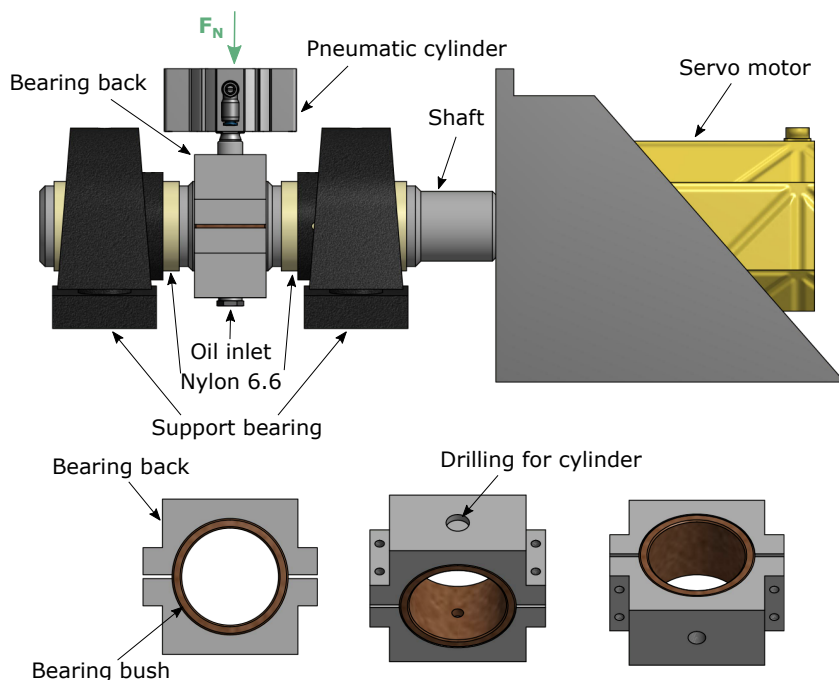


Figure 6: Journal bearing test rig

A PAC (physical acoustics cooperation) Wideband AE sensor with a frequency range of 100-900 kHz is mounted on the upper part of the bearing back next to the drilling for the cylinder. A 2/4/6 preamplifier is used to amplify and filter the AE signals. The oil temperature influences the oil viscosity, which again influences the AE signal. For this reason, the oil temperature needs to be held as constant as possible. A Pt100 sensor measures the oil temperature. A pressure transducer is used to measure the oil inlet pressure. The sensor signals are sampled at 200 kHz. Table 2 shows the test conditions at the test rig.

Table 2: Overview of the test conditions at the HJB test rig

Bearing bush diameter	50 mm
Bearing bush width	40 mm
Maximum speed	3000 rpm
Maximum load	3 kN
Oil inlet temperature	Constant at 27 °C
Oil inlet pressure	Constant at 2 bar
Oil	Hydraulic oil ISO VG 10
Bearing bush material	Red bronze
Shaft material	ST52-3

3.3 Test Description: Static hydrodynamic Friction and mixed Friction Conditions

This section describes the driven tests and their advantages for the detection of friction. At constant load and decreasing speed the gap between HJB and shaft also decreases, which ultimately results in mixed friction at lower deviation of the narrowest gap h_0 . As already described this condition should be avoided during operation because it affects the lifetime of the HJB negatively and can cause failures if it is repeated. Mixed friction is caused deliberately by decreasing the speed at constant load and oil viscosity with purpose of detecting mixed friction conditions in normal operation in the future.

With suitable evaluation methods, the border between fluid friction and mixed friction should be identified. For this purpose the Stribeck curve is used, which shows the relationship between speed, load and viscosity with the coefficient of friction. The sensor data in fluid friction condition could be used as a reference data for the safe condition of the HJB.

3.4 Results and Interpretation

Figure 7 shows the AE RMS plotted against the speed at a constant load of 1750 N. The speed was decreased from 350 rpm up to 60 rpm with 10 rpm steps. The trend shows a high AE RMS value at low speeds, which decreases with increasing speed until a minimum is reached. From this minimum the AE RMS increases again. To understand this trend the knowledge about the Stribeck curve is needed.

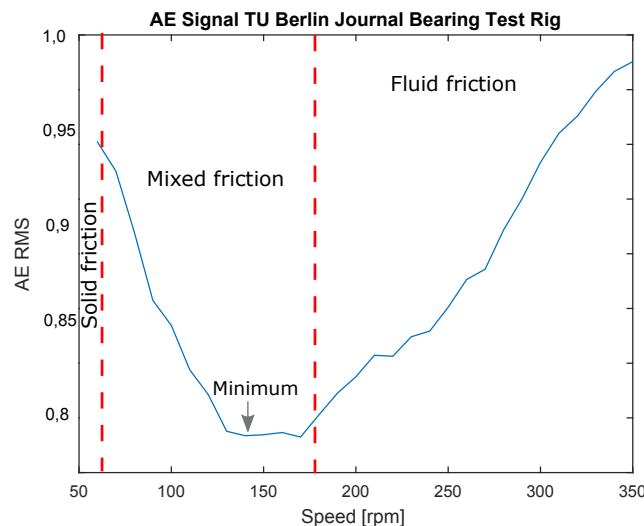


Figure 7: HJB hydrodynamic and mixed friction test; AE RMS at a load of 1750 N

The Stribeck curve indicates the relationship between the viscosity, speed and load with the coefficient of friction. At low viscosity or low speed or at high load the coefficient of friction increases. If the viscosity or speed increases or the load decreases then the gap between the shaft and HJB increases and the oil film becomes thicker. If the speed

continues increasing then the coefficient of friction increases again due to the shear stress of the fluid (Mirhadizadeh et al., 2010). The shear stress results in friction between the fluid and the shaft. This type of friction is not responsible for the wear, which is generated during friction between solid surfaces. Figure 8 (a) shows the Stribeck curve and its friction areas.

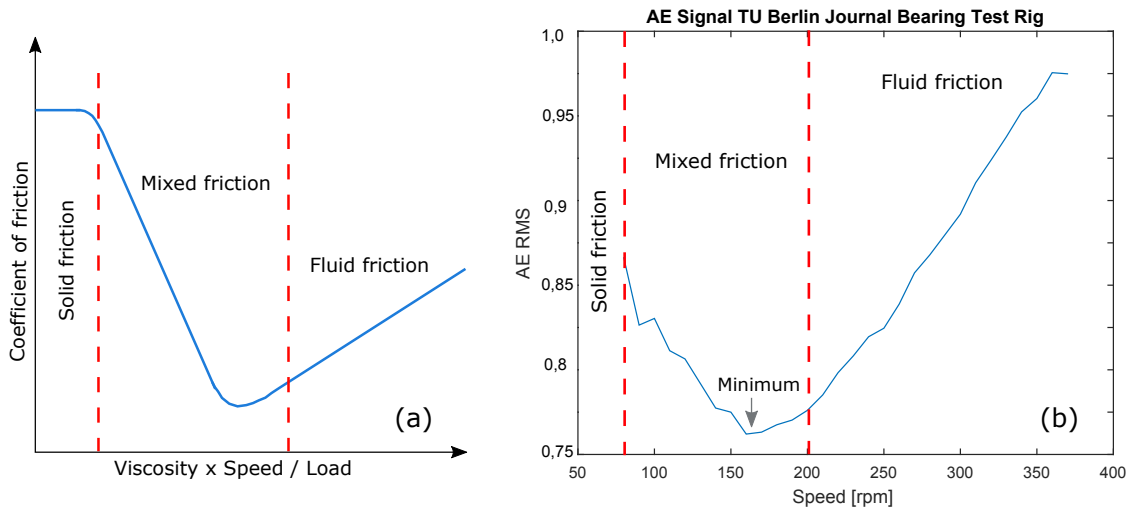


Figure 8: (a) Stribeck curve, (b) HJB hydrodynamic and mixed friction test; AE RMS at a load of 2250 N

With the knowledge about the Stribeck curve, the acquired AE RMS signal can be interpreted. Because the load and the viscosity were held constant, there is only a speed dependency. In the area with low speed and high AE RMS value solid friction occurs. The solid friction area is hardly dependent on the speed. Because of that it seems, that this area could not be recorded (motor stops at high loads). The sensor signals begin at the mixed friction area. At a speed of about 145 rpm the minimum value of AE RMS is reached. The border between fluid friction and mixed friction has not been reached yet because the real minimum oil gap is a subtraction between the theoretical oil film gap and the sum of the shafts and journals roughness. Mixed friction area ends at a speed value of ca. 175 rpm. With higher speed fluid friction begins and the AE RMS signal increases again. In this area there is no asperity contact between shaft and bearing, therefore mixed friction can not occur. Rather the shear stress of the fluid becomes important. The shear stress of the fluid generates friction between the fluid and the shaft and is responsible for the increasing of the AE RMS value. This kind of friction has theoretically no lifetime-reducing effect on the HJB. Concluding it is assumed that a higher shaft speed leads to a higher shear stress and consequently a larger AE RMS value.

The result of a second test with a constant load of 2250 N is shown in figure 8 (b). It shows a qualitatively similar trend. However, the AE RMS signals minimum is moved a little bit to the right side as expected. The minimum is reached at a speed value of ca. 155 rpm. The reason is that the journal bearing stays longer in mixed friction condition due to the higher load. The duration of mixed friction condition is longer at higher loads. Mixed friction area ends at a speed value of ca. 200 rpm.

4 Conclusion

The presented differential planet processing method, which was used within this work to detect a planet gear tooth crack on a planetary gearbox, shows that the fault detection can be improved, through windowing the time period, where a planet passes the acceleration sensor. The results demonstrate that an accurate planet position estimation can be realized by measuring the ring gear elongation with a PZT probe. In further works the planet separation processing method should be used for the development of a planetary gearbox condition monitoring system.

The tests performed at the HJB test bench show that it is possible to find mixed friction events with AE technology and suitable analysis tools. Furthermore it is possible to differentiate between mild and strong friction. This result can be used for further investigations especially for the calculation of the remaining useful lifetime of a HJB.

References

Al-Ghamd, A. M.; Mba, D.: A comparative experimental study on the use of acoustic emission and vibration analysis for bearing defect identification and estimation of defect size. *Mechanical Systems and Signal Processing*, 20, 7, (2006), 1537–1571.

Albers, A.; Dickerhof, M., eds.: *Simultaneous Monitoring of Rolling-Element and Journal Bearings Using Analysis of Structure-Born Ultrasound Acoustic Emissions*, International Mechanical Engineering Congress & Exposition (2010).

Albers, A.; Nguyen, H. T.; Burger, W.: Energy-efficient hydrodynamic journal bearings by means of condition monitoring and lubrication flow control. *International Journal of Condition Monitoring*, 2, 1, (2012), 18–21.

Blunt, D. M.; Keller, J. A.: Detection of a fatigue crack in a uh-60a planet gear carrier using vibration analysis. *Mechanical Systems and Signal Processing*, 20, 8, (2006), 2095–2111.

Deters, L.: *Dubbel - 5 Gleitlagerungen: Plain bearings*. 24 edn. (2014).

Elia, G. D.; Mucchi, E.; Dalpiaz, G.: On the time synchronous average in planetary gearboxes. In: *International Conference Surveillance* 7 (2013).

Hoffmann, L.; Müller, M. S.; Sommavilla, M.; Koch, A. W.: Wälzlagerüberwachung mit faseroptischer sensorik. *tm – Technisches Messen*, 74, 4, (2007), 204–210.

Huang, Q.; Li, L.-p.; Rao, H.-d.; Jin, F.-h.; Tang, Y.-q., eds.: *The AE Law of Sliding Bearings in Rotating Machinery and its Application in Fault Diagnosis*, Hangzhou, China (2007).

Kelm, R. D.: Journal bearing analysis. pages 221–240.

McFadden, P. D.: A technique for calculating the time domain averages of the vibration of the individual planet gears and the sun gear in an epicyclic gearbox. *Journal of Sound and Vibration*, 144, 1, (1991), 163–172.

McFadden, P. D.; Smith, J. D.: An explanation for the asymmetry of the modulation sidebands about the tooth meshing frequency in epicyclic gear vibration. *Proceedings of the Institution of Mechanical Engineers, Part C: Journal of Mechanical Engineering Science*, 199, 1, (1985), 65–70.

Mirhadizadeh, S. A.; Moncholi, E. P.; Mba, D.: Influence of operational variables in a hydrodynamic bearing on the generation of acoustic emission. *Tribology International*, 43, 9, (2010), 1760–1767.

Mohammed, O. D.; Rantatalo, M.: Dynamic response and time-frequency analysis for gear tooth crack detection. *Mechanical Systems and Signal Processing*, 66-67, (2016), 612–624.

Ompusunggu, A.; Y'Ebondo, B.; Devos, S.; Petre, F.: Towards an automatic diagnostics system for gearboxes based on vibration measurements. *International Conference on Noise and Vibration Engineering (ISMA)*, 26, (2014), 2849–2863.

Raharjo, P.: *An Investigation of Surface Vibration, Airborne Sound and Acoustic Emission Characteristics of a Journal Bearing for Early Fault Detection and Diagnosis*. Dissertation, University of Huddersfield (2013).

Reimche, W.; Scheer, C.; Bach, F.-W.: Frühzeitige schadenserkennung an rotierenden bauteilen mittels schallemissionsanalyse und einer wirbelstromtechnik unter anwendung der wavelet-transformation. *Schwingungsüberwachung und Diagnose von Maschinen VDI-Berichte Vol. 1982*, S. 39-55. Düsseldorf: VDI-Verl., 2007.

Shan, J.; Bauer, B.; Seeliger, A.: Schadensdiagnose von planetengetrieben mit hilfe der schwingungsanalyse. In: *Schwingungsüberwachung und -diagnose von Maschinen und Anlagen*, VDI-Berichte, VDI-Verl., Düsseldorf (1999).

Vecer, P.; Kreidl, M.; Smid, R.: Condition indicators for gearbox condition monitoring systems. *Acta Polytechnica*, Vol. 45 No. 6, (2005), 1–6.

Vicuna, C. M.: *Contributions to the analysis of vibrations and acoustic emissions for the condition monitoring of epicyclic gearboxes*. Dissertation, RWTH Aachen, Aachen (2009).

Yoon, J.; He, D.; Van Hecke, B.; J. Nostrand, T.; Zhu, J.; Bechhoefer, E.: Planetary gearbox fault diagnosis using a single piezoelectric strain sensor. *ANNUAL CONFERENCE OF THE PROGNOSTICS AND HEALTH MANAGEMENT SOCIETY 2014*, 5, (2014), 118–127.

Address: Technische Universität Berlin
School of Electrical Engineering and Computer Science
Department of Energy and Automation Technology
Chair of Electronic Measurement and Diagnostic Technology
Sekretariat EN13
Einsteinufer 17 - 10587 Berlin

email: noushin.mokhtari@tu-berlin.de
mateusz.grzeszkowski@tu-berlin.de
clemens.guehmann@tu-berlin.de

Vibro-acoustical Behavior of a Turbocharger Housing Excited by Oil-film Induced Rotor Oscillations

A. Boyaci, W. Seemann

This paper deals with the interaction of the turbocharger housing and the rotor to reveal the acoustic phenomena which are excited by the oil whirl/whip instabilities. Therefore, a flexible multibody model is built up for the rotor subsystem which is supported in floating ring bearings. The flexibility of the housing subsystem is taken into account by considering it as a modally reduced structure within the multibody simulation model. Primarily, the two subsystems are simulated sequentially. The first step gives the oil film forces during a typical run-up simulation of the rotor subsystem if the bearing shell deformation is neglected. In a second step, the obtained oil film forces are applied at the decoupled housing structure to analyze the vibro-acoustics of the turbocharger in detail. The vibro-acoustical behavior is judged by the occurring housing amplitudes which are predominantly influenced by the mounting concept of the turbocharger on the engine. It is found out that the subsynchronous excitation due to the oil films can be magnified through the housing structure in a quite wide speed range which is the main excitation mechanism affecting the acoustics of turbochargers. Finally, the run-up simulation is performed for the coupled subsystems of rotor and housing where the oil film forces are also dependent on the local deformation of the bearing housing.

1 Introduction

High-speed rotors in turbochargers are well-known to show synchronous oscillations due to unbalance as well as various types of subsynchronous oscillations which are induced by several whirl/whip instabilities of the oil films. The rotor oscillations are transmitted through the nonlinear oil film forces to the turbocharger housing whose acoustic emission significantly affects the driver comfort especially in passenger-car applications.

Floating ring bearings are usually chosen to support the turbocharger rotors where the inner and the outer oil films causes different types of subsynchronous oscillations (Orcutt and Ng, 1968; Tanaka and Hori, 1972) which are basically in the conical and cylindrical forward rotor mode, respectively. With regard to the oil film generating the subsynchronous frequency and the rotor mode shape, Schweizer (2009, 2010) suggested a categorization of the occurring types of subsynchronous oscillations (Sub 1: conical mode, inner oil film; Sub 2: cylindrical mode, inner oil film; Sub 3: conical mode, outer oil film) which is also adopted in this study, see also (Boyaci and Schweizer, 2015). Furthermore, typical bifurcation sequences are shown by performing transient run-up simulations of the rotor bearing systems. Recently, run-up simulations are carried out by applying more sophisticated bearing models (Chasalevris, 2016) where, for instance, the bearing geometry with feeding holes and grooves is taken into account (Nowald et al., 2015; Woschke et al., 2015). The influence of design parameters on the subsynchronous oscillations is systematically investigated in (Koutsovassis et al., 2015). The methods of numerical continuation can be applied to investigate the stability behavior of floating ring bearings in detail (Boyaci et al., 2009, 2011, 2015; Boyaci, 2016) and to detect the types of bifurcations at the critical speeds. The additional consideration of the thrust bearing leads to the damping of the subsynchronous oscillations where the conical rotor modes are involved (Chatzisavvas et al., 2016). Transient simulations are also validated with experimental measurements in (Kirk et al., 2007; Köhl et al., 2014; San Andrés et al., 2007).

The failure of floating ring bearings probably causes a rotor damage which is known as Total Instability (Schweizer, 2009) represented by the critical limit cycle (Boyaci et al., 2011). In this case, the flexibility of the bearing housing can become essential on the occurrence of the subsynchronous oscillations and is therefore simply modeled as linear spring-damper element in (Schweizer, 2009). Moreover, oil-film-induced acoustic problems of turbochargers are reported in many publications, e.g. (Nguyen-Schäfer, 2013), but not explicitly analyzed by modeling both the rotor and the housing structure. In order to improve the vibro-acoustical behavior, the physical understanding

of the interaction between rotor and housing, especially the mechanism of transmitting the oil film forces, is an important part of the research in subsynchronous oscillations of turbochargers.

Within this paper, the next section outlines the flexible multibody model of the investigated turbocharger rotor/housing system. The modal analysis of the housing structure gives hints which modes can become significant for the vibro-acoustical behavior. In Section 3, the constant-tone phenomenon is first explained by a sequential simulation of the decoupled subsystems rotor and housing where a typical bifurcation sequence of subsynchronous oscillations is considered. Then, the effect of the bearing shell deformation is examined on the subsynchronous oscillations for the coupled subsystems. Finally, the decoupled and the coupled approach are compared with each other. Section 4 shortly summarizes the paper.

2 Mechanical Model

2.1 Flexible Multibody Model of Turbocharger Rotor/Housing System

The interaction of the turbocharger rotor and housing is investigated by a flexible multibody model. The turbocharger rotor/housing system can be disassembled into two subsystems whose interfaces are the two radial bearings. As depicted in Figure 1 (a), the multibody model of the turbocharger rotor consists of a flexible shaft

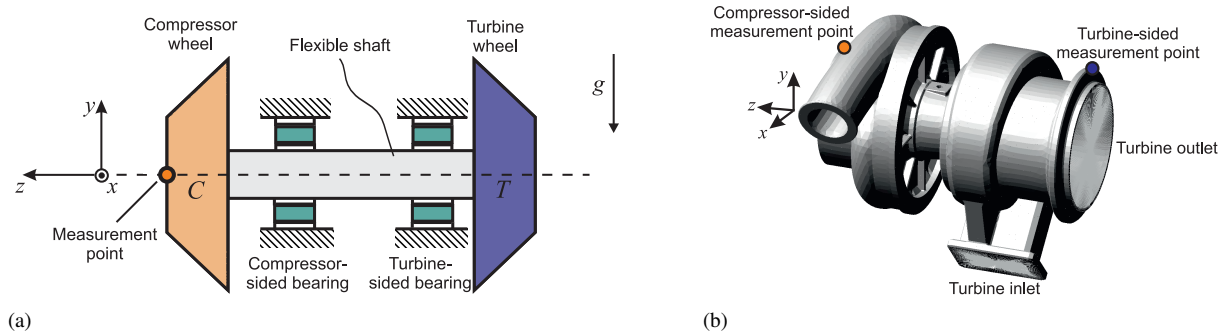


Figure 1: Mechanical model of subsystems: (a) Turbocharger rotor. (b) Housing structure.

at which two rigid disks are placed representing the compressor and the turbine wheel. The flexible shaft is incorporated as a modally reduced structure by applying component mode synthesis which is described in (Craig and Bampton, 1968; Shabana, 2005). The rotor is supported by two full-floating ring bearings where the rings are assumed to be rigid bodies with two translational and one rotational degree of freedom. The nonlinear oil film forces are given by analytical expressions, see e.g. (Boyaci et al., 2015; Childs, 1993), which can be derived by the short bearing theory of DuBois and Ocvirk (1953). Unbalance is modeled by two point masses which are attached on the compressor and turbine wheel. The complete housing structure is also discretized by finite elements and modally reduced by component mode synthesis. The system is under the influence of earth's gravitational field g . Axial and torsional motions of the multibody system are neglected in this study.

Analogously as for instance in (Chatzisavvas et al., 2016; Koutsovassis et al., 2015; Schweizer, 2009, 2010), the flexible multibody model of the turbocharger rotor/housing can be stated as a system of nonlinear Differential-Algebraic Equations (DAEs) which is here written in the stabilized index-2 formulation (Ascher and Petzold, 1998)

$$\begin{aligned} \mathbf{M}(\mathbf{q}) \dot{\mathbf{u}} &= \mathbf{f}(\mathbf{q}, \mathbf{u}, t) - \mathbf{G}^T(\mathbf{q}, t) \boldsymbol{\lambda}, & \dot{\mathbf{q}} &= \mathbf{u} - \mathbf{G}^T(\mathbf{q}, t) \boldsymbol{\mu}, \\ \mathbf{0} &= \mathbf{g}(\mathbf{q}, t), & \mathbf{0} &= \mathbf{G}^T(\mathbf{q}, t) \mathbf{u} + \frac{\partial \mathbf{g}}{\partial t}(\mathbf{q}, t), \end{aligned}$$

and which is computed by using solvers based on the backward differentiation formula (Gear et al., 1985). The vectors \mathbf{q} and \mathbf{u} collect the generalized coordinates and velocities, respectively, which also include the modal coordinates of the flexible bodies. The symmetric positive definite mass matrix is given by $\mathbf{M}(\mathbf{q})$. The vector $\mathbf{f}(\mathbf{q}, \mathbf{u}, t)$ represents all applied and gyroscopic forces. The algebraic constraint equations are considered in $\mathbf{g}(\mathbf{q}, t)$ from which the Jacobian $\mathbf{G}(\mathbf{q}, t) = \frac{\partial \mathbf{g}}{\partial \mathbf{q}}$ is obtained. Then, $-\mathbf{G}^T(\mathbf{q}, t) \boldsymbol{\lambda}$ describes the constraint forces where $\boldsymbol{\lambda}$ is the vector of Lagrange multipliers. To avoid the drift-off effect when solving the DAE, the correction term $-\mathbf{G}^T(\mathbf{q}, t) \boldsymbol{\mu}$ is added to the equations by introducing auxiliary Lagrange multipliers $\boldsymbol{\mu}$.

2.2 Modal Analysis of Turbocharger Housing Subsystem

Before the transient simulations are presented, the modal behavior of the turbocharger housing ($m_H \approx 5 \text{ kg}$) is discussed to support the result interpretation of the subsequent simulations. As shown in Figure 1, the housing structure is built up of two assembled sections which are the compressor-side section and the turbine-side section including the bearing housing. Furthermore, to model the mounting of the turbocharger on the engine block, it is assumed that the housing is rigidly clamped at both the turbine inlet (twin scroll) and outlet while free boundary conditions are chosen at the compressor side. Then, the modal analysis yields the eigenfrequencies and corresponding mode shapes of the housing (cf. Figure 2). Note that the modal behavior of the housing is strongly dependent on the chosen boundary conditions.

Figure 2 outlines four modes of the clamped housing structure which are excited by the oil film forces in the next section. The axial and torsional modes as well as the the higher modes of the turbocharger housing are not explicitly considered here since they can hardly be observed directly in the transient simulations. Primarily, it

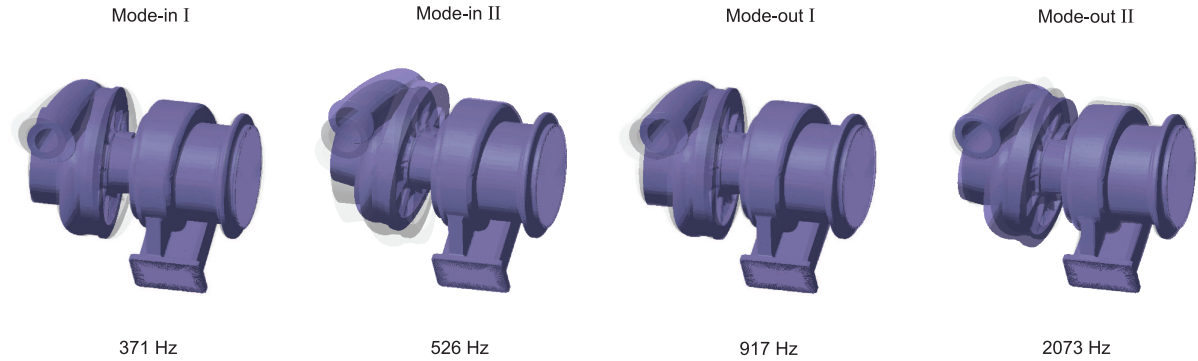


Figure 2: Modal analysis of housing structure which is rigidly clamped at the turbine inlet and outlet.

can be distinguished between two types of bending modes by considering the phase difference of the compressor and turbine section. In-phase oscillations of both sections characterize the first in-phase bending modes – Mode-in I and Mode-in II – about the principal axes of the housing. The two further bending modes – Mode-out I and Mode-out II – describe out-of-phase oscillations of both sections where the nodal point is located close to the turbine-sided bearing. However, for all types of modes, the amplitudes at the turbine section are much lower since the fixed clamping is applied on this side.

3 Run-up Simulation

In this section, a small-sized (passenger-car) turbocharger is considered to investigate the rotor-housing interaction. The multibody simulation model comprises two different subsystems which are, on the one hand, the nonlinear rotor subsystem (rotor mass $m_R \approx 0.2 \text{ kg}$, rotor length $\ell_R \approx 130 \text{ mm}$) supported in full-floating ring bearings and, on the other hand, the linear housing subsystem (housing mass $m_H \approx 5 \text{ kg}$). The coupling between the two subsystems is modeled in two different ways. The first approach is to simulate both subsystems sequentially and thus separately. For this purpose, a run-up simulation of the rotor subsystem is primarily performed to obtain the nonlinear oil film forces where the bearing shell as part of the housing structure is assumed to be rigid. In a further transient simulation, the nonlinear oil film forces are applied as external excitations on the bearing shells to compute the housing oscillations. With regard to the decoupled subsystems, the rotor subsystem only affects the housing oscillations but not vice versa. Therefore, in the second approach, both subsystems are fully coupled and a transient run-up simulation is performed for the complete system. Consequently, the elastic deformation of the bearing shells is also considered on the rotor oscillations so that both subsystems mutually interact with each other.

3.1 Decoupled Subsystems

3.1.1 Rotor Bearing Subsystem

Figure 3 shows the run-up simulation of the decoupled rotor subsystem where the rotor speed is prescribed by an increasing linear time function from rest up to 3500 Hz. As already depicted in Fig 1 (a), the nonlinear oscillations are evaluated by studying the vertical displacement of the compressor-sided measurement point and the relative bearing eccentricities (compressor-sided inner/outer and turbine-sided inner/outer oil films). Additionally, the waterfall diagram in two aspects illustrates the synchronous and subsynchronous frequencies as well as the amplitudes of the compressor-sided displacement. Here, the run-up simulation reveals the following characteristic bifurcation sequence (cf. Figure 3) which comprises the three types of subsynchronous oscillations Sub 1 \rightarrow Sub 2 \rightarrow Sub 2/3 (MM):

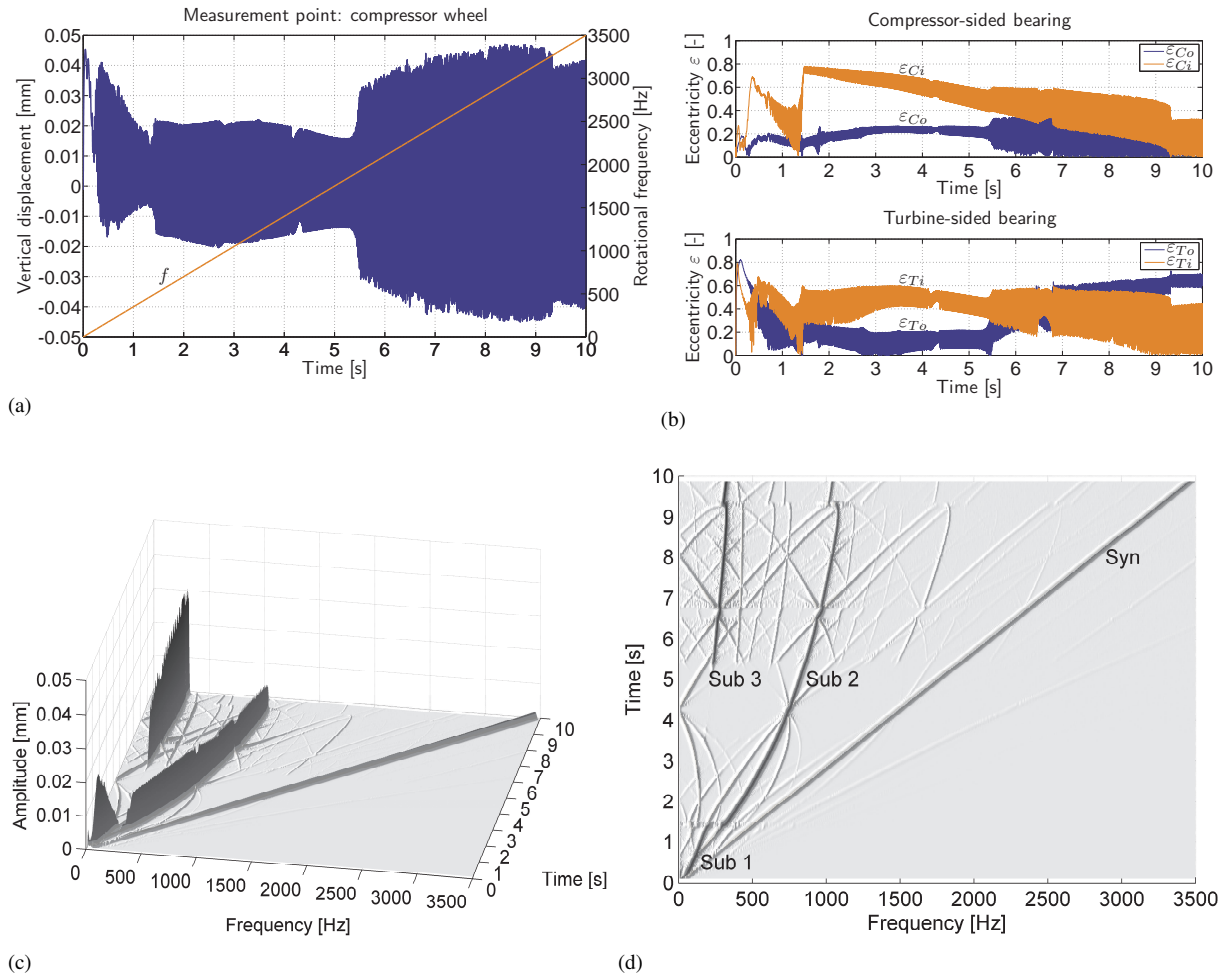


Figure 3: Run-up simulation of decoupled rotor bearing subsystem: (a) Vertical displacement of measurement point at compressor side (blue), rotational frequency f (red). (b) Compressor-sided inner/outer and turbine-sided inner/outer bearing eccentricities. (c)-(d) Waterfall diagrams (3D- and top-view) of plot (a).

- By increasing the rotational frequency from rest, the rotor bearing system needs a certain settling time before the Sub 1 oscillations are fully observed at $f \approx 105$ Hz ($t \approx 0.3$ s). They show the typical high inner bearing eccentricities of both bearings as well as the subsynchronous frequency which is associated with the conical forward rotor mode.
- Upon passing through the Sub 1 oscillations, they become unstable at $f \approx 490$ Hz ($t \approx 1.4$ s) and directly bifurcate to the Sub 2 oscillations which are characterized by a cylindrical forward rotor mode. In addition to the high inner bearing eccentricities, the subsynchronous frequency points to the inner oil films as source of the whirl/whip instability.

- In contrast to Sub 1, the Sub 2 oscillations remain apparent in the whole operation speed range up to 3500 Hz. However at $f \approx 1890$ Hz ($t \approx 5.4$ s), a further bifurcation leads to a Sub 3 component with a relatively much lower subsynchronous frequency which corresponds to a whirl/whip instability due to the outer oil films. In the case of Sub 3, the rotor mode shape is a conical forward one. By increasing the rotor speed from $f \approx 1890$ Hz ($t \approx 5.4$ s), the resulting rotor oscillations describe mixed-mode solutions of Sub 2 and Sub 3 which are denoted by Sub 2/3 (MM). The Sub 3 amplitudes grow with higher rotor speeds while the Sub 2 amplitudes remain nearly constant. Due to the higher Sub 3 amplitudes, the Sub 3 component prevails over Sub 2 during the occurrence of the mixed-mode oscillations.

To recapitulate briefly, this run-up simulation represents a classical bifurcation scenario of a small-sized turbocharger rotor bearing system. Since all three types of subsynchronous oscillations occur, it is convenient to use this reference simulation for demonstrating the vibro-acoustical behavior of the turbocharger housing.

3.1.2 Turbocharger Housing Subsystem

As noted above, the flexibility of both bearing shells is not taken into account to calculate the rotor oscillations as well as the nonlinear oil film forces. Therefore, the previously computed oil film forces lead to the excitation of the decoupled linear housing subsystem by the synchronous and the various subsynchronous frequencies in the spatial x - and y -direction, respectively. Then, the response amplitudes are significantly dependent on the modal properties of the housing structure. Figure 4 depicts the simulation results which represent the normalized housing displacements in x - and y -direction of both bearing shells, cf. Figure 1 (b). Hereafter, the housing displacements are always normalized with respect to the outer bearing clearance C_o . The response frequencies and amplitudes can be representatively taken from the waterfall diagram of the housing displacement in x -direction.

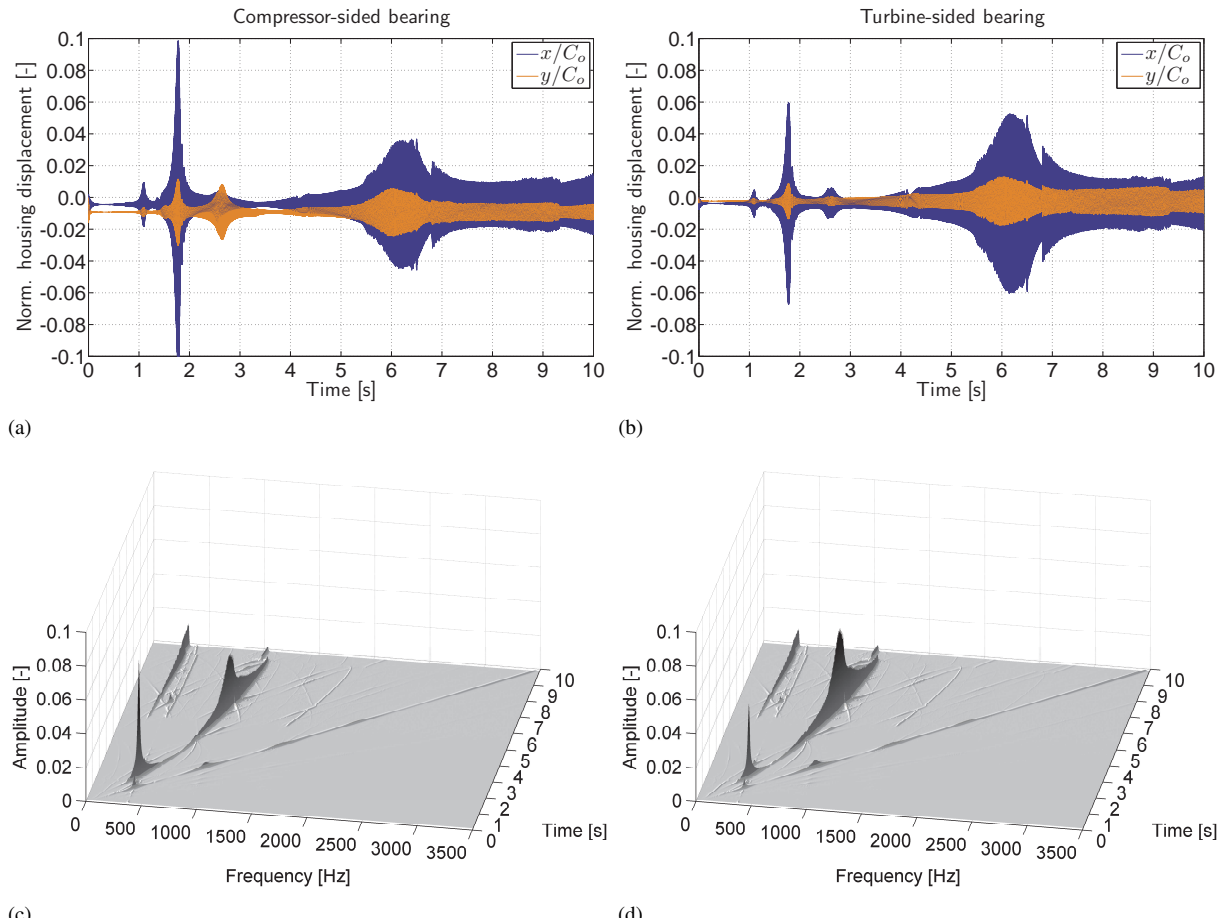


Figure 4: Transient simulation of decoupled housing subsystem: (a) Normalized housing displacement at compressor-sided bearing. (b) Normalized housing displacement at turbine-sided bearing. (c) Waterfall diagram of displacement in x -direction from plot (a). (d) Waterfall diagram of displacement in x -direction from plot (b).

If the synchronous frequency due to unbalance and the subsynchronous frequencies due to the oil films equal one of the eigenfrequencies, resonances of the housing structure can be observed in the operation speed range where four resonance peaks are clearly pronounced:

- The synchronous component of the oil film forces excites the first housing mode Mode-in I at $t \approx 1.1$ s ($f \approx 385$ Hz) where the compressor- and turbine-sided housing part apparently undergo in-phase oscillations.
- The second resonance peak again corresponds to Mode-in I at $t \approx 1.8$ s ($f \approx 630$ Hz). However, the excitation comes from the Sub 2 component of the oil film forces. Due to the higher amplitudes of the Sub 2 oscillations for the decoupled rotor subsystem (cf. Figure 3), the housing amplitudes are accordingly larger than in the case of the first resonance peak.
- The synchronous excitation leads to the resonance of Mode-out I at $t \approx 2.6$ s ($f \approx 910$ Hz) which describes out-of-phase oscillations of the compressor- and turbine-sided housing part.
- The Sub 2 excitation also gives a resonance of Mode-out I at $t \approx 6.2$ s ($f \approx 2170$ Hz) which reveals higher amplitudes than for the synchronous excitation. However, the amplitudes are still lower than for the Sub 2 excitation of the in-phase mode (Mode-in I). Since the Sub 2 frequency nearly remains constant in that speed range the resonance is slower-passed through. Thus, the resonance region becomes much broader so that a magnification of the Sub 2 is obtained for a wider speed range. The Sub 2 excitation with an almost constant frequency is also widely known as the constant-tone phenomenon (Nguyen-Schäfer, 2013).

Furthermore, it has to be remarked that the elastic deformation of the bearing shells is up to maximal 10% of the outer clearance C_o when the Sub 2 excitation reaches the first housing eigenfrequency $f_{eig} = 371$ Hz of Mode-in I. For Mode-out I at an eigenfrequency of $f_{eig} = 917$ Hz, the shell deformation attains values up to 5% of C_o while it does not exceed approximately 1% in speed ranges away from resonances. Therefore, the influence of the shell deformation is small on the rotor oscillations as shown in the next subsection. A further observation is that Mode-in II at an eigenfrequency of $f_{eig} = 526$ Hz is not obviously excited where a clear resonance peak occurs. A frequency response analysis reveals that the node of Mode-in II is located very close to the bearing locations and thus the point of application of both excitation forces. For this reason, Mode-in II plays only a negligible role in the resulting housing oscillations. Moreover, it seems that the subsynchronous frequencies of Sub 3 are too low to excite an eigenfrequency of the housing structure which means that the Sub 2 excitation is only magnified and finally may cause acoustic problems. Note that the synchronous excitation can become critical as well for higher unbalances.

For the sake of completeness, Figure 5 outlines the housing displacements in each of the three spatial directions x , y , z at the compressor- and turbine-sided measurement point. As before, the four resonance peaks are visible. The corresponding waterfall diagrams are omitted to illustrate in Figure 5 which bring no additional knowledge. The amplitudes of the compressor-sided measurement point are generally higher since the housing is rigidly supported on the turbine side.

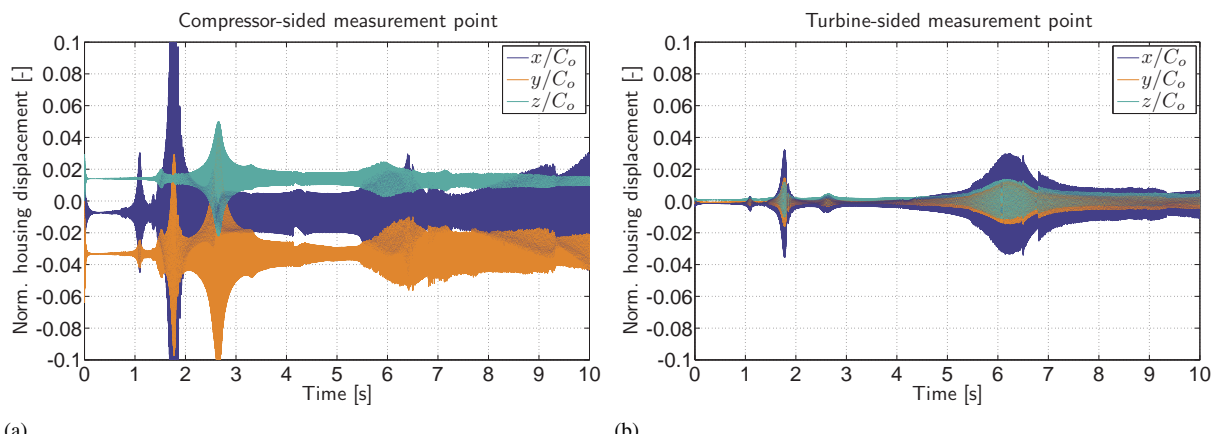


Figure 5: Normalized housing displacements for transient simulation of housing subsystem: (a) Compressor-sided measurement point. (b) Turbine-sided measurement point.

Thus, the vibro-acoustical behavior is significantly dependent on both the oil-film-induced excitation and the modal behavior of the turbocharger housing. Furthermore, the stability and bifurcation behavior of the rotor bearing system is difficult to judge if experimental measurements are only performed at points on the housing.

3.2 Coupled Subsystems

3.2.1 Rotor Bearing Subsystem

According to the previous investigations, the run-up simulation is carried out here for the coupled subsystems of rotor and housing. Figure 6 illustrates the results of the rotor subsystem which are compared to the decoupled case from Figure 3:

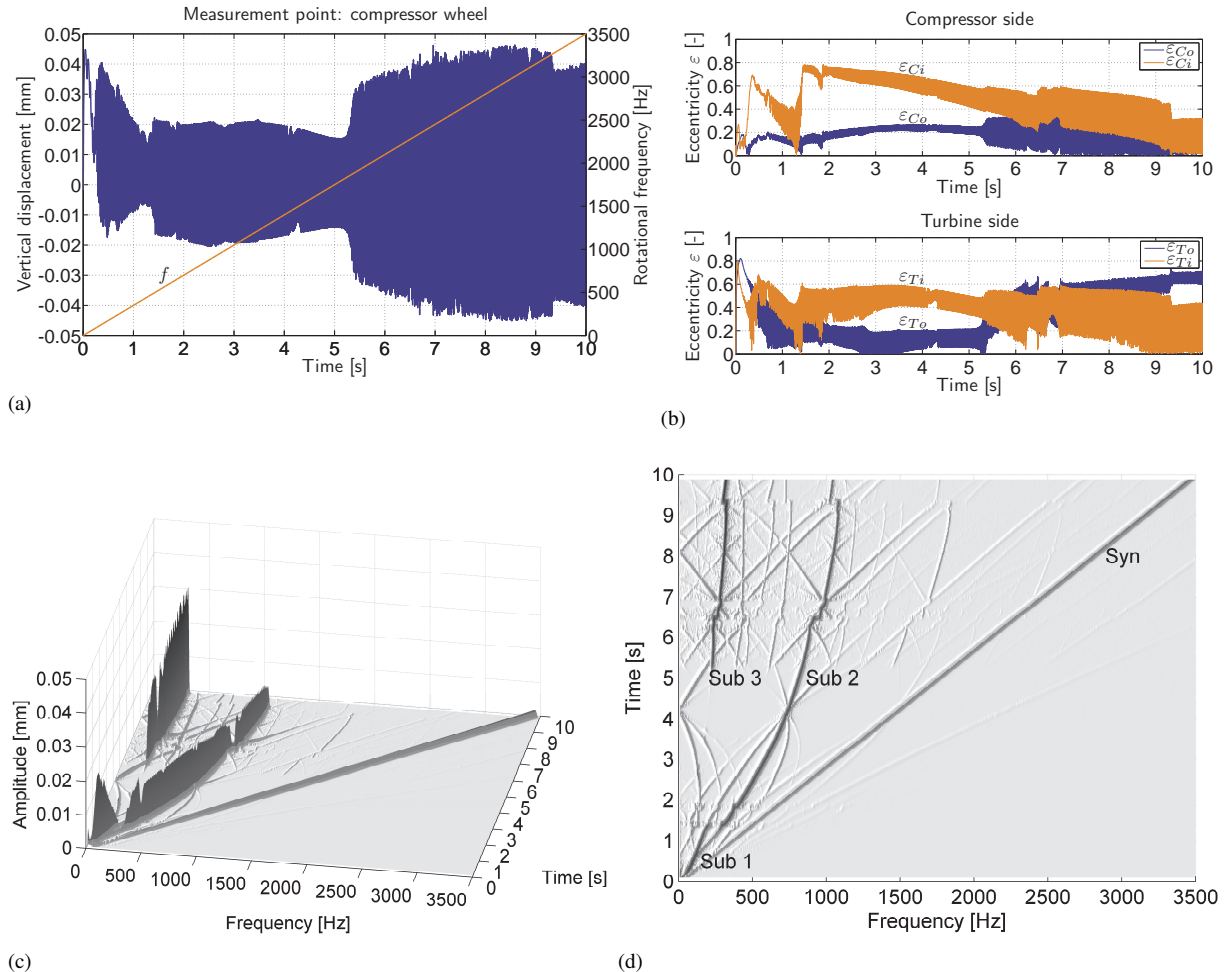


Figure 6: Run-up simulation of complete system (rotor subsystem): (a) Vertical displacement of measurement point at compressor side (blue), rotational frequency f (red). (b) Compressor-sided inner/outer and turbine-sided inner/outer bearing eccentricities. (c)-(d) Waterfall diagrams (3D- and top-view) of plot (a).

- The amplitudes of the rotor oscillations as well as the bearing eccentricities remain basically unaffected in the operation speed range.
- The subsynchronous frequencies are slightly diminished due to the additional flexibility through the bearing shells.
- Hence, the critical speeds are marginally reduced at which the types of subsynchronous oscillations occur and abruptly change, respectively.

- The main resonances of the housing structure, which are excited by Sub 2, can be traced back especially to the inner bearing eccentricity of the compressor-sided bearing and the subsynchronous frequencies. They both suddenly alter in the region of the resonance peaks and recover again very quickly after passing through.

As before supposed, the dynamical behavior of the rotor bearing system can be computed with a very good approximation by assuming rigid bearing shells. Note that the effect of shell deformation may become important on rotor oscillations in speed ranges where resonances of the housing structure occur. However, it is also conceivable that, with regard to Total Instability (Schweizer, 2009), high eccentricities associated with extremely high oil film forces can yield a bearing shell deformation which influences the rotor oscillations.

3.2.2 Turbocharger Housing Subsystem

Figure 7 shows the housing displacements and their oscillation frequencies at the bearing locations of the coupled housing subsystem. Compared to Figure 4, the following differences can be recognized:

- The oscillation amplitudes of the housing displacements are generally slightly lower than for the decoupled subsystems. This amplitude decrease is more pronounced for Mode-out I ($f_{eig} = 917$ Hz).
- Due to the lower subsynchronous frequencies, the Sub 2 excitation leads to housing resonances which are shifted to higher rotor speeds. The resonance peak of the Mode-in I appears at $t \approx 1.85$ s ($f \approx 648$ Hz) while the one of Mode-out I at $t \approx 6.5$ s ($f \approx 2275$ Hz).

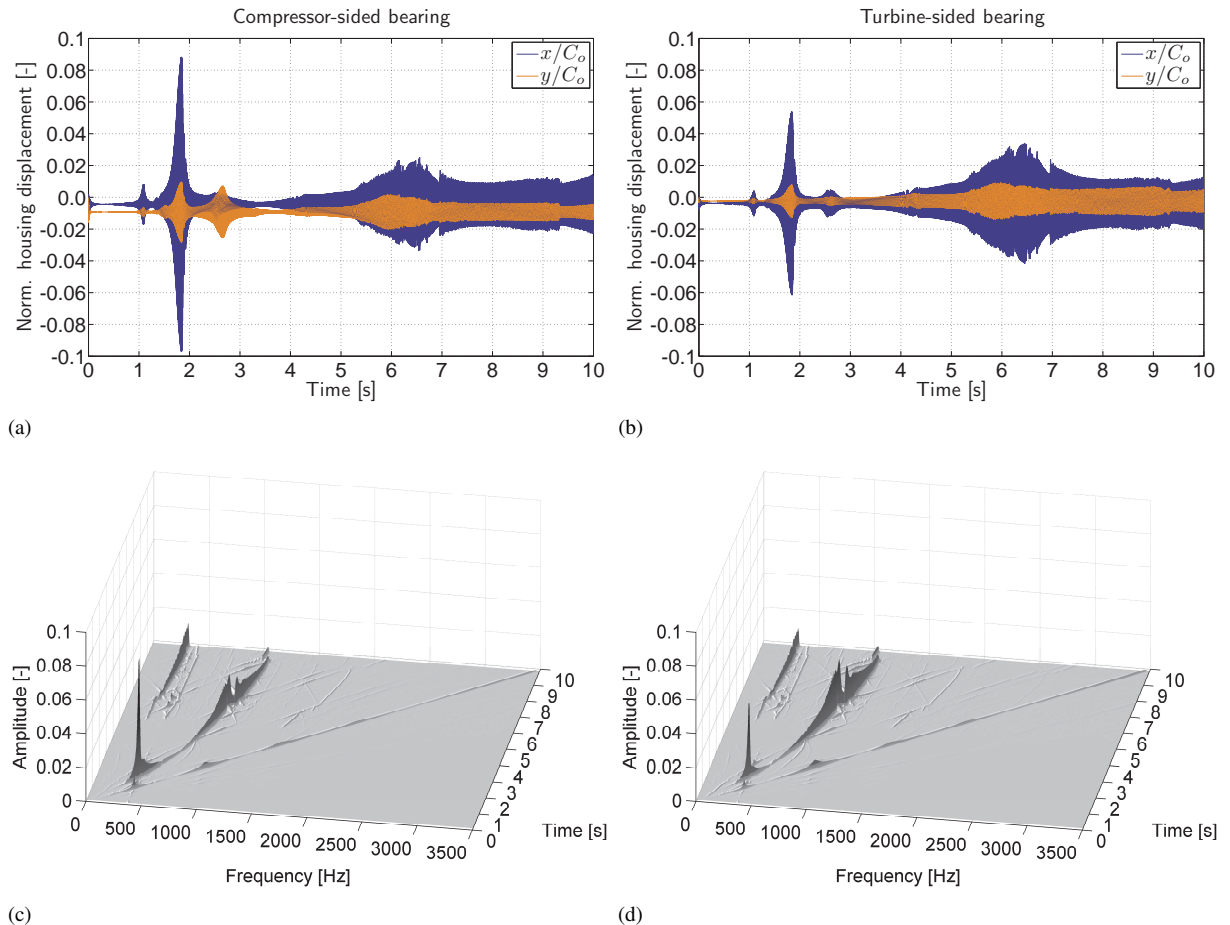


Figure 7: Run-up simulation of complete system (housing subsystem): (a) Normalized housing displacement at compressor-sided bearing. (b) Normalized housing displacement at turbine-sided bearing. (c) Waterfall diagram of displacement in x -direction from plot (a). (d) Waterfall diagram of displacement in x -direction from plot (b).

- At the resonance peaks excited by Sub 2, the response frequencies abruptly changes as already noticed for the rotor oscillations, see Figure 6.

In general, the results of the complete system show qualitatively the same behavior as for the decoupled approach and only slightly differ quantitatively. Therefore, the sequential simulation of both subsystems builds a very good approximation and can be applied to evaluate the vibro-acoustical behavior of the turbocharger housing.

For comparison purposes, the displacements are plotted on both measurement points at the housing in Figure 8. Here, the housing amplitudes are also insignificantly decreased in comparison with the decoupled approach.

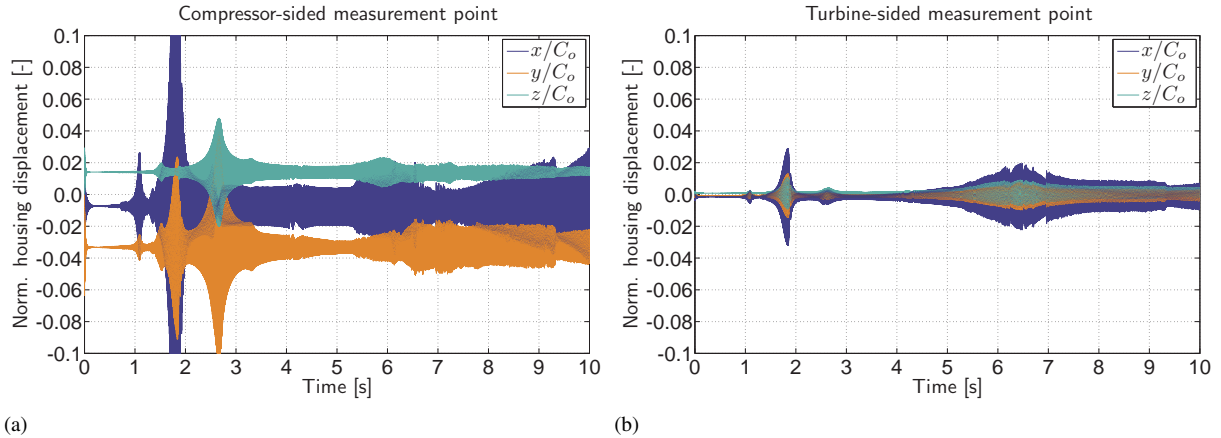


Figure 8: Normalized housing displacements for run-up simulation of complete system: (a) Compressor-sided measurement point. (b) Turbine-sided measurement point.

4 Conclusion

In this paper, the housing structure is additionally considered in the run-up simulation of a turbocharger rotor to investigate the dynamical and the vibro-acoustical behavior. The synchronous and subsynchronous oscillations of the rotor bearing system are transmitted through the oil film forces to excite the eigenfrequencies of the housing subsystem. In the considered passenger-car turbocharger, the Sub 2 excitation is critical due to its higher amplitudes. Furthermore, the response amplitudes of the housing subsystem are magnified by a resonance of an out-of-phase bending mode whose eigenfrequency lies in the speed range of the Sub 2 excitation. Since the Sub 2 frequency slightly increases with higher rotor speeds this resonance leads to a magnification in a relatively wide speed range which is well-known as constant-tone phenomenon. The excitation frequencies of Sub 1 and Sub 3 are too low to excite housing resonances. The synchronous excitation due to unbalance is passed through very quickly. Therefore, the turbocharger design demands to avoid magnification with regard to acoustic problems by shifting the housing's eigenfrequencies out of the Sub 2 excitation frequency range.

Besides the findings described above, two more conclusions can be drawn concerning a simulation of the decoupled subsystems rotor and housing. First, the influence of bearing shell deformation is negligible in the run-up simulation of turbocharger rotors if an instability phenomenon like Total Instability does not occur where extremely high oil film forces are reached. Second, a sequential computation of the two subsystems rotor and housing provides appropriate results. In future studies, a more sophisticated acoustic simulation of the turbocharger housing can follow a run-up simulation of the rotor subsystem assuming rigid bearing shells.

References

Ascher, U. M.; Petzold, L. R.: *Computer methods for ordinary differential equations and differential-algebraic equations*. Society for Industrial and Applied Mathematics, Philadelphia (1998).

Boyaci, A.: Numerical continuation applied to nonlinear rotor dynamics. *Procedia IUTAM*, 19, (2016), 255 – 265.

Boyaci, A.; Hetzler, H.; Seemann, W.; Proppe, C.; Wauer, J.: Analytical bifurcation analysis of a rotor supported by floating ring bearing. *Nonlinear Dynamics*, 57, (2009), 497 – 507.

Boyaci, A.; Lu, D.; Schweizer, B.: Stability and bifurcation phenomena of Laval/Jeffcott rotors in semi-floating ring bearings. *Nonlinear Dynamics*, 79, (2015), 1535 – 1561.

Boyaci, A.; Schweizer, B.: *Proceedings of the 9th IFTOMM International Conference on Rotor Dynamics*, chap. Nonlinear oscillations of high-speed rotor systems in semi-floating ring bearings, pages 845 – 854. Springer (2015).

Boyaci, A.; Seemann, W.; Proppe, C.: *IUTAM Symposium on Emerging Trends in Rotor Dynamics*, chap. Bifurcation analysis of a turbocharger rotor supported by floating ring bearings, pages 335 – 347. Springer Netherlands (2011).

Chasalevris, A.: Finite length floating ring bearings: Operational characteristics using analytical methods. *Tribology International*, 94, (2016), 571 – 590.

Chatzisavvas, I.; Boyaci, A.; Koutsovasilis, P.; B., S.: Influence of hydrodynamic thrust bearings on the nonlinear oscillations of high-speed rotors. *Journal of Sound and Vibration*, 380, (2016), 224 – 241.

Childs, D.: *Turbomachinery rotordynamics*. Wiley-Intersciences, New York (1993).

Craig, R. R.; Bampton, M. C.: Coupling of substructures for dynamics analyses. *AIAA Journal*, 6, (1968), 1313 – 1319.

DuBois, G. B.; Ocvirk, F. W.: Analytical derivation and experimental evaluation of short-bearing approximation for full journal bearing. *NACA Report*, 1157, (1953), 1199 – 1206.

Gear, C. W.; Leimkuhler, B.; Gupta, G. K.: Automatic integration of euler-lagrange equations with constraints. *Journal of Computational and Applied Mathematics*, 12&13, (1985), 77 – 90.

Kirk, R. G.; Alsaeed, A. A.; Gunter, E. J.: Stability analysis of a high-speed automotive turbocharger. *Tribology Transactions*, 50, (2007), 427 – 433.

Köhl, W.; Kreschel, M.; Filsinger, D.: Experimental and numerical investigations on an automotive turbocharger with a transparent bearing section. In: *11th International Conference on Turbochargers and Turbocharging*, pages 349 – 359, Woodhead Publishing, Oxford (2014).

Koutsovasilis, P.; Driot, N.; Lu, D.; Schweizer, B.: Quantification of sub-synchronous vibrations for turbocharger rotors with full-floating ring bearings. *Archive of Applied Mechanics*, 85, (2015), 481 – 502.

Nguyen-Schäfer, H.: *Aero and vibroacoustics of automotive turbochargers*. Springer, Berlin (2013).

Nowald, G.; Boyaci, A.; Schmoll, R.; Koutsouvasilis, P.; Schweizer, B.: Influence of circumferential grooves on the non-linear oscillations of turbocharger rotors in floating ring bearings. In: *The 14th IFTOMM World Congress*, Taipei, Taiwan (October 2015).

Orcutt, F. K.; Ng, C. W.: Steady-state and dynamic properties of the floating-ring journal bearing. *ASME Journal of Lubrication Technology*, 90, (1968), 243 – 253.

San Andrés, L.; Rivadeneira, J. C.; Chinta, M.; Gjika, K.; LaRue, G.: Nonlinear rotordynamics of automotive turbochargers: predictions and comparisons to test data. *ASME Journal of Engineering for Gas Turbines and Power*, 129, (2007), 488 – 493.

Schweizer, B.: Total instability of turbocharger rotors - physical explanation of the dynamic failure of rotors with full-floating ring bearings. *Journal of Sound and Vibration*, 328, (2009), 156 – 190.

Schweizer, B.: Dynamics and stability of automotive turbochargers. *Archive of Applied Mechanics*, 80, (2010), 1017 – 1043.

Shabana, A.: *Dynamics of multibody systems*. Cambridge University Press, Cambridge (2005).

Tanaka, M.; Hori, Y.: Stability characteristics of floating bush bearings. *ASME Journal of Lubrication Technology*, 93, (1972), 248 – 259.

Woschke, E.; Göbel, S.; Nitzschke, S.; Daniel, C.; Strackeljan, J.: *Proceedings of the 9th IFTOMM International Conference on Rotor Dynamics*, chap. Influence of bearing geometry of automotive turbochargers on the non-linear vibrations during run-up, pages 835 – 844. Springer (2015).

Run-up Simulation of Automatic Balanced Rotors Considering Velocity-dependent Drag Coefficients

L. Spannan, C. Daniel, E. Woschke

The paper at hand presents the modelling approach of a laboratory centrifuge with a vertically mounted rotor and an automatic balancing device, which counterbalances the unbalance in one plane. This device consists of an annulus containing the outer ring of a ball-bearing as well as steel balls and is filled with a newtonian fluid. The fluid, accelerated by the annulus' walls, flows around the balls and positions them in the annulus. In order to develop a design method for the balancing device the velocity dependency of the drag coefficient is considered and the influence of fluid density and viscosity on the balancing efficiency is examined. An experimental comparison shows that the flow in the concave bearing race can be represented by the flow around a ball in contact with a flat surface. It can be shown that, depending on the run-up acceleration, a selective choice of the fluid properties has a positive influence on the vibrations near the critical speed and the response time of the counterbalancing effect at supercritical speeds.

1 Introduction

Unbalances in high-speed rotors can lead to excessive vibrations. At the same time, balancing of unbalances due to production or assembly can be uneconomical or process dependent variations in imbalance may be present. In these cases automatic balancing systems can be implemented, which use movable fluids or solids in order to counterbalance the rotor unbalance. Applications of such systems can be found in CD-ROM drives, washing machines and angle grinders.

It is common knowledge that dynamic systems show a phase shift between excitation and deflection while passing resonances. Assuming low damping, the rotor deflects in the direction of the unbalance when operated subcritically and deflects opposing the unbalance when operated supercritically. In contrast, the balancing masses in automatic balancers are driven speed independently by the centrifugal forces F_{cf} to the position most distant to the center of rotation \mathcal{O}_R , meaning in the direction of deflection e of the center of geometry \mathcal{O}_G . Therefore, automatic balancers are increasing the unbalance excitation at subcritical speeds and act counterbalancing at supercritical speeds, see fig. 1. In order to get a good description of the transient positioning of the counterbalancing masses the modelling of the driving forces is essential. The aim of this paper is to contribute to this model with regard to the description of flow resistance. Without loss of generality the following explanations and descriptions refer to automatic balancers with one ball only.

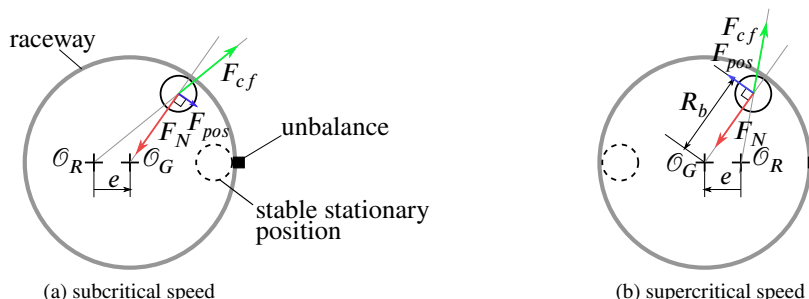


Figure 1: Functionality of automatic ball balancers. Demonstration of driving forces on the counterbalancing mass in a rotating reference frame.

2 State of Research

One of the first publications on ball balancers is the patent from Thearle (1936). Since then, multiple studies were conducted and a growing interest in this topic can be observed, especially in the last 15 years. In order to achieve an efficient balancing device multiple system parameters need to be specified. The findings from preceding publications are summarised in this section.

2.1 Friction

The contact between the balls and the raceway is inducing friction, which is directed oppositely to the ball movement along the raceway. Figure 1 shows that the driving force

$$F_{pos} = |\vec{F}_{pos}| = |\vec{F}_{cf} + \vec{F}_N|, \quad (1)$$

with \vec{F}_N describing the normal force on the ball, is decreasing with increasing approach to the stable stationary position. Therefore, an area near the stable stationary position exists where the friction is sufficient to hold the ball in place aside the ideal position. Hence the optimal counterbalancing cannot be achieved.

This negative influence of friction was identified analytically by Huang et al. (2002). Ishida et al. (2012) used different friction modelling approaches in their numerical models. They differentiated between Coulomb friction, which is proportional to the normal force, static rolling friction and rolling friction on the basis of hysteresis losses and concluded that the static rolling friction is influencing the balancing effectiveness dominantly. With respect to the design of automatic balancing devices a minimisation of the ball and raceway surface roughness is to be aspired. As described by Ishida et al. (2012), the influence of friction can be reduced by an increased number of balls, preferably in separate raceways, because the balls are not getting to rest at the same time. In addition, the static rolling friction decreases with increasing ball diameter.

2.2 Raceway Eccentricity

Due to an eccentricity ϵ of the raceway, its geometric centre \mathcal{O}_G is not coinciding with the center of mass \mathcal{O}_M of the balanced rotor, leading to a stable position ($F_{pos} = 0$) of the ball aside the ideal balancing position, see fig. 2. This negative influence was examined by Huang et al. (2002) and Majewski (1988) amongst others. From this follows that irregularities of the circular race form, see fig. 3, have negative influence on the balancing capabilities, too.

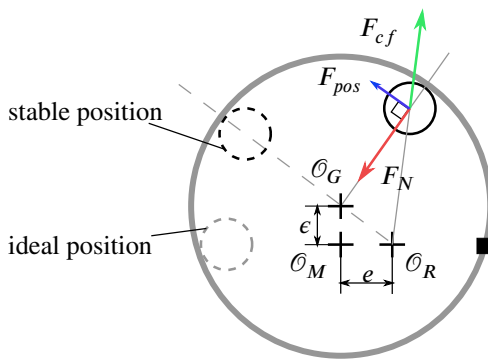


Figure 2: Influence of raceway eccentricity on the positioning at supercritical speeds.

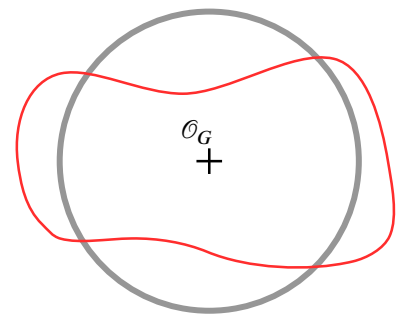


Figure 3: Exaggerated representation of an arbitrary form irregularity.

2.3 Non-synchronous Motions

Ryzhik et al. (2003) showed that in an operation range above the critical speed ω_i the balancing balls are not circulating with the rotor frequency but with the critical frequency. This causes the balls to not come to rest and therefore the rotor unbalance cannot be counterbalanced. Only after reaching a border rotating speed $\Omega_{bo,i}$ the balls get accelerated to the rotor speed resulting in the balancing effect to be performed. In order to avoid the operation

of automatic balancing devices below the critical speed and in the speed range of non-synchronous motions, the operating range has to be restricted, see fig. 4. A possible solution to avoid non-synchronous motions by using multiple balls and partitioning the annulus is described by Ishida et al. (2012). The partitioning walls are enforcing the rotor speed to the balls, avoiding non-synchronous motions. As a drawback, the maximum counterbalancing force is reduced.

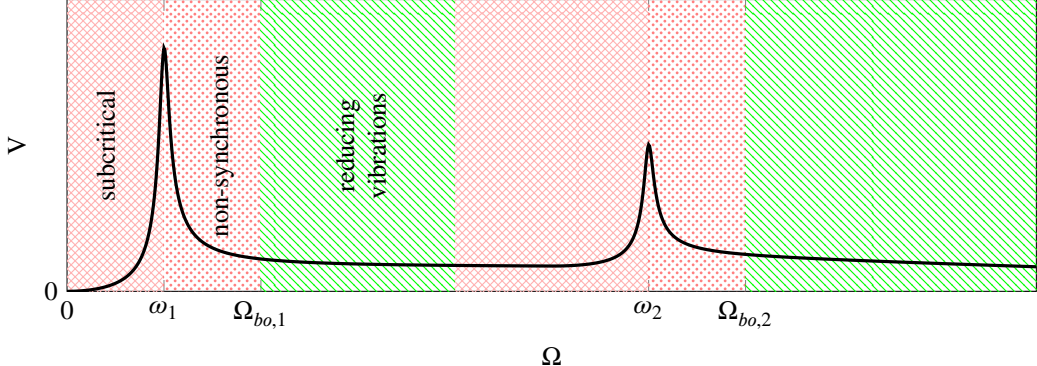


Figure 4: Exemplary magnifying function of an unbalanced rotor with operation ranges of automatic balancing devices.

2.4 Viscosity and Density of the Fluid

In contrast to the surface roughness and the raceway eccentricity, where small values are preferred, the choice of an optimal fluid in the automatic balancing system leads to a conflict of aims (Ryzhik et al. (2003)), which has to be resolved. With increasing density ρ_{fl} and viscosity ν the lag between the rotor and ball velocity is decreased due to the flow resistance. On one hand the lag is desired at subcritical speeds so that the balls are not positioned near the rotor imbalance causing an increase in rotor vibration. On the other hand a fast reduction of lag and positioning of the balls to their ideal position is desired once the critical speed is exceeded. The objective of the choice of fluid is to keep the vibrations in the run-up phase moderate and to gain a quick balancing effect at supercritical speeds. The modelling of the viscous coupling between the rotor (the annulus), the fluid and the balls has a great impact on the quality of the simulation results.

Many previous stationary (Ryzhik et al. (2003); Green et al. (2006); Ishida et al. (2012); Kim and Na (2013); Chen and Zhang (2016)) and transient (Sperling et al. (2002)) models make use of a linear correlation between the moment of fluid drag M_D and the difference in rotating speed between the rotor and the ball

$$M_D = \beta \cdot (\dot{\phi}_R - \dot{\phi}_b). \quad (2)$$

The parameter β inherits several system properties and depends on the fluid, the annulus geometry and the ball diameter and is difficult to determine without experimental data. Huang et al. (2002) make use of a physically motivated approach on the basis of the fluid drag force F_D , leading to a nonlinear correlation between the moment and the rotating speed difference based on geometric and physical quantities

$$M_D = F_D \cdot R_b = \frac{1}{2} \rho_{fl} \cdot \bar{A} \cdot C_D \cdot v_{rel}^2 \cdot R_b \cdot \text{sign}(v_{rel}) \quad (3)$$

$$= \underbrace{\frac{1}{2} \rho_{fl} \cdot \bar{A} \cdot R_b^3 \cdot C_D}_{\text{constant}} \cdot (\dot{\phi}_R - \dot{\phi}_b)^2 \cdot \text{sign}(\dot{\phi}_R - \dot{\phi}_b). \quad (4)$$

$R_b, \bar{A}, C_D, v_{rel}$ describe the radius of the ball center track, the ball cross-sectional area, the drag coefficient and the flow velocity, respectively. Huang et al. make the assumption of a constant drag coefficient C_D , which is called into question by the authors. Furthermore, it should be noted that the velocity of the fluid $\dot{\phi}_{fl}$ is not equal to the rotor speed $\dot{\phi}_R$ in transient models. The spin-up of fluids in rotating annuli cannot be calculated analytically (Benton and Clark (1974)). Hence the fluid is modelled as a rigid body and its acceleration is described by a linear correlation in the style of equation (2)

$$M_{fl} = \beta_{fl} (\dot{\phi}_R - \dot{\phi}_{fl}), \quad (5)$$

where the parameter β_{fl} is fitted to the experimental data. Additionally, the radial increase of the flow velocity, see fig. 5, is neglected for small ball diameters $d \ll R_b$, leading to a flow velocity of $v_{rel} = R_b(\dot{\varphi}_{fl} - \dot{\varphi}_b)$.

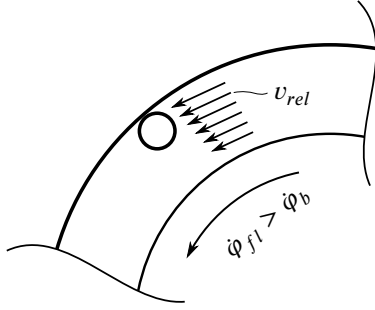


Figure 5: Flow velocity profile at stationary state.

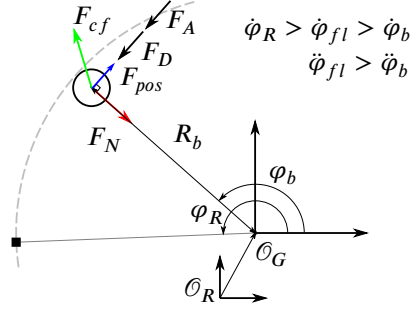


Figure 6: Coordinates and forces describing the dynamics of the balancing ball neglecting raceway eccentricity.

Another aspect of transient modelling is the added virtual mass, whose inertia is antagonising the acceleration of a rigid body in a fluid. The appropriate virtual mass coefficient for balls in contact with a flat surface was identified experimentally by Jan and Chen (1997) to be $C_A = 2$. Derived from their conclusions, the impact of the added mass effect is decreasing with an increasing ratio in the densities ρ_b/ρ_{fl} . The moment of virtual mass equals

$$M_A = F_A \cdot R_b = \rho_{fl} \cdot \frac{\pi d^3}{6} \cdot C_A \cdot (\ddot{\varphi}_{fl} - \ddot{\varphi}_b) \cdot R_b. \quad (6)$$

The recited publications neglect the dependency of the drag coefficient C_D from the flow velocity v_{rel} . This relation is usually expressed with the use of the dimensionless Reynolds number

$$Re = \frac{v_{rel} \cdot d}{\nu} = \frac{(\dot{\varphi}_{fl} - \dot{\varphi}_b) \cdot R_b \cdot d}{\nu}. \quad (7)$$

In order to describe the following experimental results a modified Reynolds number based on the rotor speed $\dot{\varphi}_R$ is introduced

$$Re^* = \frac{(\dot{\varphi}_R - \dot{\varphi}_b) \cdot R_b \cdot d}{\nu}. \quad (8)$$

The paper at hand presents a transient modelling approach of an automatic balancing device, which considers the velocity dependent drag coefficient.

3 Experimental Analysis

The test rig, which is modelled in this study and whose run-up is simulated, is depicted in fig. 7. A discoidal rotor is joint on an axis, which is mounted vertically in the stator of an electric motor. The stator itself is mounted by three elastomer bushings, which affect the systems damping and flexibility significantly. The system has an eigenfrequency at $\omega_1 = 50 \text{ rad s}^{-1}$ which is related to a translatoric eigenmode orthogonal to the axis of rotation. And a second eigenfrequency at $\omega_2 = 125 \text{ rad s}^{-1}$, which is related to a tilting eigenmode orthogonal to the axis of rotation. The conducted experiments use a maximum operation frequency of $\Omega = 70 \text{ rad s}^{-1}$, at which a self-balancing effect of the system is expected. In order to reduce the friction force on the ball an outer ring of a ball bearing is used as a race track, see fig. 8. The discoidal rotor is balanced statically in order to set defined unbalance masses into the threads located circumferentially afterwards.

In order to neglect the interaction between multiple balls only one ball with the mass $m_b = 7.6 \text{ g}$ is used whose center is moving on a circular track with a radius of R_b . The mass m_u of the added imbalance is matched, so that the ball can counterbalance this mass exactly. This results in

$$m_u \cdot r_u = (\rho_b - \rho_{fl}) \cdot \frac{\pi d^3}{6} \cdot R_b = 512 \text{ gmm}, \quad (9)$$

with ρ_b being the ball density.

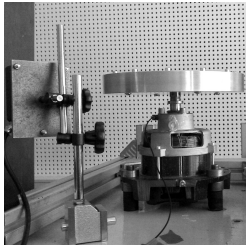


Figure 7: Test rig with the automatic balancing prototype.

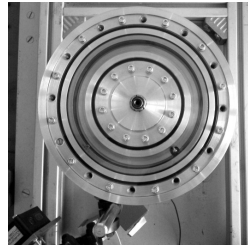


Figure 8: Cross section of the rotor.

With the use of a video camera, which is mounted above the test rig, the position of the rotor and the ball is recorded at 25 frames per second. The corresponding angular velocities, which are shown at the top of fig. 9 can be derived from the footage. It can be seen that the angular velocity of the ball is lagging behind the rotors angular velocity until it reaches the predefined nominal speed. Using equation (8) and the speed difference the Reynolds number can be derived, which is plotted at the bottom of fig. 9.

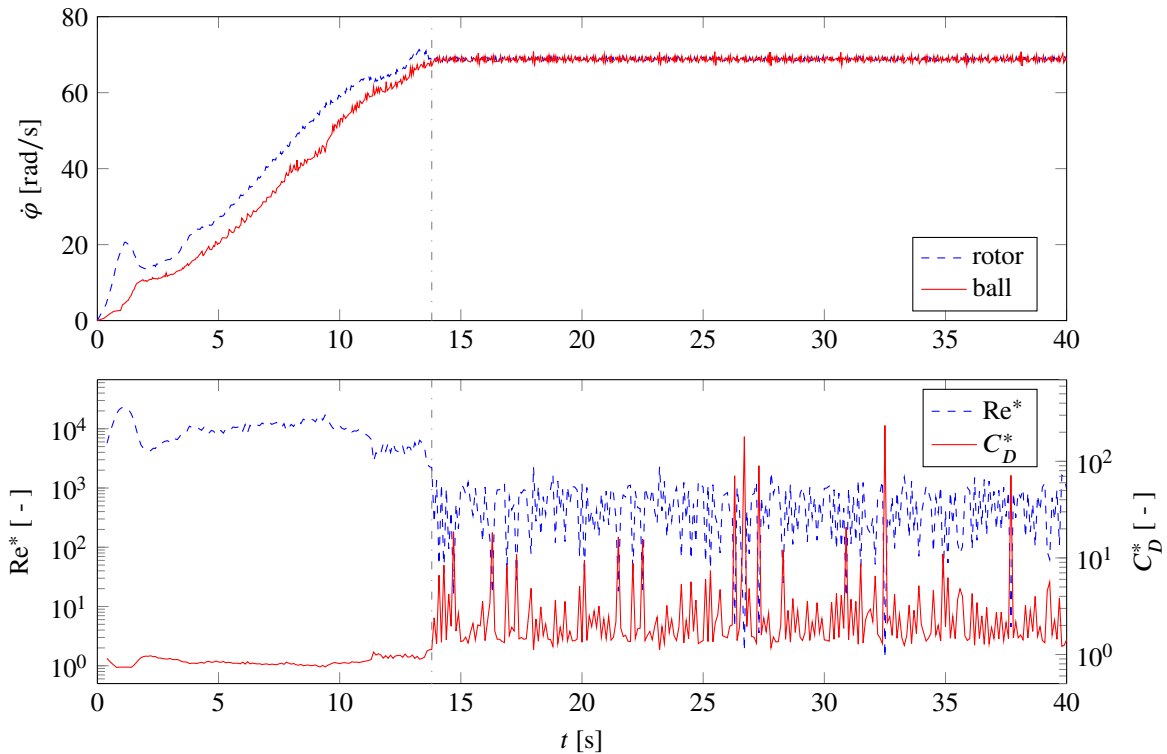


Figure 9: Time dependent quantities of a rotor run-up. Relation $C_D^* = f(Re^*)$ corresponding to fig. 10. Fluid properties: $\nu = 0.65 \text{ mm}^2 \text{s}^{-1}$, $\rho_{fl} = 760 \text{ kg m}^{-3}$.

Despite the flow velocity being relatively high during the run-up of the rotor, it is reduced in the synchronous phase in which the balls are positioned relative to the imbalance. The dependency of the drag coefficient C_D from the Reynolds number for a free flow around a sphere is well documented in the literature. One empirical approximation from Morrison (2013) is plotted in fig. 10 as a reference. The ball in automatic balancing devices of the described type is in steady contact with the race, which is often designed as a cylindrical surface. Assuming a sufficient large R_b , the flow characteristic can be described by a sphere in contact with a flat surface. Jan and Chen (1997) conducted experimentally that the drag coefficient is increased when considering the wall contact. To achieve this, they examined the terminal velocity of spheres moving down a tilted surface in fluids of different viscosities. The drag coefficient as a function of the Reynolds number is plotted in fig. 10.

Considering this relationship, the drag coefficient C_D^* for the experimental data in fig. 9 can be derived. A significant increase in the drag coefficient can be identified at the start of the positioning phase ($t = 13.8 \text{ s}$). Deviations due to the concave contour of the race are assumed to be negligible. This is supported by studies of Chhabra et al. (2000) on the drag of spheres in tubes, in which it is concluded that the influence of concavity is not significant for

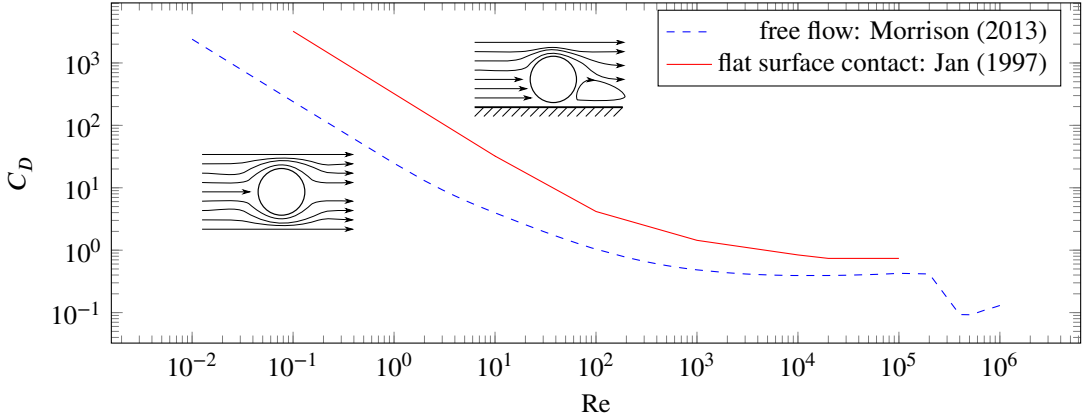


Figure 10: Drag coefficients of flows around spheres.

Reynolds numbers below 4000 and diameter ratios between sphere and tube below 0.5.

Even without knowledge of the exact flow velocity of the fluid the presented data suggest that the drag coefficient underlies high variance during the run-up process of automatic balancing devices. Therefore a significant influence on the balancing characteristic is expected. This influence is examined in the next section with the help of simulation models, which compare the consideration of velocity dependent drag coefficients to the commonly used models.

4 Influence on the Run-up Simulation

The rotor under consideration is modelled in a multi-body simulation program using force elements to represent the interaction between the bodies. The eigenfrequencies are mostly influenced by the bushings, which are modelled by using frequency dependent spring and damper elements. The run-up process is defined by the rotor speed sequence shown in fig. 9. Using a viscosity coefficient of $\beta_{fl} = 720 \times 10^{-6} \text{ N m s rad}^{-1}$ for equation (5) a good agreement with the experimental record of the ball's velocity is reached in the acceleration phase ($t < 10 \text{ s}$). With an increasing viscosity coefficient the lag between the rotor speed and the ball speed is decreasing.

Based on this model with velocity dependent drag coefficients three additional run-ups with constant drag coefficients C_D are conducted. Firstly, a value of $C_D = 0.74$ is used, which is reached for Reynolds numbers above 10^4 as shown in fig. 10. Secondly, a value of $C_D = 3.7$ is used, which corresponds to the mean value in fig. 9 for $t > 13.8 \text{ s}$. Thirdly, a value of $C_D = 2.0$ in between the prior values is chosen. Fig. 11 shows the effect of the different drag coefficient modelling approaches in the simulation on the ball velocity.

The most obvious disagreement of the simulation results is located in the time interval in which the rotor reaches its nominal speed. In view of the time difference between the rotor reaching its nominal speed and the ball getting synchronous with the rotor¹ the relative and absolute deviations with respect to the reference simulation with velocity dependent drag coefficients are shown in table 1.

This leads to the conclusion that the modelling approach of the drag coefficients has an influence on the dynamics inside the automatic balancing device and should not be neglected, if an optimal choice of the fluid properties is the objective.

Table 1: Time difference in reaching the synchronous motion of the ball with different modelling approaches.

	C_D			fig. 10	
	constant				
	0.74	2.00	3.70		
Δt [s]	4.66	3.10	2.22	3.78	
rel. deviation	+23%	-18%	-40%	—	

¹The final point in time at which the relative deviation from the nominal speed is above 1% is used to characterise synchronous motion.

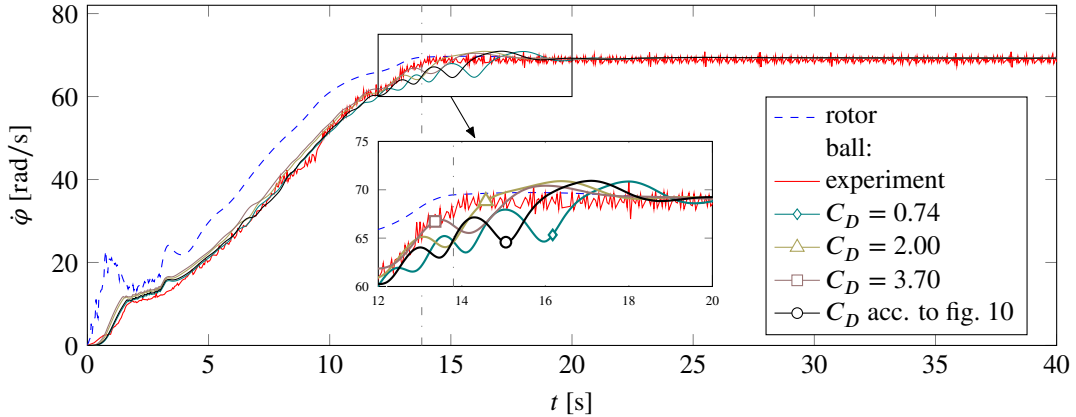


Figure 11: Influence of the drag coefficient model on the ball velocity simulation results.

5 Summary

In the design of automatic balancing devices the choice of fluids shows potential for optimisation. The density and viscosity are influencing the positioning of the counterbalancing mass directly and therefore affecting the rotor vibrations. In particular the reduction of the system-dependent vibration increase at subcritical speeds is to be aimed at.

The modelling of the driving forces on the ball becomes important in simulating the transient process. Previous studies on the influence of friction and virtual mass are implemented in the simulation model. Up to now, the dependence of the drag coefficient from the flow velocity is neglected. The experimental data in section 3 show the variation of the flow conditions during the run-up and provide the motivation to consider the velocity dependency.

Some discrepancy between the simulation and the experimental data of the ball velocity remains in the positioning phase of the ball. It is assumed that the modelled Coulomb friction is not sufficient and the simulation therefore shows oscillatory behaviour of the ball speed. Variation of the friction coefficient μ in reasonable ranges showed little effect, thus a model including rolling friction should be implemented in further research. The effect of neglecting the velocity dependency of drag coefficients is discussed on the basis of simulations in section 4. Despite this restriction the comparison of the different modelling approaches shows a significant influence on the ball velocities and therefore on the transient position of the counterbalancing mass.

The presented study neglects the difference between a flat surface and the curved ball bearing raceway on hand. In addition to that, irregularities in form and position of the mounted raceway are not taken into account leading to remaining differences in the stationary ball positions in comparison to the experimental results. These model enhancements are implemented in future studies. Furthermore, the viscous representation of the fluid acceleration is currently determined by a parametric study in order to reach a good agreement with the experimental data. An alternative based on a priori known quantities, i.e. by solving the Navier-Stokes equations numerically, is to be implemented instead.

6 Future Prospects

For future studies a test rig is planned to validate the curve $C_D = f(Re)$ as presented by Jan and Chen (1997) for the annulus geometry at hand. Moreover a more accurate model and identification of the friction coefficients is aspired in order to improve the transient simulation. Due to the fact that the acceleration of the fluid is represented by the fitted parameter β_{fl} , numerical solutions will be pursued to get a model on the basis of the annulus geometry, the fluid properties and the rotor acceleration only. The objective is a simulative a priori design of the optimal fluid properties for the automatic balancing device at hand and a subsequent experimental validation.

Acknowledgments

Funded by the German Federal Ministry of Economics and Energy.

References

Benton, E. R.; Clark, A.: Spin-up. *Annu. Rev. Fluid Mech.*, 6, 1, (1974), 257–280.

Chen, H.-W.; Zhang, Q.-J.: Dynamic analysis and design of a balancer for a three-column centrifuge. *Shock and Vibration*, 2016, (2016), 1–13.

Chhabra, R.; Kumar, M.; Prasad, R.: Drag on spheres in rolling motion in inclined smooth tubes filled with incompressible liquids. *Powder technology*, 113, 1, (2000), 114–118.

Green, K.; Friswell, M. I.; Champneys, A. R.; Lieven, N. A.: The stability of automatic ball balancers. In: *IFTOMM Seventh International Conference on Rotor Dynamics*, Citeseer (2006).

Huang, W.; Chao, C.; Kang, J.; Sung, C.: The application of ball-type balancers for radial vibration reduction of high-speed optic disk drives. *Journal of Sound and Vibration*, 250, (2002), 415–430.

Ishida, Y.; Matsuura, T.; Zhang, X. L.: Efficiency improvement of an automatic ball balancer. *J. Vib. Acoust.*, 134, 2, (2012), 021012.

Jan, C.-D.; Chen, J.-C.: Movements of a sphere rolling down an inclined plane. *Journal of Hydraulic Research*, 35, 5, (1997), 689–706.

Kim, T.; Na, S.: New automatic ball balancer design to reduce transient-response in rotor system. *Mechanical Systems and Signal Processing*, 37, 1-2, (2013), 265–275.

Majewski, T.: Position error occurrence in self balancers used on rigid rotors of rotating machinery. *Mechanism and Machine Theory*, 23, 1, (1988), 71–78.

Morrison, F. A.: *An introduction to fluid mechanics*. Cambridge University Press (2013).

Ryzhik, B.; Duckstein, H.; Sperling, L.: Automatic balancing of the unsymmetrical rigid rotor. *PAMM*, 2, 1, (2003), 70–71.

Sperling, L.; Ryzhik, B.; Linz, C.; Duckstein, H.: Simulation of two-plane automatic balancing of a rigid rotor. *Mathematics and computers in simulation*, 58, 4, (2002), 351–365.

Thearle, E. L.: Dynamic balancing machine (1936), US Patent 2043845 A.

Address: L. Spannan, C. Daniel, E. Woschke

IFME, Otto-von-Guericke-Universität Magdeburg, Universitätsplatz 2, 39106 Magdeburg, Deutschland

email: {lars.spannan, christian.daniel, elmar.woschke}@ovgu.de

Simulation and Experimental Validation of a Misaligned Rotor in Journal Bearings using Different Levels of Detail

A. Krinner, W. Tsunoda, C. Wagner, T. Berninger, T. Thümmel, D. Rixen

In this contribution, a given test rig of a rotor system with journal bearing is validated by using simulation models with different levels of detail. A special focus is placed on the misalignment between rotor and bearing axis. It is shown, how to consider misalignment in the numeric calculation of the bearing forces as well as in the modeling of the rotor system. With a model of the LAVAL rotor, the misalignment in the test rig is identified by measuring and simulating relative equilibrium positions of the rotor in the bearing at different rotational speeds. A measured rotor orbit due to unbalance is used to compare simulation results of different complex rotor models and discuss their accuracy and efficiency.

1 Introduction

The dynamic behavior of a rotor system with journal bearings, which operates at steady-state conditions like a constant rotational speed, strongly depends on its equilibrium position. At low rotational speeds, the equilibrium between gravity force, stiffness force and fluid force is found at a larger eccentricity than for higher rotational speeds, meaning that the rotor moves to the bearing center with increasing rotational speed. This fact is illustrated in Fig. 1(a) for the case of a vanishing stiffness force. Fig. 1(a) shows the equilibrium eccentricity e between shaft and bearing center in dependency of the rotational speed Ω , when vertical gravity force and the fluid force are the only acting forces in the bearing with clearance h_0 . The well-known GUEMBEL curve arises, see for instance [4, 11, 3]. In an idealized rotor bearing system, the rotor axis is assumed to be perfectly aligned with the bearing axis. In this case, the equilibrium position can be calculated by the equality of gravity, stiffness and fluid force. However, in reality, the rotor axis can be misaligned in the bearing housing, resulting in a different equilibrium position, since an additional misalignment force has to be considered in the static force equilibrium. As a consequence, misalignment affects the dynamic behavior of the rotor system and hence, it also needs to be considered in simulation models. To illustrate this fact, Fig. 1(b) sketches the equilibrium eccentricity in dependency of the rotational speed Ω for the case, in which the rotor stiffness and additionally, a misalignment a between rotor shaft and bearing axis are considered. It occurs a different curve of equilibrium positions compared to the curve of Fig. 1(a).

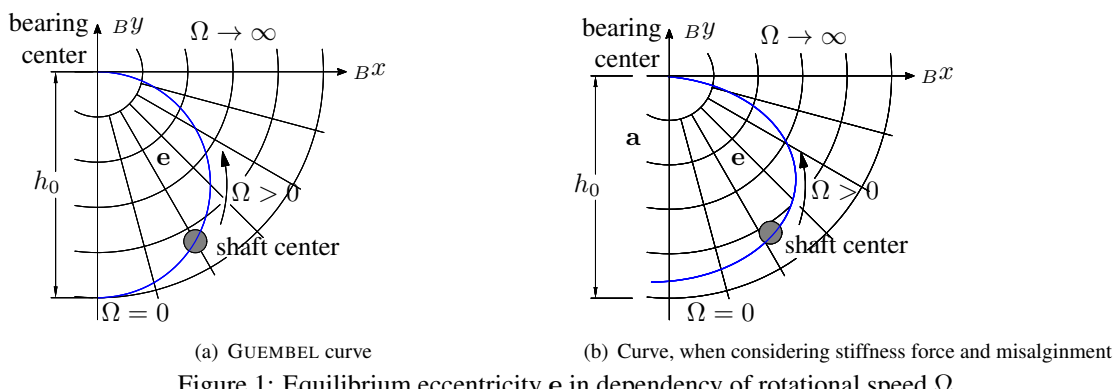


Figure 1: Equilibrium eccentricity e in dependency of rotational speed Ω .

Several contributions to a misaligned rotor system can be found in literature: The interaction between misalignment and wear is investigated by an analytical model in [9] and an experimental study on this interaction is given in [2]. In [12], a theoretical study on a misaligned shaft due to an external preload force is outlined. Angularly misaligned bearings are numerically investigated in [1]. In [7], a design of a test rig with a rotor supported by four journal

bearings suitable for the prediction of misalignment is proposed. In [10], simulation models and results for a flexible rotor system with angular and parallel misalignment are presented.

In this contribution, a rotor test rig with journal bearings is investigated with respect to parallel misalignment of rotor and bearing axis. First, a simple rotor model is applied in order to analyze the misalignment and in a next step, the dynamic behavior of the test rig due to unbalance can be investigated by further rotor models.

The paper is structured as follows: In Section 2, the hydrodynamic equations for the calculation of the fluid forces are outlined. Then, the rotor test rig with two journal bearings is described in Section 3. In Section 4, four different rotor models (LAVAL / elastic rotor with nonlinear / linearized fluid forces) are presented for the numeric simulation of the test rig. In Section 5, two experiments are validated by the different simulation models. While the first experiment serves to determine the misalignment, the second experiment is used for the evaluation of the different rotor models. At the end, a conclusion is given in Section 6.

2 Hydrodynamic Equations

In this section, the hydrodynamic equations for the calculation of the fluid forces in a hydrodynamic lubricated cylindrical joint are given. For a more detailed description, it is referred to [8].

The pressure is computed by a finite element discretization of the REYNOLDS equation, which is introduced first. A steady-state cavitation condition, also known as REYNOLDS condition, is imposed on the REYNOLDS equation in order to avoid negative pressures in the fluid film. It is further shown how to adapt the kinematics of the REYNOLDS equation to a cylindrical joint. Last, the calculation of the fluid forces is given.

REYNOLDS Equation

Fig. 2 shows a lubricated contact, which is characterized by a thin fluid film between the interface of two bodies. When the fluid inertia effects are neglected, the pressure distribution in the thin fluid film can be calculated by the REYNOLDS equation. It gives following partial differential equation for the pressure in the fluid film $h(y, z) = h_2 - h_1$ between the two bodies in the two-dimensional fluid domain $\Omega_f \subset \mathbb{R}^2$ with descriptive coordinates (y, z) (see for instance [6]):

$$\underbrace{-\frac{\partial}{\partial y} \left(\frac{h^3 \rho \partial p}{12\eta \partial y} \right) - \frac{\partial}{\partial z} \left(\frac{h^3 \rho \partial p}{12\eta \partial z} \right)}_{q_{\text{poiseuille}}} = \underbrace{-\frac{\partial}{\partial y} \left(\rho h \frac{v_1 + v_2}{2} \right)}_{-q_{\text{couette}}} - \underbrace{\rho \frac{\partial h}{\partial t}}_{-q_{\text{squeeze}}} - \underbrace{h \frac{\partial \rho}{\partial t}}_{-q_{\text{expansion}}} \quad (1)$$

where u_i and v_i are the absolute velocities of the interface of body i ($i \in \{1, 2\}$) in the local normal and tangential direction, respectively. For simplicity, the velocity w_i in z -direction is not considered here. It is also assumed that the fluid viscosity η and the fluid density ρ do neither depend on pressure nor on temperature. In Eq. (1), the POISEUILLE flow $q_{\text{poiseuille}}$ is driven by the pressure gradient, the COUETTE flow q_{couette} occurs due to the movement of surfaces in the tangential plane, the squeeze flow q_{squeeze} occurs due to squeezing motion and the local expansion flow $q_{\text{expansion}}$ occurs due to the change of density. The squeeze flow depends on the local normal velocities u_i , the tangential velocities v_i and derivatives of the heights h_i with respect to y , by the following equation (see [6]):

$$\frac{\partial h}{\partial t} = u_2 - v_2 \frac{\partial h_2}{\partial y} - u_1 + v_1 \frac{\partial h_1}{\partial y}. \quad (2)$$

A numerical discretization by the finite element method is applied to the REYNOLDS equation (1). For the discretized pressure \mathbf{P} , the following discretized equation can be obtained:

$$\mathbf{A}(\mathbf{q}) \mathbf{P} = \mathbf{b}(\mathbf{q}, \dot{\mathbf{q}}) - \mathbf{N} \mathbf{Q}_{\text{exp.}}, \quad (3)$$

where the kinematics of the two bodies are now described by the generalized coordinates \mathbf{q} and velocities $\dot{\mathbf{q}}$. The square matrix \mathbf{A} results from the numerical discretization of the POISEUILLE flow, the vector \mathbf{b} from the discretization of the terms $-q_{\text{couette}}$ and $-q_{\text{squeeze}}$ and the square matrix \mathbf{N} is the finite element mass matrix. The discretized expansion term $\mathbf{Q}_{\text{exp.}}$ is still unknown, but a cavitation condition in the next subsection gives an additional relation between pressure and expansion term. It is noted, that for the numerical discretization of the REYNOLDS equation, the standard GALERKIN method with quadrilateral finite elements (each with eight nodes) is applied and for all later simulation examples, a structured rectangular mesh with 16 elements in circumferential and 3 elements in z -direction respectively, is used.

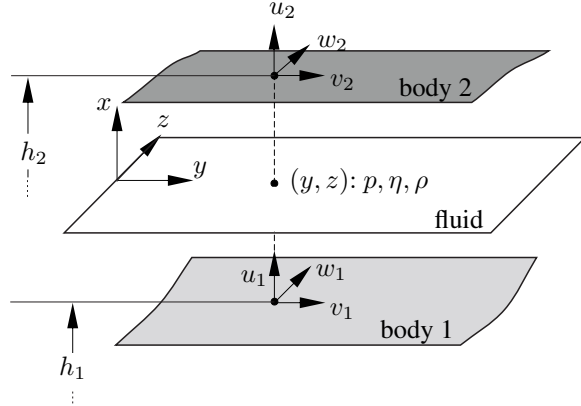


Figure 2: Notations in the fluid domain.

Cavitation Condition

Here, a stationary cavitation condition, also known as REYNOLDS condition, is imposed on the REYNOLDS equation (1) in order to eliminate the expansion term and further to avoid unphysical negative pressures in the fluid film. The REYNOLDS cavitation condition states that in the pressurized zone ($p > 0$) the change of density $\frac{\partial \rho}{\partial t}$ is zero (meaning $q_{\text{exp.}} = 0$), whereas in the cavitation zone ($p = 0$) the density starts to decrease, meaning $\frac{\partial \rho}{\partial t} < 0$, leading to a positive expansion term $q_{\text{exp.}} > 0$. This cavitation condition can be formulated mathematically by a Linear Complementarity Problem (LCP) by finding the pressure p such that:

$$0 \leq -q_{\text{exp.}} = \left(-\nabla \left(\frac{h^3 \rho}{12 \eta} \nabla p \right) + q_{\text{couette}} + q_{\text{squeezze}} \right) \perp p \geq 0 \quad \text{on } \Omega_f, \quad (4)$$

$$p = \hat{p} \quad \text{on } \Gamma_p, \quad (5)$$

$$\frac{h^3 \rho}{12 \eta} \nabla p \mathbf{n} = \hat{q} \quad \text{on } \Gamma_q, \quad (6)$$

where the symbol \perp denotes orthogonality for each point (y, z) on Ω_f (i. e. $q_{\text{exp.}}(y, z) \cdot p(y, z) = 0$). Dirichlet and Neumann boundary conditions are considered additionally in the REYNOLDS equation at the boundaries Γ_p and Γ_q respectively. With the discretized equation (3) follows:

$$\mathbf{0} \leq \mathbf{P} \perp -\mathbf{Q}_{\text{exp.}} \geq \mathbf{0} \quad \Leftrightarrow \quad \mathbf{0} \leq \mathbf{P} \perp \mathbf{N}^{-1} [\mathbf{A}(\mathbf{q}) \mathbf{P} - \mathbf{b}(\mathbf{q}, \dot{\mathbf{q}})] \geq \mathbf{0}, \quad (7)$$

where the symbol \perp stands now for component-wise orthogonality. This resulting LCP for the pressure \mathbf{P} can only be solved by different methods, e. g. a block pivot-based Murty algorithm of Goenka [5] or a projection formulation as proposed in [8].

Joint Kinematics

For a cylindrical revolute joint, the local kinematic entities can be derived according to Fig. 3. The procedure is explained for a two-dimensional problem, but it can without difficulty be extended to the three-dimensional case. In the cylindrical bearing, the local coordinates ($y = R\varphi, z$) are used for the description of the fluid domain. The joint kinematics is described in the frame (Bx, By), which is fixed to the bearing shell. For the REYNOLDS equation, local entities are needed, i. e. the velocities and heights have to be transformed into the local frame (Fx, Fy). For the eccentricity between the two center points C_1 and C_2 follows:

$$B\mathbf{e} = \begin{pmatrix} e_x \\ e_y \end{pmatrix} \quad \rightarrow \quad F\mathbf{e} = \begin{pmatrix} e_r \\ e_t \end{pmatrix} = \begin{pmatrix} e_x \cos(\varphi) + e_y \sin(\varphi) \\ -e_x \sin(\varphi) + e_y \cos(\varphi) \end{pmatrix}. \quad (8)$$

According to Fig. 3, following local heights h_1 and h_2 can be derived for the two points P_1 and P_2 , respectively:

$$h_1(y, z) = e_r(y, z) + \sqrt{R_1^2 - e_t^2(y, z)}, \quad (9)$$

$$h_2(y, z) = R_2. \quad (10)$$

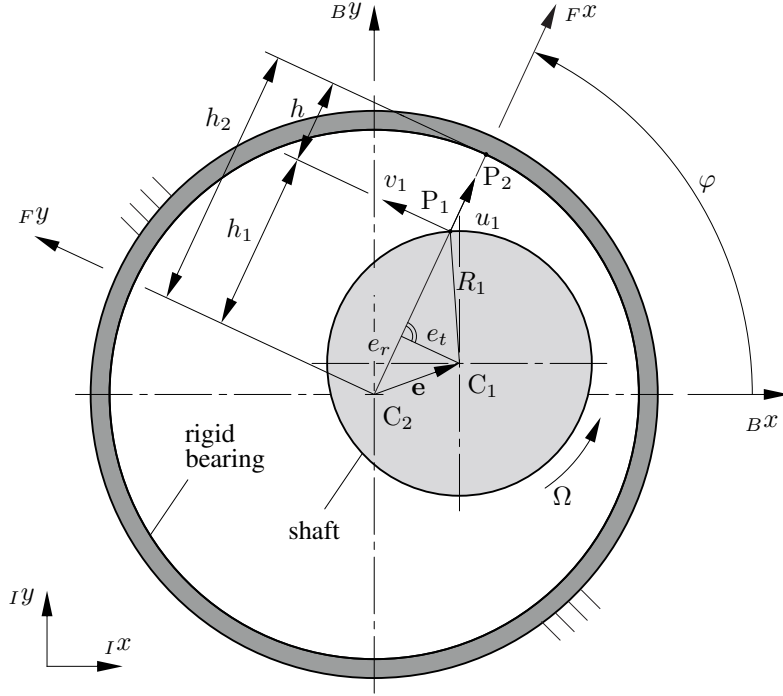


Figure 3: Kinematics in cylindrical joint.

For the local velocities, the translation velocities as well as the angular velocity vectors of the center point of shaft C_1 and bearing C_2 respectively are needed in the local (F_x, F_y) coordinate system. With them, following local velocities can be stated for a fixed bearing housing, according to Fig. 3:

$$u_1 = \Omega e_t + \dot{e}_x \cos(\varphi) + \dot{e}_y \sin(\varphi), \quad u_2 = 0 \quad (11)$$

$$v_1 = \Omega \sqrt{R_1^2 - e_t^2(y, z)} - \dot{e}_x \sin(\varphi) + \dot{e}_y \cos(\varphi), \quad v_2 = 0 \quad (12)$$

Having the kinematic entities as a function of the descriptive coordinates (y, z) , the derivatives of the local heights and velocities with respect to y can be derived for the REYNOLDS equation.

Force Calculation

When the pressure \mathbf{P} is known in the bearing by Eq. (7), the fluid forces on the two bodies can be computed. Here, it is shown only for pressure forces in normal direction, shear forces in tangential direction are not considered for simplicity. For the resulting force $\mathbf{F}_{f,i}$ on body i follows:

$$\mathbf{F}_{f,i} = \int_{\Omega_f} p \mathbf{n}_i d\Omega \approx \mathbf{W}(\mathbf{q})_i \mathbf{P}, \quad i \in \{1, 2\}, \quad (13)$$

where $\mathbf{W}(\mathbf{q})_i$ is the discrete direction matrix, which is state-dependent due to the normal directions \mathbf{n}_i .

3 Rotor Test Rig with two Journal Bearings

At the Institute of Applied Mechanics, a rotor test rig exists for the investigation of the interaction of the rotor dynamics with fluid forces coming from a journal bearing or a seal. In Fig. 4, the experimental setup is shown. It consists of an elastic rotor, which is supported by stiff roller bearings at the two ends. In the middle of the rotor, a rigid disk rotates in a pressurized journal bearing component system. This system consists of two identical journal bearings with external pressure support in the center of the two bearings, see Fig. 4. An oil distribution ring ensures an uniform oil flow through the bearings.

When pressurizing the journal bearing system at zero rotational speed, the rotor is lifted in an equilibrium position. In the following, this equilibrium position at zero rotational velocity is denoted by the misalignment parameter \mathbf{a} .

Further, it is assumed for simplicity that the lifting force due to the external pressure support remains constant in both its value and directions.

The main properties of the rotor test rig and the journal bearings are listed in Table 1. The bending stiffness of the dry rotor was identified by an operational modal analysis by determining the first bending eigenfrequency.

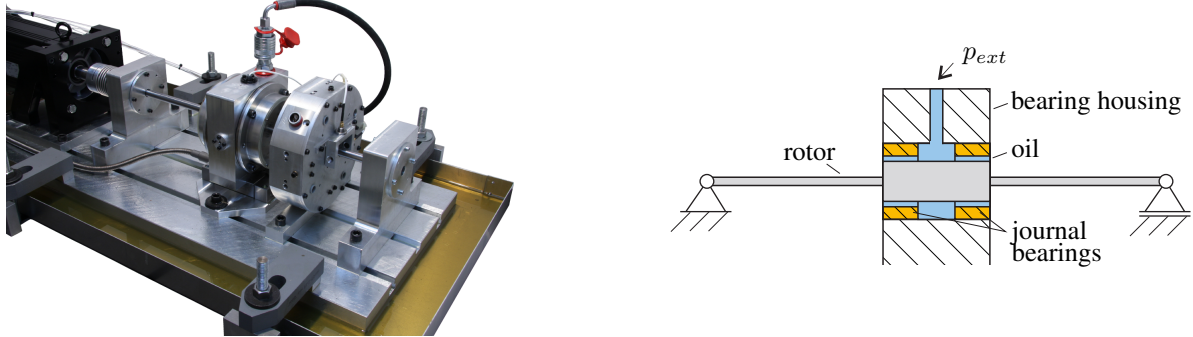


Figure 4: Rotor test rig with journal bearings.

Table 1: Properties of the test rig.

parameter	value	parameter	value	parameter	value
rotor mass m	5.0 kg	radius bearing R_2	50 mm	dyn. viscosity η	0.021 kg/m ²
bending stiffness rotor c	295 kN/m	clearance bearing	170 μ m	fluid density ρ	880 kg/m ³
length rotor	0.60 m	length bearing	20 mm	external pressure p_{ext}	2.5 bar
1. eigenfrequency (dry)	38.6 Hz	diameter shaft	15 mm		

4 Rotor Modeling

In this section, different rotor models are presented for the validation of the experimental results. As the rotor axis in the test rig is not aligned concentrically to the bearing axis, misalignment is considered for all models. Further, it will be assumed that the gravity force is always compensated due to the external pressure support.

Four different complex rotor models are introduced. The first one is a LAVAL rotor with misalignment and fluid forces. This model will be used for the experimental validation of equilibrium positions of the rotor bearing system at different rotational speeds.

The further models are a LAVAL rotor with linearized fluid forces, a complete elastic rotor model with nonlinear and linearized fluid forces, respectively. These models will be used for comparisons with the first rotor model in order to discuss their model differences with respect to experimental measurements.

Model A1: LAVAL Rotor with Misalignment and Fluid Forces

The first model is a LAVAL rotor as depicted in Fig. 5. The rotor is characterized by the mass m and the stiffness c and its deflection \mathbf{r} is described in the inertia frame, which is located in the center of the undeformed shaft. The misalignment is considered by the vector \mathbf{a} as relative alignment between bearing axis and rotor axis at zero rotational speed. Then, following dynamic equations can be stated:

$$m \ddot{\mathbf{r}} + c \mathbf{r} = 2 \mathbf{F}_f(\mathbf{r}, \dot{\mathbf{r}}, \Omega, \mathbf{a}) + \mathbf{F}_p + \mathbf{F}_g + \mathbf{F}_{ext}, \quad (14)$$

where \mathbf{F}_f is the nonlinear fluid force of one journal bearing according to (13) depending on the rotational speed Ω and the misalignment \mathbf{a} , \mathbf{F}_p is the preload force coming from the external pressure support and \mathbf{F}_g is the gravity force. In addition, external forces \mathbf{F}_{ext} can act on the rotor. Note that the misalignment \mathbf{a} enters in the fluid equations by the kinematic relation $\mathbf{B}\mathbf{e} = \mathbf{r} - \mathbf{a}$ in Eq. (8).

As mentioned in Section 3, the preload force is assumed to be constant. For that reason and when no further forces are acting, the force \mathbf{F}_p has to compensate the gravity force all the time, in order to fulfill the definition of the misalignment \mathbf{a} at zero rotational speed; it gives $\mathbf{F}_p = -\mathbf{F}_g$.

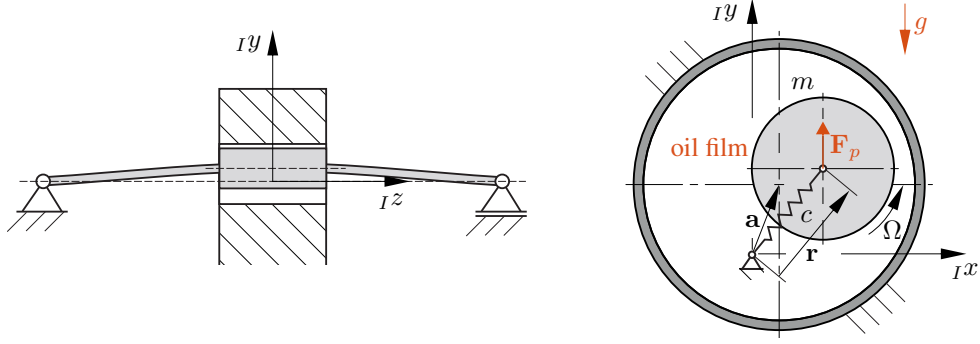


Figure 5: LAVAL rotor with misalignment, preload force and fluid forces.

For the model validation, the static equilibrium points at given rotational speeds Ω are considered. For the static deflection \bar{r} , following nonlinear equation has to be solved:

$$c\bar{r} = 2\mathbf{F}_f(\bar{r}, \Omega, \mathbf{a}). \quad (15)$$

Model A2: LAVAL Rotor with Misalignment and linearized Fluid Forces

For this rotor model, the LAVAL rotor is still used and the fluid forces are linearized around the equilibrium position \bar{r} , which is determined by the solution of Eq. (15) for a given rotational speed and a known misalignment, leading to:

$$\mathbf{F}_f(\mathbf{r}, \dot{\mathbf{r}}, \Omega, \mathbf{a}) \approx \mathbf{F}_f(\bar{r}, \Omega, \mathbf{a}) - \mathbf{K}_f(\bar{r}, \Omega, \mathbf{a})(\mathbf{r} - \bar{r}) - \mathbf{D}_f(\bar{r}, \Omega, \mathbf{a})\dot{\mathbf{r}}, \quad (16)$$

with the linearized matrices \mathbf{K}_f and \mathbf{D}_f for the fluid stiffness and damping, respectively. They are assumed to have the following form:

$$\mathbf{K}_f = -\frac{\partial \mathbf{F}_f}{\partial \mathbf{r}} \Big|_{\mathbf{r}=\bar{r}} = \begin{bmatrix} K_{xx} & k_{xy} \\ k_{yx} & K_{yy} \end{bmatrix}, \quad \mathbf{D}_f = -\frac{\partial \mathbf{F}_f}{\partial \dot{\mathbf{r}}} \Big|_{\mathbf{r}=\bar{r}} = \begin{bmatrix} D_{xx} & d_{xy} \\ d_{yx} & D_{yy} \end{bmatrix}, \quad (17)$$

where K is the direct stiffness, k the coupling stiffness, D the direct damping and d the coupling damping coefficient. Inserting Eq. (16) in Eq. (14) and using Eq. (15) gives the dynamic equations of the LAVAL rotor with misalignment and linearized fluid forces:

$$m\ddot{\mathbf{r}} + c(\mathbf{r} - \bar{\mathbf{r}}) + 2\mathbf{K}_f(\bar{\mathbf{r}}, \Omega, \mathbf{a})(\mathbf{r} - \bar{\mathbf{r}}) + 2\mathbf{D}_f(\bar{\mathbf{r}}, \Omega, \mathbf{a})\dot{\mathbf{r}} = \mathbf{F}_{ext}. \quad (18)$$

Model B1: Elastic Rotor with Misalignment and Fluid Forces

In a more detailed simulation model, the elastic deformation of the rotor is described by a set of mode shapes (Ritz ansatz). These mode shapes come from a finite element discretization of the rotor by using Bernoulli beam elements. For a better distinction from the LAVAL rotor, the elastic deformation is now described by the vector \mathbf{q} representing the modal coordinates. The dynamic behavior of the rotor is then characterized by the mass matrix \mathbf{M} and the stiffness matrix \mathbf{C} , leading for the rotor bearing system to:

$$\mathbf{M}\ddot{\mathbf{q}} + \mathbf{C}(\mathbf{q} - \bar{\mathbf{q}}) = \mathbf{F}_{f,1}(\mathbf{q}, \dot{\mathbf{q}}, \Omega, \mathbf{a}) + \mathbf{F}_{f,2}(\mathbf{q}, \dot{\mathbf{q}}, \Omega, \mathbf{a}) + \mathbf{F}_{ext}, \quad (19)$$

with the fluid forces $\mathbf{F}_{f,1}$ and $\mathbf{F}_{f,2}$ of the two bearings, external forces \mathbf{F}_{ext} and similar to the rotor models A1 and A2, a equilibrium position $\bar{\mathbf{q}}$. Damping or gyroscopic effects of the rotor are not considered.

Model B2: Elastic Rotor with Misalignment and linearized Fluid Forces

Similar to model A2, the fluid forces are linearized like in Eq. (16). Considering this in Eq. (19), following linear differential equation for the elastic rotor is obtained:

$$\mathbf{M}\ddot{\mathbf{q}} + \mathbf{C}(\mathbf{q} - \bar{\mathbf{q}}) + [\mathbf{K}_{f,1} + \mathbf{K}_{f,2}](\mathbf{q} - \bar{\mathbf{q}}) + [\mathbf{D}_{f,1} + \mathbf{D}_{f,2}]\dot{\mathbf{q}} = \mathbf{F}_{ext}, \quad (20)$$

which describes the motion of the rotor around the equilibrium position $\bar{\mathbf{q}}$.

5 Experimental Validation

In this section, an experimental validation of the rotor system of Section 3 is given by applying adequate simulation models of Section 4 depending on the specific accuracy requirements. A first experiment (static rotor equilibrium positions) is performed in order to determine the parallel misalignment between rotor and bearing axis. After having analyzed the misalignment, measurement data of a second experiment (rotor orbit at unbalance) is validated by simulation results of the four different simulation models of Section 4.

Experiment 1: Static Rotor Equilibrium Positions

The first experiment serves to determine the misalignment \mathbf{a} between rotor and bearing axis, which can not be identified by an absolute measurement.

On the test rig, the relative equilibrium positions of the rotor in the bearing can be measured for different rotational speeds Ω . Since the absolute position of the rotor can not be measured, the equilibrium positions are measured with respect to a reference position. The latter is chosen as the equilibrium position at high rotational speed, since it is known from theory that the rotor will be centered in the bearing housing for high rotational speeds [3].

The LAVAL-rotor model A1 with Eq. (15) for the equilibrium position $\bar{\mathbf{r}}$ is used for the experimental validation. With this model, an optimal misalignment parameter \mathbf{a} can be determined in such a way that the relative curve of equilibrium positions of the experiment is well approximated by the equilibrium positions calculated by Eq. (15).

In Fig. 6, the curve of equilibrium positions of the experiment and of the simulation can be seen. The misalignment parameter is chosen as $\mathbf{a} = [-0.15 \text{ mm}, 0.07 \text{ mm}]$. The measurement and the simulation start at $\Omega_1 = 3 \text{ rps}$ and move with increasing rotational speed to the reference position identical with the bearing center at $\Omega_2 = 100 \text{ rps}$.

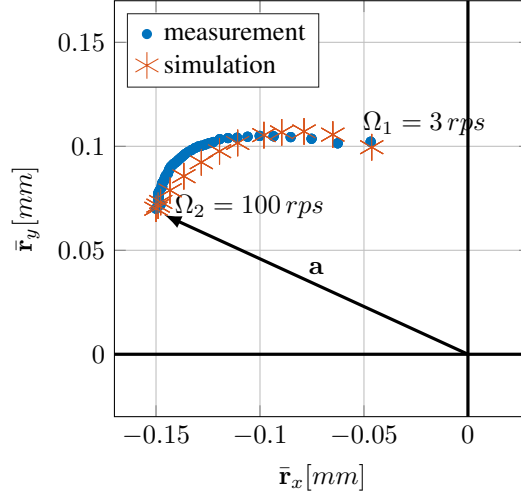


Figure 6: Measured and simulated curve of equilibrium positions with misalignment parameter $\mathbf{a} = [-0.15 \text{ mm}, 0.07 \text{ mm}]$.

When the equilibrium positions $\bar{\mathbf{r}}$ for different rotational speeds are known, the stiffness and damping coefficients of (17) can be calculated in a next step. Here, they are computed by a finite difference scheme and following mean coefficient can be determined:

$$K = (K_{xx} + K_{yy})/2, \quad k = (k_{xy} + k_{yx})/2, \quad D = (D_{xx} + D_{yy})/2, \quad d = (d_{xy} + d_{yx})/2.$$

The calculated as well as the measured mean coefficients are shown in Fig. 7. In the experiment, the coefficients are determined by exciting the rotor at different frequencies and measuring the rotor displacements and bearing reaction forces in the frequency domain. A fitting of the measured data by a reduced rotor bearing model gives the mean coefficient. The detailed measurement concept is described in [14]. Note that as far, only the mean values can be determined by this measuring method and hence, can be analyzed. The dependency of the measured coefficients on the rotational speed shows good agreement with the simulation results for the direct stiffness, direct damping and coupling stiffness coefficients (K , D and k). However, for the coupling damping coefficient d , a discrepancy is observed. The reason could be an angular misalignment of the rotor shaft in the experiment.

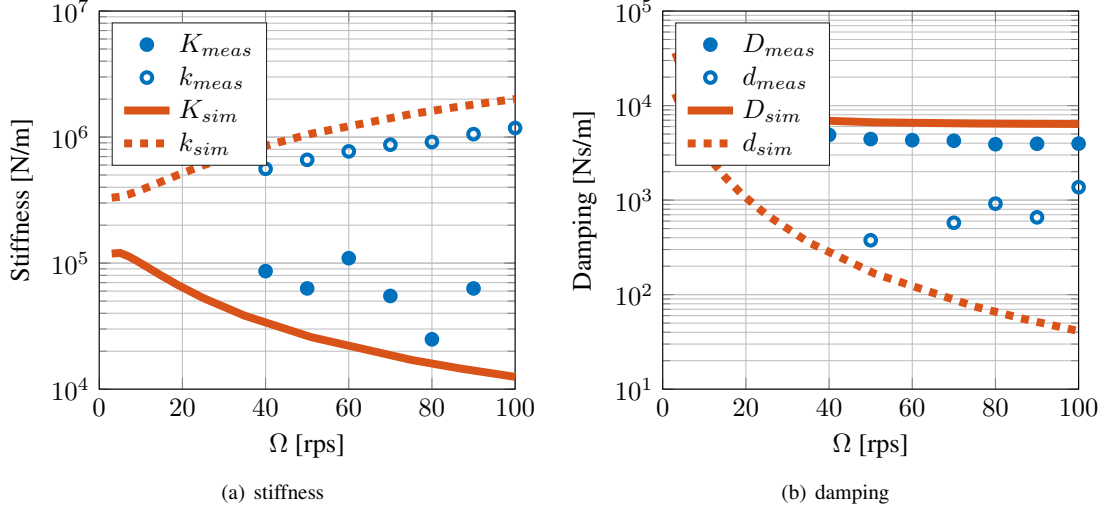


Figure 7: Calculated and measured stiffness and damping coefficients for different rotational speeds.

Experiment 2: Rotor Orbit at Unbalance

After having determined the parallel misalignment, a second experiment is performed in order to discuss the accuracy and efficiency of the four presented simulation models. Therefore, an unbalance is added at the middle of the rotor and the orbit of the rotor is measured at a constant rotational speed $\Omega = 21$ rps. The measured and simulated orbits are depicted in Fig. 8.

In Fig. 8(a), the measured and the simulated orbits are shown at their equilibrium positions. It has to be mentioned that the misalignment α determined by the first experiment is added to the measured orbit in order to get the absolute position of the orbit. The reason for that is that, as already mentioned, the absolute reference point of the measurement is unknown. For the simulation, rotor model A1 is used.

In Fig. 8(b), the form of the measured orbit is compared with the orbits obtained by the four simulation models. It can be seen that all four simulation models give nearly the same rotor orbit, meaning the model accuracy is sufficient for all simulation models. The elliptical form of the simulated orbits are characteristic for a rotor, which has an eccentric equilibrium position in the journal bearing. However, the form of the measured orbit has a tendency to a quadratic form. The reason could be that next to the unbalance an excitation with the third harmonic is present, which could cause a quadratic form, see for instance [13]. A physical source for a third harmonic excitation is usually caused by the three-jaw chuck during manufacturing of the rotor shaft.

When looking at the simulation time of the models in Table 2, it can be seen that the fastest model is model A2 – the LAVAL rotor model with linearized fluid forces. It is followed by the elastic rotor model B2, where the fluid forces are also linearized. A relatively long simulation time is needed for the full elastic rotor model B1 with nonlinear fluid forces. All the four simulation models are integrated with the `ode15s` solver of MATLAB, which uses a variable step size. The absolute and relative tolerance are set to $1e - 6$. For the elastic description of the rotor shafts of models B1 and B2, twelve RITZ modes are used.

Table 2: Simulation time for the different rotor models.

model	sim. time	rel. time
A1	11.7 s	100 %
A2	0.124 s	1.06 %
B1	1343 s	11478 %
B2	4.46 s	38.1 %

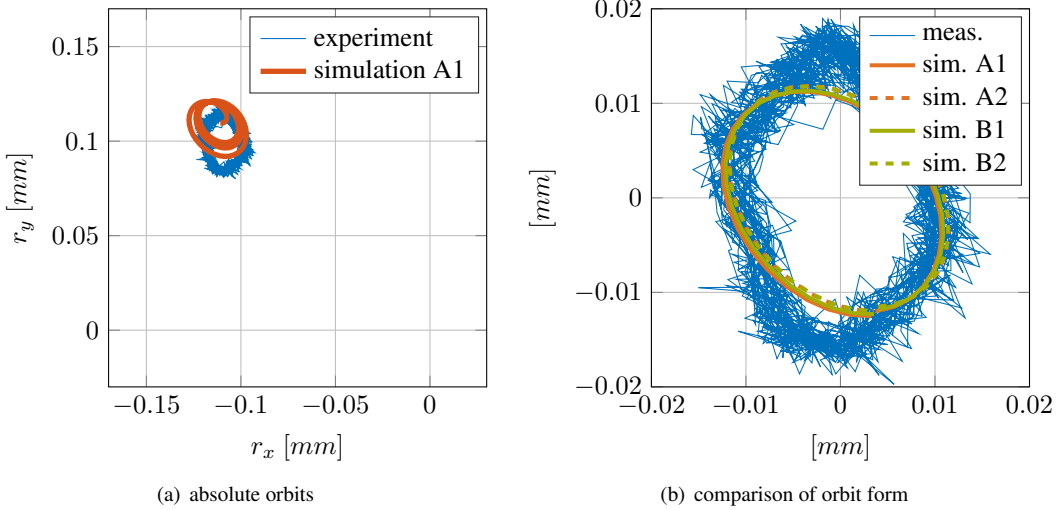


Figure 8: Rotor orbits due to unbalance at $\Omega = 21$ rps.

6 Conclusion

In this contribution, a rotor test rig with two journal bearings is validated by adequate simulation models. It becomes evident that the misalignment of rotor and bearing axis has to be considered in the simulation models.

When using simulation models with nonlinear fluid forces (models A1 and B1), the misalignment has to be known for the dynamic simulation in order to ensure that the rotor moves in the simulation to the right equilibrium position. When using simulation models with linearized fluid forces (models A2 and B2), an important step for the dynamic analysis is the determination of the equilibrium position, which again requires the misalignment parameter. When the equilibrium position is known, the fluid forces can be linearized around this equilibrium position.

With respect to the accuracy of the simulation models, the LAVAL rotor model is accurate enough for the experimental validation presented in this contribution. The use of an elastic rotor is not necessary for the here described experiments, it only requires a larger modeling effort than the simple LAVAL rotor model.

The simulation costs can be saved significantly when the fluid forces are linearized, as the evaluation of the finite element solution of the nonlinear fluid forces are the most time-consuming part. However, the linearization has to be performed in a preprocessing step, as well as the calculation of the equilibrium position.

Outlook

For the model of the fluid forces, the classical REYNOLDS equation is applied, where effects of the fluid inertia are neglected. This assumption has to be analyzed further and comparisons with the bulk flow equations, usually applied for seals, should be made. Further, the effect of the preload force has to be investigated in more detail.

In this contribution, only mean stiffness and damping coefficients are determined in the experiment. Their practical relevance is only given for a vanishing eccentricity of the shaft. Usually, the exact coefficients have to be determined for a precise dynamic analysis, see the work of GLIENICKE [4] or SOMEYA [11].

The model based determination of the parallel misalignment as described in the first experiment could be further used for rotor diagnostics, similar to concepts described in [13].

References

[1] Boedo, S. and Booker, J. (2004): Classical Bearing Misalignment and Edge Loading: A Numerical Study of Limiting Cases. *Tribology International*, **126**(3), pp. 535–541.

[2] Chasalevris, A. and Dohnal, F. (2013): An Experimental Study on the Additional Harmonics due to Worn Journal Bearings. In *Tagungsband SIRM*, Magdeburg, Germany, Feb. 23-25.

[3] Gasch, R., Nordmann, R. and Pfützner, H. (2006): *Rotordynamik*. Springer-Verlag, Berlin.

[4] Glienicke, J. (1966): *Feder- und Dämpfungskonstanten von Gleitlagern für Turbomaschinen und deren Einfluß auf das Schwingungsverhalten eines einfachen Rotors*. PHD thesis, TH Karlsruhe.

[5] Goenka, P.-K. (1984): Dynamically loaded journal bearings: finite element method analysis. *Journal of Tribology*, **106**(4), pp. 429–437.

[6] Hamrock, B., Schmid, S. and Jacobson, B. (2004): *Fundamentals of fluid film lubrication*. CRC press, New York.

[7] Hu, W., Miah, H., Feng, N. and Hahn, E. (2000): A rig for testing lateral misalignment effects in a flexible rotor supported on three or more hydrodynamic journal bearings. *Tribology International*, **33**(3), pp. 197–204.

[8] Krinner, A., Schindler, T. and Rixen D. J. (2016): Time integration of mechanical system with elastohydrodynamic joints using Quasi-Newton method and projection formulation. *International Journal of Numerical Methods in Engineering*.

[9] Nikolakopoulos, P. and Papadopoulos C. (2008): A study of friction in worn misaligned journal bearings under severe hydrodynamic lubrication. *Tribology International*, **41**(6), pp. 461–472.

[10] Pennacchi, P., Vania, A. and Chatterton, S. (2011): Analysis of the Effects of Parallel and Angular Misalignment in Hyperstatic Rotors Equipped With Oil-Film Bearings. In *Proceedings of the ASME Turbo Expo*. Vancouver, British Columbia, Canada, June 6–10.

[11] Someya, T. (1989): *Journal-Bearing Databook*. Springer-Verlag, Berlin, Heidelberg.

[12] Sun, J. and Changlin, P. (2004): Hydrodynamic lubrication analysis of journal bearing considering misalignment caused by shaft deformation. *Tribology International*, **37**(10), pp. 841–848.

[13] Thümmel, T., Roßner, M., Ulbrich, H. and Rixen, D. (2015): Unterscheidung verschiedener Fehlerarten beim modellbasierten Monitoring. In *Tagungsband SIRM*, Magdeburg, Germany, Feb. 23-25.

[14] Wagner, C., Tsunoda, W., Berninger, T., Thümmel, T. and Rixen, D. (2017): Instability Prediction and Rotordynamic with Seals: Simulations Based on the Bulk-Flow Theory and Experimental Measurements. In *Proc. of DINAME 2017*. Sao Sebastiao, Sao Paulo, Brasil, March 5–10.

Address: Chair of Applied Mechanics, Technical University of Munich, 85748 Garching, Germany,
 email: andreas.krinner@tum.de

Technische Mechanik *digital*

The journal Technische Mechanik is also available on DVD containing all volumes from the beginning in 1980 until 2016.

It also includes information and hints for authors how to prepare a paper using the style of the journal with word processors like Microsoft Word or TeX .

The price of the DVD is 30,00 € including VAT and shipping.

If you are interested in the DVD please contact the editorial office.

Ab sofort steht eine Komplettausgabe der Zeitschrift Technische Mechanik zur Verfügung. Die DVD enthält alle im Zeitraum 1980 bis 2016 erschienenen Artikel als PDF-Dateien.

Zur Suche nach Autoren/Artikeln steht unter einer HTML-Oberfläche eine Suchmaschine zur Verfügung. Ein PDF-Reader befindet sich ebenfalls auf der DVD. (Suchmaschine und PDF-Reader für Windows)

Für interessierte Autoren werden Hinweise zum Verfassen von Artikeln im Stil der Zeitschrift angeboten (TeX und MS-Word).

Der Preis der DVD beträgt 30,00 € inkl. Mehrwertsteuer und Versand.

Interessenten wenden sich bitte an die Redaktion der Zeitschrift.

Redaktion Technische Mechanik
Dr. W. Lenz
Institut für Mechanik
Otto-von-Guericke-Universität
Postfach 4120
D-39016 Magdeburg
Telefon: +49 391 67-52 459
Telefax: +49 391 67-12 439/-12 863
E-Mail: Technische.Mechanik@ovgu.de
Internet: www.ovgu.de/techmech/

TECHNISCHE MECHANIK

Scientific Journal for Fundamentals and Applications of Engineering Mechanics

Instructions for Authors

TECHNISCHE MECHANIK publishes articles in all fields of mechanics, theoretical as well as applied, including related disciplines, and in particular also articles demonstrating practical applications. The journal publishes full length papers, as well as discussions on papers which have appeared in the journal.

TECHNISCHE MECHANIK is a non-profit journal, founded by the Otto-von-Guericke-University. It can be freely downloaded from the website.

Manuscripts can be written with LaTeX. The most important features of the style guidelines are implemented in the files contained in LATEX-techmech.zip (download from <http://www.ovgu.de/techmech/>).

Other word processors may be used if the style guidelines are met by the author. An example file for Microsoft Word is available in WORD-techmech.zip (download from <http://www.ovgu.de/techmech/>).

The page size is DIN A4, no page numbers, no header, no footer, no footnotes, 25 mm left and right margin, single space, one line distance between paragraphs, no indentation for the first line of a paragraph, 40 mm margin between upper edge and title, 6 mm between title and author names, 9 mm before and 6 mm after chapter heads.

Type-face and size: Title 16pt, bold face; author names 10pt, italics; section headings 10pt, boldface; text 10pt, roman.

No bold face letters should be used within the text. All symbols used must be properly defined in the text or through appropriate equations. Equations not embedded in the text must keep an indentation of 10 mm and should be specified by continuous numbers. Reference to an equation should be made in analogy to "see equation (24)".

When using the word processor WORD for WINDOWS, then the equations editor should be set to: Full 10pt, Subscript/Superscript 7pt, Sub-Subscript/Superscript 5pt, Symbol 18pt, Sub-symbol 12pt.

Figures and tables shall not be collected in an appendix but be arranged in the text, centred between paragraphs. Figure and table headings (Roman, 10pt) should have the following structure: "Figure 3. Density distribution" or "Table 3. Density distribution".

References must follow author-year style (DIN 1505). It states that in the text the reference consists of the name of one author and the year of publication, e.g. "in Schulze (1991)" and "(Schulze, 1991)" or "in Müller and Schulze (2000)" and "(Müller and Schulze, 2000)" or "in Schulze et al. (2003)" and "(Schulze et al., 2003)". Author's names should not be typed in Small Caps.

At the end of the text the list of references, headed "References", is arranged alphabetically. The following structure should be kept:

Tejman, J.; Wu, W.: Numerically study on patterning of shear bands in a Cosserat continuum. *Acta Mech.*, 99, (1993), 61-74.

Hill, R.: *The Mathematical Theory of Plasticity*. Oxford Univ. Press (1950).

Eremeyev, V. A.: Nonlinear micropolar shells: theory and applications. In: W. Pietraszkiewicz and C. Szymczak, eds., *Shell Structures: Theory and Applications*, 11-18, Taylor & Francis, London (2005).

The complete postal and e-mail address of each authors is published at the end of the paper.

Manuscripts should be submitted in electronic version by letter or by e-mail.

Each submitted paper runs through a standard peer review process. Please suggest three international well known reviewers for your paper when you submit it.

TECHNISCHE MECHANIK

Wissenschaftliche Zeitschrift für Grundlagen und Anwendungen der Technischen Mechanik

Hinweise für Autoren

Die Zeitschrift veröffentlicht Forschungsarbeiten aus dem Gesamtgebiet der Mechanik, d. h. allen Zweigen der theoretischen und angewandten Mechanik einschließlich angrenzender Fachgebiete sowie Diskussionsbeiträge zu in dieser Zeitschrift erschienenen Arbeiten. Die Zeitschrift ist ein open-access Journal das 1980 von der Otto-von-Guericke-Universität gegründet wurde. Alle Artikel können kostenfrei von unserer Webseite herunter geladen werden.

Artikel werden ausschließlich in englischer Sprache veröffentlicht.

Die Manuskripte können in LaTeX geschrieben werden. Die wichtigsten Stil-Richtlinien sind in den Dateien umgesetzt, die in LATEX-techmech.zip (über unsere INTERNET-Adresse: <http://www.ovgu.de/techmech/> verfügbar) enthalten sind.

Andere Textverarbeitungssysteme können verwendet werden, wenn die Stil-Richtlinien eingehalten werden. Als Orientierung kann die in WORD-techmech.zip (ebenfalls über unsere INTERNET-Adresse verfügbar) enthaltene Beispiel-Datei für Microsoft-Word dienen. Das Schriftbild soll 16 cm breit sein. Die Seiten sollen mit einzeiligem Abstand beschrieben sein, im DIN A4-Format, die Hauptüberschrift in 16pt Buchstabengröße, alles andere in 10pt Buchstabengröße.

Jeder Arbeit ist ein kurzer Überblick in Kursivschrift voranzustellen.

Bilder sollten in den Text einzuordnet werden, ebenso Tabellen. Fußnoten sollten vermieden werden.

Literaturhinweise erfolgen nach DIN 15005, wonach Zitate im Text aus Namen eines Verfassers und Erscheinungsjahr bestehen, zum Beispiel: ... nach Schulze (1991) ... oder ... (Schulze, 1991) ... oder nach Schulze und Müller (2000) ... oder ... (Schulze und Müller, 2000) ... oder ... nach Müller u. a. (2003) ... oder ... (Müller u. a., 2003) ...

Im Verzeichnis am Schluss des Manuskriptes ist das Schrifttum alphabetisch einzuordnen. Bei Zeitschriften zum Beispiel ist folgende Reihenfolge einzuhalten: Namen der Verfasser, Titel der Arbeit sowie Namen, Band- und Heftnummer der Zeitschrift, Erscheinungsjahr.

Zum Beispiel:

Müller, A.D.; Schmidt, G.; Terzani, T.: Ermittlung modaler Parameter aus Übertragungsfrequenzgängen. *ZAMM*, 73, 3, (1993), 143 – 154.

Für Bücher oder Berichte sind entsprechende Angaben zu machen:

Hill, R.: *The Mathematical Theory of Plasticity*. Oxford Univ. Press (1950).

Eremeyev, V. A.: Nonlinear micropolar shells: theory and applications. In: W. Pietraszkiewicz and C. Szymczak, eds., *Shell Structures: Theory and Applications*, 11-18, Taylor & Francis, London (2005).

Die Anschrift eines jeden Autors, mit akademischen Titeln, Vor- und Zunamen sowie genauer Postanschrift und E-Mail-Adresse ist am Ende des Manuskriptes anzugeben.

Die Textdateien können auf Diskette oder CD per Post an die Redaktion geschickt werden. Ebenso ist eine Übermittlung über die unten angegebene E-Mail-Adresse möglich.

Jeder eingereichte Beitrag durchläuft einen standardmäßigen Begutachtungsprozess. Bitte schlagen Sie bei Einreichung des Artikels drei mögliche, international renommierte Gutachter vor.

Anschrift der Redaktion:
Institut für Mechanik
Otto-von-Guericke-Universität
Postfach 4120

D-39016 Magdeburg

Tel.: +49-391-67-52459
Sekretariat -58608
Fax: +49-391-67-12439
-12863

e-mail: Technische.Mechanik@ovgu.de
<http://www.ovgu.de/techmech/>

